DISSERTATION

INTERACTIONS OF BIOLOGICALLY ACTIVE MOLECULES, COFACTORS, AND DRUGS WITH MODEL MEMBRANES

Submitted by

Cameron Van Cleave

Department of Chemistry

In partial fulfillment of the requirements

For the Degree of Doctor of Philosophy

Colorado State University

Fort Collins, Colorado

Fall 2021

Doctoral Committee:

Advisor: Debbie C. Crans

Alan K. Van Orden
Nancy E. Levinger
Deborah A. Roess

ABSTRACT

INTERACTIONS OF BIOLOGICALLY ACTIVE MOLECULES, COFACTORS, AND DRUGS WITH MODEL MEMBRANES

The cell membrane is important for the structure, function, and overall homeostasis of the cell. It consists mainly of phospholipids which have different physicochemical and material properties. As such, molecular interactions between the membrane's components and its environment are of importance. This manuscript explores the interactions of different classes of molecules with model membrane systems to gain a fundamental understanding. Chapter 1 provides background on the cell membrane and current models as well as an introduction to lipoquinones and small molecule drugs.

Chapter 2 discusses the interactions of menadione and menadiol with Langmuir monolayers and reverse micelles. Menadiol and menadione are representative of the headgroup of menaquinones, a class of electron transporter, hence they are redox active. We hypothesized that the respective locations of menadione and menadiol within the membrane would vary due to their different physicochemical properties. We used Langmuir monolayers and NMR of reverse micelles to explore the location and association of menadione and menadiol with model membrane interfaces.

Chapter 3 investigates the location, association, and conformation of truncated menaquinones with Langmuir monolayers and simulated bilayers. Previous work found that truncated menaquinones fold at the interface of a reverse micelle, so we hypothesized that subtle differences in folding would cause variations in location and association with phospholipids. We used a combination of Langmuir monolayers and molecular dynamics simulations to probe location, association, and conformation of truncated menaquinone homologues, MK-1 through MK-4, in a phospholipid membrane.

Chapter 4 explores the pH-dependent effects of two anti-tubercule molecules at the membrane interface. Recent studies have suggested that pyrazinoic acid behaves as a protonophore and we further explored this suggestion while simultaneously exploring physicochemical properties of pyrazinoic acid and pyrazinamide. This chapter utilized a combination of Langmuir monolayers, NMR, and fluorescence leakage studies to characterize the molecular interactions of pyrazinoic acid with model membranes so that POA could be compared to a previous study with benzoic acid, a known protonophore.

ACKNOWLEDGEMENTS

Just as it takes a village to raise a child, so too does it take a community to earn a Ph.D. There were good times and times where I cried sitting down in the shower, but I had a fantastic community supporting me both in the lab and behind the scenes. I feel it necessary to take the time to thank all of them. This may take a couple pages, so bear with me.

Thank you to Dr. Benjamin J. Peters for training me and toughening me up. A **GIGANTIC** thank you to Dr. Jordan T. Koehn for providing compounds, a wise perspective, and a crash course in high impact writing. I'm pretty sure I would've crashed and burned multiple times without your intervention. Thank you to Dr. Kaitlin A. Doucette and Dr. Cheryle N. Beuning for their friendship and willingness to bounce ideas around so we could do better science. Thank you to my undergraduates Callan A. Knebel (a.k.a. Minion), Logan W. Stephenson, Jose J. Rivera, Andrea Basile, and especially Pablo Maldonado, Jr., and Audrey Wolfgang for their hard work collecting data and keeping things (and me!) light and positive.

Another round of "thank yous" also goes to my current lab mates. To Allison A. Haase for always being willing to collaborate and having a good eye for choicy memes. To Heide A. Murakami for work talks, strong talks, real talks, and lunch "talks." I don't know if you two will ever realize how much it meant to have been on this journey with you. Thank you to Zeyad Arhouma for teaching me the basics of microbiology and how (not) to kill a cell culture. Thank you to my ducklings Nate Gasparovic and Zhang Xiaoping for keeping me company in the office during my last months in the group.

Thank you to my undergraduate advisor Professor Peter L. Blair (a.k.a. the Phantom of the Operon) for all your support both at Earlham and later at CSU. I hope I've made you proud and that I'll be able to exchange bad puns with you again in the future.

Thank you to Professor Audra L. Goach for being a secondary advisor when it comes to Langmuir monolayers, lipids, and life. Maybe someday I'll be as awesome as you.

Thank you to Professor Dean C. Crick for allowing me to use his lab to learn bacterial culturing and for never letting me overstate myself in a paper.

Thank you to Professor Guilherme Menegon Arantes and Dr. Caroline Simões Pereira for their hard work on Chapter 3. Your willingness to work under strange conditions was and is truly appreciated.

A huge thank you to Professor Debbie C. Crans for mentoring me and never giving up on me even during the tough times. I don't think I would have made it with another advisor.

And, of course, thanks to my family, friends, and Alice the Cat for all the love and support over the past five years. I couldn't have done it without you. Last but not least, shoutout to my (not so) little brother Ryan. You can make me laugh even when I'm in a very dark place. That has helped more than you realize.

DEDICATION

To my Grandpa Ed. Your belief in me made a difference on the rough days.

Don’t crash the tea set.

TABLE OF CONTENTS

Chapter 1
Fantastic Cell Membranes and How to (Physically) Model Them

1.1 Introduction

For a molecule to enter the cell, it must interact with the phospholipids of the cell membrane in some capacity. Recently, the interest in lipid formulations as a means of drug and vaccine delivery has increased.[1-3] As such, studying the molecular interactions of both native and foreign molecules with the membrane interface is pertinent with regards to drug formulation and development. This manuscript aims to characterize these molecular interactions of different biologically relevant molecules with both eukaryotic and prokaryotic phospholipids as well as other interfacial models. Before discussing these interactions, it is appropriate to provide a short description of the cell membrane, its function, and current models used in research.

1.2. The Cell Membrane

The cell membrane is integral to both the structure and function of cells. It is the first line of defense of the cell from foreign molecules or organisms.[4] It is crucial for cell signaling, signal transduction, and overall homeostasis of the cell.[4-5] Structurally, it consists of a dynamic lipid bilayer approximately 5 nm thick interspersed with various proteins (Figure 1.1).[5-7] The current fluid mosaic model describes a fluid-like bilayer composed mainly of lipids. This bilayer, as mentioned above, is interspersed with different proteins. There have been additions to the model since it was initially proposed. It now accounts for protein microdomains, lipid rafts, less fluidity than initially proposed, and even metal-induced signal transduction.[7-10]

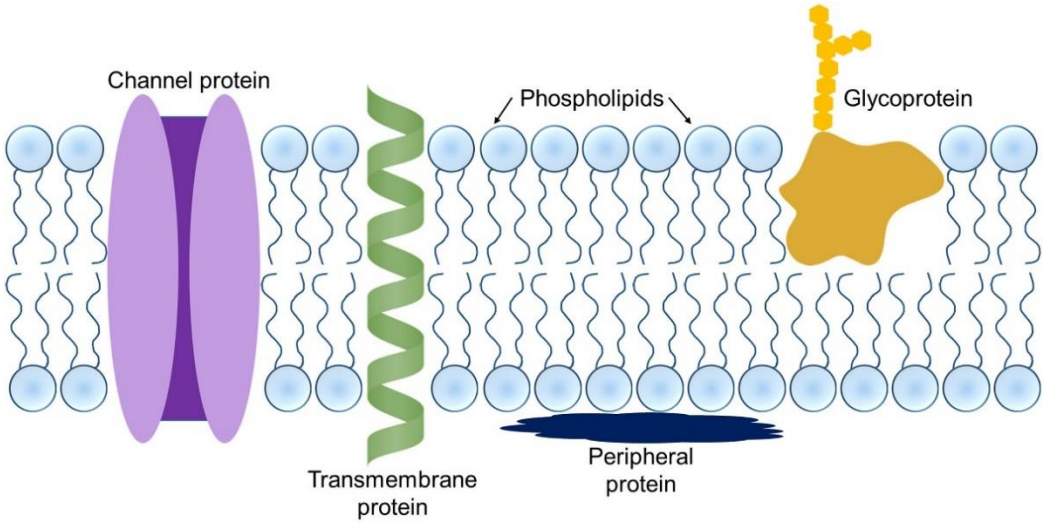

Figure 1.1. Representation of the cell membrane bilayer, consisting of various phospholipids and proteins. Reproduced with permission from Bunea *et al.* 2020.[11]

Given the various functions and processes related to the cell membrane, such as signal transduction,[4] and the interest in using synthetic cell membranes in drug and vaccine formulation, a fundamental understanding of the interactions of molecules at the cell membrane interface is needed.

1.3. Modeling the Membrane

1.3.1. Why Models are Necessary

Ideally, all measurements would be made in live cells. However, live cell models introduce many confounding variables that can make it difficult to interpret data on molecular interactions. A single living cell may have 1000 different phospholipid species within the plasma membrane, further complicating interpretation.[11] There is also an asymmetrical distribution of phospholipids within the inner and outer leaflets of the membrane bilayer, leading to different mechanical and physical properties in different areas of the membrane.[12-14] Given the complexity of live cell membranes, chemists and membrane biophysicists often seek simpler interpretable models.

Many physicochemical models have developed over the years, including liposomes, micelles, reverse micelles, Langmuir monolayers, and Langmuir-Blodgett films (Figure 1.2).[15] Short descriptions are provided for each model system, but the two focused on in this manuscript are reverse micelles and Langmuir monolayers.

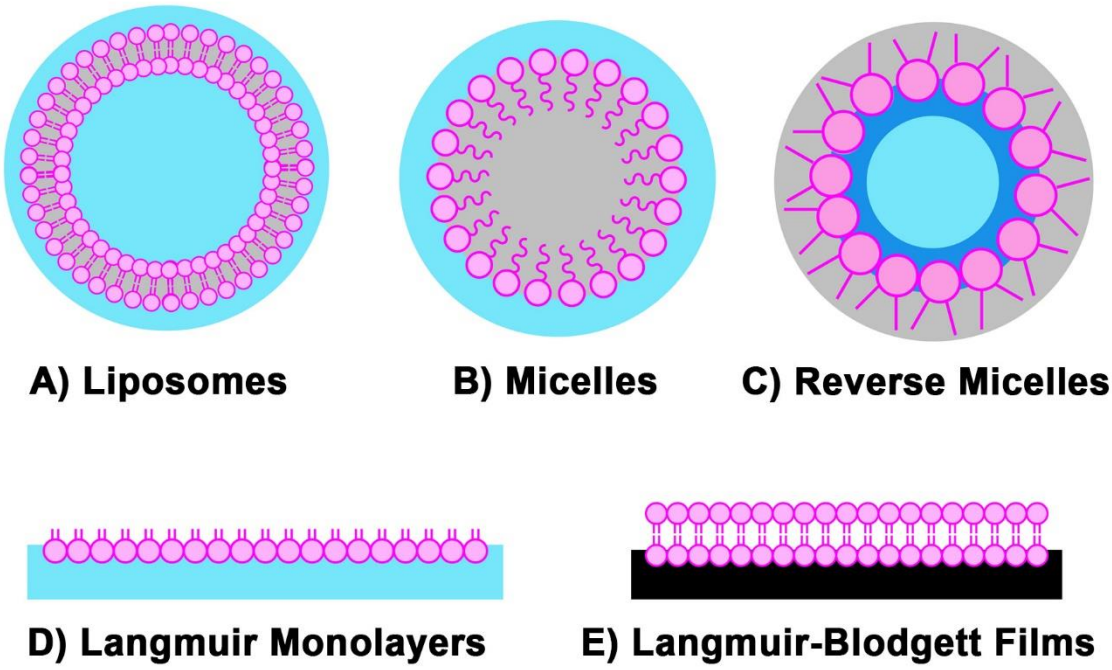

Figure 1.2. Common model membrane systems. A) Liposomes are spherical bilayers, typically phospholipid, with water both inside and outside. B) Micelles are non-polar core contained within an amphiphilic surfactant in bulk water. C) Reverse micelles are a water core encapsulated within an amphiphilic surfactant in bulk hydrophilic solvent, such as isooctane. D) Langmuir monolayers are self-assembled monolayers at the gas-liquid interface consisting of amphiphilic molecules. E) Langmuir-Blodgett films are multiple layers of amphiphilic molecules supported on either a hydrophobic or hydrophilic solid substrate. Pink represents lipids or surfactant, blue represents water, grey represents hydrophilic/non-polar regions, and black represents a solid such as glass or silicon.

1.3.2. Liposomes

Liposomes, or vesicles, are roughly spherical artificial bilayers, generally consisting of phospholipids, both enclosing and surrounded by water. They were first described in 1964 when it was discovered that phospholipids would spontaneously form vesicles in water.[16-17] They are favored among those modeling the membrane because they are arguably the most biologically relevant. Liposomal solutions may be multilamellar or unilamellar and may have a range of sizes. They may be used to study the interactions of molecules in a bilayer, drug-induced leakage, and even the function of membrane proteins.[18]

1.3.3. Micelles

Micelles are composed of a hydrophobic pool surrounded by an amphiphilic lipid or detergent in bulk water (Figure 1.2B). The lipid or detergent generally occupies a roughly conical volume so that it may pack into a small, highly curved sphere.[16] They are commonly used in solution NMR to study interactions of molecules with charged lipid headgroups.[19-20] They have even been used to perform NMR studies of membrane proteins and their structures.[21-22]

1.3.4. Reverse Micelles

As the name implies, a reverse micelle (RM) is the opposite of a micelle. RMs consist of a water pool surrounded by an amphiphilic surfactant, such as sodium dioctyl sulfosuccinate (AOT). This microemulsion is suspended in a non-polar solvent (Figure 1.3). Fully formed RMs have a Stern layer of more solid interfacial water near the charged headgroup of the surfactant, illustrated in blue in Figure 1.3.[23-24]

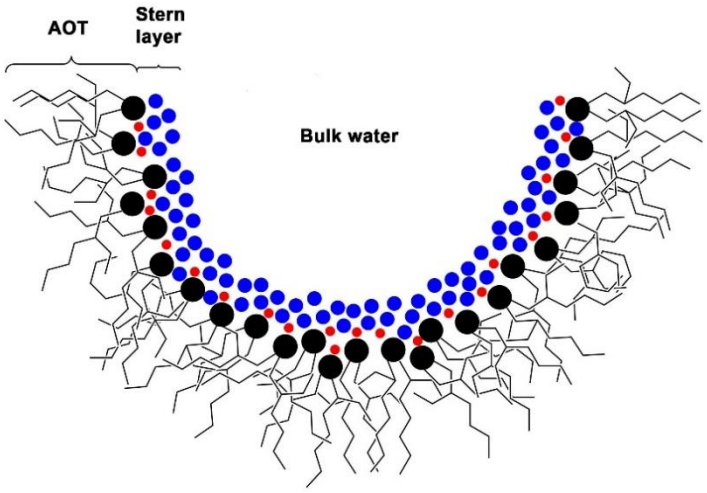

Figure 1.3. A cartoon of a w_0 12 sodium AOT reverse micelle. Interfacial water is illustrated in blue while Na^+ ions are in red. This figure was modified from Crans *et al.* 2017.[25]

RMs are characterized by their size, expressed as w_0= [H_2O]/[surfactant].[24] This system, like micelles, is often used in NMR spectroscopy studies as a model cell membrane. Association of molecules with the surfactant, location of probe molecules, and even the conformation of hydrophobic

molecules in the interface may all be investigated with RMs.[26-28] RMs are also useful to study the behavior of proteins and other molecules under confinement.[29-31]

1.3.5. Langmuir Monolayers

The material properties of the cell membrane play a key role in cell function.[32] Many of these material properties, such as packing and elasticity, can be investigated with Langmuir monolayers. Langmuir monolayers were named for Irving Langmuir, but they are based on the work of Agnes Pockles in the 19th century.[33-34]

To form a Langmuir monolayer, an amphiphilic molecule such as a phospholipid is applied at the gas-liquid interface, usually the air-water interface. The molecules then form a self-assembled monolayer on the water's surface which may then be laterally compressed to measure changes in surface pressure. The changes in pressure give information on the phase and packing of the monolayer. In this manuscript, the phospholipids dipalmitoylphosphatidylcholine (16:0 PC, DPPC) and dipalmitoylphosphatidylethanolamine (16:0 PE, DPPE) are used to create Langmuir monolayers (Figure 1.4) because they are well characterized and can be used to represent mammalian and bacterial membranes, respectively.[27] DPPC is common in mammalian pulmonary surfactant. Its cylindrical shape allows it to spread over a greater area, making it a good candidate for both Langmuir monolayers and liposomes. DPPE, on the other hand, is less common in eukaryotic cells but is prevalent in bacterial cells. Its conical shape allows it to pack tightly into smaller areas.[14] This allows for a greater number of lipids to pack into a smaller area which is required for bacterial membranes. Structurally, they are composed of 16:0 (palmitoyl) fatty acid tails, a glycerol group, a phosphate group, and then an amine headgroup.

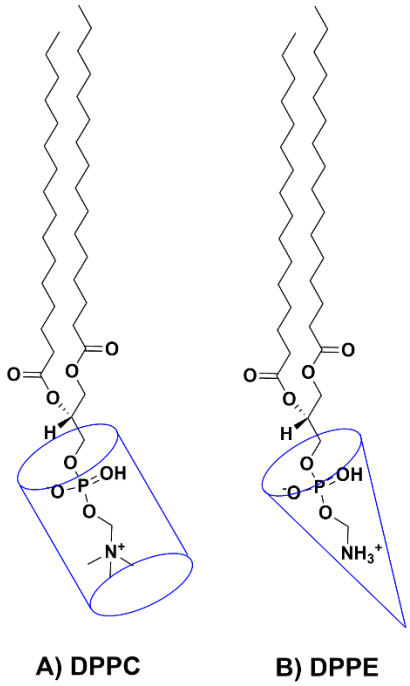

Figure 1.4. The phospholipids A) dipalmitoylphosphatidylcholine (DPPC) and B) dipalmitoylphosphatidylethanolamine (DPPE) and their "shapes." The choline headgroup of DPPC gives an overall cylindrical shape, while DPPE has an overall conical shape.

1.3.6. Langmuir-Blodgett Films

In the 1920s and 1930s, physicist Dr. Katherine Blodgett worked as an assistant to Langmuir. She found that a solid substrate dipped vertically into an aqueous solution with a Langmuir monolayer (or film) on the surface would then be homogeneously coated with the film.[35] This allows for morphological studies such as atomic force microscopy.[36-37] This technique has also been used to functionalize electrodes.[35, 38-39]

1.4. Compounds of Interest in this Manuscript

1.4.1. Lipoquinones

Lipoquinones (lipid quinones) are hydrophobic α,β-unsaturated ketones with numerous biological uses.[40] There are three major categories of lipoquinone: ubiquinones, plastoquinones, and menaquinones (Figure 1.5).[41-42] Ubiquinones are typically found in eukaryotes and some bacteria, such as *Escheria coli*,[43] while plastoquinones are typically found in plants.[44] Menaquinones (MK), the class of lipoquinones of interest in this dissertation, are generally found in Gram-positive prokaryotes

such as *Mycobacterium tuberculosis*.[45] MK structurally consists of a naphthoquinone headgroup and a tail of repeating isoprenoid units (Figure 1.5C).[46] MKs are identified based on their side chain length and saturation.[43] For example, the homologue with four unsaturated units is known as MK-4.

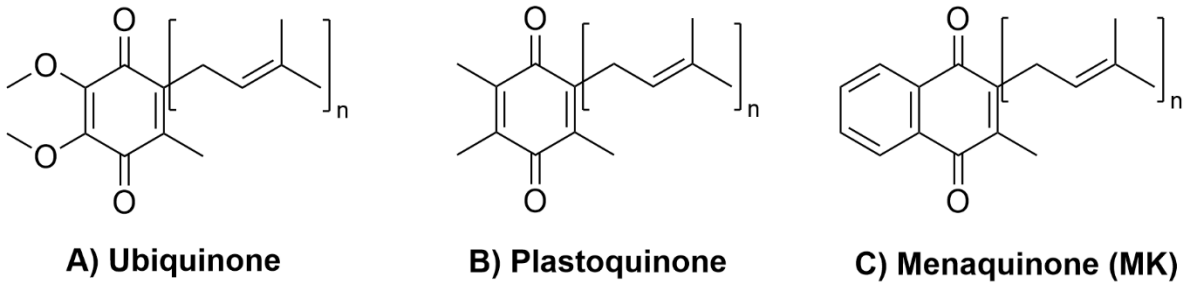

Figure 1.5. General structures of A) ubiquinone, B) plastoquinone, and C) menaquinone (MK), where *n* is the number of repeating isoprene units.

Unlike ubiquinone, MK homologues are very hydrophobic. This makes biological studies difficult as they cannot be studied in aqueous-based assays.[45] The hydrophobicity of MKs increases as their isoprenoid chain increases in length. Longer homologues, such as MK-7 and MK-9, are used in biological systems. With their hydrophobicity and relative rarity in mind, MK analogues are not as well studied as other lipoquinones. Interestingly, they are also potential drug target for the treatment of tuberculosis, as MK-9 (II-H2) is the primary electron transporter for *Mycobacterium tuberculosis*.[45] Since these lipoquinones reside within the membrane, a fundamental knowledge of location in and association with the membrane may help with drug design and formulation as well as provide insight into the bacterial electron transport chain.

1.4.2. Small Organic Drugs

All molecules entering or exiting the cell must interact with the cell membrane in some manner.[3, 47] Small organic molecules such as benzoic acid and salicylic acid are able to diffuse across the bilayer (Figure 1.6).[48-50] They are both protonophores, otherwise known as proton translocators.[51-52] Therefore, if a pH gradient exists, the neutral form may diffuse across the bilayer and then be deprotonated in the cytosol.[51] This mechanism is accepted and understood, yet fundamental studies of these molecules associating with the membrane are uncommon.

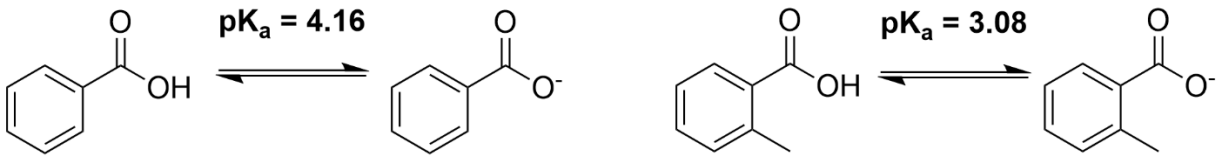

A) Benzoic Acid/Benzoate **B) Salicylic Acid/Salicylate**

Figure 1.6. Structures of A) benzoic acid and benzoate and B) salicylic acid and salicylate. The pKa values are experimental values from Serjeant and Dempsey 1979.[53]

1.5. Concluding Remarks

Chapter 2 investigates the location and interactions of the naphthoquinone and naphthoquinol headgroups of MK in model membranes. Chapter 3 addresses the interactions of truncated MKs in monolayers and bilayers. Chapter 4 investigates the interactions and locations of the anti-tuberculosis drugs pyrazinamide and pyrazinoic acid in model membranes. The primary technique in all three chapters is the compression of Langmuir monolayers, though other supporting methods such as UV-vis, NMR, and fluorimetry are presented.

References

1. Jang, H.-S., The Diverse Range of Possible Cell Membrane Interactions with Substrates: Drug Delivery, Interfaces and Mobility. *Molecules* **2017,** *22* (12), 2197.

2. Chung, Y. H.; Beiss, V.; Fiering, S. N.; Steinmetz, N. F., COVID-19 Vaccine Frontrunners and Their Nanotechnology Design. *ACS Nano* **2020,** *14* (10), 12522-12537.

3. Shinoda, W., Permeability across lipid membranes. *Biochim. Biophys. Acta* **2016,** *1858*, 2254-2265.

4. Grecco, H. E.; Schmick, M.; Bastiaens, P. I. H., Signaling from the Living Plasma Membrane. *Cell* **2011,** *144* (6), 897-909.

5. Alberts, B.; Bray, D.; Hopkin, K.; Johnson, A.; Lewis, J.; Raff, M.; Roberts, K.; Walter, P., *Essential Cell Biology*. 4 ed.; Garland Science: New York, 2014.

6. Stillwell, W., *An Introduction to Biological Membranes*. 2 ed.; Academic Press: 2016.

7. Alpern, R. J.; Herbert, S. C., *Seldin and Geibisch's the Kidney: Physiology and Pathology*. 4 ed.; Academic Press: 2008; Vol. 1.

8. Samart, N.; Althumairy, D.; Zhang, D.; Roess, D. A.; Crans, D. C., Initiation of a novel mode of membrane signaling: Vanadium facilitated signal transduction. *Coord. Chem. Rev.* **2020,** *416*, 213286.

9. Wolf-Ringwall, A. L.; Winter, P. W.; Roess, D. A.; Barisas, B. G., Luteinizing Hormone Receptors are Confined in Mesoscale Plasma Membrane Microdomains Throughout Recovery from Receptor Desensitization. *Cell Biochem. Biophys.* **2014,** *68*, 561-569.

10. Simons, K.; Toomre, D., Lipid rafts and signal transduction. *Nat. Rev. Mol. Cell Biol.* **2000,** *1*, 31-39.

11. Bunea, A.-I.; Harloff-Helleberg, S.; Taboryski, R.; Nielsen, H. M., Membrane interactions in drug delivery: Model cell membranes and orthogonal techniques. *Adv. Colloid Interface Sci.* **2020,** *281*, 102177.

12. Fadeel, B.; Xue, D., The ins and outs of phospholipid asymmetry in the plasma membrane: roles in health and disease. *Crit. Rev. Biochem. Mol. Biol.* **2009,** *44* (5), 264-277.

13. Levadnyy, V.; Hasan, M.; Saha, S. K.; Yamazaki, M., Effect of Transmembrane Asymmetric Distribution of Lipids and Peptides on Lipid Bilayers. *J. Phys. Chem. B* **2019,** *123*, 4645-4652.

14. Chakrabarti, A., Phospholipid Asymmetry in Biological Membranes: Is the Role of Phosphatidylethanolamine Underappreciated? *J. Membr. Biol.* **2021,** *254*, 127-132.

15. Yeagle, P. L., *The Membranes of Cells*. 3 ed.; Academic Press: Amsterdam, 2016.

16. Wiśniewska-Becker, A.; Gruszecki, W. I., Biomembrane models. In *Drug-biomembrane interaction studies: The application of calorimetric techniques*, Pignatello, R., Ed. Woolhead Publishing: Oxford, 2013.

17. Bangham, A. D.; Horne, R. W., Negative staining of phospholipids and their structural modification by surface-active agents as observed in the electron microscope. *J. Mol. Biol.* **1964,** *8* (5), 660-668.

18. Nasr, G.; Griege-Gerges, H.; Elaissari, A.; Khreich, N., Liposomal membrane permeability assessment by fluorescence techniques: Main permeabilizing agents, applications and challenges. *Int. J. Pharm.* **2020,** *580*, 119198.

19. Crans, D. C.; Schoeberl, S.; Gaidamauskas, E.; Baruah, B.; Roess, D. A., Antidiabetic vanadium compound and membrane interfaces: interface-facilitated metal complex hydrolysis. *J. Biol. Inorg. Chem.* **2011,** *16*, 961-972.

20. Kim, B.-J.; Im, S.-S.; Oh, S.-G., Investigation on the Solubilization Locus of Aniline-HCl Salt in SDS Micelles with ^{1}H NMR Spectroscopy. *Langmuir* **2001,** *17* (2), 565-566.

21. Fernández, C.; Hilty, C.; Wider, G.; Wüthrich, K., Lipid-protein interactions in DHPC micelles containing the integral membrane protein OmpX investigated by NMR spectroscopy. *Proc. Natl. Acad. Sci.* **2002,** *99* (21), 13533-13537.

22. Hiller, S.; Garces, R. G.; Malia, T. J.; Orekhov, V. Y.; Colombini, M.; Wagner, G., Solution Structure of the Integral Human Membrane Protein VDAC-1 in Detergent Micelles. *Science* **2008,** *321* (5893), 1206-1210.

23. De, T. K.; Maitra, A., Solution behvaior of aerosol OT in non-polar solvents. *Adv. Colloid Interface Sci.* **1995,** *59*, 95-193.

24. Maitra, A., Determination of size parameters of water-Aerosol OT-oil reverse micelles from their nuclear magnetic resonance data. *J. Phys. Chem.* **1984,** *88* (21), 5122-5125.

25. Crans, D. C.; Peters, B. J.; Wu, X.; McLauchlan, C. C., Does anion-cation organization in Na+-containing X-ray crystal structures relate to solution interactions in inhomogeneous nanoscale environments: Sodium-decavanadate in solid state materials, minerals, and microemulsions. *Coord. Chem. Rev.* **2017,** *344*, 115-130.

26. Koehn, J. T.; Magallanes, E. S.; Peters, B. J.; Beuning, C. N.; Haase, A. A.; Zhu, M. J.; Rithner, C. D.; Crick, D. C.; Crans, D. C., A Synthetic Isoprenoid Lipoquinone, Menaquinone-2, Adopts a Folded Conformation in Solution and at a Model Membrane Interface. *J. Org. Chem.* **2018,** *83*, 275-288.

27. Van Cleave, C.; Murakami, H. A.; Samart, N.; Koehn, J. T.; Maldonado, P.; Kreckel, H. D.; Cope, E. J.; Basile, A.; Crick, D. C.; Crans, D. C., Location of menaquinone and menaquinol headgroups in model membranes. *Can. J. Chem.* **2020,** *98* (6), 307-317.

28. Crans, D. C.; Rithner, C. D.; Baruah, B.; Gourley, B. L.; Levinger, N. E., Molecular Probe Location in Reverse Micelles Determined by NMR Dipolar Interactions. *J. Am. Chem. Soc.* **2006,** *128* (13), 4437-4445.

29. Van Horn, W. D.; Oglivie, M. E.; Flynn, P. F., Use of reverse micelles in membrane protein structural biology. *J. Biomol. NMR* **2008,** *40* (3), 203-211.

30. Valentine, K. G.; Peterson, R. W.; Saad, J.; Summer, M. F.; Xu, X.; Ames, J. B.; Wand, A. J., Reverse Micelle Encapsulation of Membrane-Anchored Proteins for Solution NMR Studies. *Structure* **2010,** *18*, 9-16.

31. Miller, S. L.; Wiebenga-Sanford, B. P.; Rithner, C. D.; Levinger, N. E., Nanoconfinement Raises the Energy Barrier to Hydrogen Atom Exchange between Water and Glucose. *J. Phys. Chem. B* **2021,** *125* (13), 3364-3373.

32. Kelley, E. G.; Butler, P. D.; Ashkar, R.; Bradbury, R.; Nagao, M., Scaling relationships for the elastic modululi and viscosity of mixed lipid membranes. *Proc. Natl. Acad. Sci.* **2020,** *117* (38), 23365-23373.

33. Pockles, A., On the Spreading of Oil Upon Water. *Nature* **1894,** *1288* (50), 223-224.

34. Pockles, A., On the relative contamination of the water-surface by equal quantities of different substances. *Nature* **1892,** *463* (1192), 418-419.

35. Edwards, G. A.; Bergren, A. J.; Porter, M. D., Chemically Modified Electrodes. In *Handbook of Electrchemistry*, Zoski, C. G., Ed. Elsevier: 2007; pp 295-327.

36. Picas, L.; Suárez-Germà, C.; Montero, M. T.; Hernández-Borrell, J., Force Spectroscopy Study of Langmuir-Blodgett Asymmetric Bilayers of Phosphatidylethanolamine and Phospatidylglycerol. *J. Phys. Chem. B* **2010,** *114*, 3543-3549.

37. Hagedorn, S.; Drolle, E.; Lorentz, H.; Srinivasan, S.; Leonenko, Z.; Jones, L., Atomic force microscopy and Langmuir-Blodgett monolayer technique to assess contact lens deposits and human meibum extracts. *J. Optometry* **2015,** *8* (3), 187-199.

38. Wang, F.; Wei, X.; Wang, C.; Zhang, S.; Ye, B., Langmuir-Blodgett film of *p-tert*-butylthiacalix[4]arene modified glassy carbon electrode as voltammetric sensor for the determination of Hg(II). *Talanta* **2010,** *80* (3), 1198-1204.

39. Proust, A.; Matt, B.; Villanneau, R.; Guillemot, G.; Gouzerh, P.; Izzet, G., Functionalization and post-functionalization: a step toward polyoxometalate-based materials. *Chem. Soc. Rev.* **2012,** *41*, 7605-7622.

40. Nowicka, B.; Kruk, J., Occurence, biosynthesis, and function of isoprenoid quinones. *Biochim. Biophys. Acta* **2012,** *1797*, 1587-1605.

41. Crane, F. L., Discovery of ubiquinone (coenzyme Q) and an overview of function. *Mitochondrion* **2007,** *7*, S2-S7.

42. Hauska, G., Plasto- and ubiquinone as translocators of electrons and protons through membranes - A facilitating role of the isoprenoid side chain. *FEBS Letters* **1977,** *79* (2), 345-347.

43. Collins, M. D.; Jones, D., Distribution of Isoprenoid Quinone Structural Types in Bacteria and Their Taxonomic Implications. *Microbiol. Rev.* **1981,** *45* (2), 316-354.

44. Krogmann, D. W., A requirement for plastoquinone in photosynthetic phosphorylation. *Biochem. Biophys. Res. Commun.* **1961,** *4* (4), 275-277.

45. Upadhyay, A.; Fontes, F. L.; Gonzalez-Juarrero, M.; McNeil, M. R.; Crans, D. C.; Jackson, M.; Crick, D. C., Partial Saturation of Menaquinone in *Mycobacterium tuberculosis*: Function and Essentiality of a Novel Reductase, MenJ. *ACS Cent. Sci.* **2015,** *1* (6), 292-302.

46. Braasch-Trui, M.; Crans, D. C., Synthesis of Naphthoquinone Derivatives: Menaquinones, Lipoquinones and Other Vitamin K Derivatives. *Molecules* **2020,** *25* (19), 4477.

47. Zhu, Q.; Lu, Y.; He, X.; Liu, T.; Chen, H.; Wang, F.; Zheng, D.; Dong, H.; Ma, J., Entropy and Polarity Control the Partition and Transportation of Drug-like Molecule in Biological Membrane. *Sci. Rep.* **2017,** *7*, 17749.

48. Gutknecht, J.; Tosteson, D. C., Diffusion of Weak Acids across Lipid Bilayer Membranes: Effects of Chemical Reactions in the Unstirred Layers. *Science* **1973,** *182* (4118), 1258-1261.

49. Peters, B. J.; Groninger, A. S.; Fontes, F. L.; Crick, D. C.; Crans, D. C., Differences in Interactions of Benzoic Acid and Benzoate with Interfaces. *Langmuir* **2016,** *32* (37), 9451-9459.

50. Gabba, M.; Frallicciardi, J.; van 't Klooster, J.; Henderson, R.; Syga, Ł.; Mand, R.; van Maris, A. J. A.; Poolman, B., Weak Acid Permeation in Synthetic Lipid Vesicles and Across the Yeast Plasma Membrane. *Biophys. J.* **2020,** *118* (21), 422-434.

51. Nicholls, D. G.; Ferguson, S. J., *Bioenergetics*. 4 ed.; Academic Press: Amsterdam, 2013.

52. Skulachev, V. P., Uncoupling: new approaches to an old problem of bioenergetics. *Biochim. Biophys. Acta Bioenerg.* **1998,** *1363* (2), 100-124.

53. Serjeant, E. P.; Dempsey, B., *Ionisation Constants of Organic Acids in Aqueous Solution*. Pergamon Press: Oxford, 1979.

Chapter 2
Location of Menadione and Menadiol Headgroups in Model Membranes[a]

1. Introduction

Lipoquinones are an essential group of lipids that act as electron transfer donors and acceptors within the electron transfer complex.[1-2] One type of lipoquinone typically associated with prokaryotes is menaquinone (MK), which has a naphthoquinone headgroup, as well as an isoprenyl side chain.[3-6] MK abbreviations are based on the naphthoquinone headgroup and the number of isoprene groups in the side chain, where MK-4 is a menaquinone with four isoprene units. Some of the MK derivatives are known to have biological activities in humans such as MK-4, which is important in blood coagulation.[7] Other MK homologues have been reported to have potent biological properties such as antiseizure activity in model organisms.[8-10] The native electron transport lipoquinone of *Mycobacterium* spp., specifically *M. smegmatis* and *M. tuberculosis*, is MK-9 with a reduced β isoprene unit (abbreviated as MK-9(II-H_2), Figure 2.1A).[11-12] The electron transfer complexes of most organisms are membrane-associated and thus require that the MK derivatives are also affiliated with the membrane. Native prokaryotic MKs have long isoprenyl side chains, and their conformations within their native membrane environments are poorly understood. The hydrophobic nature of MK homologues and their insolubility in aqueous assays complicate analyses of these molecules.[6] Considering the challenges of working with the native systems, we have initiated studies with truncated MK derivatives that are slightly water soluble.[1, 6, 13] Their simpler and less hydrophobic structures allow for characterization of how these MK systems interact with membrane interfaces and elucidation of their conformations.[6, 13] It was previously shown that the truncated MK-1 and MK-2 molecules fold and that such folding adjusts as the molecule associates with a model membrane interface.[1, 13]

[a] This manuscript is published in full or in part in the *Canadian Journal of Chemistry*.

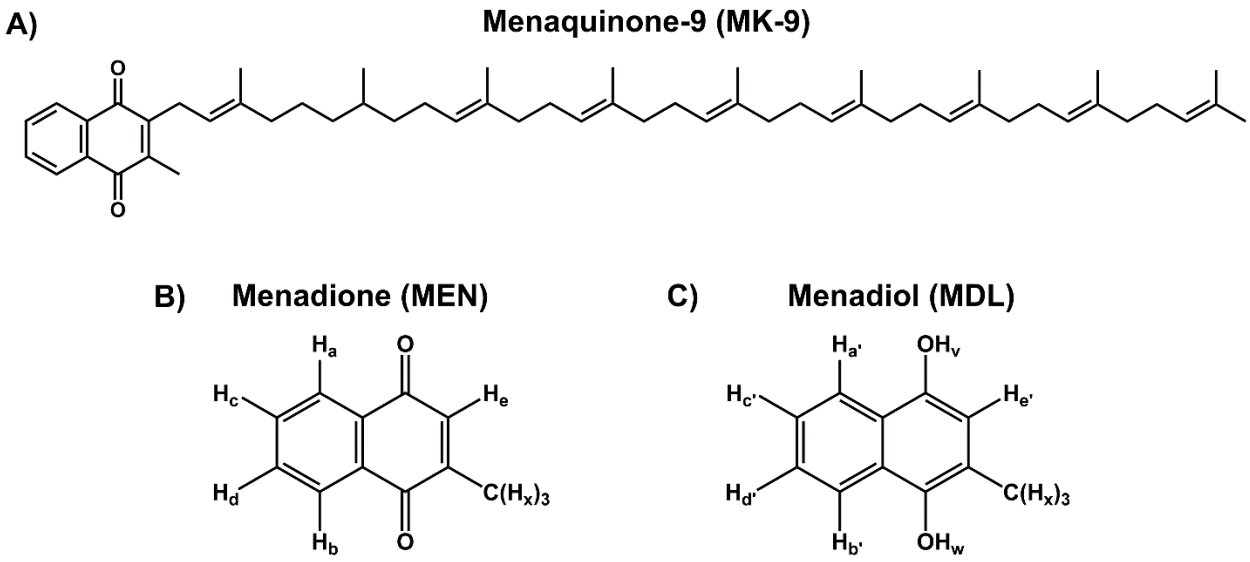

Figure 2.1. Structures for (A) menaquinone (MK-9(II-H2)) present in *M. tuberculosis*, (B) the oxidized headgroup menadione (MEN), and (C) the reduced headgroup menadiol (MDL).

The MK derivatives are reduced by the electron transfer complex to form their quinol counterparts. Reduced MKs are suggested to interact differently with the interface compared with oxidized MKs, based on computational and experimental studies on MK's counterpart, ubiquinone.[14-16] In this manuscript, we sought to obtain experimental evidence investigating whether the interaction with interfaces differs between the oxidized menadione (MEN, Figure 2.1B) and reduced menadiol (MDL, Figure 2.1C) headgroups. Previous studies of the MK derivatives with interfaces take advantage of work with two model interface systems, Langmuir monolayers[17-18] and microemulsions.[19-20] Generalized diagrams of both model membranes and potential locations of probe molecules are shown in Figure 2.2. Studies using Langmuir monolayer systems with truncated MK derivatives have been reported and support the interpretation that the MK derivatives insert into the membrane interface.[1, 21] The studies with microemulsions were carried out using a well-known model system for studying membrane interface interactions, consisting of a lipid or surfactant (aerosol-OT, abbreviated AOT), an organic solvent (isooctane), and water.[22-24] This system forms self-assembled structures with an interface resembling that of a charged membrane,[19, 25-27] making it a very useful tool for studying the interactions and potential penetration of naphthoquinone and naphthoquinol headgroups.[13, 18] Both models have been used successfully in conjunction with each other to develop

a more in-depth framework of how different biologically relevant molecules associate with the cell membrane.[28-29]

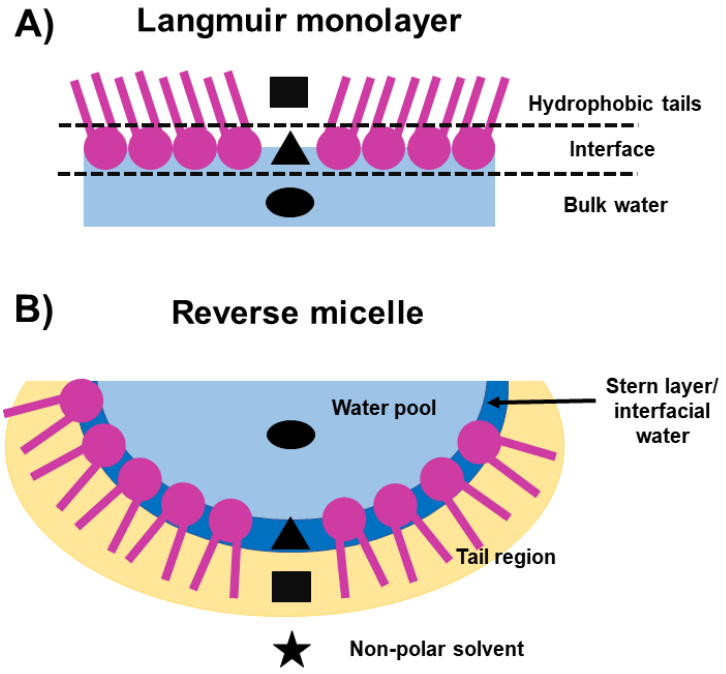

Figure 2.2. General diagrams of (A) a Langmuir monolayer and (B) a reverse micelle (RM) microemulsion. Black rectangles represent probe molecules found in the hydrophobic tails, black triangles represent molecules found in the interface, black ovals represent molecules found in the bulk water, and black stars represent molecules found in the non-polar solvent of the RM system.

Computational analysis and other studies have been carried out, which suggested that the interactions of MK and ubiquinone derivatives within the membrane were dictated mainly by the length of the isoprene side chain.[30] In other studies in neutral bilayers, the naphthoquinone headgroup was important for anchoring the lipoquinone, suggesting that the isoprene side chain may not be the only structural factor determining the location in the membrane.[14, 31] Anchoring through a headgroup has been noted with other molecules as well, lending credence to the headgroup having greater bearing on location in the interface.[32-33] In the following work, we examined the interaction of the headgroup, MEN (Figure 2.1A), and the corresponding reduced version, MDL (Figure 2.1C), with a model membrane interface. We hypothesize that MEN and MDL will both associate with and penetrate into the membrane but will sit in different locations within the interface.

2. Materials and Methods

2.1 General Materials and Methods

2.1.1 Materials

MEN was purchased from Sigma-Aldrich. MDL was prepared as reported previously.[1, 34] Chloroform (≥99.5%), dithiothreitol (DTT), monosodium phosphate (≥99.0%), disodium phosphate (≥99.0%), sodium hydroxide (≥98%), hydrochloric acid (37%), and MEN were all purchased from Sigma-Aldrich. The phospholipids dipalmitoylphosphatidylcholine (16:0 PC, DPPC, 99%) and dipalmitoylphosphatidylethanolamine (16:0 PE, DPPE, 99%) were purchased from Avanti Polar Lipids. Most materials were used without further purification. AOT (Sigma-Aldrich) was purified using charcoal and methanol as described previously.[35] The water content of the AOT was determined by NMR spectroscopy, measuring the water content in AOT solubilized in DMSO. Distilled deionized (DDI) water was generated by filtering distilled water through a water purification system until a resistance of 18.2 MΩ was obtained.

2.1.2 Instrumentation

All absorption spectra were run on an Avantes spectrophotometer (AvaSpec-USB2 with an AvaLight-DHc lamp) in 1 cm quartz cuvettes and collected with AfterMath software version 1.4.7881. The Langmuir monolayers were studied using a NIMA LB Medium Trough (Teflon) from Biolin Scientific. NMR studies were conducted on a Bruker Neo400 NMR. Dynamic light scattering (DLS) studies were performed in a Malvern Zetasizer Nano ZS equipped with a 633 nm red laser.

2.2 Synthesis of MDL

MDL was synthesized by the reduction of MEN by sodium dithionite, and NMR spectra of MDL were consistent with those reported previously.[1, 34]

2.3 Stability Studies With UV-Vis Spectroscopy

Because of the limited solubility of the oxidized and reduced headgroups, as well as the rapid oxidation of the reduced headgroup, different methods were investigated for preparation of the

solutions. Attempts to sonicate the samples under argon were not as effective as the addition of a reductant to MDL samples.

2.3.1 Stability in DDI Water

A solution of 0.10 mmol/L MEN (yellow powder) was made by sonicating 17 mg (10 µmol) of MEN in 100 mL of DDI water (18.2 MΩ) until dissolved, approximately 10 min. A solution of 0.10 mmol/L MDL (pale purple powder) was made by sonicating 17 mg (10 µmol) of MDL in 100 mmol/L of DDI water for approximately 20 min. A third sample was prepared by adding 17 mg of MDL (10 µmol) to 100 mL of DDI water, shaking for five seconds, and removing the supernatant to observe the spectra of MDL immediately after contact with water. A fourth sample was prepared by adding a small amount of solid MDL to the bottom of a cuvette and then adding water. Spectra were collected every minute for 15 min and then at the 20, 25, 30, 45, and 60 minute marks. However, one may have anticipated that MDL would be more soluble than MEN because of the two hydroxyl groups, the fact that the MDL takes longer to dissolve than MEN is not consistent with this observation. Although hydroxyl groups typically increase solubility, this is not always the case. For example, the $[VO_2(\text{dipic-OH})]^-$ complex is less soluble than the parent complex, $[VO_2\text{dipic}]^-$ complex, possibly because the former imparts greater solid-state interactions, which decrease the solubility.[36]

2.3.2 Stability of MDL in DDI Water with a Reducing Agent

DTT was used to create a reducing environment to test for an improvement in MDL stability. Due to the rapid oxidation of MDL in water, a small amount of MDL solid was added to the bottom of a quartz cuvette with a small amount of DTT. DDI water was added and a UV–vis spectrum was recorded immediately. Timepoints were taken with the same frequency as described in the previous section.

2.3.3 Stability of MDL in a Reverse Micelle Microemulsion

A stock solution of w_0 12, AOT/isooctane reverse micelles was prepared by mixing appropriate amounts of 0.50 mol/L AOT in isooctane with DDI water and agitating for 30 s until the solution became translucent. The sample for UV–vis was prepared by diluting 1.0 mL of the stock solution into 4.0 mL of isooctane and agitating for 2 min to break up aggregates. Approximately 1.0 mL of the dilution was

added to a cuvette with solid MDL and immediately placed into the UV–vis spectrophotometer (t = 0). The same timepoints were collected as described in the previous sections.

2.4 Preparation of Solutions for Langmuir Monolayers

2.4.1 Phospholipid and MEN Stock Solutions

Phospholipid stock solutions were prepared by dissolving dipalmitoylphosphatidylcholine (16:0 PC, DPPC) (0.018 g, 0.025 mmol) or dipalmitoylphosphatidylethanolamine (16:0 PE, DPPE) (0.017 g, 0.025 mmol) in 25 mL of 9:1 chloroform/methanol (v/v) for a final concentration of 1.0 mmol/L phospholipid. MEN stock solutions were prepared by dissolving MEN (0.0043 g, 0.025 mmol) in 25 mL of 9:1 chloroform/ methanol (*v/v*) for a final concentration of 1.0 mmol/L MEN. Solutions with ratios of 50:50 and 25:75 (phospholipid/MEN) were prepared in 2.0 mL glass vials and vortexed for 10 s before each experiment.

2.5 Langmuir Monolayer Studies

2.5.1 Preparation of Phospholipid Langmuir Monolayers

The aqueous subphase consisted of 230 mL of 20 mmol/L sodium phosphate buffer (pH 7.4) in DDI water (18.2 MΩ). The subphase surface was cleaned using vacuum aspiration, and the surface pressure of a compression isotherm of just the subphase (no phospholipid present) was measured (surface pressure was consistently 0.0 ± 0.5 mN/m throughout compression) before each compression measurement. To prepare the DPPC phospholipid monolayer, a total of 28 µL of phospholipid stock solution (28 ng of DPPC) was added to the surface of the subphase in a dropwise manner using a 50 µL Hamilton syringe approximately 1 inch from each expanded barrier. The film was allowed to equilibrate for 15 min during which time the chloroform and methanol evaporated. The resulting phospholipid monolayer was then used for the compression isotherm experiments.

The preparation of the Langmuir monolayer from DPPE phospholipids required a higher lipid amount and the injection volume of 58 µL was compared with the DPPC solution. Solutions with ratios of 50:50 and 25:75 (phospholipid/MEN) shared the base injection volume of phospholipid plus an appropriate amount of MEN to reach the desired ratio of phospholipid/MEN.

2.5.2 Compression Isotherm Measurements of Langmuir Monolayers

The phospholipid monolayer was compressed from two sides with a total speed of 10 mm/min (5 mm/min from opposite sides) using a NIMA LB Medium Trough from Biolin Scientific. The temperature was maintained at 25 °C using an external water bath. The trough base and Teflon barriers were rinsed three times with ethanol followed by DDI water (18.2 MΩ) before each experiment. The surface tension of the subphase during each compression was monitored using a platinum Wilhemy plate. The surface pressure was calculated from the surface tension using Eq. 1.1, where π is the surface pressure, γ_0 is the surface tension of water (72.8 mN/m), and γ is the surface tension at a given area per phospholipid after the film has been applied.

$$\pi = \gamma_0 - \gamma \qquad \textbf{Equation 1.1}$$

The compression moduli were calculated as detailed and are shown in Appendix II. Each compression isotherm experiment consisted of at least three replicates, and the averages of the area per phospholipid and the standard deviation at every 5 mN/m were calculated using Microsoft Excel. The areas of the mixed monolayers were multiplied by the mol fraction to plot curves in terms of area per phospholipid as opposed to area per molecule. This allowed for easier comparison with the control. The worked-up data were transferred to OriginPro version 9.1 to be graphed.

2.6 Reverse Micelle (RM) Solutions in Isooctane

2.6.1 MEN

Because MEN was sparingly soluble in H_2O (or D_2O), the AOT/isooctane RM samples were prepared by dissolving MEN directly into a mixture of AOT in isooctane followed by the addition of D_2O. A 0.5 mol/L stock solution of AOT in isooctane was prepared by dissolving 5.56 g, 12.5 mmol AOT in 25 mL isooctane. To prepare a 14.3 mmol/L MEN solution, 0.6 g of MEN was added to a 25 mL volumetric flask followed by the AOT/isooctane stock solution. The mixture was sonicated until MEN was fully dissolved and then diluted to the mark. The pH of a D_2O solution was adjusted to 7.0 (pD = pH + 0.4). To 2 mL of the MEN/AOT/isooctane stock of solution, varying amounts of pH adjusted

D_2O were added to prepare samples with w_0 4, w_0 8, w_0 12, w_0 16, and w_0 20 for MEN. These samples were vortexed until clear, indicating that microemulsions formed.

2.6.2 MDL

As in the case of solution preparation for studies by UV–vis spectroscopy, several methods were investigated to prepare the higher concentration solutions for NMR investigations, including the use of different solvents and solvent mixtures, as well as mixed solid systems, and the addition of the RM mixture into an NMR tube containing solid MDL at the bottom. Due to the rapid oxidation of MDL to MEN, methanol was added to the "water pool" of the RMs to both solubilize and stabilize MDL against oxidation. The mixed solvent MeOH:D_2O samples were prepared similarly to the D_2O samples in a 10 mL volumetric flask adding first MeOH (7.0, 8.0, and 9.0 mL) followed by D_2O to make up the 10 mL volume (note that MeOH:D_2O mixtures decrease in volume when combined, so the values reported here overestimate the MeOH content). Several mixed solvent pools were made but only the 70:30, 80:20, and 90:10 mixtures were able to dissolve MDL. After vortexing, the mixed solvents were used to prepare samples as described above (0.20 mg/1.15 μmol in 1.00 mL mixed solvents). As MDL was poorly soluble in aqueous and D_2O solutions, solid MDL was added to the NMR tube prior to AOT/isooctane RM solution. Specifically, microemulsion solutions for NMR studies were prepared by the addition 0.20 mg (1.2 μmol) MDL to the tube followed by 1 mL of AOT/isooctane RM solution. This experiment corresponded to the addition of solid MDL to "empty" RM. NMR spectra were collected immediately.

2.6.3 ^{1}H NMR Spectroscopic Studies of AOT/Isooctane RM Samples

One-dimensional (1D) ^{1}H NMR spectra of MEN and MDL in D2O, organic solvent, and RMs. Two-dimensional (2D) ^{1}H NMR studies of MEN and MDL were carried out in organic solvent and RMs as reported previously.[20] The parameters to record the NOESY and ROESY spectra were recorded using parameters reported previously.[1]

2.7 Dynamic Light Scattering (DLS) Studies

DLS samples were prepared similar to the RM NMR samples described above but with the following modifications: DDI water was used in place of D_2O. Once the 1 mL sample was made, 4 mL of isooctane were added to dilute the sample. Diluted samples were agitated for 2 min prior to measurements to break up RM aggregates.

3. Results

3.1 Stability of MEN and MDL in Aqueous Solution

3.1.1 MEN and MDL in Aqueous Solution

MEN was stable in aqueous solution albeit sparingly soluble, requiring agitation or sonication for dissolution. MDL, on the other hand, oxidized to MEN, so stability studies in water were conducted to determine the time over which the reaction takes place to define the parameters of the experimental design. Several different approaches to sample preparation for MDL were tested against MEN with UV–vis spectroscopy. These consisted of dissolving MDL completely in water, taking an aliquot of supernatant from a fresh mixture of MDL and water, and placing solid MDL at the bottom of a vessel such as a cuvette. The potential to carry out MDL solution preparation under argon was considered but not pursued because of the difficulties in dissolving the compound in a timely manner.

The absorption spectrum shown in Figure 1.3.1 of 0.1 mmol/L MEN contains four peaks that appear at 198 nm, 248 nm, 263 nm, and 339 nm. This solution was found to be stable over 60 min (see Appendix II, Figure A2.2.1). The UV–vis spectra of the 0.1 mmol/L MDL sample prepared by sonication had four peaks at 198 nm, 248 nm, 261 nm, and 341 nm, which was identical to that observed for MEN and thus documents complete oxidation by the time the solid MDL had dissolved (Figure 1.3.1A). After 60 min, small differences were observed for the signal at 225 nm and the two signals at 248 nm and 263 nm. An aliquot of MDL supernatant taken from a sample where MDL had just been added to water had peaks at 194 nm, 248 nm, 263 nm, and 340 nm but at a lower intensity. Some of these peaks are slightly shifted from pure MEN (Figure 2.3). In addition, the peak at 194 nm had a higher intensity than the peaks at 248 nm and 263 nm, which is the opposite spectroscopic

signature for dissolved MDL. The shifts suggests that the sample contained something other than MEN.

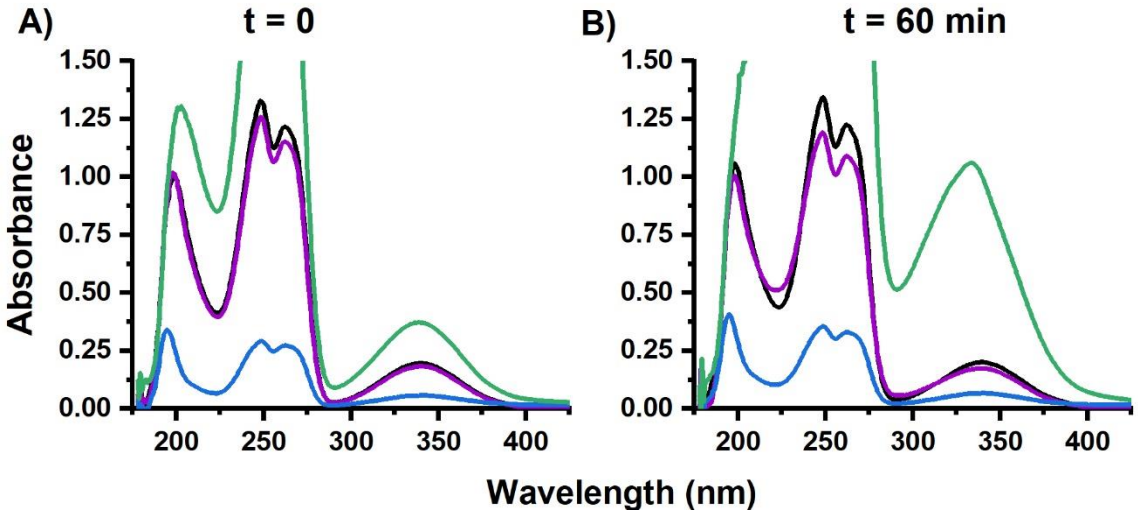

Figure 2.3. Aqueous UV–vis spectra of 0.10 mmol/L MEN (black), 0.10 mmol/L MDL that was fully dissolved before analysis (purple), supernatant from a 0.10 mmol/L MDL solution when MDL had just been added to water (blue), and aqueous solution added to solid MDL at the bottom of the quartz cuvette (green). Spectra are shown at times (A) t = 0 min and (B) t = 60 min after dissolution of the MDL material. The y axis is cut off at 1.5 as any peaks above that value in the absorbance spectrum are associated with high experimental uncertainly.

The sample of solid MDL added directly in a cuvette followed by the addition of water showed the peaks that were present at 203 nm, 249 nm, and 262 nm had coalesced into a single signal with an intensity above an absorbance where the spectrophotometer measured intensities accurately (Figure 1.3.1B). These experiments demonstrate that MDL has limited solubility and is rapidly oxidized as it dissolves. In a system where solid MDL is present at the bottom of the cuvette, the MDL can continuously dissolve and consequently continuously oxidize. The data shown for both the 0 min and 60 min time points of the MDL sample (Figure 2.3) demonstrate that even at t = 0 significantly more than 0.1 mmol/L MDL has been dissolved and oxidized to MEN. As the Langmuir monolayer studies take approximately 45 min for completion, where MDL would be exposed to bulk and interfacial water, such studies would be examinations of MEN instead of MDL. Thus, Langmuir monolayer studies were not attempted starting from MDL due to its rapid oxidation. Regardless, the data in Figure 2.3B show that the studies performed so far gives a spectrum identical to that of MEN and thus confirmed that

MDL oxidized in solutions where it was allowed to fully dissolve in the time it took to prepare the solution. To validate this interpretation, we sought to dissolve MDL under conditions where it remained in the reduced form.

3.1.2 MEN and MDL in Reducing Aqueous Solution

To keep MDL in a reduced form, solid DTT was added to the cuvette alongside solid MDL with the intent to generate a solution with a reducing environment, thus decreasing spontaneous oxidation of MDL. Such a solution allowed for the observation of MDL instead of MEN (Figure 2.4). Figure 4B shows that a solution formed from the addition of both MDL (239 nm signal) and DTT followed by the addition of water will begin oxidizing MDL to MEN as evidenced by the 263 nm signal by the 15 min timepoint. A control sample was recorded where solid DTT and MEN were added to the quartz cuvette, followed by the addition of water. This experiment verified the spectrum for MEN by the presence of the 263 nm signal as opposed to the MDL signals and is shown in Figure A1.3.2.

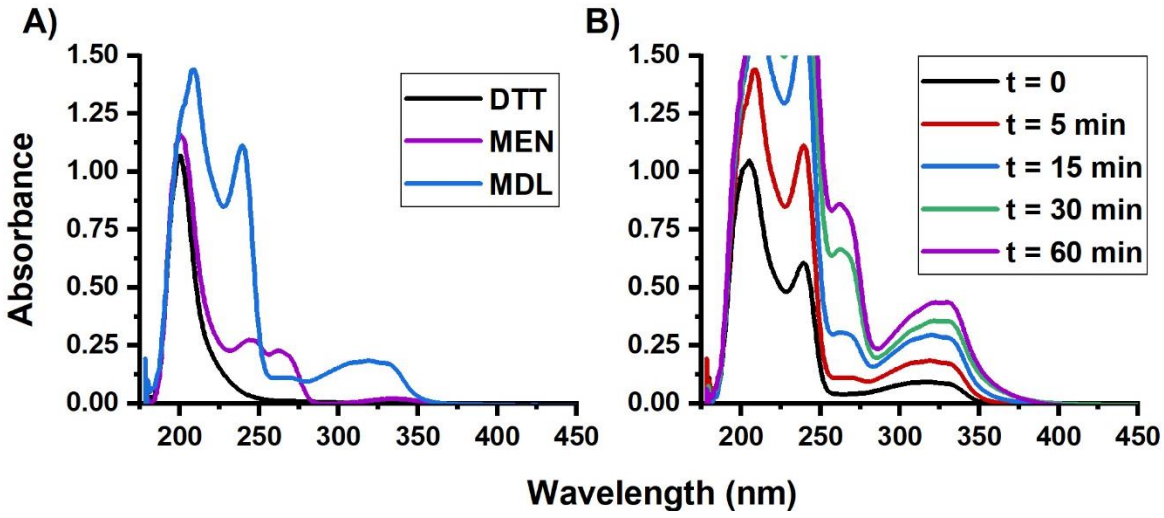

Figure 2.4. UV–vis spectra showing (A) a solution of DTT (blue), a solution formed from the addition of solid MEN and DTT (purple) in a quartz cuvette followed by the addition of DDI water, and a solution formed from the addition of solid MDL and DTT in a quartz cuvette followed by DDI water (black) and (B) a solution formed by the addition of solid MDL and DTT to a quartz cuvette followed by DDI water as a function of time from the addition of the DDI water at time 0 over 60 min. The y axis is truncated to 1.5, as any peaks above that value are associated with high error.

The use of a reducing agent did decrease the oxidation rate of MDL to MEN, and it was possible to record a spectrum of MDL in the presence of DTT. This verifies that the UV–vis spectrum

of MDL is different than that of the MEN. Considering that these spectra were recorded from solid added to the quartz cuvette, the concentrations cannot be accurately determined unlike those shown in Figure 2.3, which is why the signal intensity for the MEN is smaller than that observed for MDL. However, it is not appropriate to use such solid mixture in Langmuir monolayer studies due to the exposure to open air and continuous oxidation under those conditions, as well as the potential effects of DTT on the monolayer itself. Accordingly, an alternative model membrane system, microemulsions, was investigated in place of the Langmuir monolayer studies.

3.2 Effects of MEN on DPPC and DPPE Monolayers

The effects of MEN on a Langmuir monolayer were investigated using both DPPE and DPPC. These phospholipids were chosen as they have been thoroughly characterized in Langmuir monolayer systems and their biological relevance has also been characterized. DPPC is up to 40% of human lung surfactant, whereas DPPE is commonly found in prokaryotic cell membranes and the inner leaflet of eukaryotic cells.[37-39] Although MEN is a hydrophobic molecule, it was unable to form a monolayer on the subphase, even with increasing amounts of MEN. This implies that MEN is either surface inactive, much like geranyl bromide (Chapter 3), or that MEN was π–π stacking in the aqueous solution, thus preventing the formation of a film. As shown in Figure 2.5, the DPPC monolayers exhibited the expected gas–liquid transition between 155 and 110 $Å^2$ (0–10 mN/m), which is in accordance to the literature for the amount of lipid added.[37] The 50:50 and 25:75 DPPC:MEN curves exhibit an overall similar shape as the pure DPPC samples, though both are slightly shifted to a smaller area per phospholipid. However, the observed variation in the area measurements overlap with the variation in the control; therefore, we cannot conclude that there is a difference in area. This indicates that MEN is located in either the bulk water or the hydrophobic tail region. Given the sparing solubility of MEN in water, it is more likely that MEN was compressed into the hydrophobic phospholipid tails. This was confirmed by compression modulus calculations shown in Appendix II, Figure A2.2.1, where the compression modulus was affected by the presence of MEN in DPPC. These observations are consistent with the insertion of MEN into the monolayer.

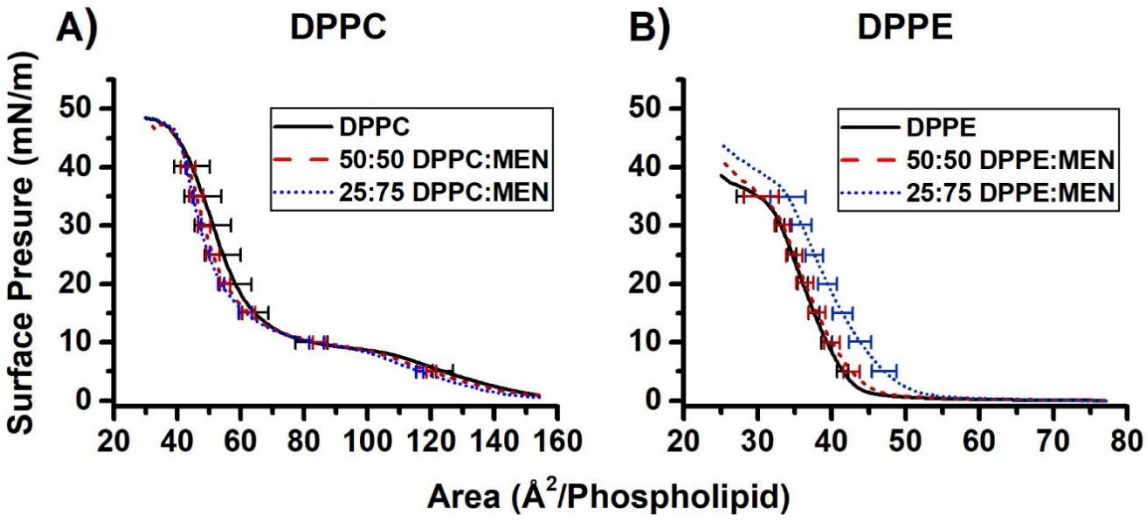

Figure 2.5. Compression isotherms of (A) DPPC and (B) DPPE with varying mol fractions of MEN as a function of area per phospholipid. Solid black curves represent DPPC or DPPE controls. Red dashed curves represent 50:50 lipid:MEN monolayers, and dotted blue curves are 25:75 lipid:MEN monolayers. Each curve is the average of a least three replicates. Error bars are the standard deviation of the area at every 5 mN/m of surface pressure.

The DPPE control curves has a shape and areas that are consistent with what is reported in the literature.[37] The curve shifts towards a greater area per phospholipid as the mol fraction of DPPE is decreased while the curve maintains its shape. These results are consistent with the possibility that MEN is located directly at the air–water interface without being compressed up into the phospholipid tails. These results support the report showing that the idebenone/idebenol pair remains at the water–lipid interface,[33] though the physical properties of the lipid or surfactant will have an effect on distribution of the molecule of interest.[40] To this effect, the packing abilities of DPPC and DPPE resulted in differing amounts of disruption by MEN, which supports that lipid composition of the cell membrane could also affect the location of lipoquinones.

3.3 MEN and MDL in the AOT RM Model Membrane System

3.3.1 MEN in Microemulsions

The solubility of MEN in aqueous solution is limited (albeit higher than MDL's solubility), but enough compound can be dissolved in D_2O that a ^1H NMR spectrum can be recorded after agitating the suspensions (Figure 2.6). The aromatic protons are in a chemical shift range well separated from the signals from the RM surfactant with the quinone proton (H_e) slightly more upfield than the benzene

protons (H_a–H_d). The aliphatic methyl group on the quinone unit on the other hand is in the range of the AOT protons around 2.3 ppm. There is a large difference between the ^{1}H NMR spectrum in D_2O and in an organic solvent such as isooctane, as shown in Figure 2.6.

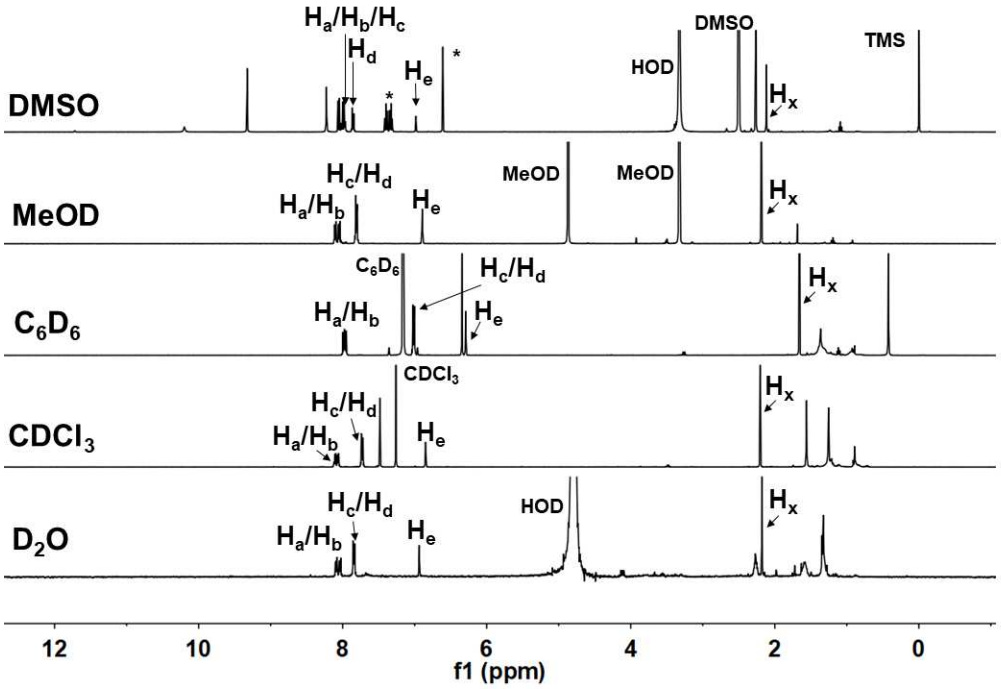

Figure 2.6. ^{1}H NMR spectra of MEN in d_6-DMSO, MeOD, d_6-benzene, $CDCl_3$, and D_2O.

3.3.2 MDL in Microemulsions

The ^{1}H NMR of MDL were recorded in a number of solvents including D_2O, MeOD, d_6- DMSO, d_6-benzene, and CDCl3, as shown in Figure 2.7. The oxidation of MDL is visually observed by the color change of the light purple MDL to the yellow MEN. Complete dissolution of MDL in D_2O, d_6-benzene, and $CDCl_3$ required incubation overnight or sonication and agitation. As a result, for the MDL samples in d_6-benzene, D_2O, and $CDCl_3$, the NMR solvent was added to solid MDL in the NMR tube and the ^{1}H NMR spectra were collected immediately. Although the rate of MDL oxidation was dependent on the solvent, the oxidation was found to be rapid in all solvents. Although some amount of the solid MDL samples was suspended in the NMR tube when the NMR spectrum was being recorded, the time it would take to dissolve the MDL sample fully would have caused significant or complete oxidation. The NMR results shown in Figure 2.7 indicate that the MDL was present in all

solvents tested regardless of the low solubility of the MDL. The ^{1}H NMR spectra of MDL show five protons in the aromatic region, with the proton on the hydroquinone group being more than 1 ppm upfield from the other aromatic protons and the aliphatic protons around 2.3 ppm. The proton most different between the MEN and MDL is the proton on the quinone or the hydroquinone, H_e. However, even recording the sample immediately after adding deuterated solvent to the NMR tube led to formation of some MEN in the samples, indicated by the * in the spectra for MDL shown in Figure 2.7.

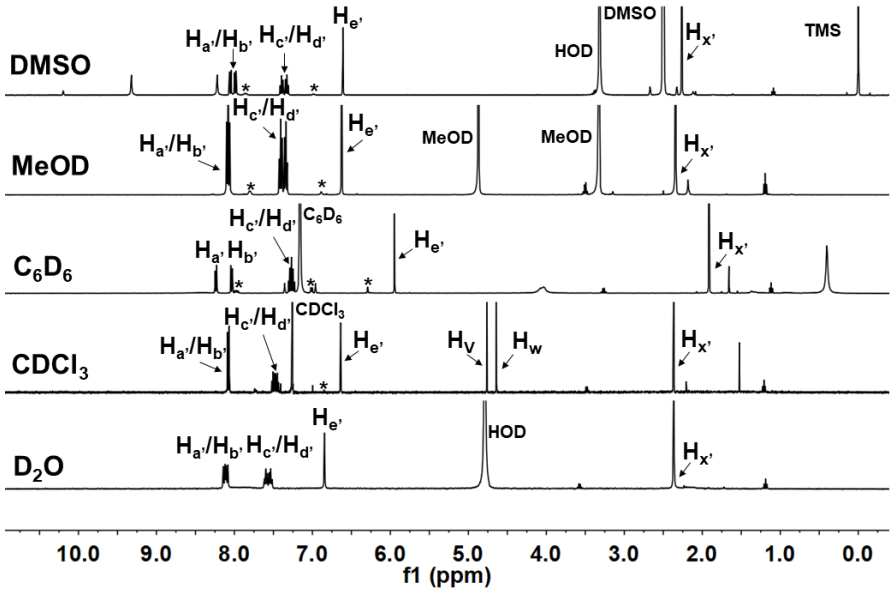

Figure 2.7. ^{1}H NMR spectra of MDL in d_6-DMSO, MeOD, d_6-benzene, $CDCl_3$, and D_2O. The signals for MEN beginning to form in these spectra are labeled with an asterisk (*).

MDL was very soluble in d_6-DMSO and MeOD. As shown in Figure 2.8, the MDL oxidized less rapidly in d_6-DMSO. The data for d_6-benzene, $CDCl_3$, and D_2O are given in Appendix II. As illustrated in Figure 2.7, it was possible to obtain spectra of not only the MDL but also the MEN that is formed in these solvents, and we show the spectra as a function of time. ^{1}H NMR spectra performed as a function of time in MeOD showed that the reduced MDL existed for about 1 h (Figure 2.8). Considering that microemulsions have been reported with “water pools” containing methanol, it was possible to record spectra of MDL in AOT reverse micelles with MeOH-containing “water pools”.[41-42]

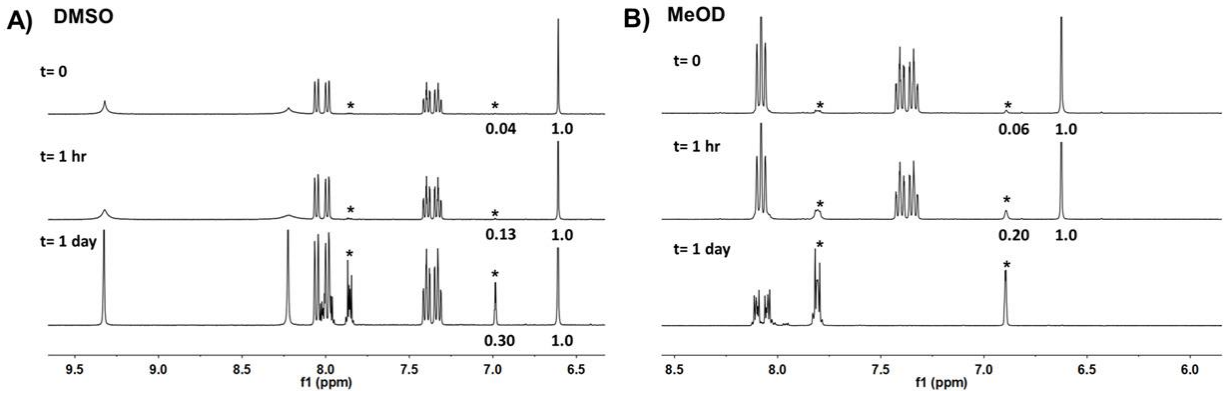

Figure 2.8. Spectra recorded of MDL as a function of time in solvents where it is readily soluble such as (A) d_6-DMSO and (B) MeOD. The increase in the ^{1}H NMR signals are due to formation of MEN and these signals are indicated by an asterisk (*).

3.3.3 Stability of MDL in RM Samples

UV–vis spectra of MDL in w_0 12 RMs were collected to assess oxidation of MDL to MEN in the RM system. As with the aqueous samples described in the above stability section, MDL was found to start oxidizing with the first 15 min of exposure to the solution, as shown in Figure 2.9. The characteristic MEN peak at 263 nm begins to appear by the fifth minute, confirming the NMR studies above in the need for a mixed solvent "water pool" to increase stability.

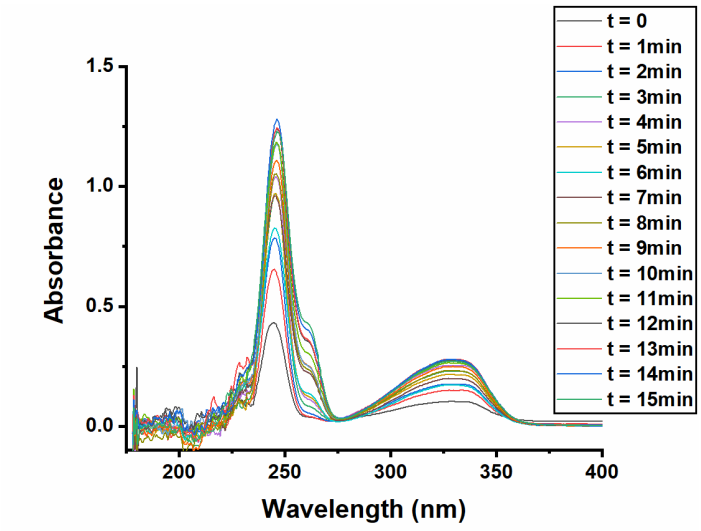

Figure 2.9. UV–vis spectra of solid MDL dissolving into a w_0 12 RM solution (0.5 mol/L AOT in isooctane) in 1 min increments over 15 min. The peak for the MDL (239 nm) increases rapidly until about 15 min, at which point a significant amount of both MDL and MEN (263 nm) have formed and the accuracy of the UV–vis spectra decreases due to experimental error.

3.4 Interactions of MEN and MDL in AOT/Isooctane RM Samples

3.4.1 MEN in Microemulsions

^{1}H NMR spectra were recorded in 0.50 mol/L AOT/isooctane to investigate the interactions of MEN with another type of model membrane interface. The w_0 sizes were varied from w_0 4 to w_0 20. The 1D ^{1}H NMR spectra show that the chemical shifts for MEN were very different from those observed in isooctane and in D_2O (Figure 2.10). The chemical shifts change for H_a was less than 0.1 ppm, whereas the shifting was 0.2 ppm for H_b and about 0.3 ppm as the quinone proton. These shifts show that MEN resides in neither the aqueous environment of the water pool, nor the organic isooctane solution, consistent with placement in the interface of the AOT RM.

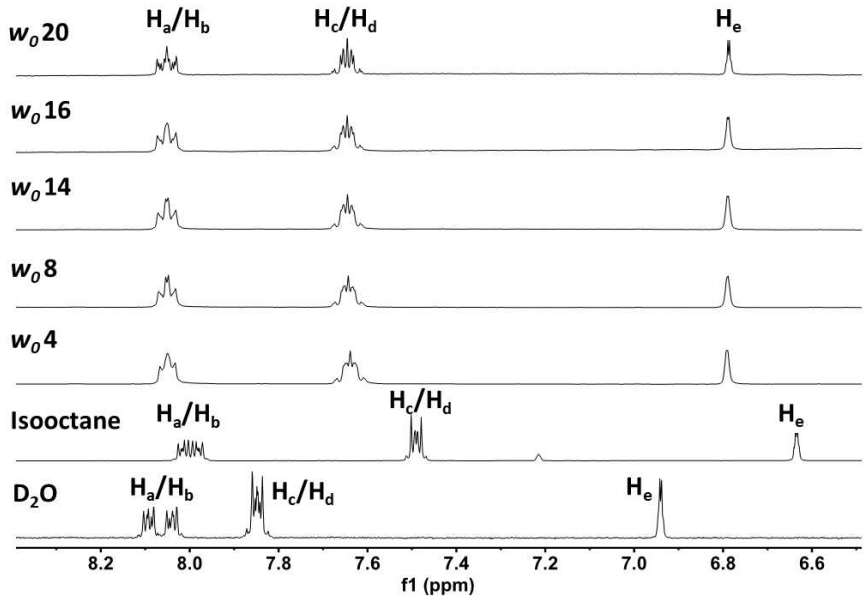

Figure 2.10. Partial ^{1}H NMR spectra of MEN in AOT/isooctane RM ranging from w_0 from 4 to 20. The ^{1}H NMR spectra of MEN in D_2O and in isooctane are shown for comparison and demonstrate that the AOT/isooctane RM environment of the MEN is very different depending on proximity to a solvent.

2D NMR spectra including NOESY and ROESY spectra (see Appendix II) were recorded for the MEN in RM samples and the partial spectra are shown in Figure 2.11. These spectra showed that proton He correlates to H_x, which serves as an internal control. Weak signals between H_a/H_b, H_c/H_d, and H_e with AOT protons H_1 and H_3 and part of the AOT CH_2 and CH_3 tail groups (H_5-H_{10}, $H_{5'}$-$H_{10'}$,

see Supplementary data for AOT labeling key) show that the placement of the MEN can vary from the headgroup to farther up in the tail region. Further investigation into whether similar conclusions could be reached with the MDL system led to the following NMR experiments.

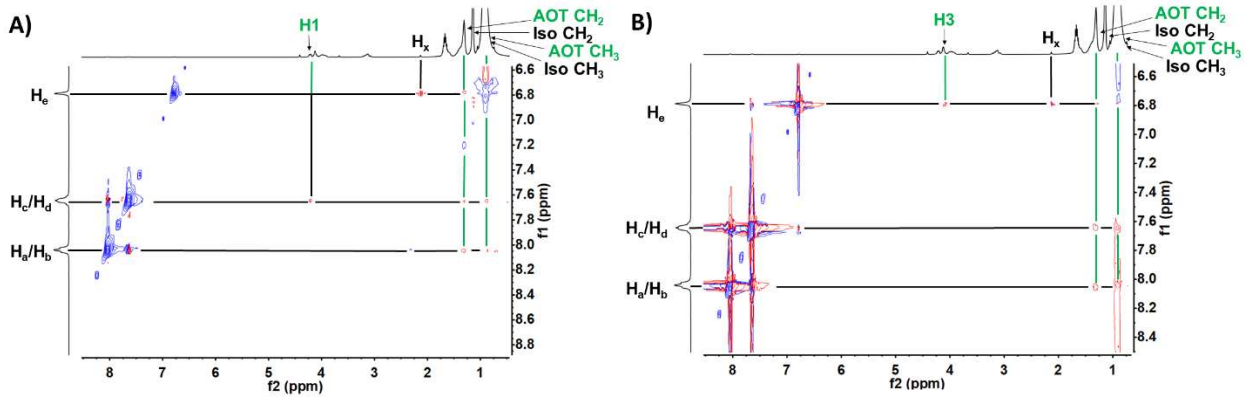

Figure 2.11. Partial ^{1}H-^{1}H 2D (A) NOESY and (B) ROESY NMR (400 MHz) spectra of MEN inside w_0 12 RM at 26 °C. Blue intensity contours represented negative NOEs or ROEs and red intensity contours represent positive NOEs or ROEs. A standard NOESY pulse consisted of 256 transients with 16 scans in the f1 domain using a 200 ms mixing time and a 1.5 s relaxation delay. A standard ROESYAD pulse consisted of 256 transients with 16 scans in the f1 domain using a 200 ms mixing time and a 2.0 s relaxation delay. Green lines indicate MEN proton interactions with AOT protons.

3.4.2 MDL in Microemulsions

Given the insolubility and instability of MDL in D_2O, an alternative co-solvent in the RM "water pool" based on MeOH/H_2O was investigated. We successfully found that MDL readily dissolved and showed an increased stability in MeOH:D_2O mixtures ranging from 70% methanol to 90% methanol. Because MeOD is known to also form RMs using AOT/isooctane,[41-42] we chose to use the mixtures with high concentrations of MeOD for better comparison with previous studies. 1D NMR studies were recorded of MDL in MeOD:D_2O mixture of AOT/isooctane. The fact that the chemical shifts of the observed protons in RMs differ from the chemical shifts of those in isooctane and MeOD:D_2O shows that the probe molecules are neither in the aqueous center or the organic outer layer; this is evidence of the probe molecules being the very least associated with the interface of the RMs (Figure 2.10). As no changes were observed in the NMR spectra as the w_0 changed (data not shown), we concluded that the MDL penetrated or associated with the interface in these MeOD:D_2O/AOT/isooctane systems. As with the aqueous stability experiments, UV–vis spectra were recorded of NMR samples prepared

from solid MDL added to the NMR tube before the MeOD:D_2O AOT RM solution was added, allowing the MDL to dissolve and then move to interact with the RM suspensions.

To obtain information on the location of the MDL, we performed 2D NMR NOESY and ROESY spectra using the w_0 16 sample in 70:30 MeOD:D_2O mixture, shown in Figure 2.12. The oxidation of MDL took place while the 2D NMR NOESY and ROESY spectra were recorded. As a result, the spectra recorded show a mixture of the MEN and MDL and the amount of MDL present depends on when the spectrum was recorded. Similar studies were performed with the 90:10 and 70:30 mixtures and these spectra gave similar patterns.

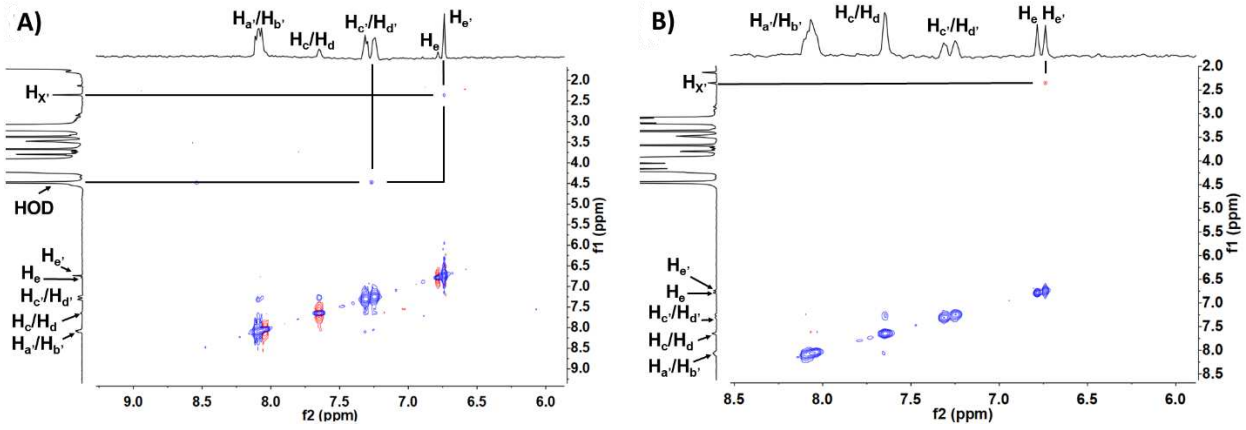

Figure 2.12. Partial ^1H-^1H 2D (A) NOESY and (B) ROESY NMR (500 MHz) spectra of MDL and MEN in a 70:30 MeOD:D2O 0.5 mol/L AOT RM suspension at 26 °C. Blue intensity contours represented negative NOEs or ROEs and red intensity contours represent positive NOEs or ROEs. A standard NOESY pulse consisted of 256 transients with 16 scans in the f1 domain using a 200 ms mixing time and a 1.5 s relaxation delay. A standard ROESYAD pulse consisted of 256 transients with 16 scans in the f1 domain using a 200 ms mixing time and a 2.0 s relaxation delay.

In Figure 2.12, there is an interaction between the internal control of $H_{e'}$ and $H_{x'}$ which shows that an NMR of MDL was obtained, but the lack of other cross peaks in the NMRs makes it difficult to determine the placement within the RM. It may be associated with the water pool, but the time span of the studies combined with the rate of oxidation of the MDL should be sufficient to observe cross peaks if there was an interaction. These results are consistent with an interaction with the interface for MEN. However, no firm conclusions can be made on the location of MDL in the RM system.

3.5 DLS

DLS confirmed that RMs were formed. The slight increase in RM size with the addition of MEN or MDL is within experimental error, suggesting that the presence of these compounds is not interfering with the formation of RMs. Data are presented in Appendix II, Table A2.3.1.

4. Discussion

MK is an important electron transport donor and accepter for bacteria, particularly pathogens like the *Mycobacterium* genus.[6, 11, 43] Despite this importance, very little experimental data are available with regard to MK's location in the cell membrane and how it moves between locations. Some experimental and computational work has been carried out with ubiquinone[14, 30, 44] while a few published computational studies have mentioned MK.[45] We have recently investigated how truncated MK derivatives interact with model membrane interfaces using both Langmuir monolayers and microemulsions. Considering the hydrophobicity of these compounds, they will undoubtedly be associated with the interface, but more experimental data detailing the nature of this association and how lipoquinones move in a lipid environment are important for future understanding of electron transfer systems.

Lipoquinones are known to shuttle electrons within cell membranes, which requires these molecules to cycle between two redox states to function. In the oxidized form, lipoquinones have a quinone headgroup, whereas the reduced form has a quinol headgroup. Quinones and quinols have different polarities, making it likely that they reside in different locations within the membrane. Current thought, however, favors the isoprenyl side chain of a lipoquinone as the main determinant of location and interaction within the membrane.[30] For lipoquinones with a larger headgroup such as MKs, it is possible that the headgroup plays a greater role than in ubiquinones. The studies in this manuscript investigate the association of MEN and MDL with two model interfaces. We anticipated that the difference in physical properties would be translated to differences in interaction and location of the compounds in the membrane bilayer.

Both MEN and MDL are hydrophobic and nearly insoluble in water. It might be expected that MDL would be more soluble than MEN due to its two hydroxyl groups. The fact that the MDL takes

longer to dissolve than MEN is not consistent with this observation (see experimental section). Furthermore, MDL only dissolved in higher concentrations with it oxidized to MEN. Generally, hydroxyl groups increase water solubility due to the increased polarity and the potential for H-bonding. This is, however, not always the case as reported previously with $[VO_2(dipic\text{-}OH)]^-$ and $[VO_2dipic]^-$ complexes.[36] Thus, spectroscopic studies for MDL were limited by rapid oxidation despite being synthesized in pure form. The most convincing MDL data were obtained in the presence of reductant or in a stabilizing organic solvent such as MeOD.

The effects of MEN on Langmuir monolayers were investigated using both DPPE and DPPC to properly characterize the interaction with different lipid interfaces. These lipids differ only in headgroup, where the choline headgroup of DPPC is a quaternary amine and the ethanolamine headgroup of DPPE is a primary amine. The different properties of these amine headgroup allow these phospholipids to fill different niches. The bulkier choline group allows for greater spreading of DPPC in conjunction with its fully saturated acyl tails, making it an ideal pulmonary surfactant.[39] The smaller ethanolamine headgroup allows for tighter packing of DPPE which is why it is more commonly found in prokaryotic membranes and the inner leaflet of eukaryotic membranes.[37-38] Our studies revealed a difference in the interaction of MEN with DPPC and DPPE. The DPPC compression isotherms showed no interaction. This implies that MEN either resides in the water or farther up into the acyl tails and thus not in the interface. The DPPE studies showed a greater area per phospholipid as the amount of MEN increased. This is consistent with MEN remaining in the interface and disrupting the ethanolamine headgroups. This is analogous to studies of idebenol and idebenol, which were found to remain in the interface.[33] Our studies also confirm that the lipid environment impacts the location and interaction of MEN in model membranes.[40]

Despite the difficulties in spectroscopic investigation of the MEN/MDL pair caused by the instability of MDL, studies were completed. We found that MEN interacted with lipids and was able to penetrate the interface. MEN was confirmed to reside in the tails by NMR. Studies with MDL were more challenging and not as clean. Although conditions were found that allowed for characterization

of the interactions of MDL with the RM interface, the 2D NMR results showed no evidence for penetration of MDL into the interface. In contrast, results showed evidence for interactions with the HOD signal. However, 1D ^{1}H NMR did show that the MDL was not in an environment akin to aqueous or organic solvent, suggesting a location in the interface. With these two pieces of evidence combined, we suggest that MDL is located at the interface near the water pool, although this and potential depth of penetration could not be confirmed. However, these results must be considered in the context of the full MK structure, where the isoprenyl side chain will impact the properties of the quinone/quinol pair.

In summary, the studies presented here show subtle differences in the location of the isolated headgroup MEN and MDL and subtle differences in the location of the isolated headgroup BEN compared with MEN in two types of model membranes, Langmuir monolayers and microemulsions. These studies provide experimental evidence that would be important to understand the location of menaquinones and menaquinols in membranes and their potential movement between membrane-bound protein complexes.

5. Summary and Conclusions

Based on structural considerations, it would not be unreasonable to expect that the MEN and MDL would occupy different locations in a membrane interface. Computational studies have been reported supporting the interpretation that lipoquinones change location in the membrane during the electron transfer process.[46] These studies also have demonstrated that the isoprenyl side chain is important for this process. We investigated the interactions and locations of the headgroups of these compounds, namely MEN and MDL, with two model membrane interface systems. We found that MEN associates with the lipid tails. The MDL system was readily oxidized, precluding any Langmuir monolayer studies. However, NMR studies of MDL in microemulsions suggest a location in the water–lipid interface, albeit no exact location was identified. Considering that these studies are of isolated headgroups, this work suggests that the headgroup, in conjunction with the isoprenyl side chain, is important for the location and interaction of lipoquinones with the cell membrane.

References

1. Koehn, J. T.; Magallanes, E. S.; Peters, B. J.; Beuning, C. N.; Haase, A. A.; Zhu, M. J.; Rithner, C. D.; Crick, D. C.; Crans, D. C., A Synthetic Isoprenoid Lipoquinone, Menaquinone-2, Adopts a Folded Conformation in Solution and at a Model Membrane Interface. *J. Org. Chem.* **2018,** *83*, 275-288.

2. Nowicka, B.; Kruk, J., Occurence, biosynthesis, and function of isoprenoid quinones. *Biochim. Biophys. Acta* **2012,** *1797*, 1587-1605.

3. Das, A.; Hugenholtz, J.; van Halbeek, H.; Ljungdahl, L. G., Structure and Function of a Menaquinone Involved in Electron Transport in Membranes of *Clostridium thermoautotrophicium* and *Clostridium thermoaceticum*. *J. Bacteriol.* **1989,** *171* (11), 5823-5829.

4. Collins, M. D., Analysis of Isoprenoid Quinones. In *Methods in Microbiology*, 1 ed.; Gottschalk, G., Ed. Academic Press: 1985; Vol. 18, pp 329-366.

5. Dhiman, R. K.; Pujari, V.; Kincaid, J. M.; Ikeh, M. A.; Parish, T.; Crick, D. C., Characterization of MenA (isoprenyl diphosphate:1,4-dihydroxy-2-napthoate isoprenyltransferase) from *Mycobacterium tuberculosis*. *PLoS ONE* **2019,** *14* (4), e0214958.

6. Upadhyay, A.; Kumar, S.; Rooker, S. A.; Koehn, J. T.; Crans, D. C.; McNeil, M. R.; Lott, J. S.; Crick, D. C., Mycobacterial MenJ: An Oxidoreductase Involved in Menaquinone Biosynthesis. *ACS Chem. Biol.* **2018,** *13* (9), 2498-2507.

7. Schwalfenberg, G. K., Vitamins K1 and K2: The Emerging Group of Vitamins Required for Human Health. *J. Nutr. Metab.* **2017,** *2017*, article 6254836.

8. Josey, B. J.; Inks, E. S.; Wen, X.; Chou, C. J., Structure-Activity Relationship Study of Vitamin K Derivatives Yields Highly Potent Neuropotective Agents. *J. Med. Chem.* **2013,** *56* (3), 1007-1022.

9. Rahn, J. J.; Bestman, J. E.; Josey, B. J.; Inks, E. S.; Stackley, K. D.; Rogers, C. E.; Chou, C. J.; Chan, S. S. L., Novel Vitamin K analogues suppress seizures in zebrafish and mouse models of epilepsy. *Neuroscience* **2014,** *259*, 142-154.

10. Chadar, D.; Camilles, M.; Patil, R.; Khan, A.; Weyhermüller; Salunke-Gawali, S., Synthesis and characterization on *n*-alkylamino derivatives of vitamin K3: Molecular structure of 2-propylamino-3-methyl-1,4-napthoquinone and antibacterial activities. *J. Mol. Struct.* **2015,** *1086*, 179-189.

11. Upadhyay, A.; Fontes, F. L.; Gonzalez-Juarrero, M.; McNeil, M. R.; Crans, D. C.; Jackson, M.; Crick, D. C., Partial Saturation of Menaquinone in *Mycobacterium tuberculosis*: Function and Essentiality of a Novel Reductase, MenJ. *ACS Cent. Sci.* **2015,** *1* (6), 292-302.

12. Kurosu, M.; Begari, E., Vitamin K_2 in Electron Transport System: Are Enzymes Involved in Vitamin K_2 Biosynthesis Promising Drug Targets? *Molecules* **2012,** *15*, 1531-1553.

13. Koehn, J. T.; Beuning, C. N.; Peters, B. J.; Dellinger, S. K.; Van Cleave, C.; Crick, D. C.; Crans, D. C., Investigating Substrate Analogues for Mycobacterial MenJ: Truncated and Partially Saturated Menaquinones. *Biochemistry* **2019,** *58* (12), 1596-1615.

14. Kaurola, P.; Sharma, V.; Vonk, A.; Vattulainen, I.; Róg, T., Distribution and dynamics of quinones in the lipid bilayer mimicking the inner membrane of mitochondria. *Biochim. Biophys. Acta* **2016,** *1858* (9), 2116-2122.

15. Quinn, P. J.; Esfahani, M. A., Ubiquinones Have Surface-Active Properties Suited to Transport Electrons and Protons across Membranes. *Biochem. J.* **1980,** *185* (3), 715-722.

16. Roche, Y.; Peretti, P.; Bernard, S., The redox state influences the interaction of ubiquinones with phospholipid bilayers. *J. Therm. Anal. Calorim.* **2007,** *89*, 867-873.

17. Möhwald, H.; Brezesinski, G., From Langmuir Monolayers to Multilayer Films. *Langmuir* **2016,** *32* (14), 10445-10458.

18. Peters, B. J.; Van Cleave, C.; Haase, A. A.; Hough, J. P. B.; Giffen-Kent, K. A.; Cardiff, G. M.; Sostarecz, A. G.; Crick, D. C.; Crans, D. C., Structure Dependence of Pyridine and Benzene Derivatives on Interactions with Model Membranes. *Langmuir* **2018,** *34* (30), 8939-8951.

19. Eskici, G.; Axelsen, P. H., The Size of AOT Reverse Micelles. *J. Phys. Chem. B* **2016,** *120* (44), 11337-11347.

20. Crans, D. C.; Rithner, C. D.; Baruah, B.; Gourley, B. L.; Levinger, N. E., Molecular Probe Location in Reverse Micelles Determined by NMR Dipolar Interactions. *J. Am. Chem. Soc.* **2006,** *128* (13), 4437-4445.

21. Koehn, J. T.; Crick, D. C.; Crans, D. C., Synthesis and Characterization of Partially and Fully Saturated Menaquinone Derivatives. *ACS Omega* **2018,** *3* (11), 14889-14901.

22. Wiebenga-Sanford, B. P.; Washington, J. B.; Cosgrove, B.; Palomares, E. F.; Vasquez, D. A.; Rithner, C. D.; Levinger, N. E., Sweet Confinement: Glucose and Carbohydrate Osmolytes in Reverse Micelles. *J. Phys. Chem. B* **2018,** *122*, 9555-9566.

23. Correa, N. M.; Silber, J. J.; Riter, R. E.; Levinger, N. E., Nonaqueous Polar Solvents in Reverse Micelle Systems. *Chem. Rev.* **2012,** *112*, 4569-4602.

24. Maitra, A., Determination of size parameters of water-Aerosol OT-oil reverse micelles from their nuclear magnetic resonance data. *J. Phys. Chem.* **1984,** *88* (21), 5122-5125.

25. Binks, B. P.; Meunier, J.; Abillon, O.; Langevin, D., Measurement of Film Rigidity and Interfactial Tension of Several Ionic Surfactant-Oil-Water Microemulsion Systems. *Langmuir* **1989,** *5* (2), 415-421.

26. Mukherjee, K.; Mukherjee, D. C.; Moulik, S. P., Thermodynamics of Microemulsion Formation. *J. Colloid Interface Sci.* **1997,** *187* (2), 327-333.

27. Van Horn, W. D.; Oglivie, M. E.; Flynn, P. F., Use of reverse micelles in membrane protein structural biology. *J. Biomol. NMR* **2008,** *40* (3), 203-211.

28. Sostarecz, A. G.; Gaidamauskas, E.; Distin, S.; Bonetti, S. J.; Levinger, N. E.; Crans, D. C., Correlation of insulin-enhancing properties of vanadium-dipicolinate complexes in model membrane systems: phospholipid langmuir monolayers and AOT reverse micelles. *Chemistry* **2014,** *20* (17), 5149-59.

29. Peters, B. J.; Groninger, A. S.; Fontes, F. L.; Crick, D. C.; Crans, D. C., Differences in Interactions of Benzoic Acid and Benzoate with Interfaces. *Langmuir* **2016,** *32* (37), 9451-9459.

30. Teixeira, M. H.; Arantes, G. M., Effects of lipid composition on membrane distribution and permeability of natural quinones. *RSC Adv.* **2019,** *9*, 16892-16899.

31. Monteiro, J. P.; Martins, A. F.; Nunes, C.; Morais, C. M.; Lúcio, M.; Reis, S.; Pinheiro, T. J. T.; Geraldes, C. F. G. C.; Oliveira, P. J.; Jurado, A. S., A biophysical approach to menadione membrane interactions: Relevance for menadione-induced mitochondria dysfunction and related deleterious/therapeutic effects. *Biochim. Biophys. Acta* **2013,** *1828*, 1899-1908.

32. Ausili, A.; Torrecillas, A.; de Godos, A. M.; Corbalán-García, S.; Gómez-Fernández, J. C., Phenolic groups of α-Tocopherol Anchors at the Lipid-Water Interface of Fully Saturated Membranes. *Langmuir* **2018,** *34* (10), 3336-3348.

33. Gómez-Murcia, V.; Torrecillas, A.; de Godos, A. M.; Corbalán-García, S.; Gómez-Fernádez, J. C., Both idebenone and idebenol are localized near the lipid-water interface of the membrane and increase its fluidity. *Biochim. Biophys. Acta* **2016,** *1858*, 1071-1081.

34. Suhara, Y.; Wada, A.; Tachibana, Y.; Watanabe, M.; Nakamura, K.; Nakagawa, K.; Okano, T., Structure-activity relationships in the conversion of vitamin K analogues into menaquinone-4. Substrates essential to the synthesis of menaquinone-4 in cultured human cell lines. *Bioorg. Med. Chem.* **2010,** *18* (9), 3116-3124.

35. Stahla, M. L.; Baruah, B.; James, D. M.; Johnson, M. D.; Levinger, N. E.; Crans, D. C., ^{1}H NMR Studies of Aerosol-OT Reverse Micelles with Alkali and Magnesium Counterions: Preparation and Analysis of MAOTs. *Langmuir* **2008,** *24* (12), 6027-6035.

36. Yang, L.; la Cour, A.; Anderson, O. P.; Crans, D. C., 4-Hydroxypyridine-2,6-dicarboxylatodioxovanadate(V) Complexes: Solid State and Aqueous Chemistry. *Inorg. Chem.* **2002,** *41* (24), 6322-6331.

37. Patterson, M.; Vogel, H. J.; Prenner, E. J., Biophysical characterization of monofilm model sytems composed fo selected tear film phospholipids. *Biochim. Biophys. Acta – Biomembr.* **2016,** *1858*, 403-414.

38. Fadeel, B.; Xue, D., The ins and outs of phospholipid asymmetry in the plasma membrane: roles in health and disease. *Crit. Rev. Biochem. Mol. Biol.* **2009,** *44* (5), 264-277.

39. Al-Saiedy, M.; Tarokh, A.; Nelson, S.; Hossini, K.; Green, F.; Ling, C.-C.; Prenner, E. J.; Amrein, M., The role of multilayers in preventing the premature buckling of the pulmonary surfactant. *Biochim. Biophys. Acta – Biomembr.* **2017,** *1859* (8), 1372-1380.

40. Baryiames, C. P.; Teel, M.; Baiz, C. R., Interfacial H-Bond Dynamics in Reverse Micelles: The Role of Surfactant Heterogeneity. *Langmuir* **2019,** *35*, 11463-11470.

41. Lu, R.; Zhu, R.; Zhong, R.; Yu, A., Locations of methanol in methanol-containing AOT reverse micelles revealed by photophysics of IR125. *J. Photochem. Photobiol. A* **2013,** *252*, 116-123.

42. Shirota, H.; Horie, K., Solvation Dynamics in Nonaqueous Reverse Micelles. *J. Phys. Chem. B* **1999,** *103* (9), 1437-1443.

43. Dhiman, R. K.; Mahapatra, S.; Slayden, R. A.; Boyne, M. E.; Lenaerts, A.; Hinshaw, J. C.; Angala, S. K.; Chatterjee, D.; Biswas, K.; Narayanasamy, P.; Kurosu, M.; Crick, D. C., Menaquinone synthesis is critical for maintaining mycobacterial viability during exponential growth and recovery from non-replicating persistence. *Mol. Microbiol.* **2009,** *72* (1), 85-97.

44. Hoyo, J.; Guaus, E.; Torrent-Burgués, J., Tuning ubiquinone position in biomimetic monolayer membranes. *Eur. Phys. J. E: Soft Matter Biol. Phys.* **2017,** *40* (62), 62.

45. Chatron, N.; Hammed, A.; Benoît, E.; Lattard, V., Structural Insights into Phylloquinone (Vitamin K1), Menaquinone (MK4, MK7), and Menadione (Vitamin K3) Binding to VKORC1. *Nutrients* **2019,** *11*, 67.

46. Galassi, V. V.; Arantes, G. M., Partition, orientation and mobility of ubiquinones in a lipid bilayer. *Biochim. Biophys. Acta* **2015,** *1847*, 1560-1573.

Chapter 3
Interactions of Truncated Menaquinones with Lipid Monolayers and Bilayers[b]

1. Introduction

Menaquinones (MK), belong to a class of molecules known as lipoquinones, or lipid-quinones. MKs are used in the electron transport system (ETS) of bacteria to generate cellular energy, such as the pathogenic *Mycobacterium tuberculosis*.[1-3] MKs consist of a naphthoquinone headgroup and an isoprenoid side chain of varying length (Figure 3.1).[4-5] We have previously found that MK's structure allows it to fold into different molecular shapes depending on environment and side chain length.[6-7] MKs must be membrane-associated to function in the ETS,[1,8,] and current knowledge regarding the interaction and conformation of MK homologues in phospholipid bilayers is limited and often conflicting. Thus, understanding MK's location, association, and conformation with membranes will ultimately provide a better understanding of bacterial energy production, which aids drug development to address the looming antibiotic resistance crisis.[9-11] MK homologues presumably reside in the hydrophobic region of the bilayer due to the hydrophobicity of the MKs, and we are seeking experimental confirmation further specifying the location of truncated MKs. Studies in model membrane systems of the structurally similar lipoquinone analogue, ubiquinone (UQ), have been used successfully to determine that UQ is located near the water interface of the membrane,[10, 16-17] though there is some debate about whether the side chain is folded or extended. We anticipate that employing similar methodology will enable us to characterize the behavior of MK homologues within membranes. In this chapter, we use a combination of experimental and computational methods to investigate the location, conformation, and disruptive potential of a series of MK homologues with varying isoprenyl side chain length (MK-1, MK-2, MK-3, MK-4) in the membrane. We used shorter MK homologues in our studies because they are less hydrophobic, which enables their study in aqueous-based systems, such as enzyme assays.[3, 18-19]

[b] This manuscript is published in full or in part in the *International Journal of Molecular Sciences.*

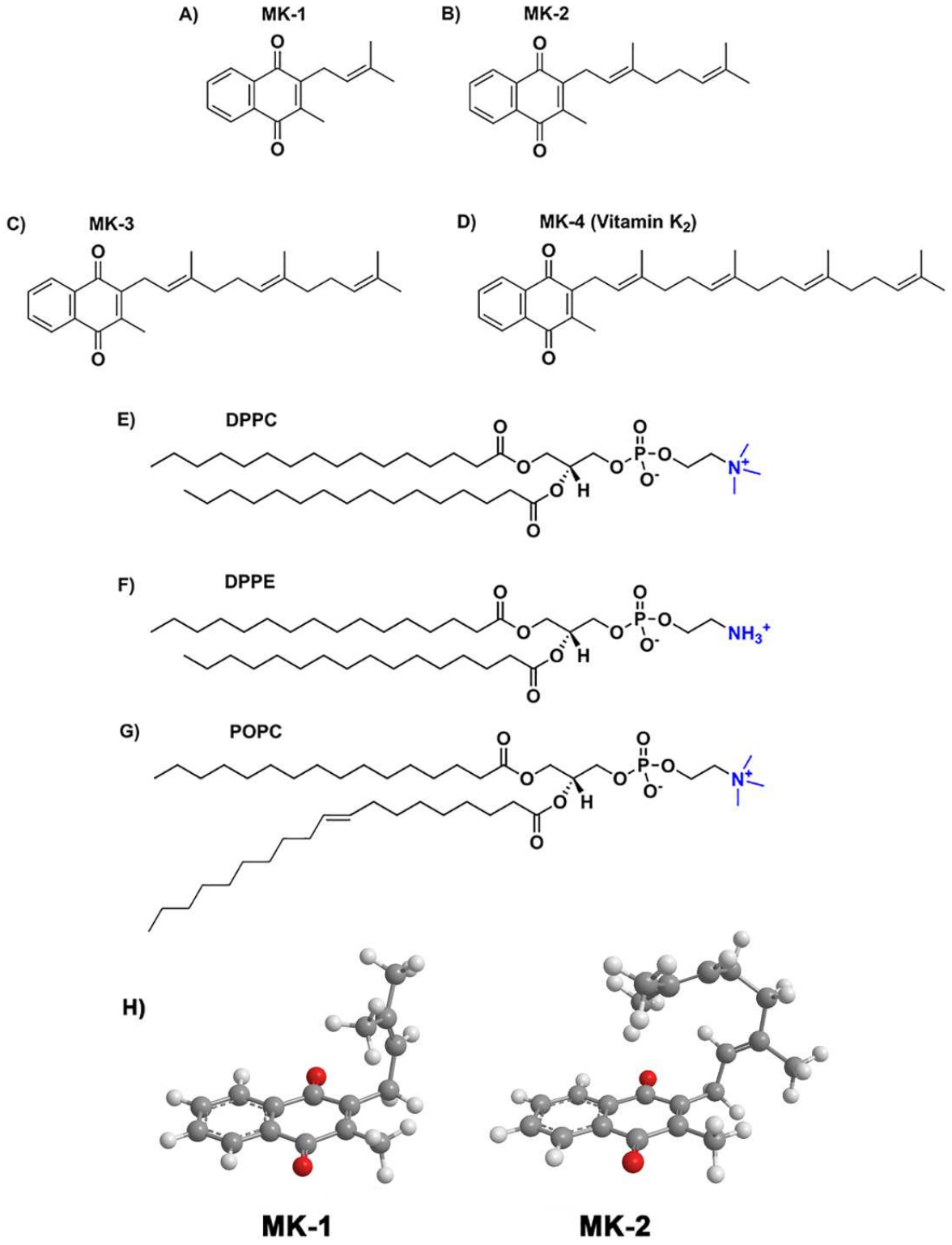

Figure 3.1. The structures of menaquinones MK-1 to MK-4 (A-D) and the lipids, E) dipalmitoylphosphatidylcholine (DPPC), F) dipalmitoylphosphatidylethanolamine (DPPE), and G) palmitoyloleyoylphosphatidylcholine (POPC) that were used. Confirmations of H) MK-1 and MK-2 in the interface of an AOT reverse micelle interface are also shown.[18-19]

Langmuir monolayers are a model membrane system that provides information on packing, disruption, and location of a target molecule in the context of a phospholipid monolayer. Langmuir monolayers consist of a single layer at the air-water interface, usually comprised of amphiphilic phospholipids or other lipid-like molecules.[20-21] In this study, we used the phospholipids dipalmitoylphosphatidylcholine (16:0 PC, DPPC) and dipalmitoylphosphatidylethanolamine (16:0 PE, DPPE), which were mixed with the hydrophobic MK homologues to form a monolayer film.[22] Previous Langmuir monolayer studies have been performed with different UQ homologues. These UQ homologues were found to expand and disrupt the packing of the phospholipids as the length of the UQ isoprenoid side chain increased until approximately physiological surface pressure (30-35 mN/m),[23] when the UQ molecules were compressed into the hydrophobic phospholipid tails.[24-26] We expect to see a similar trend with the truncated MK homologues. However, since MKs are more hydrophobic than UQs, MKs may prefer to reside farther into the phospholipid tails at lower surface pressures.

We used molecular dynamics (MD) studies to provide support for the Langmuir monolayer experimental studies.MD simulations were used to obtain a more in-depth molecular view of the location, conformational folding, and disruptiveness of the MK homologues in a simulated bilayer system. In this chapter, we used a previously validated MD bilayer system consisting of phosphatidylcholine (16:0-18:1 PC, POPC) with a single MK molecule in each membrane leaflet, which corresponds to a 2-3% concentration of MK in the phospholipid bilayer.[27-28] This is a more physiologically relevant system than what we used in the Langmuir monolayer studies. Previous MD simulations with UQ places the headgroup near the membrane interface by the phosphate group of the phospholipid with the isoprenoid side chain extended into the midplane of the bilayer.[27] We hypothesize that under physiological conditions, i) the hydrophobic MK headgroup will be located further away from the interfacial water than UQ, ii) the side chain length influences the association of MK with phospholipids, and iii) the MK homologues adopt some type of folded conformation in a membrane environment.

2. Materials and Methods

2.1 General Materials and Methods

2.1.1 Materials

Chloroform (≥99.5%), monosodium phosphate (≥99.0%), disodium phosphate (≥99.0%), sodium hydroxide (≥98%), hydrochloric acid (37%), and menaquinone-4 (MK-4, menatetrenone, vitamin K_2) were all purchased from Sigma-Aldrich. The lipids dipalmitoylphosphatidylcholine (16:0 PC, DPPC, 99%, SKU 850355P) and dipalmitoylphosphatidylethanolamine (16:0 PE, DPPE, 99%, SKU 850705P) were purchased from Avanti Polar Lipids as pure lyophilized powder. Since MK-1, MK-2, and MK-3 are commercially unavailable, they were synthesized as previously described.[6-7, 29] Distilled deionized (DDI) water was obtained by filtering distilled water through a Millipore water purification system, obtaining a resistance of 18.2 MΩ.

2.1.2 Instrumentation

The Langmuir monolayers were studied using a Kibron µTrough XS (stainless steel) equipped with a Teflon ribbon barrier.

2.2 Preparation of Solutions

2.2.1 Preparation of Subphase Solutions

The subphase consisted of 20 mM sodium phosphate buffer (pH 7.40 ± 0.02). Solutions were brought to pH 7.40 ± 0.02 with 1 M HCl or NaOH.

2.2.2 Preparation of Lipid and MK Solutions

Phospholipid stock solutions were prepared by dissolving dipalmitoylphosphatidylcholine (DPPC) (0.018 g, 0.025 nmol) or dipalmitoylphosphatidylethanolamine (DPPE) (0.017 g, 0.025 nmol) in 25 mL of 9:1 chloroform/methanol (v/v) for a final concentration of 1.0 mM phospholipid.

MK and GB stock solutions consisted of 1.0 mM MK-1 (0.0012 g, 5 nmol), MK-2 (0.0015 g, 5 nmol), MK-3 (0.0019 g, 5 mmol), or MK-4 (0.0022 g, 5 nmol) dissolved in 5 mL of 9:1 chloroform/methanol (v/v). Mixed phospholipid:MK solutions were created by mixing appropriate amounts of phospholipid and MK stock in a 2 mL glass vial to create a final volume of 1 mL and

vortexing until combined. Final molar fractions of mixes (phospholipid:MK) were 0:100, 25:75, 50:50, 75:25, or 100:0.

2.3 Langmuir Monolayer Studies

2.3.1 Preparation of Phospholipid Langmuir Monolayers

The buffered aqueous subphase consisted of 50 mL of 20 mM sodium phosphate buffer (pH 7.40 ± 0.02) in DDI water (18.2 MΩ). The subphase surface was cleaned via vacuum aspiration until a quick compression of the subphase provided a surface pressure which was consistently 0.0 ± 0.5 mN/m throughout compression. A total of 20 µL of phospholipid stock solution (20 nmol of lipid) was then added to the surface of the subphase in a dropwise manner using a 50 µL Hamilton syringe. The monolayer was allowed to equilibrate for 15 minutes.

2.3.2 Compression Isotherm Measurements of Langmuir Monolayers

The phospholipid monolayer was compressed from two sides with a total speed of 10 mm/min (5 mm/min from opposite sides). The temperature was maintained at 25 °C using an external water bath. The trough plate was scrubbed three times with isopropanol, then three times with ethanol, then rinsed with DDI water (18.2 MΩ) before each experiment. The ribbon barrier was rinsed with isopropanol followed by ethanol and then water. The surface tension was monitored via Wilhemy plate technique where a steel wire was used as the probe instead of a plate. The surface pressure was calculated from the surface tension using Equation 1, where π is the surface pressure, γ_0 is the surface tension of water (72.8 mN/m), and γ is the surface tension at a given area per phospholipid after the monolayer has been applied.

$$\pi = \gamma_0 - \gamma \qquad \textbf{Equation 1}$$

Each compression isotherm experiment consisted of at least three replicates. The averages of the area per phospholipid and the standard deviation at every 5 mN/m were calculated using Microsoft Excel. The worked-up data were then transferred to Origin 2021 to be graphed with error bars.

2.3.3 Ideal Mixing Calculations

The ideal mixing was calculated at every 1 mN/m of surface pressure with Equation 3, where A_i is the ideal mixed area (Å^2), x_{MK} is the mol fraction of MK, A_{MK} is the area per molecule (Å^2) of the control MK monolayer, x_{PL} is the molar fraction of DPPC or DPPE, and A_{PL} is the area per molecule (Å^2) of DPPC or DPPE. The possible mol fractions were 0.25, 0.5, or 0.75.

$$A_i = x_{MK}A_{MK} + x_{PL}A_{PL} \qquad \textbf{Equation 3}$$

2.3.4 Brewster Angle Microscopy

Brewster angle microscopy (BAM) images were obtained using a Biolin NIMA medium trough equipped with a MicroBAM (659 nm laser). Differing amounts of 2 mM stocks of MK-1 (800 nmol), MK-2 (120 nmol), MK-3 (80 nmol), and MK-4 (80 nmol) were applied to the subphase and allowed to equilibrate for 15 minutes before compression. The compression parameters are the same as above.

2.4 Molecular Dynamics Simulations

We employed a previously developed fully hydrated POPC (16:0-18:1 phosphatidylcholine) bilayer model system and added MK molecules (one MK in each layer, corresponding to a ~2-3% concentration), composed of n = [1-4] isoprenoid units (MK-1 through MK-4, Figure 3.1A-1D). Symmetric lipid bilayers were built containing 126 molecules of POPC and 7794 water molecules which have been previously characterized to represent a biological membrane.[27] NaCl was added until a final concentration of 150 mM was achieved. The protocol described by Javanainen was used to insert one MK-4 in each layer of the membrane.[30] The system was relaxed by a 50 ns MD run, and mean area and bilayer thickness were monitored to check for equilibration. Initial configurations for MK-1, MK-2 and MK-3 systems were derived from an equilibrated configuration from MK-4 system by deleting tail atoms and adapting the atomic connectivity to generate MK-1, MK-2, and MK-3. Conformations were sampled using classical molecular dynamics (MD) simulations were performed with GROMACS version 2020.3 [31] and the CHARMM36 force-field.[32-33] Parameters for MKs were obtained by us previously.[27-28] Water was described by TIP3P [34] and the NPT ensemble was used. Temperature was kept at physiological temperature (37℃, 310 K) with a Bussi thermostat [35] and a

coupling constant of 0.1 ps. The pressure was kept at 1.0 bar with Parrinello-Rahman barostat for productive runs [36] with a coupling constant of 1 ps and a compressibility of 0.5 10^{-5} bar^{-1}. Semi-isotropic coupling was applied. Electrostatic interactions were handled by Particle-Mesh Ewald (PME)[37] with grid spacing of 0.14 nm and quartic interpolation. All bonds were constrained using the LINCS algorithm.[38] No dispersion corrections were applied.[39] The integration time step was 2 fs and MD run 200 ns for equilibration MD was run for 200 ns. Trajectories with 350 ns were collected for MK-1, MK-2 and MK3 and with 750 ns for MK-4.

3. Results

3.1 Compression Isotherm Studies of MKs in Langmuir Monolayers

Compression isotherms of Langmuir monolayers consisting of phospholipids were obtained to provide insight into the interactions between the truncated MK-1 through MK-4 with both DPPC and DPPE phospholipids. Langmuir monolayers are often investigated to examine the ability of a molecule to penetrate an interface, disrupt packing, and affect the elasticity of the monolayer.[7, 40-42] We have previous reported compression isotherms of mixed films in terms of area per molecule for MK-1 and MK-2.[6-7] The Langmuir monolayer data may be analyzed differently depending on the system of interest (hydrophobic vs hydrophilic target molecule). Here, we normalized to the area per phospholipid because that allows for more facile interpretation of the results and comparison between multiple compounds such as MK-1, MK-2, MK-3, and MK-4. A similar analysis was previously used by Quinn and Esfahani in 1980.[43]

3.1.1 Compression Isotherms and Brewster Angle Microscopy of Pure MK Films

The pure MK-2 monolayer reached a maximum pressure of ~ 13 mN/m (figure 3.2B). This result is slightly lower than previously reported (20 mN/m).[7] As found in previous studies, target MK homologues can undergo varying degrees of aggregation and are likely to cause small differences between reported MK experiments.[7] The pure MK-3 monolayer collapsed at 12 mN/m and the pure MK-4 monolayer reached a maximum pressure of 13 mN/m. A potential decrease in collapse pressure

of these MK homologues as the isoprene side chain length increased was experimentally indistinguishable in contrast to the larger differences reported with UQs.[43]

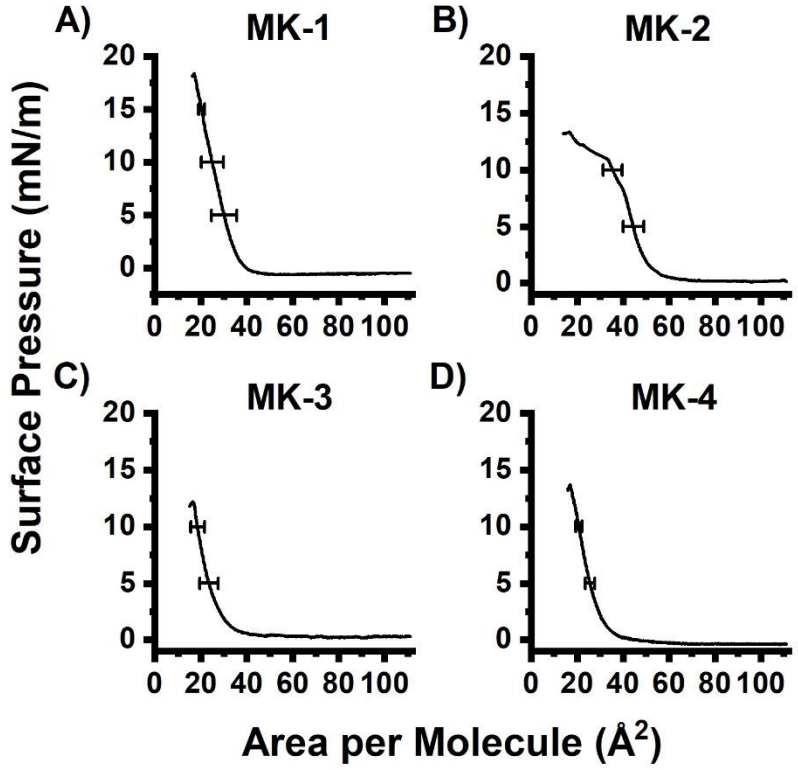

Figure 3.2. Compression isotherms for pure films of (A) MK-1, (B) MK-2, (C) MK-3, and (D) MK-4. Curves are the average of at least three replicates. Error bars represent the standard deviation of the area.

We sought verification that a film was formed because the surface pressure of the MK homologues did not begin rising until ~ 40 Å^2/molecule. Hysteresis studies were therefore performed on pure MK films to determine stability (see Appendix III). All truncated homologue films showed a decreased surface area with each compression cycle, which confirmed the formation of films Figure A3.2.1). The decreased surface area demonstrates that MK films are all unstable and inelastic. A decrease in observed surface area may indicate that MKs are either self-aggregating or dissolving into the aqueous subphase. We anticipated that the most soluble MKs would form the least stable films due to the compound continually dissolving into the subphase. In the hysteresis studies, the most elastic films are those films which are able to compress and expand multiple times and remain the

same, and as such are more stable. We would have anticipated that MK-1 and MK-2 formed less elastic films due to their ability to dissolve into the subphase. However, even though MK-1 and MK-2 are more soluble in aqueous solution, they formed more elastic films. Both MK-2 and MK-3 formed less stable films, which implies that self-aggregation is a more important contributor to film elasticity than solubility.

We obtained BAM images of MK homologues in order to visualize the surface morphology of MK films, Figure 3.3. At the start of compression, a gray surface was observed, which indicates no organization. Upon reaching pressures > 7 mN/m (collapse point in Figure 3.2), white circular features were observed, which indicates aggregation. In Figure 3.3A, we show a Bam image of MK-1 that documented some aggregation occurred. Ten times the amount of MK-1 relative to MK-3 and MK-4 was needed to obtain meaningful BAM images. This may be due to MK-1 dissolving into the aqueous subphase.[6] Images of MK-2, MK-3, and MK-4 demonstrate that the surface was densely covered with MK aggregates. It is clear from these images that MK-1 behaves differently from the other three MK homologues.

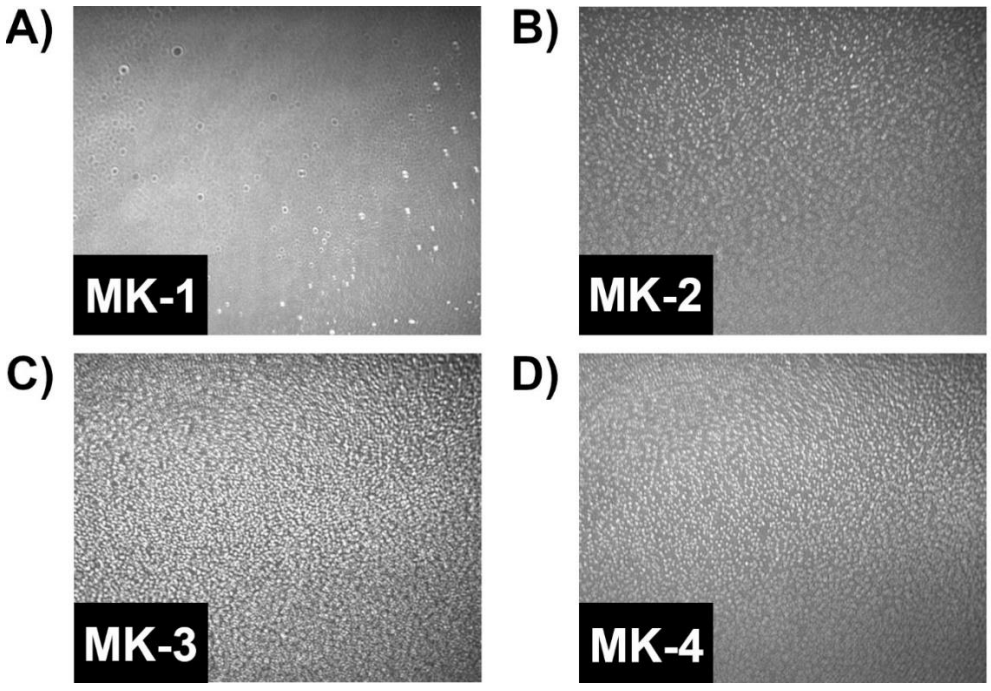

Figure 3.3. BAM images of pure MK films demonstrating the droplet-like structures formed between 7.5 mN/m and 13 mNm of surface pressure during compression. Images A) MK-1 (800 nmol), B) MK-2 (120 nmol), C) MK-3 (80 nmol), and D) MK-4 (80 nmol) were captured at 12.5 mN/m, 10.0 mN/m, 11,8 mN/m, and 10.7 mN/m, respectively. Each panel is 2387 x 1925 µm. Images in this figure were cropped from raw images (640 x 480 px) to a final size of 382 x 308 px. All images were cropped from the upper right corner for consistency. Cropped images were then scaled up to 720 x 582 px. All image manipulation was done in GIMP 2.10.22.

Geranyl bromide (*trans*-1-bromo-3,7-dimethyl-2,6-octadiene, Figure 3.4A) was used to further investigate a surface inactive compound that shares structural similarity to MK. Geranyl bromide is a relatively surface-inactive molecule that contains a two-unit isoprenoid chain and a bromine atom in place of a headgroup, which provides an appropriate comparison for MKs. The related farnesol (containing three isoprene units) and a farnesyl diphosphate have been reported to favor extended conformation in a number of solvent and in x-ray structures coordinated in proteins.[44] When geranyl bromide was applied to the air-water interface and compressed, the surface pressure remained at 0 mN/m until the end of compression when it rose to ~ 3 mN/m (Figures 3.4B and 3.4C). The surface pressure of geranyl bromide was significantly lower than the pure truncated MK films (10-17 mN/m). Given this information, MKs are surface-active but are unable to form a stable-elastic film. These compression isotherms and hysteresis studies confirmed that MK-1 through MK-4 form films, but the films are inelastic. In contrast, geranyl bromide, which lack a headgroup, did not form a film.

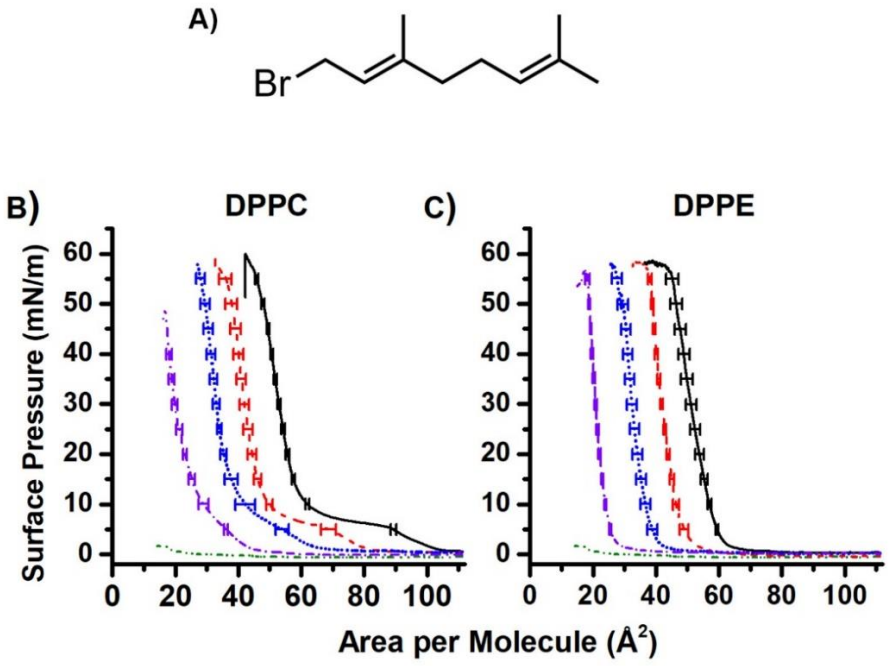

Figure 3.4. A) The structure of geranyl bromide, consisting of two isoprene units with a bromine headgroup. Panel B) shows compression isotherms of geranyl bromide and DPPC, while panel C) shows compression isotherms of geranyl bromide with DPPE. Solid black curves represent either pure DPPC or DPPE. Red dashed curves show 75:25 phospholipid:geranyl bromide films. Blue dotted curves are 50:50 phospholipid:geranyl bromide films. Purple dash-dot curves are 25:75 phospholipid:geranyl bromide films. Green dash-dot-dot curves are pure geranyl bromide films.

At high geranyl bromide concentrations above 50% molar fraction, a disappearance of the gas-liquid transition in DPPC was observed (0-6 mN/m). While geranyl bromide is relatively surface inactive, it is likely affecting the packing of the model membrane at low surface pressure, but not physiological pressure.

3.1.2. Compression Isotherms of Normalized Mixed MK/Phospholipid Films

The compression isotherm were measured for MK-1, MK-2, MK-3, and MK-4 and the normalized compression isotherm curves for the mixed monolayers of MK-1, M-2, MK-3 and MK-4 were replotted as a function of area per phospholipid, Figure 3.5. Normalization was calculated by using Equation 4 where A_N is the normalized area per phospholipid ($Å^2$), A is the measured area per molecule ($Å^2$), and x is the molar fraction of phospholipid (0, 0.25. 0.5, or 0.75, or 1).

$$A_N = A(x^{-1}) \qquad \textbf{(Equation 4)}$$

Mixed films of MK-1 and DPPC show an overall increase in area as molar fraction of MK-1 increases, though the 75:25 and 50:50 lipid:MK-1 curves are similar (Figure 3.5A). The typical gas-liquid transition (0-6 mN/m) seen in the pure DPPC curve disappears in the mixed monolayers. In addition, the 25:75 DPPC:MK-1 film did not undergo a full collapse (end of compression where there is no longer a monolayer). This trend is also seen with mixed films containing MK-2, MK-3, and MK-4. In addition, increasing amounts of MK were found to increase the compressibility of both DPPC and DPPE mixed monolayers by compression modulus analysis (see Supplemental Information).

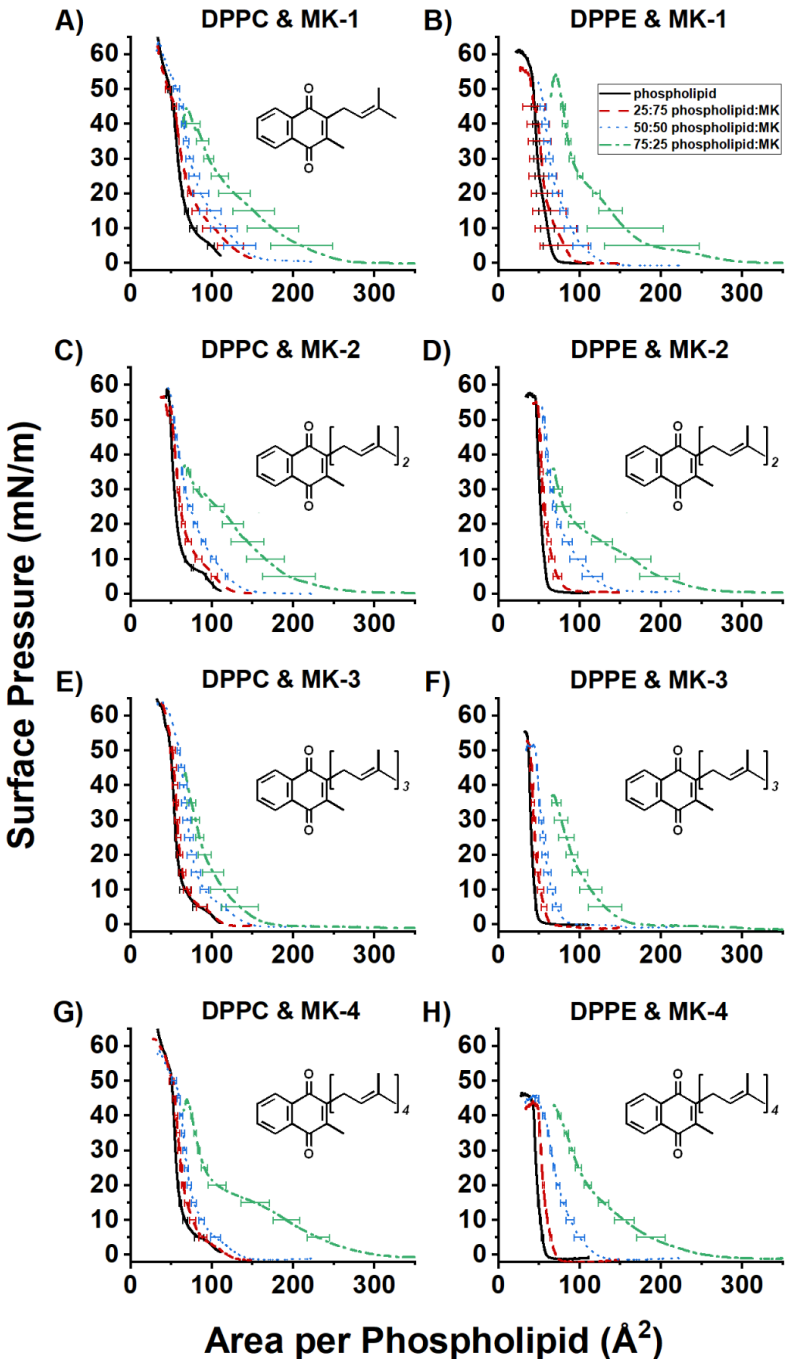

Figure 3.5. Normalized compression isotherms of mixed monolayers of either DPPC (left column) or DPPE (right column) with MK-*n*. Panels (A) and (B) are MK-1, (C) and (D) are MK-2, (E) and (F) are MK-3, and (G) and (H) are MK-4. Pure phospholipid monolayers are represented with solid black curves, 75:25 phospholipid:MK with red dashed curves, 50:50 phospholipid:MK with blue dotted curves, and 25:75 phospholipid:MK with green dash-dot curves. Each curve is the average of at least three trials. Error bars represent the standard deviation of the area at every 5 mN/m of surface pressure. Data for MK-1 and MK-2 were previously reported.[6-7]

Studies with DPPE are more difficult to interpret because there is only one phase change. Therefore, we will only focus on large differences between the data. Overall, gentler slopes were observed with increasing molar fractions of all MK molecules with DPPE. However, the 50:50 and 75:25 DPPE:MK-4 films exhibited a liquid condensed phase from 1 mN/m to 17 mN/m. The liquid condensed phases seen in the DPPE-MK-2 and DPPE-MK-4 mixed films indicate an expansive effect, which is observed in literature with UQ.[45-46] This expansion at lower surface pressure may be due to aggregation and/or conformation of the MK homologues. Interestingly, for both DPPC and DPPE, the mixed corves tended to overlap the control curve at physiological surface pressure (30-35 mN/m).[23] This has previously been reported with UQ and was interpreted as the lipoquinone migrating into the phospholipid tails.[24] These studies confirm the interpretation that MK homologues reside slightly higher in the interface than UQ, thus confirming our initial hypothesis that MKs would reside further into the interface than UQ in model membranes.

3.2 Ideal Mixing of MK and DPPC or DPPE

Ideal mixing calculations were performed to elucidate whether or not any interactions were occurring between phospholipids and MK homologues, as well as the differences in free energy of the films, Figure 3.6. The ideal mixing was plotted to show where the ideal and experimental fall relative to both the MK and phospholipid control (plotted using un-normalized data). Assuming no interactions between the two components of the film, the experimental film will match the calculated ideal. Ideal mixing curves for 50:50 phospholipid:MK mixtures are presented in the main text as representative results while curves for 25:75 and 75:25 phospholipid:MK mixtures are shown in Appendix III (Figure A3.5.1 and Figure A3.5.2).

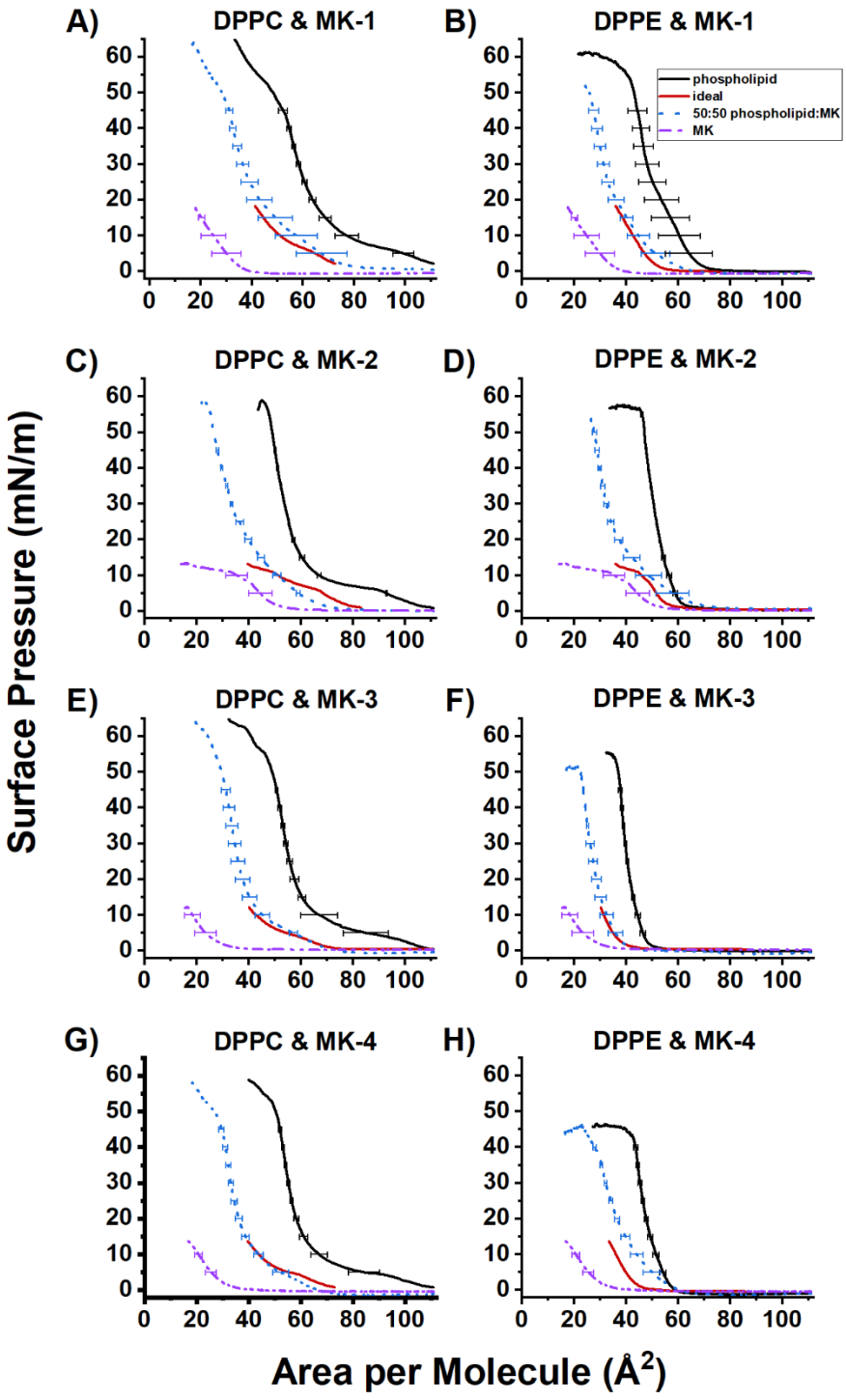

Figure 3.6. Ideal mixing of 50:50 phospholipid:MK films compared to experimental data. DPPC films are in the left column. DPPE films are in the right column. (A) and (B) show MK-1 mixed films, (C) and (D) show MK-2 mixed films, (E) and (F) show MK-3 mixed films, and (G) and (H) show MK-4 films. Solid black curves are pure phospholipid monolayers. Blue dotted curves represent experimental 50:50 phospholipid:MK films. Solid red curves represent calculated ideal mixed films. Purple dash-dot-dot curves represent put MK films.

The general trend of the 50:50 DPPC:MK films indicate ideal mixing, in that the experimental curves do not deviate significantly from the ideal. As such, DPPC and the MK homologues likely do not interact directly with each other. In the DPPE films, the 50:50 mixture containing MK-4 is expanded relative to the ideal mixing area. This suggests that MK-4 is able to associate with DPPE, possibly due toc onformational folding and molecular shape. We sought further mean of computationally investigating molecular reasoning for this, specifically MD simulations.

Langmuir monolayers studies were studied at molar fractions well above the biological molar fraction in order to be able to observe the effects of MKs on the DPPC and DPPE films.[9] As such, it is not clear whether these observed effects in the monolayers are relevant to effects observed within bilayers and native membranes. We hypothesized that conformation might be important for the exact method of disruption between phospholipids and MK homologues. We investigated this question us a computational model to probe the MK conformation in a physiologically relevant bilayer system.

3.3 Molecular Dynamic Simulations of MKs in a Membrane Bilayer

Computational studies were performed to determine the location, association, and conformation of MK homologues in a bilayer at physiological concentrations. We modeled fully hydrated bilayers based on the lipid phosphatidylcholine (POPC, 16:0-18:1 phosphatidylcholine) mixed with one MK molecule in each layer, which correspond to a ~2-3% concentration of MK-1, MK-2, MK-3, or MK-4 (Figure 3.7A). Classical MD simulations were done with the CHARMM36 force field where the parameters for menaquinones developed previously.[27-28]

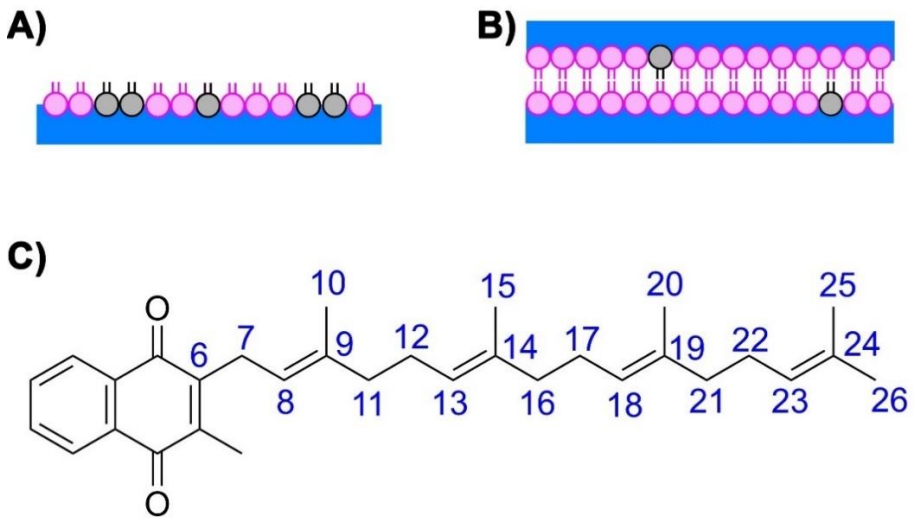

Figure 3.7. Cartoons of different model membrane systems as well as the numbering of carbons for computational studies. A) Illustration of the monolayer system with a mix of phospholipid (pink) and MK 9grey). B) Illustration of a bilayer system with a molecule of MK in each leaflet of the bilayer. C) Labeling scheme of MK-1 of MK-4 (MK composed of n = [1-4] isoprenoid units) used in computational studies. The terminal carbon (CT) groups on MK-1 are labeled 10 and 11, the CT groups on mK-2 are labeled 15 and 16, the CT groups on MK-3 are labeled 20 and 21, and the CT groups on MK-4 are 25 and 26.

The Langmuir monolayer studies showed that at lower concentration (25% molar fraction), the MK homologues were associated with the monolayer film. However, at higher concentrations the MK-homologues were compressed out of the film (Figure 3.5). In the computational studies with a phospholipid bilayer, in no example was the MK homologue compressed out from the phospholipid bilayer at physiological conditions. The lack of MK exclusion from the bilayer is likely due to two reasons: i) lower MK concentrations similar to those existing under biological conditions were investigated and ii) a finite simulation time (350-750 ns) was used, which may not be enough time to sample the water-phospholipid partition process.[9]

Figure 3.8 details the position of the MK headgroup in the bilayer in terms of center of mass. The plot shows the distance from the center of the membrane (0 nm) and the interface as indicated by the POPC phosphate group's center of mass at about 2 nm. As shown in the plot for MK-1, MK-2, MK-3, and MK-4, the centers of mass for the MK headgroups were all located around 1.3 nm. The small variations in peak position are not statistically significant. Thus, the MK headgroups are about 0.7 nm into the interface and below the water-phospholipid interface as defined by the lipid phosphate

(2 nm). Our simulations show that the MK headgroups will have the same location in the membrane, regardless of differences in hydrophobicity, length of the MK side chain, and the ability to disrupt the membrane. These studies are in line with previous simulations of UQ in POPC and mixed bilayers,[27-28] and suggest that these lipoquinone headgroups are both located in a similar membrane region, about 0.5 nm below UQ (z = 1.8 nm) toward the membrane midplane. These data also support the interpretation that for truncated MK homologues, the headgroup anchors the location of the MK homologue slightly farther into the membrane than that of UQ (MK z = 1.3 nm, UQ z = 1.8 nm, POPC phosphate z = 2 nm).[27-28] The placement of MK in a more hydrophobic region compared to UQ is consistent with Langmuir monolayer findings that placed the MK homologues in the phospholipid tails at physiological surface pressure. In addition, there was no appreciable disruption to the permeability of the bilayer, which is in agreement with previous studies.[27-28]

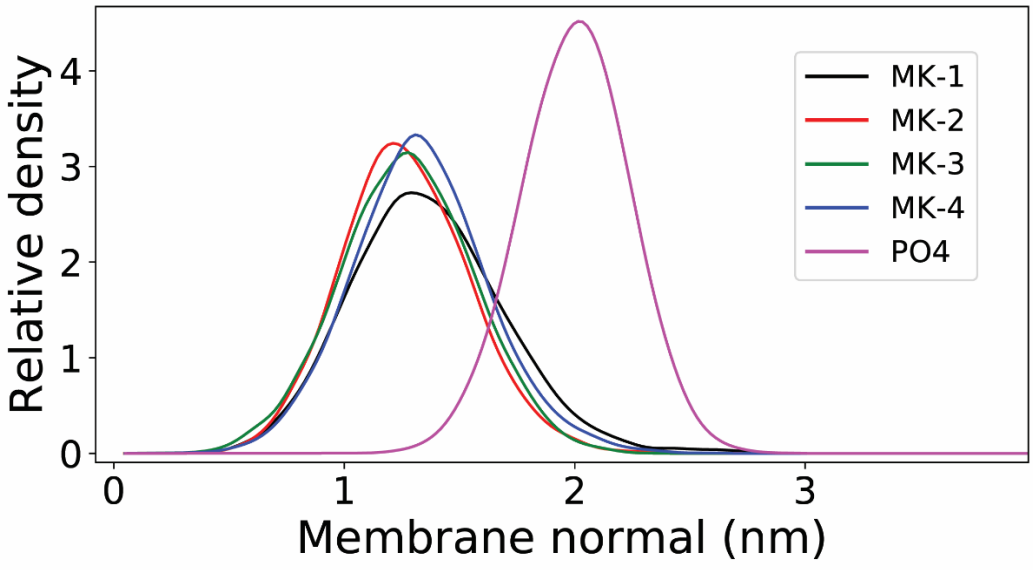

Figure 3.8. Mass density of the MK naphthoquinone headgroup along the membrane normal for MK-1 (black, MK-2 (red), MK-3 (green), and MK-4 (blue. The phosphate group of POPOC (PO4) is shown in magenta. Data from both layers were symmetrized. The normal zero corresponds to the center of the bilayer.

The MD studies provided a quantitative representation of the conformation and distribution of the dihedral angles of the side chain of MK-1 through MK-4 in a simulated phospholipid bilayer (Figure 9). Rotation around the C6-C7 bond was restrained in all MK homologues due to steric restriction

limiting rotation. Specifically, the methyl group on the naphthoquinone headgroup and the sp^2 hybridization of the C6 atom limit the rotation around the C6-C7 bond. Thus, this torsional angle is ± 110° (Figure 3.9A). Rotation around the C7-C8 bond was freer than around the C6-C7 bond but still somewhat restrained due to the methyl group on the naphthoquinone headgroup and the sp^2 hybridization of C8. The bond angle was often ± 120°, indicating folding, but the *trans* (180°, extended) configurations are also present in Figure 3.10B.

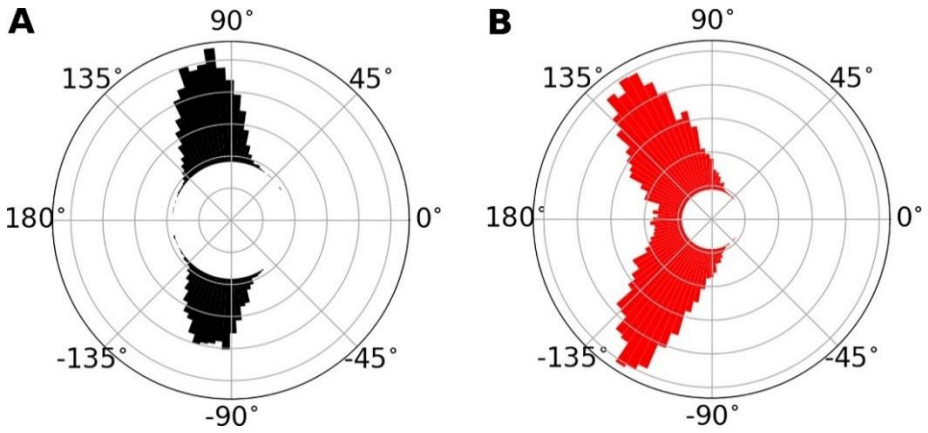

Figure 3.9. Polar plot showing distributions of dihedral angles rotating around the C6-C7 bond (panel A) and the C7-C8 bond (panel B) observed in the MD simulation of MK-4 located in the lipid POPC bilayer. Interestingly, the energy function observed when rotating around the C6-C7 bond is not symmetrical because the molecular shape is not symmetrical. Steric repulsions to the ring substitutions are directional as described previous in detail.[27]

Torsional angle distributions of corresponding rotations around C6-C7 and C7-C8 bonds similar to Figure 3.9 were observed for all MK derivatives studied here. However, MK-2, MK3, and MK-4 contain longer tails and additional C-C bonds, which are more flexible than MK-1. Figure 3.10A shows a *trans* (extended) conformer in which the C11-C12 torsional angle is ± 180°. Figure 3.10B shows that the *gauche* (folded) conformer, in which C11-C12 torsional angle is ± 60° which will allow for partial folding of the side chain over the naphthoquinone headgroup. Overall, truncated MK homologues undergo some amount of folding in a phospholipid bilayer.

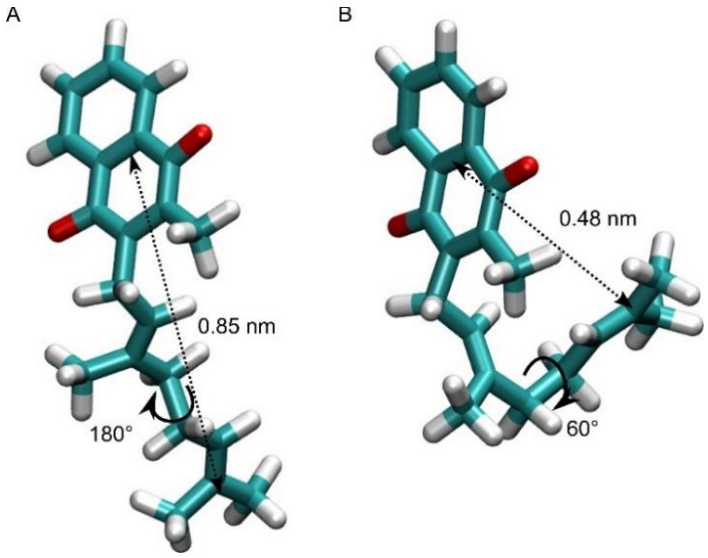

Figure 3.10. Two representative conformers observed for the MK-2 MD simulations in POPC lipid bilayer. Torsion around the C11-C12 bond modulates the distance between the terminal CH_3-carbon labeled CT and the center of the naphthoquinone ring, termed here d(CT-H). Panel A shows a *trans* conformer with a long distance and panel B, a *gauche* conformer with a much smaller distance.

Figure 3.11 shows the distances (termed d(CT-H)) generated through rotation of the dihedral angle between the terminal CH_3 group (CT) C2-C3 (UQ numbering) bond in the middle of the naphthoquinone headgroup; the different distances are observed due to rotations around the C11-C12 bond. The panels in Figure 3.11 all show conformations with angles in *trans* (~180°, extended) are more populated than conformation with *gauche* (± 60º, folded) geometry for all MK-2, MK-3, and MK-4. However as shown in Figure 3.11 for MK-3, the relative population of *gauche* is significantly lower than for MK-2 or MK-4.

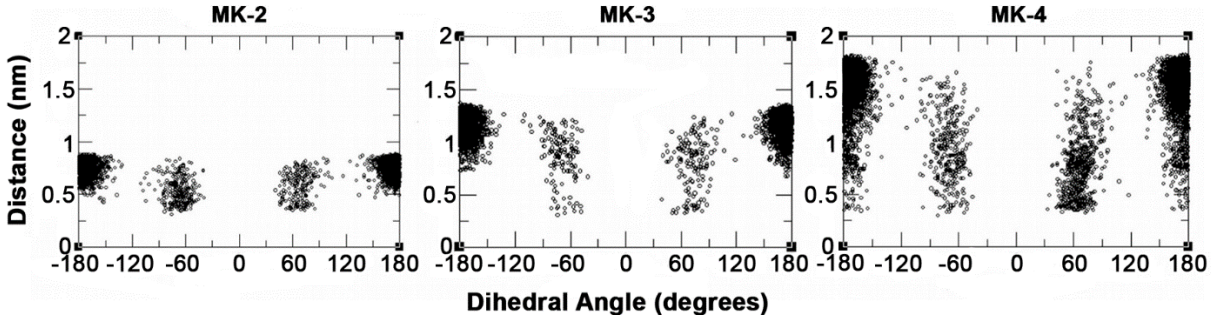

Figure 3.11. Plots of the distance between the terminal CH_3 groups in MK-2, MK-3 or MK-4 to the middle of the quinone ring**,** d(CT-H), as obtained when the dihedral angle is changing as the rotation around the C11-C12 bond takes place.

Figure 3.12 summarizes the population distribution of the terminal carbon from the C-C bond in the middle of the headgroup for all MKs. As the isoprenoid chain length increases, there is the potential for a greater distance between the terminal carbon and the headgroup. Since MK-1 has limited length and rotation, the entire distribution occurred within a small range of distances. MK-2 can reach d(CT-H) < 0.5 nm only when C11-C12 is in *gauche* conformation. In the case of MK-3 and MK-4, short distances could be reached when C11-C12 was in *gauche* or *trans* because their isoprene chains contain additional rotatable C-C bonds and are long enough to fold back over the naphthoquinone headgroup. Figure 3.11 also shows that d(CT-H) > 0.7 nm when C11-C12 in MK-3 is *trans*. Even when in *gauche*, fewer MK-3 conformers will have smaller d(CT-H). MK-4 may reach d(CT-H) < 0.5 nm when C11-C12 is *trans* due to increased side chain length and flexibility of the additional isoprene units. As demonstrated in Figure 3.10, C11-C12 torsion in gauche allows the side chain to partially fold upon itself and, thus, a lower d(CT-H) was obtained. Similar results (data not shown) are obtained if we examine the equivalent torsions for bonds closer to the terminal carbon, such as the C16-C17 bond in MK-3 and MK-4.

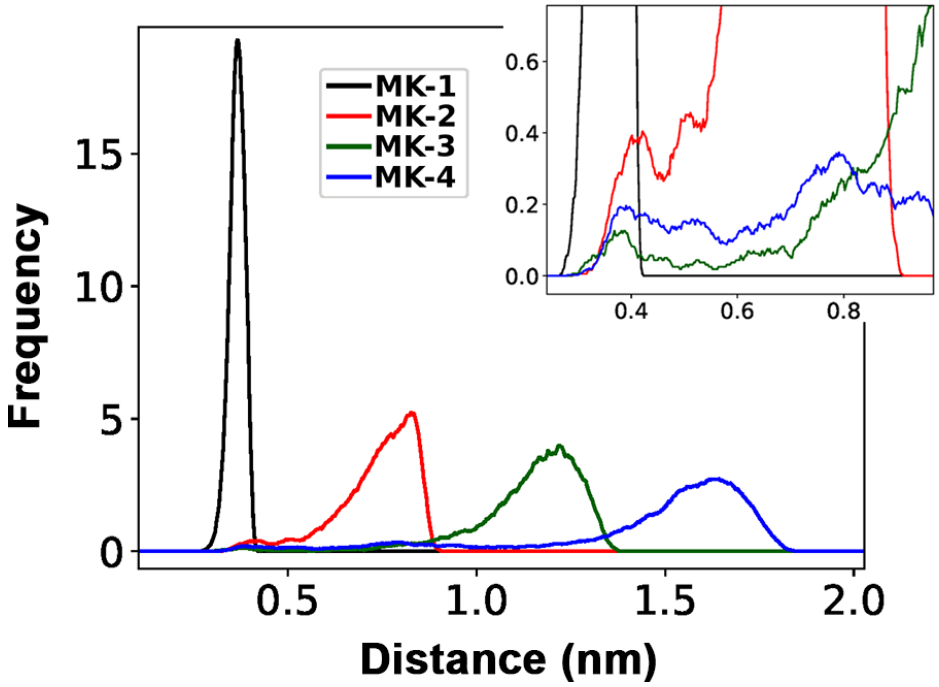

Figure 3.12. Distance distribution from terminal carbon (CT) to the center of the MK naphthoquinone head group, d(CT-H) in MK-1 (black), MK-2 (red), MK-3 (green), and MK-4 (blue). The upper right panel zooms in at the distance range 0.3 to 1.0 nm (3-10 Å).

4. Discussion

Langmuir monolayers were used to experimentally probe the location and association of truncated MK homologues within phospholipid monolayers. There are two ways to conduct Langmuir monolayer experiments depending on the solubility of the compound of interest. When the compound is water-soluble, it is added to the aqueous subphase. With hydrophobic molecules, experiments are conducted by mixing and applying different molar ratios of substrate and phospholipid as described by Hoyo *et al*. in 2015.[22] In order to observe a response on the monolayer, concentrations are typically higher than micromolar. This is above the solubility of even the water-soluble truncated MK homologues. In our studies using molar ratios of lipid vs MKs, information about potential aggregation of MK homologues and film formation was gathered.[47-48] Using the Langmuir trough, we studied how truncated MKs (MK-1, MK-2, MK-3 and MK-4) interact with DPPC and DPPE films.

Biologically, DPPC is present in up to 40 % of mammalian lung surfactant while little, if any, is found in bacterial membranes.[47, 49] However, DPPC has been well characterized in Langmuir monolayers and demonstrates distinct behavioral phases (gas, gas-liquid, liquid condensed, solid) which give information on the disruption of phospholipid packing. Therefore, it is used extensively in model membrane systems.[50] DPPE is found in bacterial cells and is only a minor component in mammalian cells, such as in the inner leaflet of eukaryotic cells.[51-53] As such, DPPE is the most biologically relevant phospholipid for the study of MKs. While the more biologically plentiful POPC has been used in Langmuir monolayer studies, it did not demonstrate the same phase changes as DPPC and is therefore less informative with regards to the association of MK homologues.[54] Compression isotherms in this manuscript were accordingly run at 25 ^{o}C to maintain the distinct phases of DPPC, as the gas-liquid phase is not present at physiological temperature.[55]

We investigated the ability of truncated MK homologues to form films. We found that MKs were surface-active even though the surface pressure did not begin to rise until ~ 40 Å^2/molecule and that these MK films were unstable. Using BAM, we were able to visualize the aggregation of the MK homologues and we observed strong aggregation of MK-2, MK-3, and MK-4. However, the self-

association with MK-1 was weaker, possibly due to enhance water solubility. Because of the limiting solubility of MK homologues, the studies of the MK derivatives on the films were performed using ratios of MK homologue to DPPC or DPPE. By mixing ratios of phospholipid, and MK, we found that the MK homologues associated with the phospholipid interface, and that at low surface pressure disruptive effects were greatest for MK-2 and MK-4, Figure 3.5. However, we observed little, if any, increase in disruptiveness between 30-35 mN/m. Moreover, the curves of 75:25 phospholipid:MK overlap the control in all but the DPPE:MK-4 trials. The conclusions of the lack of disruption at physiological surface pressure are that i) the MK homologues were compressed into the phospholipid tails from the interface and ii) that this migration to the saturated phospholipid tails allows for greater accommodation of the volume of the MK homologues, hence the lack of MK disruption. We used MD simulations to confirm he location and association with phospholipids and additionally explore the conformation of MK homologues.

The MD simulations were performed in a phospholipid bilayer, and at a phospholipid:MK ratio that approximated the concentrations found in biological systems. We chose a model bilayer composed of MK homologues embedded in a POPC bilayer, which was previously developed in out laboratory to investigate the interaction of phospholipids with native UQs or MKs in eukaryotic cells.[28] Although simulations of Langmuir monolayers are possible,[56] they would require an extensive reparameterization and testing of the force-field used for simulations[27-28] and would provide little detail on the biological context in which MKs are found. Instead, we chose to carry out simulations at a physiologically relevant MK concentration within a model phospholipid bilayer which are more reliable with our current force-field technology,[27-28] and resulted in detailed information on the intrinsic folding of MK isoprenoid chains in its (MK-4) native membrane environment. Eukaryotic membranes have a large POPC concentration and pure POPC bilayers have been well-characterized as models for the simulation of biological membranes.[57] In particular, we have previously characterized in detail the location and water-phospholipid partition of UQ with variable isoprenoid chain length to POPC bilayers, in good agreement with experimental observations.[27]

The MD simulations also showed that once the MK was associated with the membrane, the average (equilibrium) location of the MK headgroup did not depend on the number of isoprenoid units (Figure 3.8). The tiny differences observed between the four MK homologues in Figure 3.8 are not statistically significant and are due to fluctuations of the finite sampling. Thus, our simulations do not show any dependence of MK headgroup location with side chain length, in line with previous simulations of UQ with various side chain length in POPC and in mixed membranes.[27-28] The MD studies also suggested that the location of lipoquinones along the membrane midplane in an intrinsic physicochemical property of the quinone molecule due at least in part to its amphiphilic character and more polar headgroup. This finding supports the possibility that in the monolayer system, the MK headgroup location will not change with isoprenoid chain length. However, the redox state (quinone vs quinol form) of the headgroup affects its location, as we previously demonstrated within reverse micelle membrane environments.[58] Combined, our work supports the possibility that the headgroup structure and redox state, as opposed to tail length, is a major contributing factor driving the location and association of MK homologues in a membrane.

The conformational distribution of C-C bonds in the MK side chain described in the MD results have a subtle but potentially relevant impact on side chain folding upon the MK head and the related distance d(CT-H) (Figure 3.12). The possible distances for MK-1 are quite narrow due to restricted torsion around the C6-C7 bond (Figure 9). For the other MKs, longer distances are reached and the distribution spreads due to increasing the number of isoprenoid units and increased side chain flexibility. The conformations where the side chain fold over the headgroup have a different chape compared to MK-1 where the side chain is at an angle with the headgroup. Interestingly, the excerpt of Figure 12 shows that the side chain of the distance distribution in which MK-3 visits low d)CT-H) values have the lowest probabilities among MK-1 through MK-4. Thus, we suggest that the non-ideal behavior observed for these MK homologues in the monolayer insotherms may be caused by the more frequent partial folding of the side chain over the MK head group as observed in the MD simulations for MK-2 and MK-4 and the related shorter d(CT-H) (Figure 6).

The interactions of lipoquinones with membranes are a multi-faceted topic in which many different factors are important to the location, association, and conformation of the lipoquinones in the phospholipid bilayer. In order to illustrate some of these effects we compare the properties of the different MK homologues are list them in Table 3.1. We order the properties of MK-1 through MK-4 in terms of clogP, ability to disrupt a monolayer (based on increase in monolayer area at physiological surface pressure), MK headgroup location, longest average distance of the terminal carbon of the isoprene chain from the naphthoquinone headgroup, and the ability of the terminal carbon to be within 0.6 nm of the naphthoquinone headgroup (which is a measure of folding). The only two properties that show the same order are the clogP and the longest average distance of the terminal carbon of the isoprene chain from the naphthoquinone headgroup. The later correspond to the largest MK derivative and hence thus also the most hydrophobic.

Table 3.1. comparing carious physicochemical properties of the four MK homologues investigated in this work.

Property	Ranking
clogP	MK-4 (8.86) > MK-3 (7.52) > MK-2 (5.67) > MK-1 (3.83)
Ability to disrupt a phospholipid monolayer based on the increase in monolayer area between 30-35 mN/m	MK-2 > MK-4 > MK-1 > MK-3
MK headgroup location relative to the bilayer midplane	MK-1 ~ MK-2 ~ MK-3 ~ MK-4
Longest average distance from CT to naphthoquinone headgroup	MK-4 > MK-3 > MK-2 > MK-1
Frequency of CT residing within 0.6 nm of the naphthoquinone headgroup	MK-1 > MK-2 > MK-4 > MK-3

We confirmed that MK homologues occupy a more hydrophobic region of the membrane than UQ, though there was less disruption of phospholipid packing. We hypothesize that the lack of

disruption is due to the location of the MK homologues. The free rotation of the phospholipid tails allows for compensation of the MK volume while UQ's location in the interface does not.[17, 59] In addition, we also found that all MK homologues adopted some folded conformation in a simulated bilayer, though conformations varied. We would be interested in exploring the physicochemical properties of the reduced quinol forms of these MK homologues. However, menaquinols are unstable under atmospheric conditions, making experimentation difficult.[11, 58]

5. Summary and Conclusions

MKs are membrane-associated lipoquinones that are used as essential components in the ETS of many bacteria. Therefore, understanding the behavior of MKs in membranes could provide fundamental knowledge of the ETS and could aid in antimicrobial drug development. We have previously demonstrated that truncated MKs fold in a model membrane interface.[6-7] However, we sought more information on the location of MKs as well as how MKs associate with and affect the packing of phospholipid s in a membrane environment. We hypothesized, but did not confirm, that MKs would behave in a similar manner to UQs, in that there would be a side chain-dependent disruption of phospholipid packing and association with MKs. Moreover, we wanted to further explore their predicted location can conformation in a membrane bilayer. We used a combination of experimental and computational methods to probe these open questions. Langmuir monolayer studies provided experimental data pertaining to location of MK homologues as well as phospholipid packing and association while MD simulations provided molecular information of exact location, association, and conformation in a phospholipid bilayer at physiological MK concentration.

Langmuir monolayers were created with biologically relevant phospholipids, DPPC and DPPE, to experimentally model the cell membrane interface. All truncated MK homologues were found to migrate from the air-water interface into the phospholipid tails at physiological surface pressure, which is consistent with our hypothesized location. We demonstrated that truncated MKs do associate but do not disrupt the phospholipid packing at physiological surface pressure that was observed with UQs.[24-26] Using MD simulations, we found, in accordance with the hydrophobic nature of MKs, that

the MK headgroup was located closer to the phospholipid tails than UQ, which was located closer to the interfacial water, which is consistent with our hypothesized location. Furthermore, we found through MD simulations that MK-2, MK-3, and MK-4 favored an overall folded conformation, which is in agreement with our previous experimental studies with MK-1 and MK-2.[6-7] In line with Langmuir monolayer studies, there was no observed dependence on MK side chain length for MK location, association, or conformation within the bilayer under physiological conditions. However, it is possible that this lack of dependence on MK side chain length is limited to truncated MK homologues and that the longer MK homologues, a=such as MK-9, would exhibit an appreciable difference in folding and disruption due to the significantly larger volume of MK-9. As the MKs are located further into the phospholipid tails than UQs, it is possible that the tails adjust to compensate for the volume of the lipoquinones. Hence, MK would be less disruptive than UQ based on membrane location.

Combined, Langmuir studies and MD simulations demonstrated that truncated MKs are located closer to the phospholipid tails, regardless of the truncated MK side chain length. A lack of dependence on side chain length was also observed in the association and packing of truncated MK homologues with phospholipids. Additionally, truncated MKs generally demonstrated some amount of folding. In conjunction with previous studies detailing the different environment-dependent folded conformations of MK-1 and MK-2, this provides a fundamental view of the behavior of MKs in a membrane environment. Overall, MK homologues may disrupt phospholipid packing at higher concentrations as seen in Archaea,[11, 60] but not necessarily at concentrations found in most other organisms.[9] These truncated MK homologues were also found to fold, which may influence their behavior, recognition, and function in the ETS that is essential for bacterial survival.

References

1. Collins, M. D.; Jones, D. Distribution of Isoprenoid Quinone Structural Types in Bacteria and Their Taxonomic Implications. *Microbiol. Rev.* **1981,** *45*, 316–354.
2. Brennan, P. J. Mycobacterium and other actinomycetes. In *Microbial Lipids*, Ratledge, C.; Wilkinson, S. G. Eds. Academic Press: San Diego, CA, USA, **1988**, *1*, 203–298.
3. Upadhyay, A.; Kumar, S.; Rooker, S. A.; Koehn, J. T.; Crans, D. C.; McNeil, M. R.; Lott, J. S.; Crick, D. C. Mycobacterial MenJ: An Oxidoreductase Involved in Menaquinone Biosynthesis. *ACS Chem. Biol.* **2018,** *13*, 2498–2507.
4. Braasch-Turi, M.; Crans, D. C. Synthesis of Naphthoquinone Derivatives: Menaquinones, Lipoquinones and Other Vitamin K Derivatives. *Molecules* **2020,** *25*, 4477.
5. Popa, D.-S.; Bigman, G.; Rusu, M. E. The Role of Vitamin K in Humans: Implication in Aging and Age-Associated Diseases. *Antioxidants.* **2021,** *10*, 566.
6. Koehn, J. T.; Beuning, C. N.; Peters, B. J.; Dellinger, S. K.; Van Cleave, C.; Crick, D. C.; Crans, D. C. Investigating Substrate Analogues for Mycobacterial MenJ: Truncated and Partially Saturated Menaquinones. *Biochemistry* **2019,** *58*, 1596–1615.
7. Koehn, J. T.; Magallanes, E. S.; Peters, B. J.; Beuning, C. N.; Haase, A. A.; Zhu, M. J.; Rithner, C. D.; Crick, D. C.; Crans, D. C. A Synthetic Isoprenoid Lipoquinone, Menaquinone-2, Adopts a Folded Conformation in Solution and at a Model Membrane Interface. *J. Org. Chem.* **2018,** *83*, 275–288.
8. Gupta, C.; Khaniya, U.; Chan, C. K.; Dehez, F.; Shekhar, M.; Gunner, M. R.; Sazanov, L.; Chipot, C.; Singharoy, A. Charge Transfer and Chemo-Mechanical Coupling in Respiratory Complex I. *J. Am. Chem. Soc.* **2020,** *142*, 9220–9230.
9. Das, A.; Hugenholtz, J.; van Halbeek, H.; Ljungdahl, L. G. Structure and Function of a Menaquinone Involved in Electron Transport in Membranes of *Clostridium thermoautotrophicium* and *Clostridium thermoaceticum*. *J. Bacteriol.* **1989,** *171*, 5823–5829.

10. Lenaz, G.; Samori, B.; Fato, R.; Battino, M.; Castelli, C. P.; Domini, I. Localization and preferred orientations of ubiquinone homologs in model bilayers. *Biochem. Cell. Biol.* **1992,** *70*, 504–514.
11. Feng, S.; Wang, R.; Pastor, R. W.; Klauda, J. B.; Im, W. Location and Conformational Ensemble of Menaquinone and Menaquinol, and Protein-Lipid Modulations in Archaeal Membranes. *J. Phys. Chem. B* **2021,** *125*, 4714–4725.
12. Nixon, G. L.; Pidathala, C.; Shone, A. E.; Antoine, T.; Fisher, N.; O'Neill, P. M.; Ward, S. A.; Biagini, G. A. Targeting the mitochondrial electron transport chain of *Plasmodium falciparum*: new strategies towards the development of improved antimalarials for the elimination era. *Future Med. Chem.* **2013,** *5*, 1573–1591.
13. Berube, B. J.; Russell, D.; Castro, L.; Choi, S.-R.; Narayanasamy, P.; Parish, T. Novel Men A Inhibitors Are Bactericidal against *Mycobacterium tuberculosis* and Synergize with Electron Transport Chain Inhibitors. *Antimicrob. Agent Chemother.* **2019,** *63*, e02661–18.
14. Debnath, J.; Siricilla, S.; Wan, B.; Crick, D. C.; Lenaerts, A. J.; Franzblau, S. G.; Kurosu, M. Discovery of Selective Menaquinone Biosynthesis Inhibitors against *Mycobacterium tuberculosis*. *J. Med. Chem.* **2012,** *55*, 3739–3755.
15. Kurosu, M.; Begari, E. Vitamin K_2 in Electron Transport System: Are Enzymes Involved in Vitamin K_2 Biosynthesis Promising Drug Targets? *Molecules* **2012,** *15*, 1531–1553.
16. Afri, M.; Ehrenberg, B.; Talmon, Y.; Schmidt, J.; Cohen, Y.; Frimer, A. A. Active oxygen chemistry within the liposomal bilayer Part III: Locating Vitamin E, ubiquinol and ubiquinone and their derivatives in the lipid bilayer. *Chem. Phys. Lipids* **2004,** *131*, 107–121.
17. Cornell, B. A.; Keniry, M. A.; Post, A.; Roberston, R. N.; Weir, L. E.; Westerman, P. W. Location and activity of ubiquinone 10 and ubiquinone analogues in model and biological membranes. *Biochemistry* **1987,** *26*, 7702–7707.
18. Upadhyay, A.; Fontes, F. L.; Gonzalez-Juarrero, M.; McNeil, M. R.; Crans, D. C.; Jackson, M.; Crick, D. C. Partial Saturation of Menaquinone in *Mycobacterium tuberculosis*: Function and Essentiality of a Novel Reductase, MenJ. *ACS Cent. Sci.* **2015,** *1*, 292–302.

19. Kumar, S.; Koehn, J. T.; Gonzalez-Juarrero, M.; Crans, D. C.; Crick, D. C. *Mycobacterium tuberculosis* survival in J774A.1 Cells Is Dependent on MenJ Moonlighting Activity, Not Its Enzymatic Activity. *ACS Infect. Dis.* **2020,** *6*, 2661–2671.
20. Möhwald, H.; Brezesinski, G. From Langmuir Monolayers to Multilayer Films. *Langmuir* **2016,** *32*, 10445–10458.
21. Stefaniu, C.; Brezesinski, G.; Möhwald, H. Langmuir monolayers as models to study processes at membrane surfaces. *Adv. Colloid Interface Sci.* **2014,** *208*, 197–213.
22. Hoyo, J.; Guaus, E.; Torrent-Burgués, J.; Sanz, F. Biomimetic monolayer films of digalactosyldiacylglycerol incorporating plastoquinone. *Biochim. Biophys. Acta* **2015,** *1848*, 1341–1351.
23. Jones, M. N.; Chapman, D. *Micelles, Monolayers, and Biomembranes*. Wiley-Liss, New York, NY, USA, 1995.
24. Roche, Y.; Peretti, P.; Bernard, S. Influence of the chain length of ubiquinones on their interaction with DPPC mixed monolayers. *Biochim. Biophys. Acta* **2006**, *1758*, 468–478.
25. Katsikas, H.; Quinn, P. The polyisoprenoid chain length influences the interaction of ubiquinones with phospholipid bilayers. *Biochim. Biophys. Acta* **1982**, *689*, 363–369.
26. Roche, Y.; Peretti, P.; Bernard, S. DSC and Raman studies of the side chain length effect of ubiquinones on the thermotropic phase behavior of liposomes. *Thermochim. Acta* **2006,** *447*, 81–88.
27. Galassi, V. V.; Arantes, G. M. Partition, orientation and mobility of ubiquinones in a lipid bilayer. *Biochim. Biophys. Acta* **2015**, *1847*, 1560–1573.
28. Teixeira, M. H.; Arantes, G. M. Effects of lipid composition on membrane distribution and permeability of natural quinones. *RSC Adv.* **2019,** *9*, 16892–16899.
29. Aroti, A.; Leontidis, E.; Maltseva, E.; Brezesinski, G. Effects of Hofmeister anions on DPPC Langmuir monolayers at the air-water interface. *J. Phys. Chem. B.* **2004,** *108*, 15238–15245.

30. Miyoshi, T.; Kato, S. Detailed Analysis of the Surface Area and Elasticity in the Saturated 1,2-Diacylphosphatidylcholine/Cholesterol Binary Monolayer System. *Langmuir* **2015**, *31*, 9086–9096.
31. Quinn, P. J. Phase Behaviour of Binary Mixtures of Membrane Polar Lipids in Aqueous Sytems. *Nat. Prod. Rep.* **1987,** *4*, 129–137.
32. Quinn, P. J.; Esfahani, M. A. Ubiquinones Have Surface-Active Properties Suited to Transport Electrons and Protons across Membranes. *Biochem. J.* **1980,** *185*, 715–722.
33. Zhan, T. J.; Eilers, M.; Guo, Z.; Ksebati, M. B.; Simon, M.; Scholten, J. D.; Smith, S. O.; Gibbs, R. A. Evaluation of Isoprenoid Conformation in Solution and in the Active Site of Protein-Farnesyl Transferase Using Carbon-13 Labeling in Conjunction with Solution- and Solid-State NMR. *J. Am. Chem. Soc.* **2000,** *122,* 7153–7164
34. Hoyo, J.; Torrent-Burgués, J.; Guaus, E. Biomimetic monolayer films of monogalactosyldiacylglycerol incorporating ubiquinone. *J. Colloid. Interface Sci.* **2012,** *384*, 189–197.
35. Hoyo, J.; Guaus, E.; Torrent-Burgués, J. Tuning ubiquinone position in biomimetic monolayer membranes. *Eur. Phys. J. E: Soft Matter Biol. Phys.* **2017,** *40*, 62.
36. Patterson, M.; Vogel, H. J.; Prenner, E. J. Biophysical characterization of monofilm model systems composed of selected tear film phospholipids. *Biochim. Biophys. Acta Biomembr.* **2016,** *1858*, 403–414.
37. Ma, G.; Allen, H. C. Condensing effect of palmitic acid on DPPC in mixed Langmuir monolayers. *Langmuir* **2007,** *23*, 589–97.
38. Veldhuizen, E. J. A.; Haagsman, H. P. Role of pulmonary surfactant components in surface film formation and dynamics. *Biochim Biophys Acta-Biomembr.* **2000,** *1467*, 255–270.
39. Crane, J. M.; Puts, G.; Hall, S. B. Persistence of Phase Coexistence in Disaturated Phosphatidylcholine Monolayers at High Surface Pressures. *Biophys. J.* **1999,** *77*, 3134–4143.
40. Shaw, N. Lipid Composition as a Guide to the Classification of Bacteria. In *Advances in Applied Microbioligy*, Perlman, D., Ed. Academic Press: New York, **1974**, *17*, 63–108.

41. Fadeel, B.; Xue, D. The ins and outs of phospholipid asymmetry in the plasma membrane: roles in health and disease. *Crit. Rev. Biochem. Mol. Biol.* **2009,** *44*, 264–277.
42. Chakrabarti, A. Phospholipid Asymmetry in Biological Membranes: Is the Role of Phosphatidylethanolamine Underappreciated? *J. Membr. Biol.* **2021,** *254*, 127–132.
43. Olżyńska, A.; Zubek, M.; Roeselova, M.; Korchowiec, J.; Cwiklik, L. Mixed DPPC/POPC Monolayers: All-atom Molecular Dynamics Simulations and Langmuir Monolayer Experiments. *Biochim. Biophys. Acta* **2016,** *1858*, 3120–3130.
44. Träuble, H.; Eibl, H.; Sawada, H. Respiration—a Critical Phenomenon? Lipid Phase Transitions in the Lung Alveolar Surfactant. *Naturwissenschaften* **1974,** *61*, 344–354.
45. Javanainen, M.; Lamberg, A.; Cwiklik, L.; Vattulainen, I.; Ollila, O. H. S. Atomistic Model for Nearly Quantitative Simulations of Langmuir Monolayers. *Langmuir* **2018,** *34*, 2565–2572.
46. Marsh, D. *Handbook of Lipid Bilayers*. 2 ed.; CRC Press: Boca Raton, FL, USA, 2013.
47. Van Cleave, C.; Murakami, H. A.; Samart, N.; Koehn, J. T.; Maldonado, P.; Kreckel, H. D.; Cope, E. J.; Basile, A.; Crick, D. C.; Crans, D. C. Location of menaquinone and menaquinol headgroups in model membranes. *Can. J. Chem.* **2020,** *98*, 307–317.
48. Stidham, M. A.; McIntosh, T.; Siedow, J. N. On the localization of ubiquinone in phosphatidylcholine bilayers. *Biochim. Biophys. Acta.* **1984,** *767*, 423–431.
49. Koehn, J. T. Synthesis and exploration of biologically important, hydrophobic, redox-active molecules: investigation of partial saturation of mycobacterial electron transport lipids. Ph.D. Thesis, Colorado State University, Fort Collins, 2019.
50. Javanainen, M. Universal Method for Embedding Proteins into Complex Lipid Bilayers for Molecular Dynamics Simulations. *J. Chem. Theory Comput.* **2014,** *10*, 2577–2582.
51. Pronk, S.; Páll, S.; Schulz, R.; Larsson, P.; Bjelkmar, P.; Apsotolov, R.; Shirts, M. R.; Smith, J. C.; Kasson, P. M.; van der Spoel, D.; Hess, B.; Lindahl, E. GROMACS 4.5: A High-Throughput and Highly Parallel Open Source Molecular Simulation Toolkit. *Bioinformatics* **2013,** *29*, 845–854.

52. MacKrell Jr., A. D.; Bashford, D.; Bellott, M.; Dunbrack Jr., R. L.; Evanseck, J. D.; Field, M. J.; Fischer, S.; Gao, J.; Guo, H.; Ha, S. All-Atom Empirical Potential for Molecular Modeling and Dynamics Studies of Proteins. *J. Phys. Chem. B* **1998,** *102*, 3586–3616.
53. Vanommeslaeghe, K.; Hatcher, E.; Achraya, C.; Kundu, S.; Zhong, S.; Shim, J.; E., D.; Guvench, O.; Lopes, P.; Vorobyov, I. CHARMM General Force Field: A Force Field for Drug-like Molecules Compatible with the CHARMM All-atom Additive Biological Force Fields. *J. Comp. Chem.* **2010,** *31*, 671–690.
54. Jorgensen, W. L.; Chandrasekhar, J.; Madura, J. D.; Impey, R. W.; Klein, M. L. Comparison of Simple Potential Functions for Simulating Liquid Water. *J. Chem. Phys.* **1983,** *79*, 926–935.
55. Bussi, G.; Donadio, D.; Parrinello, M. Canonical Sampling through Velocity Rescaling. *J. Chem. Phys.* **2007,** *126*, 14101.
56. Parrinello, M.; Rahman, A. Polymorphic Transitions in Single Crystals: A New Molecular Dynamics Method. *J. Appl. Phys.* **1981,** *52*, 7182–7190.
57. Darden, T.; York, D.; Pedersen, L. Particle Mesh Ewald: An N· Log (N) Method for Ewald Sums in Large Systems. *J. Chem. Phys.* **1993,** *98*, 1463–1472.
58. Hess, B.; Bekker, H.; Berendsen, H. J.; Fraaije, J. G. E. M. LINCS: A Linear Constraint Solver for Molecular Simulations. *J. Comp. Chem.* **1997,** *18*, 1463–1472.
59. Anézo, C.; de Vries, A. H.; Höltje, H.-D.; Tieleman, D. P.; Marrink, S.-J. Methodological Issues in Lipid Bilayer Simulations. *J. Chem. Phys.* **2003,** *107*, 9424–9433.
60. Kellerman, M. Y.; Yoshinaga, M. Y.; Valentine, R. C.; Wörmer, L.; Valentine, D. L. Important roles for membrane lipids in haloarchaeal bioenergetics. *Biochim. Biophys. Acta. Biomembr.* **2016,** *1858*, 2940–2956.

Chapter 4
The Physicochemical Properties of Pyrazinoic Acid and Pyrazinoate are Consistent with Their Protonophore Activity in Cells[c]

1. Introduction

Two simple aromatic molecules, pyrazinamide (PZA) and isoniazid (Figure 4.1), are known first-line antituberculosis prodrugs. PZA is metabolized to pyrazinoic acid (POA) by pyrazinamidase,[1-2] though the mechanism of action remains under discussion.[2-5] Regardless, both PZA and POA must interact with the cell membrane for uptake.[6-9] In the case of POA, such interactions are important because it has been demonstrated to be a protonophore *in vivo*.[10-11] Therefore fundamental molecular interactions with lipids and membranes are of interest.[12-13] According to the Lipinski rules determined based on statistical evaluation of known drugs, successful drugs are small neutral molecules, with hydrogen acceptors and donors. These molecules have some hydrophobicity and affinity for the hydrophobic region of the cell membranes.[13] Since there are several different routes by which drugs enter cells, including active and passive transport studies, exploring drug-lipid interactions is of interest.[14-15]

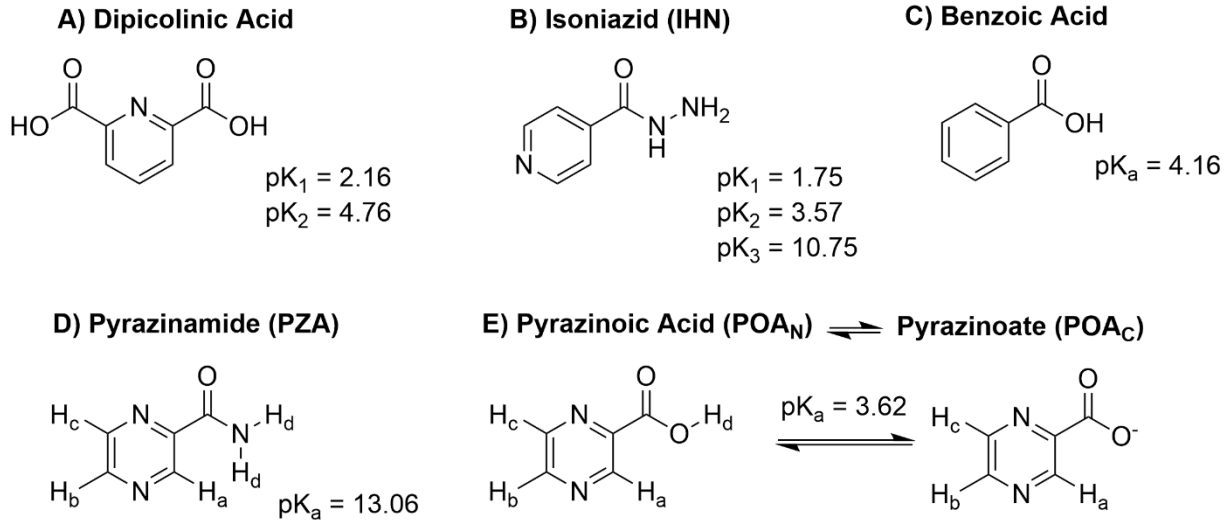

Figure 4.1. The structures and pK_a's of A) dipicolinic acid, B) isoniazid, C) benzoic acid, D) pyrazinamide (PZA), E) pyrazinoic acid (POA_N) pyrazinoate (POA_C) The pK_a values for PZA and POA are predicted values from www.chemicalize.com. The pK_a's of dipicolinic acid, isoniazid, and benzoic acid were obtained from Serjeant and Dempsey 1979.[13]

[c] This manuscript is in preparation for *Langmuir*.

Recently, POA has shown pH-dependent activity *in vitro* as well as activity as a protonophore.[10-11] Protonophores are capable of transporting protons across the bilayer, thus disrupting the pH gradient and acidifying the cytoplasm (when the outside of the cell is more acidic) without disrupting the packing of the bilayer.[2, 18] Interestingly, POA was more effective at inhibiting mycobacterial growth at acidic pH than neutral pH. This suggests that the neutral species has a greater inhibitory effect than the charged species due to its greater ability to cross the bilayer due to its neutral charge.[11] The fully protonated POA species will be referred to as POA_N, while the conjugate base, pyrazinoate, will be referred to as POA_C. We are interested in investigating PZA and POA for their interaction with model membrane systems. Three different model membranes will be used: Langmuir monolayers, reverse micelles, and liposomes.

Langmuir monolayers are a layer of phospholipids one molecule thick at the air-water interface. A probe molecule may be dissolved into the subphase, and effects on area and lipid packing can be observed.[19-20] We used the phospholipids dipalmitoylphosphatidylcholine (DPPC) and dipalmitoylphosphatidylethanolamine (DPPE) to represent both mammalian and bacterial membranes, respectively.[21-24] DPPC is prevalent in mammalian pulmonary surfactant and shows distinct behavioral phases, while DPPE is common in bacterial bilayers and the inner leaflet of eukaryotic cells due to its ability to pack tightly.[8, 25-26] Reverse micelles (RM) may be used to probe the location of a molecule within the interface. Previous work has been done by Peters *et al.* to investigate the location of benzoic acid and its charged species, benzoate, through ^1H-^1H 2D NMR in reverse micelles, similar to POA_N and POA_C.[7] RMs are self-assembled structures formed by surfactant microemulsions. The RMs consist of a polar water pool encapsulated in a surfactant (AOT) and dissolved in a non-polar solvent such as isooctane.[27-28] The water layer which is closest to the interface and exhibits tighter packing than the bulk water at the center of the RM is known as the Stern layer.[29-30] The environments in the RMs can change by varying the sizes represented by w_0 = [AOT]/[H_2O] as well as changes in pH to report on the compound interface association. When studied with ^1H NMR, detailed molecular information on the location of the probe molecule within the interface can be obtained.[7-8]

Since cells contain bilayers and not monolayers, it is desirable to investigate how POA and PZA interact with bilayers. Since pH equilibration across a membrane could take place through compound transport of the proton or by simple disruption, it is desirable that we investigate whether the bilayer is disrupted in the presence of PZA and POA. To this end, we investigated large unilamellar vesicles from phosphatidylcholine loaded with a fluorescent dye at self-quenching concentrations. These fluorophore-filled liposomes are overall stable; therefore, the ability of compounds such as POA to disrupt the membrane can be measured, as membrane disruption results in the release of the dye from within the liposome into the bulk water, diluting it and leading to an increase in fluorescence.[31]

In this paper, we characterize the physicochemical properties of the interaction of PZA and POA with a model membrane using these three methods. First, we investigate the interactions of PZA and POA in the model membrane system, Langmuir monolayers. Second, we investigate the location of PZA and POA with studies in the AOT-reverse micellar microemulsion system. Finally, examine the integrity of the lipid bilayer by preparing large unilamellar vesicles loaded with a fluorescent dye to determine whether the vesicle remains intact upon addition of PZA or the charged form of POA (POA_C). We hypothesize *that the interaction of PZA and POA with lipid monolayers and bilayers does not disrupt the lipid bilayer, leaving the membrane intact.* The studies carried out in this manuscript provide information on the effects of these compounds on both mono- and bilayers of lipids.

2. Materials and Methods

2.1 General Materials and Methods

2.1.1 Materials

The following materials were used without further purification. Chloroform (≥99.5%), monosodium phosphate (≥99.0%), disodium phosphate (≥99.0%), citric acid (≥99.5%), sodium citrate

dihydrate (>99%), sodium chloride (≥99.0%), sodium hydroxide (≥98%), hydrochloric acid (37%), 2-pyrazincarboxamoide (pyrazinamide, PZA, ≥98.0%), 2-pyrazincarboxylic acid (pyrazinoic acid, POA, 99%), 2,2,4-trimethylpentane (isooctane, 99.8%), 2,2-dimethyl-2-silapentane-5-sulfonate sodium salt (DSS, 97%), L-α-phosphatidylcholine (from egg yolk, Type XVI-E, ≥99%), 5(6)-carboxyfluorescein (≥95%), and HEPES (≥99.5%), were all purchased from Sigma-Aldrich. Phospholipids dipalmitoylphosphatidylcholine (16:0 PC, DPPC, 99%) and dipalmitoylphosphatidylethanolamine (16:0 PE, DPPE, 99%) were purchased from Avanti Polar Lipids as a pure lyophilized powder. Deuterium oxide (D_2O, ≥99%) was purchased from Cambridge Isotope laboratories. Aerosol-OT (AOT, dioctyl sulfosuccinate sodium salt, ≥99.0%) was purchased from Sigma Aldrich and purified with charcoal as previously described.[8] Distilled deionized (DDI) water was obtained by filtering distilled water through a Millipore water purification system, obtaining a resistance of 18.2 MΩ.

2.1.2 Instrumentation

The Langmuir monolayers were studied using a Kibron μTrough XS (stainless steel) equipped with a Teflon ribbon barrier. All ^1H NMR experiments were performed using a 400 MHz Varian NMR spectrometer. Dynamic light scattering studies were performed on a Malvern Zetasizer ZS equipped with a 633 nm red laser. Fluorescence studies were done on a Horiba Jobin-Yvon FluoroLog-3 where the cuvette was attached to the light source and detector by fiber optic cables. All pH values were obtained with a Thermo Orion 2 Star pH meter (pH = pD + 0.4). Liposome extrusions were performed with a mini-extruder and heating block purchased from Avanti Polar Lipids.

2.2 Langmuir Monolayer Studies

2.2.1 Preparation of Subphase Solutions

The subphase consisted of 20 mM sodium phosphate-citrate buffer. Buffers were prepared to be pH 3, 5, or 7.4. Solutions of PZA or POA were created by dissolving an appropriate amount of solid into 250 mL of buffer to create a 10 mM solution (0.3078 g PZA, 0.3105 g POA). Solutions of 1 mM and 0.1 mM were created by diluting from the 10 mM solutions. PZA solutions were brought to pH 7.40 ± 0.02 with 1 M HCl or NaOH. POA solutions were adjusted to pH 3.00, pH 5.00, or pH 7.40 ± 0.02 with 1 M HCl or NaOH.

2.2.2 Preparation of Lipid Solutions

Phospholipid stock solutions were prepared by dissolving dipalmitoylphosphatidylcholine (DPPC) (0.018 g, 0.025 mmol) or dipalmitoylphosphatidylethanolamine (DPPE) (0.017 g, 0.025 mmol) in 25 mL of 9:1 chloroform/methanol (v/v) for a final concentration of 1.0 mM phospholipid.

2.2.3 Preparation of Phospholipid Langmuir Monolayers

The buffered aqueous subphase consisted of 50 mL of 20 mmol/L sodium phosphate-citrate buffer (pH 3.00, 5.00, 7.40) in DDI water (18.2 MΩ). The subphase surface was cleaned via vacuum aspiration until a quick compression of the subphase until the surface pressure was consistently 0.0 ± 0.5 mN/m throughout compression. A total of 20 µL of phospholipid stock solution (20 nmol of lipid) was then added to the surface of the subphase in a dropwise manner using a 50 µL Hamilton syringe. The monolayer was allowed to equilibrate for 15 minutes.

2.2.4 Compression Isotherm Measurements of Langmuir Monolayers

The equilibrated monolayer was compressed from two sides with a total speed of 10 mm/min (5 mm/min from each side). The temperature was maintained at 25 °C using an external water bath. The trough plate was scrubbed three times with isopropanol, then three times with ethanol, then rinsed with DDI water (18.2 MΩ) before each experiment. The ribbon barrier was rinsed with isopropanol followed by ethanol and then water. The surface tension was monitored via Wilhemy plate technique, where a steel wire was used as the probe instead of a plate. The surface pressure was calculated from the surface tension using **Equation 1**, where π is the surface pressure, γ_0 is the surface tension of water (72.8 mN/m), and γ is the surface tension at a given area per phospholipid after the monolayer has been applied.

$$\pi = \gamma_0 - \gamma \qquad \textbf{Equation 1}$$

Each compression isotherm experiment consisted of at least three replicates. The averages of the area per phospholipid and the standard deviation at every 5 mN/m were calculated using Microsoft Excel. The worked-up data were then transferred to Origin 2021 to be graphed with error bars.

2.2.5 Compression Modulus Analysis

The compression modulus of each average was calculated according to Equation 2, where C_s^{-1} is the compression modulus, A is the area per molecule (Å^2), and π is the surface pressure.

$$C_s^{-1} = -A\left(\frac{d\pi}{dA}\right)_T \qquad \textbf{Equation 2}$$

The 1st derivative of the surface pressure with respect to temperature was calculated in Origin 2021 and smoothed with a second degree polynomial Savitsky-Golay function (350 points per window). The derivative was then multiplied by the negative area and graphed versus surface pressure in Origin 2021.

2.3 ^{1}H NMR of Reverse Micelles

2.3.1 Preparation of Aqueous Solutions and Reverse Micelles

Solutions for studies by ^{1}H NMR are done in D_2O, therefore the measured pH values are adjusted to pD with pD = pH – 0.4.[30] Stock solutions of 100 mM PZA or POA were made by dissolving 0.123 g PZA or 0.124 g POA in 20 mL of D_2O. Stocks were then aliquoted into 2 mL samples. Each sample was brought to a different pD (pH = pD + 0.4) with 0.1 M DCl and/or 0.1 M NaOD. Each of the pD values were within the range of 1.2 to 10 and were used to determine the pK_a.

A 750 mM stock solution of purified AOT in isooctane was prepared by dissolving 8.34 g (18.8 mmol AOT) in 25 mL isooctane. This mixture was sonicated and then allowed to equilibrate to room temperature. Appropriate amounts of pD-adjusted PZA or POA solution in D_2O were added to AOT/isooctane solution samples of sizes w_0 12, w_0 16, and w_0 20, where $w_0 = [H_2O]/[AOT]$. These samples were vortexed for ~ 1 minute until clear, indicating that the microemulsions had formed.

2.3.2 1H 1D NMR Spectroscopic Studies

One-dimensional (1D) ^{1}H NMR spectra of PZA and POA were conducted in both D_2O and RMs. Spectra were obtained using standard parameters (1 s relaxation time, 25℃, and 45˚ pulse angle).[8] The determination of pK_a values were measure by recording a series of spectra at different pH and plotting the chemical shifts as a function of pD. The data are shown in Appendix IV. Corresponding studies were done in RM as well, and the data are presented.

Aqueous spectra were referenced to DSS. RM spectra were referenced to the internal isooctane methyl peak at 0.90 ppm corresponding to previously reported chemical shifts recorded in reference to tetramethylsilane at 0 ppm.[8, 32-33]

2.4 Dynamic Light Scattering

DLS experiments were done to verify that the RMs were formed using methods described previously.[8] RMs were prepared as above. A 1 mL aliquot was then diluted in 5 mL of isooctane and vortexed for ~ 2 minutes to break up aggregates. The DLS cuvette was rinsed three times with isooctane, then three times with sample before each reading. Samples were allowed 15 minutes to reach temperature equilibration before data were recorded. Each reading consisted of 15 measurements, with each measurement consisting of 10 scans. The average result was recorded.

2.5 Liposome Leakage Assay

2.5.1 Preparation of Buffers

The following were based on Jimah *et al.* 2017.[34] The carboxyfluorescein (CF) buffer was prepared by dissolving 0.596 g HEPES (50 mM), 0.146 g NaCl (50 mM), and 1.88 g of 5(6)-carboxyfluorescein into 50 mL of DDI H_2O. The buffer was then brought to pH 7.4 with 1 M NaOH and 1 M H_2SO_4. Column buffer was prepared by dissolving 5.96 g HEPES (100 mM) and 1.46 g NaCl (100 mM) in 250 mL of DDI H_2O. The buffer was then adjusted to pH 6.5 with 1.0 M NaOH and 1 M H_2SO_4.

2.5.2 Preparation of Liposomes

Lipid cakes were prepared by dissolving 0.20 g of L-α-phosphatidylcholine in 25 mL of chloroform in a 100 mL round bottom flask. The solution was then lyophilized by removing the solvent with a rotary evaporator. After all excess solvent was removed, the lipid cake was then rehydrated in 5.2 mL of CF buffer to create a 50mM solution of lipid suspended in the buffer. The round bottom flask was then agitated in a 55℃ water bath for one hour. The rehydrated solution was then extruded eight times through a 0.1 μM filter to create large unilamellar vesicles. Excess CF was removed by running the sample through a size-exclusion column of Sephadex G-50 that was incubated with column buffer for a minimum of 12 hours.

2.5.3 Fluorescence Leakage Assay of Lipososmes

Liposomes were diluted in a 1:8 ratio with column buffer to make solutions of appropriate concentration to measure small increases in fluorescence as induced by membrane-disruptive drugs. Increasing amounts of 10 mM PZA or 10 mM POA in column buffer (pH 6.5) were added, up to 5 mM. Exact amounts of PZA or POA solution added to the liposomal solution are detailed in Supplemental Information. Varying concentrations of the surfactant Triton X-100 were used as a positive control for fluorescence-induced membrane leakage, as Triton X-100 is known to destabilize membrane bilayers.[35] Samples were allowed to incubate for one hour before fluorescence was measured in triplicate. Data was collected with λ_{ex} = 492 nm and λ_{em} = 517 nm.

3. Results and Discussion

3.1 Compression Isotherms of Langmuir Monolayers

3.1.1 PZA vs POA_C at pH 7.4

The interactions of PZA and POA_C were determined at physiological pH at concentrations of 0.1 mM, 1 mM, and 10 mM in Langmuir monolayers prepared from dipalmitoylphosphatidylcholine (DPPC) and dipalmitoylphosphatidylethanolamine (DPPE). The data are shown in **Figure 4.2.** For POA_C, DPPC monolayers do not exhibit a difference in area in the presence of 0.1 mM or 1 mM POA_C. However, the 10 mM POA_C experiment does exhibit statistically significant, albeit small, expansion of the monolayer at physiological surface pressure. This is consistent with the interpretation that POA_C slightly penetrates into the interface but that this observation is only detected at higher concentrations.

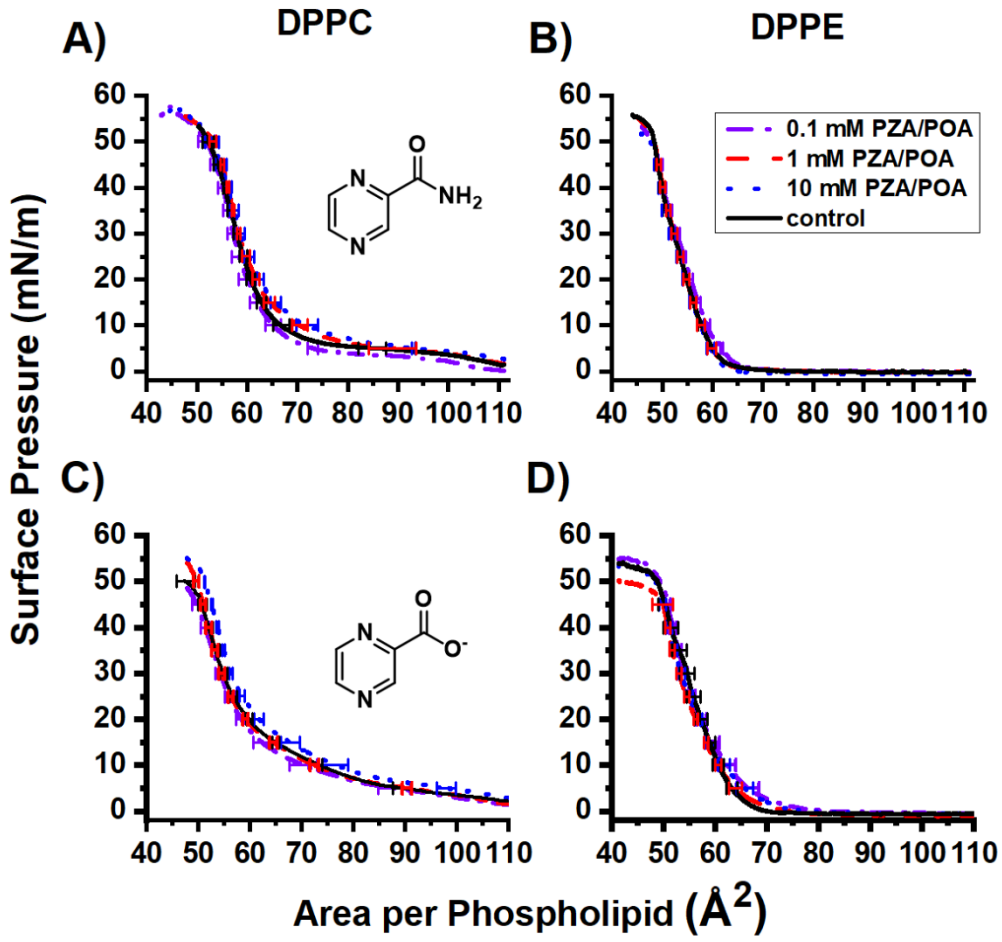

Figure 4.2. Compression isotherms of DPPC (left column) or DPPE (right column) with either PZA (A and B) or POA_C (C and D) as the analyte at pH 7.4 ± 0.02. Black solid curves represent control monolayers with no analyte present, blue dotted curves represent monolayers with 10 mM PZA/POA_C present, red dashed curves represent monolayers exposed to 1 mM PZA/POA_C, and purple dash-dot curves represent monolayers exposed to 0.1 mM PZA/POA_C. Each curve is the average of at least triplicate measurements. Error bars are the standard deviation of the area and are reported at every 5 mN/m of surface pressure.

Compression isotherms of DPPC with PZA showed only a small expansion of the monolayer from 5-20 mN/m for 1 mM and 10 mM concentrations, where the isotherm also flattens (Figure 4.2A). While it does not affect the area of the interface, it may force the monolayer into the liquid-condensed phase earlier during compression than the control. However, the error bars on at 10 and 20 mN/m overlap with the control, suggesting no real difference in area or packing. As with DPPC, there was no

appreciable difference in the isotherms of DPPE in the presence of PZA, consistent with the interpretation that PZA does not reside in the interface of DPPE (Figure 4.2B).

Compression isotherms suggest that PZA and POA do not interact with the membrane. However, considering that POA has different protonation states, the effects of pH on the interactions of the different species with the monolayer was investigated.

3.1.2 Changes in pH Change POA's Interaction with Langmuir Monolayers

Compression isotherms were obtained of POA at pH 5, where there should be a mixture of both POA_N and POA_C, and pH 3, where the majority of molecules should be POA_N (**Figure 4.3**). With DPPC, we see an overall expansion of the monolayer at all concentrations, unlike the similar responses at pH 7.4 shown above. At physiological surface pressure (30-35 mN/m)[34] and a pH of 5, DPPC is slightly condensed. However, the differences are small enough that there may not be any physiological implications. There is also an expansion of at least 2 $Å^2$ at physiological surface pressure for DPPE monolayers. As with the DPPC monolayers, this is likely not an indication of more than a moderate interaction.

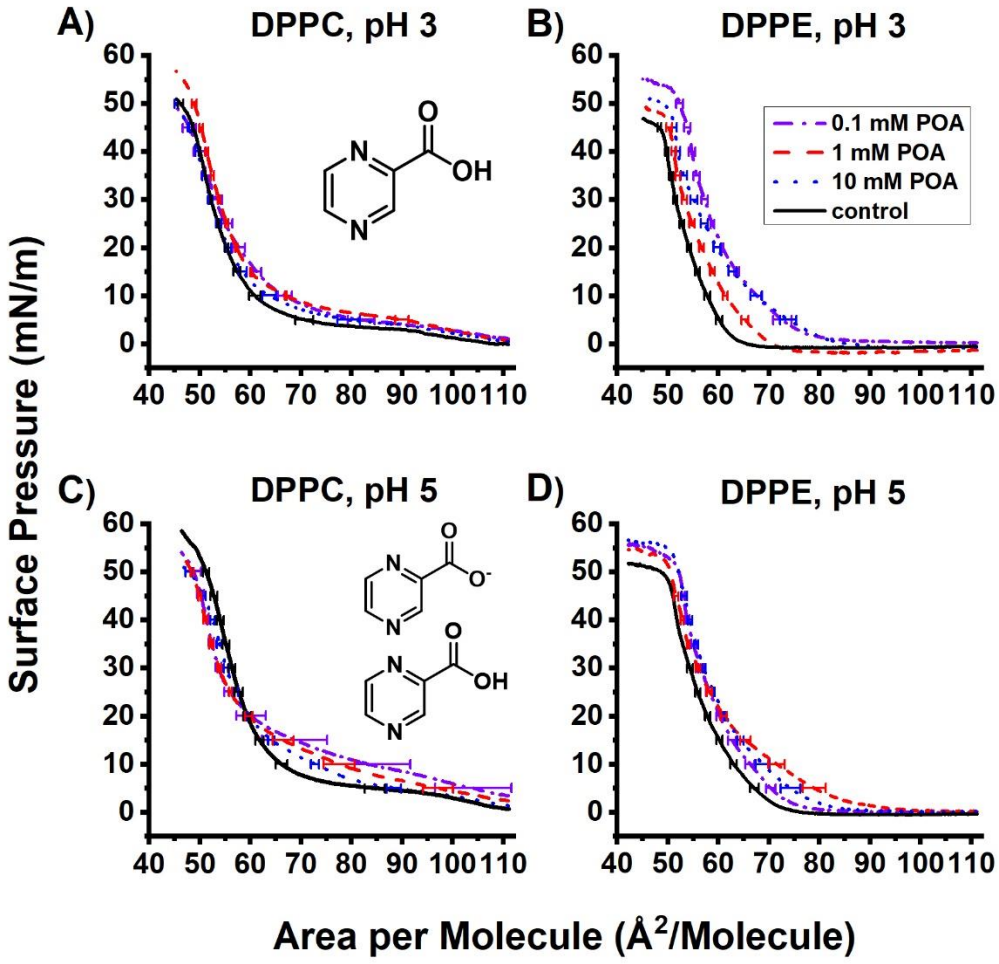

Figure 4.3. Compression isotherms of DPPC (left column) or DPPE (right column) with the subphase at either pH 3 (A and B) of pH 5 (C and D). Structures of species present are provided. Solid black curves represent control monolayers with no POA present, blue dotted curves represent 10 mM POA, red dashed curves represent 1 mM POA, and purple dash-dot curves represent 0.1 mM POA. Each curve is the average of triplicate measurements. Error bars are the standard deviation of the area.

At pH 3, there is some expansion of the DPPC monolayer, though overall, the response is moderate just like at pH 5 and pH 7.4. This can be interpreted as POA_N residing within the interface but not causing any significant differences in packing. In contrast to DPPC, DPPE demonstrates a significant expansion of the monolayer at 0.1 mM and 10 mM concentrations of POA_N. It is possible that these expansive effects are due to the pH instead of the protonation state of POA. However, the pK_a's of both DPPC and DPPE are below two;[37] thus, these differences are more likely due to the different protonation states of POA as opposed to those of the phospholipids.

3.1.3 Compression Modulus Analysis of Langmuir Monolayers

Compression moduli were calculated from the isotherms to assess monolayer elasticity and to confirm phase transitions in DPPC (**Figure 4.4)**. An increase in the compression modulus indicates increased rigidity of the monolayer, while a decrease indicates that the monolayer is becoming more elastic. When exposed to PZA, DPPC did not show a disappearance of the gas-liquid phase transition, indicating that there is not likely a rearrangement of the monolayer. The monolayers exposed to 0.1 mM and 10 mM exhibit little to no difference in compressibility, while the 1 mM showed increased elasticity. For DPPE, PZA showed no effect except at 10 mM, where the monolayer becomes more compressible. Together, the compression moduli of DPPC and DPPE exposed to PZA may make monolayers more tolerant to compression despite seeing no difference in the compression isotherms. A difference in the modulus but not the isotherm suggests that PZA is at the interface but does preferentially reside within the interface at physiological pH.

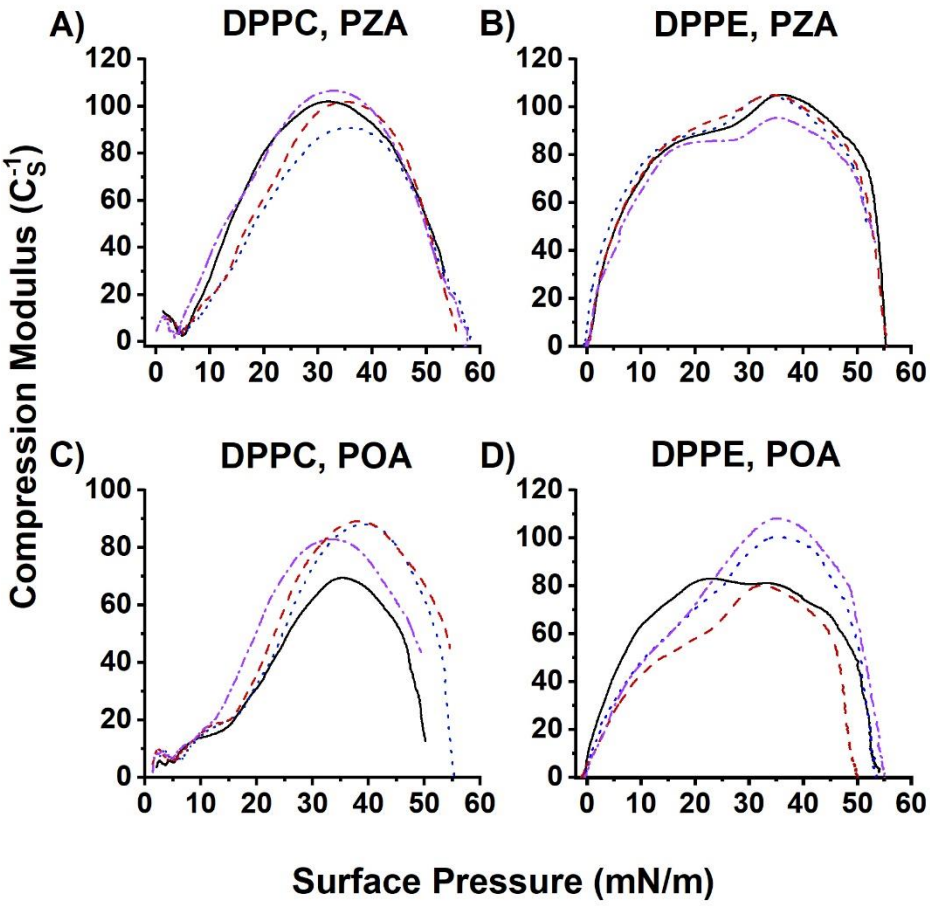

Figure 4.4. Compression moduli of DPPC (left column) or DPPE (right column). Black curves represent phospholipid controls, blue dotted curves represent 10 mM of probe molecule, red dashed curves represent 1 mM of probe molecule, and purple dash-dot curves represent 0.1 mM probe molecule. Curves are the average of at least three replicates.

POA_C increased the rigidity of DPPC at all concentrations at pH 7.4. While it may not increase the area or phase transitions of the monolayer at pH 7.4, POA_C is still exerting an effect on the monolayer by making it less tolerant to changes due to compression. In conjunction with observations of compression isotherms, it is likely that POA_C is at the interface but not within the interface at pH 7.4. The increased rigidity is of interest. To investigate this further, we carried out an NMR analysis.

3.2 ^{1}H NMR Studies of PZA and POA in Reverse Micelles

3.2.1 1H NMR Measurement of PZA in AOT Reverse Micelles

PZA was added to a series of differently sized reverse micelles (RM) prepared from NaAOT in isooctane and with w_0 ranging from 8 to 20. In Figure 4.5, we focus on the aromatic region of the spectrum, highlighting the protons from PZA. H_a in D_2O had a chemical shift of 9.22 ppm (**Figure 4.5**). When the stock solution is placed in RMs, H_a shifts downfield as the RMs size is reduced. Downfield shifts have previously been associated with a location in the interface[38] and would suggest that H_a is associated with the interface possible near the AOT headgroup. In contrast, H_b is a doublet at 8.84 ppm and shifts upfield as the RM size reduces. This implies that H_b is located further up in the interface, likely the AOT tails as reported previously.[33, 38] Similarly, H_c at 8.78 ppm shifts upfield as the RM size reduces, showing that this proton is located in a similar environment as that of H_b. Based on the differences in shifting, we suggest that Ha and the amide functionality are facing the polar headgroup of the AOT (towards the bulk water pool), whereas Hb and Hc are oriented toward the hydrophobic tail groups. The spectra of PZA were also recorded at different pD values. However, since there is no acidic proton, no major change in chemical shifts was observed (Figure A4.3.2).

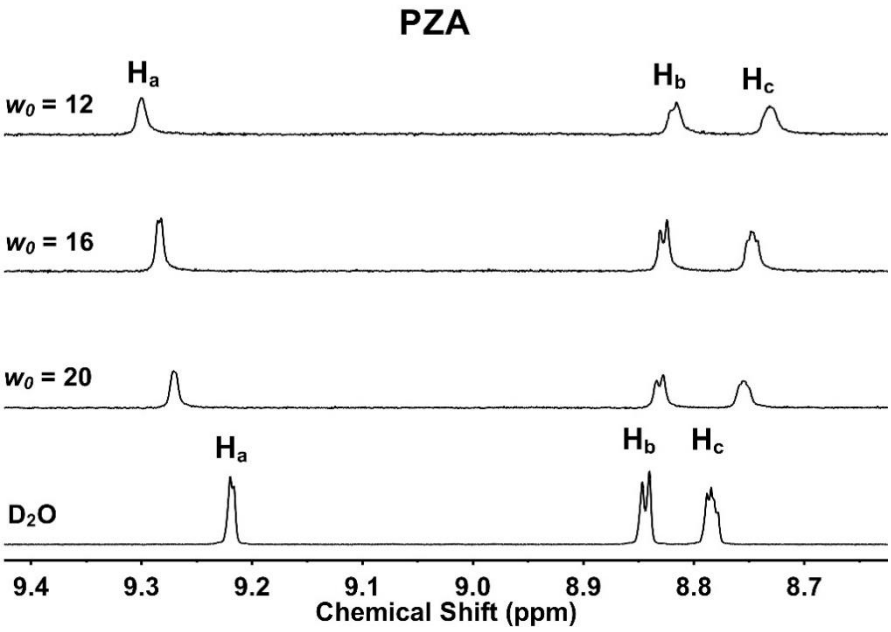

Figure 4.5. ^{1}H NMR spectra of 100 mM PZA in 0.75 MAOT/isooctane reverse micelles and 100% D_2O. The key to the proton labels are defined in Figure 4.1.

3.2.2 1H NMR Measurement of POA in AOT Reverse Micelles

Since POA has an acidic proton, ^{1}H NMR spectra were recorded from stock solutions at different pD values to represent POA_N and POA_C in the AOT/isooctane model membrane interface system, Figure 4.6. An acidic solution of POA_N was added to a series of reverse micelles sized w_0 8-20 prepared from 0.75 M NaAOT in isooctane. When dissolved in D_2O at pD 2.16 (POA_N), the chemical shift of H_a is 9.27 ppm, H_b is at 8.84, and H_c is at 8.77 ppm (Figure 4.6A). When a solution of POA_N was added to RMs of sizes w_0 12-20, H_a shifts upfield, and H_b and H_c coalesce and shift upfield. As described previously[7] these shifts are interpreted as POA_N residing further up in the interface and AOT tails than POA_C as opposed to residing in the water pool.

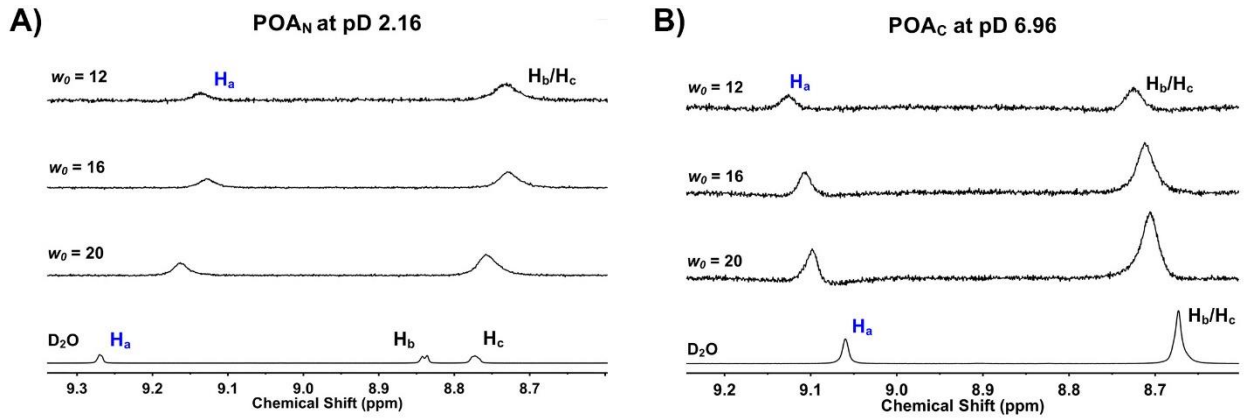

Figure 4.6. ^{1}H NMR spectra of A) 100 mM POA$_N$ at pD 2.16 and B) 100 mM POA$_C$ at pD 6.96 in D_2O and different sizes of 0.75 mM AOT/isooctane reverse micelles.

A solution of pD 6.96 (POA$_C$) was added to 0.75 M mM AOT/isooctane with w_0 ranging from 8 to 20. In the aqueous solution, the ^{1}H NMR chemical shift H_a appears at 9.06 ppm, significantly upfield from that observed at acidic pH (9.27 ppm). When this solution was added to the RMs, the chemical shifts increased above 9.1 ppm, with the peaks shifting increasingly downfield as the RM water pool becomes smaller. These observations are interpreted as the POA$_C$ being associated with the interface but will most likely reside in or near the Stern layer. This is in line with the Langmuir monolayer studies described above, where POA$_C$ interacted with the monolayer but mainly remained in the water.

^{1}H NMR spectra were recorded for a series of POA solutions with varying pD values in different sizes of RM to investigate the pK_a value of the POA associated with the interface (Figure 4.7). The is a consistent pattern across all sizes, so only w_0 16 will be discussed (Figure A4.3.4, Figure A4.3.5, Figure A4.3.6). H_a shifted downfield from 9.32 to 9.12 when the pD of the stock solution n rose from 1.26 to 2.16. H_a then shifted to 9.11 at pD 3.92 where it remained for the increasing pD values. These studies demonstrated that the pK_a of POA associated with the AOT/isooctane interface is significantly less than the calculated 3.46 (Figure 4.1). A change in pK_a value would be anticipated if the POA was associated with the interface. Spectra recorded for the H_a proton of POA in w_0 16 and w_0 12 RMs (Figure S4.3.4, Figure A4.3.5) demonstrate a consistent decrease of the pK_a value when associated with the interface. In the case of POA, the pK_a change is more than one pH unit and hence consistent with the interpretation that the POA is interacting with the AOT interface.

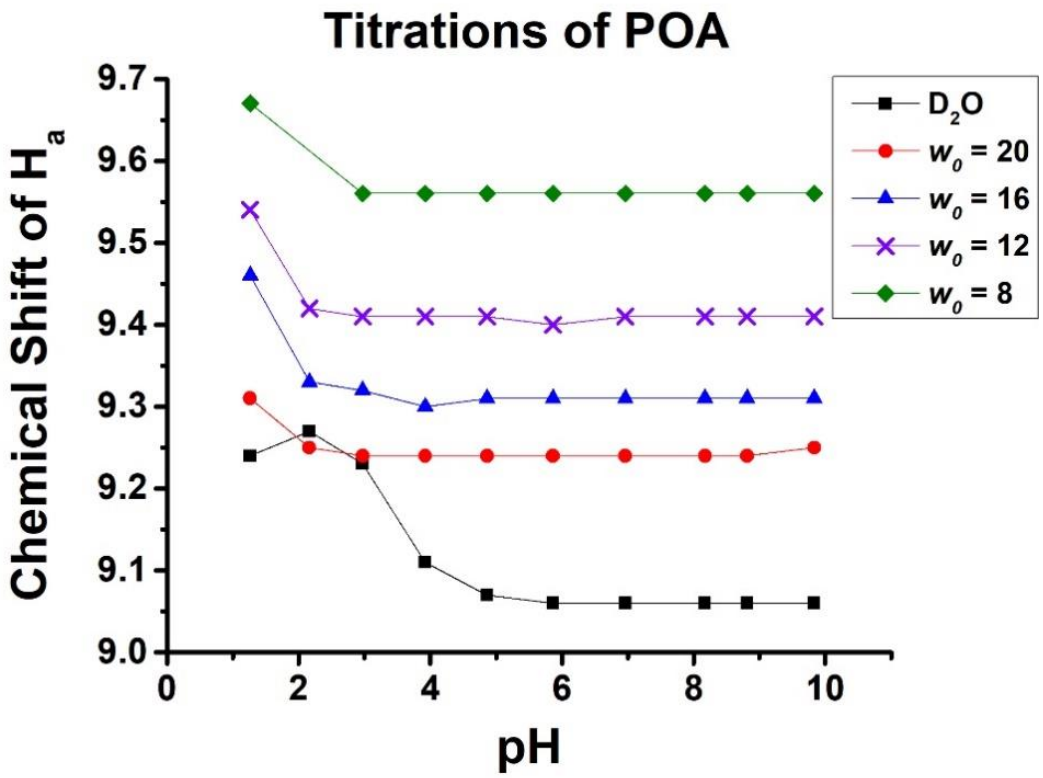

Figure 4.7. Chemical shifts of H_a of 100 mM POA in D_2O and 0.75 M AOT/isooctane reverse micelles of varying sizes. Red circles represent w_0 20, blue triangles represent w_0 16, purples X's represent w_0 12, green diamonds represent w_0 8, and black squares represent D_2O. NMR spectra of the $w_0$12, w_0 16, and w_0 20 reverse micelles are provided in Appendix IV.

Previously, several studies observed that different acids, such as the aforementioned benzoic acid and dipicolinic acid (Figure 4.1), had a decreased pK_a value upon addition to RMs.[6-7, 33] These acids were found to reside in the AOT interface using a variety of techniques, such as ^1H NMR, ^{51}V NMR, Langmuir monolayers, RMs, and other model membrane techniques.[6, 8, 29-30, 38] Previously, anilinium was found to change the pK_a value upon insertion into the AOT reverse micelle interface,[39] but these changes are smaller than the differences observed here. We conclude that the large reduction in pK_a value is also consistent with placement in the interface. In this case, the placement may be further up into the interface since there is a large change in the chemical environment, causing a greater change in pK_a value.

3.3 Liposome Leakage Assay to Determine Ability of PZA and POA to Disrupt a Bilayer Membrane

Combined, the Langmuir monoloyer and ^{1}H NMR studies suggest that POA_N and POA_C are associating weakly with the interface. Studies in cellular systems show that POA is a protonophore [9] and able to transport H^+ across a membrane, equilibrating an existing pH potential.[40] Hence it is believed that POA_N and POA_C are both able to traverse membranes without causing disruption. In the following experiments, we aim to demonstrate that neither POA_N nor POA_C are able to disrupt the membrane. In the following, we test the ability of PZA and POA_C to cause leakage in a bilayer by loading a large unilamellar vesicle (LUV) prepared from L-α-phosphatidylcholine lipids with a fluorophore to determine whether the lipid bilayer is compromised in the presence of the additive.

Specifically, LUVs encapsulating self-quenching 5(6)-carboxyfluorescein (CF) were exposed to varying concentrations of PZA or POA with the objective to determine if the additive is capable of disrupting the liposomal membrane. If the membrane is disrupted, the self-quenching dye is released and an increase in fluorescence intensity is observed.[31, 41] A positive control experiment was done in which concentrations varying from 0-0.5% of Triton X-100 were added to test the validity of the assay (Figure 4.8A). This experiment serves as a control experiment, as Triton X-100 is known to penetrate and disrupt lipid bilayers causing the dye to fluoresce when the lipid bilayer is compromised. Increasing the percent volume of Triton resulted in a linear increase in fluorescence with an $R^2 = 0.92$, thus validating the method (Figure 4.8A).

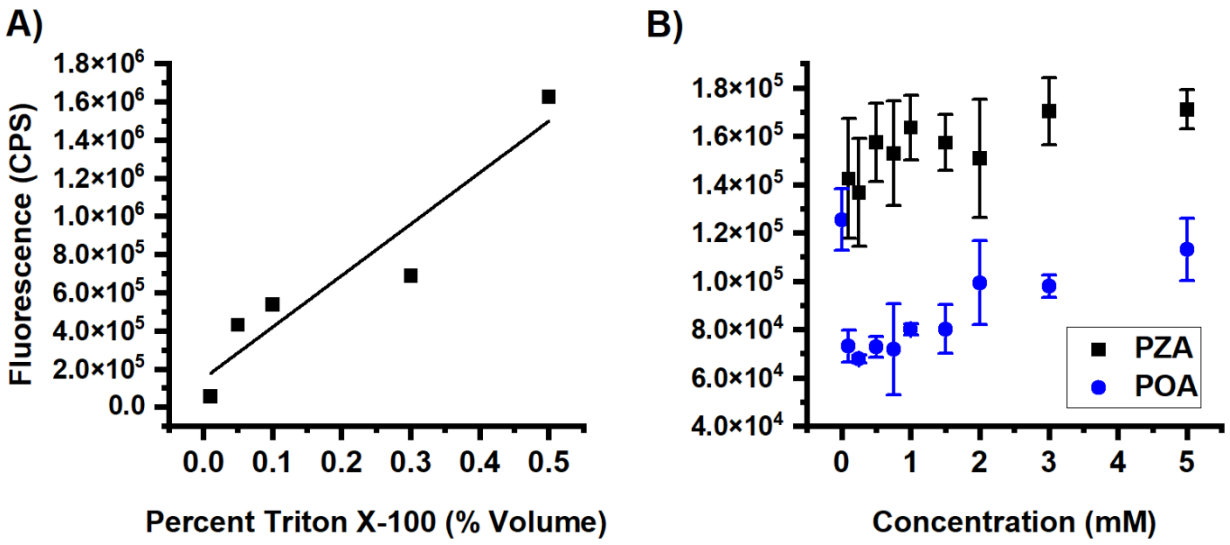

Figure 4.8. Induced CF leakage studies with A) Triton X-100 or B) PZA and POA. Panel A) shows fluorescence vs percent Triton X-100 fitter to a linear regression model (R^2 = 0.92). Panel B) shows fluorescence vs concentration of PZA (black squares) or POA (blue circles). It should be noted that the scales of B is 10-fold lower than that of Panel A. Error bars are the standard deviation of triplicate measurements. A bar graph with the average fluorescence intensity of experimental groups is provided in the Appendix IV.

Addition of 1-5 mM PZA and POA overall did not induce any appreciable fluorescence, as all values are within a magnitude of the zero (Figure 4.8B). It should also be noted that the maximum fluorescence observed in the Triton control experiment is tenfold higher than that of any sample exposed up to 5 mM of PZA or POA. This observation supports the conclusion that negligible fluorescence is resulting from adding up to 5 mM PZA or POA to a LUV documenting the integrity of the lipid bilayer in the LUV. Since the bilayer is not compromised, this conforms to our studies with Langmuir monolayers and RMs and suggests that cells in a biological system will also remain intact and not cause disorganization of a biological membrane bilayer.

3.4 Implications and Future Directions

Much like benzoic acid and benzoate, POA_N and POA_C reside in different locations of the membrane as suggested by several lines of evidence. Specifically, POA_N resides further up in the hydrophobic part of the interface while POA_C resides in the hydrophilic Stern layer. This observation is consistent with the possibility that POA, like benzoic acid, is able to behave as a protonophore in a bilayer when there is a pH gradient across the membrane. These results suggest that PZA, POA_N and

POA_C do not compromise the organization of the lipid bilayer even though we show that they are able to incorporate themselves with a membrane interface. Hence, although POA behaves as a protonophore, such disruption of the pH gradient is not due to disruption of the membrane but more likely due to the transport POA_N across the membrane and delivery of the acidic proton. Combined, these studies confirm our hypothesis that *the interaction of PZA and POA with lipid monolayers and bilayers does not disrupt the lipid bilayer but leaves the membrane intact*.

4. Summary and Conclusions

The membrane interactions of PZA and POA were investigated to determine if their interaction is able to disrupt a lipid bilayer, and their physicochemical properties are consistent with the designation of POA as a protonophore for *M. tuberculosis*. Langmuir monolayer studies show that PZA has little to no interaction with the interface, while POA_C slightly associates with the interface. POA_N showed moderate expansion of the monolayer, consistent with the neutral species residing in the interface as opposed to the bulk water. NMR studies suggest that the neutral form of POA penetrates the interface while the deprotonated and charged species of POA resides in the interfacial water layer. Large unilamellar vesicles prepared from egg phosphatidylcholine loaded with a fluorescent dye did not show any leakage of dye, documenting that the vesicles are intact and not compromised by the presence of PZA or POA_C. These studies support the interpretation that when POA acts as a protonophore, it does not disrupt the membrane bilayer. Instead, the neutral and protonated form of POA is transported across the membrane, delivers the proton and transport deprotonated and charged POA back to equilibrate the pH potential over the membrane. Computational studies may be able to provide insights into the origins of these physical processes.

References

1. Lamont, E. A.; Dillon, N. A.; Baughn, A. D., The Bewildering Antitubercular Action of Pyrazinamide. *Microbiol. Mol. Biol. Rev.* **2020,** *84* (2), e00070-19.

2. Zhang, Y.; Wade, M. M.; Scorpio, A.; Zhang, H.; Sun, Z., Mode of action of pyrazinamide: disruption of *Mycobacterium tuberculosis* membrane transport and energetics by pyrazinoic acid. *J. Antimicrob. Chemother.* **2003,** *52* (5), 790-795.

3. Sun, Q.; Li, X.; Perez, L. M.; Shi, W.; Zhang, Y.; Sacchettini, J. C., The molecular basis of pyrazinamide activity on *Mycobacterium tuberculosis panD*. *Nat. Commun.* **2020,** *11*, 339.

4. Nijire, M.; Wang, N.; Wang, B.; Tan, Y.; Cai, X.; Liu, Y.; Mugweru, J.; Guo, J.; Hameed, H. M. A.; Tan, S.; Liu, J.; Yew, W. W.; Nuremberger, E.; Lamichhane, G.; Liu, J.; Zhang, T., Pyrazinoic Acid Inhibits a Bifunctional Enzyme in *Mycobacterium tuberculosis*. *Antimicrob. Agents Chemother.* **2017,** *61* (7), e00070-17.

5. Lu, P.; Haagsma, A. C.; Pham, H.; Maaskant, J. J.; Mol, S.; Lill, H.; Bald, D., Pyrazinoic Acid Decreases the Proton Motive Force, Respiratory ATP Synthesis Activity, and Cellular ATP Levels. *Antimicrob. Agents Chemother.* **2011,** *55* (11), 5354-5357.

6. Sostarecz, A. G.; Gaidamauskas, E.; Distin, S.; Bonetti, S. J.; Levinger, N. E.; Crans, D. C., Correlation of insulin-enhancing properties of vanadium-dipicolinate complexes in model membrane systems: phospholipid Langmuir monolayers and AOT reverse micelles. *Chemistry* **2014,** *20* (17), 5149-5159.

7. Peters, B. J.; Groninger, A. S.; Fontes, F. L.; Crick, D. C.; Crans, D. C., Differences in Interactions of Benzoic Acid and Benzoate with Interfaces. *Langmuir* **2016,** *32* (37), 9451-9459.

8. Peters, B. J.; Van Cleave, C.; Haase, A. A.; Hough, J. P. B.; Giffen-Kent, K. A.; Cardiff, G. M.; Sostarecz, A. G.; Crick, D. C.; Crans, D. C., Structure Dependence of Pyridine and Benzene Derivatives on Interactions with Model Membranes. *Langmuir* **2018,** *34* (30), 8939-8951.

9. Gabba, M.; Frallicciardi, J.; van 't Klooster, J.; Henderson, R.; Syga, Ł.; Mand, R.; van Maris, A. J. A.; Poolman, B., Weak Acid Permeation in Synthetic Lipid Vesicles and Across the Yeast Plasma Membrane. *Biophys. J.* **2020,** *118* (21), 422-434.

10. Fontes, F. L. The pH-dependent activity and the protonophoric mechanism of pyrazinoic acid and its structural analogues. Colorado State University, Fort Collins, 2019.

11. Fontes, F. L.; Peters, B. J.; Crans, D. C.; Crick, D. C., The Acid-Base Equilibrium of Pyrazinoic Acid Drives the pH Dependence of Pyrazinamide-Induced *Mycobacterium tuberculosis* Growth Inhibition. *ACS Infect. Dis.* **2020,** *6* (11), 3004-3014.

12. Zhu, Q.; Lu, Y.; He, X.; Liu, T.; Chen, H.; Wang, F.; Zheng, D.; Dong, H.; Ma, J., Entropy and Polarity Control the Partition and Transportation of Drug-like Molecule in Biological Membrane. *Sci. Rep.* **2017,** *7*, 17749.

13. Shinoda, W., Permeability across lipid membranes. *Biochim. Biophys. Acta* **2016,** *1858*, 2254-2265.

14. Bunea, A.-I.; Harloff-Helleberg, S.; Taboryski, R.; Nielsen, H. M., Membrane interactions in drug delivery: Model cell membranes and orthogonal techniques. *Adv. Colloid Interface Sci.* **2020,** *281*, 102177.

15. Chen, G.; Shen, Z.; Li, Y., A machine-learning-assisted study of the permeability of small drug-like molecules across lipid membranes. *Phys. Chem. Chem. Phys.* **2020,** *22*, 19687-19696.

16. Serjeant, E. P.; Dempsey, B., *Ionisation Constants of Organic Acids in Aqueous Solution*. Pergamon Press: Oxford, 1979.

17. Zhang, Y.; Mitchison, D., The curious characteristics of pyrazinamide: a review. *Int. J. Tuberc. Lung Dis.* **2003,** *7* (1), 6-21.

18. Nicholls, D. G.; Ferguson, S. J., *Bioenergetics*. 4 ed.; Academic Press: Amsterdam, 2013.

19. Brezesinski, G.; Möhwald, H., Langmuir monolayers to study interactions at model membrane surfaces. *Adv. Colloid Interface Sci.* **2003,** *100-102*, 563-584.

20. Ariga, K., Don't Forget Langmuir-Blodgett Films 2020: Interfacial Nanoarchitectonics with Molecules, Materials, and Living Objects. *Langmuir* **2020,** *36* (26), 7158-7180.

21. Veldhuizen, E. J. A.; Haagsman, H. P., Role of pulmonary surfactant components in surface film formation and dynamics. *Biochim. Biophys. Acta - Biomembr.* **2000,** *1467* (2), 255-270.

22. Wüstneck, R.; Perez-Gil, J.; Wüstneck, N.; Cruz, A.; Fainerman, V. B.; Pison, U., Interfacial properties of pulmonary surfactant layers. *Advanced Colloid and Interface Science* **2005,** *117* (1-3), 33-58.

23. Fadeel, B.; Xue, D., The ins and outs of phospholipid asymmetry in the plasma membrane: roles in health and disease. *Crit. Rev. Biochem. Mol. Biol.* **2009,** *44* (5), 264-277.

24. Chakrabarti, A., Phospholipid Asymmetry in Biological Membranes: Is the Role of phosphatidylethanolamine Underappreciated? *J. Membr. Biol.* **2021,** *254*, 127-132.

25. Patterson, S.; Wyllie, S., Nitro drugs for the treatment of trypanosomatid disease: past, present, and future prospects. *Trends Parasitol.* **2014,** *30* (6), 289-298.

26. Shaw, N., Lipid Composition as a Guide to the Classification of Bacteria. In *Advances in Applied Microbioligy*, Perlman, D., Ed. Academic Press: New York, 1974; Vol. 17, pp 63-108.

27. Crans, D. C.; Rithner, C. D.; Baruah, B.; Gourley, B. L.; Levinger, N. E., Molecular Probe Location in Reverse Micelles Determined by NMR Dipolar Interactions. *J. Am. Chem. Soc.* **2006,** *128* (13), 4437-4445.

28. Maitra, A., Determination of size parameters of water-Aerosol OT-oil reverse micelles from their nuclear magnetic resonance data. *J Phys Chem* **1984,** *88* (21), 5122-5125.

29. Gaidamauskas, E.; Cleaver, D. P.; Chatterjee, P. B.; Crans, D. C., Effect of Micellar and Reverse Micellar Interface on Solute Location: 2,6-Pyridinedicarboxylate in CTAB Micelles and CTAB and AOT Reverse Micelles. *Langmuir* **2010,** *26* (16), 13153-13161.

30. Baruah, B.; Roden, J. M.; Sedgewick, M.; Correa, M.; Crans, D. C.; Levinger, N. E., When is Water Not Water? Exploring Water Confined in Larfe Reverse Micelles Using a Highly Charged Inorganic Molecular Probe. *J. Am. Chem. Soc.* **2006,** *128* (39), 12758-12765.

31. Liu, Y.; Liu, J., Leakage and Rupture of Lipid Membranes by Charged Polymers and Nanoparticles. *Langmuir* **2020,** *36* (3), 810-818.

32. Samart, N.; Beuning, C. N.; Haller, K. J.; Rithner, C. D.; Crans, D. C., Interaction of Biguanide Compound with Membrane Model Interface Systems: Probing the Properties of Antimalarial and Antidiabetic Compounds. *Langmuir* **2014,** *30* (29), 8697-8706.

33. Crans, D. C.; Trujillo, A. M.; Bonetti, S.; Rithner, C. D.; Baruah, B.; Levinger, N. E., Penetration of Negatively Charged Lipid Interfaces by the Doubly Deprotonated Dipicolinate. *J. Org. Chem.* **2008,** *73* (24), 9633-9640.

34. Jimah, J. R.; Schlesinger, P. H.; Tolia, N. H., Liposome Distruption Assay to Examine Lytic Properties of Biomolecules. *Bio Protoc.* **2017,** *7* (15), e2433.

35. Pizzirusso, A.; De Nicola, A.; Sevnik, G. J. A.; Correa, A.; Cascella, M.; Kawakatsu, T.; Rocco, M.; Zhao, Y.; Celino, M.; Milano, G., Biomembrane solubilization mechanism by Triton X-100: a computational study of the three stage model. *Phys. Chem. Chem. Phys.* **2017,** *19* (44), 29780-29794.

36. Jones, M. N.; Chapman, D., *Micelles, Monolayers, and Biomembranes*. Wiley-Liss, Inc.: New York, 1995.

37. Marsh, D., *Handbook of Lipid Bilayers*. 2 ed.; CRC Press: Boca Raton, 2013.

38. Horton, D. C.; VanDerveer, D.; Krzystek, J.; Tesler, J.; Pittman, T.; Crans, D. C.; Holder, A. A., Spectroscopic Characterization of L-ascorbic Acid-induced Reduction of Vanadium(V) Dipicolinates: Formation of Vanadium(III) and Vanadium(IV) Complexes from Vanadium(V) Dipicolinate Derivatives. *Inorg. Chim. Acta* **2014,** *420* (24), 112-119.

39. Sripradite, J.; Miller, S. A.; Johnson, M. D.; Tongraar, A.; Crans, D. C., How Interfaces Accet the Acidity of the Anilinium Ions. *Chemistry* **2016,** *22* (11), 3873-3880.

40. Feng, X.; Zhu, W.; Schurig-Briccio, L. A.; Lindert, S.; Shoen, C.; Hitchings, R.; Li, J.; Wang, Y.; Baig, N.; Zhou, T.; Kim, B. K.; Crick, D. C.; Cynamon, M.; McCammon, J. A.; Gennis, R. B.; Oldfield, E., Antiinfectives targeting enzymes and the proton motive force. *Proc. Natl. Acad. Sci.* **2015,** *112* (51), E7073-E7082.

41. Nasr, G.; Griege-Gerges, H.; Elaissari, A.; Khreich, N., Liposomal membrane permeability assessment by fluorescence techniques: Main permeabilizing agents, applications and challenges. *Int. J. Pharm.* **2020,** *580*, 119198.

Chapter 5
Summary and Future Directions

5.1 Summary

The research in this dissertation provides fundamental experimental insight into the location and association of small biologically relevant molecules with model membrane systems.

Chapter 2 explored the locations of menaquinone (MK) headgroups withing model membrane interfaces. For these studies, we used Langmuir monolayers and reverse micelle (RM) microemulsions to investigate how the menaquinone headgroup (menadione, MEN) and the menahydroquinone headgroup (menadiol, MDL) associate with model membrane interfaces to determine if redox state (oxidized vs reduced) caused a difference in molecule location within a model membrane interface. The literature suggested any variation in the location of MKs within the interface was mainly caused by the isoprenyl side chain rather than the headgroup quinone-to-quinol reduction during electron transport. We have now presented experimental evidence to the contrary; quinone-quinol cycling likely drives location of MKs within the cell membrane. Utilizing Langmuir monolayers and NMR of RMs, we determined that MEN resided farther into the interface while MDL resided near the interfacial water. These findings are in line with the more hydrophobic nature of MEN compared to MDL. It follows that if MKs moves within the cell membrane upon menaquinol formation, it is due at least in part, to the differences in the properties of headgroup interactions with the membrane in addition to the isoprenyl side chain.

Chapter 3 investigated the effects of varying the tail length of truncated MKs with phospholipid monolayers and bilayers We have previously demonstrated that the folded conformation of truncated MK homologues, MK-1 and MK-2, in both solution and reverse micelle microemulsions depended on environment. There is little information on how MKs associate with phospholipids in a model membrane system and how MKs affect phospholipid organization. In this chapter, we used a combination of Langmuir monolayer studies and molecular dynamics (MD) simulations to probe these questions on truncated MK homologues, MK-1 through MK-4

within a model membrane. We observed that truncated MKs reside farther away from the interfacial water than ubiquinones are located closer to the phospholipid tails. We also observed that phospholipid packing does not change at physiological pressure in the presence of truncated MKs, though a difference in phospholipid packing has been observed in the presence of ubiquinones. We found through MD simulations that for truncated MKs, the folded conformation varied, but MKs location and association with the bilayer remained unchanged at physiological conditions regardless of side chain length. Combined, Chapter 3 provides fundamental information, both experimental and computational, on the location, association, and conformation of truncated MK homologues in model membrane environments relevant to bacterial energy production.

Chapter 4 explored the physicochemical properties of two molecules related to the treatment of tuberculosis, pyrazinamide (PZA) and pyrazinoic acid (POA). PZA, a pro-drug, is converted by the host into POA, which has demonstrated anti-tubercule activity as well as protonophore-like behavior *in vitro*. To exert drug or protonophore activity, POA must inter the cell and therefore must interact with the cell membrane. However, there is little fundamental information on the physicochemical properties of POA within the cell membrane interface. To investigate, we used a combination of model membranes to explore i) association and ii) location in an interface. We observed that the charged species, POA_C, showed very minor association even at high concentration with a phospholipid monolayer while the neutral species, POA_N, showed much greater association. The increased association implied that POA_N resided within the interface, so NMR studies in RMs were pursued. We demonstrated that POA_C remained closer to the water pool while POA_N was further towards the surfactant tails. Together, these studies are comparable to studies with benzoic acid, a known protonophore, possibly providing insight into the protonophore-like activity of POA.

5.2 Future Directions

The following is a series of suggestions for future avenues of inquiry pertaining to MKs within the cell membrane. Some pathways are already underway, but I feel they deserve some mention. I will first start with the study of headgroups. The most obvious next step is to test the headgroups of other lipoquinones to see if the trend we found with MEN and MDL in model membranes holds true. Margaret (Maggi) Braasch-Turi, Dr. Jordan T. Koehn, Kateryna (Kate) Kostenkova, Heide A. Murakami, and myself have already contributed to the study of ubiquinone (UQ) and its benzoquinone headgroup in model membranes. While not presented in this dissertation, the published manuscript of Chapter 2 contains NMR of benzoquinone in RMs (see Appendix V).[1] We have not, however, run benzoquinol. The quinols are not what they seem; they are not trivial to work with due to their instability under atmospheric condition. Ubiquinols are reported to be more stable,[2-3] but I would like to see if a more robust method for working with quinols could be developed. I have received suggestions of degassing the water first and working under an argon atmosphere. I suggest that studies may be completed with liposomes, provided that any water is degassed. Simplified, the steps would consist of i) forming a lipid cake, ii) rehydrating the lipid cake with degassed D_2O under argon, iii) adding the quinol under inert atmosphere, and iv) running NMR immediately after addition of the quinol. This could be done with MEN and MDL, as well as benzoquinone and benzoquinol to compare the differences in location of the two sets. However, I anticipate that it will be difficult to answer Professor Crans's inevitable question of "what is the pH?"

In the same vein of investigating the effects of headgroup, Maggi, Jordan, and Kate are currently (September 2021) writing up a manuscript on the differences in location and association of UQ-2 and MK-2 within RMs and Langmuir monolayers. This manuscript will provide insight into how headgroup structure (as opposed to headgroup redox state) influences the location of lipoquinones within model membranes.

In Chapter 3, I discussed side chain length of MKs. I used only MK-1 through MK-4. While the next logical step may be to use MK-5 through MK-9, these are not trivial to synthesize or isolate. For

perspective, 10 mg of MK-9 costs approximately $300 USD at the writing of this manuscript (Santa Cruz Biotechnology), and the synthesis of MK-2 is seven steps.[4] While I would love to run the rest of these compounds, it just is not feasible at this time. I believe the best way forward is to study the compounds we have (MK-1 through MK-4) with liposomes made of different phospholipids, such as DPPC, DPPG, POPC, POPG, and POPE. A variety of techniques may be used to study location and behavior, such as NMR and electrochemistry. As of 2021, Dr. Kaitlin A. Doucette has performed electrochemistry of differing MKs in POPC liposomes which is described in her dissertation.[5] Dr. Kaitlin A. Doucette and Gaia R. Bublitz have also explored the location and conformation of MK-2 within POPC liposomes through the use of 2D ^{1}H-^{1}H NMR.[5-6] While POPC is one of the most biologically plentiful phospholipids, it is not found in bacteria, which use MKs in the electron transport chain.[7] As such, the phospholipids DPPG, POPG, and POPE would be of use as they are common components of bacterial cell membranes[8] with at least moderate ability to form liposomes when mixed together.[9-11] NMR and electrochemical studies of MKs with DPPG, POPG, and POPE will give fundamental information on the association of MKs with phospholipids of varying phospholipid tail length and saturation as well as varying phospholipid headgroups.

However, it will be necessary at some point to create liposomes with lipids extracted from *Mycobacterium tuberculosis* or *Mycobacterium smegmatis* in order to answer the overarching questions of location, association, conformation, and redox behavior of MKs in their native membrane environment. This will not be trivial, as we will then be analyzing a mixture of more than two lipids as opposed to a single phospholipid. This will no doubt convolute any NMR spectra, so other techniques will be needed. Dr. Kaitlin A. Doucette's aforementioned work on electrochemistry in liposomes will still be useful, but I anticipate the use of differential scanning calorimetry (DSC) and Raman spectroscopy will be helpful. A previous study carried out by Roche *et al*. in 2006 successfully combined DSC and Raman to demonstrate the location and association of UQs in DPPC liposomes whereby the location of a foreign molecule in a phospholipid bilayer may be determined based on the gel-liquid transition.[12] They demonstrated that shorter UQs were located in aggregates close to the interface while longer UQs were homogeneously dispersed in the bilayer midplane. A DSC/Raman

study does not give the same molecular information as NMR, but combined with computational modeling, there will likely be a wealth of information inaccessible with our current techniques.

I do truly believe that we are starting to paint a fuller picture of how MKs work, and I can only hope that these suggestions bear some fruit in the future. I am unsure where this will lead, but I am sure it will be fantastic.

References

1. Van Cleave, C.; Murakami, H. A.; Samart, N.; Koehn, J. T.; Maldonado, P.; Kreckel, H. D.; Cope, E. J.; Basile, A.; Crick, D. C.; Crans, D. C., Location of menaquinone and menaquinol headgroups in model membranes. *Can. J. Chem.* **2020,** *98* (6), 307-317.

2. Quinn, P. J.; Esfahani, M. A., Ubiquinones Have Surface-Active Properties Suited to Transport Electrons and Protons across Membranes. *Biochem J* **1980,** *185* (3), 715-722.

3. Roche, Y.; Peretti, P.; Bernard, S., The redox state influences the interaction of ubiquinones with phospholipid bilayers. *J. Therm. Anal. Calorim.* **2007,** *89*, 867-873.

4. Koehn, J. T.; Magallanes, E. S.; Peters, B. J.; Beuning, C. N.; Haase, A. A.; Zhu, M. J.; Rithner, C. D.; Crick, D. C.; Crans, D. C., A Synthetic Isoprenoid Lipoquinone, Menaquinone-2, Adopts a Folded Conformation in Solution and at a Model Membrane Interface. *J. Org. Chem.* **2018,** *83*, 275-288.

5. Doucette, K. A. The use of model membrane techniques for the analysis of interactions, conformation, and redox properties of menaquinones and other small molecules. Ph.D. Dissertation, Colorado State University, Fort Collins, 2021.

6. Bublitz, G. R. Characterization of Interactions of Lipoquinone Derivatives Within Model Membrane Systems. M.S. Thesis, Colorado State University, Fort Collins, 2021.

7. Marsh, D., *Handbook of Lipid Bilayers*. 2 ed.; CRC Press: Boca Raton, 2013.

8. López-Lara, I. M.; Geiger, O., Bacterial lipid diversity. *Biochim. Biophys. Acta Mol. Cell. Biol. Lipids* **2017,** *1862* (11), 1287-1299.

9. Duarte, A. A.; Bothelo do Rego, A. M.; Salerno, M.; Ribeiro, P. A.; El Bari, N.; Bouchikhi, B.; Raposo, M., DPPG Lipsosomes Adsorbed on Polymer Cusions: Effects of Roughness on AMount, Surface Composition and Topography. *J. Phys. Chem. B* **2015,** *119* (27), 8544-8552.

10. Pozo Navas, B.; Lohner, K.; Deutsch, G.; Sevcsik, E.; Riske, K. A.; Dimova, R.; Garidel, P.; Pabst, G., Composition dependence of vesicle morphology and mixing properties in a bacterial model membrane system. *Biochim. Biophys. Acta Biomembr.* **2005,** *1716* (1), 40-48.

11. Seeger, H. M.; Marino, G.; A., A.; Facci, P., Effect of physical Parameters on the Main Phase Transition of Supported Lipid Bilayers. *Biophys. J.* **2009,** *97* (4), 1067-1076.

12. Roche, Y.; Peretti, P.; Bernard, S., DSC and Raman studies of the side chain length effect of ubiquinones on the thermotropic phase behavior of liposomes. *Thermochim. Acta* **2006,** *447* (1), 81-88.

Appendix I: Distribution of Work

Chapter 1

A review. Written by Cameron Van Cleave.

Chapter 2

Writing of the manuscript was done by Cameron Van Cleave. UV-vis studies and data were performed by Cameron Van Cleave. Langmuir monolayer experiments and data workup were performed by Pablo Maldonado, Jr., Heidi D. Kreckel, and Andrea Basile with project management from Cameron Van Cleave. NMR studies of MEN were recorded by Jordan T. Koehn and Elana J. Cope and processed by Heide A. Murakami. NMR Studies of MDL were performed by Heide A. Murakami and Nuttaporn Samart. DLS studies were performed by Heidi D. Kreckel.

Chapter 3

Manuscript was written by Cameron Van Cleave and Dr. Jordan T. Koehn. Langmuir monolayer studies of MK-1 and MK-2 were performed by Cameron Van Cleave, Benjamin J. Peters, and Allison A. Haase. Langmuir monolayer studies of MK-3 were performed by Cameron Van Cleave. MK-4 Langmuir monolayer studies were performed by Cameron Van Cleave, Allison A. Haase, and Katarina J. Werst. Ideal area calculations were performed by Seth W. Croslow and Kyle G. McLaughlin. BAM images were taken by Allison A. Haase and Cameron Van Cleave. Simulations and modeling were performed by Professor Guilherme Menegon Arantes and Dr. Caroline Simões Pereira.

Chapter 4

Writing was done by Cameron Van Cleave. Langmuir monolayer studies were performed by Cameron Van Cleave, Allison A. Haase, and John Peter B. Hough with assistance from Benjamin J. Peters. 1D ^{1}H NMR studies were performed by Benjamin J. Peters. DLS experiments were performed

by Benjamin J. Peters. Fluorescence leakage studies were performed by Kaitlin A. Doucette and LaRee L. Henry.

Chapter 5

Closing remarks and future directions. Written by Cameron Van Cleave.

Appendix II: Supporting Information for Chapter 2[d]

A2.1. Stability UV-Vis Studies

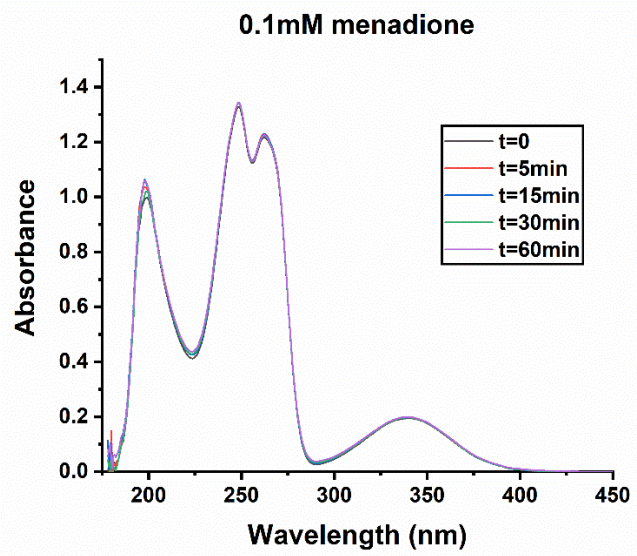

Figure A2.1.1 UV-vis spectra of 0.1 mM MEN in water over 60 minutes, demonstrating the stability of MEN in aqueous solution.

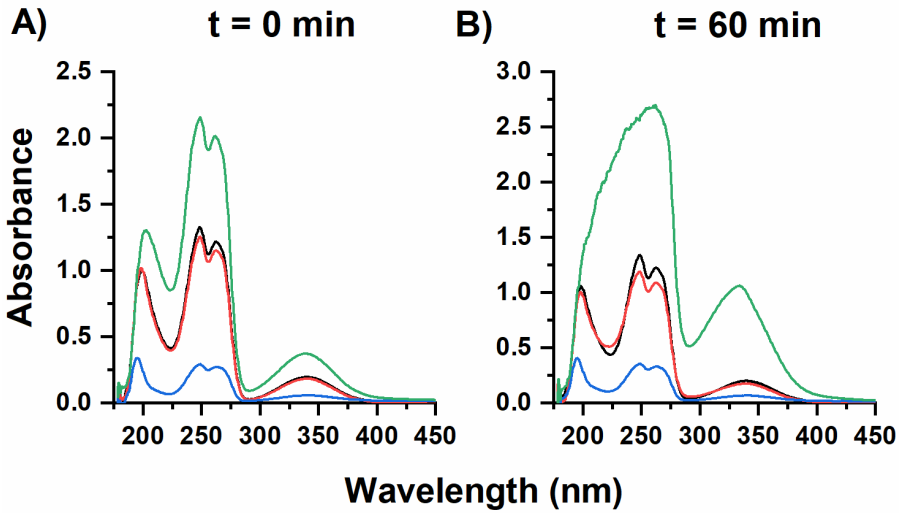

Figure A2.1.2. Full UV-vis spectra of 0.1 mM MEN (black), 0.1 mM MDL that was fully dissolved before analysis (red), supernatant from a 0.1 mM MDL solution when MDL had just been added to water (blue), and aqueous solution added to solid MDL at the bottom of the quartz cuvette (green). Spectra are shown at times A) t = 0 min and B) t = 60 min.

[d] This material is published in the *Canadian Journal of Chemistry*.

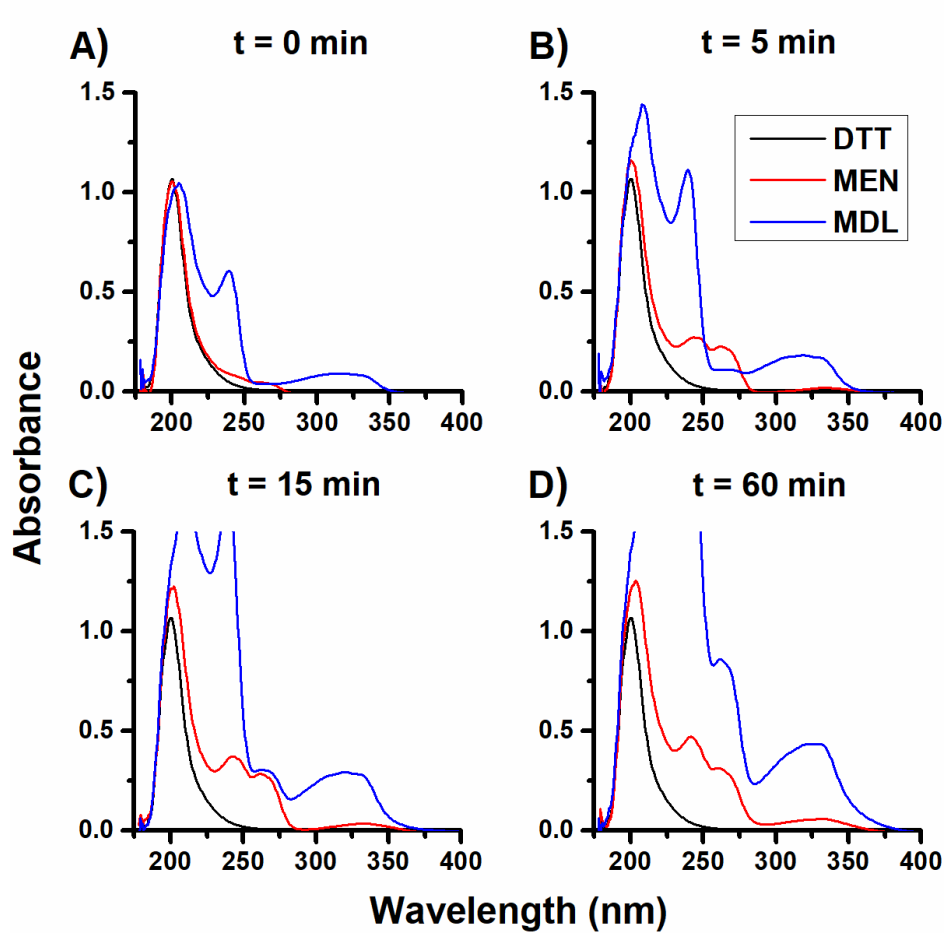

Figure A2.1.3. UV-vis of DTT reference (black), solid MEN with solid DTT (red), and solid MDL with solid DTT (blue) over 60 minutes. Panel A) represents time t = 0 min, B) is at t = 5 min, C) is at t = 15 min, and D is at t = 60 min. Figures presented in the main text truncate the y-axis to 1.5 as any measurement above 1.5 has high experimental error.

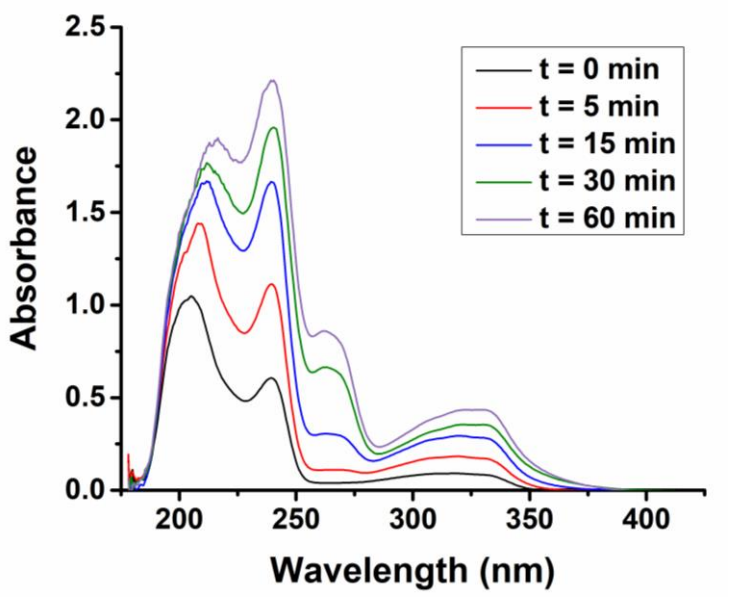

Figure A2.1.4. Full UV-vis spectra of similar amounts of MDL and DTT dissolving into aqueous solution over 60 minutes. Figures presented in the main text truncate the y-axis to 1.5 as any measurement above 1.5 has high experimental error.

A2.2. Calculation of Compression Moduli

Compression moduli were calculated using OriginPro version 9.1 from the compression isotherm average results using equation A1, where C_s^{-1} is the compression modulus, A is the surface area per molecule (Å^2), and π is the surface pressure (mN/m).

$$C_S^{-1} = -A(\frac{d\pi}{dA}) \quad \text{(A1)}$$

A Savitsky-Golay smoothing function was used (2nd degree polynomial, 250 points in the window).

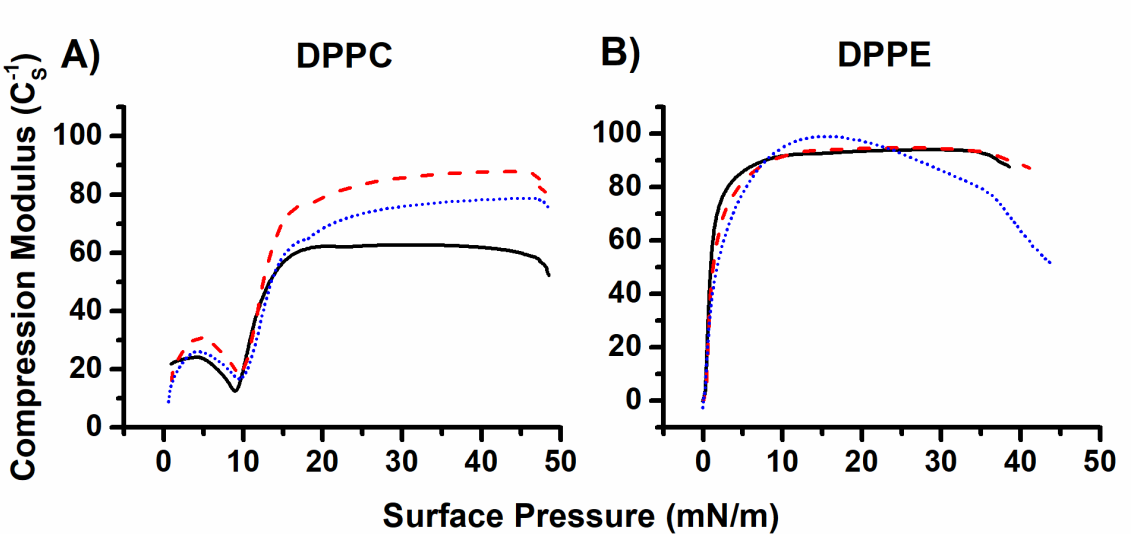

Figure A2.2.1. Compression moduli of mixed monolayers containing menadione and either DPPE (left) or DPPC (right). Pure phospholipid monolayers are represented by solid black curves, 50:50 phospholipid:MEN by red dashed curves, and 25:75 phospholipid:MEN by blue dotted curves. There is a possible increase in rigidity for DPPE monolayers with the addition of MEN and a possible decrease in DPPC monolayers. However, it is uncertain why MEN would affect the elasticity of the DPPC monolayer in a 25:75 MEN:DPPC mixture instead of a 50:50 mixture.

A2.3. Dynamic Light Scattering of RM Samples

Table A2.3.1. Hydrodynamic diameters of RM samples.

Sample	Hydrodynamic Diameter (nm)
w_0 16 RM	12.8 ± 1.5
w_0 16 RM with MEN	12.6 ± 1.5
w_0 16 RM with 90:10 MeOH:H_2O "water pool"	14.5 ± 1.6
w_0 16 RM with 90:10 MeOH:H_2O "water pool" and MDL	14.2 ± 1.9
w_0 16 RM with 80:20 MeOH:H_2O "water pool"	14.2 ± 1.6
w_0 16 RM with 90:10 MeOH:H_2O "water pool" and MDL	16.2 ± 2.3
w_0 16 RM with 70:30 MeOH:H_2O "water pool"	13.9 ± 1.4
w_0 16 RM with 90:10 MeOH:H_2O "water pool" and MDL	16.3 ± 2.1

A2.4. 1D NMR Stability Studies

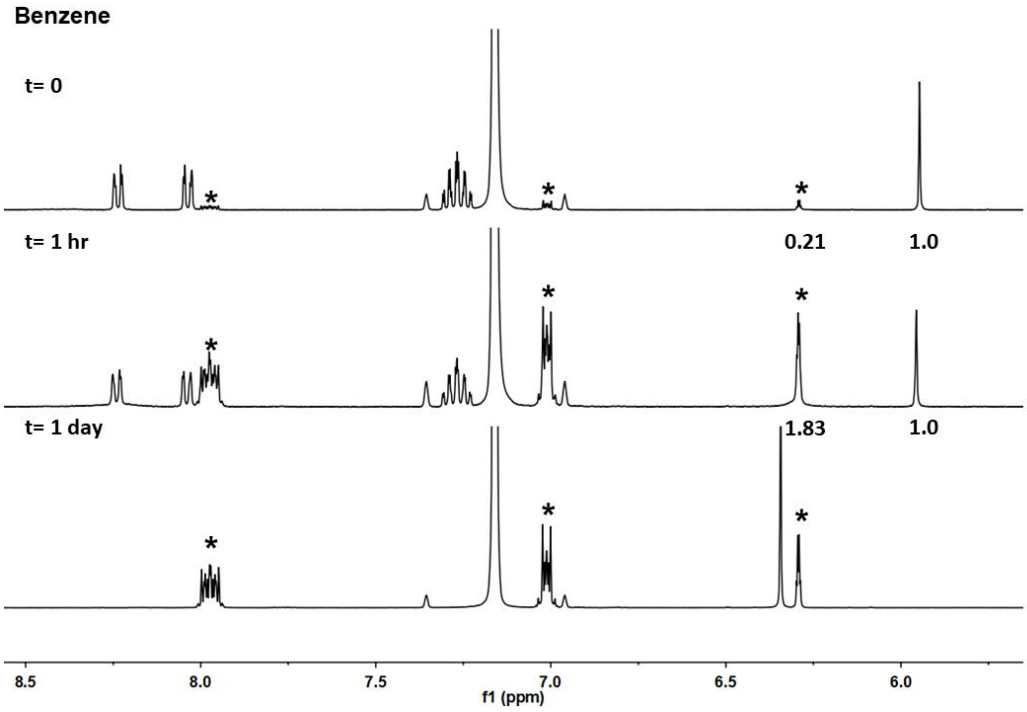

Figure A2.4.1. Stability studies of MDL in d_6-benzene at time 0 (top), 1 hour (middle), and 1 day (bottom). MEN peaks are indicated by *.

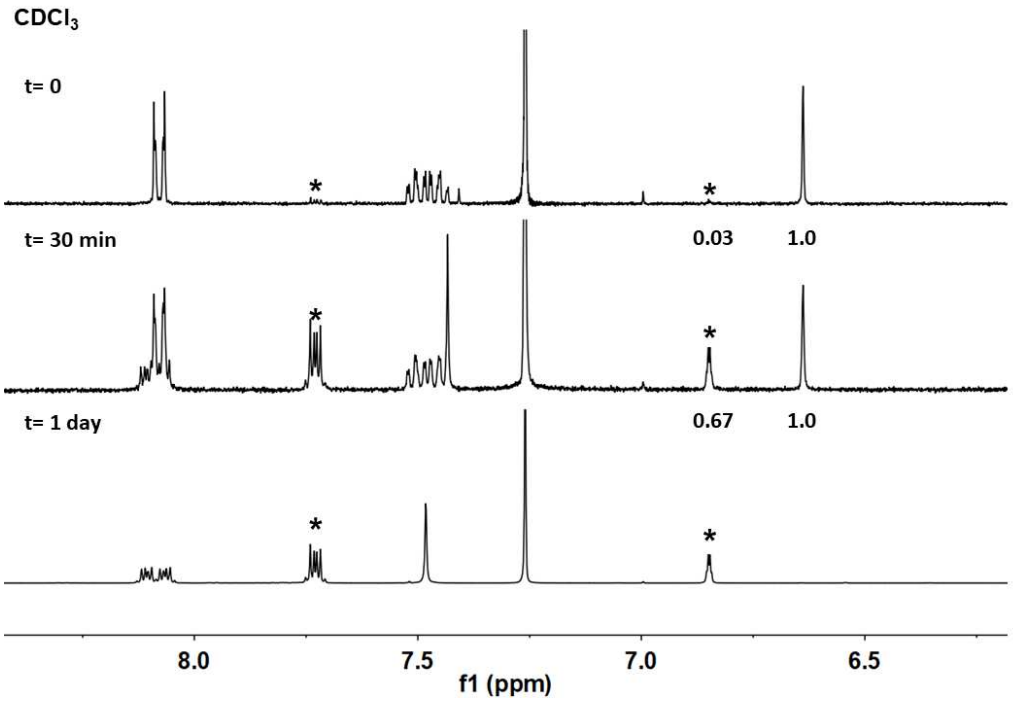

Figure A2.4.2. Stability studies of MDL in $CDCl_3$ at time 0 (top), 1 hour (middle), and 1 day (bottom). MEN peakes are indicated by *.

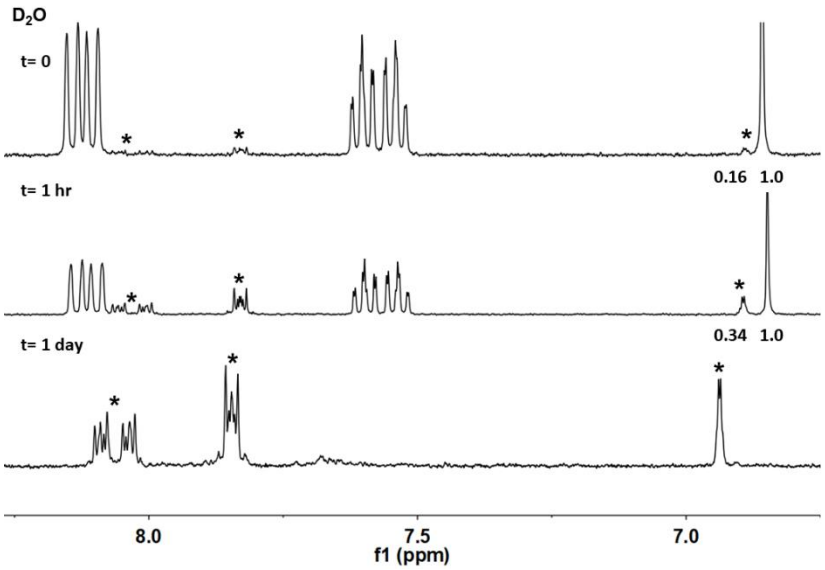

Figure A2.4.3. Stability studies of MDL in D2O at time 0 (top), 1 hour (middle), and 1 day (bottom). MEN peaks are indicated by *.

A2.5. 2D NMR Studies of MEN, MDL, and BEN in Reverse Micelles

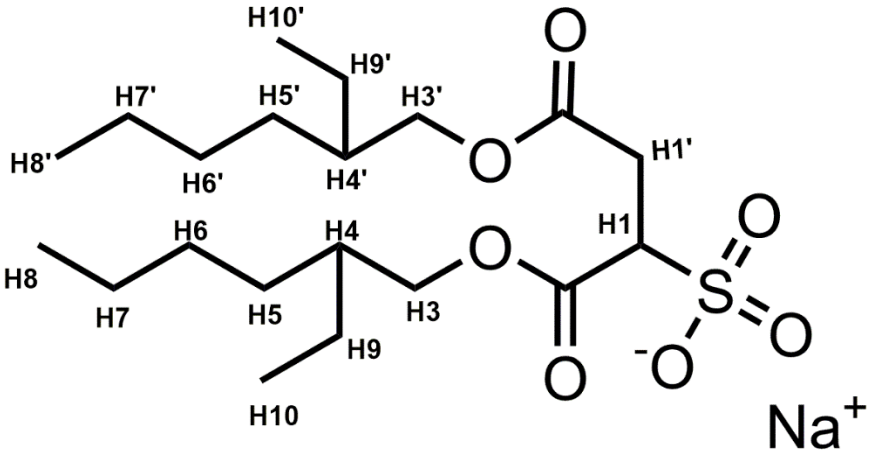

Figure A2.5.1. Proton labeling scheme of AOT.

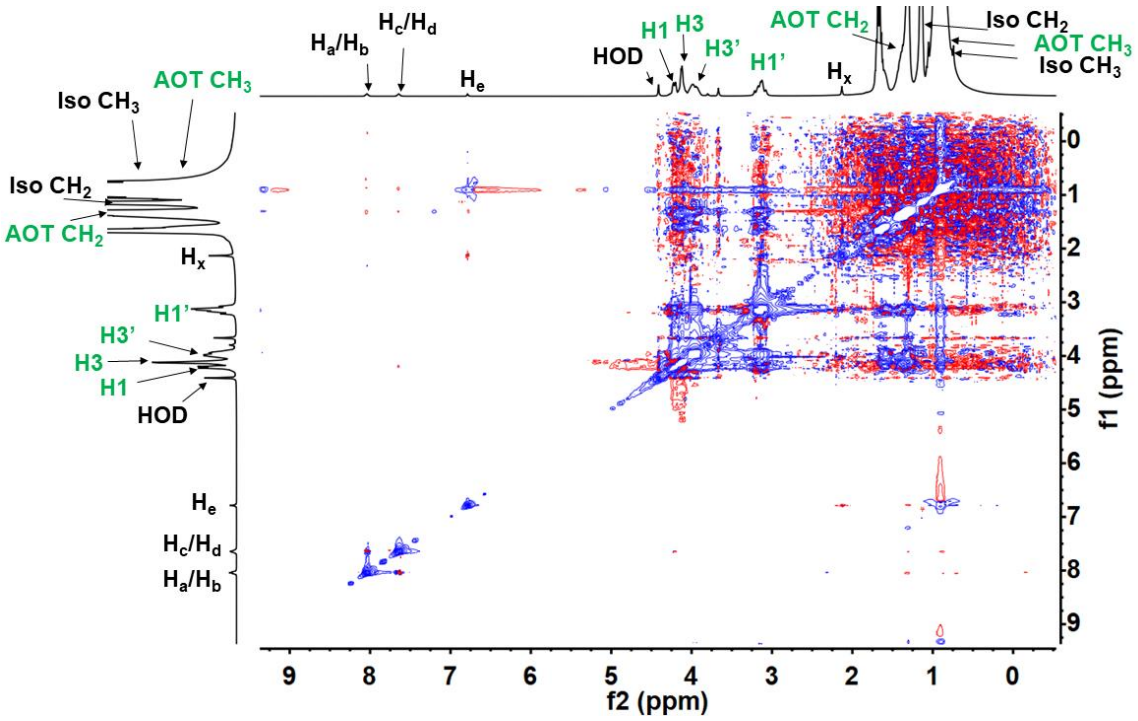

Figure A2.5.2. Full ^{1}H-^{1}H 2D NMR NOESY NMR (400 MHz) spectra of MEN (50mM) in a w_0 12 RM. A standard NOESY pulse consisted of 256 transients with 16 scans in the f_1 domain using a 200 ms mixing time and a 1.5 s relaxation delay.

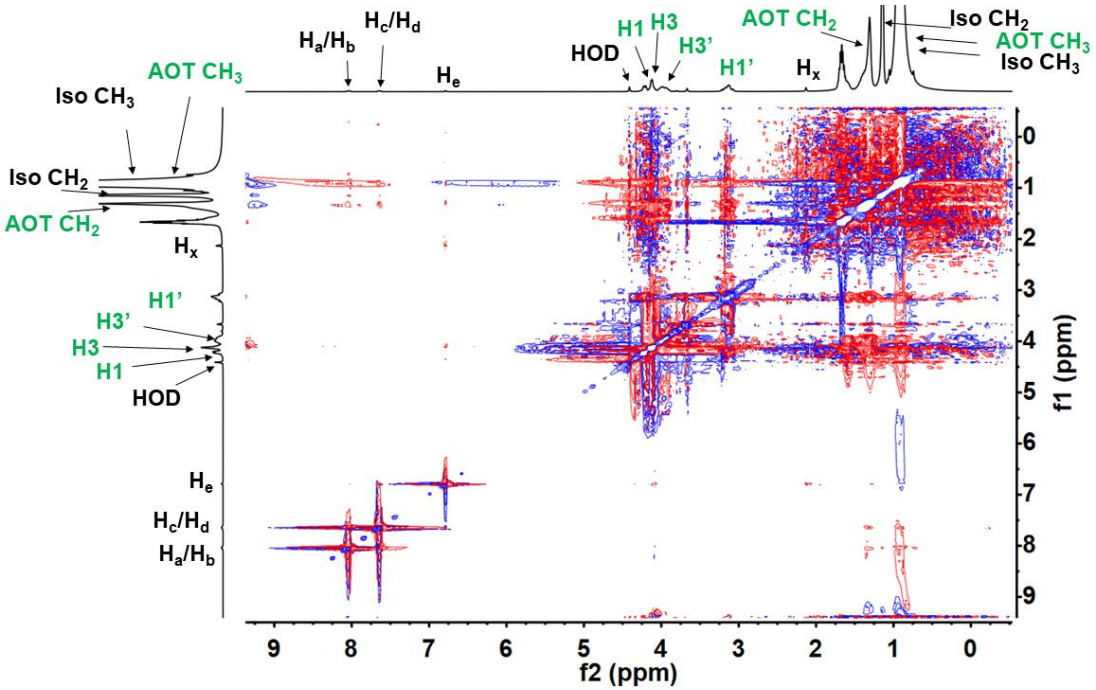

Figure A2.5.3. Full ^{1}H-^{1}H 2D NMR ROESY NMR (400 MHz) spectra of MEN (50mM) in a w_0 12 RM. A standard ROESY pulse consisted of 256 transients with 16 scans in the f_1 domain using a 200 ms mixing time and a 1.5 s relaxation delay.

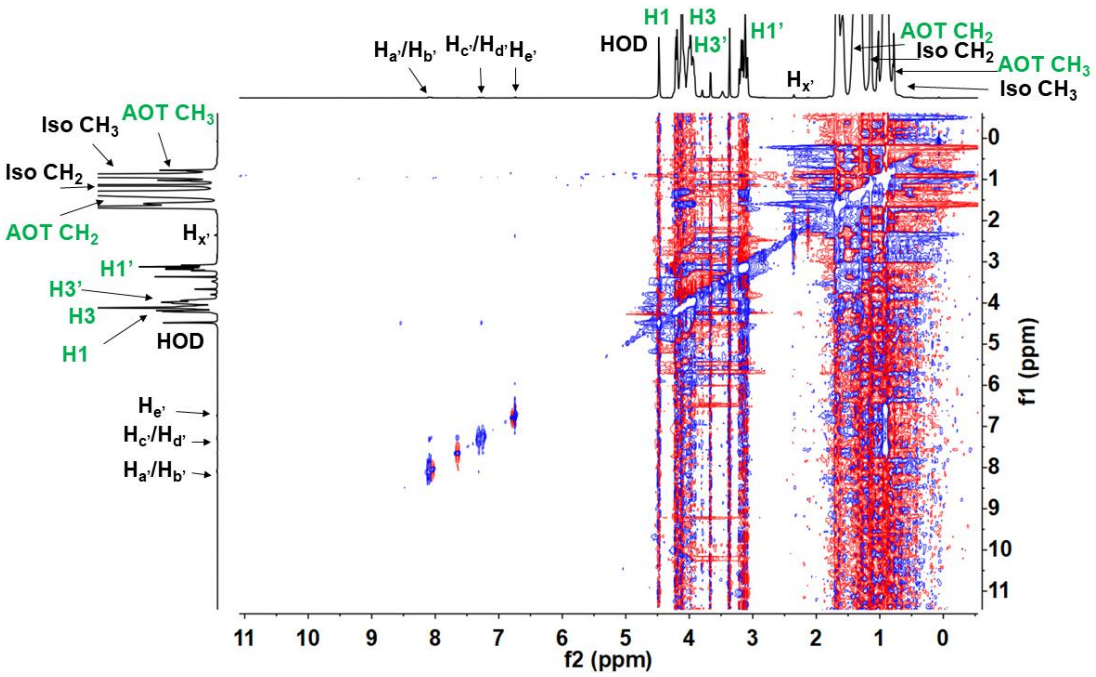

Figure A2.5.4. Full ^{1}H-^{1}H2D NOESY (500 MHz) spectra of menadiol (30mM) in a 70:30 MeOD:D_2O AOT RM suspension at 26˚C. A standard NOESY pulse consisted of 256 transients with 16 scans in the f_1 domain using a 200 ms mixing time and a 1.5 s relaxation delay.

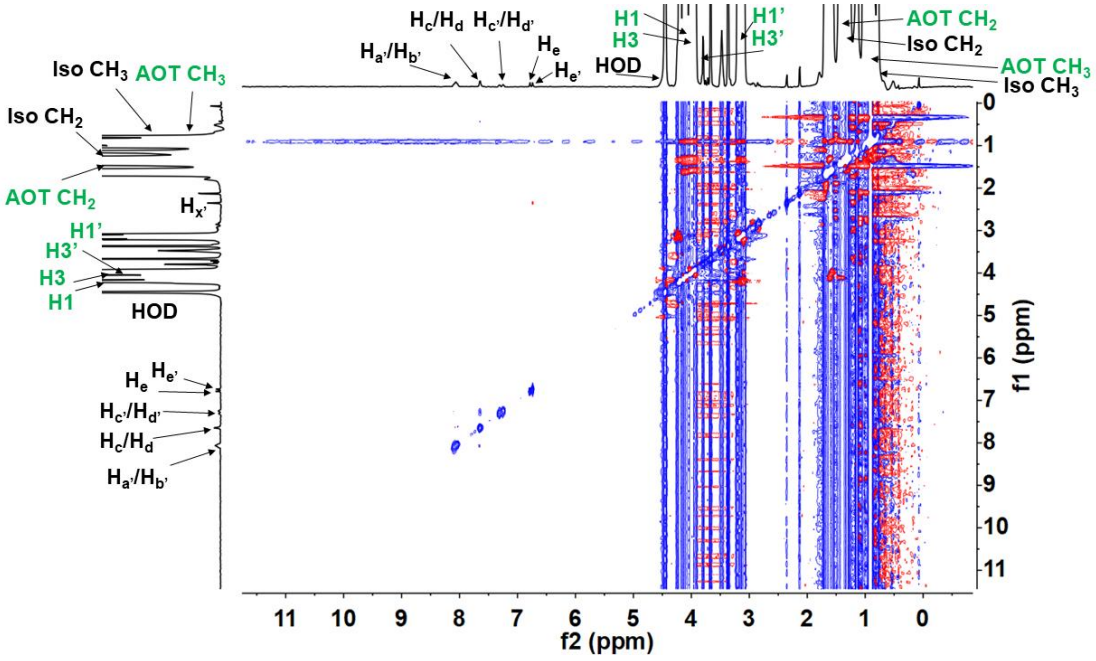

Figure A2.5.5. Full ^{1}H-^{1}H2D ROESY NMR (500 MHz) spectra of menadiol and menadione (30mM) in a 70:30 MeOD:D_2O AOT RM suspension at 26˚C. A standard ROESYAD pulse consisted of 256 transients with 16 scans in the f_1 domain using a 200 ms mixing time and a 2.0 s relaxation delay.

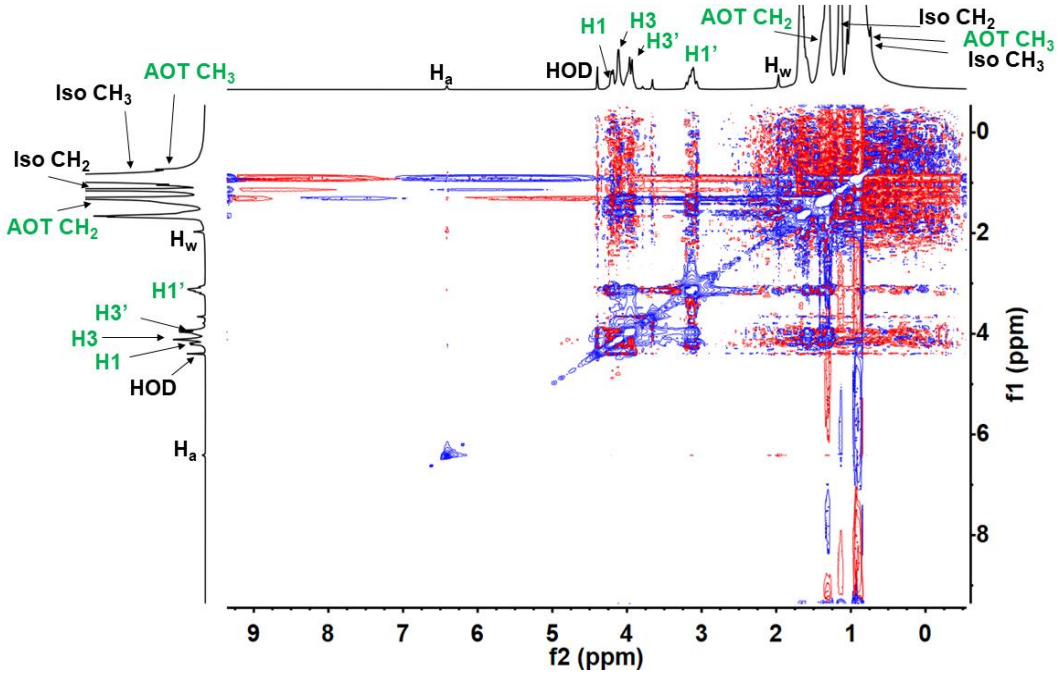

Figure A2.5.6. Full ^{1}H-^{1}H2D NOESY (400 MHz) spectra of BEN (50mM) inside w_0 12 RM at 26˚C. (A standard NOESY pulse consisted of 256 transients with 16 scans in the f_1 domain using a 200 ms mixing time and a 1.5 s relaxation delay.

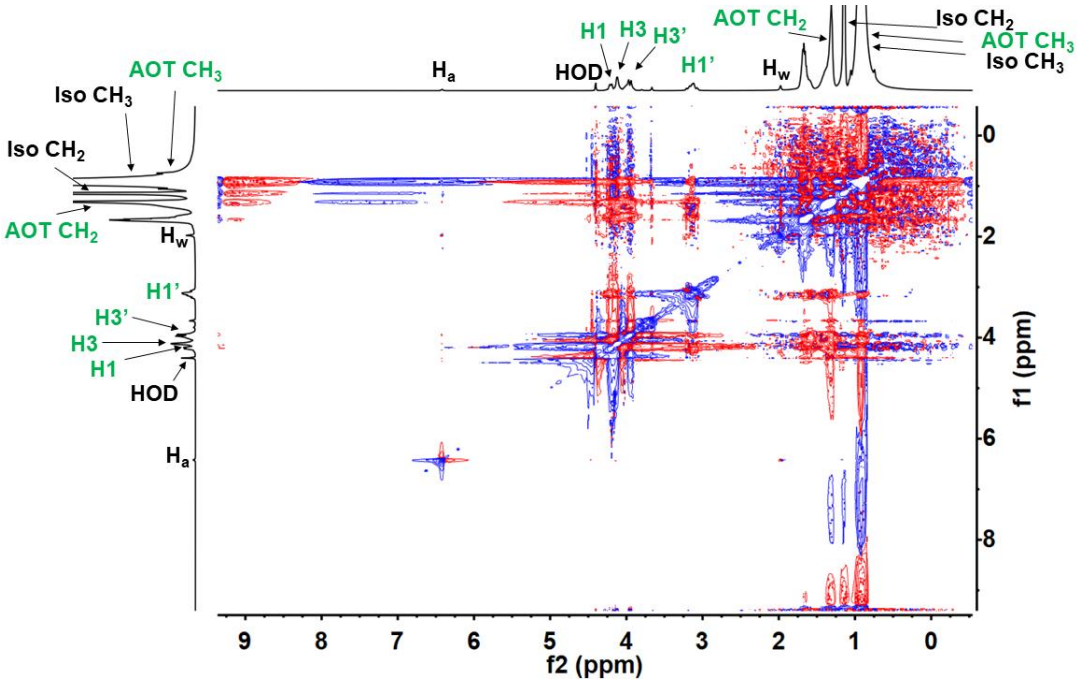

Figure A2.5.7. Full ^{1}H-^{1}H 2D ROESY NMR (400 MHz) spectra of BEN (50mM) inside w_0 12 RM at 26˚C. A standard ROESYAD pulse consisted of 256 transients with 16 scans in the f_1 domain using a 200 ms mixing time and a 1.5 s relaxation delay

Appendix III: Supporting Information for Chapter 3[e]

A.3.1. Partition Coefficients

Table A3.1.1. Calculated logP values of truncated MK analogues obtained from molinspiration.com.

Analogue	Structure	Calculated logP
MK-1	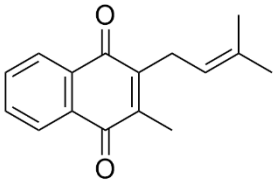	3.83
MK-2	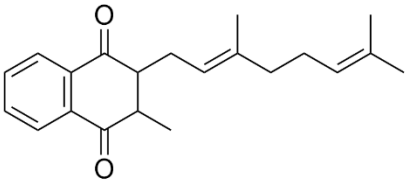	5.67
MK-3	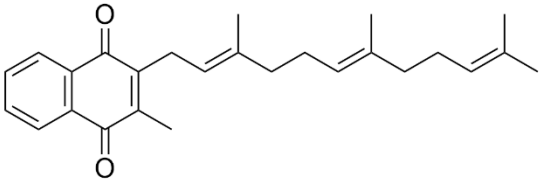	7.52
MK-4	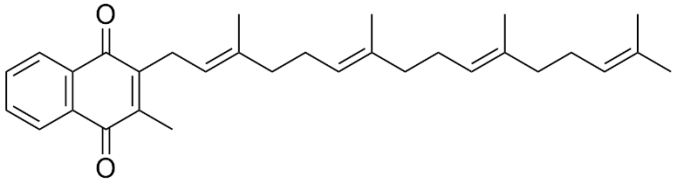	8.86

A.3.2. Hysteresis

A3.2.1 Hysteresis Methods

The hystereses of MK films were performed on a NIMA trough (Teflon) with Teflon block barriers. The injection volumes of 2 mM MK varied based on the ability to generate a surface pressure greater than 1 mN/m. MK-1 required an injection of 400 µL (800 nmol), MK-2 required a 60 µL (120 nmol) injection, and both MK-3 and MK-4 required a 40 µL (80 nmol) injection. As with the compression isotherms, films were allowed to equilibrate for 15 minutes before hysteresis. Films were compressed at a speed of 10 mm/min until a surface pressure between 6 and 8 mN/m. Compression was paused for one second, then expansion proceeded at a speed of 10 mm/min until a surface pressure of 1

[e] This material is published in the *International Journal of Molecular Sciences*.

mN/m was achieved. This compression/expansion cycle was repeated until the trough ran out of area for compression.

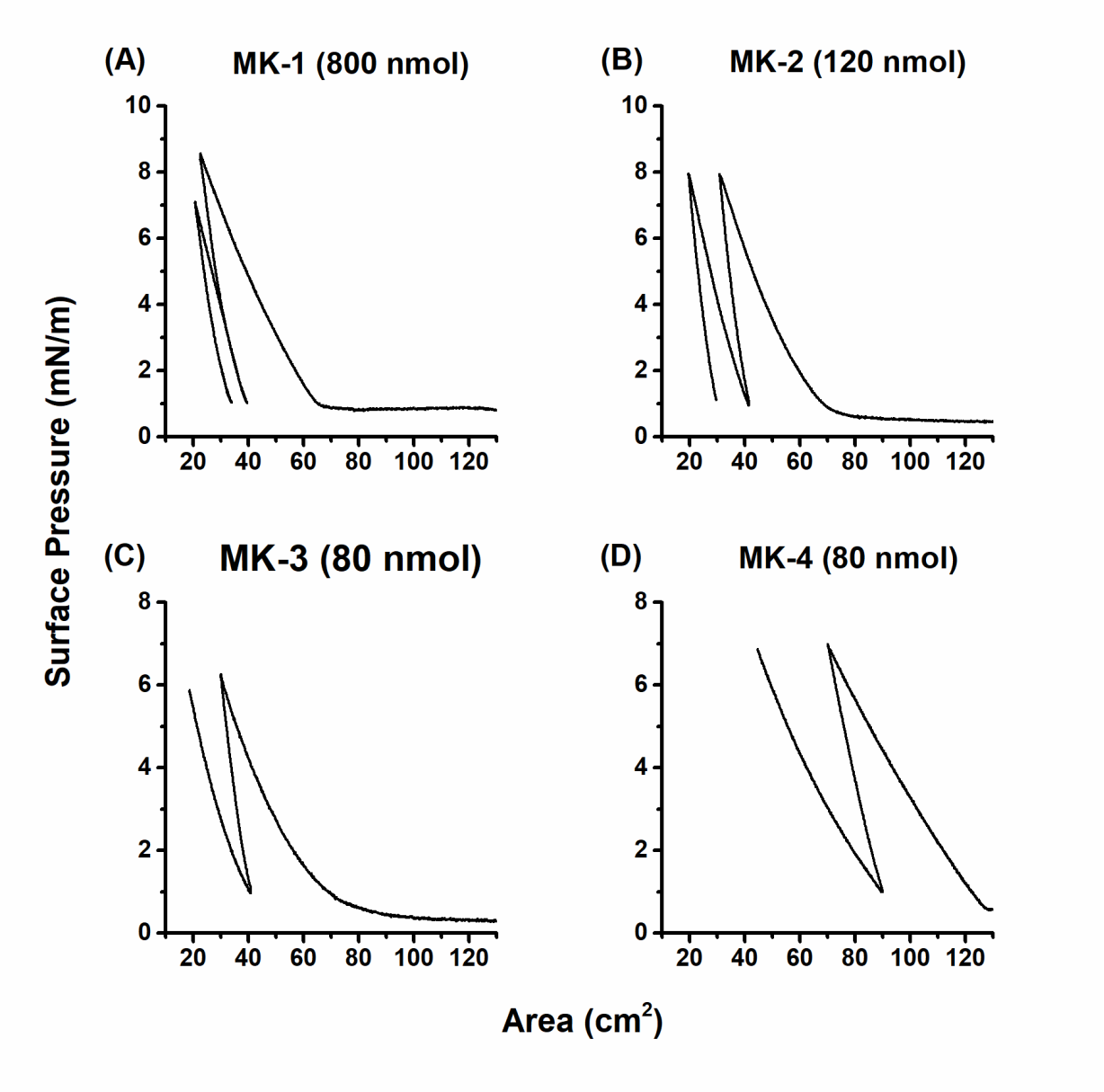

Figure A3.2.1. Hysteresis of pure MK films as a function of surface pressure (mN/m) vs film area (cm^2). Panels are representative of (A) 800 nmol of MK-1, (B) 120 nmol of MK-2, (C) 80 nmol of MK-3, and (D) 80 nmol of MK-4.

A3.3 Visualization of Compression Modulus Terminology

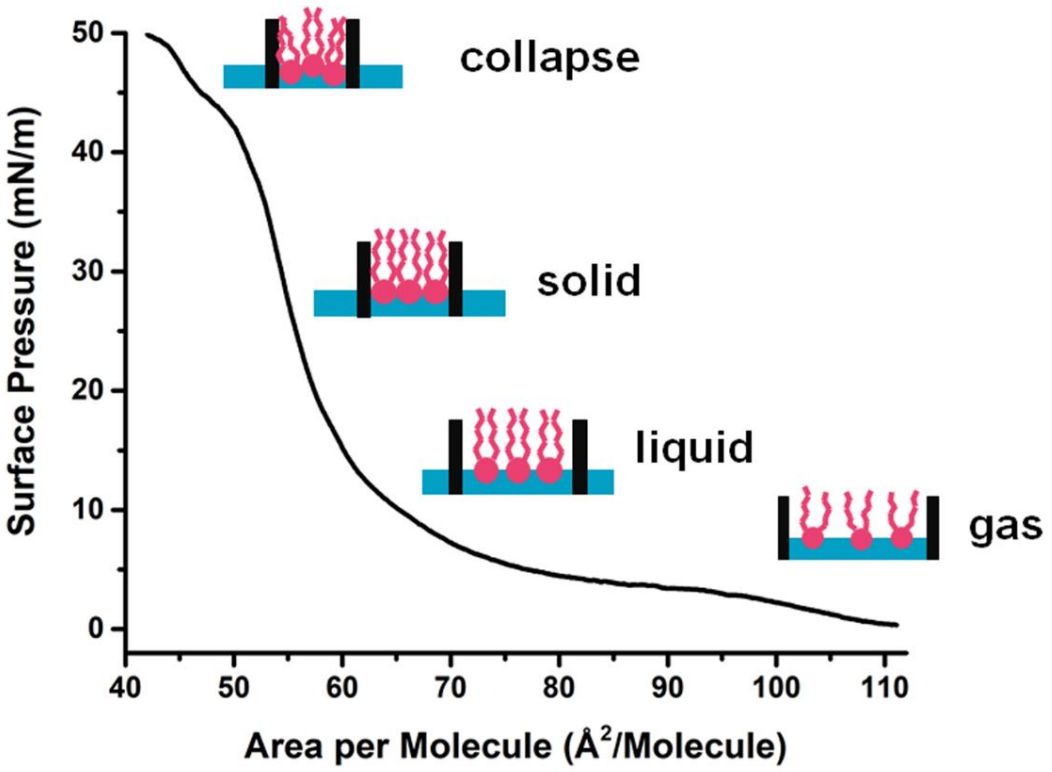

Figure A3.3.1. A representative compression isotherm demonstrating and visualizing the different behavioral phases that are observed and described in Langmuir monolayer studies.

A3.4. Compression Modulus Analysis

A3.4.1. Compression Modulus Methods

The compression modulus of each average was calculated according to Equation A3.1, where C_s^{-1} is the compression modulus, A is the area per molecule (Å^2), and π is the surface pressure.

$$C_S^{-1} = -A\left(\frac{d\pi}{dA}\right)_T$$ **Equation A3.1**

The first derivative of the surface pressure with respect to the area at a constant temperature was calculated in Origin 2021 and smoothed with a second degree polynomial Savitsky-Golay function (500 points per window). The first derivative was then multiplied by the negative of the area and graphed versus surface pressure in Origin 2021.

A3.4.2. Interpretation

The calculated compression modulus showed phase transitions and changes in monolayer compressibility (Figure A3.4.1). The maximum compression modulus (highest point of the curve) may be used to indicate the state of the film (such as liquid or solid). These states are thought of as a range as opposed to one indicative value.[1] For example, a maximum compression modulus between 50 and 100 mN/m is indicative of a liquid condensed film. The values obtained in Figure A3.4.1 mixed phospholipid:MK films are either liquid or liquid-expanded. A general trend for DPPC films mixed with MK is that the maximum compression modulus decreased with increasing MK homologue concentration, indicating a more fluid film. Likewise, increasing MK concentration suppressed the gas-liquid phase transition peak between 0 and 10 mN/m. The DPPE:MK films all demonstrated decrease in maximum compression modulus as the molar fraction of MK increased, similar to DPPC. Despite errors (Figures A3.4.2 and A3.4.3), the overall trend of decreased compression modulus with increased MK fraction is clear.

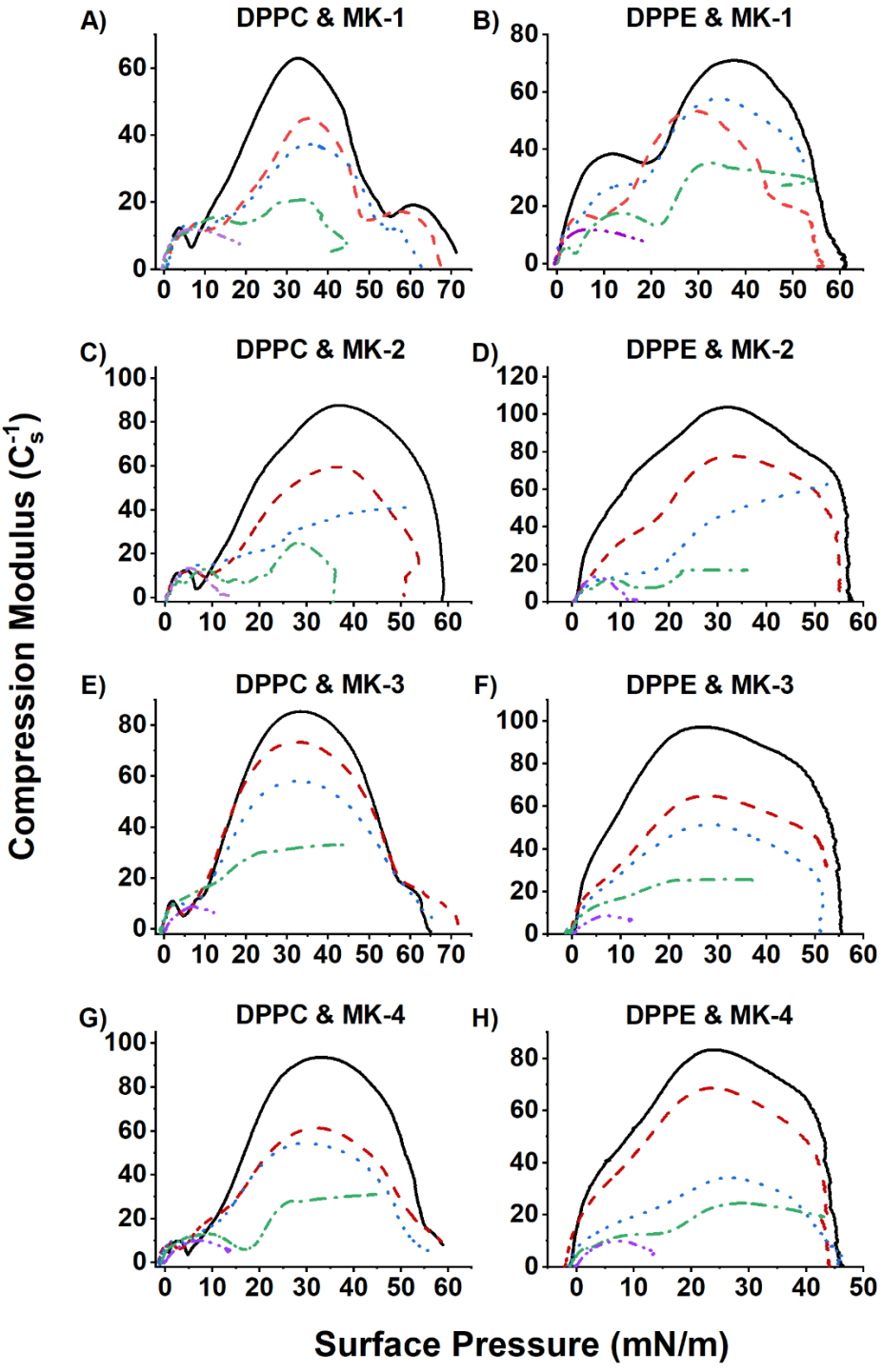

Figure A3.4.1. Compression modulus (C_S^{-1}) versus surface pressure (mN/m) of DPPC (left column) and DPPE (right column) and phospholipid:MK films. Panels A) and B) are MK-1, C) and D) are MK-2, E) and F) are MK-3, and G) and H) are MK-4. Solid black curves represent pure lipid, red dashed curves represent 75:25 phospholipid:MK, blue dotted curves represent 50:50 phospholipid:MK, green dash-dot curves represent 25:75 phospholipid:MK, and purple dash-dot-dot curves represent pure MK.

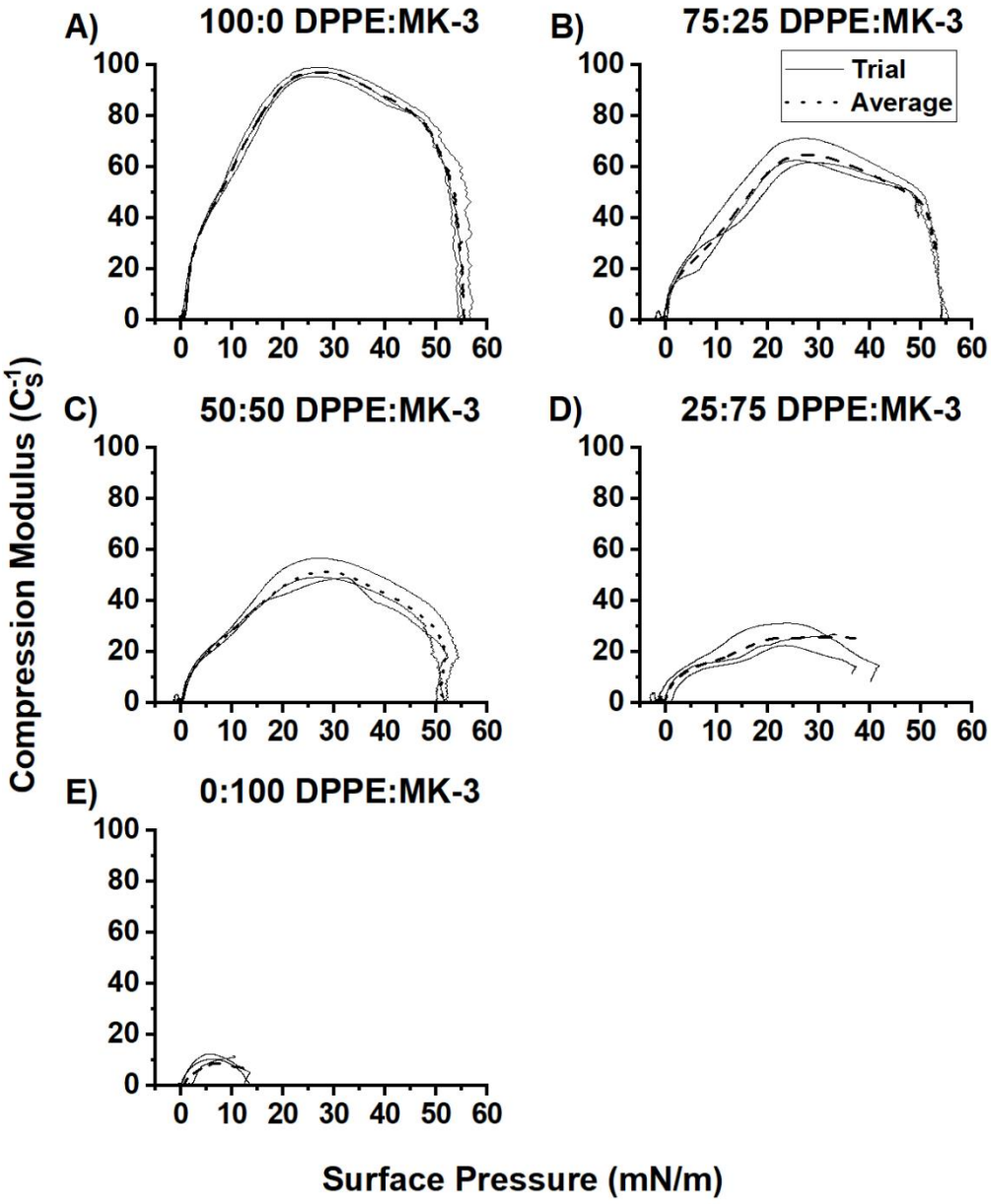

Figure A3.4.2. Representative compression modulus versus surface pressure plots demonstrating experimental trials versus calculated averages of A) DPPE, B) 75:25 DPPE:MK-3, C) 50:50 DPPE:MK-3, D) 25:75 DPPE:MK-3, and E) MK-3. These plots demonstrate that the average curve is a decent representation of compression modulus data.

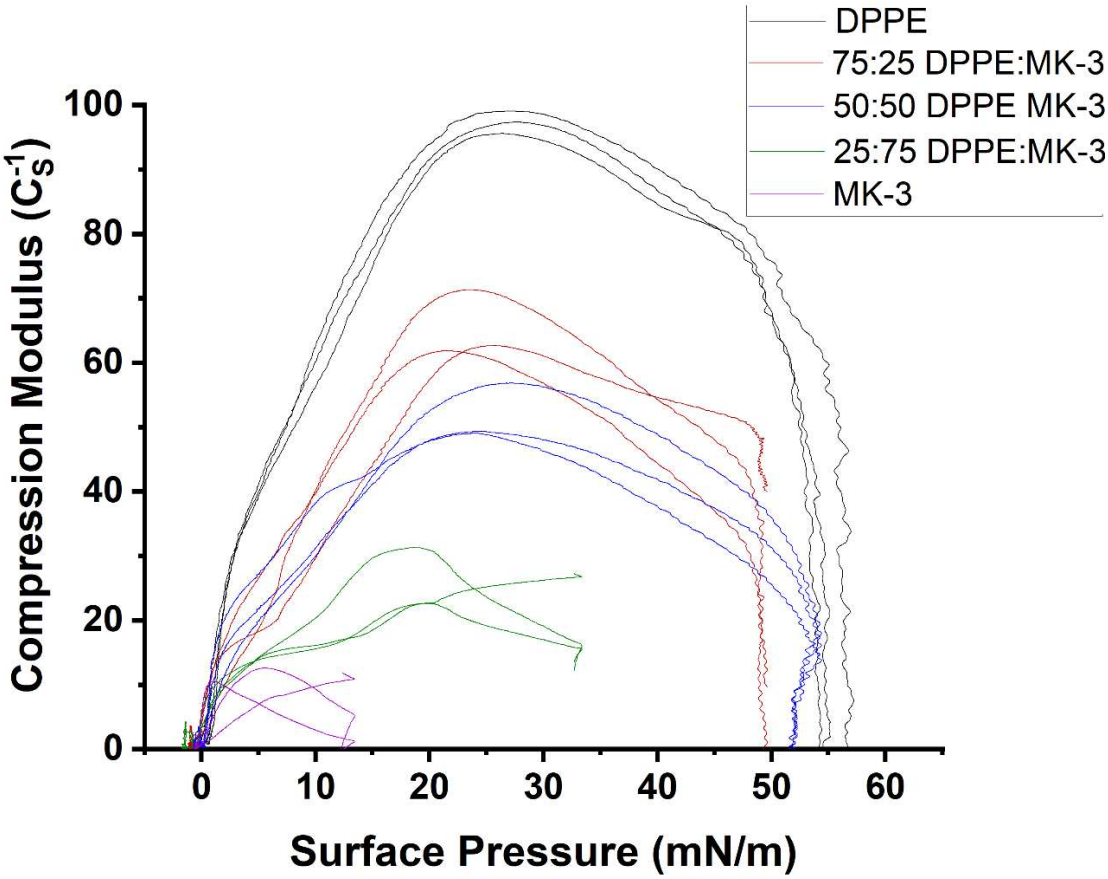

Figure A3.4.3. A representative compression modulus versus surface pressure graph in which all experimental trials of the DPPE:MK-3 monolayers were transformed into compression modulus and plotted versus surface pressure. This demonstrates that while there may be large error, an overall trend of increased compressibility (decreased compression modulus) is identifiable.

A3.5. Ideal Mixing

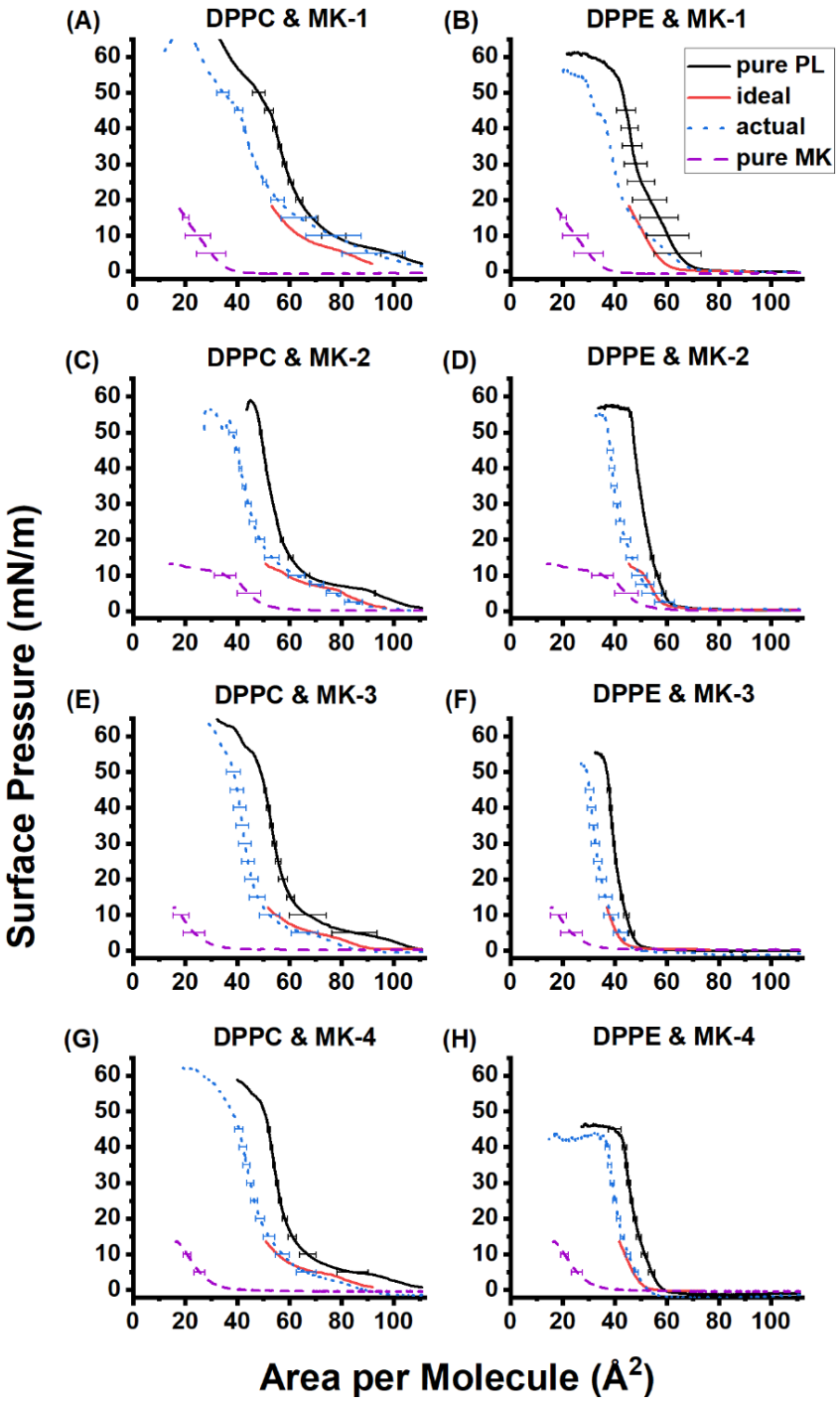

Figure A3.5.1. Ideal mixing of 75:25 phospholipid:MK films compared to experimental DPPC films are in the left column. DPPE films are in the right column. A) and B) show MK-1 mixed films, C) and D) show MK-2 mixed films, E) and F) show mixed MK-3 films, and G) and H) show mixed MK-4 films. Solid black curves are pure phospholipid monolayers. Blue dotted curves represent experimental 75:25 phospholipid:MK films. Solid red curves represent calculated ideal mixed films. Purple dash-dot curves represent pure MK films.

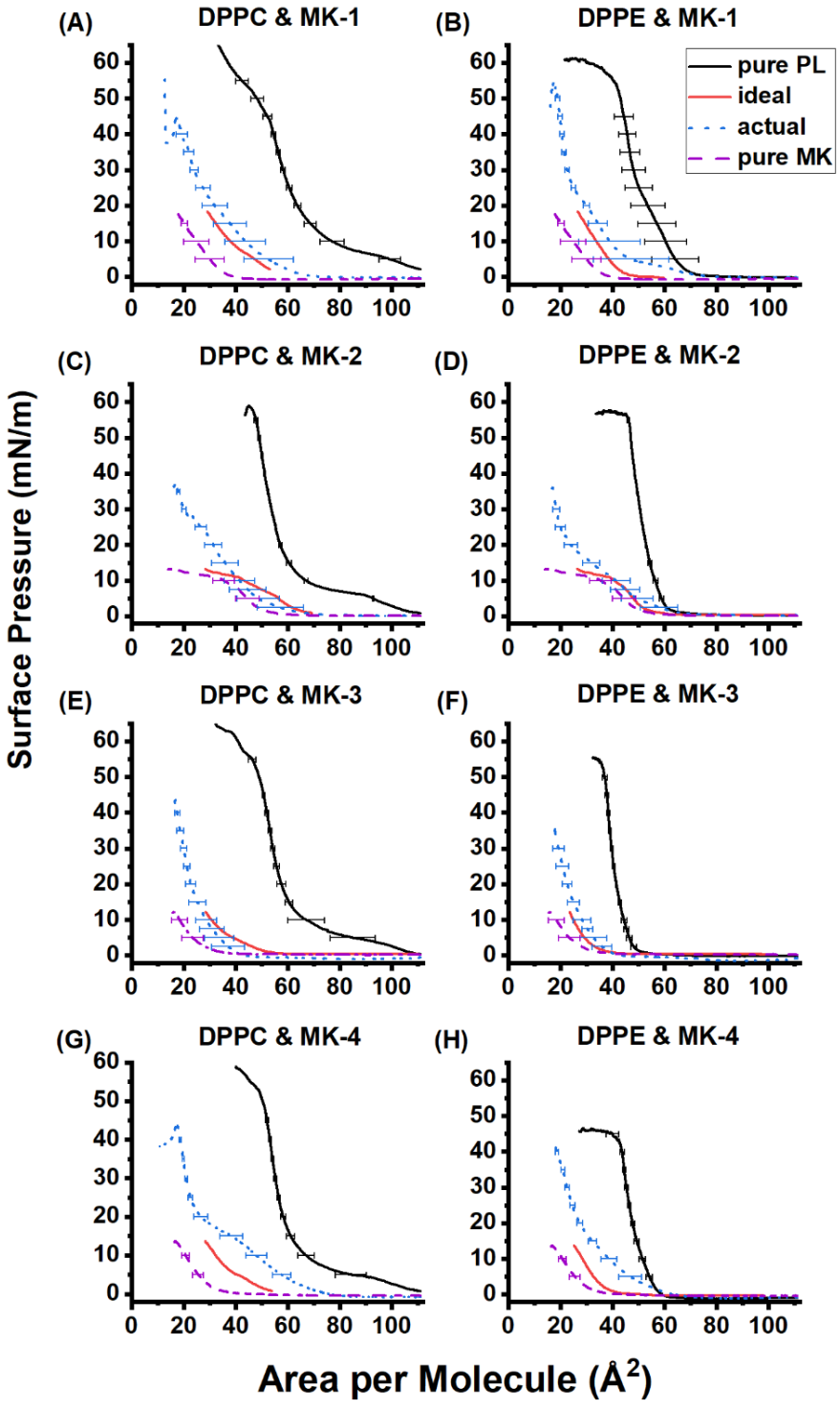

Figure A3.5.2. Ideal mixing of 25:75 phospholipid:MK films compared to experimental DPPC films are in the left column. DPPE films are in the right column. A) and B) show MK-1 mixed films, C) and D) show MK-2 mixed films, E) and F) show mixed MK-3 films, and G) and H) show mixed MK-4 films. Solid black curves are pure phospholipid monolayers. Blue dotted curves represent experimental 25:75 phospholipid:MK films. Solid red curves represent calculated ideal mixed films. Purple dash-dot curves represent pure MK films.

A3.6. Labeling and Nomenclature

The IUPAC name of MK-4 is 2-methyl-3-(3,7,11,15-tetramethylhexadeca-2,6,10,14-tetraenyl)naphthalene-1,4-dione. The labeling scheme is provided below in Figure A3.4.1. This differs from the labeling scheme in the main manuscript as we used the UQ scheme (Figure A3.4.2) for easier comparison.

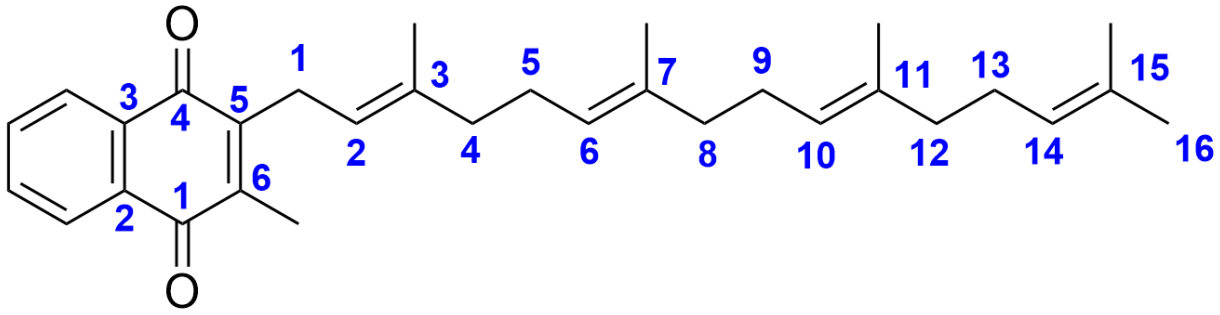

Figure A3.6.1. IUPAC labeling of MK-4.

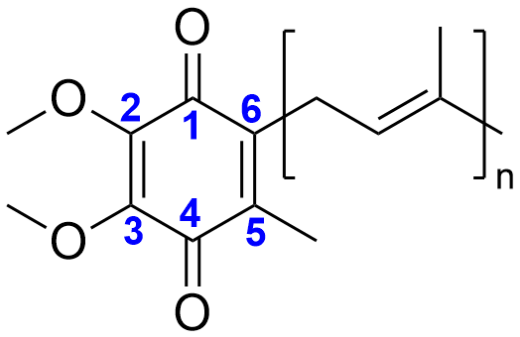

Figure A3.6.2. IUPAC labeling of UQ molecules.

References

1. Patterson, M.; Vogel, H. J.; Prenner, E. J., Biophysical characterization of monofilm model sytems composed of selected tear film phospholipids. *Biochim. Biophys. Acta Biomembr.* **2016,** *1858*, 403-414.

Appendix IV: Supporting Information for Chapter 4

A4.1. Area Values at Physiological Surface Pressure[1] of Langmuir Monolayers

Table A4.1.1. Area values of monolayers with PZA present at pH 7.4. The selected surface pressures are physiological. An * denotes the value is significantly different from the control at $p < 0.05$.

Concentration of PZA (mM)	Surface Pressure (mN/m)	Area per Molecule – DPPC (Å^2)	Area per Molecule – DPPE (Å^2)
0	30	57.9 ± 0.7	52.2 ±0.7
	35	56.7 ± 0.6	50.9 ± 0.7
0.1	30	57 ± 1	52.2 ± 0.7
	35	56.2 ± 0.9	51.4 ± 0.7
1	30	58.2 ± 0.3	52.3 ± 0.6
	35	57.2 ± 0.2	51.2 ± 0.5
10	30	58.6 ± 0.9	51.9 ± 0.7
	35	57.8 ± 0.8	50.7 ± 0.8

Table A4.1.2. Area values of monolayers with POA_C present at pH 7.4. The selected surface pressures are physiological. An * denotes the value is significantly different from the control at $p < 0.05$.

Concentration of POA_C (mM)	Surface Pressure (mN/m)	Area per Molecule – DPPC (Å^2)	Area per Molecule – DPPE (Å^2)
0	30	54.8 ± 0.7	55 ± 1
	35	53.3 ± 0.7	53 ± 1
0.1	30	54 ± 1	54.0 ± 0.6
	35	52.8 ±	52.8 ± 0.6
1	30	54.4 ± 0.6	52.9 ± 0.6
	35	53.2 ± 0.6	51.6 ± 0.5
10	30	56.4 ± 0.3*	53.4 ± 0.7
	35	54.9 ± 0.3*	51.9 ± 0.7

Table 4.1.3. Area values of monolayers with a mix or POA_N and POA_C at pH 5. The selected surface pressures are physiological. An * denotes the value is significantly different from the control at $p < 0.05$.

Concentration of $POA_{N/C}$ (mM)	pH	Surface Pressure (mN/m)	Area per Molecule – DPPC (Å^2)	Area per Molecule – DPPE (Å^2)
0	5	30	56.4 ± 0.7	54.4 ± 0.5
		35	55.1 ± 0.7	52.9 ± 0.5
0.1	5	30	53.7 ± 0.6*	56.5 ± 0.5*
		35	52.3 ± 0.5*	52.3 ± 0.4*
1	5	30	53.9 ± 0.4*	56.0 ± 0.5*
		35	52.3 ± 0.4*	55.7 ± 0.2*
10	5	30	55.3 ± 0.7	57.2 ± 0.3*
		35	53.9 ± 0.7	53.1 ± 0.4*

Table A4.1.4. Area values of monolayers with a mix or POA_N at pH 3. The selected surface pressures are physiological. An * denotes the value is significantly different from the control at $p < 0.05$.

Concentration of POA_N (mM)	pH	Surface Pressure (mN/m)	Area per Molecule – DPPC (Å²)	Area per Molecule – DPPE (Å²)
0	3	30	52.2 ± 0.1	51.5 ± 0.4
		35	51.11 ± 0.09	50.6 ± 0.4
0.1	3	30	53 ± 1	57.3 ± 0.6*
		35	51 ± 1	55.7 ± 0.6*
1	3	30	53.8 ± 0.3*	53.2 ± 0.5*
		35	52.5 ± 0.3*	52.0 ± 0.5*
10	3	30	52.1 ± 0.4	55.2 ± 0.7*
		35	50.8 ± 0.3	53.1 ± 0.6*

A4.2 ^{1}H Spectra of PZA and POA in Different w_0 Reverse Micelles

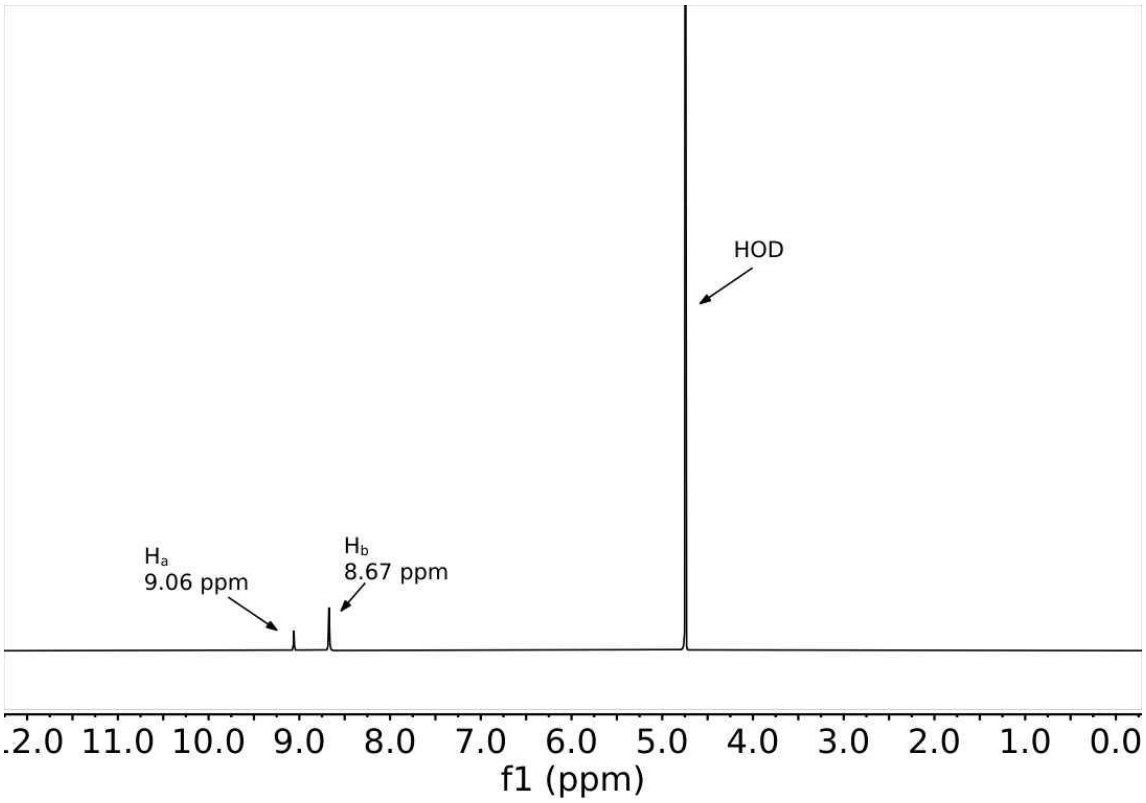

Figure A4.2.1. Full ^{1}H NMR spectrum of 100 mM POA at pD 6.96 in D_2O.

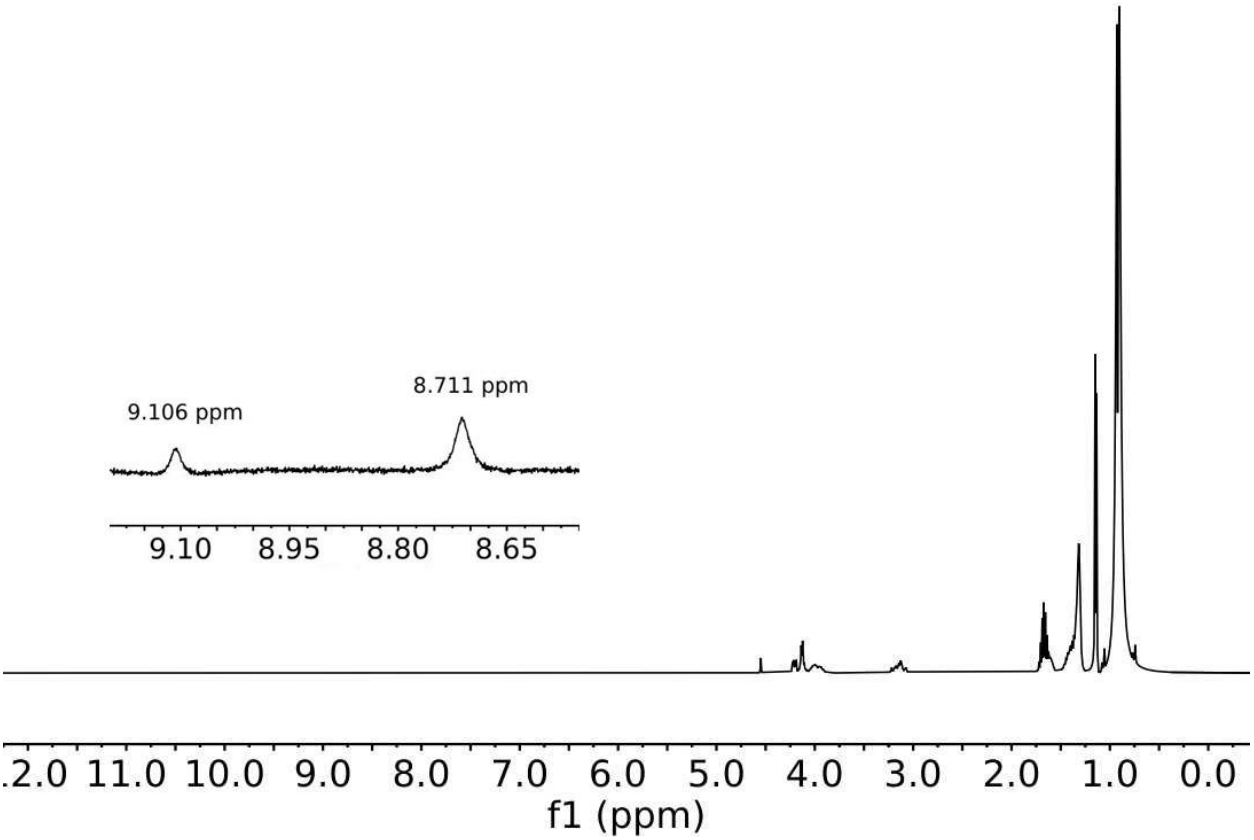

Figure A4.2.2. An example full ^{1}H NMR spectrum of a w_0 16 RM containing POA at pD 6.96. A zoom-in of the aromatic region is provided.

A4.3. Determination of pK_a by ^{1}H 1D NMR

The procedure for determining pK_a was adapted from Gift *et al.* 2012.[2] Briefly, chemical shift was plotted against pD for each proton. Curves were then fit using a sigmoidal function (Boltzmann) in Origin 2021. The first derivative was then taken of the fit to determine the point where the slope was the steepest. Figure A4.3.1 gives a visual demonstration.

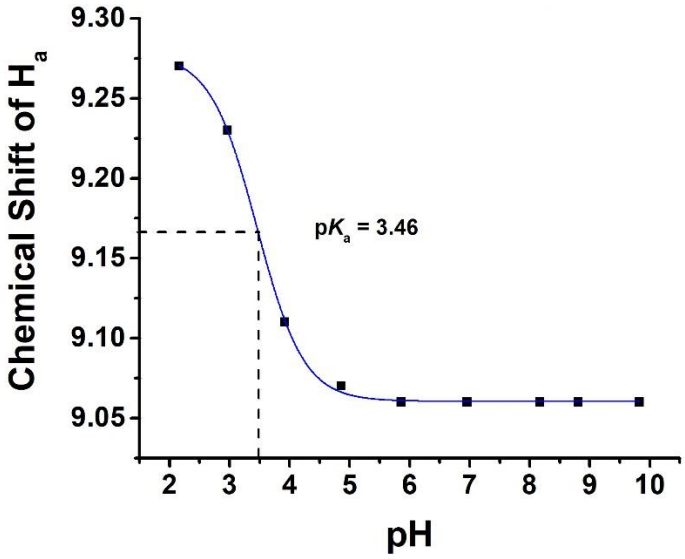

Figure A4.3.1. A demonstration of how pK_a was calculated for 100 mM POA in D_2O. Points were fit with a Boltzmann sigmoidal fit. The first derivative was then taken. The smallest value in the derivative was representative of the steepest slope, which is correlated to pK_a.

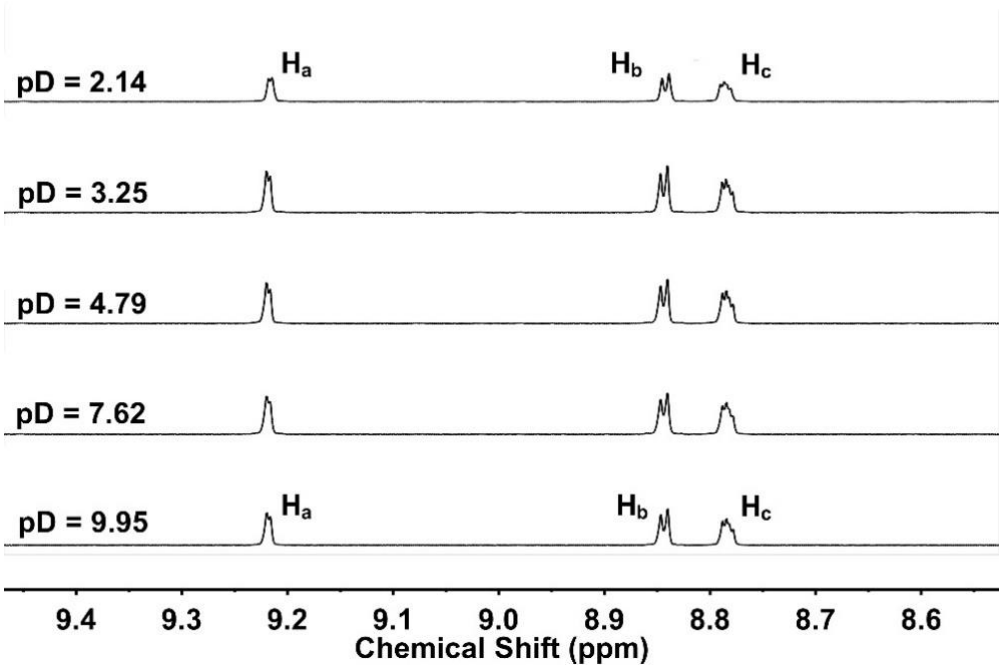

Figure A4.3.2. Proton NMR chemical shifts of 100 mM PZA in D_2O, demonstrating no significant change in chemical shift with a change in pD of the stock solution.

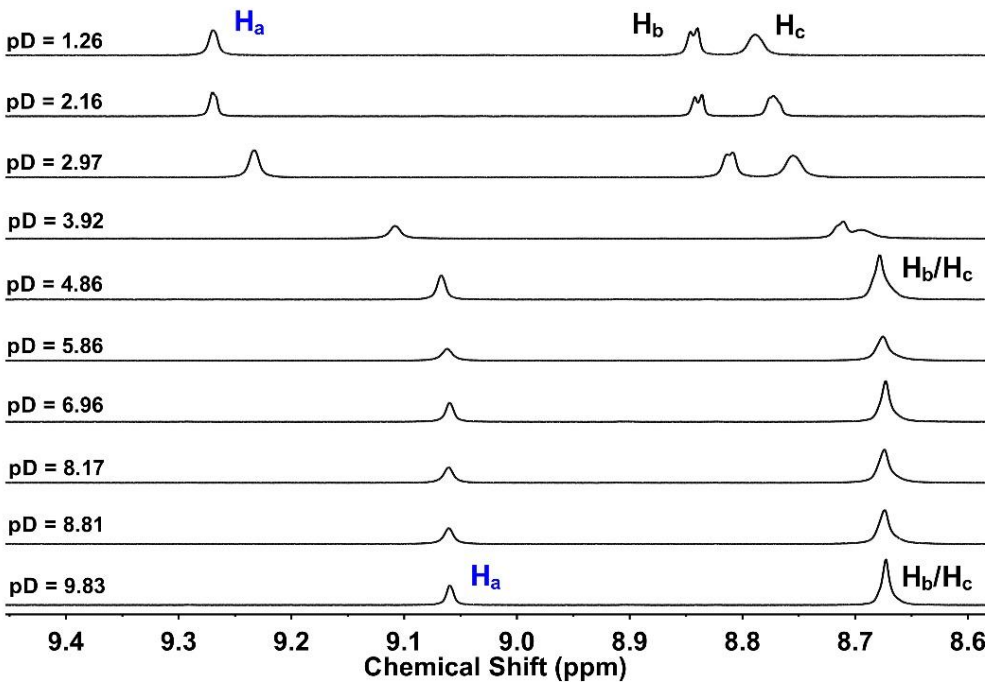

Figure A4.3.3. Proton NMR chemical shifts of 100 mM POA in D_2O. Each spectrum was recorded at a different stock pD.

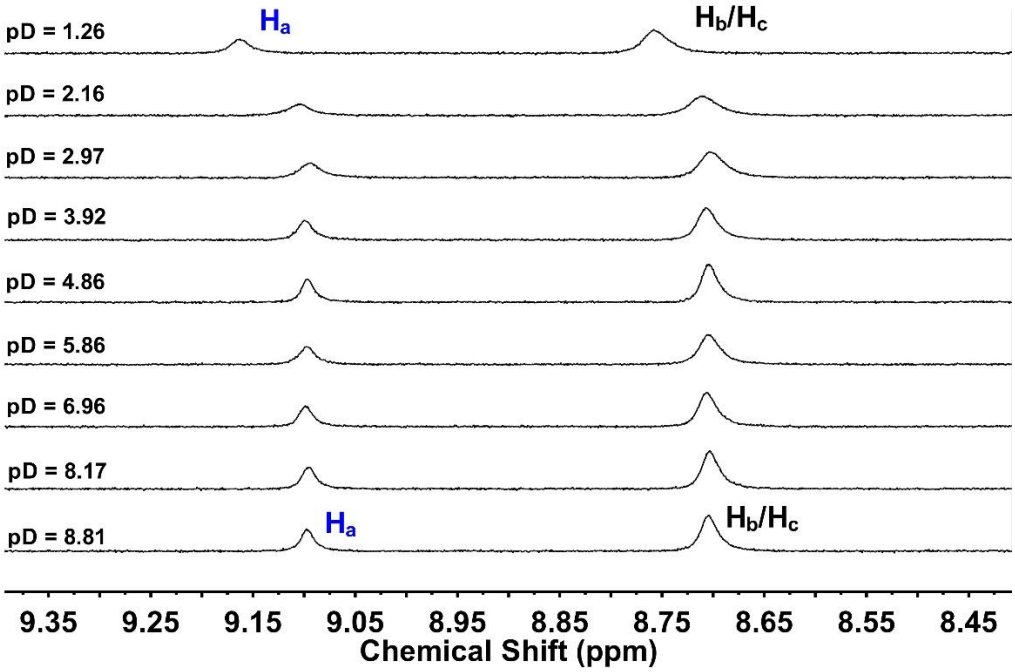

Figure A4.3.4. Proton NMR chemical shifts of 100 mM POA in w_0 20 AOT/isooctane (0.75 M) reverse micelles. Each spectrum was recorded with stock solutions of differing pD.

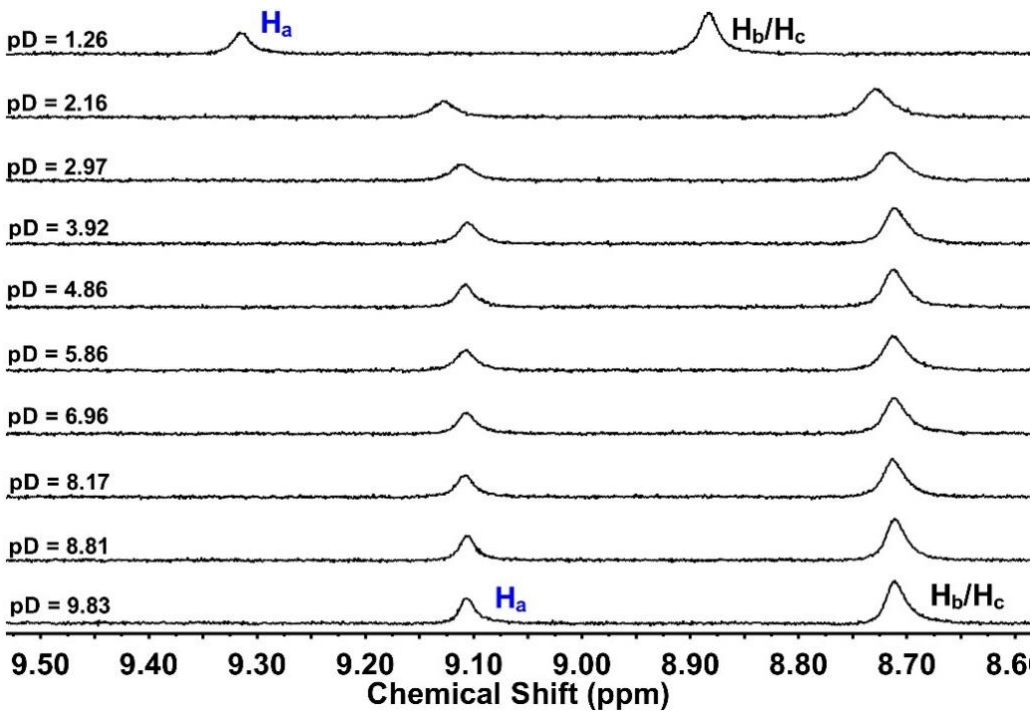

Figure A4.3.5. Proton NMR chemical shifts of 100 mM POA in w_0 16 AOT/isooctane (0.75M) reverse micelles. Each spectrum was recorded with stock solutions of differing pD.

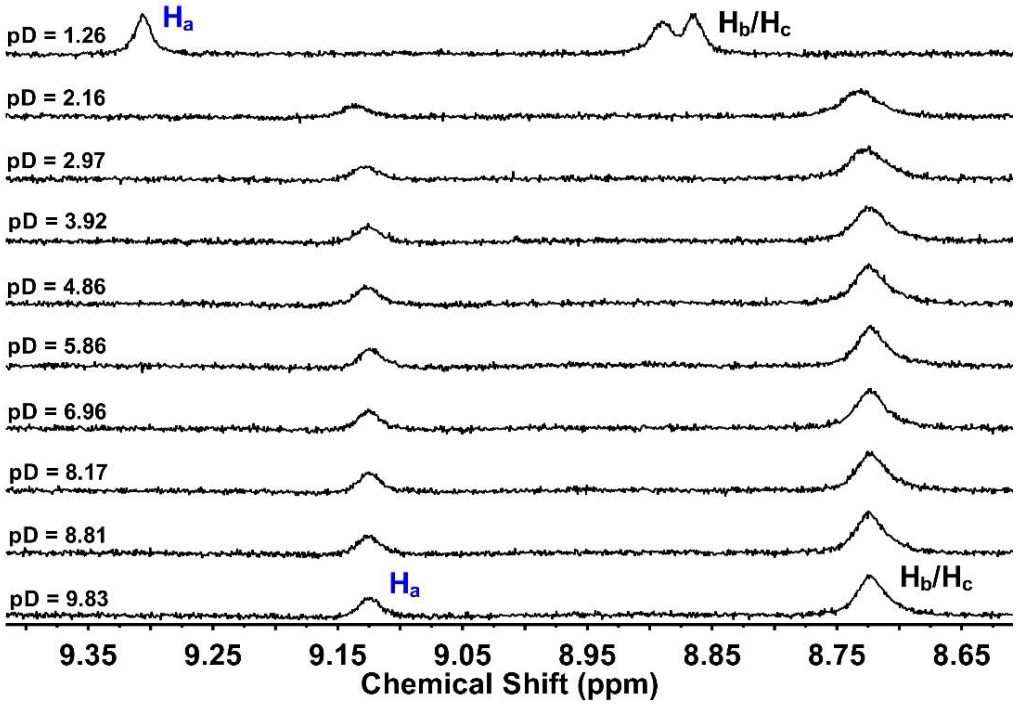

Figure A4.3.6. Proton NMR chemical shifts of 100 mM POA in w_0 12 AOT/isooctane (0.75 M) reverse micelles. Each spectrum was recorded with stock solutions of differing pD.

A4.4. Fluorescence Studies

To test the validity of the fluorescence leakage assay, different concentrations of Triton X-100 were used to induce leakage. A linear fit of the data was calculated in Origin 2021. A positive linear relationship of fluorescence intensity vs concentration was found with an R^2 of 0.92, thus validating the method.

Table A4.4.1. Exact amounts of each component added to the liposome solution for leakage experiments.

Drug Concentration (mM)	Liposome Solution (µL)	POA/PZA Solution (µL)	Buffer Solution (µL)
0.10 mM	500 µL	10	490
0.25 mM	500 µL	25	475
0.50 mM	500 µL	50	450
0.75 mM	500 µL	75	425
1 mM	500 µL	100	400
1.5 mM	500 µL	150	350
2 mM	500 µL	200	300
3 mM	500 µL	300	200
5 mM	500 µL	500	0

References

1. Jones, M. N.; Chapman, D., *Micelles, Monolayers, and Biomembranes*. Wiley-Liss, Inc.: New York, 1995.

2. Gift, A. D.; Stewart, S. M.; Bokashanga, P. K., Experimental Determination of pK_a Values by Use of NMR Chemical Shifts, Revisited. *J. Chem. Ed.* **2012,** *89* (11), 1458-1460.

Appendix V: Location of menaquinone and menaquinol headgroups in model membranes

This is the manuscript that corresponds to Chapter 2 and is published in the *Canadian Journal of Chemistry*.[1]

References

1. Van Cleave, C.; Murakami, H. A.; Samart, N.; Koehn, J. T.; Maldonado, P.; Kreckel, H. D.; Cope, E. J.; Basile, A.; Crick, D. C.; Crans, D. C., Location of menaquinone and menaquinol headgroups in model membranes. *Can. J. Chem.* **2020,** *98* (6), 307-317.

NRC Research Press

ARTICLE

Location of menaquinone and menaquinol headgroups in model membranes

Cameron Van Cleave, Heide A. Murakami, Nuttaporn Samart, Jordan T. Koehn, Pablo Maldonado, Jr., Heidi D. Kreckel, Elana J. Cope, Andrea Basile, Dean C. Crick, and Debbie C. Crans

Abstract: Menaquinones are lipoquinones that consist of a headgroup (naphthoquinone, menadione) and an isoprenyl sidechain. They function as electron transporters in prokaryotes such as *Mycobacterium tuberculosis*. For these studies, we used Langmuir monolayers and microemulsions to investigate how the menaquinone headgroup (menadione) and the menahydroquinone headgroup (menadiol) interact with model membrane interfaces to determine if differences are observed in the location of these headgroups in a membrane. It has been suggested that the differences in the locations are mainly caused by the isoprenyl sidechain rather than the headgroup quinone-to-quinol reduction during electron transport. This study presents evidence that suggests the influence of the headgroup drives the movement of the oxidized quinone and the reduced hydroquinone to different locations within the interface. Utilizing the model membranes of microemulsions and Langmuir monolayers, it is determined whether or not there is a difference in the location of menadione and menadiol within the interface. Based on our findings, we conclude that the menadione and menadiol may reside in different locations within model membranes. It follows that if menaquinone moves within the cell membrane upon menaquinol formation, it is due at least in part, to the differences in the properties of headgroup interactions with the membrane in addition to the isoprenyl sidechain.

Key words: menaquinone, menadione, menadiol, Langmuir monolayer, reverse micelle.

Résumé : Les ménaquinones sont des lipoquinones formées d'un groupement de tête (naphtoquinone, ménadione) et d'une chaîne latérale isoprényle. Elles servent de transporteurs d'électrons dans les procaryotes tels que *Mycobacterium tuberculosis*. Dans le cadre des présents travaux, nous avons employé des monocouches de Langmuir et des microémulsions pour étudier la manière dont le groupement de tête de la ménaquinone (la ménadione) et le groupement de tête de la ménahydroquinone (le ménadiol) interagissent avec les interfaces du modèle membranaire. Cette étude avait pour but de déterminer si des différences peuvent être décelées quant aux endroits où ces groupements de tête se situent à l'intérieur d'une membrane. L'hypothèse selon laquelle ces différences de position seraient essentiellement attribuables à la chaîne latérale plutôt qu'à la réduction de la quinone en quinol durant le transport d'électrons a été posée. Cette étude présente des éléments qui tendent à démontrer que la quinone oxydée et l'hydroquinone réduite se déplacent à des endroits différents dans la membrane cellulaire, et ce, sans influence de la chaîne latérale. À l'aide de membranes modèles de microémulsions et de monocouches de Langmuir, nous avons pu déterminer s'il y avait ou non une différence de position entre la ménadione et le ménadiol dans la membrane. Nos résultats ont permis de conclure que la ménadione et le ménadiol peuvent se situer à des endroits différents dans les membranes modèles. Par conséquent, si la ménaquinone se déplace dans la membrane cellulaire lorsqu'elle se transforme en ménaquinol, ce déplacement est attribuable non seulement à la chaîne isoprényle, mais aussi, du moins en partie, à la différence des propriétés des interactions entre le groupement de tête et la membrane. [Traduit par la Rédaction]

Mots-clés : ménaquinone, ménadione, ménadiol, monocouche de Langmuir, micelle inversée.

1. Introduction

Lipoquinones are an essential group of lipids that act as electron transfer donors and acceptors within the electron transfer complex.[1,2] One type of lipoquinone typically associated with prokaryotes is menaquinone (MK), which has a naphthoquinone headgroup, as well as an isoprenyl sidechain.[3–6] The menaquinone abbreviations are based on the naphthoquinone headgroup and the number of isoprene groups in the sidechain, where MK-4 is a menaquinone with four isoprene units. Some of the MK derivatives are known to have biological activities in humans such as MK-4, which is important in blood coagulation.[7] Other MK analogs have been reported to have potent biological properties such as antiseizure activity in model organisms.[8–10] The native electron transport lipoquinone of *Mycobacterium* spp., specifically *M. smegmatis* and *M. tuberculosis*, is MK-9 with a reduced β isoprene unit (abbre-

Received 15 January 2020. Accepted 30 March 2020.

C. Van Cleave, H.A. Murakami, J.T. Koehn, P. Maldonado, Jr., H.D. Kreckel, E.J. Cope, and A. Basile. Department of Chemistry, Colorado State University, Fort Collins, CO 80523, USA.
N. Samart. Department of Chemistry, Colorado State University, Fort Collins, CO 80523, USA; Department of Chemistry, Rajabhat Rajanagarindra University, Chachoengsao, Thailand.
D.C. Crick. Cell and Molecular Biology Program, Colorado State University, Fort Collins, CO 80523, USA; Department of Microbiology, Immunology, and Pathology, Colorado State University, Fort Collins, CO 80523, USA.
D.C. Crans. Department of Chemistry, Colorado State University, Fort Collins, CO 80523, USA; Cell and Molecular Biology Program, Colorado State University, Fort Collins, CO 80523, USA.
Corresponding author: Debbie Crans (email: debbie.crans@colostate.edu).
This paper is part of a special issue to honour Professor Jim Wuest.

Can. J. Chem. 98: 307–317 (2020) dx.doi.org/10.1139/cjc-2020-0024 Published at www.nrcresearchpress.com/cjc on 16 April 2020.

Fig. 1. Structures for (A) menaquinone (MK-9(II-H_2)) present in *M. tuberculosis*, (B) the oxidized headgroup menadione (MEN), and (C) the reduced headgroup menadiol (MDL).

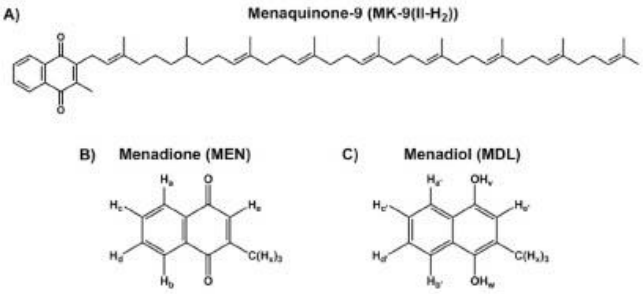

viated as MK-9(II-H_2), Fig. 1A).[11,12] The electron transfer complexes of most organisms are membrane associated and thus require that the MK derivatives are also affiliated with the membrane. Native prokaryotic MKs have long isoprenyl sidechains and their native conformations are poorly understood. Their hydrophobic nature and insolubility in aqueous assays complicates analyses of these molecules.[6] Considering the challenges of working with the native systems, we have initiated studies with truncated MK derivatives that are slightly water soluble.[1,6,13] Their simpler and less hydrophobic structures allow for characterization of how these MK systems interact with membrane interfaces and elucidation of their conformations.[6,13] We have recently shown that the truncated MK-1 and MK-2 molecules fold and that such folding adjusts as the molecule associates with a model membrane interface.[1,13]

The MK derivatives are reduced by the electron transfer complex to form their quinol counterparts. Reduced MKs are suggested to interact differently with the interface compared with oxidized MKs, based on computational and experimental studies on MK's counterpart, ubiquinone.[14–16] In this manuscript, we sought to obtain experimental evidence investigating whether the interaction with interfaces differs between the oxidized menadione (MEN) and reduced menadiol (MDL) headgroups. Previous studies of the MK derivatives with interfaces take advantage of work with two model interface systems, Langmuir monolayers[17,18] and microemulsions.[19,20] Generalized diagrams of both model membranes and potential locations of probe molecules are shown in Fig. 2. Studies using Langmuir monolayer systems with truncated MK derivatives have been reported and support the interpretation that the MK derivatives insert into the membrane interface.[1,21] The studies with microemulsions were carried out using a well-known model system for studying membrane interface interactions, consisting of a lipid or surfactant (aerosol-OT, abbreviated AOT), an organic solvent (isooctane), and water.[22–24] This system forms self-assembled structures with an interface resembling that of a charged membrane,[19,25–27] making it a very useful tool for studying the interactions and potential penetration of naphthoquinone and naphthoquinol headgroups.[13,18] Both models have been used successfully in conjunction with each other to develop a more in-depth framework of how different biologically relevant molecules interact with the cell membrane.[28,29]

Computational analysis and other studies have been carried out, which suggest that the interactions of MK and ubiquinone derivatives within the membrane are dictated mainly by the length of the isoprene sidechain.[30] In other studies in neutral bilayers, the naphthoquinone headgroup was important for anchoring the lipoquinone, suggesting that the isoprene may not be the only structural factor determining the location in the membrane.[14,31] Anchoring through a headgroup has been noted with other molecules as well.[32,33] In the following work, we examined

Fig. 2. General diagrams of (A) a Langmuir monolayer and (B) a reverse micelle (RM) microemulsion. Black rectangles represent probe molecules found in the hydrophobic tails, black triangles represent molecules found in the interface, black ovals represent molecules found in the bulk water, and black stars represent molecules found in the non-polar solvent of the RM system. [Colour online.]

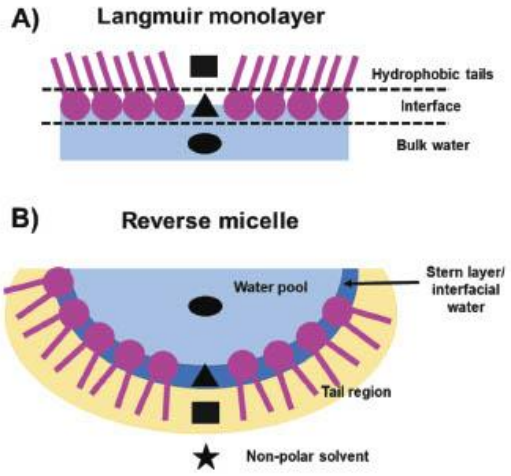

the interaction of the headgroup, MEN (Fig. 1A), and the corresponding reduced version, MDL (Fig. 1C), with a model membrane interface. We hypothesize that the headgroup will interact and penetrate into the membrane but that there are differences in how MEN and MDL interact with the interface. These studies are important and provide experimental evidence for the role of the headgroup in the interaction of the MK derivatives at the cell membrane interface.

2. Materials and methods

2.1. General materials and methods

2.1.1. *Materials*

MEN was purchased from Sigma-Aldrich. MDL was prepared as reported previously.[1,34] Chloroform (≥99.5%), dithiothreitol (DTT), monosodium phosphate (≥99.0%), disodium phosphate (≥99.0%), sodium hydroxide (≥98%), hydrochloric acid (37%), and MEN were all purchased from Sigma-Aldrich. Dipalmitoylphosphatidylcholine

(DPPC, ≥99%) and dipalmitoylphosphatidylethanolamine (DPPE, 99%) were purchased from Avanti Polar Lipids. Most materials were used without further purification. AOT (Sigma-Aldrich) was purified using charcoal and methanol as described previously.[35] The water content of the AOT was determined by NMR spectroscopy, measuring the water content in AOT solubilized in DMSO. Distilled deionized (DDI) water was obtained by filtering distilled water through a water purification system, obtaining a resistance of 18.2 MΩ.

2.1.2. Instrumentation

All absorption spectra were run on an Avantes spectrophotometer (AvaSpec-USB2 with an AvaLight-DHc lamp) in 1 cm quartz cuvettes and collected with AfterMath software version 1.4.7881. The Langmuir monolayers were studied using a NIMA LB Medium Trough (Teflon) from Biolin Scientific. NMR studies were conducted on a Bruker Neo400 NMR. Dynamic light scattering (DLS) studies were performed in a Malvern Zetasizer Nano ZS equipped with a 633 nm red laser.

2.2. Synthesis of MDL

MDL was synthesized by the reduction of MEN by sodium dithionite, and NMR spectra of MDL were consistent with those reported previously.[1,34]

2.3. Stability studies with UV–vis spectroscopy

Because of the limited solubility of the oxidized and reduced headgroups, as well as the rapid oxidation of the reduced headgroup, a number of different methods were investigated for preparation of the solutions. Attempts to sonicate the samples under argon were not as effective as the addition of a reductant of MDL samples.

2.3.1. Stability in DDI water

A solution of 0.10 mmol/L MEN (yellow powder) was made by sonicating 17 mg (10 μmol) of MEN in 100 mL of DDI water (18.2 MΩ) until dissolved, approximately 10 min. A solution of 0.10 mmol/L MDL (pale purple powder) was made by sonicating 17 mg (10 μmol) of MDL in 100 mmol/L of DDI water for approximately 20 min. A third sample was prepared by adding 17 mg of MDL (10 μmol) to 100 mL of DDI water, shaking for five seconds, and removing the supernatant to observe the spectra of MDL immediately after contact with water. A fourth sample was prepared by adding a small amount of solid MDL to the bottom of a cuvette and then adding water. Spectra were collected every minute for 15 min and then at the 20, 25, 30, 45, and 60 minute marks. Although one may have anticipated that MDL would be more soluble than MEN because of the two hydroxyl groups, the fact that the MDL takes longer to dissolve than MEN is not consistent with this observation. Although hydroxyl groups typically increase solubility, this is not always the case. For example, the $[VO_2(dipic\text{-}OH)]^-$ complex is less soluble than the parent complex, $[VO_2dipic]^-$ complex, possibly because the former imparts greater solid-state interactions, which decrease the solubility.[36]

2.3.2. Stability in DDI water with a reducing agent

DTT was used to create a reducing environment to test for an improvement in MDL stability. Due to the rapid oxidation of MDL in water, a small amount of MDL solid was added to the bottom of a quartz cuvette with a small amount of DTT. DDI water was added and a UV–vis spectrum was recorded immediately. Timepoints were taken with the same frequency as described in the previous section.

2.3.3. Stability of MDL in a reverse micelle microemulsion

A stock solution of w_0 12, AOT/isooctane reverse micelles was prepared by mixing appropriate amounts of 0.50 mol/L AOT in isooctane with DDI water and agitating for 30 s until the solution became translucent. The sample for UV–vis was prepared by diluting 1.0 mL of the stock solution into 4.0 mL of isooctane and agitating for 2 min to break up aggregates. Approximately 1.0 mL of the dilution was added to a cuvette with solid MDL and immediately placed into the UV–vis spectrophotometer (t = 0). The same timepoints were collected as described in the previous sections.

2.4. Preparation of solutions for Langmuir monolayers studies

2.4.1. Phospholipid and menaquinone stock solutions

Phospholipid stock solutions were prepared by dissolving dipalmitoylphosphatidylcholine (DPPC) (0.018 g, 0.025 mmol) or dipalmitoylphosphatidylethanolamine (DPPE) (0.017 g, 0.025 mmol) in 25 mL of 9:1 chloroform/methanol (*v*/*v*) for a final concentration of 1.0 mmol/L phospholipid. MEN stock solutions were prepared by dissolving MEN (0.0043 g, 0.025 mmol) in 25 mL of 9:1 chloroform/methanol (*v*/*v*) for a final concentration of 1.0 mmol/L MEN. Solutions with ratios of 50:50 and 25:75 (phospholipid/MEN) were prepared in 2.0 mL glass vials and vortexed for 10 s before each experiment.

2.5. Langmuir monolayers studies

2.5.1. Preparation of phospholipid Langmuir monolayers

The aqueous subphase consisted of 230 mL of 20 mmol/L sodium phosphate buffer (pH 7.4) in DDI water (18.2 MΩ). The subphase surface was cleaned using vacuum aspiration, and the surface pressure of a compression isotherm of just the subphase (no phospholipid present) was measured (surface pressure was consistently 0.0 ± 0.5 mN/m throughout compression) before each compression measurement. To prepare the DPPC phospholipid monolayer, a total of 28 μL of phospholipid stock solution (28 ng of DPPC) was added to the surface of the subphase in a dropwise manner using a 50 μL Hamilton syringe approximately 1 inch from each expanded barrier. The film was allowed to equilibrate for 15 min during which time the chloroform and methanol evaporated. The resulting phospholipid monolayer was then used for the compression isotherm experiments.

The preparation of the Langmuir monolayer from DPPE phospholipids required a higher lipid amount and the injection volume of 58 μL was compared with the DPPC solution. Solutions with ratios of 50:50, and 25:75 (phospholipid/MEN) shared the base injection volume of phospholipid plus an appropriate amount of MEN to reach the desired ratio of phospholipid/MEN.

2.5.2. Compression isotherm surface pressure measurements of Langmuir monolayers

The phospholipid monolayer was compressed from two sides with a total speed of 10 mm/min (5 mm/min from opposite sides) using a NIMA LB Medium Trough from Biolin Scientific. The temperature was maintained at 25 °C using an external water bath. The trough base and Teflon barriers were rinsed three times with ethanol followed by DDI water (18.2 MΩ) before each experiment. The surface tension of the subphase during each compression was monitored using a platinum Wilhemy plate. The surface pressure was calculated from the surface tension using eq. 1, where π is the surface pressure, γ_o is the surface tension of water (72.8 mN/m), and γ is the surface tension at a given area per phospholipid after the film has been applied.

$$\pi = \gamma_o - \gamma \quad (1)$$

The compression moduli were calculated and are shown as detailed in the Supplementary data. Each compression isotherm experiment consisted of at least three replicates, and the averages of the area per phospholipid and the standard deviation at every 5 mN/m were calculated using Microsoft Excel. The areas of the mixed monolayers were multiplied by the mol fraction to plot curves in terms of area per phospholipid as opposed to area per

molecule. This allowed for easier comparison with the control. The worked-up data were transferred to OriginPro version 9.1 to be graphed showing the variation in the measurements.

2.6. Reverse micelle (RM) solutions in AOT/isooctane

2.6.1. MEN

Because MEN was sparingly soluble in H_2O (or D_2O) the AOT/isooctane RM samples were prepared by dissolving MEN directly into a mixture of AOT in isooctane followed by the addition of D_2O. A 0.5 mol/L stock solution of AOT in isooctane was prepared by dissolving 5.56 g, 12.5 mmol AOT in 25 mL isooctane. To prepare a 14.3 mmol/L MEN solution, 0.6 g of MEN was added to a 25 mL volumetric flask followed by the AOT/isooctane stock solution. The mixture was sonicated until MEN was fully dissolved and then diluted to the mark. The pH of a D_2O solution was adjusted to 7.0 (pD = pH + 0.4). To 2 mL of the MEN/AOT/isooctane stock of solution varying amounts of pH adjusted D_2O was added to prepare samples with w_0 4, w_0 8, w_0 12, w_0 16, and w_0 20 for MEN. These samples were vortexed until clear, indicating that the microemulsions were formed.

2.6.2. MDL

As in the case of solution preparation for studies by UV–vis spectroscopy, several methods were investigated to prepare the higher concentration solutions for NMR investigations including use of different solvents and solvent mixtures, as well as mixed solid systems, and the addition of the RM mixture into an NMR tube containing the solid at the bottom. Due to the rapid oxidation of MDL to MEN, methanol was added to the "water pool" of the RMs to both solubilize and stabilize MDL against oxidation. The mixed solvent MeOH/D_2O samples were prepared similarly to the D_2O samples in a 10 mL volumetric flask adding first MeOH (7.0, 8.0, and 9.0 mL) followed by D_2O to make up the 10 mL volume (note that MeOH/D_2O decrease volume when combined, so the values reported here overestimate the MeOH content). Several mixed solvent pools were made but only the 70:30, 80:20, and 90:10 mixtures were able to dissolve MDL. After vortexing, the mixed solvents were used to prepare samples as described above (0.20 mg/1.15 μmol in 1.00 mL mixed solvents). As MDL was poorly soluble in aqueous and D_2O solutions, solid MDL was added to the NMR tube prior to AOT/isooctane RM solution. Specifically, microemulsion solutions for NMR studies were prepared by the addition of 0.20 mg (1.2 μmol) MDL to the tube followed by 1 mL of AOT/isooctane RM solution. This experiment corresponded to the addition of solid MDL to an "empty" RM. NMR spectra were collected immediately.

2.6.3. ^{1}H NMR spectroscopic studies of AOT/isooctane RM samples

One-dimensional (1D) ^{1}H NMR spectra of MEN and MDL in D_2O, organic solvent, and RMs. Two-dimensional (2D) ^{1}H NMR studies of MEN and MDL were carried out in organic solvent and in RMs as reported previously.[20] The parameters to record the NOESY and ROESY spectra were recorded using parameters reported previously.[1]

2.7. Dynamic light scattering (DLS) studies

DLS samples were prepared similar to the RM NMR samples described above but with the following modifications: DI water was used in place of D_2O, and once the 1 mL sample was made, 4 mL of isooctane were added to dilute the sample. Diluted samples were agitated for 2 min prior to measurements to break up RM aggregates.

3. Results

3.1. Stability of MEN and MDL in aqueous solution

3.1.1. MEN and MDL in aqueous solution

MEN is stable in aqueous solution albeit sparingly soluble, requiring agitation or sonication for dissolution. MDL, on the other hand, oxidizes to MEN, so stability studies in water were conducted to determine the time that the reaction takes place to define the parameters of the experimental design. Several different approaches to sample preparation for MDL were tested against MEN with UV–vis spectroscopy. These consisted of dissolving MDL completely in water, taking an aliquot of supernatant from a fresh mixture of MDL and water, and placing solid MDL at the bottom of a vessel such as a cuvette. The potential to carry out MDL solution preparation under argon was considered but not pursued because of the difficulties in dissolving the compound in a timely manner.

The absorption spectrum shown in Fig. 3 of 0.1 mmol/L MEN contains four peaks that appear at 198 nm, 248 nm, 263 nm, and 339 nm. This solution was found to be stable over 60 min (see Supplementary Fig. S1). The UV–vis spectra of the 0.1 mmol/L MDL

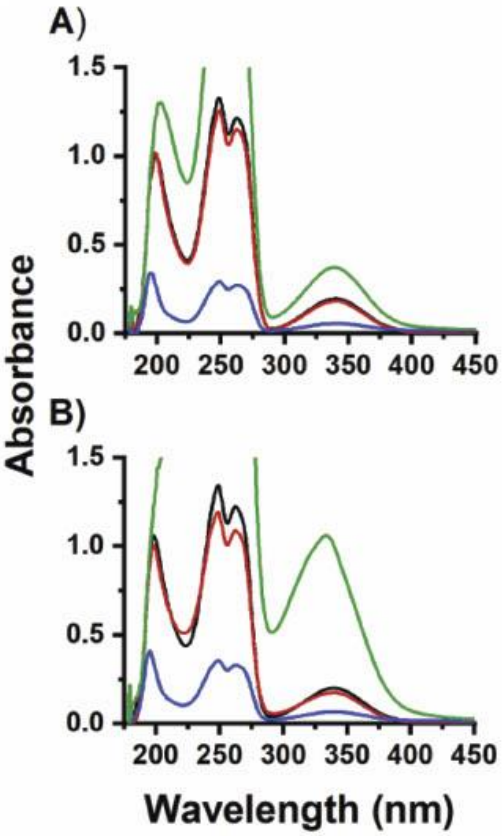

Fig. 3. Aqueous UV–vis spectra of 0.10 mmol/L MEN (black), 0.10 mmol/L MDL that was fully dissolved before analysis (red), supernatant from a 0.1 mmol/L MDL solution when MDL had just been added to water (blue), and aqueous solution added to solid MDL at the bottom of the quartz cuvette (green). Spectra are shown at times (A) t = 0 min and (B) t = 60 min after dissolution of the MDL material. The y axis is cut off at 1.5 as any peaks above that value in the absorbance spectrum are associated with high experimental uncertainly. Full spectra are provided in Supplementary Fig. S2. [Colour online.]

sample prepared by sonication has four peaks at 198 nm, 248 nm, 261 nm, and 341 nm, which is identical to that observed for MEN and thus documents complete oxidation by the time the solid MDL had dissolved (Fig. 3A). After 60 min, small differences were observed for the signal at 225 nm and the two signals at 248 nm and 263 nm. An aliquot of MDL supernatant taken from a sample where MDL had just been added to water had peaks at 194 nm, 248 nm, 263 nm, and 340 nm but at a lower intensity. Some of these peaks are slightly shifted from pure MEN (Fig. 3). In addition, the peak at 194 nm had a higher intensity than the peaks at 248 nm and 263 nm, which is the opposite spectroscopic signature for dissolved MDL. This suggests that the sample contained something other than MEN.

The sample of solid MDL added directly in a cuvette followed by the addition of water showed the peaks that were present at 203 nm, 249 nm, and 262 nm had coalesced into a single signal with an intensity above an absorbance where the spectrophotometer measured intensities accurately (Fig. 3B). These experiments demonstrate that MDL has limited solubility and it rapidly oxidizes as it dissolves. In a system where solid MDL is present at the bottom of the cuvette, the MDL can continuously dissolve and consequently continuously oxidize. The data shown for both the 0 min and 60 min time points of the MDL sample (Fig. 3) demonstrate that even at $t = 0$ significantly more than 0.1 mmol/L MDL has been dissolved and oxidized to MEN. As the Langmuir monolayer studies take approximately 45 min for completion, where MDL would be exposed to bulk and interfacial water, such studies would be examinations of MEN as opposed to MDL. Thus, Langmuir monolayer studies were not attempted starting from MDL due to its rapid oxidation. Regardless, the data in Fig. 3B show that the studies performed so far gives a spectrum identical to that of MEN and thus confirmed that MDL oxidized in solutions where it was allowed to fully dissolve in the time it took to prepare the solution. To validate this interpretation, we sought to dissolve MDL under conditions where it remained in the reduced form.

3.1.2. *MEN and MDL in reducing aqueous solution*

To keep MDL in a reduced form, solid DTT was added to the cuvette alongside solid MDL with the intent to generate a solution with a reducing environment, thus decreasing spontaneous oxidation of MDL. Such a solution should allow for the observation of MDL instead of MEN (Fig. 4). Figure 4B shows that a solution formed from the addition of both MDL (239 nm signal) and DTT followed by the addition of water will begin oxidizing MDL to MEN as evidenced by the 263 nm signal by the 15 min timepoint. A control sample was recorded where solid DTT and MEN were added to the quartz cuvette followed by the addition of water. This experiment verifies the spectrum for MEN by the presence of the 263 nm signal as opposed to the MDL signals and is shown in Fig. 4A.

The use of a reducing agent did decrease the oxidation rate of MDL to MEN, and it was possible to record a spectrum of MDL in the presence of DTT. This verifies that the UV–vis spectrum of MDL is different than that of the MEN. Considering that these spectra were recorded from solid added to the quartz cuvette, the concentrations cannot be accurately determined unlike those shown in Fig. 3, which is why the signal intensity for the MEN is smaller than that observed for MDL. However, it is not appropriate to use such solid mixture in Langmuir monolayer studies due to the exposure to open air and continuous oxidation under those conditions, as well as the potential effects of DTT on the monolayer itself. Accordingly, an alternative model membrane system, microemulsions, was investigated in place of the Langmuir monolayer studies.

3.2. Effects of MEN on DPPE and DPPC monolayers

The effects of MEN on a Langmuir monolayer were investigated using both DPPE and DPPC. These phospholipids were chosen as they have been thoroughly characterized in Langmuir monolayer systems and their biological relevance has also been characterized. DPPC is up to 40% of human lung surfactant, whereas DPPE is commonly found in prokaryotic cell membranes and the inner leaflet of eukaryotic cells.[37–39]

Although MEN is a hydrophobic molecule, it was unable to form a monolayer on the subphase, even with increasing amounts of MEN. This implies that MEN is either surface inactive, much like

Fig. 4. UV–vis spectra showing (A) a solution of DTT (blue), a solution formed from the addition of solid MEN and DTT (red) in a quartz cuvette followed by the addition of DDI water, and a solution formed from the addition of solid MDL and DTT in a quartz cuvette followed by DDI water (black) and (B) a solution formed by the addition of solid MDL and DTT to a quartz cuvette followed by DDI water as a function of time from the addition of the DDI water at time 0 over 60 min. The *y* axis is truncated to 1.5, as any peaks above that value are associated with high error. [Colour online.]

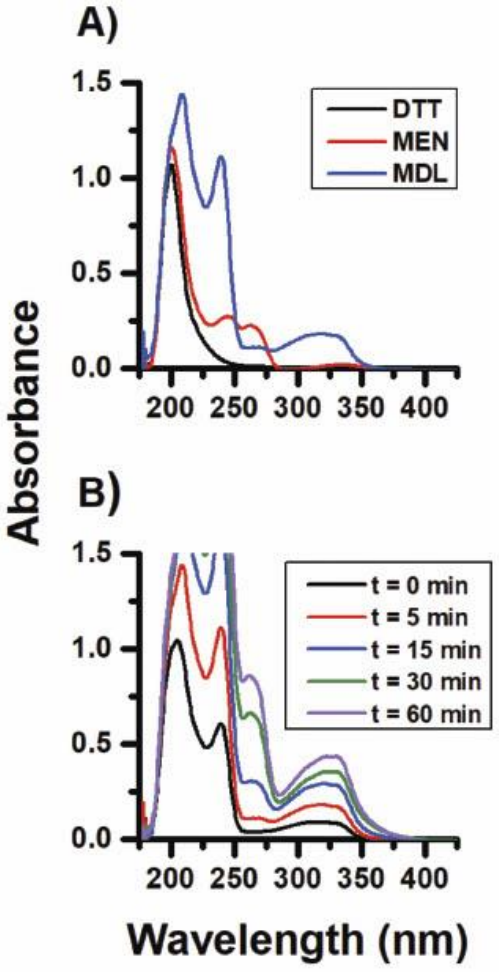

Fig. 5. Compression isotherms of (A) DPPC and (B) DPPE with varying mol fractions of MEN as a function of area per phospholipid. Solid black curves represent DPPC or DPPE controls. Red dashed curves represent 50:50 lipid/MEN monolayers, and dotted blue curves are 25:75 lipid/MEN monolayers. [Colour online.]

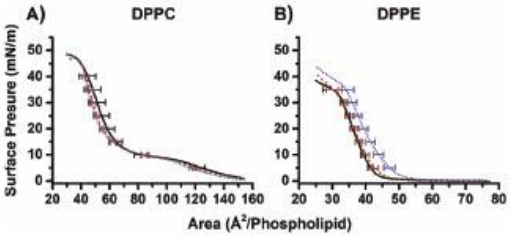

geranyl bromide (unpublished data), or that MEN was π–π stacking in the aqueous solution, thus preventing the formation of a film.

As shown in Fig. 5, the DPPC monolayers exhibited the expected gas–liquid transition between 155 and 110 Å^2 (0–10 mN/m), which is in accordance to the literature for the amount of lipid added.[18,37] The 50:50 and 25:75 DPPC/MEN curves exhibit an overall similar shape as the pure DPPC samples, though both are slightly shifted to a smaller area per phospholipid. However, the observed variation in the area measurements overlap with the variation in the control; therefore, we cannot conclude that there is a difference in area. This indicates that MEN is located in either the bulk water or the hydrophobic tail region. Given the sparing solubility of MEN in water, it is more likely that MEN was compressed into the hydrophobic phospholipid tails. This was confirmed by compression modulus calculations shown in Supplementary Fig. S5, where the compression modulus was affected by the presence of MEN in DPPC. These observations are consistent with the insertion of MEN into the monolayer.

The DPPE control curves has a shape and areas that are consistent with what is reported in the literature.[37] The curve shifts towards a greater area per phospholipid as the mol fraction of DPPE is decreased while the curve maintains its shape. These results are consistent with the possibility that MEN is located directly at the air–water interface without being compressed up into the phospholipid tails. These results support the report showing that the idebenone/idebenol pair remains at the water–lipid interface,[33] though the physical properties of the lipid or surfactant will have an effect on distribution of the molecule of interest.[40] To this effect, the physical properties of DPPC and DPPE resulted in different interaction with MEN, which supports that lipid composition of the cell membrane could also affect the location of lipoquinones.

3.3. MEN and MDL in the AOT RM model membrane system

3.3.1. *MEN in microemulsions*

The solubility of MEN in aqueous solution is limited (albeit higher than MDL's solubility), but enough compound can be dissolved in D_2O that a ^{1}H NMR spectrum can be recorded after agitating the suspensions (Fig. 6). The aromatic protons are in a chemical shift range well separated from the signals from the RM surfactant with the quinone proton (H_e) slightly more upfield than the benzene protons (H_a–H_d). The aliphatic methyl group on the quinone unit on the other hand is in the range of the AOT protons around 2.3 ppm. There is a large difference between the ^{1}H NMR spectrum in D_2O and in an organic solvent such as isooctane, as shown in Fig. 6.

3.3.2. *MDL in microemulsions*

The ^{1}H NMR of MDL were recorded in a number of solvents including D_2O, MeOD, d_6-DMSO, d_6-benzene, and $CDCl_3$, as shown

Fig. 6. ^{1}H NMR spectra of MEN in d_6-DMSO, MeOD, d_6-benzene, $CDCl_3$, and D_2O.

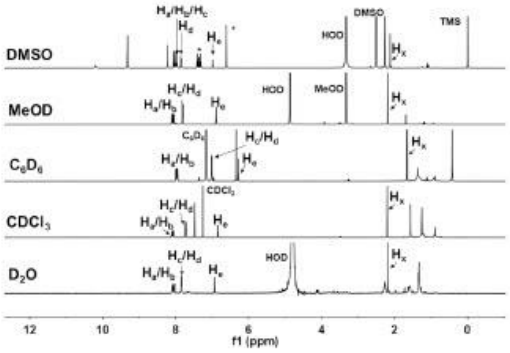

in Fig. 7. The oxidation of MDL is visually observed by the colour change of the light purple MDL to the yellow MEN. Complete dissolution of MDL in D_2O, d_6-benzene, and $CDCl_3$ required incubation overnight or sonication and agitation. As a result, for the MDL samples in d_6-benzene, D_2O, and $CDCl_3$, the NMR solvent was added to solid MDL in the NMR tube and the ^{1}H NMR spectra were collected immediately. Although the rate of MDL oxidation was dependent on the solvent, the oxidation was found to be rapid in all solvents. Although some amount of the solid MDL samples was suspended in the NMR tube when the NMR spectrum was being recorded, the time it would take to dissolve the MDL sample fully would have caused significant or complete oxidation. The NMR results shown in Fig. 7 indicate that the MDL was present in all solvents tested regardless of the low solubility of the MDL. The ^{1}H NMR spectra of MDL show five protons in the aromatic region, with the proton on the hydroquinone group being more than 1 ppm upfield from the other aromatic protons and the aliphatic protons around 2.3 ppm. The proton most different between the MEN and MDL is the proton on the quinone or the hydroquinone, H_e. However, even by recording the sample immediately after adding deuterated solvent to the NMR tube led to formation of some MEN in the samples, indicated by the * in the spectra for MDL shown in Fig. 7.

MDL was very soluble in d_6-DMSO and MeOD. As shown in Fig. 8, the MDL oxidized less rapidly in d_6-DMSO and the data for d_6-benzene, $CDCl_3$, and D_2O are given in the Supplementary data. As illustrated in Fig. 7, it was possible to obtain spectra of not only the MDL but also the MEN that is formed in these solvents, and we show the spectra as a function of time. ^{1}H NMR spectra performed as a function of time in MeOD showed that the reduced MDL existed for about 1 h (Fig. 8). Considering that microemulsions have been reported with "water pools" containing methanol, it was possible to record spectra of MDL in AOT reverse micelles with MeOH-containing "water pools".[41,42]

3.3.3. *Stability of MDL in RM samples*

UV–vis spectra of MDL in w_0 12 RMs were collected to assess oxidation of MDL to MEN in the RM system. As with the aqueous samples described in the above stability section, MDL was found to start oxidizing with the first 15 min of exposure to the solution, as shown in Fig. 9. The characteristic MEN peak at 263 nm begins to appear by the fifth minute, confirming the NMR studies above in the need for a mixed solvent "water pool" to increase stability.

Fig. 7. ^{1}H NMR spectra of MDL in d_6-DMSO, MeOD, d_6-benzene, $CDCl_3$, and D_2O. The signals for MEN beginning to form in these spectra are labeled with an asterisk (*).

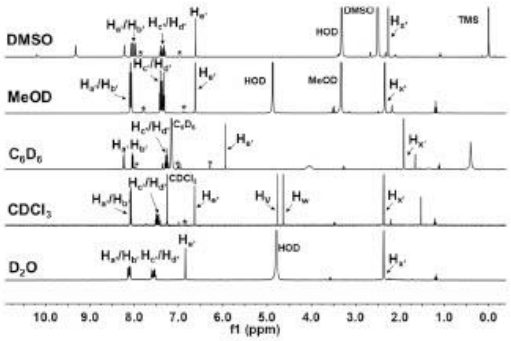

Fig. 8. Spectra recorded of MDL as a function of time in solvents where it is readily soluble such as (A) d_6-DMSO and (B) MeOD. The increase in the ^{1}H NMR signals are due to formation of MEN and these signals are indicated by an asterisk (*).

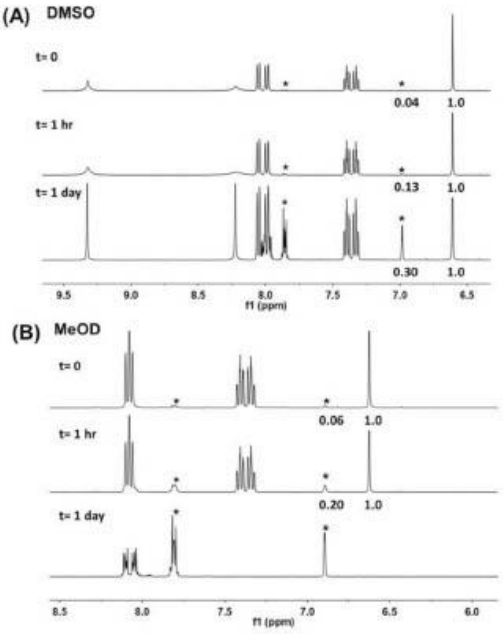

3.4. Interactions of MEN and MDL in AOT/isooctane RM samples

3.4.1. *MEN in microemulsions*

^{1}H NMR spectra were recorded in 0.50 mol/L AOT/isooctane to investigate the interactions of MEN with another type of model membrane interface. The w_0 sizes were varied from w_0 4 to w_0 20. The 1D ^{1}H NMR spectra show that the chemical shifts for MEN were very different from those observed in isooctane and in D_2O (Fig. 10). The chemical shifts change for H_a was less than 0.1 ppm,

Fig. 9. UV–vis spectra of solid MDL dissolving into a w_0 12 RM solution (0.5 mol/L AOT in isooctane) in 1 min increments over 15 min. The peak for the MDL (239 nm) increases rapidly until about 15 min, at which point a significant amount of both MDL and MEN (263 nm) have formed and the accuracy of the UV–vis spectra begins to decrease due to experimental error. [Colour online.]

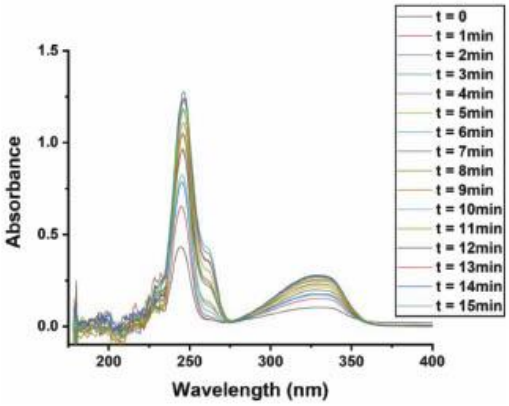

Fig. 10. Partial ^{1}H NMR spectra of MEN in AOT/isooctane RM ranging from w_0 from 4 to 20. The ^{1}H NMR spectra of MEN in D_2O and in isooctane are shown for comparison and demonstrate that the AOT/isooctane RM environment of the MEN is very different depending on proximity to a solvent.

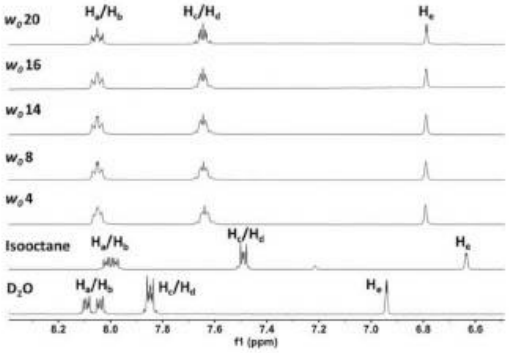

whereas the shifting was 0.2 ppm for H_b and about 0.3 ppm as the quinone proton. These shifts show that MEN resides in neither the aqueous environment of the water pool, nor the organic isooctane solution, consistent with placement in the interface of the AOT RM.

2D NMR spectra including NOESY and ROESY spectra (see Supplementary data) were recorded for the MEN in RM samples and the partial spectra are shown in Fig. 11. These spectra showed that proton H_e correlates to H_x, which serves as an internal control. Weak signals between H_a/H_b, H_c/H_d, and H_e with AOT protons H_1 and H_3 and part of the AOT CH_2 and CH_3 tail groups (H5-H10, H5′-H10′, see Supplementary data for AOT labeling key) show that the placement of the MEN can vary from the headgroup to farther up in the tail region. Further investigation into whether similar conclusions could be reached with the MDL system led to the following NMR experiments.

Fig. 11. Partial ^{1}H-^{1}H 2D (A) NOESY and (B) ROESY NMR (400 MHz) spectra of MEN inside w_0 12 RM at 26 °C. Blue intensity contours represented negative NOEs or ROEs and red intensity contours represent positive NOEs or ROEs. A standard NOESY pulse consisted of 256 transients with 16 scans in the f_1 domain using a 200 ms mixing time and a 1.5 s relaxation delay. A standard ROESYAD pulse consisted of 256 transients with 16 scans in the f_1 domain using a 200 ms mixing time and a 2.0 s relaxation delay. Green lines indicate MEN proton interactions with AOT protons. [Colour online.]

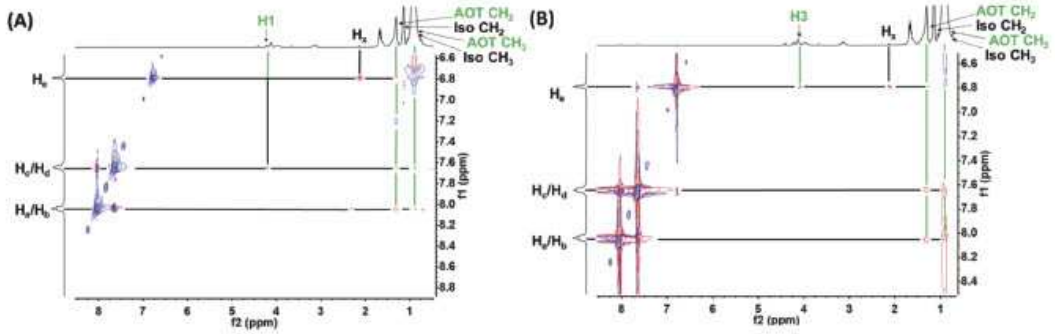

3.4.2. *MDL in microemulsions*

Given the insolubility and instability of MDL in D_2O, an alternative co-solvent in the RM "water pool" based on MeOH/H_2O was investigated. We successfully found that MDL readily dissolved and showed an increased stability in MeOH/D_2O mixtures ranging from 70% methanol to 90% methanol. Because MeOD is known to also form RMs using AOT/isooctane,[41,42] we chose to use the mixtures with high concentrations of MeOD for better comparison with previous studies. 1D NMR studies were recorded of MDL in MeOD/D_2O mixture of AOT/isooctane. The fact that the chemical shifts of the observed protons in RMs differ from the chemical shifts of those in isooctane and MeOD/D_2O shows that the probe molecules are neither in the aqueous center or the organic outer layer; this is evidence of the probe molecules being the very least associated with the interface of the RMs (Fig. 10). As no changes were observed in the NMR spectra as the w_0 changed (data not shown), we concluded that the MDL penetrated or associated with the interface in these MeOD/D_2O/AOT/isooctane systems. As with the aqueous stability experiments, UV–vis spectra were recorded of NMR samples prepared from solid MDL added to the NMR tube before the MeOD/D_2O AOT RMs solution was added, allowing for the MDL to dissolve and move to interact with the RM suspensions.

To obtain information on the location of the MDL, we performed 2D NMR NOESY and ROESY spectra using the w_0 16 sample in 70:30 MeOD/D_2O mixture, shown in Fig. 12. The oxidation of MDL took place while the 2D NMR NOESY and ROESY spectra were recorded. As a result, the spectra recorded show a mixture of the MEN and MDL and the amount of MDL present depends on when the spectrum was recorded. Similar studies were performed with the 90:10 and 70:30 mixtures and these spectra gave similar patterns.

In Fig. 12, there is an interaction between the internal control of $H_{c'}$ and $H_{x'}$ which shows that an NMR of MDL was obtained, but the lack of other cross peaks in the NMRs makes it difficult to determine the placement within the RM. It may be associated with the water pool, but the time span of the studies combined with the rate of oxidation of the MDL should be sufficient to observe cross peaks if there was an interaction. These results are consistent with an interaction with the interface for MEN. However, no firm conclusions can be made on the location of MDL in the RM system.

3.4.3. *Benzoquinone (BEN) in microemulsions*

To investigate the similarity of the interactions of 2,3-dimethoxy-5-methyl-1,4-benzoquinone (BEN), the headgroup of ubiquinone, with a model membrane interface, ^{1}H NMR spectra were recorded in 0.50 mol/L AOT/isooctane (Fig. 13). The w_0 sizes were varied from w_0 4 to w_0 20. The 1D ^{1}H NMR spectra show that the chemical shifts for BEN are very different from those observed in isooctane and in D_2O (Figs. 13A and 13B). These shifts are consistent with BEN residing in neither the aqueous environment of the water pool, nor the organic isooctane solution, suggesting placement in the interface of the AOT RM. There is a small chemical shift change for H_a as the w_0 changes from 4 to 20. That is consistent with the fact that the BEN is located more in the Stern layer of the interface, placing it closer to the water pool than the tail region of interface.

To obtain confirmation regarding the location of BEN at the aqueous part of the interface, we performed ^{1}H-^{1}H 2D NOESY and ROESY NMR (400 MHz) spectra of BEN inside w_0 12 RM at 26 °C (Figs. 13C and 13D). The partial ^{1}H-^{1}H 2D NOESY spectrum of BEN inside w_0 12 RM show an interaction between H_a with the CH_2 groups in the AOT consistent with penetration of BEN into the interface. The partial ^{1}H-^{1}H 2D NMR ROESY NMR spectra in a w_0 12 RM (Fig. 13D) show this interaction, as well are some additional interactions between H_a and the AOT protons, confirming the penetration of BEN with the interface.

3.5. DLS

DLS confirmed that RMs were formed and that the slight increase in RM size with the addition of MEN or MDL is within experimental error and suggest that overall the presence of these compounds is not interfering with the formation of the RMs. Data are presented in Supplementary Table S1.

4. Discussion

MK is a very important electron transport donor and accepter for bacteria and particularly pathogens like the *Mycobacterium* family.[6,11,43] Despite this importance, very little experimental data are available with regard to MK's location in the cell membrane and how it moves from one location to another. Some experimental and computational work has been carried out for ubiquinone.[14,30,44] A few computational studies have been reported that mention MK.[45] We have recently investigated how truncated MK derivatives interact with interfaces using both Langmuir monolayers and microemulsions. Considering the hydrophobicity of these compounds, they will undoubtedly be associated with the interface, but experimental data, more details on the nature of this association, and how lipoquinones move in a

Fig. 12. Partial ^{1}H-^{1}H 2D (A) NOESY and (B) ROESY NMR (500 MHz) spectra of MDL and MEN in a 70:30 MeOD/D_2O 0.5 mol/L AOT RM suspension at 26 °C. Blue intensity contours represented negative NOEs or ROEs and red intensity contours represent positive NOEs or ROEs. A standard NOESY pulse consisted of 256 transients with 16 scans in the f_1 domain using a 200 ms mixing time and a 1.5 s relaxation delay. A standard ROESYAD pulse consisted of 256 transients with 16 scans in the f_1 domain using a 200 ms mixing time and a 2.0 s relaxation delay. [Colour online.]

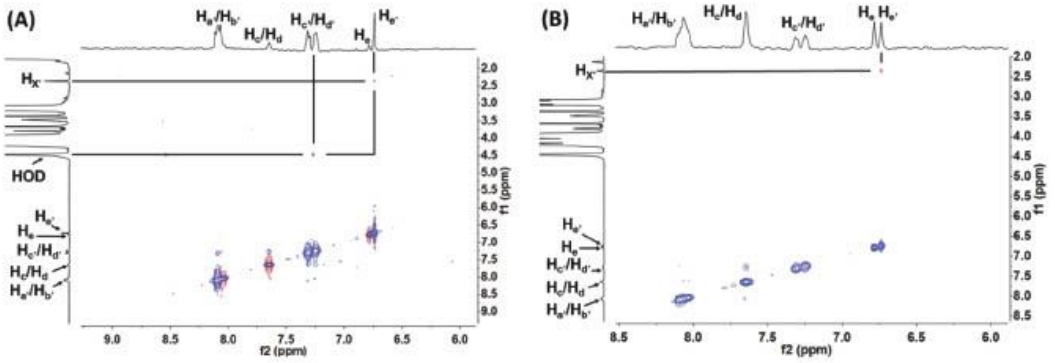

Fig. 13. (A) Structure with proton assignments of BEN. (B) 1D NMR of BEN in varying sizes of RM demonstrating that BEN is in the interface. Partial ^{1}H-^{1}H 2D (C) NOESY and (D) ROESY NMR (400 MHz) spectra of BEN inside w_0 12 RM at 26 °C. Blue intensity contours represented negative NOEs or ROEs and red intensity contours represent positive NOEs or ROEs. A standard NOESY pulse consisted of 256 transients with 16 scans in the f_1 domain using a 200 ms mixing time and a 1.5 s relaxation delay. A standard ROESYAD pulse consisted of 256 transients with 16 scans in the f_1 domain using a 200 ms mixing time and a 1.5 s relaxation delay. Blue lines indicate BEN proton interactions with AOT protons. [Colour online.]

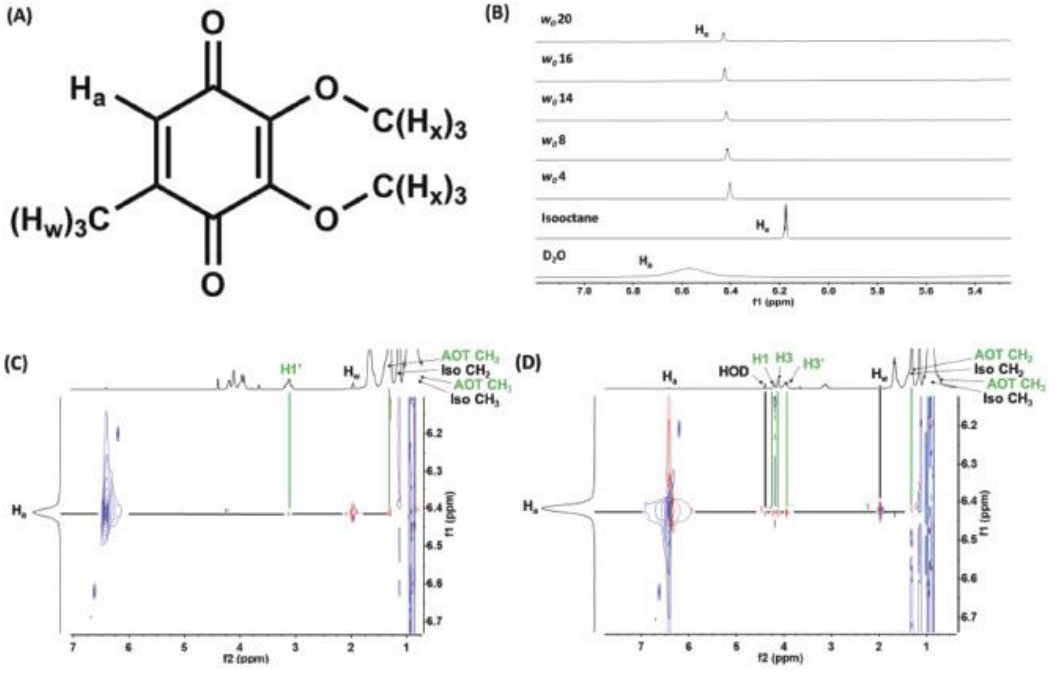

lipid environment are important for future understanding of electron transfer systems.

Lipoquinones are known to shuttle electrons within cell membranes, which requires these molecules to cycle between two redox states to function. In the oxidized form, lipoquinones have a quinone headgroup, whereas the reduced form has a quinol headgroup. Quinones and quinols have different polarities, making it likely that they reside in different locations within the membrane. Current thought, however, favors the isoprenyl sidechain of a lipoquinone as the main determinant of location and inter-

action within the membrane.[30] For lipoquinones with the larger headgroup such as in menaquinones, it is possible that the headgroup plays a greater role than in ubiquinones. The studies in this manuscript investigate the association of MEN and MDL with two model interfaces. We anticipated that the difference in physical properties would be translated to differences in interaction and location of the compounds in the membrane bilayer.

Both MEN and MDL are hydrophobic and insoluble compounds. One may have anticipated that MDL would be more soluble than MEN because of the two hydroxyl groups. The fact that the MDL takes longer to dissolve than MEN is not consistent with this observation (see experimental section); furthermore, MDL only dissolved to higher concentrations when it oxidized to MEN. Generally, hydroxyl groups increase water solubility due to the increased polarity and the potential for H-bonding; however, this is not always the case as reported previously with, for example, the $[VO_2(dipic\text{-}OH)]^-$ and $[VO_2dipic]^-$ complexes.[36] Thus, spectroscopic studies for MDL were limited by rapid oxidation despite being synthesized in pure form. The most convincing MDL data were obtained in the presence of reductant or in a stabilizing organic solvent such as MeOD.

The effects of MEN on a Langmuir monolayer were investigated using both DPPE and DPPC in Langmuir monolayers to properly characterize the interaction with different lipid interfaces. These lipids differ only in headgroup, where the choline headgroup of DPPC is a quaternary amine and the ethanolamine headgroup of DPPE is a primary amine. The different properties of these amine headgroups allow these phospholipids to fill different niches. The bulkier choline group allows for greater spreading of DPPC in conjunction with its fully saturated acyl tails, making it an ideal pulmonary surfactant.[39] The smaller ethanolamine headgroup allows for tighter packing of DPPE, which is why it is more commonly found in the inner leaflet of the cell membrane.[37,38] Our studies revealed a difference in the interaction of MEN with DPPC and DPPE. The DPPC compression isotherms showed no interaction. This implies that MEN either resides in the water or father up into the acyl tails and thus not in the interface. The DPPE studies showed a greater area per phospholipid as the amount of MEN increased. This is consistent with MEN remaining in the interface and disrupting the packing of the ethanolamine headgroups. This is analogous to studies of idebenone and idebenol, which were found to remain in the interface.[33] Our studies also confirm that the lipid environment impacts the location and interaction of MEN in model membranes.[40]

Despite the difficulties in spectroscopic investigation of the MEN/MDL pair caused by the instability of MDL, studies were completed. We found that MEN interacted with the lipids and was able to penetrate the interface. Indeed, the isolated headgroup was found to reside in the tail ends of the interface. The NMR studies in the microemulsion model system supported the findings from the Langmuir monolayers with regard to the localization of the isolated headgroup. Studies with the MDL were more challenging and not as clean. Although conditions were found that allowed for characterization of the interactions of MDL with the reverse micellar interface, the 2D NMR results showed no evidence for penetration of the MDL into the interface. In contrast, results showed evidence for interactions with the HOD signal. However, 1D ^1H NMR data did show that the MDL was not in an environment akin to aqueous or organic solvent, which suggests a location at the interface. With these two pieces of evidence combined, we suggest that the MDL is located at the interface near the water pool, although if and how deep the molecule penetrated could not be confirmed. Importantly, these results must be considered in the context of the full MK structure, where the isoprenyl sidechain will impact the properties of the quinone/quinol pair.

We have recently shown that the truncated MK derivatives, MK-1 and MK-2, adopt a folded conformation observed near the model AOT/RM membrane interface.[1,13] Such a folded conformation would impact the location of the molecule. However, it is clear from these studies that the headgroup has the ability to direct the location of the lipoquinone, which in turn affects the action of these electron carriers and their travels between protein complexes within the membrane. Undoubtedly, structural and polarity differences in the lipoquinone headgroups contribute to different redox potentials, but perhaps less recognized is the fact that these differences may also aid in shuttling of these essential electron transport lipids in the membrane, aiding their function.

We were able to obtain experimental evidence that MEN is associated with the interface, likely through interactions with the AOT tail groups. This may be differentiated from headgroups of other lipoquinones such as BEN, the headgroup of ubiquinone. Additional NOESY and ROESY of BEN were collected under similar conditions to MEN as described in this manuscript. Spectra of BEN are shown in Fig. 13, and we observe interactions between H_a and the AOT protons found in the headgroup (H1, H1′, H3, H3′), as well as the water pool. Comparing the two quinones, this implies that there are several factors in lipoquinone structure that may affect the location in the interface. Although we do not have data on the benzoquinol headgroup, it is likely that it would be located in a more polar environment, similar to both MDL and BEN. Previous studies with quinone/quinol pairs found that both molecules remained at the lipid–water interface.[33] However, we cannot identify an exact location of MDL at the water–lipid interface. Further studies on compounds with quinol headgroups are desirable.

Interestingly, but not unexpectedly, MEN is located father up in the hydrophobic tail region than BEN considering that MEN is significantly more hydrophobic than BEN. Computational studies have found ubiquinone low in the tail region, nearer the water interface, which is consistent with the interactions of the head groups of AOT observed in the spectrum shown in Fig. 13.[46] These findings suggest that both the isoprenyl sidechain and the headgroup will influence the location of lipoquinones.

In summary, the studies presented here show subtle differences in the location of the isolated headgroup MEN and MDL and subtle differences in the location of the isolated headgroup BEN compared with MEN in two types of model membranes, Langmuir monolayers and microemulsions. These studies provide experimental evidence that would be important to understand the location of menaquinones and menaquinols in membranes and their potential movement between membrane-bound protein complexes.

5. Conclusions

Based on structural considerations, it would not be unreasonable to expect that the MEN and MDL would occupy different locations in a membrane interface. Computational studies have been reported supporting the interpretation that lipoquinones change location in the membrane during the electron transfer process.[46] These studies also have demonstrated that the isoprenyl side chain is important for this process. We investigated the interactions and locations of the headgroups of these compounds, namely MEN and MDL, with two model membrane interface systems. We found that MEN associates with the lipid tails. The MDL system was readily oxidized, precluding any Langmuir monolayer studies. However, NMR studies of MDL in microemulsions suggest a location in the water–lipid interface, albeit no exact location was identified. Considering that these studies are of isolated headgroups, this work suggests that the headgroup, in conjunction with the isoprenyl sidechain, is important for the location and interaction of lipoquinones with the cell membrane.

Supplementary data

Supplementary data are available with the article through the journal Web site at http://nrcresearchpress.com/doi/suppl/10.1139/cjc-2020-0024.

Acknowledgements

DCC and DCC thank NSF for partial funding (CHE-1709564). DCC and PM thank the NSF REU program for summer funding to PM (CHE-1461040).

References

(1) Koehn, J. T.; Magallanes, E. S.; Peters, B. J.; Beuning, C. N.; Haase, A. A.; Zhu, M. J.; Rithner, C. D.; Crick, D. C.; Crans, D. C. *J. Org. Chem.* **2018**, *83*, 275. doi:10.1021/acs.joc.7b02649.
(2) Nowicka, B.; Kruk, J. *Biochim. Biophys. Acta* **2012**, *1797*, 1587. doi:10.1016/j.bbabio.2010.06.007.
(3) Das, A.; Hugenholtz, J.; van Halbeek, H.; Ljungdahl, L. G. *J. Bacterid.* **1989**, *171* (11), 5823. doi:10.1128/JB.171.11.5823-5829.1989.
(4) Collins, M. D., Analysis of isoprenoid quinones. In: G. Gottschalk, editor. *Methods in Microbiology*. 1st ed. Academic Press, 1985; Vol. 18, pp. 329–366.
(5) Dhiman, R. K.; Pujari, V.; Kincaid, J. M.; Ikeh, M. A.; Parish, T.; Crick, D. C. *PLoS One* **2019**, *14* (4), e0214958. doi:10.1371/journal.pone.0214958.
(6) Upadhyay, A.; Kumar, S.; Rooker, S. A.; Koehn, J. T.; Crans, D. C.; McNeil, M. R.; Lott, J. S.; Crick, D. C. *ACS Chem. Biol.* **2018**, *13* (9), 2498. doi:10.1021/acschembio.8b00402.
(7) Schwalfenberg, G. K. *J. Nutr. Metab.* **2017**, 2017, article 6254836. doi:10.1155/2017/6254836.
(8) Josey, B. J.; Inks, E. S.; Wen, X.; Chou, C. J. *J. Med. Chem.* **2013**, *56* (3), 1007. doi:10.1021/jm301485d.
(9) Rahn, J. J.; Bestman, J. E.; Josey, B. J.; Inks, E. S.; Stackley, K. D.; Rogers, C. E.; Chou, C. J.; Chan, S. S. L. *Neuroscience* **2014**, *259*, 142. doi:10.1016/j.neuroscience.2013.11.040.
(10) Chadar, D.; Camilles, M.; Patil, R.; Khan, A.; Weyhermüller, T.; Salunke-Gawali, S. *J. Mol. Struct.* **2015**, *1086*, 179. doi:10.1016/j.molstruc.2015.01.029.
(11) Upadhyay, A.; Fontes, F. L.; Gonzalez-Juarrero, M.; McNeil, M. R.; Crans, D. C.; Jackson, M.; Crick, D. C. *ACS Cent. Sci.* **2015**, *1* (6), 292. doi:10.1021/acscentsci.5b00212.
(12) Kurosu, M.; Begari, E. *Molecules* **2010**, *15*, 1531. doi:10.3390/molecules15031531.
(13) Koehn, J. T.; Beuning, C. N.; Peters, B. J.; Dellinger, S. K.; Van Cleave, C.; Crick, D. C.; Crans, D. C. *Biochemistry* **2019**, *58* (12), 1596. doi:10.1021/acs.biochem.9b00007.
(14) Kaurola, P.; Sharma, V.; Vonk, A.; Vattulainen, I.; Róg, T. *Biochim. Biophys. Acta* **2016**, *1858* (9), 2116. doi:10.1016/j.bbamem.2016.06.016.
(15) Quinn, P. J.; Esfahani, M. A. *Biochem. J.* **1980**, *185* (3), 715. doi:10.1042/bj1850715.
(16) Roche, Y.; Peretti, P.; Bernard, S. J. *Therm. Anal. Calorim.* **2007**, *89*, 867. doi:10.1007/s10973-006-7916-4.
(17) Möhwald, H.; Brezesinski, G. *Langmuir* **2016**, *32* (14), 10445. doi:10.1021/acs.langmuir.6b02518.
(18) Peters, B. J.; Van Cleave, C.; Haase, A. A.; Hough, J. P. B.; Giffen-Kent, K. A.; Cardiff, G. M.; Sostarecz, A. G.; Crick, D. C.; Crans, D. C. *Langmuir* **2018**, *34* (30), 8939. doi:10.1021/acs.langmuir.8b01661.
(19) Eskici, G.; Axelsen, P. H. *J. Phys. Chem. B* **2016**, *120* (44), 11337. doi:10.1021/acs.jpcb.6b06420.
(20) Crans, D. C.; Rithner, C. D.; Baruah, B.; Gourley, B. L.; Levinger, N. E. *J. Am. Chem. Soc.* **2006**, *128* (13), 4437. doi:10.1021/ja0583721.
(21) Koehn, J. T.; Crick, D. C.; Crans, D. C. *ACS Omega* **2018**, *3* (11), 14889. doi:10.1021/acsomega.8b02620.
(22) Wiebenga-Sanford, B. P.; Washington, J. B.; Cosgrove, B.; Palomares, E. F.; Vasquez, D. A.; Rithner, C. D.; Levinger, N. E. *J. Phys. Chem. B* **2018**, *122*, 9555. doi:10.1021/acs.jpcb.8b07406.
(23) Correa, N. M.; Silber, J. J.; Riter, R. E.; Levinger, N. E. *Chem. Rev.* **2012**, *112*, 4569. doi:10.1021/cr200254q.
(24) Maitra, A. *J. Phys. Chem.* **1984**, *88* (21), 5122. doi:10.1021/j150665a064.
(25) Binks, B. P.; Meunier, J.; Abillon, O.; Langevin, D. *Langmuir* **1989**, *5* (2), 415. doi:10.1021/la00086a022.
(26) Mukherjee, K.; Mukherjee, D. C.; Moulik, S. P. *J. Colloid Interface Sci.* **1997**, *187* (2), 327. doi:10.1006/jcis.1996.4696.
(27) Van Horn, W. D.; Oglivie, M. E.; Flynn, P. F. *J. Biomol. NMR* **2008**, *40* (3), 203. doi:10.1007/s10858-008-9227-5.
(28) Sostarecz, A. G.; Gaidamauskas, E.; Distin, S.; Bonetti, S. J.; Levinger, N. E.; Crans, D. C. *Chemistry* **2014**, *20* (17), 5149. doi:10.1002/chem.201201803.
(29) Peters, B. J.; Groninger, A. S.; Fontes, F. L.; Crick, D. C.; Crans, D. C. *Langmuir* **2016**, *32* (37), 9451. doi:10.1021/acs.langmuir.6b02073.
(30) Teixeira, M. H.; Arantes, G. M. *RSC Adv.* **2019**, *9*, 16892. doi:10.1039/C9RA01681C.
(31) Monteiro, J. P.; Martins, A. F.; Nunes, C.; Morais, C. M.; Lúcio, M.; Reis, S.; Pinheiro, T. J. T.; Geraldes, C. F. G. C.; Oliveira, P. J.; Jurado, A. S. *Biochim. Biophys. Acta* **2013**, *1828*, 1899. doi:10.1016/j.bbamem.2013.04.006.
(32) Ausili, A.; Torrecillas, A.; de Godos, A. M.; Corbalán-García, S.; Gómez-Fernández, J. C. *Langmuir* **2018**, *34* (10), 3336. doi:10.1021/acs.langmuir.7b04142.
(33) Gómez-Murcia, V.; Torrecillas, A.; de Godos, A. M.; Corbalán-García, S.; Gómez-Fernández, J. C. *Biochim. Biophys. Acta* **2016**, *1858*, 1071. doi:10.1016/j.bbamem.2016.02.034.
(34) Suhara, Y.; Wada, A.; Tachibana, Y.; Watanabe, M.; Nakamura, K.; Nakagawa, K.; Okano, T. *Bioorg. Med. Chem.* **2010**, *18* (9), 3116. doi:10.1016/j.bmc.2010.03.035.
(35) Stahla, M. L.; Baruah, B.; James, D. M.; Johnson, M. D.; Levinger, N. E.; Crans, D. C. *Langmuir* **2008**, *24* (12), 6027. doi:10.1021/la8002965.
(36) Yang, L.; la Cour, A.; Anderson, O. P.; Crans, D. C. *Inorg. Chem.* **2002**, *41*, 6322. doi:10.1021/ic0201598.
(37) Patterson, M.; Vogel, H. J.; Prenner, E. J. *Biochim. Biophys. Acta* **2016**, *1858*, 403. doi:10.1016/j.bbamem.2015.11.025.
(38) Fadeel, B.; Xue, D. *Crit. Rev. Biochem. Mol. Biol.* **2009**, *44* (5), 264. doi:10.1080/10409230903193307.
(39) Al-Saiedy, M.; Tarokh, A.; Nelson, S.; Hossini, K.; Green, F.; Ling, C.-C.; Prenner, E. J.; Amrein, M. *Biochim. Biophys. Acta* **2017**, *1859* (8), 1372. doi:10.1016/j.bbamem.2017.05.004.
(40) Baryiames, C. P.; Teel, M.; Baiz, C. R. *Langmuir* **2019**, *35*, 11463. doi:10.1021/acs.langmuir.9b01693.
(41) Lu, R.; Zhu, R.; Zhong, R.; Yu, A. *J. Photochem. Photobiol. A* **2013**, *252*, 116. doi:10.1016/j.jphotochem.2012.12.004.
(42) Shirota, H.; Horie, K. *J. Phys. Chem. B* **1999**, *103* (9), 1437. doi:10.1021/jp983605e.
(43) Dhiman, R. K.; Mahapatra, S.; Slayden, R. A.; Boyne, M. E.; Lenaerts, A.; Hinshaw, J. C.; Angala, S. K.; Chatterjee, D.; Biswas, K.; Narayanasamy, P., et al. *Mol. Microbiol.* **2009**, *72* (1), 85. doi:10.1111/j.1365-2958.2009.06625.x.
(44) Hoyo, J.; Guaus, E.; Torrent-Burgués, J. *Eur. Phys. J. E: Soft Matter Biol. Phys.* **2017**, *40* (62), 62. doi:10.1140/epje/i2017-11552-2.
(45) Chatron, N.; Hammed, A.; Benoît, E.; Lattard, V. *Nutrients* **2019**, *11*, 67. doi:10.3390/nu11010067.
(46) Galassi, V. V.; Arantes, G. M. *Biochim. Biophys. Acta* **2015**, *1847*, 1560. doi:10.1016/j.bbabio.2015.08.001.

Appendix VI: Interactions of Truncated Menaquinones in Lipid Monolayers and Bilayers

This manuscript corresponds to Chapter 3 and is published in the *International Journal of Molecular Sciences*.[1]

References

1. Van Cleave, C.; Koehn, J.T.; Pereira, C.S.; Haase, A.A.; Peters, B.J.; Croslow, S.W.; McLaughlin, K.G., Werst, K.R.; Goach, A.L.; Crick, D.C.; Arantes, G.M.; Crans, D.C., Interactions of Truncated Menaquinones with Lipid Monolayers and Bilayers. *Int. J. Mol. Sci.* **2021**, *22* (18), 9755.

International Journal of
Molecular Sciences

MDPI

Article

Interactions of Truncated Menaquinones in Lipid Monolayers and Bilayers

Cameron Van Cleave [1], Jordan T. Koehn [1], Caroline Simões Pereira [2], Allison A. Haase [1], Benjamin J. Peters [1], Seth W. Croslow [3], Kyle G. McLaughlin [3], Katarina R. Werst [1], Audra L. Goach [3], Dean C. Crick [4,5], Guilherme Menegon Arantes [2] and Debbie C. Crans [1,4,*]

[1] Department of Chemistry, Colorado State University, Fort Collins, CO 80523, USA; camvc@colostate.edu (C.V.C.); jordan_koehn@med.unc.edu (J.T.K.); Allison.Haase@colostate.edu (A.A.H.); ben.peters252@gmail.com (B.J.P.); katarina.werst@gmail.com (K.R.W.)
[2] Department of Biochemistry, Institutio de Química, Universidade de São Paulo, Av. Prof. Lineu Prestes 748, São Paulo 05508-900, SP, Brazil; caroline013@gmail.com (C.S.P.); garantes@iq.usp.br (G.M.A.)
[3] Department of Chemistry, Monmouth College, Monmouth, IL 61462, USA; SCROSLOW@monmouthcollege.edu (S.W.C.); kmclaughlin@mcw.edu (K.G.M.); ASOSTARECZ@monmouthcollege.edu (A.L.G.)
[4] Cell and Molecular Biology Program, Colorado State University, Fort Collins, CO 80523, USA; dean.crick@colostate.edu
[5] Department of Microbiology, Immunology and Pathology, Colorado State University, Fort Collins, CO 80523, USA
* Correspondence: Debbie.Crans@colostate.edu; Tel.: +1-(970)-491-7635

check for updates

Citation: Van Cleave, C.; Koehn, J.T.; Pereira, C.S.; Haase, A.A.; Peters, B.J.; Croslow, S.W.; McLaughlin, K.G.; Werst, K.R.; Goach, A.L.; Crick, D.C.; et al. Interactions of Truncated Menaquinones in Lipid Monolayers and Bilayers. *Int. J. Mol. Sci.* **2021**, *22*, 9755. https://doi.org/10.3390/ijms22189755

Academic Editor: Claudiu T. Supuran

Received: 12 July 2021
Accepted: 5 September 2021
Published: 9 September 2021

Publisher's Note: MDPI stays neutral with regard to jurisdictional claims in published maps and institutional affiliations.

Abstract: Menaquinones (MK) are hydrophobic molecules that consist of a naphthoquinone headgroup and a repeating isoprenyl side chain and are cofactors used in bacterial electron transport systems to generate cellular energy. We have previously demonstrated that the folded conformation of truncated MK homologues, MK-1 and MK-2, in both solution and reverse micelle microemulsions depended on environment. There is little information on how MKs associate with phospholipids in a model membrane system and how MKs affect phospholipid organization. In this manuscript, we used a combination of Langmuir monolayer studies and molecular dynamics (MD) simulations to probe these questions on truncated MK homologues, MK-1 through MK-4 within a model membrane. We observed that truncated MKs reside farther away from the interfacial water than ubiquinones are are located closer to the phospholipid tails. We also observed that phospholipid packing does not change at physiological pressure in the presence of truncated MKs, though a difference in phospholipid packing has been observed in the presence of ubiquinones. We found through MD simulations that for truncated MKs, the folded conformation varied, but MKs location and association with the bilayer remained unchanged at physiological conditions regardless of side chain length. Combined, this manuscript provides fundamental information, both experimental and computational, on the location, association, and conformation of truncated MK homologues in model membrane environments relevant to bacterial energy production.

Keywords: Menaquinone (MK); Vitamin K_2; lipoquinone; phospholipid; Langmuir monolayer; bilayer; conformation

1. Introduction

Menaquinones (MK) belong to a class of molecules known as lipoquinones or lipidquinones. MKs are cofactors used in the electron transport system (ETS) of bacteria to generate cellular energy, such as in the pathogenic *Mycobacterium tuberculosis*. [1–3] MKs consist of a naphthoquinone headgroup and an isoprenoid side chain of varying length (Figure 1) [4,5]. We have previously found that MK's structure allows it to fold into different molecular shapes depending on environment and side chain length [6,7]. MKs must be

membrane-associated to function in the ETS [1,8], and current knowledge regarding the interaction and conformation of MK homologues in phospholipid bilayers is limited and often conflicting [9–11]. Thus, understanding MK's location, association, and conformation with membranes will ultimately provide a better understanding of bacterial energy production, which aids drug development to address the looming antibiotic resistance crisis [12–15]. MK homologues presumably reside in the hydrophobic region of the bilayer membrane due to the hydrophobicity of the MKs, and we are seeking experimental confirmation further specifying the location of truncated MKs. Studies in model membrane systems of the structurally similar lipoquinone analogue, ubiquinone (UQ), have been used successfully to determine that UQ is located near the water interface of the membrane [10,16,17], though there is some debate about whether the side chain is folded or extended. We anticipate that employing a similar methodology will enable us to characterize the behavior of MK homologues within membranes. In this manuscript, we use a combination of experimental and computational methods to investigate the location, association, and conformation of a series of MK homologues with varying isoprenyl side chain length (MK-1, MK-2, MK-3, MK-4) in the membrane. We used shorter MK homologues in our studies because they are less hydrophobic, which enables their study in aqueous-based systems, such as enzyme assays [3,18,19].

Langmuir monolayers are a model membrane system that provides information on packing, disruption, and location of a target molecule in the context of a phospholipid monolayer. Langmuir monolayers consist of a single layer at the air-water interface, usually comprised of amphiphilic phospholipids or other lipid-like molecules [20,21]. In this study, we used the phospholipids dipalmitoylphosphatidylcholine (16:0 PC, DPPC) and dipalmitoylphosphatidylethanolamine (16:0 PE, DPPE), which were mixed with the hydrophobic MK homologues to form a monolayer film [22]. Previous Langmuir monolayer studies have been performed with different UQ homologues. These UQ homologues were found to expand and disrupt the packing of the phospholipids as the length of the UQ isoprenoid side chain increased until approximately physiological surface pressure (30–35 mN/m) [23], when the UQ molecules were compressed into the hydrophobic phospholipid tails [24–26]. We expect to see a similar trend with the truncated MK homologues. However, since MKs are more hydrophobic than UQ, MKs may prefer to reside farther into the phospholipid tails at lower surface pressures.

We used molecular dynamics (MD) studies to provide support for the Langmuir monolayer experimental studies. Furthermore, MD simulations were used to obtain a more in-depth molecular view of the location, association, and conformational folding of the MK homologues in a simulated bilayer membrane system. In this manuscript, we used a previously validated MD bilayer system consisting of POPC with a single MK molecule in each membrane leaflet, which corresponds to an approximately 3% concentration of MK in the phospholipid bilayer [27,28]. This is a more physiologically relevant system than what we used in the Langmuir monolayer studies, but nonetheless complements the DPPC and DPPE Langmuir monolayer studies. Previous MD simulations with UQ placed the headgroup near the membrane interface by the phosphate group of the phospholipid with the isoprenoid side chain extended into the middle of the bilayer [27]. We hypothesize that under physiological conditions, (i) the hydrophobic MK headgroup will be located further away from the interfacial water than UQ, (ii) the side chain length influences the association of MKs with phospholipids, and (iii) the MK homologues adopt some type of folded conformation in a membrane environment.

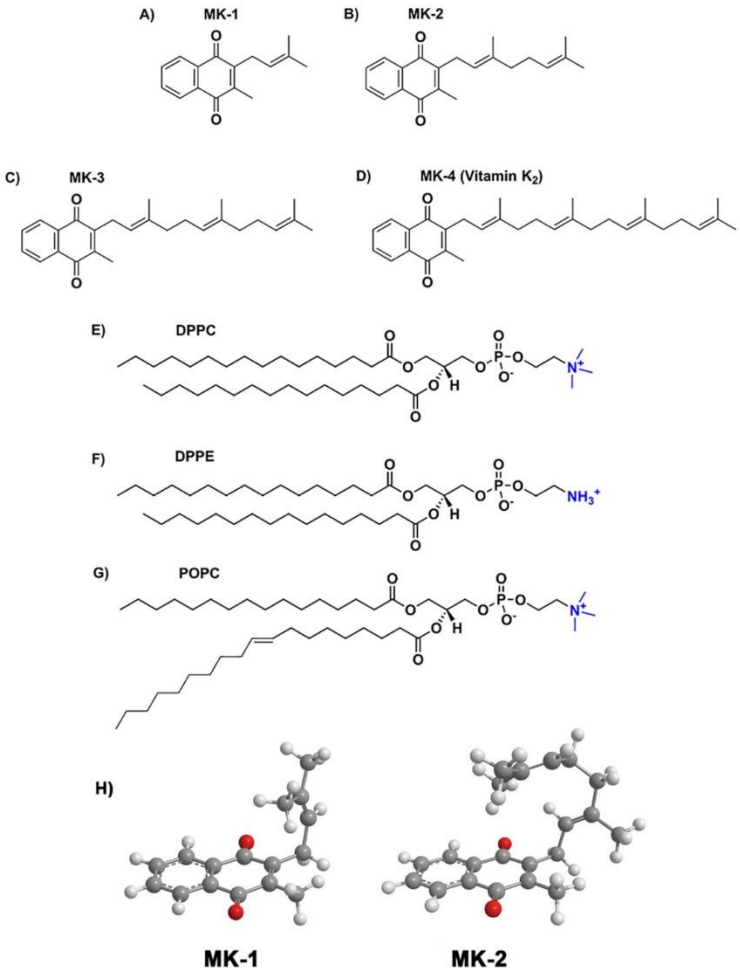

Figure 1. The structures of MK-1 through MK-4 (**A**–**D**) and the phospholipids (**E**) dipalmitoylphosphatidylcholine (DPPC), (**F**) dipalmitoylphosphatidylethanolamine, and (**G**) palmitoyloleyoylphosphatidylcholine (POPC). Conformations of (**H**) MK-1 and MK-2 within the AOT reverse micelle interface are adapted from refs [6,7].

2. Results

2.1. Compression Isotherm Studies of MKs in Langmuir Monolayers

Compression isotherms of Langmuir monolayers were obtained to provide insight into the interactions between the truncated MK-1 through MK-4 homologues with both DPPC or DPPE phospholipids. Langmuir monolayers are often used to examine the ability of a molecule to penetrate an interface, to disrupt packing, and to affect the elasticity of the monolayer [7,29–31]. We have previously reported compression isotherms of mixed films in terms of area per molecule for MK-1 and MK-2 [6,7]. The Langmuir monolayer data may be analyzed differently depending on the system of interest (hydrophilic vs. hydrophobic target molecule). Here, we normalized to the area per phospholipid because that allows for more facile interpretation of the results and comparison between multiple compounds

such as MK-1, MK-2, MK-3, and MK-4. A similar analysis was previously used by Quinn and Esfahani in 1980 [32].

The pure MK-2 monolayer reached a maximum pressure of ~13 mN/m (Figure 2B). This result is slightly lower than previously reported (20 mN/m) [7]. As found in previous studies, target MK homologues can undergo varying degrees of self-aggregation and are likely to cause small differences reported between MK experiments [7]. The pure MK-3 monolayer collapsed at 12 mN/m and the pure MK-4 monolayer reached a maximum pressure of 13 mN/m. A potential decrease in collapse pressure of these MK homologues as the isoprene side chain length increased was experimentally indistinguishable in contrast to the larger differences reported with ubiquinones [32].

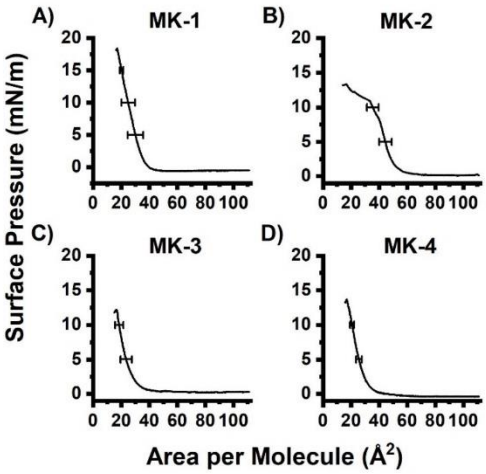

Figure 2. Compression isotherms of pure films of (**A**) MK-1, (**B**) MK-2, (**C**) MK-3, and (**D**) MK-4. Curves are the average of triplicate measurements. Error bars represent the standard deviation of the area.

We sought verification that a film was formed because the surface pressure does not begin to rise until ~40 Å^2/molecule. Hysteresis studies were therefore performed on pure MK films to determine film stability (See Supplemental Information). All truncated MK homologue films showed a decreased surface area with each compression cycle, which confirmed the formation of films (Figure S2a). The decreased surface area demonstrates that MK films are all unstable and inelastic. A decrease in observed surface area may indicate that MKs are either self-aggregating or dissolving into the aqueous subphase. We anticipated that the most soluble MKs would form the least stable films due to the compound continually dissolving into the subphase. In hysteresis studies. the most elastic films are those films which are able to compress and expand multiple times and remain the same, such as the most stable film. We would have anticipated that MK-1 and MK-2 formed less elastic films due to their ability to dissolve into the subphase. However, even though MK-1 and MK-2 are more soluble in aqueous solutions, and they formed more elastic films. Both MK-3 and MK-4 form less stable films, which implies that self-aggregation is a more important contributor to film inelasticity than solubility.

We obtained BAM images of MK homologues in order to obtain visualize the surface morphology of MK films, as shown in Figure 3. At the start of compression, a gray surface was observed, which indicates no organization. Upon reaching pressures >7 mN/m (collapse point in Figure 2), white circular features were observed, which indicates aggregation. In Figure 3A, we show a BAM image captured of MK-1, documenting that some aggregation occurred. Ten times the amount of MK-1 relative to MK-3 and MK-4 was needed to

obtain meaningful BAM images. This may be due to MK-1 dissolving into the aqueous subphase [6]. Images of MK-2, MK-3, and MK-4 demonstrate that the surface was densely covered with MK aggregates. It is clear from these images that MK-1 behaves differently from the other three MK homologues.

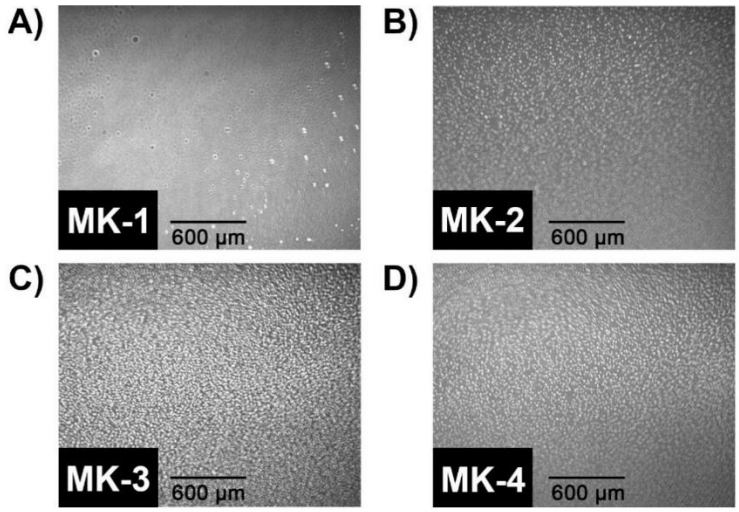

Figure 3. BAM images of pure MK films that demonstrated droplet-like structures were formed between 7.5 and 13 mN/m of surface pressure during compression. Images are shown at the approximate collapse pressure of each MK homologue. Images of (**A**) MK-1 (800 nmol), (**B**) MK-2 (120 nmol), (**C**) MK-3 (80 nmol), and (**D**) MK-4 (80 nmol) were captured at 12.5 mN/m, 10.0 mN/m, 11.8 mN/m, and 10.7 mN/m, respectively. Each panel is 2387 × 1925 µm. Images in this figure were cropped from raw images (640 × 480 px) to a final size of 382 × 308 px. All images were cropped from the upper right corner for consistency. Cropped images were then scaled up to 720 × 582 px. All image manipulation was performed in GIMP 2.10.22.

Geranyl bromide (*trans*-1-bromo-3,7-dimethyl-2.6-octadiene, Figure 4A) was used to further investigate a surface inactive compound that shares structurally similarity to MK. Geranyl bromide is a relatively surface-inactive molecule that contains a two-unit isoprenoid chain and a bromine atom in place of a headgroup, which provides an appropriate comparison for MKs. The related farnesol (containing three isoprene units) and farnesyl diphosphate have been reported to favor extended conformations in a number of solvents and in X-ray structures coordinated to proteins [33]. When applying geranyl bromide to the air-water interface and then compressing, the surface pressure remained at 0 mN/m until the end of compression when it rose to ~3 mN/m (Figure 4B,C). The surface pressure of geranyl bromide was significantly lower than the pure truncated MK films (10–17 mN/m). Given this information, MKs are surface-active but are unable to form a stable, elastic film. These compression isotherm and hysteresis studies confirmed that MK-1 through MK-4 form films, but the films are inelastic. In contrast, geranyl bromide, which lacks a headgroup, did not form a film.

At high geranyl bromide concentrations above 50% mol fraction, a disappearance of the gas-liquid transition in DPPC was observed (0–6 mN/m). While geranyl bromide is relatively surface inactive, it is likely affecting the packing of the model membrane at low surface pressure, but not at physiological pressure.

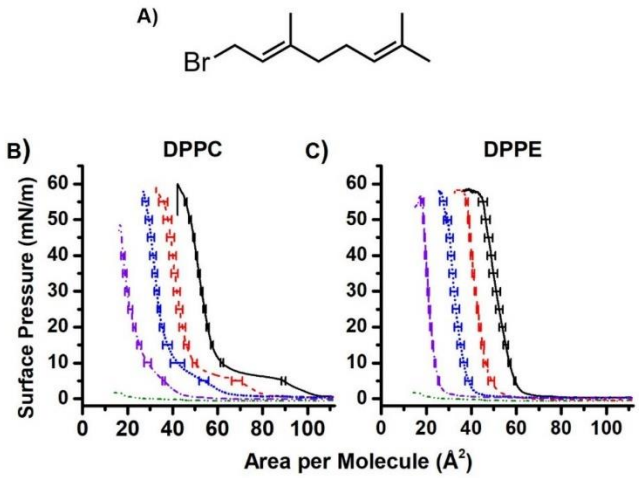

Figure 4. Compression isotherms of mixed films containing geranyl bromide. (**A**) The structure of geranyl bromide. (**B**) Compression isotherms of geranyl bromide and DPPC. (**C**) Compression isotherms of geranyl bromide with DPPE. Red dashed curves show 75:25 phospholipid:geranyl bromide films. Blue dotted curves are 50:50 phospholipid:geranyl bromide films. Purple dash-dot curves are 25:75 phospholipid:geranyl bromide films. Green dash-dot-dot curves are pure geranyl bromide films.

2.2. Compression Isotherms of Normalized Mixed MK and DPPC or DPPE Films

The compression isotherms were measured for MK-1, MK-2, MK-3, and MK-4 and the normalized compression isotherm curves for the mixed monolayers of MK-1, M-2, MK-3, and MK-4 were replotted as a function of area per phospholipid, Figure 5. Normalization occurs by using Equation (1) where A_N is the normalized area per phospholipid (Å^2), A is the measured area per molecule (Å^2), and x is the molar fraction of phospholipid (either 0, 0.25, 0.5, 0.75, or 1).

$$A_N = A\left(x^{-1}\right). \quad (1)$$

Mixed films of MK-1 and DPPC show an overall increase in area as the molar fraction of MK-1 increases, though the 75:25 and 50:50 phospholipid:MK-1 curves are similar (Figure 5A). The typical gas-liquid transition (0–6 mN/m) seen in the pure DPPC curve disappears in the mixed monolayers. In addition, the 25:75 DPPC:MK-1 film did not undergo a full collapse (end of compression where there is no longer a monolayer). This trend is also seen with mixed film containing MK-2, MK-3, and MK-4. In addition, increasing amounts of MK were found to increase the compressibility of both DPPC and DPPE mixed monolayers by compression modulus analysis (see Supplemental Information).

Studies with DPPE are more difficult to interpret because there is only one phase change. Therefore, we will only focus on large differences observed between the data. Overall, gentler slopes were observed with increasing molar fractions of all MK molecules with DPPE. However, the 50:50 and 75:25 DPPE:MK-4 films exhibited a liquid condensed phase from 1 mN/m to 17 mN/m. The liquid condensed phases seen in the DPPE:MK-2 and DPPE:MK-4 mixed films indicate an expansive effect, which is observed in literature with UQ [34,35]. This expansion at lower surface pressures may be due to aggregation and/or conformation of the MK homologues. Interestingly, for both DPPC and DPPE, the mixed curves tended to overlap the control curve at physiological surface pressure (30–35 mN/m) [23]. This has previously been observed with UQ and was interpreted as the lipoquinone migrating out of the interface and into the phospholipid tails [24]. These studies confirm the interpretation that MK homologues reside slightly higher in

the interface than UQ, thus confirming our initial hypothesis that MK and UQ reside in differing locations in model membranes.

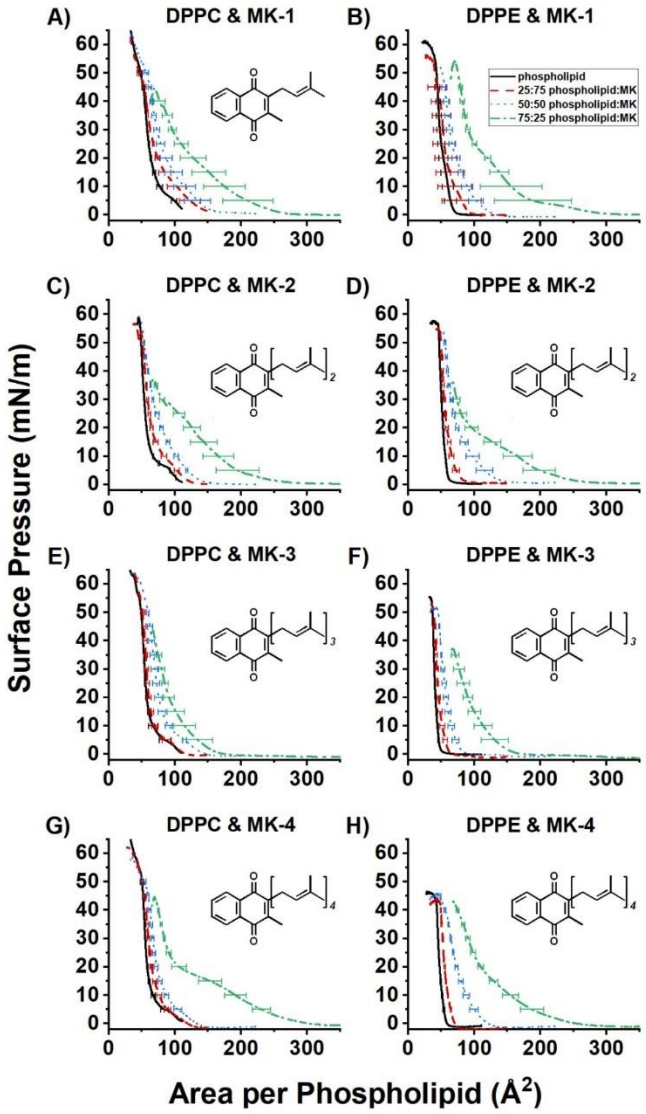

Figure 5. Normalized compression isotherms of mixed monolayers of either DPPC (left column) or DPPE (right column) with MK. Panels (**A**) and (**B**) are MK-1, (**C**) and (**D**) are MK-2, (**E**) and (**F**) are MK-3, and (**G**) and (**H**) are MK-4. Pure phospholipid monolayers are represented with solid black curves, 75:25 phospholipid:MK with red dashed curves, 50:50 phospholipid:MK with blue dotted curves, and 25:75 phospholipid:MK with green dash-dot curves. Each curve is the average of at least three replicates. Error bars are the standard deviation at every 5 mN/m of surface pressure. Data for MK-1 and MK-2 were previously reported [6,7].

2.3. Ideal Mixing of MK and DPPC or DPPE

Ideal mixing calculations were performed to confirm whether or not any interactions were occurring between phospholipids and MK homologues, as well as the differences in the free energy of the films, as shown in Figure 6. The ideal mixing was plotted to show where the ideal and experimental fall relative to both the MK and phospholipid control (plotted using un-normalized data). Assuming no interactions between the two components of the film, the experimental film will match the calculated ideal. Ideal mixing curves for 50:50 phospholipid:MK mixtures are presented in the main text as representative results while curves for 25:75 and 75:25 phospholipid:MK mixtures are shown in Supplemental Information (Figure S5a,b).

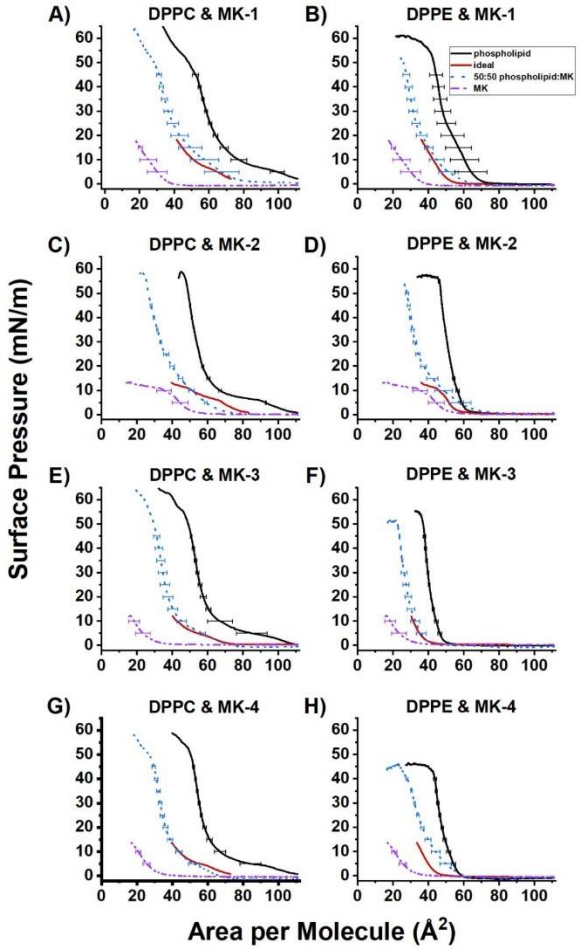

Figure 6. Ideal mixing of 50:50 phospholipid:MK films compared to experimental data. DPPC films are in the left column. DPPE films are in the right column. (**A**,**B**) show MK-1 mixed films, (**C**,**D**) show MK-2 mixed films, (**E**,**F**) show MK-3 mixed films, and (**G**,**H**) show MK-4 films. Solid black curves are pure phospholipid monolayers. Blue dotted curves represent experimental 50:50 phospholipid:MK films. Solid red curves represent calculated ideal mixed films. Purple dash-dot-dot curves represent pure MK films. Each MK homologue experiments were run independently, hence differences in control isotherms were observed.

The general trend of the 50:50 DPPC:MK films indicate ideal mixing, in that the experimental curves do not deviate significantly from the ideal. As such, DPPC and the MK homologues likely do not interact directly with each other. In the DPPE films, the 50:50 mixture containing MK-4 is expanded relative to the ideal mixing area. This suggests that MK-4 is able to associate with DPPE, possibly due to conformational folding and molecular shape. We sought further means of computationally investigating molecular reasoning for this, specifically MD simulations.

Langmuir monolayers studies were studied at both low and high molar fractions that were well above the biological molar fraction to observe the association of MK homologues on the DPPC and DPPE films [9]. As such, it is not clear whether the observed effects at higher molar fractions in the monolayers are relevant to effects observed within bilayers and native membranes. We hypothesized that conformation might be important for the disruptive association of MK homologues at high molar fractions. However, Langmuir monolayer studies were unable to provide molecular information on folding and the exact mechanism of disruption between phospholipids and MK homologues. As such, we investigated this question using a computational model to probe the MK conformation in a physiologically relevant bilayer system.

2.4. Molecular Dynamics Simulations of MKs in a Membrane Bilayer

Computational studies were performed to determine the location, association, and conformation of MK homologues embedded in a bilayer at physiological concentrations. We modeled fully hydrated bilayers based on the phospholipid phosphatidylcholine (POPC, 16:0–18:1 PC) mixed with one MK molecule in each layer, which correspond to a ~2–3% concentration of MK-1, MK-2, MK-3, or MK-4 (Figure 7A). Classical MD simulations were performed with the CHARMM36 force field using parameters for MKs developed previously [27,28].

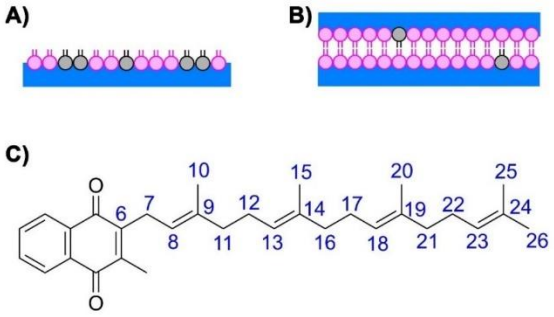

Figure 7. Cartoons of different model membrane systems as well as the numbering of carbons for computational studies. (**A**) Illustration of the monolayer system with a mix of phospholipid (pink) and MK (grey). (**B**) Illustration of a bilayer system with a molecule of MK in each of the phospholipid layer in the bilayer, (**C**) Labeling scheme of MK-1 through MK-4 (MK composed by n = [1–4] isoprenoid units) used in computational studies. The terminal carbon (CT) groups on MK-1 are labeled 10 and 11, the CT groups on MK-2 are labeled 15 and 16, the CT groups on MK-3 are labeled 20 and 21, the CT groups on MK-4 are 25 and 26.

The Langmuir monolayer studies showed that at lower MK concentrations (25% molar fraction), the MK homologues were associated with the monolayer film. However, at higher concentrations the MK homologues were compressed out of the film (Figure 5). In the computational studies with the phospholipid bilayer, in no example was the MK homologue compressed out from the phospholipid bilayer at physiological conditions. The lack of MK exclusion from the bilayer is likely due to two reasons: (i) lower MK concentrations similar to those existing under biological conditions were investigated and

(ii) a finite simulation time (350–750 ns) was used, which may not be enough time to sample the water-phospholipid partition process [9].

Figure 8 details the position of the MK headgroup in the bilayer in terms of center of mass. The plot shows the distance from the center of the membrane (0 nm) and the interface as indicated by the POPC phosphate group's center of mass at about 2 nm. As shown in the plot for MK-1, MK-2, MK-3, and MK4, the center of mass for the MK headgroups were all located around z = 1.3 nm. The small variations in peak position are not statistically significant. Thus, the MK headgroups are about 0.7 nm up in the interface and below the water-phospholipid interface as defined by the phospholipid phosphate (2 nm). Our simulations show that the MK headgroups will have the same location in the membrane, regardless of difference in hydrophobicity, length of the MK side chain, and ability to disrupt the membrane. These studies are in line with previous simulations of native UQ in POPC and mixed membranes [27,28], and suggest that these lipoquinone headgroups are both located in a similar membrane region, about 0.5 nm below UQ (z = 1.8 nm) toward the membrane midplane. These data also support the interpretation that for truncated MK homologues, the headgroup anchors the location of the MK homologue slightly farther into the membrane than that of UQ (MK z = 1.3 nm, UQ z = 1.8 nm, POPC phosphate z = 2 nm) [27,28]. The location of MK in a more hydrophobic region compared to UQ is consistent with Langmuir monolayer findings that placed the MK homologues in the phospholipid tails at physiological surface pressure. In addition, there was no appreciable disruption to the permeability of the bilayer noted in simulations which is in agreement with previous studies [27,28].

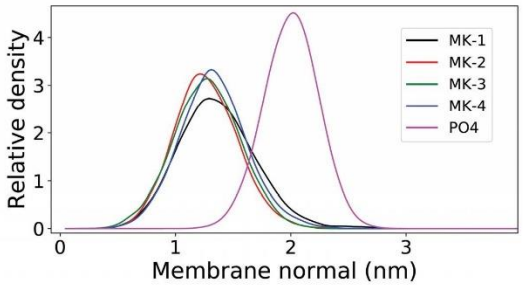

Figure 8. Mass density of the MK quinone headgroup along the membrane normal for MK-1 (black), MK-2 (red), MK-3 (green), and MK-4 (blue). The phosphate group of POPC (PO4) is shown in magenta. Data from both layers were symmetrized. The normal zero corresponds to the center of the bilayer.

The MD studies provided a quantitative representation of the conformation and distribution of the dihedral angles of the side chain of MK-1 through MK-4 in a simulated phospholipid bilayer (Figure 9). Rotation around the C6-C7 bond was restrained in all MK homologues due to the steric restriction that limits rotation. Specifically, the methyl group on the naphthoquinone headgroup and the sp^2 hybridization of the C6 atom limit the rotation around the C6-C7 bond. Thus, this torsional angle is $\pm 110^\circ$ (Figure 9A). Rotation around the C7-C8 bond was freer than around the C6-C7 bond but still somewhat restrained due to the methyl group on the naphthoquinone headgroup and the sp^2 hybridization of C8. The bond angle was often $\pm 120^\circ$, but some trans (180°, extended) conformations were also present in Figure 9B.

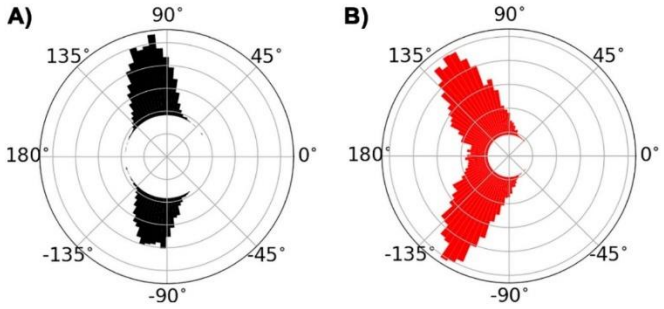

Figure 9. Polar plot showing distributions of dihedral angles rotating around the C6-C7 bond (panel (**A**)) and the C7-C8 bond (panel (**B**)) observed in the MD simulation of MK-4 located in the phospholipid POPC bilayer. Interestingly, the energy function observed when rotating around the C6-C7 bond is not symmetrical because the molecular shape is not symmetrical. Steric repulsions to the naphthoquinone ring substitutions are directional as described previously in detail [27].

Torsional angle distributions of corresponding rotations around C6-C7 and C7-C8 bonds similar to Figure 9, were observed for all MK homologues studied here. However, MK-2, MK3, and MK-4 contain longer side chains and additional C-C bonds, which are more flexible than MK-1. Figure 10A shows a trans (extended) conformer in which the C11-C12 torsional angle is ±180°. Figure 10B shows that the gauche (folded) conformer (C11-C12 torsion is ±60°) will allow for partial folding of the side chain over the naphthoquinone headgroup. Overall, truncated MK homologues undergo some amount of folding in a phospholipid bilayer.

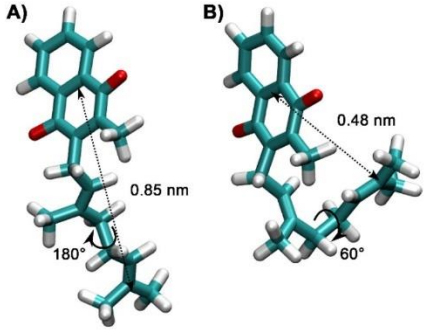

Figure 10. Two representative conformers observed for the MK-2 MD simulations in the POPC bilayer. Torsion around the C11-C12 bond modulates the distance between the terminal CH_3-carbon labeled CT and the center of the quinone ring, termed here d(CT-H). Panel (**A**) shows a trans conformer with a long intramolecular distance and panel (**B**), a gauche conformer with a much smaller intramolecular distance.

Figure 11 shows the distances (termed d(CT-H)) generated through rotation of the dihedral angle (rotation around the C11-C12 bond) between the terminal CH_3 group (CT) and the C2-C3 (UQ numbering) bond in the middle of the naphthoquinone headgroup; the different distances are observed due to rotations around the C11-C12 bond. The panels in Figure 11 all show conformations with angles in *trans* (~180°, extended) more populated than the conformation with *gauche* (±60°, folded) geometry for MK-2, MK-3, and MK-4. However as shown in Figure 11 for MK-3, the relative population of *gauche* is significantly lower than for MK-2 or MK-4.

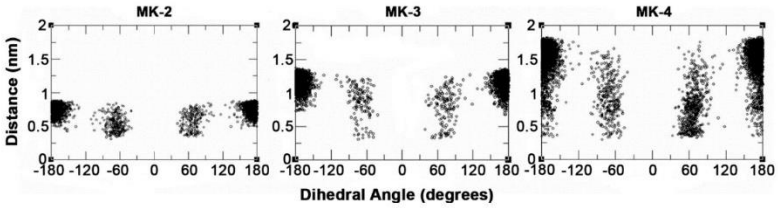

Figure 11. Plots of the distance between the terminal CH_3 groups in MK-2, MK-3 or MK-4 to the middle of the center C-C bond of the naphthoquinone headgroup, d(CT-H), as obtained when the dihedral angle is changing as the rotation around the C11-C12 bond takes place.

Figure 12 summarizes the population distribution of the terminal carbon from the C-C bond in the middle of the headgroup for all MKs. As the isoprenoid side chain length increases, there is the potential for a greater distance between the terminal carbon and the headgroup. Since MK-1 has limited length and rotation, the entire distribution occurs within a small range of distances. MK-2 can reach d(CT-H) <0.5 nm only when C11-C12 is in gauche conformation. In the case of MK-3 and MK-4, short distances can be reached when C11-C12 in gauche as well as trans because their isoprene chains contain additional rotatable C-C bonds and are long enough to fold back over the headgroup. Figure 11 shows that d(CT-H) >0.7 nm when C11-C12 in MK-3 is trans. Even when in gauche, fewer MK-3 conformations will have a smaller d(CT-H). MK-4 may reach d(CT-H) <0.5 nm when C11-C12 is trans, because of increased side chain length and flexibility of the additional isoprenoid units. As shown in Figure 10, C11-C12 torsion in gauche allows the side chain to partially fold upon itself and, thus, a lower d(CT-H) to be visited. Similar results (data not shown) are obtained if we examine the equivalent torsions for bonds closer to the CT, such as the C16-C17 bond in MK-3 and MK-4.

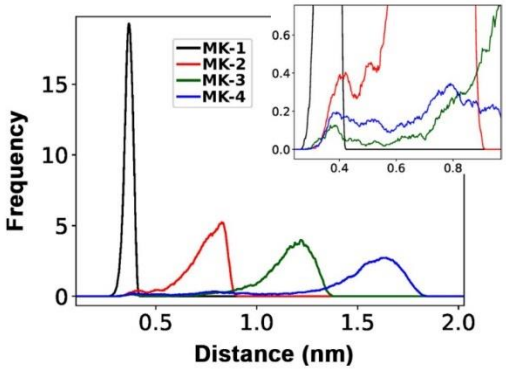

Figure 12. Distance distribution from terminal carbon (CT) to the center of the MK quinone headgroup, d(CT-H) in MK-1 (black), MK-2 (red), MK-3 (green), and MK-4 (blue). The upper right panel is a zoom-in of the distance range 0.3–1.0 nm (3–10 Å).

3. Discussion

Langmuir monolayers were used to experimentally probe the location and association of MK homologues within phospholipid monolayers. There are two ways to conduct Langmuir monolayer experiments depending on the solubility of the compound of interest. When the compound is water-soluble, it is added to the aqueous subphase. With hydrophobic molecules, experiments are conducted by mixing and applying different molar ratios of substrate and phospholipid, as described by Hoyo et al. in 2015 [22]. In order to observe a response on the monolayer, concentrations of the target compound are typically higher

than micromolar. This is above the solubility of even the water-soluble truncated MK homologues. In our studies using molar ratios of phospholipid vs. MKs, information about potential aggregation of MK homologues and film formation was gathered [36,37]. Using the Langmuir trough, we studied how truncated MKs (MK-1, MK-2, MK-3, and MK-4) associated with DPPC and DPPE films.

Biologically, DPPC is present in up to 40% of mammalian lung surfactant while little, if any, is found in bacterial membranes [36,38]. However, DPPC has been well characterized in Langmuir monolayers and demonstrates distinct behavioral phases (gas, gas-liquid, liquid condensed, solid) which give information on the disruption of phospholipid packing. Therefore, it is used extensively in model membrane systems [39]. DPPE is found in bacterial cells and is only a minor component in mammalian cells, such as in the inner leaflet of eukaryotic cells [40–42]. As such, DPPE is the most biologically relevant phospholipid for the study of MKs. While the more biologically plentiful POPC has been used in Langmuir monolayer studies, it did not demonstrate the same phase changes as DPPC and is therefore less informative with regards to the association of MK homologues [43]. Compression isotherms in this manuscript were accordingly measured at 25 °C to maintain the distinct phases of DPPC, as the gas-liquid phase is not present at physiological temperature [44].

We investigated the ability of truncated MK homologues to form films. We found that MKs were surface-active even though the surface pressure did not begin rising until ~40 $Å^2$/molecule and that these MK films were unstable. Using BAM, we were able to visualize the aggregation of the MK homologues and we observed strong aggregation of MK-2, MK-3, and MK-4. However, the self-association with MK-1 was weaker, possibly to enhance water solubility. Because of the limiting solubility of the MK homologues, the studies of the MK derivatives on the films were performed using ratios of MK homologue to DPPC or DPPE. By mixing ratios of phospholipid and MK, we found that the MK homologues associated with the phospholipid interface, and that the at low surface pressure disruptive effects were greatest for MK-2 and MK-4, as shown in Figure 5. However, we observed little, if any, increase in disruptiveness between 30 and 35 mN/m. Moreover, the curves of 75:25 phospholipid:MK overlap the phospholipid control in all but the DPPE:MK-4 trials. The conclusions of the lack of disruption at physiological surface pressure are that (i) the MK homologues were compressed into the phospholipid tails from the interface and (ii) that this migration to the saturated phospholipid tails allows for greater accommodation of the volume of the MK homologues, hence the lack of disruption. We used MD simulations to confirm the location and association with phospholipids and additionally explore the conformation of MK homologues.

The MD simulations were performed in a phospholipid bilayer, and at a phospholipid:MK ratio that approximated the concentrations found in biological systems. We chose a model bilayer composed of MK homologues embedded in a POPC bilayer, which was previously developed in our laboratory to investigate the interaction with native UQs or MKs in eukaryotic cells [28]. Although simulations of Langmuir monolayers are possible [45], they would require an extensive reparametrization and testing of the force-field used for simulations [27,28] and would provide little detail on the biological context in which MKs are found. Instead, we chose to carry out simulations at a physiologically relevant MK concentration within a model phospholipid bilayer, which are more reliable with our current force-field technology [27,28], and resulted in detailed information on the intrinsic folding of MK isoprenoid chains in its (MK-4) native membrane environment. Eukaryotic membranes have a large POPC concentration and pure POPC bilayers have been well-characterized as models for the simulation of biological membranes [28,46]. In particular, we have previously characterized in detail the location and water-phospholipid partition ofUQ with variable isoprenoid chain length to POPC bilayers, in good agreement with experimental observations [27].

The MD simulations also show that once the MK was associated with the membrane, the average (equilibrium) location of the MK headgroup did not depend on the number of MK isoprenoid units (Figure 8). The tiny differences observed between the four MKs in

Figure 8 are not statistically significant and are due to fluctuations of the finite sampling. Thus, our simulations do not show any dependence of MK headgroup location with side chain length, in line with previous simulations of UQ with various side chain lengths in POPC and in mixed membranes [27,28]. The MD studies also suggested that the location of lipoquinones along the membrane midplane is an intrinsic physicochemical property of the quinone molecule due at least in part to its amphiphilic character and more polar headgroup. This finding supports the possibility that in the monolayer system the MK headgroup location will not change with isoprenoid chain length. However, the redox state (quinone vs. quinol form) of the headgroup affects location, as we previously demonstrated within reverse micelle membrane environments [47]. Combined, our work supports the possibility that the headgroup structure and redox state, as opposed to side chain length, is a major contributing factor driving the location and association of MK homologues in a membrane.

The conformational distribution of C-C bonds in the MK side chain described in the MD bilayer simulation results have a subtle but potentially relevant impact on side chain folding upon the MK headgroup and the related distance d(CT-H) (Figures 9–11). The possible distances for MK-1 are quite narrow due to rather restricted torsion around the C6-C7 bond (Figure 11). For the other MK, longer distances are reached and the distribution spreads due to increasing the number of isoprenoid units and increased side chain flexibility (Figure 11). The conformations where the side chain folds over the headgroup have a different shape compared to MK-1 where the side chain is at an angle with the headgroup. Interestingly, the exerpt in Figure 12 shows the terminal carbon of MK-3 is less likely to reside near the naphthoquinone headgroup than MK-2 or MK-4. Thus, we suggest that the non-ideal behavior observed for these MK homologues in the monolayer isotherms (Figure 6) may be caused by the more frequent partial folding of the side chain over the MK head group as observed in the MD simulations for MK-2 and MK-4 and the related shorter d(CT-H) (Figure 12).

The interactions of lipoquinones with membranes are a multi-faceted topic in which many different factors are important to the conformation and location of the lipoquinones in the phospholipid bilayer. In order to illustrate some of these effects, we compared the properties of the different MK homologues, as shown in Table 1. We ordered the properties of MK-1 through MK-4 in terms of clogP, ability to disrupt a monolayer (based on increase in monolayer area at physiological surface pressure), MK headgroup location, longest average distance of the terminal carbon of the isoprene chain from the naphthoquinone headgroup, and the ability of the terminal carbon to reside within 0.6 nm of the naphthoquinone headgroup (which is a measure of folding). The only two properties that showed the same order are the clogP and the longest average distance of the terminal carbon of the isoprene side chain from the naphthoquinone headgroup.

Table 1. Comparing various physicochemical properties of the four MK homologues investigated in this work.

Property	Ranking
clogP	MK-4 (8.86) > MK-3 (7.52) > MK-2 (5.67) > MK-1 (3.83)
Ability to disrupt a phospholipid monolayer based on increase in monolayer area between 30 and 35 mN/m	MK-4 > MK-2 > MK-1 ~ MK-3
MK headgroup location relative to the midplane	MK-1 ~ MK-2 ~ MK-3 ~ MK-4
Longest average distance from CT to naphthoquinone headgroup	MK-4 > MK-3 > MK-2 > MK-1
Ability of CT to be within 0.6 nm of the naphthoquinone headgroup	MK-1 > MK-2 > MK-4 > MK-3

We confirmed that MK homologues occupy a more hydrophobic region of the membrane than UQ, though there was less disruption of phospholipid packing. We hypothesize that the lack of disruption is due to the location of the MK homologues. The free rotation of the phospholipid tails allows for compensation of the molecular volume of MK while UQ's location close to the phospholipid headgroups in the interface does not [17,48]. In addition, we also found that all MK homologues adopted some folded conformation in a simulated bilayer, though conformations varied. We would be interested in exploring the physicochemical properties of the reduced quinol forms of these MK homologues. However, menaquinols are unstable under atmospheric conditions, making experimentation difficult [11,47].

4. Materials and Methods

General Materials and Methods. Chloroform (≥99.5%, monosodium phosphate (≥99.0%), disodium phosphate (≥99.0%), sodium hydroxide (≥98%), hydrochloric acid (37%), geranyl bromide (*trans*-1-bromo-3,7-dimethyl-2,6-octadiene, 95%), and manequinone-4 (MK-4, menatetrenone, Vitamin K_2) were all purchased from Sigma Aldrich (St. Louis, MO, USA) and used without further purification. The phospholipids dipalmitoylphosphatidylcholine (16:0 PC, DPPC, 99%, SKU 850355P) and dipalmitoylphosphatidylethanolamine (16:0 PE, DPPE, 99%, SKU 850705P) were purchased from Avanti Polar Lipids (Alabaster, AL, USA) and pure lyophilized powder. Since MK-1, MK-2, and MK-3 are not commercially available, they were synthesized and purified as previously described [6,7,49]. Distilled deionized (DDI) water was filtered through a Millipore water purification system (Burlington, MA, USA) until water with a measured resistance of 18.3 MΩ was achieved. Langmuir monolayers were studied using a Kibron μTrough XS (stainless steel, Helsinki, Finland) equipped with a Teflon ribbon barrier.

Preparation of Solutions. The aqueous subphase of monolayers consisted of 20 mM sodium phosphate buffer (pH 7.40 ± 0.02).

Solutions were brought to pH with 1 M HCl or NaOH. Phospholipid stock solutions were prepared by dissolving DPPC (18 mg, 25 nmol) or DPPE (17 mg, 25 nmol) in 25 mL of 9:1 chloroform/methanol (v/v) for a final concentration of 1 mM phospholipid. MK and geranyl bromide stocks consisted of 1.0 mM MK-1 (12 mg, 5 nmol), MK-2 (15 mg, 5 nmol), MK-3 (19 mg, 5 nmol), MK-4 (22 mg, 5 nmol), or geranyl bromide (1.1 mg, 5 nmol) dissolved in 5 mL of 9:1 chloroform/methanol (v/v). Mixed phospholipid solutions were created by mixing appropriate amounts of phospholipid and either MK or geranyl bromide stock in a 2 mL glass vial to create a final volume of 1 mL and vortexed until combined. Final mol fractions (phospholipid:MK) were 100:0, 25:75, 50:50, 75:25, or 0:100.

Preparation of Langmuir Monolayers. The buffered aqueous subphase consisted of 50 mL of 20 mM sodium phosphate buffer (pH 7.40 ± 0.02) in DDI water (18.2 MΩ). The subphase surface was cleaned via vacuum aspiration until a quick compression of the subphase provided a surface pressure which was consistently 0.0 ± 0.5 mN/m throughout compression. A total of 20 μL of phospholipid stock solution (20 nmol of phospholipid) was then added to the surface of the subphase in a dropwise manner using a 50 μL Hamilton syringe. The monolayer was allowed to equilibrate for 15 min.

Compression Isotherm Measurements of Langmuir Monolayers. The phospholipid monolayer was compressed from two sides with a total speed of 10 mm/min (5 mm/min from opposite sides). The temperature was maintained at 25 °C using an external water circulator. The stainless-steel trough plate was scrubbed three times with isopropanol, then three times with ethanol, then rinsed with DDI water (18.2 MΩ) before each experiment. The Teflon ribbon barrier was rinsed with isopropanol followed by ethanol and then DDI water. The surface tension was monitored via Wilhemy plate technique where a steel wire was used as the probe instead of a metal or paper plate. The surface pressure was calculated from the surface tension using Equation (2), where π is the surface pressure

(mN/m), γ_0 is the surface tension of water (71.99 mN/m), and γ is the surface tension at a given area per phospholipid after the monolayer has been applied.

$$\pi = \gamma_0 - \gamma. \quad (2)$$

Each compression isotherm experiment consisted of at least three replicates. The averages of the area per phospholipid and the standard deviation at every 5 mN/m were calculated using Microsoft Excel (=AVERAGE, =STDEV). The worked-up data were then transferred to Origin 2021 (Northampton, MA USA) to be graphed with error bars.

Ideal Mixing of Monolayers. The ideal mixing sets were calculated by averaging the mean molecular area of two isotherms at the same surface pressure using Equation (3), where A_i is the ideal mixed area (Å^2), x_{MK} is the molar fraction of MK, A_{MK} is the area per molecule (Å^2) of the control MK monolayer, x_{PL} is the molar fraction of DPPC or DPPE, and A_{PL} is the area per molecule (Å^2) of DPPC or DPPE. The possible mol fractions were 0.25, 0.50, or 0.75.

$$A_i = x_{MK}A_{MK} + x_{PL}A_{PL}. \quad (3)$$

Brewster Angle Microscopy. Brewster angle microscopy (BAM) images were obtained using a Biolin NIMA medium trough (Gothenberg, Sweden) equipped with a MicroBAM (659 nm laser). Differing amounts of 2 mM stocks of MK-1 (800 nmol), MK-2 (120 nmol), MK-3 (80 nmol), and MK-4 (80 nmol) were added.

Molecular Dynamics Simulations. We employed a previously developed fully hydrated POPC (16:0-18:1 phosphatidylcholine) bilayer model system and added MK molecules (one MK in each layer, corresponding to a ~2–3% concentration), composed by n = [1–4] isoprenoid units (MK-1 through MK-4, Figures 1A and 4D). Symmetric phospholipid bilayers were built containing 126 molecules of POPC and 7794 water molecules which have previously been characterized to represent a biological membrane [27]. NaCl was added until a final concentration of 150 mM was achieved. The protocol described by Javanainen was used to insert one MK-4 in each layer of the membrane [50]. The system was relaxed by a 50 ns MD run, and mean area and bilayer thickness were monitored to check for equilibration. Initial equilibrated configurations were derived from the MK-4 system by deleting side chain atoms and adapting the atomic connectivity to generate MK-1, MK-2, and MK-3 species. Conformations were sampled using classical MD simulations with the program GROMACS version 2020.3 [51] and the CHARMM36 force-field [52,53]. Parameters for MK were obtained by us previously [27,28]. Water was described by TIP3P [54] and the NPT ensemble was used. The temperature was kept at physiological temperature (37 °C, 310 K) with a Bussi thermostat [55] and a coupling constant of 0.1 ps. The pressure was kept at 1.0 bar with Parrinello-Rahman barostat for productive runs [56] with a coupling constant of 1 ps and a compressibility of 0.5 10^{-5} bar^{-1}. Semi-isotropic coupling was applied. Electrostatic interactions were handled by Particle-Mesh Ewald (PME) [57] with grid spacing of 0.14 nm and quartic interpolation. All bonds were constrained using the LINCS algorithm [58]. No dispersion corrections were applied [59]. The integration time step was 2 fs and MD simulations were run 200 ns for equilibration. Trajectories with 350 ns were collected for MK-1, MK-2 and MK-3 and with 750 ns for MK-4.

5. Conclusions

MKs are membrane-associated lipoquinones that are used as essential components in the ETS of many bacteria. Therefore, understanding the behavior of MKs in membranes could provide fundamental knowledge of the ETS and could aid in antimicrobial drug development. We have previously demonstrated that truncated MKs fold in a model membrane interface. However, we sought more information on the location of MKs as well as how MKs associate with and affect the packing of phospholipids in a membrane environment. We hypothesized, but did not confirm, that MKs would behave in a similar manner to UQs, in that there would be a side chain-dependent disruption of phospholipid packing and association with MKs. Moreover, we wanted to further explore their predicted

location and conformation in a membrane bilayer. We used a combination of experimental and computational methods to probe these open questions. Langmuir monolayer studies provided experimental data pertaining to phospholipid packing and association and MD simulations provided molecular information of exact location, association, and conformation in a membrane bilayer at physiological MK concentration.

Langmuir monolayers were created with biologically relevant phospholipids, DPPC and DPPE, to experimentally model the cell membrane interface. All truncated MK homologues were found to migrate from the air-water interface into the phospholipid tails at physiological surface pressure, which is consistent with our hypothesized location. We demonstrated that truncated MKs associate with the phospholipids but do not disrupt the phospholipid packing at physiological surface pressure that was observed with UQs [24–26]. We found using MD simulations that, in accordance with MKs hydrophobic nature, the MK headgroup was located closer to the phospholipid tails than UQ (UQ was located closer to the interfacial water) which is consistent with the hypothesized location. Furthermore, we found through MD simulations that MK-2, MK-3, and MK-4 overall favored a gauche, or folded, conformation, which is in agreement with our previous experimental studies with MK-1 and MK-2 [6,7]. In line with Langmuir monolayer studies, there was no observed dependence on MK side chain length for either MK conformation or location within the bilayer under physiological conditions. However, it is possible that this lack of dependence on MK side chain length is limited to truncated MK homologues and that the longer MK homologues, such as MK-9, would exhibit an appreciable difference in folding and disruption due to the significantly larger volume of MK-9. As the MKs are located further into the phospholipid tails than UQs, it is possible that the phospholipid tails adjust to compensate for the volume of the MK molecule. Hence, MK would be less disruptive than UQ based on membrane location.

Combined, Langmuir studies and MD simulations demonstrated that truncated MKs are located closer to the phospholipid tails, regardless of the truncated MK side chain length. A lack of dependence on side chain length was also observed in the association and packing of truncated MK homologues with phospholipids. Additionally, truncated MKs generally demonstrated some amount of folding. In conjunction with previous studies detailing the different, environment-dependent folded conformations of MK-1 and MK-2, this provides a fundamental view of the behavior of MKs in a membrane environment. Overall, MK homologues may disrupt phospholipid packing at higher concentrations as seen in Archaea [11,60], but not necessarily at concentrations found in most other organisms [9]. These truncated MK homologues were also found to adopt folded conformations, which may influence their behavior, recognition, and function in the ETS that is essential for bacterial survival.

Supplementary Materials: The following are available online at https://www.mdpi.com/article/10.3390/ijms22189755/s1.

Author Contributions: Conceptualization, C.V.C., B.J.P., D.C.C. (Dean C. Crick), and D.C.C. (Debbie C. Crans); data curation, C.V.C. and D.C.C. (Debbie C. Crans); formal analysis, C.V.C., C.S.P., B.J.P., S.W.C., K.G.M., A.L.G., G.M.A., and D.C.C. (Debbie C. Crans); funding acquisition, D.C.C. (Dean C. Crick) and D.C.C. (Debbie C. Crans); investigation, C.V.C., A.A.H., C.S.P., B.J.P., J.T.K., K.R.W., and G.M.A.; methodology, C.V.C., A.A.H., C.S.P., B.J.P., J.T.K., S.W.C., A.L.G., G.M.A., and D.C.C. (Debbie C. Crans); project administration, D.C.C. (Debbie C. Crans).; supervision, D.C.C. (Debbie C. Crans); validation, J.T.K., A.L.G., and D.C.C. (Debbie C. Crans), visualization, C.V.C. and G.M.A.; writing—original draft, C.V.C., J.T.K., G.M.A., and D.C.C. (Debbie C. Crans); writing—review and editing, C.V.C., A.A.H., C.S.P., B.J.P., J.T.K., S.W.C., A.L.G., D.C.C. (Dean C. Crick), G.M.A., and D.C.C. (Debbie C. Crans). All authors have read and agreed to the published version of the manuscript.

Funding: D.C. Crans thanks the NSF for funding (grant CHE-1709564). D.C. Crans also thanks the Arthur Cope Foundation administered by the American Chemical Society and Colorado State University for partial support. G.M.A. acknowledges funding from Fundacao de Amparo a Pesquisa do Estado de São Paulo (FAPESP, grant 2019/21856-7).

Institutional Review Board Statement: Not applicable.

Informed Consent Statement: Not applicable.

Data Availability Statement: The manuscript will be deposited on the NSF repository site. Additional data has been provided in Supplemental Information.

Acknowledgments: C.V. and D.C. Crans thank Julia. L. Sharp for discussion regarding error analysis on compression isotherms.

Conflicts of Interest: The authors declare no conflict of interest.

References

1. Collins, M.D.; Jones, D. Distribution of Isoprenoid Quinone Structural Types in Bacteria and Their Taxonomic Implications. *Microbiol. Rev.* **1981**, *45*, 316–354. [CrossRef] [PubMed]
2. Brennan, P.J. Mycobacterium and other actinomycetes. In *Microbial Lipids*; Ratledge, C., Wilkinson, S.G., Eds.; Academic Press: San Diego, CA, USA, 1988; Volume 1, pp. 203–298.
3. Upadhyay, A.; Kumar, S.; Rooker, S.A.; Koehn, J.T.; Crans, D.C.; McNeil, M.R.; Lott, J.S.; Crick, D.C. Mycobacterial MenJ: An Oxidoreductase Involved in Menaquinone Biosynthesis. *ACS Chem. Biol.* **2018**, *13*, 2498–2507. [CrossRef]
4. Braasch-Turi, M.; Crans, D.C. Synthesis of Naphthoquinone Derivatives: Menaquinones, Lipoquinones and Other Vitamin K Derivatives. *Molecules* **2020**, *25*, 4477. [CrossRef] [PubMed]
5. Popa, D.-S.; Bigman, G.; Rusu, M.E. The Role of Vitamin K in Humans: Implication in Aging and Age-Associated Diseases. *Antioxidants* **2021**, *10*, 566. [CrossRef] [PubMed]
6. Koehn, J.T.; Beuning, C.N.; Peters, B.J.; Dellinger, S.K.; Van Cleave, C.; Crick, D.C.; Crans, D.C. Investigating Substrate Analogues for Mycobacterial MenJ: Truncated and Partially Saturated Menaquinones. *Biochemistry* **2019**, *58*, 1596–1615. [CrossRef]
7. Koehn, J.T.; Magallanes, E.S.; Peters, B.J.; Beuning, C.N.; Haase, A.A.; Zhu, M.J.; Rithner, C.D.; Crick, D.C.; Crans, D.C. A Synthetic Isoprenoid Lipoquinone, Menaquinone-2, Adopts a Folded Conformation in Solution and at a Model Membrane Interface. *J. Org. Chem.* **2018**, *83*, 275–288. [CrossRef] [PubMed]
8. Gupta, C.; Khaniya, U.; Chan, C.K.; Dehez, F.; Shekhar, M.; Gunner, M.R.; Sazanov, L.; Chipot, C.; Singharoy, A. Charge Transfer and Chemo-Mechanical Coupling in Respiratory Complex I. *J. Am. Chem. Soc.* **2020**, *142*, 9220–9230. [CrossRef] [PubMed]
9. Das, A.; Hugenholtz, J.; van Halbeek, H.; Ljungdahl, L.G. Structure and Function of a Menaquinone Involved in Electron Transport in Membranes of *Clostridium thermoautotrophicium* and *Clostridium thermoaceticum*. *J. Bacteriol.* **1989**, *171*, 5823–5829. [CrossRef] [PubMed]
10. Lenaz, G.; Samori, B.; Fato, R.; Battino, M.; Castelli, C.P.; Domini, I. Localization and preferred orientations of ubiquinone homologs in model bilayers. *Biochem. Cell. Biol.* **1992**, *70*, 504–514. [CrossRef]
11. Feng, S.; Wang, R.; Pastor, R.W.; Klauda, J.B.; Im, W. Location and Conformational Ensemble of Menaquinone and Menaquinol, and Protein-Lipid Modulations in Archaeal Membranes. *J. Phys. Chem. B* **2021**, *125*, 4714–4725. [CrossRef]
12. Nixon, G.L.; Pidathala, C.; Shone, A.E.; Antoine, T.; Fisher, N.; O'Neill, P.M.; Ward, S.A.; Biagini, G.A. Targeting the mitochondrial electron transport chain of *Plasmodium falciparum*: New strategies towards the development of improved antimalarials for the elimination era. *Future Med. Chem.* **2013**, *5*, 1573–1591. [CrossRef]
13. Berube, B.J.; Russell, D.; Castro, L.; Choi, S.-R.; Narayanasamy, P.; Parish, T. Novel Men A Inhibitors Are Bactericidal against *Mycobacterium tuberculosis* and Synergize with Electron Transport Chain Inhibitors. *Antimicrob. Agent Chemother.* **2019**, *63*, e02661-18. [CrossRef] [PubMed]
14. Debnath, J.; Siricilla, S.; Wan, B.; Crick, D.C.; Lenaerts, A.J.; Franzblau, S.G.; Kurosu, M. Discovery of Selective Menaquinone Biosynthesis Inhibitors against *Mycobacterium tuberculosis*. *J. Med. Chem.* **2012**, *55*, 3739–3755. [CrossRef] [PubMed]
15. Kurosu, M.; Begari, E. Vitamin K_2 in Electron Transport System: Are Enzymes Involved in Vitamin K_2 Biosynthesis Promising Drug Targets? *Molecules* **2012**, *15*, 1531–1553. [CrossRef]
16. Afri, M.; Ehrenberg, B.; Talmon, Y.; Schmidt, J.; Cohen, Y.; Frimer, A.A. Active oxygen chemistry within the liposomal bilayer Part III: Locating Vitamin E, ubiquinol and ubiquinone and their derivatives in the lipid bilayer. *Chem. Phys. Lipids* **2004**, *131*, 107–121. [CrossRef]
17. Cornell, B.A.; Keniry, M.A.; Post, A.; Roberston, R.N.; Weir, L.E.; Westerman, P.W. Location and activity of ubiquinone 10 and ubiquinone analogues in model and biological membranes. *Biochemistry* **1987**, *26*, 7702–7707. [CrossRef]
18. Upadhyay, A.; Fontes, F.L.; Gonzalez-Juarrero, M.; McNeil, M.R.; Crans, D.C.; Jackson, M.; Crick, D.C. Partial Saturation of Menaquinone in *Mycobacterium tuberculosis*: Function and Essentiality of a Novel Reductase, MenJ. *ACS Cent. Sci.* **2015**, *1*, 292–302. [CrossRef] [PubMed]
19. Kumar, S.; Koehn, J.T.; Gonzalez-Juarrero, M.; Crans, D.C.; Crick, D.C. *Mycobacterium tuberculosis* survival in J774A.1 Cells Is Dependent on MenJ Moonlighting Activity, Not Its Enzymatic Activity. *ACS Infect. Dis.* **2020**, *6*, 2661–2671. [CrossRef] [PubMed]
20. Möhwald, H.; Brezesinski, G. From Langmuir Monolayers to Multilayer Films. *Langmuir* **2016**, *32*, 10445–10458. [CrossRef]
21. Stefaniu, C.; Brezesinski, G.; Möhwald, H. Langmuir monolayers as models to study processes at membrane surfaces. *Adv. Colloid Interface Sci.* **2014**, *208*, 197–213. [CrossRef]

22. Hoyo, J.; Guaus, E.; Torrent-Burgués, J.; Sanz, F. Biomimetic monolayer films of digalactosyldiacylglycerol incorporating plastoquinone. *Biochim. Biophys. Acta* **2015**, *1848*, 1341–1351. [CrossRef]
23. Jones, M.N.; Chapman, D. *Micelles, Monolayers, and Biomembranes*; Wiley-Liss: New York, NY, USA, 1995.
24. Roche, Y.; Peretti, P.; Bernard, S. Influence of the chain length of ubiquinones on their interaction with DPPC mixed monolayers. *Biochim. Biophys. Acta* **2006**, *1758*, 468–478. [CrossRef]
25. Katsikas, H.; Quinn, P. The polyisoprenoid chain length influences the interaction of ubiquinones with phospholipid bilayers. *Biochim. Biophys. Acta* **1982**, *689*, 363–369. [CrossRef]
26. Roche, Y.; Peretti, P.; Bernard, S. DSC and Raman studies of the side chain length effect of ubiquinones on the thermotropic phase behavior of liposomes. *Thermochim. Acta* **2006**, *447*, 81–88. [CrossRef]
27. Galassi, V.V.; Arantes, G.M. Partition, orientation and mobility of ubiquinones in a lipid bilayer. *Biochim. Biophys. Acta* **2015**, *1847*, 1560–1573. [CrossRef] [PubMed]
28. Teixeira, M.H.; Arantes, G.M. Effects of lipid composition on membrane distribution and permeability of natural quinones. *RSC Adv.* **2019**, *9*, 16892–16899. [CrossRef]
29. Aroti, A.; Leontidis, E.; Maltseva, E.; Brezesinski, G. Effects of Hofmeister anions on DPPC Langmuir monolayers at the air-water interface. *J. Phys. Chem. B.* **2004**, *108*, 15238–15245. [CrossRef]
30. Miyoshi, T.; Kato, S. Detailed Analysis of the Surface Area and Elasticity in the Saturated 1,2-Diacylphosphatidylcholine/Cholesterol Binary Monolayer System. *Langmuir* **2015**, *31*, 9086–9096. [CrossRef]
31. Quinn, P.J. Phase Behaviour of Binary Mixtures of Membrane Polar Lipids in Aqueous Sytems. *Nat. Prod. Rep.* **1987**, *4*, 129–137. [CrossRef] [PubMed]
32. Quinn, P.J.; Esfahani, M.A. Ubiquinones Have Surface-Active Properties Suited to Transport Electrons and Protons across Membranes. *Biochem. J.* **1980**, *185*, 715–722. [CrossRef]
33. Zhan, T.J.; Eilers, M.; Guo, Z.; Ksebati, M.B.; Simon, M.; Scholten, J.D.; Smith, S.O.; Gibbs, R.A. Evaluation of Isoprenoid Conformation in Solution and in the Active Site of Protein-Farnesyl Transferase Using Carbon-13 Labeling in Conjunction with Solution- and Solid-State NMR. *J. Am. Chem. Soc.* **2000**, *122*, 7153–7164. [CrossRef]
34. Hoyo, J.; Torrent-Burgués, J.; Guaus, E. Biomimetic monolayer films of monogalactosyldiacylglycerol incorporating ubiquinone. *J. Colloid. Interface Sci.* **2012**, *384*, 189–197. [CrossRef] [PubMed]
35. Hoyo, J.; Guaus, E.; Torrent-Burgués, J. Tuning ubiquinone position in biomimetic monolayer membranes. *Eur. Phys. J. E: Soft Matter Biol. Phys.* **2017**, *40*, 62. [CrossRef]
36. Patterson, M.; Vogel, H.J.; Prenner, E.J. Biophysical characterization of monofilm model systems composed of selected tear film phospholipids. *Biochim. Biophys. Acta Biomembr.* **2016**, *1858*, 403–414. [CrossRef]
37. Ma, G.; Allen, H.C. Condensing effect of palmitic acid on DPPC in mixed Langmuir monolayers. *Langmuir* **2007**, *23*, 589–597. [CrossRef]
38. Veldhuizen, E.J.A.; Haagsman, H.P. Role of pulmonary surfactant components in surface film formation and dynamics. *Biochim Biophys Acta-Biomembr.* **2000**, *1467*, 255–270. [CrossRef]
39. Crane, J.M.; Puts, G.; Hall, S.B. Persistence of Phase Coexistence in Disaturated Phosphatidylcholine Monolayers at High Surface Pressures. *Biophys. J.* **1999**, *77*, 3134–4143. [CrossRef]
40. Shaw, N. Lipid Composition as a Guide to the Classification of Bacteria. In *Advances in Applied Microbioligy*; Perlman, D., Ed.; Academic Press: New York, NY, USA, 1974; Volume 17, pp. 63–108.
41. Fadeel, B.; Xue, D. The ins and outs of phospholipid asymmetry in the plasma membrane: Roles in health and disease. *Crit. Rev. Biochem. Mol. Biol.* **2009**, *44*, 264–277. [CrossRef]
42. Chakrabarti, A. Phospholipid Asymmetry in Biological Membranes: Is the Role of Phosphatidylethanolamine Underappreciated? *J. Membr. Biol.* **2021**, *254*, 127–132. [CrossRef]
43. Olżyńska, A.; Zubek, M.; Roeselova, M.; Korchowiec, J.; Cwiklik, L. Mixed DPPC/POPC Monolayers: All-atom Molecular Dynamics Simulations and Langmuir Monolayer Experiments. *Biochim. Biophys. Acta* **2016**, *1858*, 3120–3130. [CrossRef]
44. Träuble, H.; Eibl, H.; Sawada, H. Respiration—A Critical Phenomenon? Lipid Phase Transitions in the Lung Alveolar Surfactant. *Naturwissenschaften* **1974**, *61*, 344–354. [CrossRef]
45. Javanainen, M.; Lamberg, A.; Cwiklik, L.; Vattulainen, I.; Ollila, O.H.S. Atomistic Model for Nearly Quantitative Simulations of Langmuir Monolayers. *Langmuir* **2018**, *34*, 2565–2572. [CrossRef] [PubMed]
46. Marsh, D. *Handbook of Lipid Bilayers*, 2nd ed.; CRC Press: Boca Raton, FL, USA, 2013.
47. Van Cleave, C.; Murakami, H.A.; Samart, N.; Koehn, J.T.; Maldonado, P.; Kreckel, H.D.; Cope, E.J.; Basile, A.; Crick, D.C.; Crans, D.C. Location of menaquinone and menaquinol headgroups in model membranes. *Can. J. Chem.* **2020**, *98*, 307–317. [CrossRef]
48. Stidham, M.A.; McIntosh, T.; Siedow, J.N. On the localization of ubiquinone in phosphatidylcholine bilayers. *Biochim. Biophys. Acta.* **1984**, *767*, 423–431. [CrossRef]
49. Koehn, J.T. Synthesis and Exploration of Biologically Important, Hydrophobic, Redox-Active Molecules: Investigation of Partial Saturation of Mycobacterial Electron Transport Lipids. Ph.D. Dissertation, Colorado State University, Fort Collins, CO, USA, 2019.
50. Javanainen, M. Universal Method for Embedding Proteins into Complex Lipid Bilayers for Molecular Dynamics Simulations. *J. Chem. Theory Comput.* **2014**, *10*, 2577–2582. [CrossRef]

51. Pronk, S.; Páll, S.; Schulz, R.; Larsson, P.; Bjelkmar, P.; Apsotolov, R.; Shirts, M.R.; Smith, J.C.; Kasson, P.M.; van der Spoel, D.; et al. GROMACS 4.5: A High-Throughput and Highly Parallel Open Source Molecular Simulation Toolkit. *Bioinformatics* **2013**, *29*, 845–854. [CrossRef]
52. MacKrell, A.D., Jr.; Bashford, D.; Bellott, M.; Dunbrack, R.L. Jr.; Evanseck, J.D.; Field, M.J.; Fischer, S.; Gao, J.; Guo, H.; Ha, S. All-Atom Empirical Potential for Molecular Modeling and Dynamics Studies of Proteins. *J. Phys. Chem. B* **1998**, *102*, 3586–3616. [CrossRef]
53. Vanommeslaeghe, K.; Hatcher, E.; Achraya, C.; Kundu, S.; Zhong, S.; Shim, J.; Darian, E.; Guvench, O.; Lopes, P.; Vorobyov, I. CHARMM General Force Field: A Force Field for Drug-like Molecules Compatible with the CHARMM All-atom Additive Biological Force Fields. *J. Comp. Chem.* **2010**, *31*, 671–690. [CrossRef] [PubMed]
54. Jorgensen, W.L.; Chandrasekhar, J.; Madura, J.D.; Impey, R.W.; Klein, M.L. Comparison of Simple Potential Functions for Simulating Liquid Water. *J. Chem. Phys.* **1983**, *79*, 926–935. [CrossRef]
55. Bussi, G.; Donadio, D.; Parrinello, M. Canonical Sampling through Velocity Rescaling. *J. Chem. Phys.* **2007**, *126*, 14101. [CrossRef]
56. Parrinello, M.; Rahman, A. Polymorphic Transitions in Single Crystals: A New Molecular Dynamics Method. *J. Appl. Phys.* **1981**, *52*, 7182–7190. [CrossRef]
57. Darden, T.; York, D.; Pedersen, L. Particle Mesh Ewald: An N· Log (N) Method for Ewald Sums in Large Systems. *J. Chem. Phys.* **1993**, *98*, 1463–1472. [CrossRef]
58. Hess, B.; Bekker, H.; Berendsen, H.J.; Fraaije, J.G.E.M. LINCS: A Linear Constraint Solver for Molecular Simulations. *J. Comp. Chem.* **1997**, *18*, 1463–1472. [CrossRef]
59. Anézo, C.; de Vries, A.H.; Höltje, H.-D.; Tieleman, D.P.; Marrink, S.-J. Methodological Issues in Lipid Bilayer Simulations. *J. Chem. Phys.* **2003**, *107*, 9424–9433. [CrossRef]
60. Kellerman, M.Y.; Yoshinaga, M.Y.; Valentine, R.C.; Wörmer, L.; Valentine, D.L. Important roles for membrane lipids in haloarchaeal bioenergetics. *Biochim. Biophys. Acta. Biomembr.* **2016**, *1858*, 2940–2956. [CrossRef]

Appendix VII: Investigating Substrate Analogues for Mycobacterial MenJ: Truncated and Partially Saturated Menaquinones

This manuscript contains Langmuir monolayer data previously reported in *Biochemistry*.[1] This data was incorporated in the comparison of MK-1 through MK-4 presented in Chapter 3.

References

1. Koehn, J. T.; Beuning, C. N.; Peters, B. J.; Dellinger, S. K.; Van Cleave, C.; Crick, D. C.; Crans, D. C., Investigating Substrate Analogues for Mycobacterial MenJ: Truncated and Partially Saturated Menaquinones. *Biochemistry* **2019,** *58* (12), 1596-1615.

Biochemistry
Cite This: Biochemistry 2019, 58, 1596−1615
Article
pubs.acs.org/biochemistry

Investigating Substrate Analogues for Mycobacterial MenJ: Truncated and Partially Saturated Menaquinones

Jordan T. Koehn,[†] Cheryle N. Beuning,[†] Benjamin J. Peters,[†] Sara K. Dellinger,[†] Cameron Van Cleave,[†] Dean C. Crick,[‡,§] and Debbie C. Crans*[,†,‡]

[†]Chemistry Department, [‡]Cell and Molecular Biology Program, and [§]Microbiology, Immunology, and Pathology Department, Colorado State University, Fort Collins, Colorado 80523, United States

Supporting Information

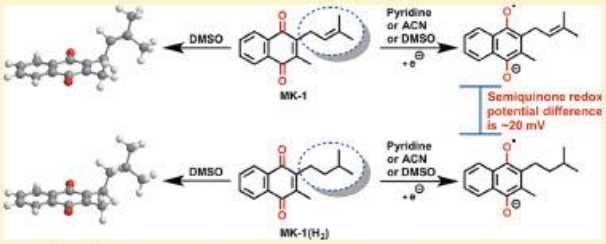

ABSTRACT: Menaquinones (MKs) are essential for electron transport in prokaryotes, and importantly, partially saturated MKs represent a novel virulence factor. However, little is known regarding how the degree of saturation in the isoprenyl side chain influences conformation or quinone redox potential. MenJ is an enzyme that selectively reduces the second isoprene unit on MK-9 and is contextually essential for the survival of *Mycobacterium tuberculosis* in J774A.1 macrophage-like cells, suggesting that MenJ may be a conditional drug target for pathogenic mycobacteria. Therefore, fundamental information about the properties of this system is important, and we synthesized the simplest MKs, unsaturated MK-1 and the saturated analogue, MK-1(H_2). Using two-dimensional nuclear magnetic resonance spectroscopy, we established that MK-1 and MK-1(H_2) adopted similar folded−extended conformations (i.e., the isoprenyl side chain folds upward) in each solvent examined but the folded−extended conformations differed slightly between organic solvents. Saturation of the isoprenyl side chain slightly altered the MK-1 analogue conformation in each solvent. We used molecular mechanics to illustrate the MK-1 analogue conformations. The measured quinone redox potentials of MK-1 and MK-1(H_2) differed between organic solvents (presumably due to differences in dielectric constants), and remarkably, an ~20 mV semiquinone redox potential difference was observed between MK-1 and MK-1(H_2) in pyridine, acetonitrile, and dimethyl sulfoxide, demonstrating that the degree of saturation in the isoprenyl side chain of MK-1 influences the quinone redox potential. Finally, MK-1 and MK-1(H_2) interacted with Langmuir phospholipid monolayers and Aerosol-OT reverse micelle (RM) model membrane interfaces, where MK-1 adopted a slightly different folded conformation within the RM model membrane interface.

Quinones are a unique type of α,β-unsaturated ketone existing as metabolites in numerous pathways where they have many functions in nature.[1−6] The importance of quinone chemistry has been recognized since the mid-1800s. Quinone-containing compounds can be antioxidants, antitumoral agents, or carcinogenic agents and are the inherent components of biological systems such as photosystem II.[1−6] Menaquinones (MKs) (or naphthoquinones) are members of the lipoquinone (lipid-quinone) class of molecules and are essential components of the respiratory electron transport system (ETS), where they shuttle electrons and protons between protein complexes by acting as electron donors and acceptors.[6] Partial saturation of the isoprenyl side chain of MK has been known for a long time, but MenJ was recently shown to selectively reduce MK-9 at the second isoprene unit, demonstrating the origin and necessity of partially saturated MKs for the survival of the bacteria.[7,8] Currently, little is known regarding the conformation of MKs in solution or within cell membranes and how partial saturation of the isoprenyl side chain affects conformation and quinone reactivity, even though the structures and biological significance of lipoquinones and isoprenoids have been known for more than 50 years.[6,9−13] It is well-known that evolutionarily conserved structural differences in the lipoquinone headgroup alter quinone redox potential,[1] but how partial saturation of the isoprenyl side chain affects quinone redox potential remains uncertain. Therefore, this work aims to characterize the conformation of the most fundamental MKs containing

Received: January 3, 2019
Revised: February 19, 2019
Published: February 21, 2019

DOI: 10.1021/acs.biochem.9b00007
Biochemistry 2019, 58, 1596−1615

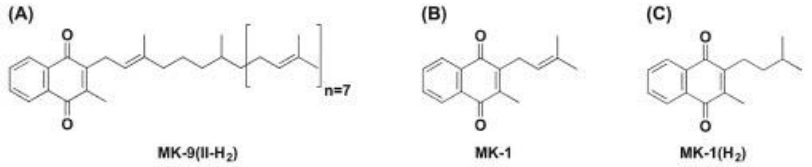

Figure 1. Structures of (A) MK-9(II-H_2), present within *Mycobacterium tuberculosis*, (B) the unsaturated MK analogue, MK-1, and (C) the saturated MK analogue, MK-1(H_2).

one isoprene unit (unsaturated vs saturated side chain) in an organic solution and a model membrane interface and to determine the quinone redox potentials of unsaturated MK-1 and saturated MK-1(H_2) in organic solutions.

MKs are structurally characterized by a naphthoquinone moiety and a repeating isoprenyl side chain of varying length (Figure 1), where the latter is a characteristic that has long been used to assist taxonomic efforts.[14,15] The most widely known MK compound is vitamin K_2 (or MK-4), which is essential for life in humans as it is a key cofactor in blood coagulation.[16] MK-4 was recently shown to be biosynthesized in humans[17] and as a part of the ETS in *Drosophila*.[18] Vitamin K_3 (or menadione), the simplest 1,4-naphthoquinone derivative lacking the isoprenyl side chain, has been reported to have significant antitumoral properties.[2] N-Alkylated MK derivatives have also been synthesized and characterized in the literature, with several exhibiting interesting biological properties.[19−22] The truncated MK analogues, menaquinone-1 (MK-1) and menaquinone-1(H_2) [MK-1(H_2)], are vital to study as they are the simplest, most fundamental MKs, where they retain the core requirements (i.e., a naphthoquinone moiety and a one-unit isoprenyl side chain). MK-1(H_2) is crucial to study as it lacks the double bond in the isoprenyl side chain, and importantly, biologically isolated MK analogues containing partial saturation (reduced double bond) in the isoprenyl side chain have been reported (Figure 1).[6−8] Truncated MK analogues are more soluble than the natural MK substrate, thus allowing rigorous characterization in aqueous assays.[8] Furthermore, MK-9 contains 80 hydrogens with significant spectral overlap, making conformational analysis nontrivial. Therefore, the conformational analysis of these two truncated MK-1 analogues is essential as the conformation of the first isoprene unit will influence the conformation of the rest of the isoprenyl side chain in naturally occurring longer MK analogues [e.g., MK-4, MK-9, or MK-9(II-H_2) (Figure 1)].

The synthesis of truncated MK analogues is necessary as it allows experimental conformational analysis to be carried out. Molecular conformations are significant for manifesting physical and chemical reactivity as well as recognition in biological systems. MKs contain alkyl side chains of varying lengths, and conformations have been reported for various alkanes, alkenes, and fatty acids, which all contain alkyl chains of varying lengths.[23−35] For example, the degree of folding of C_5−C_{32} *n*-alkanes in solution depends on the strength of the dispersion force of the solvent and increases with an increase in chain length.[27−29] Furthermore, studies of *n*-hexane and *n*-pentane in various solvents suggested that the solvent environment had only minor effects on the conformational equilibrium.[35] Interestingly, conformations observed in polar and spherical solvents such as dimethyl sulfoxide (DMSO) favored *gauche* conformations.[35] Computational studies have been carried out on MK analogues in which folded conformations were found to be favorable.[34,36] Importantly, we recently reported that menaquinone-2 (MK-2) adopts a folded, U-shaped conformation in solution and within a model membrane interface.[37] However, MK-1 contains only one isoprene unit and presents the best opportunity for a flat−extended conformation to exist, and therefore, it is important to determine if a flat−extended (i.e., trans or extended configuration of the side chain and isoprene planar), folded−extended (i.e., isoprene folded upward), or U-shaped conformation (i.e., isoprene folded up and back toward the naphthoquinone in a U shape) is preferred (see the illustration below). On the basis of these selected examples, we hypothesized that MK-1 analogues adopt folded conformations regardless of the degree of saturation in their isoprenyl side chain.

The conformation and electronic properties of a molecule can affect both the reactivity and function of a molecule in solution and within biological environments. The longer partially saturated isoprenyl side chain MK analogue, MK-9(II-H_2) (Figure 1), is an electron transporter within *Mycobacterium tuberculosis*, and the synthesis of MK-9(II-H_2) was found to be essential for the survival of pathogenic *M. tuberculosis* in host macrophages; thus, partially saturated MKs represent a novel virulence factor.[7,8] In addition, partially saturated MK analogues have been reported in other organisms such as members of the genera *Streptomyces* and *Actinomadura*.[11] It is unclear whether hydrogenation of the double bond in specific isoprene units changes the reactivity of the quinone system. The double bonds present within the isoprenyl side chain are not conjugated to the quinone system within MK. Therefore, it would not be anticipated that a significant change in the quinone redox potential would occur upon reduction of an isoprenyl unit. However, it has been reported that even when there is no direct conjugation between the quinone system and a substituent group, electrochemical reduction of the quinone system is sensitive to the electronic perturbation of the substituents.[1] Thus, it is possible that partial saturation in the isoprenyl side chain could influence the quinone redox potential, where an indirect through-bond effect could be a contributing factor and/or conformational effects of the substituent. Therefore, we hypothesized that the quinone redox potential of MK-1 may

DOI: 10.1021/acs.biochem.9b00007
Biochemistry 2019, 58, 1596−1615

be influenced by the degree of saturation in the isoprenyl side chain.

In this work, MK-1 and MK-1(H_2) (Figure 1) were first synthesized and then their conformations within organic solvents were elucidated by one-dimensional (1D) and two-dimensional (2D) ^{1}H nuclear magnetic resonance (NMR) spectroscopy. MK-1 and MK-1(H_2) adopted similar folded–extended conformations in each solvent, but the preferred folded–extended conformations differed slightly between solvent environments. The quinone redox potentials of MK and MK-1(H_2) were measured in three organic solvents, where a solvent effect (presumably due to a change in the dielectric constant) was observed, and most interestingly, an ~20 mV difference in semiquinone redox potential was observed between MK-1 and MK-1(H_2). The interaction of MK-1 and MK-1(H_2) with phospholipid monolayers was characterized using Langmuir phospholipid monolayers, and the two MK-1 analogues were found to interact with the phospholipid interface. Finally, using a complementary study, the location, orientation, and conformation of MK-1 and MK-1(H_2) within a reverse micelle (RM) model membrane interface were determined using 1D and 2D NMR spectroscopy. The two MK-1 analogues interacted similarly with the RM model membrane interface, and MK-1 adopted a slightly different folded conformation within the RM interface compared to that observed in an organic solution.

EXPERIMENTAL SECTION

Materials. Menadione (crystalline), sodium hydrosulfite (85.0%), 1,4-dioxane (99.9%), 3-methyl-2-buten-1-ol (99%), BF_3 etherate (≥46.5%), Luperox A98 benzoyl peroxide (≥98%), 1-iodo-3-methylbutane (97%), dioctyl sulfosuccinate sodium salt (AOT, 97.0%), isooctane (2,2,4-trimethylpentane, ≥99.0%), chloroform (99.8%), methanol (99.9%), tetrabutylammonium perchlorate (TBAP, ≥99.0%), ferrocene (Fc, anhydrous), silver nitrate ($AgNO_3$, ≥99.0%), and activated charcoal were purchased from Sigma-Aldrich and used as received unless otherwise noted. Absolute ethanol and ultra-high-purity argon gas (99.9%) were acquired from Pharmco-Aaper and Airgas, respectively. Deuterated solvents of acetonitrile (d_3-ACN or CD_3CN) (99.8% D), dimethyl sulfoxide (d_6-DMSO) (99.9% D, 0.05% (v/v) tetramethylsilane), and d_6-benzene (≥99.6%) were acquired from Sigma-Aldrich. Deuterium oxide (D_2O, 99.9%), d_2-dichloromethane (99.9%), and d_4-methanol (99.8%) were acquired from Cambridge Isotope Laboratories, Inc. Deuterated pyridine (99.8% D) was purchased from Arcos Organics. DPPC (1,2-dipalmitoyl-*sn*-glycero-3-phosphocholine, ≥99.0%) and DPPE (1,2-dipalmitoyl-*sn*-glycero-3-phosphoethanolamine, ≥99.0%) were purchased from Avanti Polar Lipids Inc. Monosodium phosphate (NaH_2PO_4, 96.0%) and sodium phosphate dibasic anhydrous (Na_2HPO_4) were purchased from Fisher Scientific, and distilled deionized water (DDI H_2O) was purified with a Barnstead E-pure system (~18 MΩ cm).

General Methods. All non-aqueous reactions were carried out under an argon atmosphere in flame-dried glassware, and all mixtures were stirred on a magnetic stir plate using an anhydrous solvent unless otherwise noted. Reactions were monitored by thin layer chromatography (TLC) on Whatman Partisil K6F TLC plates (silica gel 60 Å, 0.250 mm thickness) and visualized using an ultraviolet lamp (366 or 254 nm). Products were purified by flash chromatography (SiliCycle SiliaFlash F60, 43–60 μm, 60 Å). Yields refer to chromatographically and spectroscopically (^{1}H NMR) homogeneous materials unless otherwise noted. All chemicals were used without purification except AOT and the organic solvents. AOT was purified using activated charcoal and methanol to remove acidic impurities using previously reported methods.[38] Organic solvents dimethyl sulfoxide (DMSO), acetonitrile (CH_3CN or ACN), and pyridine were purified by distillation and then dried over activated 3 Å molecular sieves (40 g/200 mL of solvent) for 3 days. Benzene was dried by being passed through an alumina drying column (Solv-Tek Inc.) under argon pressure. When samples were prepared for RM NMR experiments, deuterium oxide was used instead of H_2O and the pH was adjusted to consider the presence of deuterium (pD = 0.4 + pH).[39] ^{1}H and ^{13}C NMR spectra were recorded on a 400 MHz Varian Model MR400, 400 MHz Varian iNova400, or 500 MHz Varian iNova500 spectrometer. Chemical shift values (δ) are reported in parts per million and referenced against the internal solvent peaks in ^{1}H NMR ($CDCl_3$, δ 7.26; d_3-acetonitrile, δ 1.94; d_6-DMSO, δ 2.50; d_4-methanol, δ 4.87; d_2-methylene chloride, δ 5.32; d_6-benzene, δ 7.16; d_5-pyridine, δ 8.74; D_2O, δ 4.79) and in ^{13}C NMR ($CDCl_3$, δ 77.16; d_6-benzene, δ 128.06).

Preparation of 2-Methyl-3-(3-methylbut-2-en-1-yl)-naphthalene-1,4-dione, MK-1 (3). Menadiol 2 was synthesized as previously described[37] from menadione 4, and MK-1 3 was synthesized previously.[8] However, in this work, the reaction to form MK-1 3 was scaled up and characterization reported data in $CDCl_3$. To a dry 100 mL Schlenk flask were added a stir bar, EtOAc (16 mL), and 1,4-dioxane (16 mL), which was then purged/evacuated with argon repeatedly. Then, crude menadiol 2 (2.50 g, 4:1 menadiol:menadione by NMR integration; note that menadiol is prone to autoxidation in $CDCl_3$, 11.48 mmol) was added followed by 3-methyl-2-buten-1-ol 1 (1.08 g, 12.52 mmol) and then dropwise addition of distilled BF_3 etherate (0.8 mL). The reaction solution turned dark orange and was refluxed at 70 °C for 3 h under argon. The reaction was quenched with ice and H_2O (100 mL), and then the mixture extracted with diethyl ether (3 × 100 mL). The yellow organic extracts were washed with saturated $NaHCO_3$ (100 mL), washed with brine (100 mL), dried with anhydrous Na_2SO_4, and then concentrated under reduced pressure at ambient temperature to yield 3.50 g of crude red oil. The crude oil was purified by flash column chromatography (1000 mL of 230–400 mesh SiO_2, 70 mm column, 20:1 *n*-pentane:EtOAc). The red oil obtained was dried under reduced pressure (~125 mTorr) overnight to yield 0.628 g of a deep red oil (2.61 mmol, 22.7% yield): ^{1}H NMR (400 MHz, $CDCl_3$) δ 8.06–8.08 (m, 2H), 7.67–7.69 (m, 2H), 5.02 (t, J = 7.0 Hz, 1H), 3.36 (d, 2H, J = 7.0 Hz), 2.19 (s, 3H), 1.79 (s, 3H), 1.69 (s, 3H); ^{13}C NMR (101 MHz, $CDCl_3$) δ 185.6, 184.7, 146.2, 143.4, 134.1, 133.47, 133.42, 132.33, 132.30, 126.4, 126.3, 119.3, 26.3, 25.9, 18.2, 12.8; HRMS (DART) m/z [(M + H)$^+$] calcd for $C_{16}H_{17}O_2$ 241.1223, found 241.1222.

Preparation of 2-Isopentyl-3-methylnaphthalene-1,4-dione, MK-1(H_2) (6). To a dry 100 mL round-bottom Schlenk flask were added a stir bar and dry and degassed benzene (30 mL) followed by 1-iodo-3-methylbutane 5 (1.98 g, 10.0 mmol, 1 equiv), which was then purged/evacuated with argon repeatedly. To a dry 20 mL vial was added dry benzene (15 mL), which was then degassed via argon needle purge, followed by addition of menadione 4 (1.72 g, 10.0 mmol) and benzoyl peroxide (2.42 g, 10.0 mmol, 1 equiv). This solution

DOI: 10.1021/acs.biochem.9b00007
Biochemistry 2019, 58, 1596–1615

was sonicated until dissolution occurred under argon. The naphthoquinone/benzoyl peroxide solution was added dropwise over 135 min to the refluxing prenyl iodide solution, which was under an argon atmosphere during the reaction. After the addition was complete, the solution was refluxed for an additional 1 h. The solution was then diluted with saturated $NaHCO_3$ (100 mL) and diethyl ether (100 mL), and then the two phases were separated. The aqueous layer was extracted with diethyl ether (3 × 100 mL), and the combined organic extracts were washed with saturated $NaHCO_3$ (100 mL), washed with brine (100 mL), dried with anhydrous Na_2SO_4, and then concentrated under reduced pressure at ambient temperature to yield a crude yellow powder. The crude powder was purified by flash column chromatography (10:1.5 *n*-pentane:EtOAc) to yield 0.493 g of a yellow solid (2.03 mmol, 20.3% yield) after drying overnight under reduced pressure (~125 mTorr): ^{1}H NMR (400 MHz, C_6D_6) δ 8.05−8.07 (m, 2H), 7.04−7.06 (m, 2H), 2.41−2.45 (m, 2H), 1.92 (s, 3H), 1.45−1.55 (m, 1H), 1.16−1.21 (m, 2H), 0.89 (d, J = 6.6 Hz, 2H); ^{13}C NMR (101 MHz, C_6D_6) δ 184.9, 184.3, 147.5, 142.7, 133.09, 133.08, 132.74, 132.71, 126.26, 126.21, 37.8, 28.9, 25.2, 22.5, 12.3; HRMS (DART) m/z [$(M + H)^+$] calcd for $C_{16}H_{19}O_2$ 243.1380, found 243.1378.

Mass Spectrometry. High-resolution mass spectrometry (HRMS) experiments were conducted on an Agilent 6224 TOF LC/MS instrument [O-time-of-flight (TOF)] interfaced with the Direct Analysis in Real Time (DART) source (IonSense DART-100). A standard of Jeffamine was used as an internal standard calibration for HRMS DART experiments carried out in positive mode.

NMR Spectroscopic Studies. 1D and 2D ^{1}H NMR spectroscopic studies were carried out both in organic solvents and in an RM model membrane system. ^{1}H and ^{13}C NMR spectra were recorded using either a Varian model MR400, model Inova400, or model Inova500 spectrometer operating at either 400, 500, or 101 MHz, respectively. Chemical shift values (δ) are reported in parts per million and referenced against the internal solvent peaks in ^{1}H NMR ($CDCl_3$, δ 7.26; d_3-ACN, δ 1.94; d_6-DMSO, δ 2.50; d_4-methanol, δ 4.87; d_2-methylene chloride, δ 5.32; d_6-benzene, δ 7.16; d_5-pyridine, δ 8.74; D_2O, δ 4.79) and in ^{13}C NMR ($CDCl_3$, δ 77.16; d_6-benzene, δ 128.06). All NMR spectra were recorded at either 22, 25, or 26 °C. See figure captions and the Supporting Information for more details.

Solution 1D ^{1}H NMR Spectroscopic Studies. Samples were prepared by dissolving ~5.0 mg of MK-1 in 0.5 mL of either d_1-chloroform, d_2-methylene chloride, d_4-methanol, d_6-DMSO, d_5-pyridine, d_3-ACN, or d_6-benzene. The NMR instrument was locked onto the respective deuterium signal in the deuterated solvent used. NMR spectra were then collected using 32 scans for each sample. The data were processed using MestReNova NMR processing software version 10.0.1. The spectra were manually phased, and then the baseline was corrected using a Bernstein Polynomial Fit (polynomial order 3). The obtained spectra were referenced to the proper internal solvent peak.

Sample Preparation for ^{1}H−^{1}H 2D NOESY and ^{1}H−^{1}H 2D ROESY NMR Spectroscopic Studies. To prepare the solutions of MK-1 or MK-1(H_2) in d_5-pyridine, d_3-ACN, and d_6-DMSO, 0.0024 g of MK-1 or 0.0024 g of MK-1(H_2) was dissolved in 0.5 mL of a deuterated solvent to produce a 20 mM solution of MK-1 or MK-1(H_2), respectively. The NMR samples containing the MK-1 or MK-1(H_2) solution were purged with argon briefly and capped prior to data collection.

^{1}H−^{1}H 2D NOESY and ^{1}H−^{1}H 2D ROESY NMR Spectroscopic Solution Studies. ^{1}H−^{1}H 2D NOESY NMR and ^{1}H−^{1}H 2D ROESY NMR spectroscopic experiments were conducted using a 400 MHz Varian MR400 NMR spectrometer operating at 26 °C. A standard NOESY pulse sequence was used consisting of 256 transients with 16 scans in the f1 domain using a 500 ms mixing time, a 45° pulse angle, and a 1.5 s relaxation delay. The standard ROESYAD pulse sequence consisted of 256 transients with 16 scans in the f1 domain using a 400 ms mixing time, a 45° pulse angle, and a 2.0 s relaxation delay. The NMR was locked onto either d_5-pyridine, d_3-ACN, or d_6-DMSO. The resulting spectrum was processed using MestReNova NMR software version 10.0.1 (see the Supporting Information for further details). The spectra were referenced to the proper internal solvent peak.

Molecular Mechanics Calculations. To illustrate conformations for MK-1 and MK-1(H_2), Merck Molecular Force Field 94 (MMFF94) molecular mechanics gas phase simulations were conducted using ChemBio3D Ultra 12.0 at 25 °C. Starting conformations were obtained by building ChemDraw structures and rotating desired bonds, and then simulations were run followed by energy optimization or simply an energy minimization to achieve the desired conformation. Conformations A, A1, B, B1, C, and C1 in Figure 5 were constructed and then energy minimized with a root-mean-square (RMS) gradient of 0.1 and up to 50 iterations to obtain MK-1 and MK-1(H_2) conformations that agreed with our interpretation of the cross peak observations and intensities in the ^{1}H−^{1}H 2D NOESY and ROESY NMR spectral data. Two simulations were run for 10000 iterations and then energy minimized using an MMFF94 energy minimization calculation using 500 iterations with an RMS gradient of 0.001 to achieve conformations D and D1 in Figure S27. Conformations E, E1, F, and F1 in Figure S27 were generated by rotating bonds to achieve the desired conformation followed by an energy minimization using 20−50 iterations and an RMS gradient of 0.1. A table of structural parameters such as selected distances between hydrogens within the conformations in Figure 5 and Figure S27 and energies calculated for the three-dimensional (3D) conformations can be found in the Supporting Information. Tables of Cartesian coordinates for the MK-1 analogue conformations can be found in the Supporting Information.

Electrochemistry Methods. The electrochemistry was performed on a CHI 750D potentiostat. For cyclic voltammetry, a classical three-electrode system was used with a scan rate of 100 mV/s at ambient temperature. A glassy carbon working electrode (BASi MF2012, 3 mm) was lightly polished between runs with alumina powder and then rinsed with water and ethanol. A platinum wire counter electrode (BASi MW1032) was gently polished between runs with 600 grit sandpaper. A Ag^+/Ag reference electrode (BASi MW1085) was constructed by using the Ag wire gently polished with 600 grit sandpaper inserted into a freshly prepared solution of organic solvent (ACN, pyridine, or DMSO) with 0.1 M TBAP and 0.01 M $AgNO_3$. This reference electrode was equilibrated in the MK-1 or MK-1(H_2) solution (2 mM) of the same organic solvent for 10 min. The solutions were bubbled for ~5−10 min with argon gas to ensure as much dissolved O_2(g) was removed as possible before the cyclic voltammogram was recorded. All half-wave potentials recorded were referenced to

DOI: 10.1021/acs.biochem.9b00007
Biochemistry 2019, 58, 1596−1615

the internal standard Fc^+/Fc couple by subtracting the averaged potential in each solvent. The Fc^+/Fc couple against the Ag^+/Ag reference in ACN was 0.081 ± 0.002 V, in DMSO was 0.176 ± 0.004 V, and in pyridine was 0.562 ± 0.001 V. The reliability of the Fc^+/Fc couple half-wave potential in each solvent was within experimental error.

$$E_{1/2} = \frac{E_{pc} + E_{pa}}{2} \quad (1)$$

$$\frac{i_{pc}}{i_{pa}} = 1, \text{ for a reversible process} \quad (2)$$

$$\Delta E_p = E_{pc} - E_{pa}, n = x \times \frac{0.059V}{\Delta E_p} \quad (3)$$

The half-wave potentials are calculated using eq 1, where E_{pc} and E_{pa} are the cathodic and anodic peak potentials, respectively. The cathodic and anodic peak currents, i_{pc} and i_{pa}, respectively, were measured manually with a ruler on the cyclic voltammograms in centimeters to determine reversibility as a measure of the closeness to unity (eq 2). The number of electrons, n, in each process was determined using eq 3, where x is the adjustment factor in each solvent determined by setting the standard ferrocene number of electrons to 1 (n = 1). Electrochemistry performed in non-aqueous solvents may have ΔE_p values that are not indicative of the number of electrons; therefore, the ferrocene standard was used to determine the true value. See the Supporting Information for more detailed electrochemistry methods and discussion.

Langmuir Monolayer Compression Isotherms. Langmuir phospholipid monolayers were prepared using a Kibron μtroughXS. The subphase consisted of ~50 mL of a 20 mM phosphate buffer (pH 7.4). Phospholipid stock solutions of 18.4 mg (1 mM) of DPPC or 17.3 mg (1 mM) of DPPE were prepared by dissolving the phospholipid in 25 mL of a chloroform/methanol solvent [9:1 (v/v)]. Stock solutions (1 mM) of both MK-1 and MK-1(H_2) were prepared with 0.97 and 0.96 mg, respectively, in 4 mL of a chloroform/methanol solvent [9:1 (v/v)]. Then, 20 μL of a stock solution [20 nmol of DPPC, DPPE, MK-1, or MK-1(H_2)] or a mixture (10 nmol of lipid and 10 nmol of MK) was applied in dropwise fashion to the surface of the subphase. This was then allowed to equilibrate for 15 min, allowing the lipids to spread and the solvent to evaporate. The DPPC/DPPE mixed solution and MK-1 or MK-1(H_2) were prepared by mixing equimolar amounts of phospholipid and MK analogue in a separate vial before application to the subphase. The resulting monolayer was compressed at a rate of 10 mm min^{-1} (5 mm min^{-1} from two sides) with a Teflon ribbon, and the surface tension was measured using the Wilhemy plate method using a wire probe as the Wilhemy plate. The temperature of the compression isotherm experiments was kept consistent at 25 °C using a circulating water bath. The surface pressure reported is calculated from eq 4, where π is the surface pressure, γ_o is the surface tension of water without lipid (72.8 mN/m[40,41]), and γ is the surface tension of water with lipid present during compression. Each compression isotherm presented herein is an average of three measurements. The data acquired were processed using OriginPro version 9.1 graphing software. The compression modulus was calculated as described in the Supporting Information.

$$\pi = \gamma_o - \gamma \quad (4)$$

Sample Preparation for RM NMR Spectroscopic Studies. A 0.50 M AOT stock solution was prepared by dissolving AOT (5.56 g, 12.5 mmol) in isooctane (25.0 mL). Empty RMs were prepared by mixing a 0.50 M AOT stock solution with a D_2O water pool and then vortexed. MK-1 and MK-1(H_2) RMs were made in a similar manner, the only difference being a 14.3 mM stock solution for MK-1 or MK-1(H_2) was prepared by dissolving MK-1 or MK-1(H_2), respectively, in a 0.50 M AOT/isooctane solution. The RMs were then prepared using the MK-1 or MK-1(H_2) AOT/isooctane stock solution. First, 2.0 mL samples were made using specific amounts of MK-1 or MK-1(H_2) AOT/isooctane stock solution and then diluting the sample to 2.0 mL with the 0.50 M AOT/isooctane solution. From the 2.0 mL solutions, 1.0 mL RM samples were prepared using designated amounts of the 2.0 mL sample and then adding the proper amount of D_2O at pH 6.65 (see General Methods for pH measurements) for MK-1 [the D_2O pH was 6.71 for the MK-1(H_2) samples] to form RMs of the desired size. The samples were then vortexed until the solution was clear. The overall concentrations for the 1.0 mL MK-1 RM samples are as follows: w_0 4, 13.8 mM; w_0 8, 6.5 mM; w_0 12, 3.5 mM; w_0 16, 1.9 mM; and w_0 20, 1.3 mM. The overall concentrations for the 1.0 mL MK-1(H_2) RM samples are as follows: w_0 4, 13.8 mM; w_0 8, 6.4 mM; w_0 12, 3.5 mM; w_0 16, 2.0 mM; and w_0 20, 1.4 mM.

1D ^{1}H NMR Spectroscopic Studies of AOT/Isooctane RMs Containing MK-1 or MK-1(H_2). NMR spectra of MK-1 and MK-1(H_2) in various size RMs, isooctane, and D_2O were obtained using a Varian Inova 400 MHz instrument operating at 22 °C using routine parameters (45° pulse angle and 1 s relaxation delay) and 64 scans. The NMR instrument was locked onto the 10% D_2O signal for the RM samples and locked onto 100% D_2O for the sample in D_2O. The 1D ^{1}H NMR spectra of MK-1 or MK-1(H_2) in isooctane were doped with ~5% d_6-benzene for the NMR instrument to lock onto and to achieve properly shimmed spectra. The spectral data were processed using MestReNova NMR processing software version 10.0.1. The spectra were manually phased, and then the baseline was corrected using a multipoint baseline correction (cubic splines). The spectrum in D_2O was referenced to the internal D_2O peak, and the spectra in isooctane and RMs were referenced to the isooctane methyl peak (0.904 ppm) as previously reported.[39]

Sample Preparation for ^{1}H–^{1}H 2D NOESY and ^{1}H–^{1}H 2D ROESY NMR Spectroscopic Studies in AOT/Isooctane RMs. RM samples of MK-1 and MK-1(H_2) were prepared in the following manner. A 0.50 M AOT stock solution was first prepared by dissolving AOT (5.56 g, 12.5 mmol) in isooctane (25.0 mL). A 1.0 mL stock solution of 112 mM MK-1 in an AOT/isooctane solution was prepared by dissolving 27.7 mg of MK-1 in 1.0 mL of a 0.50 M AOT/isooctane stock solution. To prepare a w_0 12 RM, 894.68 μL of a 112 mM MK-1 AOT/isooctane stock solution and 105.32 μL of D_2O at pH 7.03 were mixed together and then vortexed until the solution was clear. The MK-1(H_2) w_0 12 RM sample was prepared like that of MK-1 using a 112 mM stock solution and D_2O (pH 7.01). This final mixture results in a w_0 12 RM microemulsion with an overall concentration of MK-1 or MK-1(H_2) of ~100 mM (~29 molecules per RM). The NMR samples containing the MK-1 or MK-1(H_2) RM solution were purged with argon briefly and capped prior to data collection.

^{1}H–^{1}H 2D NOESY and ^{1}H–^{1}H 2D ROESY NMR Spectroscopic Studies in a w_0 12 AOT/Isooctane RM.

DOI: 10.1021/acs.biochem.9b00007
Biochemistry 2019, 58, 1596−1615

Scheme 1. (A) Synthetic Scheme for the Allylic Alcohol Coupling Reaction To Form MK-1 3 and (B) Synthetic Scheme for the Radical Alkylation of Menadione 4 and 1-Iodo-3-methylbutane 5 To Form MK-1(H_2) 6[8,37,51−53]

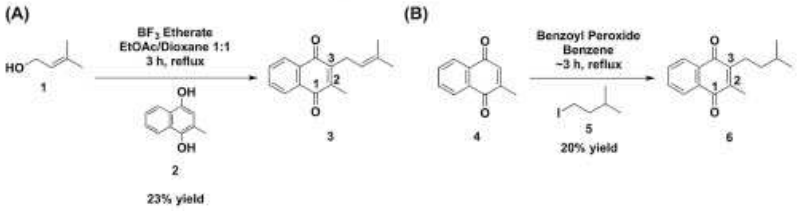

2D NMR spectra of MK-1 and MK-1(H_2) in RMs were obtained using similar conditions and methods described previously[37,42,43] using a 400 MHz Varian MR400 NMR spectrometer operating at 26 °C for MK-1 and were obtained using a 500 MHz Varian Inova 500 spectrometer operating at 25 °C for MK-1(H_2). A standard NOESY pulse sequence was used consisting of 200 or 256 transients with either 16 or 32 scans in the f1 domain using a 200 ms mixing time, a 45° pulse angle, and a 1.5 s relaxation delay. A standard ROESYAD pulse sequence was used consisting of 256 transients with 16 scans in the f1 domain using a 200 ms mixing time, a 45° pulse angle, and a 2.0 s relaxation delay. The NMR instrument was locked onto the 10% D_2O signal. The resulting spectrum was processed using MestReNova NMR software version 10.0.1 (see the Supporting Information for further details). The spectrum was referenced to the isooctane methyl peak at 0.904 ppm on both axes as previously reported.[39] The 3D conformation illustration within an RM interface was constructed using ChemDraw Professional 15.0 and Chem-Bio3D Ultra 12.0 based on spectral parameters described in Results and Discussion.

Dynamic Light Scattering (DLS) Studies. RMs for DLS studies were prepared as described for the NMR spectroscopic studies except that DDI H_2O was used as the water pool instead of D_2O and 0.50 M AOT was diluted with isooctane after the RM had formed to a final AOT concentration of 0.1 M. The hydrodynamic radius of the RMs was determined by DLS measurements performed on a Malvern Zetasizer Nano ZS instrument (Malvern Instruments, Malvern, U.K.). The DLS cuvette (1 cm × 1 cm, glass) was washed three times with isooctane followed by three washes with the RM sample. Then, the cuvette was filled with 1 mL of the RM sample and closed with a Teflon cap. Each experiment was conducted at 25 °C and consisted of a 700 s sample equilibration period followed by 10 measurements consisting of 15 scans each.[42] Each sample was measured in triplicate, and the radius and polydispersity (PDI) were recorded. The data were analyzed using Malvern Zetasizer Software version 7.11 and compared to values reported in the literature.[44] See the Supporting Information for data and interpretation.

■ RESULTS AND DISCUSSION

Synthesis and Characterization of MK-1 Analogues. We have previously synthesized MK-1,[8] and it has been synthesized by other reported routes;[45−49] however, here we present a scaled-up version and NMR spectral characterization in chloroform-*d* (Scheme 1). Menadiol 2 was synthesized as previously described from menadione 4.[37,50,51] To introduce the isoprenyl side chain, menadiol 2 was treated with 3-methyl-2-buten-1-ol 1 in the presence of the Lewis acid catalyst, boron trifluoride.[37,51] MK-1 3 was obtained as a red oil in a 23% yield (Scheme 1). Although the route to obtain MK-1(H_2) has been reported in the literature[52] (Scheme 1), the product was not isolated in pure form or characterized by NMR spectroscopy. We modified and optimized the reported route to increase the yield and scaled the reaction up to a preparatory scale using a similar methodology we recently reported.[53] MK-1(H_2) 6 was synthesized by a one-step radical alkylation reaction in which menadione 4 and 1-iodo-3,7-dimethylbutane 5 were coupled using benzoyl peroxide as the radical initiator.[52,53] MK-1(H_2) 6 was obtained as a yellow powder in a 20% yield (Scheme 1). The menadione/benzoyl peroxide solution was added dropwise over ~2 h to the refluxing prenyl iodide solution to keep the stationary menadione 4 concentration sufficiently low in the reaction to ensure good selectivity of alkylation, favoring alkylation at C3 over C2 (Scheme 1).[52,53]

1D ^{1}H NMR Spectroscopic Studies of MK-1 in Organic Solvents. The synthesis of MK-1 and MK-1(H_2) provided material to investigate if the solvent environment induced chemical shift changes. NMR spectra of MK-1 were collected in various organic solvents ranging from aromatic to non-aromatic and of differing polarity (Figure 2). The most drastic chemical shift change observed for MK-1 was in the aromatic solvents, d_6-benzene and d_5-pyridine, compared to the other solvents in Figure 2. This is seen by focusing on the chemical

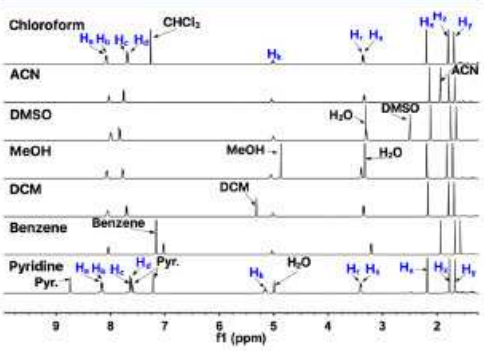

Figure 2. 1D ^{1}H NMR (400 MHz) spectra illustrating chemical shift differences of MK-1 hydrogens between various organic solvent environments. Abbreviations: ACN, d_3-acetonitrile; DMSO, d_6-dimethyl sulfoxide; MeOH, d_4-methanol; DCM, d_2-dichloromethane; Pyr, d_5-pyridine. A structure of MK-1 with a hydrogen labeling scheme key is shown in Figure 3.

DOI: 10.1021/acs.biochem.9b00007
Biochemistry 2019, 58, 1596−1615

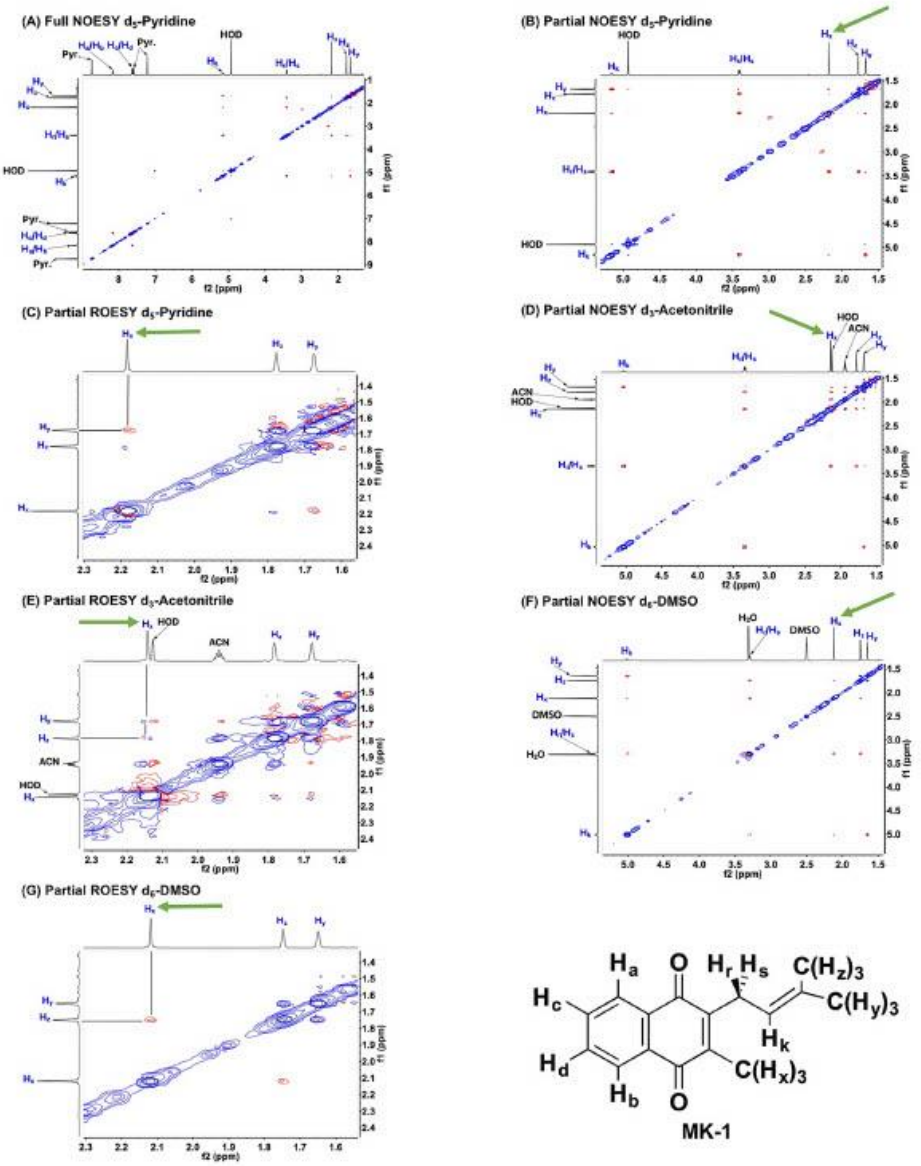

Figure 3. ^{1}H−^{1}H 2D NOESY and ^{1}H−^{1}H 2D ROESY NMR (400 MHz) spectra of 20 mM MK-1 in d_5-pyridine, d_3-acetonitrile (d_3-ACN), and d_6-DMSO at 26 °C. (A) Full ^{1}H−^{1}H 2D NOESY NMR spectrum of MK-1 in d_5-pyridine. (B) Partial ^{1}H−^{1}H 2D NOESY NMR spectrum of MK-1 in d_5-pyridine. (C) Partial ^{1}H−^{1}H 2D ROESY NMR spectrum of MK-1 in d_5-pyridine. (D) Partial ^{1}H−^{1}H 2D NOESY NMR spectrum of MK-1 in d_3-ACN. (E) Partial ^{1}H−^{1}H 2D ROESY NMR spectrum of MK-1 in d_3-ACN. (F) Partial ^{1}H−^{1}H 2D NOESY NMR spectrum of MK-1 in d_6-DMSO. (G) Partial ^{1}H−^{1}H 2D ROESY NMR spectrum of MK-1 in d_6-DMSO. Blue intensity contours represent negative NOEs or ROEs, and red intensity contours represent positive NOEs or ROEs. A standard NOESY pulse sequence consisting of 256 transients with 16 scans in the f1 domain using a 500 ms mixing time and a 1.5 s relaxation delay was used. A standard ROESYAD pulse sequence consisting of 256 transients with 16 scans in the f1 domain using a 400 ms mixing time and a 2.0 s relaxation delay was used. The structure of MK-1 is shown with a hydrogen labeling scheme key. Green arrows indicate hydrogen H_s where the observed cross peaks differed the most between the three solvents studied.

DOI: 10.1021/acs.biochem.9b00007
Biochemistry 2019, 58, 1596−1615

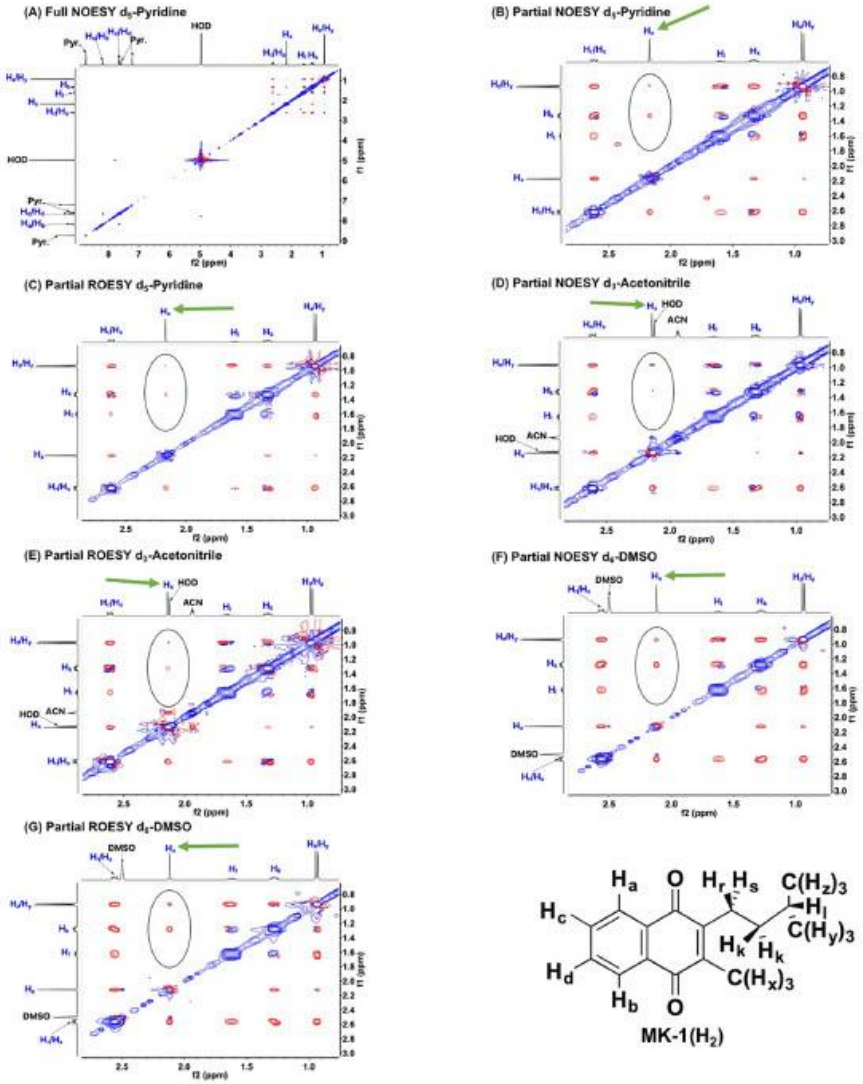

Figure 4. ^{1}H−^{1}H 2D NOESY and ^{1}H−^{1}H 2D ROESY NMR (400 MHz) spectra of 20 mM MK-1(H_2) in d_5-pyridine, d_3-acetonitrile (d_3-ACN), and d_6-DMSO at 26 °C. (A) Full ^{1}H−^{1}H 2D NOESY NMR spectrum of MK-1(H_2) in d_5-pyridine. (B) Partial ^{1}H−^{1}H 2D NOESY NMR spectrum of MK-1(H_2) in d_5-pyridine. (C) Partial ^{1}H−^{1}H 2D ROESY NMR spectrum of MK-1(H_2) in d_5-pyridine. (D) Partial ^{1}H−^{1}H 2D NOESY NMR spectrum of MK-1(H_2) in d_3-ACN. (E) Partial ^{1}H−^{1}H 2D ROESY NMR spectrum of MK-1(H_2) in d_3-ACN. (F) Partial ^{1}H−^{1}H 2D NOESY NMR spectrum of MK-1(H_2) in d_6-DMSO. (G) Partial ^{1}H−^{1}H 2D ROESY NMR spectrum of MK-1(H_2) in d_6-DMSO. Blue intensity contours represent negative NOEs or ROEs, and red intensity contours represent positive NOEs or ROEs. A standard NOESY pulse sequence consisting of 256 transients with 16 scans in the f1 domain using a 500 ms mixing time and a 1.5 s relaxation delay was used. A standard ROESYAD pulse sequence consisting of 256 transients with 16 scans in the f1 domain using a 400 ms mixing time and a 2.0 s relaxation delay was used. The structure of MK-1(H_2) is shown with a hydrogen labeling scheme key. Green arrows indicate hydrogen H_w, where the observed cross peaks differed the most between the two solvents studied, and black ovals highlight the region that changes the most between spectra.

shift differences observed between the MK-1 aromatic hydrogens, H_a/H_b and H_c/H_d. The chemical shift difference is nearly 1 ppm in d_6-benzene compared to 0.2−0.4 ppm in the other solvents. The methylene hydrogens, H_r/H_s and the

DOI: 10.1021/acs.biochem.9b00007
Biochemistry 2019, 58, 1596−1615

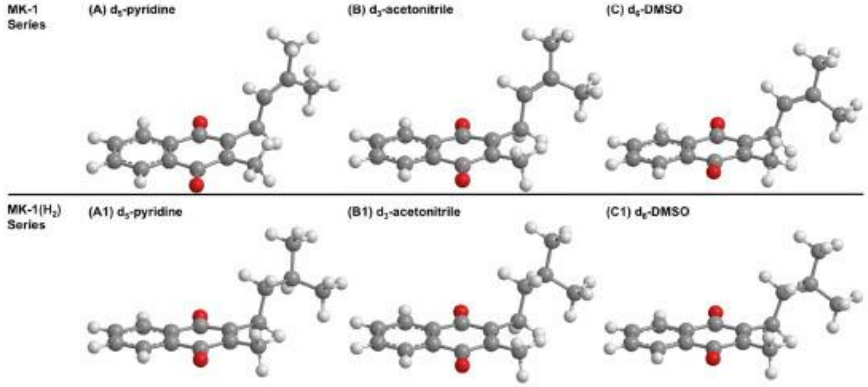

Figure 5. MK-1 and MK-1(H_2) conformations generated using MMFF94 calculations to illustrate the possible conformations consistent with the $^1H-^1H$ 2D NOESY and ROESY NMR spectral studies in which conformations agree with observed cross peak interactions and intensities. MK-1 series: (A) proposed MK-1 conformation in d_5-pyridine determined from $^1H-^1H$ 2D NOESY and ROESY NMR spectral data for cross peak interactions (51.8 kcal/mol; H_x-H_y, 4.3 Å), (B) proposed MK-1 conformation in d_3-ACN determined from $^1H-^1H$ 2D NOESY and ROESY NMR spectral data for cross peak interactions (48.6 kcal/mol; H_x-H_y, 3.9 Å), and (C) proposed MK-1 conformation in d_6-DMSO determined from $^1H-^1H$ 2D NOESY and ROESY NMR spectral data for cross peak interactions (47.3 kcal/mol; H_x-H_y, 3.2 Å). MK-1(H_2) series: (A1) proposed MK-1(H_2) conformation in d_5-pyridine determined from $^1H-^1H$ 2D NOESY and ROESY NMR spectral data for cross peak interactions (42.1 kcal/mol; H_x-H_y, 3.6 Å), (B1) proposed MK-1(H_2) conformation in d_3-ACN determined from $^1H-^1H$ 2D NOESY and ROESY NMR spectral data for cross peak interactions (43.0 kcal/mol; H_x-H_y, 4.0 Å), and (C1) proposed MK-1(H_2) conformation in d_6-DMSO determined from $^1H-^1H$ 2D NOESY and ROESY NMR spectral data for cross peak interactions (41.9 kcal/mol; H_x-H_y, 3.4 Å).

naphthoquinone methyl (H_x) also shift in d_6-benzene compared to the other solvents. Via examination of the chemical shift differences in the spectra in Figure 2, it is clear that MK-1 is influenced by solvent environment, but whether MK-1 adopts different conformations in these organic solvent environments remains unclear.

$^1H-^1H$ 2D NOESY and $^1H-^1H$ 2D ROESY NMR Spectroscopic Studies of MK-1 and MK-1(H_2) in d_5-Pyridine, d_3-Acetonitrile, and d_6-DMSO. The 1D ^1H NMR experiments demonstrated that the solvent environment impacts the chemical environment surrounding MK-1 enough to change the observed chemical shift. However, whether the conformation of MK-1 and MK-1(H_2) changes depending on the solvent environment remained unclear. Therefore, we used two different complementary 2D NMR spectroscopic techniques ($^1H-^1H$ 2D NOESY and $^1H-^1H$ 2D ROESY NMR) to elucidate the conformation of the MK analogues in organic solutions. We present the 2D NMR data for MK-1 in Figure 3, the 2D NMR data for MK-1(H_2) in Figure 4, and the 3D conformations for MK-1 and MK-1(H_2) in Figure 5. We used a semiquantitative approach for the 2D NMR conformational analysis in which NOE/ROE distance intensities are as follows: a strong cross peak intensity is an ~2−3 Å distance, a medium cross peak intensity is an ~3−4 Å distance, and a weak cross peak intensity is a >4 Å distance.[54] We standardized the signal intensities on the basis of the intensity of the H_a-H_c cross peak of MK-1 or MK-1(H_2), which was used as the internal intensity calibrant (the actual distance is 2.5 Å, which indicates a strong cross peak). Figure 3 shows $^1H-^1H$ 2D NOESY and $^1H-^1H$ 2D ROESY NMR spectra of MK-1 in d_5-pyridine, d_3-acetonitrile (d_3-ACN), and d_6-DMSO (see Figures S3−S11 and S16−S24 for full 2D NMR spectra and Figure S26 for ROE/NOE correlation traces). These organic solvents were chosen because they differed sufficiently with regard to shape, polarity, and aromatic versus non-aromatic and are well behaved in electrochemical studies.

The conformation of MK-1 in d_5-pyridine was determined by analyzing the $^1H-^1H$ 2D NOESY and ROESY NMR spectra (Figure 3A−C and Figures S3 and S4). Figure 3B shows a strong NOE cross peak observed between hydrogens $H_{z/s}$ and H_x and a weak NOE cross peak between $H_{z/s}$ and H_y (see the Supporting Information for hydrogen peak assignments of H_x and H_y). Weak NOE/ROE cross peaks are also observed between H_x and H_y (Figure 3B,C), which supports a folded−extended conformation in which the terminal methyl groups orient themselves in a manner to fold upward (C−C bond rotation allows the methyl groups to rotate upward) positioning H_y close enough to H_x to observe a NOE/ROE cross peak. The weak cross peak (same phase as the diagonal) observed between H_x and H_z is likely due to TOCSY exchange. The weak NOE cross peak in Figure 3B between H_x and H_k has an intensity similar to that of the NOE cross peak observed between H_x and H_y, which is not explained by an extended−flat conformation (see Figure S27E and Table S1 for structure and internuclear distances of the MK-1 flat−extended conformation). Together, these observations provide evidence that MK-1 adopts a folded-extended conformation in d_5-pyridine in which the isoprenyl side chain folds upward.

With regard to the conformation of MK-1 in d_3-ACN, panels D and E of Figure 3 (Figures S6 and S7) show a weak NOE/ROE cross peak observed between H_x and H_z and no cross peak observed between H_x and H_y. The cross peak observed is opposite in phase to the diagonal and possibly due to chemical exchange or TOCSY exchange. TOCSY exchange is more likely as are there are no readily exchangeable hydrogens in the molecule. There is a weak NOE cross peak between H_x and H_k that is visible only in the spectrum upon zooming in on lower floors, which is not consistent with an extended−flat

DOI: 10.1021/acs.biochem.9b00007
Biochemistry 2019, 58, 1596−1615

conformation and is different from that observed in d_5-pyridine, indicating slightly different conformations adopted between solvent environments. However, the cross peak intensity between $H_{z/s}$ and H_x or H_y is similar to that in d_5-pyridine. There is also a NOE/ROE cross peak observed between H_y and HOD and between H_y and the solvent, d_3-ACN, and interactions between MK and the solvent were not observed in the 2D NMR spectra of MK-1 in d_5-pyridine or d_6-DMSO. On the basis of observations described above, MK-1 likely adopts a folded−extended conformation in d_3-ACN that differs slightly from the folded−extended conformation in d_5-pyridine.

Finally, the conformation of MK-1 in d_6-DMSO was determined. Panels F and G of Figure 3 (Figures S9 and S10) show a weak NOE cross peak between H_x and H_k and a medium NOE/ROE cross peak between H_x and H_z and with no NOE/ROE cross peak observed between H_x and H_y. This is similar to the cross peaks observed in d_3-ACN, but the H_x to H_z cross peak is stronger in d_6-DMSO, indicating slightly different conformations. These observations would not be explained by a flat−extended conformation, and MK-1 likely adopts a folded−extended conformation in d_6-DMSO more similar to that in d_3-ACN than in d_5-pyridine.

To investigate whether saturation of the alkene in the isoprenyl side chain influences the conformation of MK-1(H_2), ^{1}H−^{1}H 2D NOESY and ^{1}H−^{1}H 2D ROESY NMR spectra were collected in d_5-pyridine, d_3-ACN, and d_6-DMSO (Figure 4). Similar NOE/ROE cross peaks were observed for MK-1(H_2) in d_5-pyridine and MK-1 in d_5-pyridine (Figure 4A−C and Figures S16 and S17). Specifically, a weak NOE/ROE cross peak between H_x and H_x/H_y, a medium NOE/ROE cross peak between H_x and $H_{z/s}$, and a medium NOE/ROE cross peak between $H_{z/s}$ and H_y were observed. There is also no NOE/ROE cross peak observed between H_x and H_k, which further supports a folded−extended conformation. This is suggestive of a similar conformation for MK-1(H_2) and MK-1 in d_5-pyridine, where both adopt a similar folded−extended conformation. Similar NOE/ROE cross peaks were observed for MK-1(H_2) in d_3-ACN and MK-1 in d_3-ACN (Figure 4D,E and Figures S19 and S20). Specifically, the lack of an observable cross peak between H_x and H_x/H_y (compared to a weak NOE/ROE cross peak in the case of MK-1), a medium NOE/ROE cross peak between H_x and $H_{z/s}$, a medium NOE/ROE cross peak between $H_{z/s}$ and H_y, and a very weak NOE/ROE cross peak between H_x and H_k was observed. There is also no NOE/ROE cross peak observed between H_x and H_l. This is suggestive of a similar conformation for MK-1(H_2) and MK-1 in d_3-ACN, where both adopt a similar folded−extended conformation. Comparable NOE/ROE cross peaks were observed for MK-1(H_2) in d_6-DMSO and MK-1 in d_6-DMSO (Figure 4F,G and Figures S22 and S23). For instance, a medium NOE/ROE cross peak between H_x and H_x/H_y, a medium NOE/ROE cross peak between H_x and $H_{z/s}$, a medium NOE/ROE cross peak between $H_{z/s}$ and H_y/H_z, and a medium NOE/ROE cross peak between H_x and H_k were observed. There was also no NOE/ROE cross peak observed between H_x and H_l. This is suggestive of a comparable conformation for MK-1(H_2) and MK-1 in d_6-DMSO, where both adopt a similar folded−extended conformation.

Considering the similar trends in cross peaks and intensities observed for MK-1 and MK-1(H_2) in d_5-pyridine, d_3-ACN, and d_6-DMSO, it appears that saturation does not affect the conformation significantly. The subtle differences observed for MK-1 and MK-1(H_2) in the different organic solvents suggest that slightly different folded−extended conformations are adopted between each of the organic solvents, but MK-1 and MK-1(H_2) have very similar conformations in each solvent. This suggests that there could be a correlation between a preferred conformation in each solvent environment and that a simple change such as saturation of a double bond only slightly influences this preferred conformation. Overall, these truncated MK analogues appear to adopt folded−extended conformations in organic solutions based on the 2D NMR data and the folded−extended conformations differ slightly between solvent environments. However, it is possible that an equilibrium population exists between multiple conformations (e.g., folded and/or nonfolded conformations). The observations from the 2D NMR spectroscopic studies support our first hypothesis that the most fundamental MK-1 analogues adopt folded conformations regardless of the degree of saturation in their isoprenyl side chain.

Illustrating MK-1 and MK-1(H_2) Conformations Using Molecular Mechanics. To clearly show illustrations of MK-1 and MK-1(H_2), conformations were generated on the basis of our interpretation of observed cross peak intensities in the ^{1}H−^{1}H 2D NOESY and ROESY NMR spectral data using a semiquantitative approach. We used molecular mechanics (MM) calculations to illustrate and model these conformations. This allowed us to explore the energy surface of conformations corresponding to MK-1 or MK-1(H_2) in either d_5-pyridine, d_3-ACN, or d_6-DMSO determined from the spectral data and provided a means for a visual comparison between conformations (Figure 5). Specific conformations were generated by constraining internuclear distances consistent with the observed 2D NMR spectral data and then energy optimized to calculate an energy value as well as produce realistic bond lengths and angles.

One of the low-energy conformations generated for MK-1 (Figure 5A; 51.8 kcal/mol; H_x−H_y, 4.3 Å) is consistent with the 2D NOESY/ROESY spectral parameters in d_5-pyridine. A lower-energy conformation for MK-1 (Figure 5B; 48.6 kcal/mol; H_x−H_y, 3.9 Å) is consistent with the 2D NOESY/ROESY spectral parameters in d_3-ACN. A slightly lower-energy conformation for MK-1 (Figure 5C; 47.3 kcal/mol; H_x−H_y, 3.2 Å) is consistent with the 2D NOESY/ROESY spectral parameters in d_6-DMSO. One of the low-energy conformations generated for MK-1(H_2) (Figure 5A1; 42.1 kcal/mol; H_x−H_y, 3.6 Å) is consistent with the NOESY/ROESY spectral parameters in d_5-pyridine. A conformation with a slightly higher energy for MK-1(H_2) (Figure 5B1; 43.0 kcal/mol; H_x−H_y, 4.0 Å) is consistent with the 2D NOESY/ROESY spectral parameters in d_3-ACN. A lower-energy conformation for MK-1(H_2) (Figure 5C1; 41.9 kcal/mol; H_x−H_z, 3.4 Å) is consistent with the 2D NOESY/ROESY spectral parameters in d_6-DMSO. All six of these conformations exhibit folding of the isoprenyl side chain upward out of the quinone plane (Figure 5) and can be described as folded−extended conformations. Each conformation for MK-1(H_2) is very similar to that of MK-1 in each organic solvent environment examined based on 2D NMR studies.

For comparison, conformations seen in panels D and D1 of Figure S27 are the lowest-energy conformations we found for MK-1 or MK-1(H_2), where an extended−flat conformation was subjected to a MM simulation using 10000 iterations followed by an energy minimization, which illustrates that folded conformations are easily reached and energetically

DOI: 10.1021/acs.biochem.9b00007
Biochemistry 2019, 58, 1596−1615

Scheme 2. Illustration of the One-Electron Reduction of the Quinone (Q) of MK-1 to the Semiquinone Radical Anion ($Q^{\bullet-}$) and the Second One-Electron Reduction to the Dianion (Q^{2-})

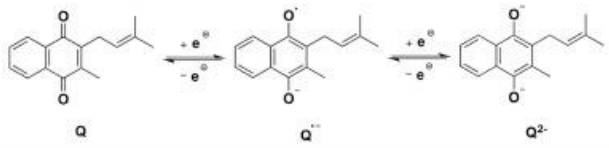

favorable. In addition to the folded conformations shown in Figure 5, a series of alternative flat conformations for MK-1 and MK-1(H_2) (panels E, E1, F, and F1 of Figure S27) were also generated on the basis of what is commonly seen in life science textbooks and literature and then subjected to energy optimization.[12,55,56] These flat−extended conformations are ∼11−20 kcal/mol higher than the lowest-energy conformations of MK-1 and MK-1(H_2). A table of selected internuclear distances for conformations seen in Figure 5 and Figure S27 is given in the Supporting Information.

Importantly, the folded−extended conformations for MK-1 determined in an organic solution closely resemble the folded conformation of the first isoprene unit of MK-2 (containing two isoprene units), which we determined previously in the same organic solvent environments.[37]

Reactivity of MK-1 and MK-1(H_2) in Different Organic Solvents: Electrochemistry. To determine the effect of saturation of the MK isoprenyl side chain on the quinone redox potential, we used cyclic voltammetry to measure the redox potentials of MK-1 and MK-1(H_2). Both MK-1 and MK-1(H_2) have two reversible single-electron redox processes; the first is the quinone to semiquinone ($Q/Q^{\bullet-}$) process, and the second the semiquinone to dianion ($Q^{\bullet-}/Q^{2-}$) process (Scheme 2). The half-wave potentials for each redox process $Q/Q^{\bullet-}$ and $Q^{\bullet-}/Q^{2-}$ in each solvent for MK-1 and MK-1(H_2) are listed in Table S9, and cyclic voltammograms are shown in Figure 6. The electrolyte tetrabutylammonium perchlorate (TBAP) was chosen because of its excellent solubility in all organic solvents. Furthermore, the addition of TBAP to MK-1 solutions in each solvent did not affect the observed chemical shifts of the MK-1 hydrogens, and thus, no evidence of ion pairing or association was found (see Figure S28). The water content of the solvents can affect the semiquinone $Q^{\bullet-}/Q^{2-}$ process as acidic hydrogens influence hydroquinone production, which results in potentials that approach the quinone $Q/Q^{\bullet-}$ half-wave potentials, and therefore, we compared only the first redox process, $Q/Q^{\bullet-}$, in our analyses.[57,58] Thus, it was important that we carried out our electrochemical experiments in anhydrous aprotic organic solvents as this issue is then avoided and organic solvents more closely resemble the native MK environment within a cellular membrane compared to aqueous solutions.

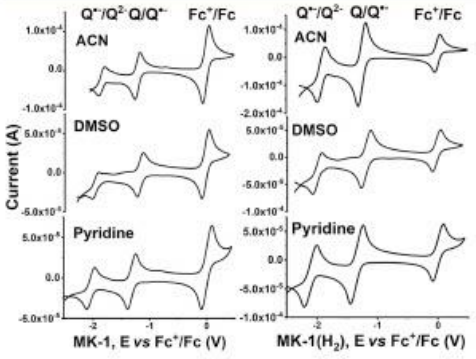

Figure 6. Six cyclic voltammograms of 2 mM MK-1 and MK-1(H_2) in ACN, DMSO, and pyridine. The potentials are referenced to the Fc^+/Fc couple internal standard (2 mM) determined in each solvent. From left to right, redox processes are $Q^{\bullet-}/Q^{2-}$, $Q/Q^{\bullet-}$, and Fc^+/Fc, respectively. Each sample has 0.1 M TBAP and was degassed with argon gas for 10 min at ambient temperature before spectra were recorded. Current sweeps are in the anodic direction from −2 to 1 V and back to −2 V vs Ag/AgCl. A 100 mV/s scan rate was used.

As shown in Figure 6, the ferrocene couple, Fc^+/Fc, was used as an internal reference standard so that the half-wave potentials are set to 0 V versus Fc^+/Fc. The values of $Q/Q^{\bullet-}$ $E_{1/2}$ versus Fc^+/Fc for MK-1 in ACN, DMSO, and pyridine were measured to be −1.227 ± 0.002, −1.158 ± 0.002, and −1.319 ± 0.001 V, respectively. The values of $Q/Q^{\bullet-}$ $E_{1/2}$ versus Fc^+/Fc for MK-1(H_2) in ACN, DMSO, and pyridine were measured to be −1.247 ± 0.007, −1.179 ± 0.002, and −1.343 ± 0.001 V, respectively. The values of $Q/Q^{\bullet-}$ $E_{1/2}$ versus Fc^+/Fc are near those reported for 1,4-naphthoquinone and those previously reported by our group for MK-2.[37,59,60] The values $Q^{\bullet-}/Q^{2-}$ $E_{1/2}$ versus Fc^+/Fc for MK-1 in ACN, DMSO, and pyridine were measured to be −1.882 ± 0.014, −1.949 ± 0.006, and −2.037 ± 0.005 V, respectively. The values of $Q^{\bullet-}/Q^{2-}$ $E_{1/2}$ versus Fc^+/Fc for MK-1(H_2) in ACN, DMSO, and pyridine were measured to be −1.912 ± 0.009, −1.9947 ± 0.0008, and −2.109 ± 0.005 V, respectively. The measured quinone half-wave redox potential differences in these solvents are statistically significant as they are distinctly different from each other at high confidence intervals (see Figure 7 caption and the Supporting Information).

The difference in millivolts between the unsaturated MK-1 and the saturated MK-1(H_2) quinone redox potential in each solvent of the less variable $Q/Q^{\bullet-}$ process is of the same magnitude as ∼20 mV with specific values of 20.033 ± 0.007, 21.333 ± 0.002, and 23.917 ± 0.001 mV for ACN, DMSO, and pyridine, respectively (Figure 7). The $Q/Q^{\bullet-}$ process potentials are less variable as the presence of acidic hydrogens and/or water can create the hydroquinone species, which results in the $Q^{\bullet-}/Q^{2-}$ process coalescing onto the first redox potential. Our previous work with MK-2 demonstrated that the isoprenyl side chain folds over toward the naphthoquinone moiety and that the solvent environment can influence the preferred conformation.[37] The mixing of molecular orbitals (MOs) on the naphthoquinone moiety with the isoprenyl side chain may potentially result in different energies of the electrochemical band gap (or HOMO to LUMO gap) needed

DOI: 10.1021/acs.biochem.9b00007
Biochemistry 2019, 58, 1596−1615

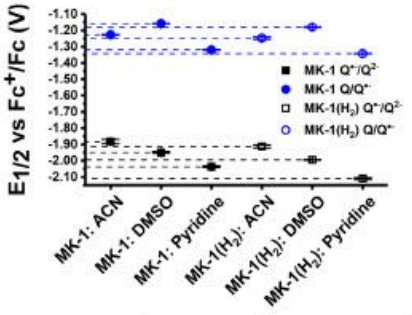

Figure 7. Measured $E_{1/2}$ (vs Fc^+/Fc in volts) of MK-1 and MK-1(H_2) $Q/Q^{\bullet-}$ and $Q^{\bullet-}/Q^{2-}$ redox process vs solvent. Each solvent was run in triplicate, with error bars shown. Added horizontal lines show the distinction between each solvent for each redox process. All solvent comparisons (ACN vs DMSO, etc.) for each redox process half-wave potential for MK-1 or MK-1(H_2) are statistically different with Student's t test confidence intervals of 99.9% ($p < 0.0001$), except for that of the ACN vs DMSO $Q/Q^{\bullet-}$ of MK-1, which was 99.5% ($p < 0.0016$) (four degrees of freedom). Comparisons between MK-1 and MK-1(H_2) half-wave potentials of $Q/Q^{\bullet-}$ and $Q^{\bullet-}/Q^{2-}$ for each solvent were at the 99.9% ($p < 0.0001$) confidence level, except for those of ACN, which were 98% ($p < 0.0089$) and 95% ($p < 0.0355$), respectively (four degrees of freedom). See the Supporting Information for data.

to reduce the quinone carbonyl oxygen to an anionic oxygen radical. The electrochemical band gap is suggestive of the potential observed or the energy required to reduce or oxidize an electrochemical process. This difference in the band gap energy results in unique half-wave potentials as the energy (E) and potential difference (V) are directly proportional as shown clearly by the electrostatic equation $E = VQ$, where Q is charge. The saturation or unsaturation of the isoprenyl side chain can therefore potentially influence these MOs and may alter the quinone redox potential in this manner. The semiquinone redox potential difference of ~20 mV between MK-1 and MK-1(H_2) could indicate the band gap energy difference between the saturated and unsaturated double bond in the one-unit isoprenyl side chain. However, the difference of ~20 mV is most likely due to an indirect effect manifested by a through-bond electronic change by the isoprenyl substituent on the quinone. An indirect substituent effect was used to explain a redox potential change for an N-aromatic substituent on a quinone.[1] The conformational differences in MK-1 between solvents were small, and the short isoprenyl side chain has limited spatial reach toward the naphthoquinone. If such an effect existed between conformation and redox potential, it may not be evident in the one-isoprene unit system. However, suitable high-level computational calculations should be carried out to characterize the HOMO−LUMO gap of this system and determine the exact contributions to the observed ~20 mV difference.

We also observed a trend in the data of the potential difference for the $Q/Q^{\bullet-}$ process as compared by solvent versus degree of saturation (Table S10). For MK-1 and MK-1(H_2), the potential differences in the $Q/Q^{\bullet-}$ process between ACN and DMSO are 69.250 ± 0.003 and 67.950 ± 0.008 mV, respectively. The other solvent comparisons also yield values that agree with each other. For MK-1 and MK-1(H_2), the potential differences in the $Q/Q^{\bullet-}$ process between DMSO and pyridine are 161.050 ± 0.002 and 163.633 ± 0.002 mV, respectively. Similarly, the potential differences of MK-1 and MK-1(H_2) of the $Q/Q^{\bullet-}$ process between ACN and pyridine are 91.800 ± 0.003 and 95.683 ± 0.008 mV, respectively. This conserved difference in the $Q/Q^{\bullet-}$ half-wave potentials between MK-1 and MK-1(H_2) in each solvent may signify that how the isoprenyl side chain folds is truly solvent-dependent and/or may suggest that the conformation of the short isoprenyl side chain (five carbons) of MK-1 has little effect on the observed quinone redox potential in the one-isoprene unit system.

In summary, both MK-1 and MK-1(H_2) during the first electrochemical process producing the semiquinone have the most positive potentials in DMSO and the most negative potentials in pyridine, demonstrating MK-1 or MK-1(H_2) is slightly more reducible in DMSO than in ACN or pyridine. Most remarkably, the observation of an ~20 mV change in quinone $Q/Q^{\bullet-}$ $E_{1/2}$ between MK-1 and MK-1(H_2) supports our second hypothesis that saturation of the isoprenyl side chain of MK-1 affects the observed quinone redox potential. This is the first time that these subtle changes have been demonstrated in a quinone/MK system. The difference is presumably mainly due to a through-bond indirect effect, which results in an electronic perturbation of the quinone system upon saturation of the isoprenyl side chain. There was not a large difference between the MK-1 analogue conformations, and therefore, changes in the observed redox potentials are not likely due to conformational differences. However, a potential correlation should be investigated using the appropriate fully unsaturated and partially saturated MK-2 analogues in combination with computational methods to determine if conformational folding of the second isoprene unit can alter the quinone redox potential in MK analogues with an unsaturated versus a partially saturated isoprenyl side chain.

Interaction of Langmuir Phospholipid Monolayers with MK-1 and MK-1(H_2). To understand the interaction and conformation of fundamental MK analogues within a membrane environment, we focused on characterizing the interaction of the most simple, truncated MK analogues, MK-1 and MK-1(H_2), with model membrane interfaces. Model membrane systems, such as Langmuir phospholipid monolayers, liposomes, micelles, and RM microemulsions, have been used to characterize the interaction and location of probe molecules with membranelike interfaces (Figure 8).[44,61−69] Langmuir phospholipid monolayers and RMs are two complementary model membrane systems that together can be used to characterize the interaction, location, placement, and conformation of MKs within a model membrane interface. Using these two model membrane systems together allowed us to determine whether MK-1 analogues interact with model membrane interfaces and if a folded conformation is adopted within the RM model membrane interface.

Surface-pressure compression isotherm experiments using Langmuir monolayers (Figure 8A) have been useful in characterizing interactions among lipids, lipids and fatty acids,[37,40,70−72] and lipids and hydrophilic molecules.[42,61,70] During a surface-pressure compression isotherm experiment, condensing and expanding effects caused by the presence of another lipid (such as MK) can be observed and changes in phase transitions of the lipids can indicate an interaction between the two lipids. To establish that the two MK

DOI: 10.1021/acs.biochem.9b00007
Biochemistry 2019, 58, 1596−1615

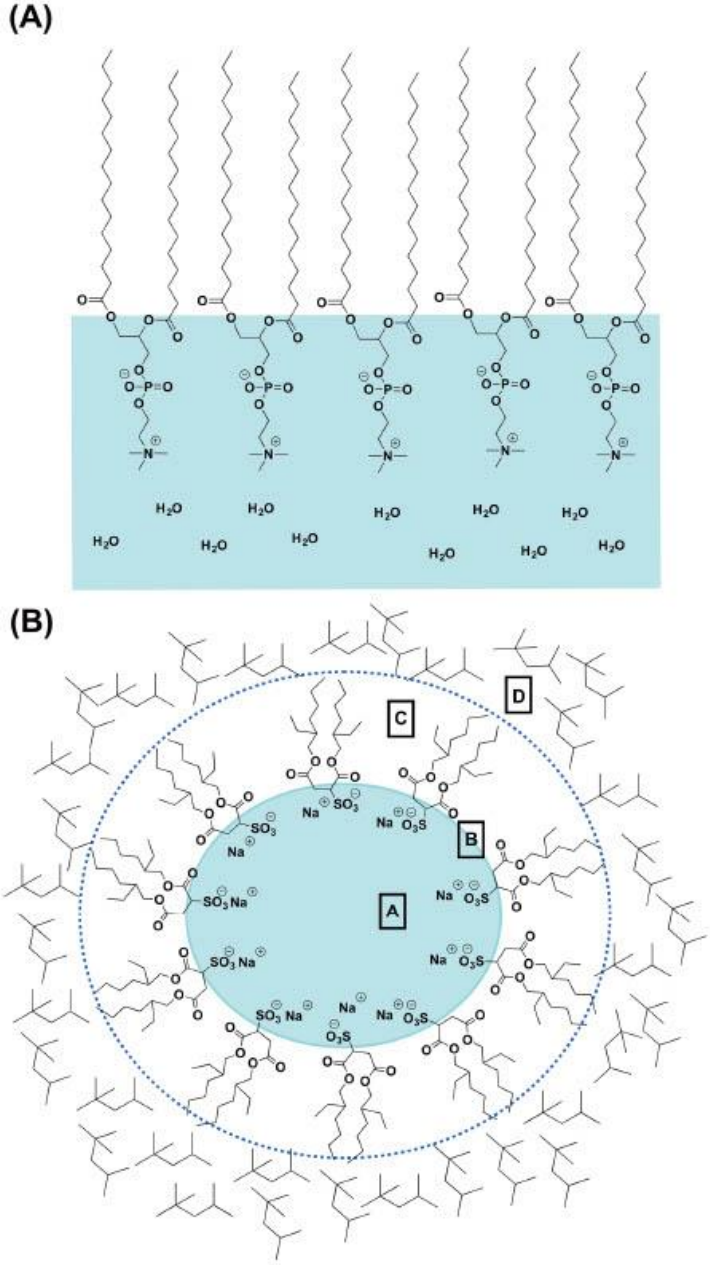

Figure 8. Schematic diagram of (A) a Langmuir phospholipid monolayer (top) and (B) a reverse micelle (bottom) present in a microemulsion with the following labeling: (A) water pool, (B) Stern layer, (C) hydrophobic surfactant tails, and (D) organic solvent isooctane. Adapted with permission from ref 37. Copyright 2018 American Chemical Society.

DOI: 10.1021/acs.biochem.9b00007
Biochemistry 2019, 58, 1596−1615

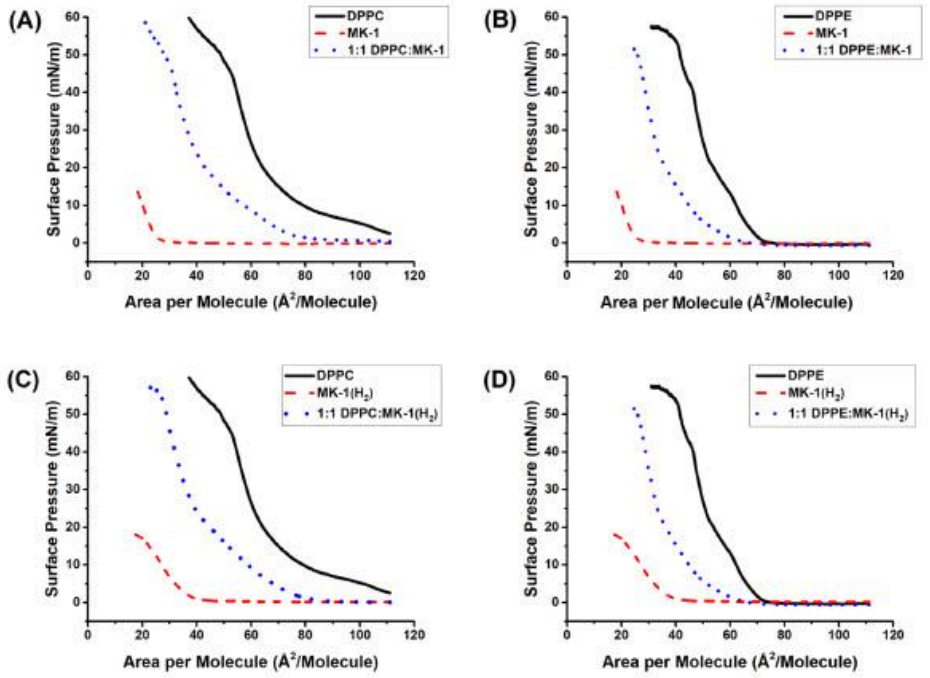

Figure 9. Compression isotherms of MK-1 and MK-1(H_2) films (dashed red lines), DPPC or DPPE phospholipid monolayers (solid black lines), or a 50:50 mixture of MK-1 or MK-1(H_2) and a phospholipid (dotted blue lines): (A) compression isotherms of MK-1 and DPPC, (B) compression isotherms of MK-1 and DPPE, (C) compression isotherms of MK-1(H_2) and DPPC, and (D) compression isotherms of MK-1(H_2) and DPPE.

analogues interact with membrane interfaces, compression isotherms of Langmuir monolayers were used to characterize the interactions of MK-1 and MK-1(H_2) with phospholipid interfaces of common phospholipids found in biological systems such as dipalmitoylphosphatidylcholine (DPPC) or dipalmitoylphosphatidylethanolamine (DPPE).[73−75] Therefore, surface-pressure compression isotherms of Langmuir monolayers consisting of DPPC, DPPE, MK-1, MK-1(H_2), or a mixture of a phospholipid and an MK analogue were performed to determine if the MK analogues had any effect on the packing and compressibility of the phospholipids. The resulting compression isotherms are shown in Figure 9. The control monolayers of DPPC and DPPE are comparable to what has been found in the literature.[40,76] The DPPC monolayers both show a characteristic gas−liquid phase transition at 5 mN/m and collapse at 55 mN/m. The DPPE monolayers also collapsed at 55 mN/m, which aligns well with results in the literature.[40,76]

The MK-1 and MK-1(H_2) pure films were compressed in the same manner as the phospholipid films. Both MK-1 and MK-1(H_2) monolayers did not reach a pressure above 20 mN/m similar to findings reported for ubiquinone-10 (UQ-10) and plastoquinone.[40,71,77] The films were not able to reach a high pressure like other lipoquinones, suggesting that the MK films either slightly soluble in the subphase (similar to UQ-2[40]) as the pressure was increased or aggregation was occurring, which has been shown for lipoquinones with longer isoprenyl side chains.[40,71] Most likely, the MK-1 analogues are aggregating as neither analogue was soluble in D_2O (see 1D ^{1}H NMR RM Spectroscopic Studies).

When the MKs are mixed with DPPC or DPPE phospholipids, differences in phase transitions and compression moduli indicate that an interaction with the MK analogues and phospholipids can be observed. First, the gas to liquid phase transition for DPPC is nonexistent when either MK-1 or MK-1(H_2) is present. This suggests a condensing effect at low pressures. Within all the compression isotherms of the mixed monolayers, a change in slope occurs at ~20 mN/m [similar to the collapse pressure of MK-1 and MK-1(H_2)], which follows the pattern in the literature with the MK analogues being compressed out of the monolayer to the top of the monolayer similar to UQ.[40,71] To determine if the MK-1 analogues still affected the phospholipid monolayers even at higher surface pressures, the compression moduli of each curve are compared in Figure S29 (see the Supporting Information for compression moduli data and interpretation). In each case, the mixed monolayer exhibited a decrease in its compression modulus (easier to compress) than the pure phospholipid monolayers, indicating that the MK analogues affect the phospholipid monolayer throughout compression even at physiologically relevant surface pressures (~30−35 mN/m).[41]

Overall, the MK analogues do not form stable monolayers at high pressures (>20 mM/m) and have a compressing effect on the phospholipid monolayers, and at higher pressures, the MK

DOI: 10.1021/acs.biochem.9b00007
Biochemistry 2019, 58, 1596−1615

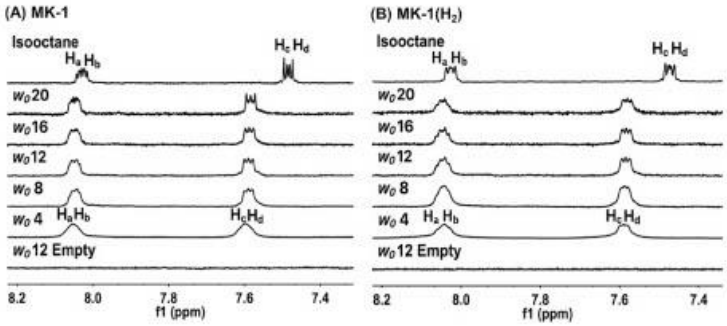

Figure 10. 1D ^{1}H NMR (400 MHz) spectra of (A) MK-1 and (B) MK-1(H_2) aromatic hydrogens H_a, H_b, H_c, and H_d in different sized RMs (w_0 4, 8, 12, 16, and 20) prepared from a 0.50 M AOT/isooctane stock solution. MK-1 or MK-1(H_2) in isooctane is used as a comparison reference spectrum, and w_0 12 Empty is a control spectrum without MK-1 or MK-1(H_2). Peaks are labeled with corresponding hydrogens for MK-1 and MK-1(H_2) (see Figures 3 and 4 for the hydrogen labeling scheme key). Hydrogens, H_a, H_b, H_c, and H_d, undergo a shift upon insertion into the RMs for both MKs. The overall concentrations for the 1.0 mL MK-1 RM samples are as follows: w_0 4, 13.8 mM; w_0 8, 6.5 mM; w_0 12, 3.5 mM; w_0 16, 1.9 mM; w_0 20, 1.3 mM. The overall concentrations for the 1.0 mL MK-1(H_2) RM samples are as follows: w_0 4, 13.8 mM; w_0 8, 6.4 mM; w_0 12, 3.5 mM; w_0 16, 2.0 mM; w_0 20, 1.4 mM.

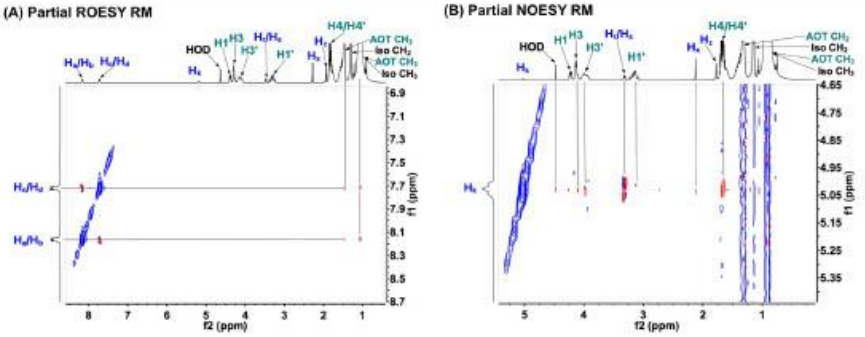

Figure 11. Partial ^{1}H−^{1}H 2D ROESY and ^{1}H−^{1}H 2D NOESY NMR (400 MHz) spectra of MK-1 in a w_0 12 RM. (A) Partial ROESY spectrum illustrating interactions of MK-1 aromatic hydrogens with AOT. (B) Partial NOESY spectrum illustrating interactions of MK-1 H_6 hydrogens with AOT. Blue to blue hydrogen text labeling shows MK-1−MK-1 interactions, and blue to teal hydrogen text labeling shows MK-1−AOT interactions. Blue intensity contours represent negative NOEs or ROEs, and red intensity contours represent positive NOEs or ROEs. See Figure 3 for the MK-1 hydrogen labeling scheme key and Figure 13 for the AOT hydrogen labeling scheme key. A standard NOESY pulse sequence consisting of 256 transients with 16 scans in the f1 domain using a 200 ms mixing time and a 1.5 s relaxation delay was used. A standard ROESYAD pulse sequence consisting of 256 transients with 16 scans in the f1 domain using a 200 ms mixing time and a 2.0 s relaxation delay was used.

analogues most likely are compressed out of the monolayer onto the phospholipid tails similar to previously reported lipoquinones with longer isoprenyl side chains.[37,40,71,77] It is important to note that the Langmuir phospholipid monolayers do not provide evidence of a folded MK conformation due to the nature of the experiment; however, they do demonstrate that MK-1 and MK-1(H_2) interact with the phospholipid model membrane interface even at physiological surface pressures like other quinones, and there was not a large difference observed between the unsaturated and saturated MK-1 analogue.[37,40,71,77]

1D ^{1}H NMR Spectroscopic Studies of MK-1 and MK-1(H_2) in RMs. The studies carried out using Langmuir phospholipid monolayers established that the two MKs interacted with the phospholipid interface. However, the placement, orientation, and conformation of the MK-1 analogues within an interface were still uncertain. Therefore, to fully characterize the location, orientation, and conformation of the MKs within a model membrane interface, we used RMs (Figure 8B), which are ternary microemulsion systems in which the surfactant is dissolved in an organic solvent and the addition of water creates nanosized water droplets encased in the surfactant.[44,64−66,78,79] MK-1 or MK-1(H_2) was placed in RMs of various sizes (w_0 4, 8, 12, 16, and 20; where w_0 = [H_2O]/[AOT]), and then 1D ^{1}H NMR spectra were obtained for each RM size as well as a spectrum in isooctane (2,2,4-trimethylpentane) (Figure 10).

The chemical shift difference between MK-1 aromatic hydrogens, H_a/H_b and H_c/H_d, is greater with a value of 0.55 ppm in isooctane versus that of MK-1 in w_0 20 = 0.47 ppm or w_0 4 = 0.45 ppm RMs, which is diagnostic of a change in the environment surrounding MK-1 (Figure 10). Similarly, the chemical shift difference between MK-1(H_2) aromatic hydrogens, H_a/H_b and H_c/H_d, is greater with a value of 0.56 ppm in

DOI: 10.1021/acs.biochem.9b00007
Biochemistry 2019, 58, 1596−1615

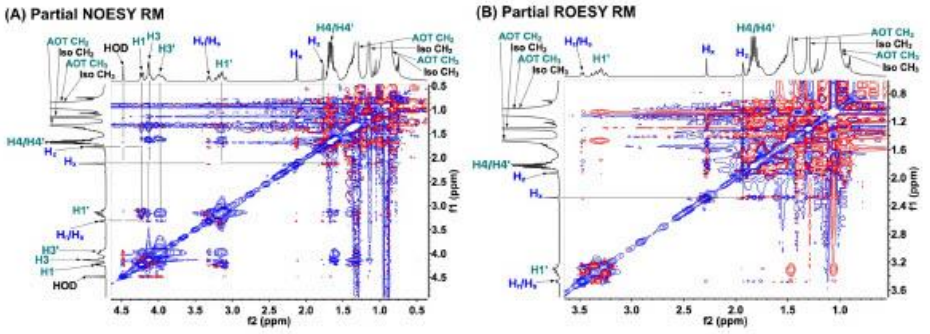

Figure 12. Partial ^{1}H−^{1}H 2D NOESY and ^{1}H−^{1}H 2D ROESY NMR (400 MHz) spectra of MK-1 in a w_0 12 RM. (A) Partial ^{1}H-^{1}H 2D NOESY NMR spectrum in a w_0 12 RM. (B) Partial ^{1}H-^{1}H 2D ROESY NMR spectrum in a w_0 12 RM. Blue to blue hydrogen text labeling shows MK-1−MK-1 interactions, and blue to teal hydrogen text labeling shows MK-1−AOT interactions. Blue intensity contours represent negative NOEs or ROEs, and red intensity contours represent positive NOEs or ROEs. See Figure 3 for the MK-1 hydrogen labeling scheme key and Figure 13 for the AOT hydrogen labeling scheme key. A standard NOESY pulse sequence consisting of 256 transients with 16 scans in the f1 domain using a 200 ms mixing time and a 1.5 s relaxation delay was used. A standard ROESYAD pulse sequence consisting of 256 transients with 16 scans in the f1 domain using a 200 ms mixing time and a 2.0 s relaxation delay was used.

isooctane versus that of MK-1(H_2) in w_0 20 = 0.47 ppm or w_0 4 = 0.45 ppm RMs (Figure 10). The loss of splitting (peak broadening) observed for the aromatic hydrogens as the RM size decreases is attributed to the poorer ability of MK-1 or MK-1(H_2) to tumble freely within the RM interface of smaller sized RMs (e.g., w_0 4). We were unable to obtain a spectrum in D_2O as neither MK was soluble even after extended sonication due to the hydrophobicity of the two MK analogues and it is not likely that either of the MKs are in the water pool due to the very poor water solubility of each compound. Together, the results demonstrated that there was a significant chemical shift difference between the aromatic hydrogens in isooctane and the RMs for both MK-1 analogues. Therefore, we can conclude that neither of the MK-1 analogues are interacting with the isooctane and are residing either at the RM interface or within the AOT alkyl tail region. Furthermore, DLS experiments were carried out and demonstrated that inserting MK-1 or MK-1(H_2) into the RM does not alter the size of the RM or destroy the RMs once inside and the RMs are stable over the course of NMR experiments (see Table S12). Overall, we concluded that MK-1 and MK-1(H_2) interacted with RMs and resided within the RM model membrane interface.

^{1}H−^{1}H 2D NOESY and ^{1}H−^{1}H 2D ROESY NMR Spectroscopic Studies of MK-1 and MK-1(H_2) in a RM Model Membrane System. The 1D ^{1}H NMR spectra of MK-1 and MK-1(H_2) in RMs demonstrated that MK-1 analogues reside within the interface of RMs. However, more information was needed to determine the orientation, position, and conformation while the MK-1 species is residing inside the RM interface. MK-1 was placed inside a w_0 12 RM, and ^{1}H−^{1}H 2D NOESY and ^{1}H−^{1}H 2D ROESY NMR spectra were obtained (Figures 11 and 12 and Figures S12 and S13). NOE/ROE cross peaks between MK-1 and AOT provide evidence for the location, orientation, and conformation within the RM interface. Figure 11A shows ROE cross peaks among all four aromatic hydrogens of MK-1 and the CH_2/CH_3 groups of the AOT alkyl tails. Figure 11B shows cross peaks between MK-1's alkene hydrogen H_k and HOD, H1, H3/H3′, and H4/H4′. Figure 12A also shows cross peaks between hydrogens H_x/H_s and H1, H3, and H3′, which together indicate that MK-1 is located within the RM interface. Panels A and B of Figure 12 show NOE/ROE cross peaks between H_x/H_s and H_z, between H_x and H_z, and between H_x and H1 and H3 and the lack of a cross peak between H_x and H_k, which supports a folded conformation for MK-1 while it is residing in the interface (see Figure S26 for ROE/NOE correlation traces). On the basis of these observations, MK-1 is oriented in a manner in which the naphthoquinone is positioned toward the AOT alkyl tails and the folded isoprenyl side chain is positioned between hydrogens H1/H1′ and H3/H3′ as illustrated in Figure 13. A proposed folded MK-1 conformation that is consistent with the 2D NOESY and ROESY spectral data is illustrated in Figure 14. The phase of the MK-1 to MK-1 cross peaks observed in the NOESY spectrum (Figures 11 and 12) within the RM interface is the opposite phase of the diagonal, indicating MK-1 is behaving as a small molecule within the RM interface and likely tumbling freely but

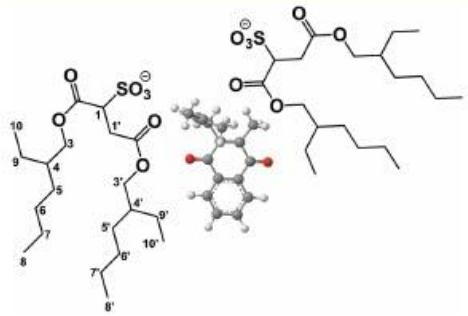

Figure 13. Illustration of the placement and proposed conformation of MK-1 penetrating the RM interface. This arrangement is consistent with the ^{1}H−^{1}H 2D NOESY and ^{1}H−^{1}H 2D ROESY NMR spectral data obtained in a w_0 12 RM. However, MK-1 likely tumbles freely within the interface but maintains interactions with the region of AOT shown in the illustration. The AOT hydrogen labeling scheme key is shown.

DOI: 10.1021/acs.biochem.9b00007
Biochemistry 2019, 58, 1596−1615

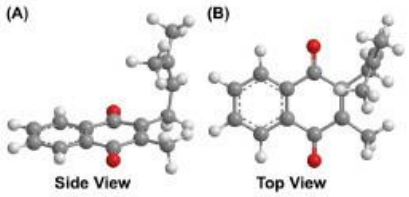

Figure 14. Proposed conformation of MK-1 at an RM interface illustrated using MMFF94 calculations that is consistent with ^{1}H−^{1}H 2D NOESY and ^{1}H−^{1}H 2D ROESY NMR spectral data. (A) Side view of the energy-minimized folded MK-1 conformation (50.3 kcal/mol; H_z−H_x internuclear distance, 2.8 Å). (B) Top view of the energy-minimized proposed MK-1 conformation showing the isoprene methyl groups positioned folded upward.

maintaining interactions with the AOT regions shown in Figure 13.

To determine if saturation of the isoprenyl side chain affects the location and orientation within the RM interface, the same experiment was carried out with MK-1(H_2) (Figure S25). NOE cross peaks are observed between MK-1(H_2) aromatic hydrogens, H_a−H_d, and AOT's CH_2 and CH_3 alkyl tail groups (Figure S25). NOE cross peaks are observed between methylene hydrogens, H_z/H_y, and HOD, H1/H1′, H3/H3′, and H4/H4′. NOE cross peaks are observed between the naphthoquinone methyl, H_w, and HOD, H1/H1′, H3/H3′, and H4/H4′ (Figure S25). The AOT and isooctane hydrogens overlapped with MK-1(H_2)'s terminal methyl hydrogens, H_z and H_y, and the methine hydrogen, H_y, signals in the spectrum for MK-1(H_2) within the RM interface; therefore, we were unable to determine the conformation of MK-1(H_2) within the interface with confidence. Despite this, we would anticipate that MK-1(H_2) adopts a folded conformation similar to that of MK-1 within the RM interface based on similar interactions observed in the 1D and 2D NMR experiments carried out for MK-1. Together, these observations demonstrate that MK-1(H_2) interacted with the interface and has a position and orientation similar to those of MK-1, indicating that saturation of the isoprenyl side chain does induce an observable change in the position and orientation within the RM interface.

Overall, the ^{1}H−^{1}H 2D NOESY and ROESY NMR spectral data of MK-1 inside an RM interface are consistent with MK-1 adopting a folded conformation within an RM model membrane interface. Interestingly, the conformation of MK-1 inside the RM interface remains folded but differs slightly from the folded conformations observed in organic solutions. The observation that MK-1 adopts a folded conformation within the RM model membrane interface is important as understanding the conformational preferences of the first isoprene unit of MK will be crucial in determining and understanding conformations of the naturally occurring longer MK analogues within cellular membranes.

■ CONCLUSIONS

Lipoquinones such as MK, are special types of lipid-quinones and are essential components of the ETS. Partial saturation of MK in these biological systems is necessary for some organisms to survive such as pathogenic *M. tuberculosis*.[7,8,11] The rationale for the observation of partially saturated MK derivatives in various organisms remains unclear. It is intriguing as the double bonds present in the isoprenyl side chain of MK are not conjugated with each other or to the redox active quinone system and therefore would not be expected to affect the redox potential. Interestingly, we recently showed that MK-2 adopts a folded conformation in which the double bond in the second isoprene unit is in the proximity of the quinone carbonyl groups on the naphthoquinone and may potentially have an influence on the reactivity of the quinone.[37] The studies described herein improve our understanding of the chemical, conformational, and biochemical properties on an important class of quinone-containing compounds involved in electron transfer processes. The partially saturated MKs represent an unrecognized group of biologically significant molecules that are essential for pathogenic taxonomic classification.

In this work, we first demonstrated using a semiquantitative 2D NMR spectroscopy approach that the two simplest, most fundamental MK analogues, unsaturated MK-1 and saturated MK-1(H_2), adopt similar folded−extended conformations in each organic solvent but differ slightly between each organic solvent environment. We also observed that the degree of saturation in the isoprenyl side chain of MK-1 only slightly alters the conformation. Importantly, the conformations observed for MK-1 closely resembled the conformation of the first isoprene unit in MK-2, which we previously showed adopted folded conformations in solution and within a model membrane interface.[37] Together, these results support the first hypothesis that MK-1 analogues adopt folded conformations regardless of the degree of saturation in their isoprenyl side chain.

The quinone redox potentials of MK-1 and MK-1(H_2) were measured in various anhydrous organic solvent environments. The organic solvent environments studied more closely resemble the environment of the cellular membrane in which native MKs are located and serve as better comparisons for biological reactivity than those carried out in aqueous solutions. We demonstrated that the measured quinone redox potentials of MK-1 and MK-1(H_2) varied with the solvent environment (presumably mainly due to differences in dielectric constants) where the ease of quinone reduction for the $Q/Q^{\bullet-}$ process follows the trend DMSO > ACN > pyridine. Remarkably, we report for the first time that the degree of saturation in the isoprenyl side chain of MK-1 influences the observed quinone redox potential, where unsaturation in the isoprenyl side chain of MK-1 makes the quinone easier to reduce by ~20 mV and the difference is conserved across several organic solvents (pyridine, ACN, and DMSO). The observed ~20 mV redox potential difference is presumably due mostly to a perturbation of the electronics of the quinone system upon saturation of the double bond by an indirect through-bond effect. The observation of a 20 mV difference in the redox potential between the two MK-1 derivatives with a saturated and unsaturated isoprenyl side chain observed in three different solvents is unexpected and may reflect some important general reactivity pattern of this system. We speculate that if such a difference is also observed for the MKs with longer isoprenyl side chains that it may reflect the biological function of these molecules and provide evidence for the possibility that such a small difference in redox potential may be biologically significant. However, in the simple MK-1 system containing one isoprene unit, the side chain may not have the spatial reach needed present in the MK-9 system, and therefore, more data are needed to properly evaluate the longer MK derivatives. The electrochemical results

DOI: 10.1021/acs.biochem.9b00007
Biochemistry 2019, 58, 1596−1615

confirm our second hypothesis that saturation of the isoprenyl side chain of MK-1 affects the observed quinone redox potential.

Finally, combining results, we found MK-1 and MK-1(H_2) both interacted with Langmuir phospholipid monolayers and RM model membrane interfaces, where MK-1 and MK-1(H_2) had very similar interactions with the Langmuir phospholipid monolayers (DPPC and DPPE phospholipids) and similar placement and location within the RM interface. Importantly, MK-1 also adopted a folded conformation within the RM model membrane interface, further supporting our first hypothesis. The results combined from all the conformational analysis studies presented herein for MK-1 and MK-1(H_2) indicated a folded−extended conformation to be a favorable and stable conformation for MK-1 analogues. Altogether, these results are significant as the conformation and reactivity of these MKs in organic solution and model membrane interfaces provide a first prediction/consideration of the form that exists within the native hydrophobic cellular membrane interface.

Overall, the findings of this study improve our understanding of how the conformation and the degree of saturation in the isoprenyl side chain affect the reactivity and function of biologically relevant molecules. The elucidation of the conformation of MK-1 and MK-1(H_2) in organic solutions and at a model membrane interface is essential and necessary as understanding the conformational preferences of the first isoprene unit of MK is useful for predicting the conformations of the naturally occurring longer MK analogues within solution and cellular membranes. We observed that partial saturation in the isoprenyl side chain only minimally alters the conformation of MK-1 but may potentially affect the reactivity and function within biologically relevant environments because a difference in the redox potential is observed. MK analogues with longer isoprenyl side chains (e.g., MK-9) may also adopt folded conformations, although likely much more complex. Saturation of the double bond in the first isoprene unit of the isoprenyl side chain serves to only minimally alter the preferred conformation but distinctly affects the redox function. The results presented here provide a working model involving the role of structure and redox potential that explains why partial saturation of MK is a virulence factor for pathogenic *M. tuberculosis*, which is responsible for the deaths of ~1.3 million people annually.[7,8,80]

■ ASSOCIATED CONTENT

Supporting Information

The Supporting Information is available free of charge on the ACS Publications website at DOI: 10.1021/acs.biochem.9b00007.

General experimental information, 1D and 2D NMR spectroscopic and structural data for MK-1 and MK-1(H_2), MK-1 and MK-1(H_2) conformations and conformational analysis and tables of relevant internuclear hydrogen distances, energies, and Cartesian coordinates, electrochemistry methods and data and discussion, ^{1}H NMR spectra of MK-1 with TBAP, Langmuir monolayer compression moduli of MK-1 and MK-1(H_2) and interpretation, and DLS data and interpretation (PDF)

■ AUTHOR INFORMATION

Corresponding Author

*E-mail: Debbie.Crans@colostate.edu.

ORCID

Jordan T. Koehn: 0000-0003-3008-6303
Benjamin J. Peters: 0000-0002-6219-4897
Cameron Van Cleave: 0000-0002-0924-1738
Dean C. Crick: 0000-0001-9281-7058
Debbie C. Crans: 0000-0001-7792-3450

Funding

D. C. Crans and D. C. Crick thank the National Institutes of Health (Grant AI119567) and the National Science Foundation (Grant CHE-1709564) for funding. D. C. Crans also thanks the Arthur Cope Foundation administered by the American Chemical Society for partial support.

Notes

The authors declare no competing financial interest.

■ ACKNOWLEDGMENTS

The authors thank Dr. Christopher Rithner for assistance with NMR spectroscopy and Taylor Lucia and Lining Yang for early contributions to this project.

■ REFERENCES

(1) Aguilar-Martínez, M., Macías-Ruvalcaba, N. A., Bautista-Martínez, J. A., Gómez, M., González, F. J., and González, I. (2004) Review: Hydrogen Bond and Protonation as Modifying Factors of the Quinone Reactivity. *Curr. Org. Chem. 8*, 1721−1738.

(2) Astudillo-Sánchez, P. D., Morales-Martínez, D., Sánchez, A., Rocha-Ortiz, G., and Salas-Reyes, M. (2017) Electrochemical Study of the Interactions Between Anionic Species of Menadione and Alkylated Nucleobases in Dimethylsulfoxide. *J. Electroanal. Chem. 801*, 104−113.

(3) Gunner, M. R., Madeo, J., and Zhu, Z. (2008) Modification of Quinone Electrochemistry by the Proteins in the Biological Electron Transfer Chains: Examples from Photosynthetic Reaction Centers. *J. Bioenerg. Biomembr. 40* (5), 509−519.

(4) Monks, T. J., Hanzlik, R. P., Cohen, G. M., Ross, D., and Graham, D. G. (1992) Quinone Chemistry and Toxicity. *Toxicol. Appl. Pharmacol. 112* (1), 2−16.

(5) Abraham, I., Joshi, R., Pardasani, P., and Pardasani, R. T. (2011) Recent Advances in 1,4-Benzoquinone Chemistry. *J. Braz. Chem. Soc. 22* (3), 385−421.

(6) Nowicka, B., and Kruk, J. (2010) Occurrence, Biosynthesis and Function of Isoprenoid Quinones. *Biochim. Biophys. Acta, Bioenerg. 1797*, 1587−1605.

(7) Upadhyay, A., Fontes, F. L., Gonzalez-Juarrero, M., McNeil, M. R., Crans, D. C., Jackson, M., and Crick, D. C. (2015) Partial Saturation of Menaquinone in *Mycobacterium tuberculosis*: Function and Essentiality of a Novel Reductase, MenJ. *ACS Cent. Sci. 1* (6), 292−302.

(8) Upadhyay, A., Kumar, S., Rooker, S. A., Koehn, J. T., Crans, D. C., McNeil, M. R., Lott, J. S., and Crick, D. C. (2018) Mycobacterial MenJ: An Oxidoreductase Involved in Menaquinone Biosynthesis. *ACS Chem. Biol. 13*, 2498−2507.

(9) da Costa, M. S., Albuquerque, L., Nobre, M. F., and Wait, R. (2011) The Extraction and Identification of Respiratory Lipoquinones of Prokaryotes and Their Use in Taxonomy. In *Methods in Microbiology, Vol 38: Taxonomy of Prokaryotes* (Rainey, F., and Oren, A., Eds.) Vol. *38*, pp 197−206, Elsevier Academic Press Inc., San Diego.

(10) Kroppenstedt, R. M., and Mannheim, W. (1989) Lipoquinones in Members of the Family Pasteurellaceae. *Int. J. Syst. Bacteriol. 39* (3), 304−308.

DOI: 10.1021/acs.biochem.9b00007
Biochemistry 2019, 58, 1596−1615

(11) Collins, M. D., and Jones, D. (1981) Distribution of Isoprenoid Quinone Structural Types in Bacteria and Their Taxonomic Implications. *Microbiol. Rev. 45* (2), 316−354.
(12) Meganathan, R. (2001) Biosynthesis of Menaquinone (Vitamin K_2) and Ubiquinone (Coenzyme Q): A Perspective on Enzymatic Mechanisms. *Vitam. Horm. 61*, 173−218.
(13) Jarchow-Choy, S. K., Koppisch, A. T., and Fox, D. T. (2014) Synthetic Routes to Methylerythritol Phosphate Pathway Intermediates and Downstream Isoprenoids. *Curr. Org. Chem. 18*, 1050−1072.
(14) Collins, M. D., Shah, H. N., and Minnikin, D. E. (1980) A Note on the Separation of Natural Mixtures of Bacterial Menaquinones Using Reverse-phase Thin-layer Chromatography. *J. Appl. Bacteriol. 48* (2), 277−282.
(15) Thomson, R. H. (1971) *Naturally Occurring Quinones*, Academic Press Inc.
(16) Kurosu, M., and Begari, E. (2010) Vitamin K_2 in Electron Transport System: Are Enzymes Involved in Vitamin K_2 Biosynthesis Promising Drug Targets? *Molecules 15* (3), 1531−1553.
(17) Nakagawa, K., Hirota, Y., Sawada, N., Yuge, N., Watanabe, M., Uchino, Y., Okuda, N., Shimomura, Y., Suhara, Y., and Okano, T. (2010) Identification of UBIAD1 as a Novel Human Menaquinone-4 Biosynthetic Enzyme. *Nature 468*, 117−121.
(18) Vos, M., Esposito, G., Edirisinghe, J. N., Vilain, S., Haddad, D. M., Slabbaert, J. R., Van Meensel, S., Schaap, O., De Strooper, B., Meganathan, R., Morais, V. A., and Verstreken, P. (2012) Vitamin K_2 Is a Mitochondrial Electron Carrier That Rescues Pink1 Deficiency. *Science 336*, 1306−1310.
(19) Josey, B. J., Inks, E. S., Wen, X., and Chou, C. J. (2013) Structure−Activity Relationship Study of Vitamin K Derivatives Yields Highly Potent Neuroprotective Agents. *J. Med. Chem. 56*, 1007−1022.
(20) Rahn, J. J., Bestman, J. E., Josey, B. J., Inks, E. S., Stackley, K. D., Rogers, C. E., Chou, C. J., and Chan, S. S. L. (2014) Novel Vitamin K Analogs Suppress Seizures in Zebrafish and Mouse Models of Epilepsy. *Neuroscience 259*, 142−154.
(21) Chadar, D., Camilles, M., Patil, R., Khan, A., Weyhermuller, T., and Salunke-Gawali, S. (2015) Synthesis and Characterization of *n*-alkylamino Derivatives of Vitamin K3: Molecular Structure of 2-propylamino-3-methyl-1,4-naphthoquinone and Antibacterial Activities. *J. Mol. Struct. 1086*, 179−189.
(22) Kathawate, L., Joshi, P. V., Dash, T. K., Pal, S., Nikalje, M., Weyhermuller, T., Puranik, V. G., Konkimalla, V. B., and Salunke-Gawali, S. (2014) Reaction Between Lawsone and Aminophenol Derivatives: Synthesis, Characterization, Molecular Structures and Antiproliferative Activity. *J. Mol. Struct. 1075*, 397−405.
(23) Klauda, J. B., Brooks, B. R., MacKerell, A. D., Venable, R. M., and Pastor, R. W. (2005) An Ab Initio Study on the Torsional Surface of Alkanes and Its Effect on Molecular Simulations of Alkanes and a DPPC Bilayer. *J. Phys. Chem. B 109*, 5300−5311.
(24) Woodward, R. B., and Bloch, K. (1953) The Cyclization of Squalene in Cholesterol Synthesis. *J. Am. Chem. Soc. 75*, 2023−2024.
(25) Chum, S. P., Knight, G. W., Ruiz, J. M., and Phillips, P. J. (1994) Computer Modeling of {110} Adjacent Reentry of Polyethylene Molecules. *Macromolecules 27*, 656−659.
(26) Robertson, M. B., Klein, P. G., Ward, I. M., and Packer, K. J. (2001) NMR Study of the Energy Difference and Population of the *gauche* and *trans* Conformations in Solid Polyethylene. *Polymer 42*, 1261−1264.
(27) Nikki, K., Inakura, H., Wu-Le, Suzuki, N., and Endo, T. (2001) Remarkable Changes in Conformations of *n*-alkanes with thier Carbon Numbers and Aromatic Solvents. *J. Chem. Soc., Perkin Trans. 2*, 2370−2373.
(28) Nikki, K., and Nakagawa, N. (1983) Elucidation of the Structure of Alkane Chains in Solution by Means of ^{1}H NMR. *Org. Magn. Reson. 21* (9), 552−554.
(29) Nikki, K. (1990) ^{1}H and ^{13}C NMR Aromatic Solvent-induced Shifts of *n*-alkanes. *Magn. Reson. Chem. 28* (5), 385−388.
(30) Schramm, M. P., and Rebek, J., Jr. (2006) Moving Targets: Recognition of Alkyl Groups. *Chem. - Eur. J. 12*, 5924−5933.
(31) Choudhury, R., Barman, A., Prabhakar, R., and Ramamurthy, V. (2013) Hydrocarbons Depending on the Chain Length and Head Group Adopt Different Conformations within a Water-Soluble Nanocapsule: ^{1}H NMR and Molecular Dynamics Studies. *J. Phys. Chem. B 117*, 398−407.
(32) Ko, Y. H., Kim, Y., Kim, H., and Kim, K. (2011) U-Shaped Conformation of Alkyl Chains Bound to a Synthetic Receptor Cucurbit[8]uril. *Chem. - Asian J. 6*, 652−657.
(33) Ko, Y. H., Kim, H., Kim, Y., and Kim, K. (2008) U-Shaped Conformation of Alkyl Chain Bound to a Synthetic Host. *Angew. Chem., Int. Ed. 47*, 4106−4109.
(34) Zakharov, A. V., and Vogt, N. (2011) Conformational Analysis of Vitamin K_1 Model Molecule: A Theoretical Study. *Struct. Chem. 22* (2), 305−311.
(35) Tynkkynen, T., Hassinen, T., Tiainen, M., Soininen, P., and Laatikainen, R. (2012) ^{1}H NMR Spectral Analysis and Conformational Behavior of *n*-alkanes in Different Chemical. *Magn. Reson. Chem. 50*, 598−607.
(36) Ishihara, M., and Sakagami, H. (2007) QSAR of Molecular Structure and Cytotoxic Activity of Vitamin K_3 Derivatives with Concept of Absolute Hardness. *Anticancer Res. 27*, 4059−4063.
(37) Koehn, J. T., Magallanes, E. S., Peters, B. J., Beuning, C. N., Haase, A. A., Zhu, M. J., Rithner, C. D., Crick, D. C., and Crans, D. C. (2018) A Synthetic Isoprenoid Lipoquinone, Menaquinone-2, Adopts a Folded Conformation in Solution and at a Model Membrane Interface. *J. Org. Chem. 83*, 275−288.
(38) Stahla, M. L., Baruah, B., James, D. M., Johnson, M. D., Levinger, N. E., and Crans, D. C. (2008) ^{1}H NMR Studies of Aerosol-OT Reverse Micelles with Alkali and Magnesium Counterions: Preparation and Analysis of MAOTs. *Langmuir 24* (12), 6027−6035.
(39) Samart, N., Beuning, C. N., Haller, K. J., Rithner, C. D., and Crans, D. C. (2014) Interaction of a Biguanide Compound with Membrane Model Interface Systems: Probing the Properties of Antimalaria and Antidiabetic Compounds. *Langmuir 30* (29), 8697−8706.
(40) Quinn, P. J., and Esfahani, M. A. (1980) Ubiquinones have Surface-Active Properties Suited to Transport Electrons and Protons Across Membranes. *Biochem. J. 185*, 715−722.
(41) Jones, M. N., and Chapman, D. (1995) *Micelles, Monolayers, and Biomembranes*, Wiley-Liss, New York.
(42) Peters, B. J., Groninger, A. S., Fontes, F. L., Crick, D. C., and Crans, D. C. (2016) Differences in Interactions of Benzoic Acid and Benzoate with Interfaces. *Langmuir 32* (37), 9451−9459.
(43) Peters, B. J., Van Cleave, C., Haase, A. A., Hough, J. P. B., Giffen-Kent, K. A., Cardiff, G. M., Sostarecz, A. G., Crick, D. C., and Crans, D. C. (2018) Structure Dependence of Pyridine and Benzene Derivatives on Interactions with Model Membranes. *Langmuir 34*, 8939−8951.
(44) Maitra, A. (1984) Determination of Size Parameters of Water-aerosol-OT Oil Reverse Micelles From Their Nuclear Magnetic-resonance Data. *J. Phys. Chem. 88* (21), 5122−5125.
(45) Hagiwara, E., Hatanaka, Y., Gohda, K.-i., and Hiyama, T. (1995) Allylation of Quinones with Allyl(trifluoro)silanes: Direct Synthesis of Isoprenoid Quinones. *Tetrahedron Lett. 36* (16), 2773−2776.
(46) Mal, D., Ghosh, K., and Jana, S. (2015) Synthesis of Vitamin K and Related Naphthoquinones via Demethoxycarbonylative Annulations and a Retro-Wittig Rearrangement. *Org. Lett. 17*, 5800−5803.
(47) Teitelbaum, A. M., Scian, M., Nelson, W. L., and Rettie, A. E. (2015) Efficient Syntheses of Vitamin K Chain-Shortened Acid Metabolites. *Synthesis 47*, 944−948.
(48) Yamago, S., Hashidume, M., and Yoshida, J.-i. (2002) A New Synthetic Route to Substituted Quinones by Radical-mediated Coupling of Organotellurium Compounds with Quinones. *Tetrahedron 58*, 6805−6813.
(49) Daines, A. M., Payne, R. J., Humphries, M. E., and Abell, A. D. (2003) The Synthesis of Naturally Occurring Vitamin K and Vitamin K Analogues. *Curr. Org. Chem. 7*, 1625−1634.

DOI: 10.1021/acs.biochem.9b00007
Biochemistry 2019, 58, 1596−1615

(50) Payne, R. J., Daines, A. M., Clark, B. M., and Abell, A. D. (2004) Synthesis and Protein Conjugation Studies of Vitamin K Analogues. *Bioorg. Med. Chem.* 12 (22), 5785−5791.
(51) Suhara, Y., Wada, A., Tachibana, Y., Watanabe, M., Nakamura, K., Nakagawa, K., and Okano, T. (2010) Structure-activity Relationships in the Conversion of Vitamin K Analogues into Menaquinone-4. Substrates Essential to the Synthesis of Menaquinone-4 in Cultured Human Cell Lines. *Bioorg. Med. Chem.* 18 (9), 3116−3124.
(52) Coppa, F., Fontana, F., Minisci, F., Nogueira Barbosa, M. C., and Vismara, E. (1991) Homolytic Alkylation of Naphthoquinone and Methyl-naphthoquinone. Enthalpic, Steric and Polar Effects. *Tetrahedron* 47 (35), 7343−7352.
(53) Koehn, J. T., Crick, D. C., and Crans, D. C. (2018) Synthesis and Characterization of Partially and Fully Saturated Menaquinone Derivatives. *ACS Omega* 3, 14889−14901.
(54) Jones, C. R., Butts, C. P., and Harvey, J. N. (2011) Accuracy in Determining Interproton Distances using Nuclear Overhauser Effect Data from a Flexible Molecule. *Beilstein J. Org. Chem.* 7, 145−150.
(55) Cooper, G. M., and Hausman, R. E. (2009) *The Cell: A Molecular Approach*, 5th ed., p 820, Sinauer Associates, Inc., Sunderland, MA.
(56) Nelson, D. L., and Cox, M. M. (2008) *Lehninger Principles of Biochemistry*, 5th ed., p 1158, W. H. Freeman and Co., New York.
(57) Dryhurst, G., Kadish, K. M., Scheller, F., and Renneberg, R. (1982) *Biological Eletrochemistry*, Academic Press, New York.
(58) Wawzonek, S., Berkey, R., Blaha, E. W., and Runner, M. E. (1956) Polarographic Studies in Acetonitrile and Dimethylformamide: III. Behavior of Quinones and Hydroquinones. *J. Electrochem. Soc.* 103 (8), 456−459.
(59) Jaworski, J. S., Leniewska, E., and Kalinowski, M. K. (1979) Solvent Effect on the Redox Potential of Quinone-semiquinone Systems. *J. Electroanal. Chem. Interfacial Electrochem.* 105 (2), 329−334.
(60) Prince, R. C., Leslie Dutton, P., and Malcolm Bruce, J. (1983) Electrochemistry of Ubiquinones. *FEBS Lett.* 160 (1), 273−276.
(61) Sostarecz, A. G., Gaidamauskas, E., Distin, S., Bonetti, S. J., Levinger, N. E., and Crans, D. C. (2014) Correlation of Insulin-Enhancing Properties of Vanadium-Dipicolinate Complexes in Model Membrane Systems: Phospholipid Langmuir Monolayers and AOT Reverse Micelles. *Chem. - Eur. J.* 20 (17), 5149−5159.
(62) Riter, R. E., Kimmel, J. R., Undiks, E. P., and Levinger, N. E. (1997) Novel Reverse Micelles Partitioning Nonaqueous Polar Solvents in a Hydrocarbon Continuous Phase. *J. Phys. Chem. B* 101 (41), 8292−8297.
(63) Durantini, A. M., Falcone, R. D., Silber, J. J., and Correa, N. M. (2016) Effect of Confinement on the Properties of Sequestered Mixed Polar Solvents: Enzymatic Catalysis in Nonaqueous 1,4-Bis-2-ethylhexylsulfosuccinate Reverse Micelles. *ChemPhysChem* 17 (11), 1678−1685.
(64) Lepori, C. M. O., Correa, N. M., Silber, J. J., and Falcone, R. D. (2016) How the Cation 1-butyl-3-methylimidazolium Impacts the Interaction Between the Entrapped Water and the Reverse Micelle Interface Created with an Ionic Liquid-like Surfactant. *Soft Matter* 12 (3), 830−844.
(65) Baruah, B., Roden, J. M., Sedgwick, M., Correa, N. M., Crans, D. C., and Levinger, N. E. (2006) When Is Water Not Water? Exploring Water Confined in Large Reverse Micelles Using a Highly Charged Inorganic Molecular Probe. *J. Am. Chem. Soc.* 128, 12758−12765.
(66) Odella, E., Falcone, R. D., Silber, J. J., and Correa, N. M. (2016) Nanoscale Control Over Interfacial Properties in Mixed Reverse Micelles Formulated by Using Sodium 1,4-bis-2-ethylhexylsulfosuccinate and Tri-n-octyl Phosphine Oxide Surfactants. *ChemPhysChem* 17 (15), 2407−2414.
(67) Diaz-Fernandez, Y., Foti, F., Mangano, C., Pallavicini, P., Patroni, S., Perez-Gramatges, A., and Rodriguez-Calvo, S. (2006) Micelles for the Self-Assembly of "Off−On−Off" Fluorescent Sensors for pH Windows. *Chem. - Eur. J.* 12, 921−930.
(68) Pallavicini, P., Diaz-Fernandez, Y., and Pasotti, L. (2009) Micelles as Nanosized Containers for the Self-assembly of Multicomponent Fluorescent Sensors. *Coord. Chem. Rev.* 253, 2226−2240.
(69) Stefaniu, C., Brezesinski, G., and Mohwald, H. (2014) Langmuir Monolayers as Models to Study Processes at Membrane Surfaces. *Adv. Colloid Interface Sci.* 208, 197−213.
(70) Choi, Y., Attwood, S. J., Hoopes, M. I., Drolle, E., Karttunen, M., and Leonenko, Z. (2014) Melatonin Directly Interacts with Cholesterol and Alleviates Cholesterol Effects in Dipalmitoylphosphatidylcholine Monolayers. *Soft Matter* 10, 206−213.
(71) Hoyo, J., Torrent-Burgues, J., and Guaus, E. (2012) Biomimetic Monolayer Films of Monogalactosyldiacylglycerol Incorporating Ubiquinone. *J. Colloid Interface Sci.* 384, 189−197.
(72) Panda, A. K., Nag, K., Harbottle, R. R., Possmayer, F., and Petersen, N. O. (2004) Thermodynamic Studies on Mixed Molecular Langmuir Films: Part 2. Mutual Mixing of DPPC and Bovine Lung Surfactant Extract with Long-chain Fatty Acids. *Colloids Surf., A* 247 (1), 9−17.
(73) Veldhuizen, E. J. A., Batenburg, J. J., van Golde, L. M. G., and Haagsman, H. P. (2000) The Role of Surfactant Proteins in DPPC Enrichment of Surface Films. *Biophys. J.* 79, 3164−3171.
(74) Wustneck, R., Perez-Gil, J., Wustneck, N., Cruz, A., Fainerman, V. B., and Pison, U. (2005) Interfacial Properties of Pulmonary Surfactant Layers. *Adv. Colloid Interface Sci.* 117 (1), 33−58.
(75) Sohlenkamp, C., and Geiger, O. (2016) Bacterial Membrane Lipids: Diversity in Structures and Pathways. *FEMS Microbiol. Rev.* 40 (1), 133−159.
(76) Toimil, P., Prieto, G., Minones, J., Jr, and Sarmiento, F. (2010) A Comparative Study of F-DPPC/DPPC Mixed Monolayers. Influence of Subphase Temperature on F-DPPC and DPPC Monolayers. *Phys. Chem. Chem. Phys.* 12, 13323−13332.
(77) Hoyo, J., Guaus, E., Torrent-Burgues, J., and Sanz, F. (2015) Biomimetic Monolayer Films of Digalactosyldiacylglycerol Incorporating Plastoquinone. *Biochim. Biophys. Acta, Biomembr.* 1848 (6), 1341−1351.
(78) Sedgwick, M. A., Trujillo, A. M., Hendricks, N., Levinger, N. E., and Crans, D. C. (2011) Coexisting Aggregates in Mixed Aerosol OT and Cholesterol Microemulsions. *Langmuir* 27 (3), 948−954.
(79) Zan, G. T., and Wu, Q. S. (2016) Biomimetic and Bioinspired Synthesis of Nanomaterials/Nanostructures. *Adv. Mater.* 28 (11), 2099−2147.
(80) Glaziou, P., Sismanidis, C., Floyd, K., and Raviglione, M. (2015) Global Epidemiology of tuberculosis. *Cold Spring Harbor Perspect. Med.* 5, a017798.

DOI: 10.1021/acs.biochem.9b00007
Biochemistry 2019, 58, 1596−1615

Appendix VIII: Structure Dependence of Pyridine and Benzene Derivatives on Interactions with Model Membranes

This manuscript discusses the interactions of hydrophilic structural analogues with model membranes and is published in *Langmuir*.[1] Although C. Van Cleave partook in this work, it was presented in the thesis of Benjamin J. Peters.

References

1. Peters, B. J.; Van Cleave, C.; Haase, A. A.; Hough, J. P. B.; Giffen-Kent, K. A.; Cardiff, G. M.; Sostarecz, A. G.; Crick, D. C.; Crans, D. C., Structure Dependence of Pyridine and Benzene Derivatives on Interactions with Model Membranes. *Langmuir* **2018,** *34* (30), 8939-8951.

LANGMUIR Article
Cite This: Langmuir 2018, 34, 8939−8951 pubs.acs.org/Langmuir

Structure Dependence of Pyridine and Benzene Derivatives on Interactions with Model Membranes

Benjamin J. Peters,[†] Cameron Van Cleave,[†] Allison A. Haase,[†] John Peter B. Hough,[†,‡] Keisha A. Giffen-Kent,[†] Gabriel M. Cardiff,[†,§] Audra G. Sostarecz,[#] Dean C. Crick,[∥,⊥] and Debbie C. Crans*[,†,⊥]

[†]Department of Chemistry, [‡]Department of Biochemistry, [§]Department of Biology, [∥]Department of Microbiology, Immunology, and Pathology, and [⊥]Cell and Molecular Biology Program, Colorado State University, Fort Collins, Colorado 80523, United States
[#]Department of Chemistry, Monmouth College, Monmouth, Illinois 61462, United States

Supporting Information

ABSTRACT: Pyridine-based small-molecule drugs, vitamins, and cofactors are vital for many cellular processes, but little is known about their interactions with membrane interfaces. These specific membrane interactions of these small molecules or ions can assist in diffusion across membranes or reach a membrane-bound target. This study explores how minor differences in small molecules (isoniazid, benzhydrazide, isonicotinamide, nicotinamide, picolinamide, and benzamide) can affect their interactions with model membranes. Langmuir monolayer studies of dipalmitoylphosphatidylcholine (DPPC) or dipalmitoylphosphatidylethanolamine (DPPE), in the presence of the molecules listed, show that isoniazid and isonicotinamide affect the DPPE monolayer at lower concentrations than the DPPC monolayer, demonstrating a preference for one phospholipid over the other. The Langmuir monolayer studies also suggest that nitrogen content and stereochemistry of the small molecule can affect the phospholipid monolayers differently. To determine the molecular interactions of the simple N-containing aromatic pyridines with a membrane-like interface, ^{1}H one-dimensional NMR and ^{1}H−^{1}H two-dimensional NMR techniques were utilized to obtain information about the position and orientation of the molecules of interest within aerosol-OT (AOT) reverse micelles. These studies show that all six of the molecules reside near the AOT sulfonate headgroups and ester linkages in similar positions, but nicotinamide and picolinamide tilt at the water−AOT interface to varying degrees. Combined, these studies demonstrate that small structural changes of small N-containing molecules can affect their specific interactions with membrane-like interfaces and specificity toward different membrane components.

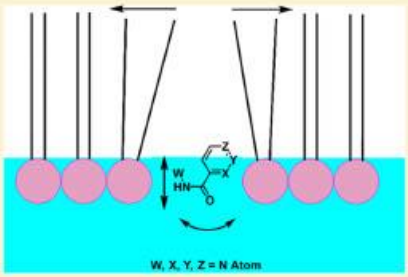

INTRODUCTION

Small molecules (<500 Da) have been the cornerstone for medical treatment, supplements, and preservatives, with many diffusing through the cellular membrane to reach their target.[1−5] One such example is a very successful first-line anti-tuberculosis drug, isoniazid (INH, Figure 1), which has been shown to diffuse across the membrane of *Mycobacterium tuberculosis*, where INH is then able to reach the target, KatG.[6,7] Similar to INH, the method of entry into a cell for many small molecules has been studied in detail,[8−12] but there is a lack of information pertaining to the specific interactions of small molecules with the membrane interfaces. This lack of information is in large part due to the difficulty of determining the specific interactions of molecules with the lipids that make up the membranes and the complexity of the biological membranes themselves.[13−15] The specific small-molecule−lipid interactions of a series of aromatic N-containing compounds were studied here (Figure 1) to understand how small molecules are taken into cells and how they affect the membrane and may elucidate aspects of the small molecules' mode of action.

Many of these small molecules, used to treat diseases such as tuberculosis, contain a pyridine as their main structural component.[16−18] The presence and placement of nitrogen within the pyridine ring have great affect on these small molecules and their inter- and intramolecular interactions. For example, the amide group of picolinamide (PIC) is ortho to the pyridine nitrogen, allowing for intramolecular hydrogen bonding (Figure 1).[19,20] This increases the molecule's hydrophobicity and allows it to penetrate a membrane interface deep enough to affect the packing of the phospholipid tails.[21,22] This behavior is not observed for nicotinamide (NIC, meta) nor isonicotinamide (iNIC, para) because the amide and pyridine nitrogens are not in proximity for intramolecular

Received: May 18, 2018
Revised: June 29, 2018
Published: June 29, 2018

DOI: 10.1021/acs.langmuir.8b01661
Langmuir 2018, 34, 8939−8951

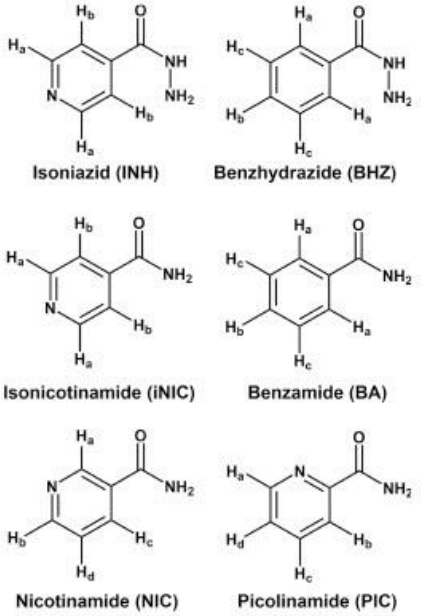

Figure 1. Structures of isoniazid (INH), benzhydrazide (BHZ), isonicotinamide (iNIC), benzamide (BA), nicotinamide (NIC), and picolinamide (PIC), with protons labeled for ^{1}H NMR peak labeling. The protons in the ^{1}H NMR spectra have H_a as the most downfield ^{1}H NMR peak, H_b as the next one, etc. See Figure S1 for enlarged versions.

hydrogen bond formation.[19,20] Despite this difference, Olsson *et al.* were able to show that NIC tightly binds to plasma membrane extracts of human leukemic K-562 cells (K_d between 3.2 and 12.7 μM).[9] Because such small differences in structure have such profound effects on inter- and intramolecular interactions, we hypothesize here that these molecules may interact with a membrane interface differently despite having similar structures, as shown in Figure 1.

To study how small structural differences can affect interactions with membrane interfaces, this study aims to explore the interactions of the molecules shown in Figure 1 with two model membrane interfaces (Figure 2). The first model membrane, Langmuir monolayer, has been used to obtain free energies of mixing of hydrophobic molecules,[23−25] explore phenomena within the membrane,[26−28] and to test how molecules affect a lipid interface.[29−32] While compressing a phospholipid Langmuir monolayer in the presence of the molecules shown in Figure 1, it is possible to determine if the molecules expand, reorganize, or affect the compressibility of the phospholipid monolayer.[33] A commonly used phospholipid, dipalmitoylphosphatidylcholine (DPPC), can comprise up to 40% of lung phospholipid content because of its superior ability to expand and spread at the lung alveolar air−liquid interface.[34−36] Similarly, dipalmitoylphosphatidylethanolamine (DPPE) is utilized to model the inner leaflet of bacterial and eukaryotic membranes for drug and lipid interactions.[37,38] These two lipids have become a very appealing model interface to study drug and lipid interactions and therefore were used in

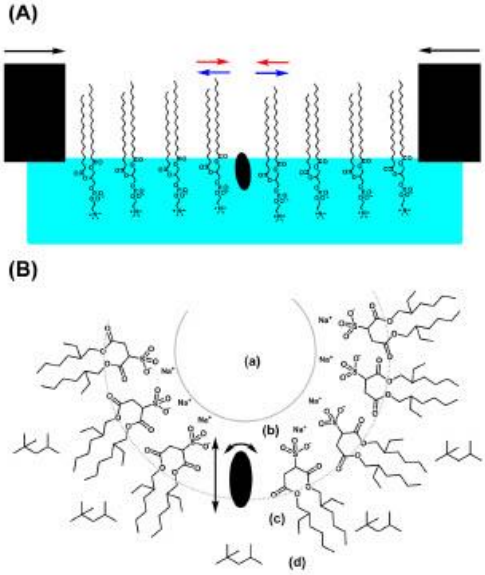

Figure 2. Langmuir monolayer (A) showing how a molecule can affect a phospholipid interface by penetrating and condensing (red arrows) or spreading (blue arrows) the phospholipids during a compression isotherm. The schematic depiction of a RM (B) outlining the area in which a molecule may reside, such as the bulk water (a), interfacial Stern layer (b), AOT tail region (c), and isooctane (d). The black oval demonstrates how a molecule can have varying depths within the RM interface along with different orientations. Figure adapted from Peters *et al.*[30]

this study as a model membrane interface to study the interactions of the N-containing compounds in Figure 1.[34−38] To determine the molecular details of interactions of small aromatic N-containing compounds with an interface, their interactions with aerosol-OT (AOT) reverse micelles (RMs)[39−42] were examined.[30,43−47] RMs are self-assembled microemulsions that form at low water concentration. In these systems, the placement and orientation could be identified by monitoring interactions with the AOT headgroup and/or lipid tails using one-dimensional (1D) and two-dimensional (2D) NMR spectroscopic techniques.[30,43−47] With the combination of these two model membrane systems (Figure 2), information about how the compounds in Figure 1 interact with membrane-like interfaces was obtained in this study.

■ MATERIALS AND METHODS

General Materials. Most materials were used without further purification. Benzamide (BA) (99%), PIC (98%), NIC (98%), iNIC (99%), INH (≥99%), benzhydrazide (BHZ) (98%), isooctane (2,2,4-trimethylpentane, 99.8%), methanol (≥99.9%), activated charcoal (99.5%), chloroform (≥99.5%), deuterium oxide (99.9%), 2,2-dimethyl-2-silapentane-5-sulfonate sodium salt (DSS, 97%), monosodium phosphate (≥99.0%), disodium phosphate (≥99.0%), sodium hydroxide (≥98%), and hydrochloric acid (37%) were all purchased from Sigma-Aldrich. DPPC (≥99%) and DPPE (99%) were purchased from Avanti Polar Lipids. Sodium aerosol-OT (AOT) (bis(2-ethylhexyl)sulfosuccinate sodium salt, ≥99.0%) was purchased from Sigma-Aldrich and was purified further as has been reported

DOI: 10.1021/acs.langmuir.8b01661
Langmuir 2018, 34, 8939−8951

previously to remove any acidic impurities.[30] Briefly, 50.0 g of AOT was dissolved into 150 mL of methanol to which 15 g of activated charcoal was added. This suspension was stirred for 2 weeks. After mixing, the suspension was filtered to remove the activated charcoal. The filtrate was then dried under rotary evaporation at 50 °C until the water content was below 0.2 molecules of water per AOT as determined by ^{1}H NMR spectroscopy. The pH was adjusted throughout this study using varying concentrations of NaOH or HCl dissolved/mixed in either D_2O or H_2O depending on experimental requirements. NaOH or HCl dissolved in D_2O is referred to as NaOD or DCl, respectively.

Preparation of Phospholipid Langmuir Monolayers. Phospholipid stock solutions were prepared by dissolving DPPC (0.018 g, 0.025 mmol) or DPPE (0.017 g, 0.025 mmol) in 25 mL of 9:1 chloroform/methanol (v/v) for a final concentration of 1 mM phospholipid. The aqueous subphase consisted of 50 mL of 20 mM sodium phosphate buffer (pH 7.4) and varying concentrations of hydrazide of amide (10, 1.0, 0.10, or 0 mM hydrazide or amide). Sodium phosphate buffer (20 mM, pH 7.4) instead of distilled deionized H_2O (DDI H_2O) was used as the subphase for the compression isotherms for better pH control (Figure S2).[30] Before addition of the phospholipid monolayers, the surface of the subphase was cleaned using vacuum aspiration, and to make sure the surface was clean, the surface pressure of a compression isotherm of just the subphase (no phospholipid present) was measured (surface pressure was consistently 0.0 ± 0.5 mN/m throughout compression). To prepare the phospholipid monolayer, 20 μL of phospholipid stock solution (20 nmol of phospholipid, 112 Å^2/molecule) was added to the surface of the subphase in a dropwise manner using a Hamilton syringe. The film was allowed to equilibrate for 15 min. The resulting phospholipid monolayer was then used for the compression isotherm experiments (see Figure 2A).

Compression Isotherm Surface Pressure Measurements of Langmuir Monolayers. The phospholipid monolayer was compressed from two sides with a total speed of 10 mm/min (5 mm/min from opposite sides, Figure 2A) using Kibron μTroughXS equipped with a Teflon ribbon (poly(tetrafluoroethylene), hydrophobic barrier). The temperature was maintained at 25 °C using an external water bath.

The surface tension of the subphase during each compression was monitored using a wire probe as a Wilhemy plate. The surface pressure was calculated from the surface tension using eq 1, where π is the surface pressure, γ_o is the surface tension of water (72.8 mN/m), and γ is the surface tension at a given area per phospholipid after the film has been applied.

$$\pi = \gamma_o - \gamma \quad (1)$$

Each compression isotherm experiment consisted of at least three replicates, and the averages with standard deviations of the area per phospholipid at every 5 mN/m were calculated using Microsoft Excel. The worked-up data were transferred to OriginPro version 9.1 to be graphed. From the averages of the compression isotherms, the percent differences from the control of each sample at 5, 30, and 35 mN/m were calculated. The compression moduli were calculated using OriginPro version 9.1 from the compression isotherm average results using eq 2, where C_s^{-1} is the compression modulus, A is the surface area, and π is the surface pressure.

$$C_s^{-1} = -A(d\pi/dA) \quad (2)$$

Preparation of RMs for Dynamic Light Scattering (DLS). RMs were prepared as has previously been reported.[30] To prepare the 100 mM AOT stock solution, 2.2 g of purified AOT (4.9 mmol) was dissolved into 50 mL of isooctane. The 10 mM aqueous stock solutions of amide or hydrazide were prepared by dissolving 50 μmol of amide or hydrazide into 5 mL of DDI H_2O, and then the pH was adjusted to pH 7.0. To prepare the RM solutions, specific volumes of the AOT stock solution and aqueous solution were added for a total of 5 mL to form RM sizes of w_0 8, 12, 16, and 20, where $w_0 = [H_2O]/[AOT]$. Upon mixing the AOT stock solution with aqueous solution, a white aggregate formed at the water–isooctane interface. Then, the mixture was vortexed until clear (~30 s), consistent with the formation of RMs.[30]

Parameters for DLS Analysis. Once the glass cuvettes (1 cm × 1 cm) had been washed with isooctane and RM sample (three times each), the cuvettes were filled with 1 mL of sample and analyzed using Zetasizer Nano ZS. The wavelength of light used was 632.8 nm, and scattering was obtained at an angle of 173°. Each sample was equilibrated for 700 s at 25 °C and then run for 10 scans per acquisition for 15 acquisitions. Each sample was run in triplicate, and the hydrodynamic radii (R_h) and polydispersity index were averaged with the standard deviations reported in Table S1.

Preparation of Aqueous Stock Solutions of Amides and Hydrazides for RM Samples for ^{1}H NMR. The aqueous stock solutions were prepared by dissolving 0.25 mmol (0.50 mmol for NIC) of amide or hydrazide into 25 mL of D_2O for a final concentration of 10 mM (20 mM for NIC). The NIC concentration was increased to obtain a greater signal-to-noise ratio in the ^{1}H NMR spectra of the RMs. Each aqueous stock solution was then pipetted into 2 mL aliquots, and the pD (pD = pH + 0.4)[30,46] of each aliquot was adjusted using NaOD or DCl solutions (5.0, 1.0, and 0.1 M). The pD will be referred to as pH in the rest of this article as is commonly done.[30,46] The pD of the aliquots was adjusted to a range between 1.2 and 9.0 for later use in the determination of the pK_a in D_2O and in the w_0 16 RMs.

Preparation of AOT–Isooctane Stock Solution and RMs for ^{1}H NMR. The 750 mM AOT stock solution was prepared by dissolving 8.34 g of AOT (18.8 mmol) in 25 mL of isooctane. This mixture was sonicated and vortexed until clear (approximately 15 min). Once dissolved, the solution was equilibrated to ambient room temperature. RMs of w_0 values of 8, 12, 16, and 20 were prepared by adding specific volumes of the stock AOT solution and the pH 7.0 aqueous aliquot. The other aqueous aliquots (215 μL) of pH's ranging from 1.2 to 9.0 and the AOT stock solution (785 μL) were mixed to form w_0 16 RMs at varying pH values. The indicated pH values of the RMs are assumed to be the same from the measured aqueous samples. All of the RM mixtures were vortexed until clear as was done for DLS experiments.

^{1}H NMR of D_2O and RM Samples. The ^{1}H NMR experiments were performed using a 400 MHz Varian NMR spectrometer using standard parameters (1 s relaxation time, 25 °C, and 45° pulse angle). The aqueous samples were referenced to an external DSS sample at pH values of 1.2, 1.5, 2.0, 2.5, and 3.0. Above pH 3.0, the DSS methyl silane peak was consistent and therefore the pH 3 DSS standard was used as the standard for the aqueous samples at higher pH values. RM samples were referenced to the isooctane methyl peak at 0.90 ppm as has been previously reported and were originally referenced to tetramethylsilane.[30,43,46] The resulting spectra were analyzed using MestReNova version 10.0.1. The pK_a values were determined by plotting the chemical shifts of the samples at different pH values in D_2O and in w_0 16 RMs and then taking the first derivative of the best-fit curve using OriginPro version 9.1 (see Figure S3).[30]

Preparation of RMs for ^{1}H–^{1}H 2D Nuclear Overhauser Enhancement Spectroscopy (NOESY) and Rotating-Frame Overhauser Effect Spectroscopy (ROESY) NMR. The 750 mM AOT stock solution was prepared by dissolving 0.34 g of AOT (0.76 mmol) in 1 mL of isooctane. To form the RM (w_0 12), 839 μL of the AOT stock solution was added to 161 μL of D_2O and vortexed until clear. This suspension was then mixed with 32 μmol of amide or hydrazide for an average concentration of 200 mM amide or hydrazide within the RM water pool (32.2 mM overall). The mixture was vortexed until the solid dissolved into the RM microemulsion.

Parameters for Recording the ^{1}H–^{1}H 2D NOESY and ROESY NMR Spectra. The ^{1}H–^{1}H 2D NOESY and ROESY experiments were conducted using 400 MHz Varian NMR at 26 °C with 16 scans per transient and 256 transient pairs in the f1 dimension. The ^{1}H–^{1}H 2D NOESY spectrum was acquired using a standard pulse sequence with a mixing time of 200 ms and a 1.5 s relaxation delay. The ^{1}H–^{1}H 2D ROESY spectra were acquired using a standard pulse sequence with a 200, 100, or 0 ms mixing time and a 1.5 s relaxation delay. The resulting spectra were analyzed using MestReNova version 10.0.1 by

DOI: 10.1021/acs.langmuir.8b01661
Langmuir 2018, 34, 8939–8951

subjecting the spectra to a 90° sine^2 weighting function with a first point at 0.50. The spectra were then phased and baselined using a third-order Bernstein polynomial baseline. Each spectrum was referenced to the isooctane methyl peak at 0.904 ppm in both dimensions.[30]

■ RESULTS AND DISCUSSION

Interactions of Aromatic Hydrazides with Langmuir Monolayers. Surface pressure compression isotherms of DPPC and DPPE were measured to model phospholipids commonly found in eukaryotic and bacterial membranes.[34−38] The minor structural difference in the lipid headgroup results in significant differences in the properties of the resulting lipid monolayer. DPPE has a conical shape and packs much more tightly when compared with DPPC, which has a cylindrical shape. This is thought to be due to the hydrogen bonding capability of DPPE (ethanolamine headgroup) that DPPC (choline headgroup) is lacking.[48,49] For these reasons, both DPPC and DPPE zwitterionic phospholipids were used to form Langmuir monolayers to study the interactions of small molecules with phospholipid interfaces.

Surface pressure compression isotherms of DPPC or DPPE were initially conducted in the presence of INH or BHZ hydrazides (Figure 3A−D). The area per phospholipid of the

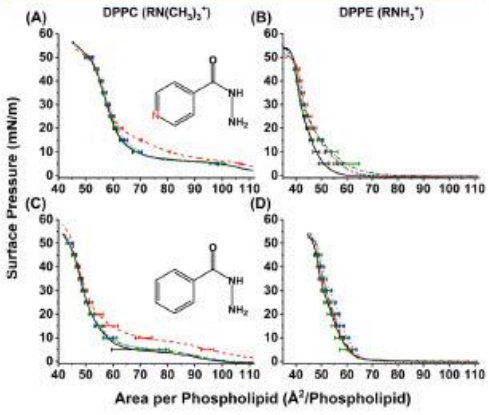

Figure 3. Average compression isotherm curves of DPPC (left column) or DPPE (right column) in the presence of INH (A, B) or BHZ (C, D). The solid black curves correspond to the control films without any hydrazide present. The other curves correspond to 10 mM (red dashed line), 1 mM (blue dotted line), and 0.1 mM (green dashed and dotted line) hydrazide present in the 20 mM sodium phosphate buffered subphase (pH 7.4). Each curve is an average of at least three trials with standard deviations. The R group for each phospholipid includes the phosphate, glycerol, and fully saturated C_{16} tails. See Figures S4 and S5 for enlarged versions.

DPPC monolayer in the presence of 10 mM INH increased, until 20−25 mN/m. The area per phospholipid of the DPPE monolayer in the presence of all concentrations of INH tested increased until 25−30 mN/m. In the presence of 10 mM BHZ, the area per phospholipid of the DPPC monolayer increased until 15−20 mN/m and the area per phospholipid of the DPPE monolayer was unaffected. Briefly, INH affected the area per phospholipid of both monolayers, but all concentrations affected the DPPE monolayer. BHZ affected only the area per phospholipid of the DPPC monolayer.

To determine if the compressibility of the monolayers was affected, the compression modulus was calculated from the average compression isotherms (Figure S6). In the presence of 10 mM INH, the compression modulus of the DPPC monolayer decreased and all concentrations of INH tested caused a decrease in the compression modulus of the DPPE monolayer. The presence of 10 mM BHZ decreased the compression modulus of the DPPC monolayer and increased the compression modulus in the presence of 1 mM BHZ. All concentrations of BHZ tested increased the compression modulus of the DPPE monolayer. In summary, INH decreased the compression modulus of both DPPC and DPPE monolayers, but only the DPPE monolayer was affected at all concentrations tested. BHZ decreased the compression modulus of the DPPC monolayer, and with 1 mM BHZ present, the compression modulus of the DPPE monolayer increased.

Generally, an increase in area per phospholipid of a monolayer indicates an uptake of the small molecule, causing the monolayer to spread, and a decrease in area per phospholipid indicates either solubilization of lipid or a reorganization to allow for tighter packing of the phospholipid monolayer. A decrease in compression modulus has been commonly interpreted as an increase in compressibility and vice versa.[29,50] INH did increase the area per phospholipid of both the DPPC and DPPE monolayers, indicating an uptake into the phospholipid monolayers, but did so at lower concentrations present for DPPE. A similar trend was observed with the decrease of compression moduli in the presence of INH. This suggests that INH has a higher affinity for DPPE than DPPC, indicating that INH would interact more favorably with the ethanolamine than with the choline headgroup. This is presumably due to hydrogen bonding with the ethanolamine headgroup, which would disrupt the intermolecular hydrogen bonding between individual DPPE molecules of the DPPE monolayer.[48,49] BHZ affected the area per phospholipid of only the DPPC monolayer at 10 mM and decreased the compression modulus, suggesting that at high concentration, BHZ is taken inside and allows for easier compression of the DPPC monolayer. At 1 mM for DPPC and all concentrations tested for DPPE, BHZ does not affect the area per phospholipid but increases the compression modulus, showing that the BHZ did not spread the phospholipids but did cause the monolayer to be more difficult to compress than the control monolayers. This suggests that BHZ is reorganizing the phospholipid tails, but more information would be needed for confirmation. In summary, INH was shown to prefer the ethanolamine headgroup and allowed for easier compression than the control phospholipid monolayers, whereas BHZ allowed for easier compression and spread the DPPC monolayer when 10 mM was present in the subphase but, otherwise, caused the phospholipid monolayers to be less compressible without affecting the area per phospholipid.

Interactions of Aromatic Amides with Langmuir Monolayers. To determine if the amides in Figure 1 interact with phospholipid interfaces differently, the surface pressure compression isotherms of DPPC and DPPE were conducted in the presence of BA, PIC, NIC, and iNIC, shown in Figure 4, and compression moduli are given in Figure S11.

First, the compression isotherm experiments using BA were conducted as a nitrogen-deficient comparison. In the presence

DOI: 10.1021/acs.langmuir.8b01661
Langmuir 2018, 34, 8939−8951

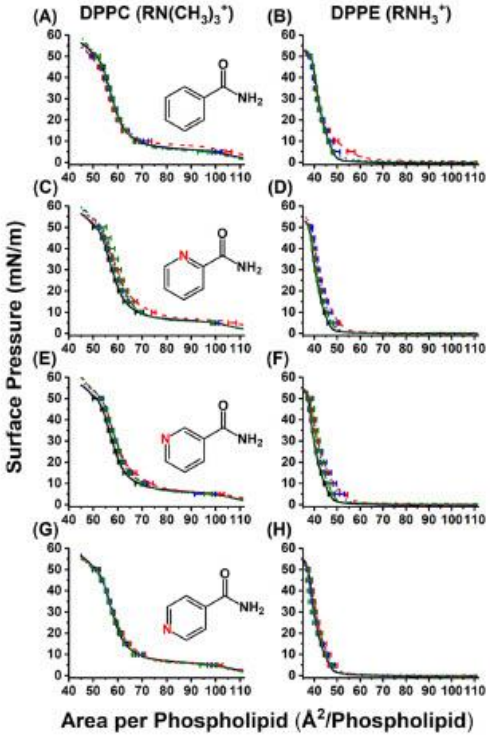

Figure 4. Resulting average surface pressure compression isotherms of DPPC (left column) and DPPE (right column) in the presence of BA (A, B), PIC, (C, D), NIC (E, F), and iNIC (G, H) at concentrations of 0 mM (black solid line), 0.1 mM (green dashed and dotted line), 1.0 mM (blue dotted line), and 10 mM (red dashed line) in the 20 mM sodium phosphate buffered subphase (pH 7.4). Each curve is an average of at least three trials with standard deviations. The R group for each phospholipid includes the phosphate, glycerol, and fully saturated C_{16} tails. See Figures S7–S10 for enlarged images.

of 10 mM BA, the DPPC monolayer exhibited an increase in pressure below 15–20 mN/m and then above 15–20 mN/m exhibited a slight decrease in area per phospholipid. The DPPE monolayer increased in area per phospholipid until 15–20 mN/m. The compression modulus (Figure S11) of the DPPC monolayer decreased in the presence of 10 and 0.1 mM BA and increased when 1.0 mM was present. Concentrations of 10 and 0.1 mM BA also decreased the compression modulus of the DPPE monolayer. This data suggests that BA can spread the phospholipids of both DPPC and DPPE until higher pressures, but it can still affect the compressibility of the phospholipid monolayers, showing that BA still does interact with the monolayer at higher pressures.

In the presence of 10 mM PIC, the DPPC and DPPE monolayers exhibited an increase in area per phospholipid as compared with the control monolayers until 35–40 mN/m. Also, depending on the concentration of PIC within the subphase, the compression modulus for DPPC decreased (10 mM), increased (1 mM), or no effect was observed (0.1 mM). The DPPE monolayer compression modulus was increased only by the presence of 0.10 mM PIC. The increase in area per phospholipid of DPPC and DPPE in the presence of PIC suggests that PIC is spreading the lipids, but depending on the concentrations of PIC, the compressibility of the phospholipid monolayers is affected (Figure S11). The dependence of the compressibility on the concentration may be due to counteracting effects where a large amount of PIC (10 mM) increases compressibility solely because PIC exists in excess within the monolayer, so it is compressed out of the monolayer. At lower concentrations (1 mM for DPPC and 0.10 mM for DPPE), PIC caused the monolayers to become more rigid and less compressible. Briefly, PIC did increase the area per phospholipid of both phospholipid monolayers and had varying effects on the compression moduli of the phospholipid monolayers.

The DPPC and DPPE monolayers in the presence of NIC both exhibited an increase in area per phospholipid. All concentrations of NIC tested increased the area per phospholipid of DPPC above 10 mN/m. The DPPE monolayer was affected in a concentration-dependent manner where 10 mM NIC increased the area per molecule the most. The presence of 10 mM NIC caused an increase in area per phospholipid of DPPE across at all surface pressures below collapse (55 mN/m). There was not much of an effect of NIC on the compression modulus of the DPPC monolayer (Figure S11); however, there was a decrease in the compression modulus for the DPPE monolayer at all concentrations of NIC tested. The presence of NIC caused a spreading of both phospholipid monolayers but only affected the compressibility of the DPPE monolayer, allowing it to become more compressible than the control monolayer.

Unlike the other molecules tested, iNIC had no effect on either the DPPC or the DPPE monolayer area per phospholipid. The presence of 10 and 1.0 mM iNIC did however decrease the compression modulus of the DPPE monolayer but did not have much of an effect on the compressibility of the DPPC monolayer (Figure S11). This suggests that iNIC has a higher affinity for DPPE than for DPPC and allows the DPPE monolayer to be more easily compressed without spreading the phospholipids.

By comparing the interactions of all of the molecules of interest with DPPC and DPPE monolayers, it is clear that not all of the aromatic N-substituted compounds interact with the phospholipid monolayers in the same manner (Figure 4 and Table 1). Out of the six compounds tested, INH and iNIC exhibited more of an effect on the DPPE monolayer than on the DPPC monolayer, suggesting a preference for the ethanolamine headgroup more so than for the choline headgroup. This is most likely due to the ethanolamine's greater hydrogen bonding capacity than that of choline, allowing for intermolecular interaction. When comparing PIC, NIC, and iNIC, the data is consistent with PIC and NIC, affecting the phospholipid monolayers similarly, but iNIC had the least effect on the phospholipid monolayers. As shown in Table 1, NIC and PIC were the only compounds to significantly increase the area per phospholipid of the DPPC and DPPE monolayers at physiologically relevant surface pressures (30–35 mN/m),[51] whereas iNIC did not have much of an effect on the area per phospholipid. Of all of the compounds, BA was the only molecule to cause a decrease in area per phospholipid for DPPC at higher surface pressures (above 15–20 mN/m, Table 1), suggesting that BA was the only compound tested that either reorganized DPPC to

DOI: 10.1021/acs.langmuir.8b01661
Langmuir 2018, 34, 8939–8951

Table 1. Percent Difference of Monolayer Surface Area in the Presence of Aromatic N-Substituted Compounds[a]

		DPPC	DPPE
compound	surface pressure (mN/m)	% difference from control	% difference from control
INH	5	7.36	12.25
	30	0.89	3.61
	35	0.10	3.22
BHZ	5	38.84	1.06
	30	1.86	2.02
	35	1.14	1.95
BA	5	6.21	16.19
	30	−2.20*	−0.92
	35	−2.19*	1.46
PIC	5	2.41	7.65
	30	3.32*	3.65**
	35	2.47**	3.44**
NIC	5	3.42	13.33
	30	3.01**	4.08**
	35	2.77**	3.62**
iNIC	5	1.22	3.32
	30	1.03	1.87
	35	0.55	1.89

[a]Surface pressures were chosen based on initial curve (5 mN/m) and physiological relevance (30−35 mN/m).[51] Significance of the percent difference was determined using Student's t test with *$p < 0.10$ and **$p < 0.05$.

condense further or assist in the solvation of the DPPC. Interestingly, BHZ did not have the same effect as BA but still interacted with the phospholipid monolayers, causing the phospholipids to spread. In summary, INH and iNIC both exhibited a preference for DPPE over DPPC, PIC and NIC affect the phospholipid monolayers similarly even at high pressures, BA reorganizes the DPPC monolayer or helps solubilize the DPPC, and BHZ does interact with both monolayers, causing spreading of the phospholipids.

Placement of Small Aromatic Hydrazides and Amides within the AOT RM. Molecular information on the specific interaction and placement of the compounds with respect to a membrane interface was sought using AOT RMs and NMR spectroscopy.[30,43−47,52] To this end, the ^{1}H NMR spectrum of each N-containing compound was acquired in D_2O and varying sizes of RM. By varying the sizes of the RM (w_0), small changes in the RM microenvironment occur. Comparing the chemical shifts of the N-containing compounds caused by varying environmental differences, it is possible to place the compounds within the RM.[30,43−47,52] The following paragraphs describe the chemical shifting and our placement of compounds as a result of the observed chemical shifting patterns.

The ^{1}H NMR spectra of INH and iNIC are presented as stack plots of ^{1}H NMR spectra in D_2O at the bottom and the RM microemulsions with the smallest RMs as the top spectrum (w_0 8, Figure 5). In the INH spectra, the H_a doublet peak shifts slightly downfield from the D_2O spectrum at 8.67−8.71 ppm in the w_0 20 spectrum and then gradually shifts upfield to 8.70 ppm in the w_0 8 spectrum. The doublet H_b peak for INH shifted gradually downfield from 7.69 ppm in D_2O to 7.80 ppm in the w_0 8 spectrum. A similar shifting pattern was observed with iNIC. The peak corresponding to the doublet H_a for iNIC barely shifts from 8.70 ppm in D_2O to 8.74 ppm in the w_0 20 spectrum followed by a slight upfield shift to the w_0 8 spectrum at 8.72 ppm. The doublet peak corresponding to H_b shifts gradually downfield from 7.76 ppm in the D_2O spectrum to 7.86 ppm in the w_0 8 spectrum. The downfield shifting of both H_a and H_b peaks of INH and iNIC from the D_2O spectrum to the w_0 20 spectrum is consistent with a more charged (deshielded) environment interpreted as placement near the sulfonates of the AOT.[53] The upfield shifting pattern of H_a of both compounds is consistent with the reduction of a charged environment as the RM sizes are reduced, suggesting that H_a is more toward the hydrophobic region than H_b.[53] Together this data suggests that both INH and iNIC reside near the AOT headgroups with the pyridine nitrogen facing toward the AOT tails and the amide/hydrazide toward the water pool similar to benzoate and phenyl biguanide.[30,46]

Next, the interactions of the benzene-based hydrazide and amide, BHZ and BA, with the AOT RM interface are described by ^{1}H NMR. The doublet corresponding to H_a for BHZ shifted from 7.74 ppm in the D_2O spectrum to 7.94 ppm gradually as the RM sizes were reduced to the w_0 8 spectrum.

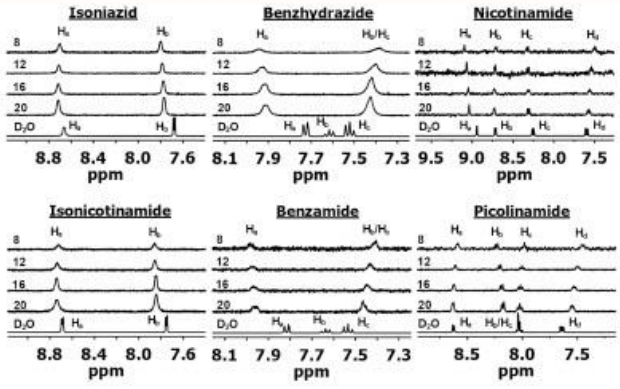

Figure 5. One-dimensional (1D) ^{1}H NMR spectra obtained using a 400 MHz Varian NMR of INH, iNIC, BHZ, BA, NIC, and PIC in D_2O and varying sizes of RMs (w_0) given on the left of each stack of spectra. See Figure 1 for labeled structures corresponding to peak labels.

DOI: 10.1021/acs.langmuir.8b01661
Langmuir 2018, 34, 8939−8951

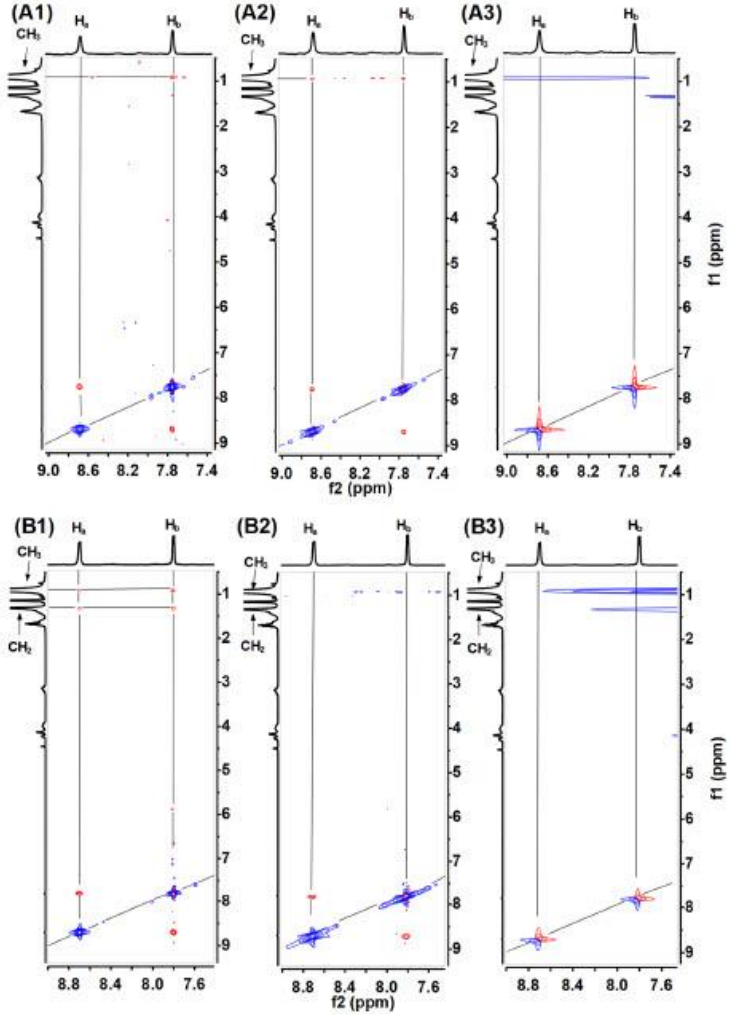

Figure 6. $^1H-^1H$ 2D ROESY NMR spectra acquired using a 400 MHz Inova NMR of INH (A1−A3) and iNIC (B1−B3) using 200, 100, and 0 ms mixing times (1−3) and a relaxation delay of 1.5 s. The diagonal is indicated by the diagonal line. The lines also highlight any off-diagonal cross-peaks.

The triplets corresponding to H_b and H_c for BHZ are at 7.62 and 7.52 ppm, respectively, in the D_2O spectrum and then coalesce in the RM spectra while gradually shifting upfield to 7.38 ppm in the w_0 8 spectrum. The peak corresponding to H_a for BA shifts from 7.83 ppm in D_2O gradually to 7.99 ppm in the w_0 8 spectrum. The peaks corresponding to H_b and H_c of BA in the D_2O spectrum are at 7.64 and 7.53 ppm, respectively, and then coalesce in the RM spectra and gradually shift upfield until 7.40 ppm in the w_0 8 spectrum. The downfield shifting pattern of H_a for both BHZ and BA from the D_2O spectrum to the w_0 8 spectrum is consistent with the RM interface. The upfield shifting pattern of H_b and H_c of both BHZ and BA is consistent with a deep placement within the RM interface toward the AOT tails. Using this data, it is possible to place BHZ and BA within the water−AOT interface with the benzene ring of both compounds placed a little more toward the AOT tails than INH and iNIC and with the amide/hydrazide toward the water pool. This is similar to what has been previously found for benzoic acid.[30]

The position and orientation of NIC within the RM were explored by itself unlike the previous compounds. The doublet corresponding to H_a for NIC shifted gradually downfield from 8.94 ppm in the D_2O spectrum to 9.10 ppm in the w_0 8 spectrum. The H_b doublet shifts from 8.72 ppm in the D_2O

DOI: 10.1021/acs.langmuir.8b01661
Langmuir 2018, 34, 8939−8951

spectrum to 8.74 ppm in the w_0 20 spectrum and then shifts upfield to 8.71 ppm in the w_0 8 spectrum. The H_c doublet shifts from 8.27 ppm in the D_2O spectrum gradually to 8.34 ppm in the w_0 8 spectrum, and the H_d peak is the only peak for NIC to gradually shift upfield from 7.62 ppm in the D_2O spectrum to 7.52 ppm in the w_0 8 spectrum. The downfield shifting for the H_d and H_a peaks for NIC is consistent with placement toward the water−AOT interface. The H_c peak initially shifted downfield and then slightly upfield, suggesting a placement near the water−AOT interface but more toward the AOT tails than H_d and H_a. The H_b peak was the only peak that consistently shifted upfield, suggesting the deepest placement (toward AOT tails) of all of the NIC protons. This data is consistent with NIC residing near the water−AOT interface with NIC tilted at the interface. This position would have H_a pointing toward the water pool and the amide tilted more toward the AOT headgroups. A similar finding was determined for the *ortho*-fluorobenzoate anion at the micellar interface.[53]

Finally, the placement and orientation of PIC within the RM samples were determined. The H_a doublet for PIC shifts slightly upfield from 8.63 ppm in the D_2O spectrum to 8.60 ppm in the w_0 8 spectrum. The peaks corresponding to H_b and H_c are overlapping in the D_2O spectrum but then separate within the RM samples with H_b shifting downfield gradually from 8.04 ppm in the D_2O spectrum to 8.24 ppm in the w_0 8 spectrum and H_c gradually shifting upfield from 8.02 ppm in the D_2O spectrum to 7.98 ppm in the w_0 8 spectrum. The H_d peak for PIC gradually shifts upfield from 7.64 ppm in the D_2O spectrum to 7.45 ppm in the w_0 8 spectrum. The upfield shifting pattern of H_a, H_c, and H_d peaks is consistent with the protons being placed toward the AOT tails. The downfield shifting pattern of H_b is consistent with it being placed more toward the AOT interface. This data is consistent with PIC residing near the AOT headgroups, with only H_b being near the AOT headgroups and the other protons toward the AOT tails causing a tilt of the molecule within the interface.

In summary, this data shows that these N-containing molecules interact differently with the AOT RM but reside at similar positions within the water−AOT interface. INH and iNIC were shown to reside within the AOT interface with the pyridine nitrogen facing toward the AOT tails and the hydrazide/amide toward the AOT headgroups. BHZ and BA were shown to reside deeper toward the AOT tails than INH or iNIC but with the same orientation. PIC was shown to reside at the AOT interface as INH and iNIC but slightly tilted at the interface with the nitrogen of the pyridine and the amide facing toward the AOT headgroup and water pool. NIC was also shown to be tilted with the proton between the amide and pyridine nitrogen facing the water pool. Generally, each molecule resided in similar positions, but the pyridine nitrogen to amide orientation did affected the overall molecular orientation at the water−AOT RM interface. This finding is similar to what has been shown for fluorobenzoate derivatives with micelles.[53]

^{1}H−^{1}H 2D NMR of Hydrazides and Amides within the AOT RM Interface. More information was sought to confirm the placement and orientation based on ^{1}H 1D NMR experiments; therefore, through-space ^{1}H−^{1}H 2D NOESY and ROESY experiments were conducted.[30,43−45] Both ^{1}H−^{1}H 2D NOESY and ROESY spectra with a 200 ms mixing time and higher concentration of BA were acquired to explore which experiment would provide the best signal-to-noise ratio (Figure S13). With the ROESY data producing a better signal-to noise ratio than NOESY for these samples, other ROESY spectra were sought using 100 or 0 ms mixing times. The 0 ms mixing time serves as a negative control to confirm no magnetization transfer was observed between magnetically different protons.

A portion of the ^{1}H−^{1}H 2D ROESY NMR spectra for INH and iNIC within w_0 12 RMs is shown in Figure 6. The spectra of INH within the w_0 12 RM microemulsion show a diagonal with two, negative, blue peaks corresponding to the H_a and H_b peaks of INH at 7.71 and 7.77 ppm, respectively. The positive, red, off-diagonal cross-peaks corresponding to H_a and H_b are observed in the spectra of 200 and 100 ms mixing time, whereas no cross-peaks are observed in the 0 ms mixing time spectrum as would be expected. In the 200 ms mixing time spectrum for INH, an off-diagonal cross-peak corresponding to H_b on INH and the methyl peak of either AOT or isooctane at 0.90 ppm on the f2 axis were observed. In the 100 ms mixing time spectrum, off-diagonal cross-peaks for both H_a and H_b at 0.90 ppm on the f2 axis were observed and correspond to the AOT or isooctane methyl peak. Considering that the previous ^{1}H 1D NMR experiments have shown that INH resides within the water−AOT interface, INH is most likely residing near the AOT ethyl CH_3 protons with the CH_3 protons tilted toward the interface (see Figure S12 for AOT assignments).

The spectra of the w_0 12 RM microemulsion with iNIC also indicated an interaction with the AOT interface similar to that for INH. Along the diagonal shown in Figure 6, two, negative, blue peaks corresponding to iNIC protons H_a and H_b at 8.70 and 7.80 ppm, respectively, are observed. Positive, red, off-diagonal cross-peaks between H_a and H_b in the 200 and 100 ms mixing time spectra are observed. Finally, no cross-peaks are observed in the 0 ms mixing time spectrum. In the 200 ms mixing time spectrum, positive, red, off-diagonal cross-peaks with H_a and H_b of iNIC are observed at 1.30 and 0.90 ppm on the f2 axis corresponding to the AOT CH_2 and an isooctane or AOT CH_3 peak, respectively. These peaks were not observed in either the 100 or 0 ms mixing time spectra. Because of iNIC's insolubility in isooctane and its similar placement determined by the ^{1}H 1D NMR studies, these results support the interpretation that iNIC interacts within the RM water−AOT resides at the interface near the sulfonate headgroups of the AOT similar to that in the vanadium dipicolinate complex.[54]

The ^{1}H−^{1}H 2D ROESY spectra of RMs containing BHZ and BA (Figure S14) were very similar. In the following, these compounds will be discussed concurrently. As can be seen on the diagonal of the spectra of BHZ, there are two negative, blue peaks at 7.97 and 7.43 ppm corresponding to H_a and H_b/H_c, respectively. Within the 200 and 100 ms mixing time spectra, positive, red, off-diagonal cross-peaks are observed between the H_a and H_b/H_c peaks, whereas no cross-peaks are observed for the 0 ms mixing time spectrum. In the 200 ms mixing time spectrum, positive, red, off-diagonal cross-peaks at 1.30 and 0.90 ppm on the f1 axis corresponding to the AOT CH_2, AOT CH_3, or isooctane CH_3 peak and H_a and H_b/H_c can be observed. In the spectrum using 100 ms mixing time, the same off-diagonal peaks are observed except for the off-diagonal cross-peak at 1.30 ppm on the f1 axis and 7.97 ppm on the f2 axis corresponding to the AOT CH_2 and the H_a protons, respectively. These cross-peaks were also observed for BA where the only differences in the spectra were from the placement of the BA negative, blue peaks on the diagonal at 7.92 ppm for H_a and 7.39 ppm for H_b/H_c. This data suggests

DOI: 10.1021/acs.langmuir.8b01661
Langmuir 2018, 34, 8939−8951

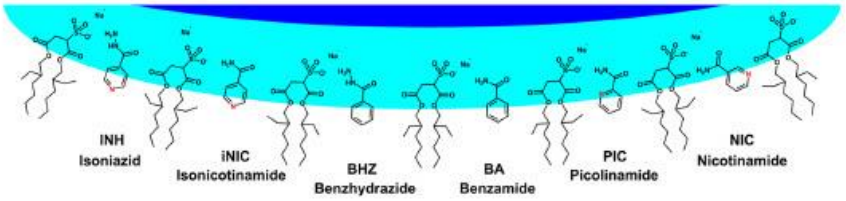

Figure 7. Pictorial representation of the placement of INH, iNIC, BHZ, BA, PIC, and NIC within the RM as determined through 1D and 2D ^{1}H NMR studies. It is important to note that this system is highly dynamic and therefore these are average positions/orientations within the AOT interface based on the 1D and 2D NMR data presented in this study.

that BHZ and BA are both positioned nearby the AOT ethyl with the hydrazide/amide facing the water pool consistent with the ^{1}H 1D NMR studies.

The ^{1}H−^{1}H 2D ROESY spectra of PIC, within RMs, were acquired to confirm the placement and orientation within the RM water−AOT interface. Figure S15 shows the ^{1}H−^{1}H 2D ROESY NMR spectra of PIC within the w_0 12 RM microemulsion acquired using 200, 100, and 0 ms mixing times. Observed in each of these spectra are negative, blue peaks along the diagonal corresponding to H_a (8.60 ppm), H_b (8.19 ppm), H_c (7.99 ppm), and H_d (7.47 ppm). In the spectra acquired using 200 and 100 ms mixing times, there are positive, red, off-diagonal cross-peaks between the peaks corresponding to the PIC peaks, whereas no off-diagonal cross-peaks are observed in the spectrum acquired using a 0 ms mixing time. In the 200 ms mixing time spectrum, positive, red, off-diagonal cross-peaks at 0.90 in the f1 dimension corresponding to all of the PIC peaks are observed. The same positive, red, off-diagonal cross-peaks are observed using a 100 ms mixing time with the exception of the off-diagonal cross-peak at 0.90 ppm in the f1 dimension and 7.99 ppm in the f2 dimension corresponding to H_c of PIC. This confirms that PIC resides within the AOT interface and does interact with the CH_3 of the ethyl of AOT.

The placement and orientation within RMs of NIC were explored using ^{1}H−^{1}H 2D ROESY NMR in the w_0 12 RM spectra shown in Figure S15. The peaks on the diagonal are negative, blue peaks corresponding to H_a (9.02 ppm), H_b (8.68 ppm), H_c (8.29 ppm), and H_d (7.50 ppm). Positive, red, off-diagonal cross-peaks between the NIC aromatic protons can be observed in the spectra acquired using 200 and 100 ms mixing times but not for the 0 ms mixing time spectrum. Positive, red, off-diagonal cross-peaks corresponding to AOT peaks can be observed at 0.90 ppm in the f1 dimension and at 9.02, 8.68, 8.29, and 7.50 ppm in the f2 dimension. These peaks suggest that all of the aromatic protons of NIC reside near a methyl. Three other positive, red, off-diagonal cross-peaks can be observed at 1.30 ppm in the f1 dimension and at 8.68, 8.29, and 7.50 ppm in the f2 dimension corresponding to the CH_2 AOT peak and H_b, H_c, and H_d. This data is consistent with NIC residing at the same position within the RM interface as the other probe molecules but H_a is not in proximity to the CH_2 of the AOT ethyl. By rotating the C−C bonds of the ethyl of AOT, the CH_3 of the ethyl can reach further than the CH_2, suggesting that H_a is in a position away from the CH_2. This would suggest a tilt in NIC at the water−AOT interface supporting the interpretation of the ^{1}H 1D NMR spectra.

In summary, the ^{1}H−^{1}H 2D ROESY NMR spectra of w_0 12 RMs containing the compounds of interest did support the results from the ^{1}H 1D NMR spectra. The placement of each of these molecules using data from both the 1D and 2D NMR experiments is illustrated in Figure 7. First of which, INH and iNIC both can be positioned near the AOT ethyl. Due to the similar ^{1}H 1D NMR chemical shifting patterns and similar ^{1}H-^{1}H 2D NMR experiments, they can be placed in similar positions near within the RM interface. BHZ and BA both can be placed at the same position and slightly deeper than iNIC and INH. The 2D NMR of PIC confirmed that it does reside within the interface of the water pool and AOT, whereas the 1D NMR suggested a tilt at the water−AOT interface. Briefly, all of the molecules resided near the water−AOT interface; however, PIC and NIC exhibited a tilted orientation within the interface (see Figure 7).

pK_a Measurement of the Hydrazides and Amides within the AOT RM. To explore how the AOT interface affects the aromatic N-containing molecules, the pK_a values of the small aromatic molecules were determined. The pH within the RM water pool is not just simply the $-\log[H^+]$ as is normally used in the United States to calculate pK_a in aqueous solutions.[55] The pH value within the RM water pool is much more complicated. Depending on the charge of the headgroup surfactant used to form the RM microemulsion, a proton gradient can form.[56,57] The AOT RMs used in this study have a negative charge and therefore can cause an increase in proton concentration at the interface.[47,55] The pK_a values of molecules have also been known to change within varying environments, such as the difference in pK_a values of a specific amino acid depends on whether or not it is in the center or on the surface of a protein; therefore, the RM may affect the small aromatic molecules' pK_a values.[58]

The pK_a values of the aromatic N-containing molecules in D_2O and in w_0 16 RMs are shown and compared to those in the literature and calculated values in Table 2.[59] The pK_a for BA was not determined in this study because of BA's low pK_a value. The pK_a values of each of the probe molecules in D_2O are all very similar to both the predicted pK_a values and the experimentally determined pK_a values.[59] The small differences between the pK_a values found in this study and the experimental studies in aqueous solutions is most likely caused by differences in ionic strength, temperature, and differences caused by H_2O (reported pK_a values) or D_2O (this study). Within the RMs, the pK_a of each molecule lowered beyond measurement. This would support an interaction with the AOT itself or an effect of the high ionic strength of the interface.[30,39,40,55] Either possibility supports that the molecules reside within the RM interface.

DLS of RMs Containing Aromatic Hydrazides and Amides. DLS was used to determine that RMs formed. In

DOI: 10.1021/acs.langmuir.8b01661
Langmuir 2018, 34, 8939−8951

Table 2. pK_a Values of the Hydrazides and Amides of Interest in Aqueous and RM Solutions[a]

compound	predicted pK_a	reported pK_a[59]	pK_a in D_2O	pK_a in w_0 16 RM
INH	3.4, 2.4*	3.5, 1.9*	3.3	<1
BHZ	2.8*	3.0*	2.8*	<1*
BA	−0.36	N.A.	N.A.	N.A.
PIC	2.2	2.1	2.4	<1
NIC	3.6	3.3	3.7	<1
iNIC	3.5	3.6	3.9	<1

[a]The table outlines the pK_a values determined using the method outlined in Figure S3. The pK_a values of the amine protons for INH and BZH are given by *. The predicted pK_a values are from http://www.chemicalize.org. The reported pK_a values are from ref 59.

addition to confirming that the RMs form, we also demonstrated that the sizes of the systems measured were consistent with those reported in the literature (Table S1).[41] Furthermore, the measurements were done to investigate whether the addition of the compound alters the overall structure of the RMs studied. As shown in Table S1, no differences in sizes of RMs with and without the aromatic hydrazides and aromatic amides were observed.[41]

Evaluation and Implication of Findings in Studies of Langmuir Monolayers and Interfaces in AOT−Isooctane RMs. Studies on model systems are done to obtain information that may not be accessible in studies of the biological membranes. The two model systems used in the studies here both have advantages and limitations. Regardless, it is important to note that there are substantial differences between the AOT interface and a phospholipid interface. The differences in structure, curvature, surfactant/lipid density, and headgroup charge (negative vs zwitterionic, respectively), may impact the interactions of the molecules under investigation with regard to their interaction with interfaces.[14,39,40,51] Although these differences exist, there are similarities between how the molecules of interest interact with the AOT interface and the phospholipid interface. By comparing the findings of the RM experiments with those of phospholipid Langmuir monolayer experiments, the combination can shed light on crucial differences behind the interactions of molecules with the surfactant or lipid interfaces.[30,45]

Interestingly, all of the molecules studied here were found to reside near the headgroup of the AOT surfactant interface. The RM studies provide information about how small structural changes in the aromatic amide or hydrazide can affect compound placement and orientation at a surfactant interface. This finding, albeit on a different type of interface, is consistent with the results reported in computational studies of NIC and PIC with phosphatidylcholine and phosphatidylethanolamine phospholipids[21,22] along with experimental studies with INH interacting with a liposome consisting of phosphotidylcholine.[60,61] We found that the distance of amide to the pyridine nitrogen and the molecular orientation of the amide can impact the interactions with the water−AOT interface. Similarly using computational methods in studies by Borba *et al.* and Martini *et al.*, specific hydrogen bondings with NIC and PIC were found using phosphatidylcholine and phosphatidylethanolamine phospholipids.[21,22] Although the findings in our studies with the RMs do not directly demonstrate the specific interactions with the phospholipid headgroups found in these computational studies, but the locations identified in our studies of the small aromatic N-containing molecules with the sulfonate headgroup of AOT were comparable, that is, placing the drug near the interface.

Conversely, if the small aromatic N-containing compounds interacted primarily with the phospholipid tails, then the headgroup would not have affected the overall interactions with the phospholipids and the area per phospholipid would have been affected similarly between DPPC and DPPE. Because this was shown to not be the case in the Langmuir monolayer studies, the molecules of interest most likely also reside near the phospholipid headgroups as found in the AOT RM experiments. The difference in interaction with DPPC versus DPPE was especially evident with INH and iNIC (see Figure 3A,B). The previous study by Marques *et al.* was able to determine a dissociation constant (K_d) of INH with dimyristoylphosphatidylcholine-supported bilayers to be 0.031 μmol by plasmon waveguide resonance.[60,62] With the observation that INH most likely prefers DPPE over DPPC, the K_d of INH with DPPE would be lower than that found by Marques *et al.* More studies are needed to determine the exact values and whether the difference in tail length would affect the K_d.

The Langmuir monolayer studies also support the interpretation that the orientation of the amide to pyridine nitrogen affects the phospholipid interface. This result was apparent from the differences in compression isotherm area per phospholipid caused by the presence of iNIC compared with NIC and PIC. NIC and PIC affected the monolayers similarly, in contrast to iNIC that affected the monolayers differently. iNIC was more similar to INH where it preferred DPPE, but iNIC did not spread the lipids like NIC and PIC did. The similar overall effects on the phospholipid monolayers by PIC and NIC were most likely caused by different molecular interactions that happen to have similar outcomes, as supported by a difference in tilting at the RM interface. To summarize, the specific structural characteristics of these compounds can influence their interactions with phospholipid and surfactant interfaces in a comparable manner.

When combining the information from these two model membrane systems, a few conclusions about the placement and interactions of the molecules of interest with surfactant and phospholipid interfaces can be made. The RM experiments show that despite a similar placement of all of the molecules of interest within the water−AOT interface, the orientation of the pyridine nitrogen to the amide can affect the specific orientation of the whole molecule of interest within an interface. This tilt of PIC and NIC suggests that within other interfaces, such as a phospholipid interface, the small difference between these molecules can allow for differences in the interactions with a phospholipid monolayer. However, these interactions will likely not be the same as those determined from the RM experiments.[21] The phospholipid Langmuir monolayer studies build on this idea by also supporting the expectation that the specifics behind the interactions of the headgroup of the phospholipid with the molecule of interest can affect binding such as what was observed with INH and iNIC. To summarize, the hypothesis that small differences in structure can lead to differences in the interactions of these small molecules with membrane interfaces was supported by these observations.

Although this study focused exclusively on monolayers, the observations gathered can cautiously be used to provide some

DOI: 10.1021/acs.langmuir.8b01661
Langmuir 2018, 34, 8939−8951

projections about how these molecules might pass through a bilayer membrane. With each molecule studied here, they all resided within the water−AOT RM interface and interacted differently with phospholipids containing the same tail but different headgroups. Together, these observations would support a headgroup-based interaction of the drugs in contrast to interactions with the choline, phosphate, or glycerol of phospholipids. Therefore, these compounds may not passively diffuse through a bilayer membrane-like weak acid preservatives (e.g., benzoic acid and formic acid) or protonophores (e.g., carbonyl cyanide *m*-chlorophenyl hydrazine).[8,10,30] If the molecules are able to traverse a membrane by passive diffusion, then it would be expected that the molecules would reside deeper within the RM tails/organic solvent.[30] The data obtained in this study does not support passive transport of these small aromatic N-containing compounds.

Other methods for crossing a bilayer have been extensively studied using different cations and anions. In these method, cations or anions are transported through forming a complex with phospholipids and then flip with the phospholipid across the bilayer or through a hydrophobic pore that may form allowing traversing of ions.[63−67] Some of these mechanisms have been studied through computational studies, and Borba *et al.* were able to show that the binding of PIC and NIC to the phosphatidylcholine or phosphatidylethanolamine headgroups can cause conformational differences in the phospholipid tails.[22] Considering that all of the molecules within this study interacted with the headgroups of AOT and the phospholipids, it is feasible that at least some of these molecules may affect the phospholipid tails as well. If these molecules affect the phospholipid tails, then such interaction might aid in the diffusion of the drugs across the phospholipid bilayer. Additional studies are needed to determine if these small molecules passively diffuse across bilayers, but these studies provide the framework to build a more in-depth understanding of small-molecule interactions with membrane interfaces.

■ CONCLUSIONS

We found that INH, BHZ, BA, PIC, NIC, and iNIC all interact with phospholipid and surfactant interfaces specficially with the phospholipid/surfactant headgroups but have different effects on phospholipid interfaces. The phospholipid Langmuir monolayer studies show a difference in interaction of the small molecules that were dependent on the structure of not only the small molecules but also the phospholipids themselves. All of the molecules tested reside within the water−AOT surfactant interface of RMs with the amide/hydrazide facing toward the water pool except for NIC and PIC. NIC and PIC resided at the interface but were tilted with the amide of NIC facing more away from the water pool than the amide of PIC. In summary, we show here that interactions of small aromatic N-containing molecules with lipid surfactant interfaces are not straightforward and that structural changes of the small aromatic compounds can alter their affinity for different phospholipid interfaces, how they affect different phospholipid interfaces, and the specifics behind the interactions with these interfaces.

■ ASSOCIATED CONTENT

Supporting Information

The Supporting Information is available free of charge on the ACS Publications website at DOI: 10.1021/acs.langmuir.8b01661.

Enlargement of Figures 1, 3, and 4; compression isotherm curves of DPPC and DPPE with DDI H_2O or 20 mM phosphate buffer (pH 7.4); the compression moduli graphs of DPPC and DPPE in the presence of the hydrazides and amides; an example for determination of the pK_a values using ^{1}H NMR; a table outlining the DLS results; a labeled AOT molecule for w_0 12 RM ^{1}H NMR spectrum; a comparison between ^{1}H−^{1}H 2D NMR NOESY and ROESY spectra of w_0 12 RMs containing BA; and ^{1}H−^{1}H 2D ROESY spectra obtained using varying mixing times of w_0 12 RMs containing BA, BHZ, PIC, and NIC (PDF)

■ AUTHOR INFORMATION

Corresponding Author

*E-mail: Debbie.crans@colostate.edu.

ORCID

Benjamin J. Peters: 0000-0002-6219-4897
Cameron Van Cleave: 0000-0002-0924-1738
Allison A. Haase: 0000-0001-6574-2599
Dean C. Crick: 0000-0001-9281-7058
Debbie C. Crans: 0000-0001-7792-3450

Author Contributions

The manuscript was written through contributions of all authors. All authors have given approval to the final version of the manuscript.

Notes

The authors declare no competing financial interest.

■ ACKNOWLEDGMENTS

We thank Dr. Christopher D. Rithner for assistance with the NMR studies. D.C.C. and D.C.C. thank NIH for funding for this research (Grant # AI119567) and the later by NSF (Grant # CHE-1709564).

■ ABBREVIATIONS

AOT, aerosol-OT; RM, reverse micelle; DPPC, dipalmitoylphosphatidylcholine; DPPE, dipalmitoylphosphatidylethanolamine; INH, isoniazid; BHZ, benzhydrazide; iNIC, isonicotinamide; NIC, nicotinamide; PIC, picolinamide; BA, benzamide; DLS, dynamic light scattering; NMR, nuclear magnetic resonance; R_h, hydrodynamic radius; DSS, 2,2-dimethyl-2-silapentane-5-sulfonate sodium salt; ROESY, rotating-frame Overhauser spectroscopy; NOESY, nuclear Overhauser effect spectroscopy; DDI H_2O, distilled deionized water

■ REFERENCES

(1) Azuma, K.; Ouchi, Y.; Inoue, S. Vitamin K: Novel Molecular Mechanisms of Action and Its Roles in Osteoporosis. *Geriatr. Gerontol. Int.* **2014**, *14*, 1−7.

(2) Lambert, R. J.; Stratford, M. Weak-Acid Preservatives: Modelling Microbial Inhibition and Response. *J. Appl. Microbiol.* **1999**, *86*, 157−164.

(3) Ullah, A.; Orij, R.; Brul, S.; Smits, G. J. Quantitative Analysis of the Modes of Growth Inhibition by Weak Organic Acids in *Saccharomyces cerevisiae*. *Appl. Environ. Microbiol.* **2012**, *78*, 8377−8387.

(4) Westfall, D. A.; Krishnamoorthy, G.; Wolloscheck, D.; Sarkar, R.; Zgurskaya, H. I.; Rybenkov, V. V. Bifurcation Kinetics of Drug Uptake by Gram-Negative Bacteria. *PLoS One* **2017**, *12*, No. e0184671.

(5) Zhang, Y.; Wade, M. M.; Scorpio, A.; Zhang, H.; Sun, Z. H. Mode of Action of Pyrazinamide: Disruption of *Mycobacterium*

tuberculosis Membrane Transport and Energetics by Pyrazinoic Acid. *J. Antimicrob. Chemother.* **2003**, *52*, 790−795.
(6) Bardou, F.; Raynaud, C.; Ramos, C.; Laneelle, M. A.; Laneelle, G. Mechanism of Isoniazid Uptake in *Mycobacterium tuberculosis*. *Microbiology* **1998**, *144*, 2539−2544.
(7) Unissa, A. N.; Subbian, S.; Hanna, L. E.; Selvakumar, N. Overview on Mechanisms of Isoniazid Action and Resistance in *Mycobacterium tuberculosis*. *Infect., Genet. Evol.* **2016**, *45*, 474−492.
(8) Finkelstein, A. Weak-Acid Uncouplers of Oxidative Phosphorylation - Mechanism of Action on Thin Lipid Membranes. *Biochim. Biophys. Acta, Bioenerg.* **1970**, *205*, 1−6.
(9) Olsson, A.; Olofsson, T.; Pero, R. W. Specific Binding and Uptake of Extracellular Nicotinamide in Human Leukemic K-562 Cells. *Biochem. Pharmacol.* **1993**, *45*, 1191−1200.
(10) Piper, P.; Mahe, Y.; Thompson, S.; Pandjaitan, R.; Holyoak, C.; Egner, R.; Muhlbauer, M.; Coote, P.; Kuchler, K. The Pdr12 Abc Transporter Is Required for the Development of Weak Organic Acid Resistance in Yeast. *EMBO J.* **1998**, *17*, 4257−4265.
(11) Silve, A.; Mir, L. M. Cell Electropermeabilization and Cellular Uptake of Small Molecules: The Electrochemotherapy Concept. *Clin. Asp. Electroporation* **2011**, *69*−82.
(12) Wilson, D. F.; Ting, H. P.; Koppelman, M. S. Mechanism of Action of Uncouplers of Oxidative Phosphorylation. *Biochemistry.* **1971**, *10*, 2897−2902.
(13) Ivanova, N.; Ivanova, A. Testing the Limits of Model Membrane Simulations-bilayer Composition and Pressure Scaling. *J. Comput. Chem.* **2018**, *39*, 387−396.
(14) Singer, S. J.; Nicolson, G. L. The Fluid Mosaic Model of the Structure of Cell Membranes. *Scienœ* **1972**, *175*, 720−730.
(15) van Meer, G.; Voelker, D. R.; Feigenson, G. W. Membrane Lipids: Where They Are and How They Behave. *Nat. Rev. Mol. Cell Biol.* **2008**, *9*, 112−124.
(16) Alvarez, R.; Aramburu, L.; Puebla, P.; Caballero, E.; González, M.; Vicente, A.; Medarde, M.; Peláez, R. Pyridine Based Antitumour Compounds Acting at the Colchicine Site. *Curr. Med. Chem.* **2016**, *23*, 1100−1130.
(17) Nayyar, A.; Jain, R. Recent Advances in New Structural Classes of Anti-Tuberculosis Agents. *Curr. Med. Chem.* **2005**, *12*, 1873−1886.
(18) Prachayasittikul, S.; Pingaew, R.; Worachartcheewan, A.; Sinthupoom, N.; Prachayasittikul, V.; Ruchirawat, S.; Prachayasittikul, V. Roles of Pyridine and Pyrimidine Derivatives as Privileged Scaffolds in Anticancer Agents. *Mini-Rev. Med. Chem.* **2017**, *17*, 869−901.
(19) Borba, A.; Albrecht, M.; Gomez-Zavaglia, A.; Lapinski, L.; Nowak, M. J.; Suhm, M. A.; Fausto, R. Dimer Formation in Nicotinamide and Picolinamide in the Gas and Condensed Phases Probed by Infrared Spectroscopy. *Phys. Chem. Chem. Phys.* **2008**, *10*, 7010−7021.
(20) Borba, A.; Gomez-Zavaglia, A.; Fausto, R. Molecular Structure, Vibrational Spectra, Quantum Chemical Calculations and Photochemistry of Picolinamide and Isonicotinamide Isolated in Cryogenic Inert Matrixes and in the Neat Low-Temperature Solid Phases. *J. Phys. Chem. A* **2008**, *112*, 45−57.
(21) Martini, M. F.; Disalvo, E. A.; Pickholz, M. Nicotinamide and Picolinamide in Phospholipid Monolayers. *Int. J. Quantum Chem.* **2012**, *112*, 3289−3295.
(22) Borba, A.; Lairion, F.; Disalvo, A.; Fausto, R. Interaction of Nicotinamide and Picolinamide with Phosphatidylcholine and Phosphatidylethanolamine Membranes: A Combined Approach Using Dipole Potential Measurements and Quantum Chemical Calculations. *Biochim. Biophys. Acta, Biomembr.* **2009**, *1788*, 2553−2562.
(23) Gzyl-Malcher, B.; Handzlik, J.; Nowak-Stępniowska, A. Interactions of Phenytoin with Lipids in Mixed Langmuir Monolayers. *Colloids Surf., A* **2008**, *321*, 52−59.
(24) Gzyl-Malcher, B.; Handzlik, J.; Klekowska, E. Interaction of Prazosin with Model Membranes - a Langmuir Monolayer Study. *Bioelectrochemistry* **2012**, *87*, 96−103.
(25) Jurak, M. Thermodynamic Aspects of Cholesterol Effect on Properties of Phospholipid Monolayers: Langmuir and Langmuir-Blodgett Monolayer Study. *J. Phys. Chem. B* **2013**, *117*, 3496−3502.
(26) Hoyo, J.; Torrent-Burgues, J.; Guaus, E. Biomimetic Monolayer Films of Monogalactosyldiacylglycerol Incorporating Ubiquinone. *J. Colloid Interface Sci.* **2012**, *384*, 189−197.
(27) Nerdal, W.; Nilsen, T. R. S.; Steinkopf, S. Coenzyme Q(10), Localizations in Model Membranes. A Langmuir Monolayer Study. *Biophys. Chem.* **2015**, *207*, 74−81.
(28) Roche, Y.; Peretti, P.; Bernard, S. Influence of the Chain Length of Ubiquinones on Their Interaction with DPPC in Mixed Monolayers. *Biochim. Biophys. Acta, Biomembr.* **2006**, *1758*, 468−478.
(29) Choi, Y.; Attwood, S. J.; Hoopes, M. I.; Drolle, E.; Karttunen, M.; Leonenko, Z. Melatonin Directly Interacts with Cholesterol and Alleviates Cholesterol Effects in Dipalmitoylphosphatidylcholine Monolayers. *Soft Matter.* **2014**, *10*, 206−213.
(30) Peters, B. J.; Groninger, A. S.; Fontes, F. L.; Crick, D. C.; Crans, D. C. Differences in Interactions of Benzoic Acid and Benzoate with Interfaces. *Langmuir* **2016**, *32*, 9451−9459.
(31) Sostarecz, A. G.; Gaidamauskas, E.; Distin, S.; Bonetti, S. J.; Levinger, N. E.; Crans, D. C. Correlation of Insulin-Enhancing Properties of Vanadium-Dipicolinate Complexes in Model Membrane Systems: Phospholipid Langmuir Monolayers and AOT Reverse Micelles. *Chem. − Eur. J.* **2014**, *20*, 5149−5159.
(32) Chimote, G.; Banerjee, R. Effect of Antitubercular Drugs on Dipalmitoylphosphatidylcholine Monolayers: Implications for Drug Loaded Surfactants. *Respir. Physiol. Neurobiol.* **2005**, *145*, 65−77.
(33) Kaganer, V. M.; Mohwald, H.; Dutta, P. Structure and Phase Transitions in Langmuir Monolayers. *Rev. Mod. Phys.* **1999**, *71*, 779−819.
(34) Veldhuizen, E. J. A.; Haagsman, H. P. Role of Pulmonary Surfactant Components in Surface Film Formation and Dynamics. *Biochim. Biophys. Acta, Biomembr.* **2000**, *1467*, 255−270.
(35) Veldhuizen, R.; Nag, K.; Orgeig, S.; Possmayer, F. The Role of Lipids in Pulmonary Surfactant. *Biochim. Biophys. Acta, Mol. Basis Dis.* **1998**, *1408*, 90−108.
(36) Wüstneck, R.; Perez-Gil, J.; Wüstneck, N.; Cruz, A.; Fainerman, V. B.; Pison, U. Interfacial Properties of Pulmonary Surfactant Layers. *Adv. Colloid Interface Sci.* **2005**, *117*, 33−58.
(37) Nowotarska, S. W.; Nowotarski, K. J.; Friedman, M.; Situ, C. Effect of Structure on the Interactions between Five Natural Antimicrobial Compounds and Phospholipids of Bacterial Cell Membrane on Model Monolayers. *Molecules* **2014**, *19*, 7497−7515.
(38) Sohlenkamp, C.; Geiger, O. Bacterial Membrane Lipids: Diversity in Structures and Pathways. *FEMS Microbiol. Rev.* **2016**, *40*, 133−159.
(39) De, T. K.; Maitra, A. Solution Behavior of Aerosol Ot in Nonpolar-Solvents. *Adv. Colloid Interface Sci.* **1995**, *59*, 95−193.
(40) Eicke, H. F.; Rehak, J. Formation of Water-Oil-Microemulsions. *Helv. Chim. Acta* **1976**, *59*, 2883−2891.
(41) Maitra, A. Determination of Size Parameters of Water Aerosol OT Oil Reverse Micelles from Their Nuclear Magnetic-Resonance Data. *J. Phys. Chem.* **1984**, *88*, 5122−5125.
(42) Zulauf, M.; Eicke, H. F. Inverted Micelles and Microemulsions as Studied by Photon Correlation Spectroscopy. *J. Phys. Chem.* **1979**, *83*, 480−486.
(43) Crans, D. C.; Trujillo, A. M.; Bonetti, S.; Rithner, C. D.; Baruah, B.; Levinger, N. E. Penetration of Negatively Charged Lipid Interfaces by the Doubly Deprotonated Dipicolinate. *J. Org. Chem.* **2008**, *73*, 9633−9640.
(44) Crans, D. C.; Trujillo, A. M.; Pharazyn, P. S.; Cohen, M. D. How Environment Affects Drug Activity: Localization, Compartmentalization and Reactions of a Vanadium Insulin-Enhancing Compound, Dipicolinatooxovanadium(V). *Coord. Chem. Rev.* **2011**, *255*, 2178−2192.
(45) Koehn, J. T.; Magallanes, E. S.; Peters, B. J.; Beuning, C. N.; Haase, A. A.; Zhu, M. J.; Rithner, C. D.; Crick, D. C.; Crans, D. C. A Synthetic Isoprenoid Lipoquinone, Menaquinone-2, Adopts a Folded

DOI: 10.1021/acs.langmuir.8b01661
Langmuir 2018, 34, 8939−8951

Conformation in Solution and at a Model Membrane Interface. *J. Org. Chem.* **2018**, *83*, 275−288.
(46) Samart, N.; Beuning, C. N.; Haller, K. J.; Rithner, C. D.; Crans, D. C. Interaction of a Biguanide Compound with Membrane Model Interface Systems: Probing the Properties of Antimalaria and Antidiabetic Compounds. *Langmuir* **2014**, *30*, 8697−8706.
(47) Sripradite, J.; Miller, S.; Tongraar, A.; Johnson, M.; Crans, D. How Interfaces Affect the Acidity of the Anilinium Ion. *Chem. - Eur. J.* **2016**, *22*, 3873−3880.
(48) Leekumjorn, S.; Sum, A. K. Molecular Simulation Study of Structural and Dynamic Properties of Mixed DPPC/DPPE Bilayers. *Biophys. J.* **2006**, *90*, 3951−3965.
(49) Leekumjorn, S.; Sum, A. K. Molecular Investigation of the Interactions of Trehalose with Lipid Bilayers of DPPC, DPPE and Their Mixture. *Mol. Simul.* **2006**, *32*, 219−230.
(50) Wang, Z.; Yang, S. Effects of Fullerenes on Phospholipid Membranes: A Langmuir Monolayer Study. *ChemPhysChem* **2009**, *10*, 2284−2289.
(51) Jones, M. N. *Micelles, Monolayers, and Biomembranes*; Wiley-Liss: New York, 1995.
(52) Crans, D. C.; Peters, B. J.; Wu, X.; McLauchlan, C. C. Does Anion-Cation Organization in Na^+-Containing X-Ray Crystal Structures Relate to Solution Interactions in Inhomogeneous Nanoscale Environments: Sodium-Decavanadate in Solid State Materials, Minerals, and Microemulsions. *Coord. Chem. Rev.* **2017**, *344*, 115−130.
(53) Vermathen, M.; Stiles, P.; Bachofer, S. J.; Simonis, U. Investigations of Monofluoro-Substituted Benzoates at the Tetradecyltrimethylammonium Micellar Interface. *Langmuir* **2002**, *18*, 1030−1042.
(54) Crans, D. C.; Rithner, C. D.; Baruah, B.; Gourley, B. L.; Levinger, N. E. Molecular Probe Location in Reverse Micelles Determined by NMR Dipolar Interactions. *J. Am. Chem. Soc.* **2006**, *128*, 4437−4445.
(55) Crans, D. C.; Levinger, N. E. The Conundrum of Ph in Water Nanodroplets: Sensing Ph in Reverse Micelle Water Pools. *Acc. Chem. Res.* **2012**, *45*, 1637−1645.
(56) Baruah, B.; Roden, J. M.; Sedgwick, M.; Correa, N. M.; Crans, D. C.; Levinger, N. E. When Is Water Not Water? Exploring Water Confined in Large Reverse Micelles Using a Highly Charged Inorganic Molecular Probe. *J. Am. Chem. Soc.* **2006**, *128*, 12758−12765.
(57) Majumder, R.; Sarkar, Y.; Das, S.; Ray, A.; Parui, P. P. Interfacial Ph and Polarity Detection of Amphiphilic Self-Assemblies Using a Single Schiff-Base Molecule. *New J. Chem.* **2017**, *41*, 8536−8545.
(58) Moran, L.; Scrimgeour, K.; Horton, H.; Ochs, R.; Rawn, J. *Biochemistry*, 2nd ed.; Neil Patterson, 1994.
(59) Perrin, D. D. International Union of Pure and Applied Chemistry, Analytical Chemistry Division, Commission on Electroanalytical Chemistry. *Dissociation Constants of Organic Bases in Aqueous Solution*; Butterworths: London, 1965.
(60) Marques, A. V.; Trindade, P. M.; Marques, S.; Brum, T.; Harte, E.; Rodrigues, M. O.; D'Oca, M. G. M.; da Silva, P. A.; Pohlmann, A. R.; Alves, I. D.; de Lima, V. R. Isoniazid Interaction with Phosphatidylcholine-Based Membranes. *J. Mol. Struct.* **2013**, *1051*, 237−243.
(61) Rodrigues, C.; Gameiro, P.; Prieto, M.; de Castro, B. Interaction of Rifampicin and Isoniazid with Large Unilamellar Liposomes: Spectroscopic Location Studies. *Biochim. Biophys. Acta, Gen. Subj.* **2003**, *1620*, 151−159.
(62) Tollin, G.; Salamon, Z.; Hruby, V. J. Techniques: Plasmon-Waveguide Resonance (PWR) Spectroscopy as a Tool to Study Ligand-Gpcr Interactions. *Trends Pharmacol. Sci.* **2003**, *24*, 655−659.
(63) Contreras, F. X.; Sánchez-Magraner, L.; Alonso, A.; Goñi, F. M. Transbilayer (Flip-Flop) Lipid Motion and Lipid Scrambling in Membranes. *FEBS Lett.* **2010**, *584*, 1779−1786.
(64) Gurtovenko, A. A.; Vattulainen, I. Molecular Mechanism for Lipid Flip-Flops. *J. Phys. Chem. B* **2007**, *111*, 13554−13559.
(65) Henseleit, U.; Plasa, G.; Haest, C. Effects of Divalent-Cations on Lipid Flip-Flop in the Human Erythrocyte-Membrane. *Biochim. Biophys. Acta, Biomembr.* **1990**, *1029*, 127−135.
(66) Kandasamy, S. K.; Larson, R. G. Cation and Anion Transport through Hydrophilic Pores in Lipid Bilayers. *J. Chem. Phys.* **2006**, *125*, No. 07491.
(67) Smeets, E. F.; Comfurius, P.; Bevers, E. M.; Zwaal, R. F. A. Calcium-Induced Transbilayer Scrambling of Fluorescent Phospholipid Analogs in Platelets and Erythrocytes. *Biochim. Biophys. Acta, Biomembr.* **1994**, *1195*, 281−286.

DOI: 10.1021/acs.langmuir.8b01661
Langmuir 2018, 34, 8939−8951

Appendix IX: The First-Row Transition Metals in the Periodic Table of Medicine

This manuscript is a review of the uses of first-row transition metals in medicine and is published in *Inorganics*.[1]

References

1. Van Cleave, C.; Crans, D.C., The First-Row Transition Metals in the Periodic Table of Medicine. *Inorganics* **2019**, *7*, 111.

inorganics

MDPI

Review

The First-Row Transition Metals in the Periodic Table of Medicine

Cameron Van Cleave [1] and Debbie C. Crans [1,2,*]

[1] Department of Chemistry, Colorado State University, Fort Collins, CO 80523, USA
[2] Cell and Molecular Biology Program, Colorado State University, Fort Collins, CO 80523, USA
* Correspondence: Debbie.Crans@colostate.edu

Received: 21 June 2019; Accepted: 27 August 2019; Published: 6 September 2019

check for updates

Abstract: In this manuscript, we describe medical applications of each first-row transition metal including nutritional, pharmaceutical, and diagnostic applications. The 10 first-row transition metals in particular are found to have many applications since there five essential elements among them. We summarize the aqueous chemistry of each element to illustrate that these fundamental properties are linked to medical applications and will dictate some of nature's solutions to the needs of cells. The five essential trace elements—iron, copper, zinc, manganese, and cobalt—represent four redox active elements and one redox inactive element. Since electron transfer is a critical process that must happen for life, it is therefore not surprising that four of the essential trace elements are involved in such processes, whereas the one non-redox active element is found to have important roles as a secondary messenger.. Perhaps surprising is the fact that scandium, titanium, vanadium, chromium, and nickel have many applications, covering the entire range of benefits including controlling pathogen growth, pharmaceutical and diagnostic applications, including benefits such as nutritional additives and hardware production of key medical devices. Some patterns emerge in the summary of biological function andmedical roles that can be attributed to small differences in the first-row transition metals.

Keywords: first-row transition metals; metals in medicine; periodic table; speciation

1. Introduction

Cations are counter ions in biology and critical for maintaining charge balance. Proteins, DNA, and RNA contain charged residues where counter ions are important to the specific three-dimensional structure and function of each [1]. Metal cations that neutralize these charges include main group metal ions and transition metals ions. Transition metal ions are generally less commonly found in nature compared to the alkali metal ions, such as sodium and potassium ions, and the alkaline earth metal ions, such as magnesium and calcium ions. However, they do play a critical role, whether it be structural or catalytic [2]. In the following manuscript, we summarize the medicinal properties of the first-row transition metals and include a comparison of the different metal ions and their speciation. Because medical applications often rely on the roles of the elements in biology, we also included some brief summaries and a discussion of the occurances of the first-row elements. Indeed, the use of each metal ion as counterions plays an important role for the medicial applications, and by summarizing the speciation of each of these metals ions, the reader will recognize the properties that are important to the action and applications of each element. To summarize the applications of the first-row transition metals, a medicinal periodic table of the elements is presented (Figure 1). Details of the medicinal applications of all the elements within the periodic table are shown in this figure and the particulars are identified in the caption. However, in this manuscript we focused on the pharmaceutical, diagnostic, and other medicinal applications of the first-row transition metals in the periodic table.

The year 2019 is designated by the United Nations as the International Year of the Periodic Table in celebration of the first report of the periodic table in 1869 by Dmitri Mendeleev of Russia. There were many key discoveries that led to the organization of the elements in the manner we recognize today, examples of which have been highlighted elsewhere [3,4]. A total of six scientists worked on the periodic table around the same time, though only two are well known [5]. In addition to Mendeleev's periodic table, Julius Lothar Meyer of Germany continued his earlier work and reported a periodic table in 1870. As elegantly articulated by Eric R. Scerri [5], "the periodic table of the elements is one of the most powerful icons in science: a single document that captures the essence of chemistry in an elegant pattern. Nothing like it exists in biology or physics or any other branch of science". Although both periodic tables properly describe the succession of the first-row metals, only Mendeleev's periodic table has the changes in properties consistent with the medicinal applications summarized in this manuscript. We have generated a periodic table of medicines shown in Figure 1, of which nutritional, pharmaceutical, and diagnostic applications as well as roles in medicinal hardware of first-row transition metals are a small part.

Metal ions have important catalytic and structural roles in biology. One-third of the proteins in the human genome contain a metal ion that playa a key role as a cofactor. For example, iron (abbreviated Fe from the Latin *ferrum*) is an important ion for the proteins involved in respiration and electron transport [6]. This means that this metal ion, found in oxidation states II and III, will coordinate to a protein and play an either structural or catalytic role. Each of the first-row transition elements have medical applications, many of which are components of materials used in medical procedures as well as roles as pharmaceuticals or diagnostic agents. Application of metal-based drugs are different from carbon-based drugs, because upon processing, the carbon-based drugs generally break down into CO_2 and various metabolites. Metal-based drugs will metabolise and form a simple metal ion which will interact with cellular components and form new compounds. Such new compounds may have a biological effect and, thus, extend the effects of the original drug added to the system. In this work, we briefly summarized the medical applications, followed by a section on speciation of metal ions highlighting the metal ions that form at neutral physiological pH for each element. Although other conditions exist in nature in the biosphere, such as the acidic environment of the stomach or in bacteria, fungi, and algea, we here focus on the metal ions forming near neutral pH in cells and the blood. The images shown in the periodic table of medicines (Figure 1) not only demonstrate the versatile uses of the first-row transition metals but illustrate the fact that nearly all elements of the periodic table have some direct medicinal use.

Several first-row transition metals, including the elements iron, copper, zinc, manganese, and cobalt, are essential elements for humans. The simplest definition of an essential element is that the element is required for life and its absence will result in the organisms death and/or severe malfunction [7]. However, in addition to mammals the biosphere includes many organisms for which additional metal ions are critical for growth and development [8–10]. It is important to emphasize that an element's essentiality can vary depending on whether the focus is for humans or other organisms. For example, an element such as nickel is essential for the bacterial enzyme urease that is an essential component for bacteria but not for human beings. This means that nickel is required for bacteria and needed for their growth, but since such metabolic pathways are not found in human beings, it is not essential for human beings. Experiments addressing essentiality are very difficult to conduct particularly with elements such as the first-row transition metals, because materials containing the metal ions are very similar and most metals preparations will contain trace levels of the related elements. For examples, iron supplements will contain trace levels of cobalt, manganese, nickel, and vanadium. Thus, the question of the essentiality of vanadium will be difficult to address experimentally because vanadium will be administered with the iron in supplements and food. Consequently, a number of controversies exist with regard to a chromium and whether it is essential or not.

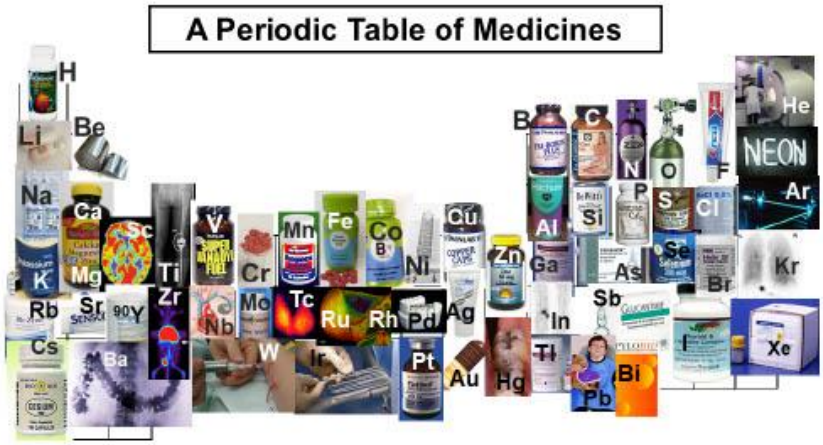

Figure 1. The periodic table with known medicinal uses of each main group or transition metal element when available. In the following, we list the use of each element. Hydrogen (H), boron (B), carbon (C), calcium (Ca), phosphorous (P), potassium (K), magnesium (Mg), vanadium (V), manganese (Mn), iron (Fe), cobalt (Co), copper (Cu), zinc (Zn), selenium (Se), rubidium (Ru), molybdenum (Mo), and cesium (Cs) are commonly found in supplements readily available to the public and are illustrated as such. Helium (He) is crucial in the operation of MRI machines. Lithium (Li) as lithium carbonate is the most common treatment of bipolar disorder. Beryllium (Be) foil is used as shielding in radiographic instruments. Nitrogen (N), as nitrous oxide, is a common anesthetic. Oxygen (O) has many medical uses, including anesthetics and resuscitation, and is illustrated here for use in ventilation. Fluorine (F) and tin (Sn) as stannous fluoride are a common ingredient in toothpaste. Sodium (Na) and chlorine (Cl) are used as NaCl in saline solutions. Aluminum (Al) compounds are a common active ingredient in antiperspirant deodorants. Silicon (Si) is used in antacid products. Sulfur (S) is illustrated as campden tablets, which are used for sterilization in beer fermentation. Argon (Ar) lasers are used in eye surgery. Zirconium (Zr) is used in immuno-positron emission tomography (PET) imaging while scandium (Sc) is a candidate for the same technique. Titanium (Ti), palladium (Pd), niobium (Nb), nickel (Ni), and tantalum (Ta) are used in medical implants. Chromium (Cr) is shown as Cr(III) picolinate, which is a controversial supplement used in lowering insulin resistance. Gallium (Ga), yttrium (Y), technetium (Tc), lanthanum (La), astatine (At), and actinium (Ac) are all used in nuclear medicine. Arsenic (As), as As(III) trioxide, is used to treat certain forms of leukemia. Bromine (Br) as KBr is an active ingredient in canine seizure medication. Krypton (Kr) was used in lung ventilation studies but has since been phased out. Strontium (Sr) is used in Sensodyne® toothpaste. Rhodium (Rh), ruthenium (Ru), and rhenium (Re) complexes are used as anticancer agents. Silver (Ag) is used in antibacterial ointments. Indium (In) is used in white blood cell scans. Antimony (Sb) is used in leishmania medicine. Barium (Ba) is used in X-ray imaging of the gastrointestinal tract. Tungsten (W) is used in shielded syringes. Iridium (Ir) is used in brachytherapy. Gold (Au) was used as a treatment for rheumatoid arthritis but has been phased out. Mercury (Hg) is used in dental amalgams. Lead (Pb) is used in X-ray aprons. Bismuth (Bi) is used in stomach ulcer medicine. Neon (Ne), germanium (Ge) cadmium (Cd), tellurium (Tl), hafnium (Hf), osmium (Os), polonium (Po), francium (Fr), radon (Rn), and radium (Ra) although most of these are toxic elements for human life, some of these elements are under development as potential agents for disease treatment but to our knowledge they are not currently used for benefical applications in medicine. References to most of these facts are dispersed throughout the manuscript.

The human body consists mainly (96%) of four elements, carbon (C), oxygen (O), hydrogen (H), and nitrogen (N). The rest of the elements make up 4% and that includes all the first-row transition metal ions as well as the rest of the periodic table. Scandium is present in very low to non-existent

concentrations in humans and the biosphere, but it is more plentiful in the Earth's crust even though its minerals are rare and it is considered a rare-earth element. In contrast, iron is considered a trace element in the human body despite being the most plentiful of the first-row transition metals in the Earth's crust (see Figure 2) [11]. Summarizing the most common minerals in which the first-row transition elements occur in the environment is important for the technological development of the applications of these elements. Table 1 lists these minerals, which are also referred to as oxides and sulfides. Each first-row transition element lends different colors to their respective minerals, the diversity of which is demonstrated, as described in Table 1. Although most of these minerals are not very soluble in water, they can leech into groundwater with rainfall. As a result, the metal ions are transported to the water supply and end up being distributed to human beings. Most countries have government agencies, such as the Environmental Protection Agency in the United States, that have stringent regulations on the allowable concentrations of these metals in drinking water because while many of these metals are largely considered non-toxic, overload of any element in the human body can lead to undesirable health effects.

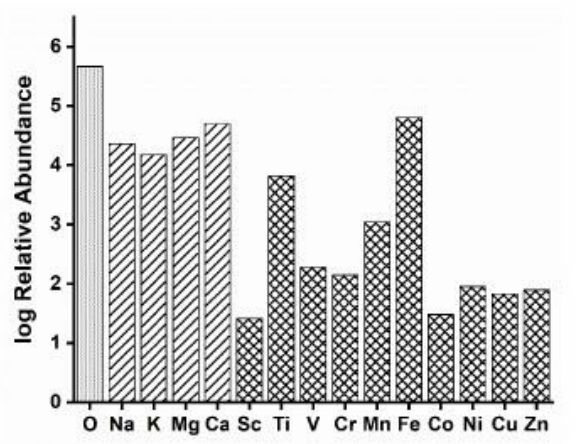

Figure 2. The relative abundance (ppm) on a log scale of oxygen (small dashes), biologically relevant main group metals (diagonal lines), and the first-row transition metals (cross hatching) in the Earth's crust on a log scale. This figure was redrawn and modified from Reference [12].

It is generally recognized that some metal ions are necessary for life but that too much of the metal can be problematic and lead to disease. It therefore seems obvious that the addition of some compounds containing essential metals will, in some cases, benefit organisms. However, the ability of some metal ions to be involved in the formation of reactive oxygen species (ROS) underlines the need for systemic control. Uptake and excretion of metal ions are biological processes that are increasingly important in medicine, and the formulation of metal ions for supplements and therapeutic purposes are two conditions appreciated as important for human health. Drug delivery has also received recent consideration as an important facet of health. For example, the form of Fe in Fe-containing supplements matters given that uptake of iron citrate salts differs from iron chloride salts since uptake of Fe in citrate salts are more effective than that of Fe in chloride salts. Medicinal effects of any therapeutic agent is therefore a complex matter in which the delivery, uptake, biodistribution, and mode of action all play a role. In the following, we focused on summarizing the information on each first-row transition element and their activities and applications in biological systems and medicine.

Table 1. Common minerals of first-row transition metals.

Element	Common Minerals	Mineral Crystal System	Mineral Color	References
Scandium (Sc)	Thortveitite ($Sc_2Si_2O_7$)	Monoclinic	Grayish green	[13–16]
Titanium (Ti)	Ilmenite ($FeTiO_3$) rutile (TiO_2)	Hexagonal; tetragonal	Iron black; reddish brown	[11,12,15]
Vanadium (V)	Vanadinite [$Pb_5(VO_4)_3Cl$] carnotite [$K(UO_2)VO_4{\cdot}1.5\ H_2O$]	Hexagonal; monoclinic	Red to brownish yellow; bright yellow to dark yellow	[11,12,15]
Chromium (Cr)	Chromite ($FeCr_2O_4$)	Cubic	Black	[11,12,15]
Manganese (Mn)	Pyrolusite (MnO_2)	Tetragonal	Black or dark grey	[12,15,17]
Iron (Fe)	Hematite, (Fe_2O_3) magnetite (Fe_3O_4)	Hexagonal; cubic	Red or black; iron black	[11,12,15]
Cobalt (Co)	Smaltite ($CoAs_2$) cobaltite (CoAsS) linnaetite (Co_3S_4)	All cubic	Grey to white; white to grey with purple tint; light gray to dark grey	[11,12,15]
Nickel (Ni)	Garnierite [$(Ni,Mg)_6Si_4O_{10}(OH)_8$] pentladite [$(Ni,Fe)_9S_8$]	N/A; cubic	N/A; bronze yellow	[11,12,15]
Copper (Cu)	Native metal, chalcopyrite ($CuFeS_2$) chalcocite (Cu_2S)	Cubic; tetragonal; orthorhombic	Pale rose to copper red; brass yellow; blackish grey to black	[12,15]
Zinc (Zn)	Sphalerite (ZnS) smithsonite ($ZnCO_3$)	Cubic; hexagonal	Various colors possible	[11,12,15]

2. Properties of First-Row Transition Metals

The International Union of Pure and Applied Chemistry (IUPAC) definition of a transition metal is "an element whose atom has a partially filled d-subshell or which can give rise to cations with an incomplete d-subshell" [18]. Cotton and Wilkinson [11] expanded the IUPAC definition by including scandium and yttrium in group 3 as first- and second-row transition metals, respectively. The first transition metal, element 21—scandium, has an electronic configuration of $1s^22s^22p^63s^23p^64s^23d^1$ (also described as an argon core with 4s filled and one electron in the 3d subshell, $[Ar]4s^23d^1$) and the last first-row transition metal, element 30—zinc, has the electronic configuration of $1s^22s^22p^63s^23p^64s^23d^{10}$. Few of these metals exist in nature in their native metallic state. In general, they are found as metal ion complexes in the form of minerals, a number of which are listed in Table 1. The properties of these metal ions vary dramatically as illustrated in Figure 3a,b. In Figure 3a, the difference between the oxidation state of the blue vanadium(IV), vanadyl sulfate, and the white (colorless) vanadium(V), potassium metavanadate is visibly shown. Also, Figure 3b presents the metal chloride salts of Cr, Mn, Fe, Co, Ni, Cu, and Zn, in that order, where the variation in color from dark green to white demonstrates the differences in these systems even when the same anion is being compared. These changes originate in the systematic succession of completing the d-shell in the first-row-transition metal series and the consequence of this is described in many text books [11–13].

Depending on the group number and the nature of the ligand and redox environments, the first-row transition metals can exist in several oxidation states [19]. Table 2 summarizes the possible oxidation states of the first-row transition metals as well as the most common oxidation state(s) under physiological conditions. The conditions suitable for most living matter consequently limits the chemistry exerted by the metal ions. The structure of metal ion complexes depends on whether the material is in the solid state or dissolved in solution. Under physiological conditions, the most common form of the first-row transition metals are oxidation states II or III, or in the case of vanadium (V),

IV and V, and IV for titanium. Vanadium, in particular, tends to form oxides, being found in the oxidation state IV as the hydrated form of $V=O^{2+}$, and for oxidation state V, it is found in the form of VO_2^+ at low pH, as a coordination complex, or in the form of $H_2VO_4^-$ at neutral or basic pH. The structures of the hydrated cations vary; however, they all include octahedral geometries. Some metals, such as titanium, vanadium, copper, and zinc, can have stable four- and five-coordinate geometries, whereas most of the others tend to be six-coordinate [10]. There is a wide range of reactivity depending on the electronic composition, but there are some generalizations. For example, low oxidation state metal ions prefer to coordinate to nitrogen-based ligands, whereas higher oxidation states prefer to coordinate to oxygen-based ligands. This preference is very important, particularly with regards to the chemistry that each of these metals can undergo in physiological conditions. The properties of these are very different, as evidenced by the different aspect and color of the metal chloride salts shown in Figure 3.

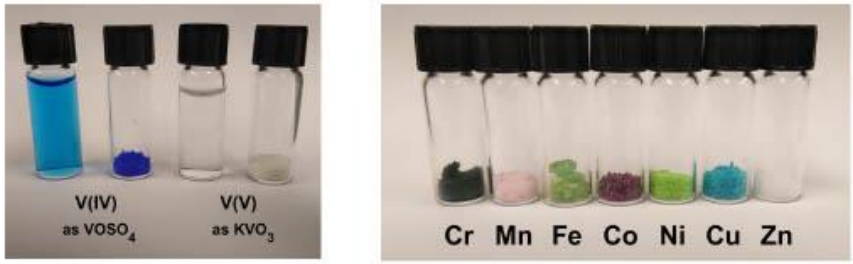

(a) (b)

Figure 3. Demonstration of the diversity of metal chemistry. (**a**) Oxidation state affects chemistry, as V(IV) is a blue solution and solid, while V(V) is a colorless solution and white powder; (**b**) chloride salts of the first-row transition metals have different colors. Shown are mainly the oxidation state (II) and (III) metal complexes $CrCl_3$, $MnCl_2$, $FeCl_3$, $CoCl_2$, $NiCl_2$, $CuCl_2$, and $ZnCl_2$ with varying amounts of hydration.

Table 2. Possible oxidation states and likely oxidation states in blood at pH 7.4 and under other biological conditions of first-row transition metals, where oxidation states in parentheses indicate rare but possible states.

Element	Possible Oxididation States	Oxidation States at pH 7.4 in Blood	Other Possible Oxidation States in the Biosphere	Reference(s)
Scandium (Sc)	III	III	III	[11,12,16]
Titanium (Ti)	0, II, III, IV	IV	0, III, IV	[11,12]
Vanadium (V)	−II, −I, I, II, III, IV, V	IV, V as metal oxides	III, IV, V	[11,12]
Chromium (Cr)	−IV, −II, 0, I, II, III, V, VI	III	III, (IV), V, VI	[11,12,20]
Manganese (Mn)	−III, −II, −I, 0, I, II, III, V, VI, VII	II, IV, VII	II, III, IV, VII	[11,12]
Iron (Fe)	−II, 0, I, II, III, IV, V, VI	II, III	II, III, (IV)	[11,12,21]
Cobalt (Co)	−I, 0, I, II, III, IV	II, III	II, III	[11,12]
Nickel (Ni)	0, I, II, III, IV	I, II, III	0, II	[11,12]
Copper (Cu)	(0), I, II, III, (IV)	Mainly II	I, II	[11,12]
Zinc (Zn)	(I), II	II	II	[11,12]

In the following, we will first summarize the aqueous speciation chemistry of each first-row transition metal complex and then briefly describe the discovery, occurrence, and detailed physical

properties of each element as we discuss each element seperately. If relevant, we then summarize the biological roles of each element, followed by a description of their medical applications.

3. Speciation of First-Row Transition Metal Ions in Aqueous Solutions

Because bodily fluids are responsible for the distribution of nutrients and drugs, it is important to know the form that the first-row transition metal ions exist in solution. Although some applications of the first-row transition metals are not based on their aqueous chemistry, there is no doubt that the speciation chemistry is important for the metal–protein, metal–DNA, metal–RNA or metal–metabolite complexation reactions that occur under physiological conditions.

Many first-row transition metals form divalent cations (oxidation state II) as one of the major oxidation states in blood and in the biosphere, as summarized in Table 2. However, Sc and Cr prefer oxidation state III, and Ti prefers oxidation state IV at pH 7.4. Vanadium prefers oxidation IV and V but forms metal oxides VO^{2+} and $VO_2{}^+$. Oxidation state V of V also forms anionic species such as $H_2VO_4{}^-$ at pH 7.4. Most of the transition metal ions undergo pH-dependent hydrolysis in aqueous solution and, thus, the concentration of a particular cation may be significantly reduced depending on the overall concentration. The properties of each metal ion are related to crystal field theory and ligand field stabilization resulting in the description of speciation chemistry. The following summary is taken from speciation diagrams in the book by Baes and Mesmer [21] and serves to illustrate the nature of the aqueous solutions of each first-row transition metal ions.

Scandium forms mononuclear ($Sc(OH)^+$), dinuclear ($Sc_2(OH)_2{}^{4+}$), or trinuclear ($Sc_3(OH)_5{}^{4+}$) species in aqueous solution depending on pH and Sc concentration: these multinuclear species form at high concentration (0.1 M), whereas at 10 µM concentration there are very few dinuclear or trinuclear species. Titanium mainly forms cations in oxidation state II and IV, although some in oxidation state III can also form. Ti^{2+} forms at low pH and low redox potential and Ti in oxidation state IV is the major oxidation state forming several species depending on pH: $Ti(OH)_3{}^+$, $Ti(OH)_4$ and TiO_2. Titanium in oxidation state III forms $Ti(OH)_2{}^+$ and a dinuclear species $Ti_2(OH)_2{}^{4+}$.

Vanadium is mainly present in the form of V(IV) and V(V). Both these ions form oxo species for V(IV), it is the vanadyl cation, VO^{2+}, and for V(V) the main species at low concentration and neutral pH is $H_2VO_4{}^-$, also referred to as vanadate. However, neither VO^{2+} or $H_2VO_4{}^-$ forms in high concentration near neutral pH, because both these species form oligomeric species. For V(IV), the species $VOOH^+$ and $(VOOH)_2{}^{2+}$ and polymeric species forms. For V(V) the polymeric species are $V_2O_7{}^{4-}$, $V_4O_{12}{}^{4-}$, and $V_5O_{15}{}^{5-}$ and other corresponding species in different protonation states. Thus, at neutral pH and at mM concentrations there is very little of the mononuclear species in solution. However, at basic pH, the speciation will be very different. Recently, it was discovered that V(III) is much more stable than anticipated, and it was found to form in aqueous solution by the reduction with ascorbate [22]. The fact that this form of V was previously missed under physiological conditions is because some of the V(III) species are only observable using high-frequency and high-field EPR spectroscopy. Chromium exists in oxidation states II, III, and VI. Oxidation state II is reactive at various pH values and will react with water. Oxidation state III is stable under most physiological conditions forming the $Cr(OH)^{2+}$, $Cr(OH)_2{}^+$, $Cr(OH)_4{}^-$, and probably $Cr(OH)_3$. Even at µM concentration, oligomeric or polymolecular species form, including $Cr_2(OH)_2{}^{4+}$ and $Cr_3(OH)_4{}^{5+}$, so the specific species depends on the pH and the concentration. Oxidation state VI is toxic, forming $HCrO_4{}^-$, and above 10 mM, $Cr_2O_7{}^{2-}$.

Manganese exists in most different oxidation states, but only oxidation state II, III, and VII form in significant amounts in solution. Mn^{2+} hydrolyzes at pH 8 at 0.1 M concentration and the dinuclear species $Mn_2(OH)_3{}^+$ forms. At 10 µM, Mn^{2+} exists up until pH 10, at which point $Mn(OH)^+$ and the dinuclear species $Mn_2(OH)_3{}^+$ form. Iron in oxidation state II and III form over a wide potential and pH range. The octahedral ferric iron (Fe(III)) complexes such as the purple hexa-aquo ion begin to hydrolyze at about pH 1 forming first the yellow $Fe(H_2O)_5OH^{2+}$. At 10 µM, monomeric species form including $Fe(H_2O)_4(OH)_2{}^+$, $Fe(H_2O)_3(OH)_3{}^-$, and $Fe(H_2O)_2(OH)_4{}^-$. At 0.1 M, in addition to

the $Fe(H_2O)_5OH^{2+}$, polynuclear species form beginning with $Fe_2(OH)_2^{4+}$, $Fe_3(OH)_4^{5+}$, $Fe(OH)_2^{+}$, $Fe(OH)_3$, and $Fe(OH)_4^{-}$. In contrast, the high spin ferrous hexa-aquo $Fe(H_2O)_6^{2+}$ is stable up until about pH 10 at which point the $Fe(OH)^{+}$, $Fe(OH)_2$, and $Fe(OH)_3^{-}$ species form.

Cobalt, in aqueous solutions, exists in the form of a cobaltous ion (Co^{2+}) because Co^{3+} is a powerful oxidizing agent which decomposes water. Co^{2+} is d^7 and ligand field stabilization energies disfavor the tetrahedral configuration compared to the octahedral configuration and, therefore, conditions exist in which both species are present in solution as $Co(H_2O)_6^{2+}$ and $Co(H_2O)_4^{2+}$. Speciation of CO^{2+} at 0.1 M results in Co^{2+} until about pH 8 when $Co_4(OH)_4^{4+}$, $Co(OH)_2$, and $Co(OH)_3^{-}$ form. At low concentration, the speciation of Co^{2+} at 10 µM results in Co^{2+} until about pH 9.5 when $Co(OH)^{+}$, $Co(OH)_2$, and $Co(OH)_3^{-}$ form. For Ni^{2+}, the major hydrolysis product is $Ni(OH)^{+}$. At high concentration (0.1 M), a tetranuclear species ($Ni_4(OH)_4^{4+}$) is formed at pH 7.5 just prior to the precipitation of $Ni(OH)_2$ and formation of $Ni(OH)_3^{-}$. At 10 µM, concentrations of Ni^{2+} exist until about pH 9.5 when $Ni(OH)_2$, $Ni(OH)_3^{-}$, and $Ni(OH)_4^{2-}$ form.

Solutions of Cu^{+} hydrolyze to form Cu_2O, which is insoluble. Cu^{2+} hydrolyzes at 0.1 M concentrations, forming $Cu_2(OH)_2^{2+}$ before precipitation at pH 6. At pH 10, the mononuclear species forms $Cu(OH)_2^{0}$, $Cu(OH)_3^{-}$, and $Cu(OH)_4^{2-}$. For speciation at 10 µM concentrations, Cu^{2+} exists until about pH 8.0, at which point $Cu_2(OH)_2^{2+}$, $Cu(OH)^{+}$, $Cu(OH)_2^{0}$, $Cu(OH)_3^{-}$, and $Cu(OH)_4^{2-}$ form. The major form of Zn is the divalent Zn(II) ion, and little hydrolysis is observed in solution to about pH 8.5. At that point, $Zn(OH)_2$ forms and above pH 11 $Zn(OH)_3^{-}$ and $Zn(OH)_4^{2-}$. The Zn speciation curves are similar at 0.1 M and 10 µM.

This section has described the hydrolysis reactions that all the first-row transition metal ions undergo. It is daunting how the differences among elements impact on the speciation chemistry summarized above. For example, the Zn speciation is very simple compared to the Cu speciation where Cu and Zn are adjacent first-row transition metal elements. Similarly, Ni and Cu are adjacent elements and the Ni speciation is much simpler than the Cu speciation. The most complex speciation was observed for Fe(III) and V. These two ions are very complex and the aqueous chemistry follows correspondingly to the speciation diagram for Fe(II) which is much simpler. These differences show that a change in oxidation state will dramatically change the solubility of the system. The stability of the complexes impact how the species exist in biological systems and, consequently, the applications to medicine.

4. Medicinal Uses of First-Row Transition Metals

Medicinal use of first-row transition metals in this document included both therapeutic and diagnostic uses of the first-row transition metals as well as examples of when the element is incorporated into materials that are used for medicinal purposes. In order for us to properly describe the uses of the each elements, we have included brief comments on basic information on the discovery and the fundamental chemistry as well as the occurrence of the element and its essentiality for humans and potential essentiality in other organisms in the biosphere.

4.1. Scandium (Sc)

The first transition metal, named scandium (Sc, element 21), was isolated as an oxide by Lars Fredrik Nilsen of Sweden in 1879, although the pure metal was not produced until the 1930s [3,13]. While Sc can exist in its metallic state, it is more commonly found in compounds and complexes as Sc(III), with predominantly octahedral geometry [16]. Scandium has a relatively high abundance in Earth's crust, comparable to cobalt (Co), but the presence of Sc-containing minerals is rare, with thortveitite being the main source [12,17]. Because of this scarcity, uses for Sc were not developed until recently [23,24] and there is still no known role for it in the biosphere.

Scandium is non-essential to human health and has been shown to be moderately toxic in a few toxicology studies [22–28]. It was found to be one of the more toxic rare-earth elements in mice [26]. It has also been tested in algae and *Caenorhabditis elegans*, a nematode used to model the nervous system;

Sc was found to inhibit growth in algae and exhibit neurotoxicity in *C. elegans* [27,28]. Work carried out in the past decade suggests that the isotopes ^{44}Sc and ^{47}Sc are promising as imaging agents and therapeutics in nuclear medicine, but have yet to reach clinical trial in the USA and Europe as of July 2019 [8,29–34]. One promising technique is Immuno-Positron Emission Tomography, or Immuno-PET, which uses radiolabeled monoclonal antibodies to visualize tumor metastases and cancer [35,36]. Two clinical trials involving the treatment of various dental diseases have been completed using an Er,Cr:YSGG laser (erbium, chromium: yttrium, scandium, gallium, garnet) [37,38]. Another application of Sc for materials is in strengthening aluminum alloys [25,39] as well as a component in very strong lights [12]. Of the first-row transition metals, it is the least used element for medicinal purposes.

4.2. Titanium (Ti)

Element 22, titanium, was discovered in 1791 by William Gregor of Britain [3]. Titanium is widely distributed in Earth's crust, with its major mineral sources being ilmenite and rutile [13]. Aside from the metallic state, titanium can also exist as Ti(II) or Ti(IV), and in rare cases as Ti(III), with oxidation state IV being the most physiologically relevant form [10,40]. Titanium dioxide (TiO_2) is a common form of Ti and is widely used in sunscreen. The convential amorphous form has a milky white appearance and is effective in scattering UV rays. However, the nanoparticle form of TiO_2 is transparent but still retains its scattering ability [41,42].

Titanium is found readily in the human body, although no reports suggest it plays an essential physiological role. It binds to human serum albumin and other proteins and is thus readily transported in the blood [43]. The element is not believed to be essential, although many reports in plants, animals, and human beings document its benefit. Titanium is able to support bone implant by osseointegration as was discovered in the 1950s [44,45]. The ability of Ti to integrate and be structurally accepted by bone without the requirement of soft tissue connection allows it to aid in healing and regrowth of bones [46].

Titanium is found readily in the human body, although no reports suggest that it plays an essential physiological role. It binds to human serum albumin and other proteins and is thus readily transported in the blood [43]. In medicine, Ti complexes and compounds have been examined as anticancer agents, in particular as titanocene dichloride. Even though the titanocene dichloride complex showed promising in vitro results and was evaluated in a clinical trial, it failed to perform satisfactorily in human studies. This is likely explained by the rapid hydrolysis of the complex [47]. However, studies continue to explore the potential of Ti as an anticancer agent and, recently, reports with dinuclear complexes are showing significantly improved anticancer activity against renal and prostate cancer cells [40,46]. Titanium dioxide (TiO_2) films have documented antimicrobial properties when irradiated by light, but there is a concern for the toxicity of TiO_2 nanoparticles [48].

The most common and well-known medical use of Ti is in implants [8,49]. Titanium and Ti-alloy implants are known to be biocompatible with excellent ability to integrate with bone. There are 488 clinical trials involving Ti are listed, of which 212 are completed. Therefore, there is no surprise that this element is used extensively, and many new applications are currently being investigated involving a wide range of applications ranging from dental implants to orthopedic prostetics. The widespread applications of Ti have been driven by the belief that it is safe and inert to processing within the human body. This belief was based on simplistic studies in aqueous solution demonstrating the high stability of Ti-complexes or alloys at physiological pH values. Recently, however, reports have been made demonstrating that Ti can corrode, which can not only lead to implant breakage, but also formation of ROS species and production of a type IV allergen [50]. There are also reports of Ti(0) becoming physiochemically corroded to Ti(IV) ions which can result in inflammation and necrosis [49,51–53]. The leached forms of titanium, either soluble Ti(IV)tricitrate or as TiO_2 nanoparticles, have resulted in toxicity [40,52]. Considering the widespread use of TiO_2 in sunscreens and particularly in the form of nanoparticles, there are several UV and non-UV debilitating cellular effects caused by TiO_2 and it is important that the form and use of TiO_2 is carefully considered [41].

4.3. Vanadium (V)

Vanadium is element 23 and was first discovered by Andres Manuel del Rio in 1801 in Mexico. Unfortunately, four years later the discovery was withdrawn because del Rio had been convinced that the element was chromium (Cr) [3]. Thirty years later, V was rediscovered by the Swedish Nils Gabriel Sefstrøm [3] who named it after the Nordic goddess of beauty and fertility, Vanadis (also called Freyja in Norse mythology). Vanadium exists in the Earth's crust in the form of numerous minerals as well as in fossil fuel deposits bound to porphyrin analogues [54–56]. It turns out that VO_2^+-porphyrin analogs are among the most stable porphyrins [55] and, thus, are found in several coal deposits, such as Venezuelian coals. Processing of this coal results in a large release of vanadium-containing aerosols [54,57].

Figure 4 shows the mushroom *Amanita muscaria* that contains amavadin, which is a V(IV)-containing natural product of specific interest to the scientific community for not containing the V=O unit, common in V(IV) coordination complexes [58,59]. Although it has been controversial whether vanadium is an essential element for human beings [60], it is known to be essential for some organisms [61]. High levels of V are found in V-accumulating tunicates, and the form in these organisms have been explored and is currentlty believed to be the V-binding proteins (VanaBin) [61,62]. The function and role of vanadium in these organisms are still being investigated [61,62]. Other V-containing enzymes were isolated from certain types of algae, seaweed, and fungi, and the class of V-dependent haloperoxidases have been characterized extensively and the X-ray structures of the vanadium-dependent chloroperoxidase and the vanadium-dependent bromoperoxidase have been reported [61]. The vanadium nitrogenase from *Azobacter vinelandii* have recently been characterized spectroscopically [63–68].

Figure 4. A photo of the *Amanita muscaria* mushroom with the V(IV)-containing natural product amavadin. The image was reproduced from JJ Harrison/Wikimedia Commons under the Creative Commons Attribution-Share Alike 3.0 Unported license (https://creativecommons.org/licenses/by-sa/3.0/deed.en).

Vanadium in oxidation state V, in the form of vanadate, is a structural and electronic phosphate analog [63–66]. Vanadyl sulfate, a simple salt with V in oxidation state IV, is used as a nutritional additive by athletes to improve glucose metabolism [69]. As a phosphate analogue, it is a potent phosphatase and phosphorylases inhibitor [70,71]. Specifically, vanadate was first discovered to be a Na^+- and K^+-ATPase inhibitor [72] and later an inhibitor for ribonucleases [73], and, for some time, vanadate was added to buffers when isolating DNA because this protected the DNA strands from hydrolysis. Recently, the inhibition of protein tyrosine phosphatases have received interest, because this signal transduction enzyme has been implicated in the action of vanadium compound to reduced elevated blood glucose in diabetic mammals [70,71]. Both vanadate and vanadyl sulfate as well as one coordination complex, bis(ethylmaltolato)oxovanadium(IV), have been investigated for potential treatment against diabetes in Phase I and II clinical trials [69,74,75]. Vanadium coordination complexes also have activities as anticancer compounds [76,77], and recently both salts and select complexes

were found to enhance an oncolytic virus, VSVΔ51, in combatting cancers that are resistant to existing therapeutics [78,79].

4.4. Chromium (Cr)

Chromium is element 24 and was discovered in 1798 by Nicholas Louis Vauquelin of France [3]. The physiologically relevant oxidation states are Cr(III), Cr(V), and Cr(VI). Cr(IV) can sometimes be observed in biological systems as an intermediate [20]. Chromium(III) generally has a coordination number of six with an octahedral geometry and, since it is hydrolytically stable at neutral pH, conversions involve redox processes [10,20]. Chromium(IV) tends to be an unstable intermediate under physiological conditions, preferring coordination number six with octahedral geometry [10,20]. Cr(V) and Cr(VI) are often found with lower coordination numbers. Chromic acid ($HCrO_4$) is a strong acid that is commonly used in acid baths for cleaning glassware. Much work has been done on the speciation of this element, and Cr(III) is reported to oxidize to higher and reduced forms [20]. Although Cr(III) is being taught as inert in introductory chemistry classes, this is only the case at neutral and slightly basic conditions.

The question of essentiality with Cr is complex because up until the 1980s, Cr was believed to be essential. Chromium(III) is therefore a component of various vitamin preparations and is still believed to be beneficial for the regulation of glucose metabolism. However, Cr is no longer believed to be essential by many scientists [80] and the matter of CrO- essentiality and its benefits is highly controversial despite a billion dollar industry supporting Cr additives [81]. The problem relating to the use of Cr(III) as a nutritional additive revolves around the fact that Cr(III) is not as stable as previously believed and will convert to the highly toxic Cr(VI) under biological conditions [49,82]. The major concern remains that some forms of Cr, generally the high oxidation states, are toxic as determined by various cancer tests, such as the Ames test [20,83–85].

Chromium has been reported to be beneficial for humans with impared glucose metabolism and treatment was effective in normalizing glucose levels [86]. These studies were fueled by the report of a chromium-containing Glucose Tolerance Factor [87]. This material was reported to have beneficial effects on diabetics, and have carried through to clinical trials and other studies with Cr-containing materials [86]. Disagreements began to appear once the question of essentiallity for Cr was questioned leading to the current general view, which no longer support the essentiallity of Cr [80].

The risk of cancer with exposure to occupational hexavalaent Cr (Cr(VI)) was studied more than 100 years ago [88]. Workers in certains industries such as chromate production, pigment production, and chrome plating have a significant greater increase in the risk for developing lung cancer [89]. Furthemore, Cr(VI) is classified as a known human carcinogen by the International Agency for Research on Cancer, known for causing cancer of the lung and positive associations with cancer of the nose and nasal sinuses [90]. However, conflicting evidence and analysis have been provided for stomach or other cancers, but a recent analysis reported that Cr(VI) does not pose a stomach cancer hazard in human beings [88]. Although Cr(III) may not have been reported to be toxic, when it oxidizes to Cr(VI), it is toxic [91]. Detailed speciation analyses have been carried out and demonstrate that Cr(III) is not as inert as previously believed, thus contributing to the debate on the safety of Cr-containing food supplements readily available online and in food stores [49,82]. However, other studies have been carried out exploring the complexity of the issue because detoxification mechanisms are also in effect [85].

4.5. Manganese (Mn)

Element 25 is manganese, which was first isolated in its metallic form from pyrolusite in 1774 by Johann Gottlieb Gahn of Sweden [3]. For Mn), there are several oxidation states that are common under physiological conditions: II, III, IV, and VII. Six-coordinate octahedral Mn(II) is the most common of the physiologically relevant valencies and coordination geometries [10]. There is, however, some variability in coordination geometries for this metal in biological systems. For example, Mn(II) forms

six-coordinate octahedral mononuclear complexes and dinuclear complexes but clusters with a Mn in coordination number of four or six.

Manganese is essential for humans and a multitude of other organisms, ranging from bacteria, to plants, to animals. The US Institute of Medicine updated the estimated average requirements and recommended dietary allowances for 22 elements for which there were sufficient data available. For adults, the tolerable upper intake level is set at 11 mg/day, while far less is recommended for children [92]. Manganese is less toxic than other transition metals such as Ni, and waterborne Mn is more readily taken up than dietary Mn [93]. However, Mn, as other essential elements, have a concentration range of acceptable range of oral intake illustrated in Figure 5.

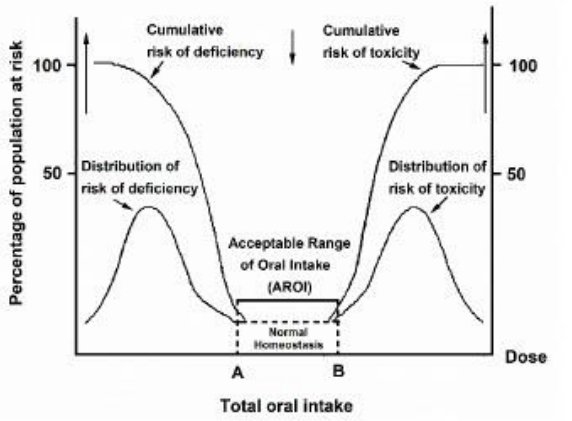

Figure 5. An illustration representing oral intake resulting in deficiency and overload of essential trace elements such as Fe, Cu, and Zn. The area between points A and B on the *x*-axis referred to as normal homeostasis, describes the ideal range of Cu for a normal and healthy organism. Reproduced with permission from Chambers et al. [94].

Manganese-based enzymes include hydrolases, superoxide dismutase, and photosystem II [1]. Several Mn-containing enzymes have the active site Mn ion involved in catalytic processes [82]. For example, glutamine synthase catalyzes the condensation of glutamate and ammonia to gluthamine [95]. Gluthamine synthase in mammals is mainly present in the brain astrocytes, liver, and kidneys. Brain astrocytes regulate glutamate and ammonium levels while recycling neurotransmitters [96]. Manganese complexes are now of interest as MRI contrast agents in part because of their presence in the brain (for references see Section 4.6).

Perhaps most well known is the role of Mn in photosystem II, which contains a Mn_4CaO_5 cluster [97]. Photosynthesis is a biochemical mechanism in plants by which chlorophyll absorbs light energy for photosynthesis. There are two families of reaction centers: type I reaction centers utilizing iron–sulfur cluster proteins in chloroplasts and type II reaction centers utilizing a quinone terminal electron acceptor in plant chloroplasts. The oxygen-evolving complex is part of photosystem two and contains a Mn_4CaO_5 cluster [97].

Superoxide dismutase (SOD) enzymes are involved in scavenging radical oxygen species (ROS) including superoxide, and the mitochondrial forms of the enzyme contain Mn as a cofactor [98]. Other SOD enzymes contain Cu or Fe instead of Mn. Manganese can participate in Fenton reactions and, thus, induce oxidative damage as supported by toxicology studies in welders [99]. Small SOD mimics have received interest as new therapeutics as anticancer compounds [100]. Manganese-based SOD mimics are generally based on porphyrin, polyamine, and salen ligands and are thought to show anticancer effects due to the fact of their ability to act as pro-oxidants within cancer cells [100,101].

Manganese-containing catalase mimics target non-radicals such as H_2O_2 and reduces neurotoxicity, acting as pro-oxidants [102].

Manganese supplements are commonly sold to treat deficiencies which can lead to improper bone growth. However, Mn is known to have neurotoxic effects in high doses, sometimes leading to a Parkinson's-like disease called manganism [103,104]. This disease often presents itself after chronic exposure to Mn in excess of 5 $\mu g/m^3$ and is distinguished from Parkinson's by a lack of Lewy bodies (protein aggregates in nerve cells) and no response to drugs used in the treatment of early Parkinson's [105]. Treatment has included chelation therapy, although the patient responses have not been encouraging, suggesting the damage had already occurred [106].

4.6. Iron (Fe)

Iron is element 26 and has been known for more than 1000 years since at least the Iron Age. While Fe is the most abundant metal on Earth, pure Fe is rare in the Earth's crust and generally comes from meteorites. However, Fe-containing minerals are readily available and often recognizable in nature with a warm rusty red color, although the common hematite and magnetite minerals appear as a darker red/black color [10]. Fe(II) and Fe(III) are the most physiologically common oxidation states although higher oxidation states are formed in some catalytic cycles. Iron complexes are commonly six-coordinate in an octahedral geometry, though a coordination number of five can be important in some systems.

Ironis an essential element in most, if not all, forms of life and a component in many biological processes with perhaps the most important being associated with respiration [6]. The complex relationships between the need to consume enough of an essential element and the problems associated with consuming to much is illustrated in Figure 5. However, Fe overload is a serious condition because the overload allows for sufficient Fe to engage in Fenton chemistry and ROS generation [107]. Formation of ROS is generally detrimental to an organism, so there are regulatory systems in place to maintain Fe homeostasis.

In blood, Fe is bound to a porphyrin, which is coordinated to the iron in the equatorial plane and, depending on the location of the complex, may contain one or two axial ligands [19]. This type of complex, known as a heme, is the major oxygen carrier in the blood. The Fe(II)-containing heme is not free but is bound to one of two proteins, hemoglobin in blood or myoglobin in muscle [6]. Hemoglobin exists in two forms: oxyhemoglobin when complexed to oxygen in arterial blood or deoxyhemoglobin when oxygen-free in venous blood [108]. The hemoglobin system is responsible for the red color of blood. For free hemoglobinis critical for life in cases when a ligand such as CO or CN binds to the heme, oxygen transport is no longer possible and the organism dies [109]. Treatment of such conditions include administration of 100% oxygen.

In addition to respiration, Fe is an important cofactor for many enzymes, too many to be described here and the reader is referred to reviews and textbooks on the topic of Fe metabolism [110]. Iron is generally a catalytically active metal ion that supports redox processes in in enzymes such as oxidases, electron transfer reactions, and in plants it is involved in nitrogen fixation [6]. The plant enzyme nitrogenase contains a Fe-containing cluster. The protein transferrin is primarily responsible for transporting Fe in the blood throughout the body, including dietary Fe shown in a simplified schematic illustration in Figure 6 [111]. The Fe levels in the body are tightly regulated, making Fe homeostasis an important medical field. Diseases from both Fe overload or deficiency are common. These problems are treated with Fe supplements or hemachromocytosis with various Fe chelators. Unfortunately, both Fe deficiency and overload conditions are common in our modern society.

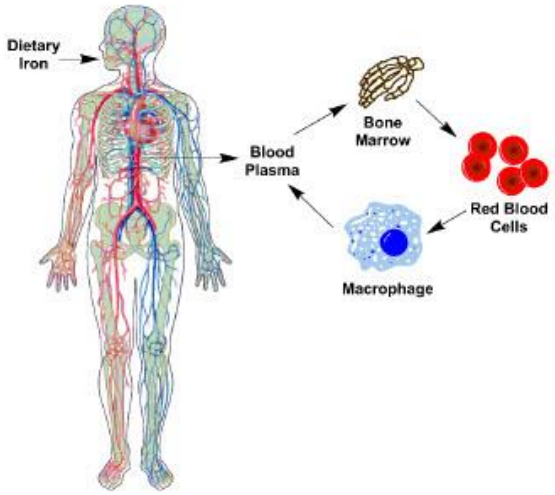

Figure 6. A simplified diagram of Fe metabolism from dietary Fe redrawn and modified from Sanghae and Nemeth [111].

There has been a significant amount of research done exploring the potential of Fe-based pharmaceuticals for treatment of cancer [112]. Because of the roles of Fe in biology, these applications are monitored carefully because doses that are too high will be detrimental [113]. Three classes of Fe compounds have been used [112], the largest group being that of ferrocene derivatives [114,115]. These organometallic compounds include ferrocerone, which is currently the only Fe-based compound used in the clinic [112]. One such ferrocene compound, ferroquine, is a derivatives which is currently in Phase II clinical trials [112,116]. In addition, a third group of ferrocene coordination compounds containing natural products have been reported with anticancer properties [115]. Coordination complexes are the second class of Fe-containing compounds have also recently been studied and they were found to have some beneficial effects. As described in detail elsewhere, these compounds are successful in treatment of several types of cancer including those that are resistent to cisplatin [112]. Although these complexes have not been investigated as extensively as ferrocene, recent studies suggest that there may be some potential applications of such systems. The third class of Fe-containing compounds recent investigation into Fe-chelators have yielded particulary interesting results [117]. A particularly intriguing system within this class of compounds, is when the chelator is a protein, such as lactoferrin. Lactoferrin is a non-heme protein binding Fe(III) at the same time as binging a carbonate anion [118]. Although it is in the blood, it does not appear to be involved in transport of Fe with the exception of lactoferrin from milk, which seems to be important for delivering Fe to newborns [107]. This system and its protolytic derivatives show anticancer properties particular when administered in combination with other agents. Recently other diseases are investigated as potential being treated with Fe-based compounds.

Recently, other applications and diseases have been investigated for treatment with Fe-based compounds. For example, Fe(II) and Fe(III) complexes are of interest as MRI contrast agents [119–121]. These complexes are alternative agents to the current standard agents that contain the lanthanide metal gadolinium, and provides options in cases when the MRI patient cannot clear the imaging agent, such as patients with kidney disorders [120]. Iron has well-characterized biochemistry and predictable physiology, making it a promising candidate for new contrast agents [120]. However, such applications must take the patients' Fe levels into account due to the potential for Fe overload.

4.7. Cobalt (Co)

Cobalt, element 27, has been known for centuries for its ability to add a blue color to glass and ceramic glazes, but it was officially discovered by Georg Brandt of Sweden in 1735 [3]. Cobalt(II) complexes typically show a four-coordinate tetrahedral or six-coordinate geometry while Co(III) complexes are often six-coordinate octahedral coordination geometry [10]. Co-compounds are very colorful. For example, the color of $CoCl_2$ salt is based on hydration. The dry form of $CoCl_2$ is sky blue; however, as the compound absorb water the color changes to purple and finally to pink. In Figure 7b, the color of purple $CoCl_2$ is compared to that of vitamin B_{12} (also referred to as cobalamin, see below) in the solid state and in solution.

Vitamin B12 is the most well-known bioactive Co-containing compound and is utilized by many organisms, from phytoplankton to humans, thus making Co an essential element to humans and many other organisms in the biosphere [122]. The vitamin's structure was solved in 1956 by the British scientist Dorothy Hodgkin and led to her receiving the 1964 Nobel Prize [123]. The structure of vitamin B_{12} is shown in Figure 7a illustrating the six-coordinate Co(III) in an octahedral geometry [10]. Vitamin B_{12} deficiency leads to fatigue, breathlessness, and poor memory [124]. Vitamin B_{12} deficiency is also found in older women that have lost the ability to extract B_{12} from foods. The condition of hypochlorhydria is found in about 47% of the population in the US caused by excessive use of antacids and low acidity in the stomach. These individuals are treated with injections of vitamin B_{12} when diagnosed.

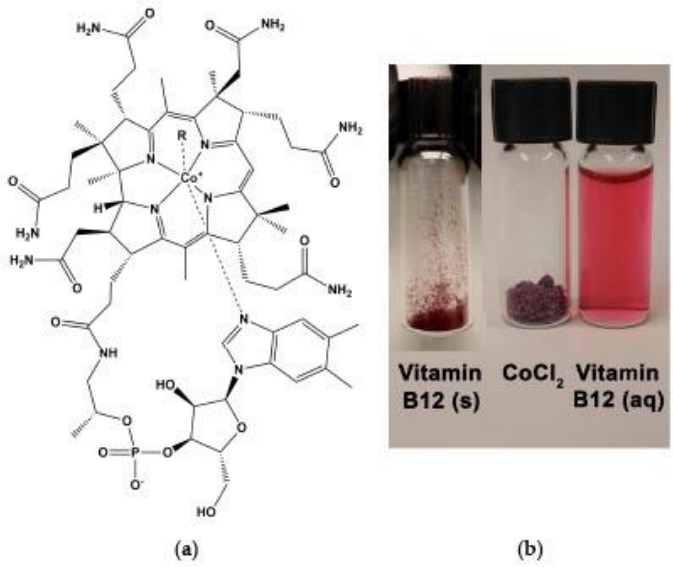

Figure 7. (**a**) The structure of vitamin B_{12}, where R is 5′-deoxyadenosyl, OH or CN; (**b**) solid vitamin B_{12} comes in the form of dark red crystals as opposed to cobalt(II) chloride, which forms blue crystals that turn purple with increasing amounts of absorbed water. When dissolved in water, vitamin B_{12} forms a pink solution.

Several forms of Co are currently used for medical purposes. Vitamin B_{12} is used in the treatment of acute cyanide poisoning in France [125] because Co(III), like Fe(III), also binds strongly to CN^- and, thus can extract the CN^- that is bound to the Fe(II) in the heme and regenerate the Fe(II)-heme complex so that it can carry oxygen. Early uses of cobalt chloride involved treatment of certain types of anemia but it has since been replaced with synthetic erythropoietin [126]. Schiff base ligands form

complexes readily with Co and have been used in a variety of medical applications. For example, the Co(III) Schiff base compound CTC-96 has completed Phase II clinical trial for the treatment of herpes simplex virus [127,128]. Compound CTC-96 is believed to prevent membrane fusion of the virus. Anticancer activity has been observed in a number of Co(II) and Co(III) Schiff base complexes [127,129]. Dinuclear heterometallic Co compounds have also been investigated, such as a cobalt-ruthenium cobaltocene derivatives which showed increased autophagic activity relative to the mononuclear Co derivative [130,131]. In addition, the radioisotope ^{60}Co has been used as a source of high-energy radiation to destroy cancerous tissue [132].

4.8. Nickel (Ni)

Element 28 is nickel, which was discovered in 1751 Axel Frederik Cronstedt of Sweden who later isolated it in 1754 [3]. The most common oxidations states for Ni are Ni(0) and Ni(II). Within these oxidation states, coordination numbers of four (square or tetrahedral geometry) and six (distorted octahedral geometry) are the most common [10]. Heteronuclear metal compounds have been suggested to be precursors to metalloenzymes and early representative of Ni–Fe-containing enzymes because they are able to catalyze a range of reactions [133]. Nickel has a high affinity for porphyrins and since it is the most stable prophyrin derivative, it is often found in coals. Exploitations of coal as an energy source releases Ni-containing aerosols [54,57].

The essentiality of Ni is somewhat controverisal, with scientists supporting both positions. While no essential role for Ni has been identified, it is a cofactor in multiple enzymes in bacteria, archaea, and fungi [134]. One well-kown Ni-containing enzyme is urease, which catalyzes the hydrolysis of urea [135]. Since urease, as a Ni-dependent enzyme, is often found in human gut bacteria, human gut health is correlated with the presence of Ni and indirectly important to human health [136]. Conversely, urease is virulence a factor for *Helicobacter pylori*, which is a causative agent of stomach ulcers [137]. Thus, the presence of Ni in vitamins supports the well being of beneficial bacteria by inhibiting some of the 40 known pathogenic species potentially residing in the human gut and, thus indirectly benefitting the human host [135].

Nickel is a common component of strong alloys, some of which have been used in implantable medical devices such as joint replacements or arterial stents. For example, The Ti–Ni alloy nitinol is used for arterial stents because of its excellent shape memory [138]. Nickel compounds have also been used to support weak bones in osteoperosis as well as to increase Fe absorption in anemia. However, there is a duality to Ni, since Ni sensitization is linked to many cases of allergic contact dermatitis, such as in body jewelry [136,139]. There have been recent cases of individuals developing Ni irritation and allergies to these implants [49]. Furthermore, the US Environmental Protection Agency has determined that Ni dust and Ni sulfide are human carcinogens. A few pharmaceutical applications of Ni are emerging. For example, Ni is one of the metals of choice in the formation of metal-containing complexes that bind to nucleic acid quadruplexes that are currently being investigated for potential use as anticancer agent [140].

4.9. Copper (Cu)

Copper is element 29 and has been known for over five thousand years. It is one of the few transition metals known to exist in nature in its native metallic form. While it can exist as Cu(I), Cu(II), and Cu(III), the most common oxidation state under physiological conditions is Cu(II). For Cu(II), the most common coordination numbers are four and six, with four generally having square planar geometry and six having distorted octahedral geometry, whereas Cu(I) prefers tetrahedral geometry [10]. The different geometric coordinations properties of Cu(I) and Cu(II) have been utilized to create molecular motion in rotaxanes [141]. This work was awarded the Nobel Prize in 2017.

Copper is an essential element to many, if not all, organisms and is found as a cofactor in a multitude of enzymes, typically coordinated to histidine, cysteine, and methionine ligands [10,113]. Copper(II) is known to coordinate both to structural or functional sites for proteins [142]. The most

well-known Cu-containing enzyme is cytochrome c oxidase, a large transmembrane protein that is vital to cellular respiration by translocating protons across the membrane to create an electrochemical gradient that drives ATP synthesis [143]. Two heme groups and two Cu sites, Cu_A and Cu_B, are present within cytochrome c oxidase. The second Cu ion Cu_B forms a binuclear center with the Fe in a heme and together they are responsible for the reduction of molecular oxygen to water. At the same time, Cu_A is involved in electron transfer to an internal heme [9,144,145]. In Cu_B, the Cu ion is coordinated to three histidine residues via the imidazole rings and has a trigonal pyramidal geometry [9]. The multivalent Cu_A site is two copper ions, both with tetrahedral geometry, bridged by two cysteine residues [10,145].

Much like Fe, Cu deficiency and overload lead to diseases. Figure 5 illustrates the potential Cu levels that an individual would experience under various doses. In excess, Cu causes toxicity via ROS generation which leads to DNA damage and is commonly treated by administration of Zn(II), which induces synthesis of small proteins rich in cysteine known as metallothioneins [113,146,147]. These proteins have a high affinity for both dietary and gastrointestinal Cu, binding Cu and sequestering it. Truncated metallothioneins were found to have Cu bound to cysteines with trigonal geometry [10]. Copper is known to cause oxidative stress in the brain, linking it to neurodegenerative diseases such as Alzheimer's and Parkinson's [148]. Copper(II) shows two different pH-dependent binding modes in the native amyloid-β peptide, both of which bind in a distorted square-planar geometry [149]. A deficiency of dietary Cu leads to anemia-like symptoms as well as neurological issues such as myelopathy [150,151].

Coppercomplexes, like Fe complexes, are of interest for anticancer theraputics. Several Cu complexes have been investigated for treatment against cancer [152,153]. These complexes are classified as chelators and ionophores, where chelators remove Cu to limit angiogenesis and cancer progression while ionophores transport Cu into cells where the ions can then exert cytotoxicity [153]. Copper anticancer compounds have been reported with a variety of ligands, such as thiosemicarbazones, thiosemicarbazides, dithiocarbamates, pyridine N-oxides, phenanthrolines, and napthoquinones, though a multitude of others have also been studied [154,155]. Investigations of dinuclear metal complexes involving Cu have also been prepared and reported to have anticancer properties. Tetrathiomolybdate is the most well-studied of the Cu-chelating compounds and has advanced to several Phase II and III clinical trials for treatment of various cancers as well as Wilson's disease, a genetic disorder that causes an accumulation of Cu in the body and is currently treated with tetrathiomolybdate [156].

Over 280 applications of Cu-containing compounds and materials have been investigated for treatment in human beings. Of these clinical trials, 184 studies have been completed and 98 are currently recruiting or active. Some of these applications include intrauterine devices (IUD). Although non-metal devices have been used for hormonal IUDs, Cu remains the most used non-hormonal devices with 150+ million being used worldwide [157]. The generally accepted mechanism for contraceptive IUDs is inflammation of the uterine lining, allowing for increased presence of white blood cells that prevent the fertilization of oocytes [158]. Other applications include Cu-infused textiles for the prevention of hospital-acquired infections. These textiles take advantage of Cu's antibacterial properties, making a type of self-sanitizing bandage to cover the wound [159,160].

4.10. Zinc (Zn)

Zinc is element 30 on the periodic table. The pure metallic form was discovered in 1746 by the German Andreas Sigismund Marggraf [3]. Zinc exists in two oxidation states: the metallic form, Zn(0), and as the cation Zn(II). Because Zn(II) has a ligand stabilization energy of zero in all potential geometries, no coordination geometry is more stable than others. Zinc is often found in four-coordinate tetrahedral geometry or six-coordinate octahedral geometry [10]. Surveys of the Cambridge Structural Database show zinc ions in four- and six-coordinate systems with frequencies of 59% and 23%, respectively [161].

Approximately one hundred years after its initial discovery, Zn(II) was reported to be essential to life and its importance in biology has been thoroughly investigated since then. As an essential element, deficiency can result in a variety of health disorders including hearing and vision impairment [10]. Since Zn is a non-redox active metal ion, its use complements that of Fe and Cu, which are also widespread in biology. The lack of redox activity may be one reason that the abundance of Zn rivals that of Ca and is important as a cofactor for metabolic enzymes, transcription factors, and facilitators of gene expression. For example, Zn is required in more than 200 transcription factors. Zinc present in vitamins and nutritional supplements. It is also in zinc lozenges which are recommended for treatment of the common cold and reduce the duration of the illness [162]. It has been proposed that the Zn may work by preventing the rhinovirus from propagating and supporting its infestation of the host, though this is a topic of debate [162].

Zinc is a key component in a number of enzymes as well as DNA-stabilizing proteins and other structural components in biology. The coordination geometry of Zn varies with its role, be it structural or catalytic [163]. When Zn(II)'s role is to structurally organize proteins, its coordination numbers are 79%, 6%, and 12%, respectively, for four, five, and six coordination [161]. Even though five-coordinate geometry is usually rare, it is found in Zn porphyrins [161]. One important group of proteins is the Zn finger proteins, which are critical for the organization and transcription of DNA [164]. Figure 8 shows DNA transcription assisted by a Zn finger protein.

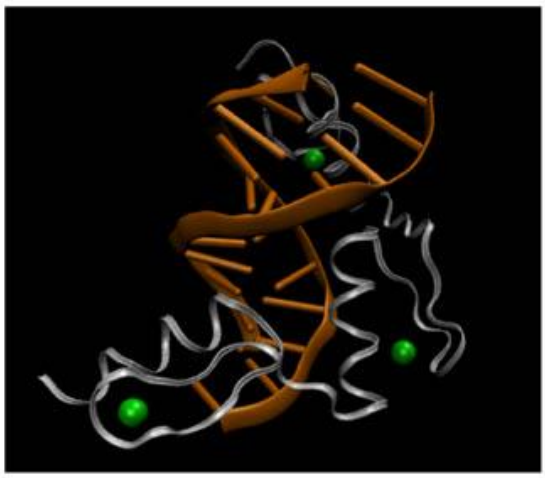

Figure 8. A Zn finger protein domain assisting in DNA transcription, where DNA is colored orange, the protein is gray, and green spheres are Zn. The image was generated with VMD software from PDB file 1A1L [165,166].

Although a non-redox active metal ion, it is now known that Zn(II) acts as a second messenger that can activate some signaling pathways within a few minutes of an extracellular stimulus such as the release of Zn(II) from intracellular compartments. Since Zn(II) cannot passively diffuse through cell membranes, homeostasis requires Zn transporter proteins that are controlled by different mechanisms. There are two families of Zn(II) transporters: SLC30A (ZnT transporters) and SLC39A (ZIP transporters) [167]. These proteins all have transmembrane domains with both N- and C-terminal peptides in the cytoplasm (ZnT transporters) or both C- and N-terminal peptides in the extracellular space (ZIP transporters). The ZnT transporters are Zn exporters, transporting Zn from the inside of the cell to the outside, while ZIP transporters are importers, transporting Zn into the cell from outside. Most of the ZIP transporters reside on the plasma membrane and transport Zn(II) into the cell, but ZIP7

resides in the endoplasmic reticulum membrane and ZIP13 is in the Golgi membrane. Both ZIP7 and ZIP13 transport Zn(II) from these stores to the cell. Recent discoveries investigating the Zn(II) ZIP transporters have linked these proteins to Zn(II) signaling related to cancer. Figure 9 is a schematic showing the members of the LIV-1 family of ZIP transporters and the different cancers in which they have been implicated. Most of these studies involve biochemical investigations and specific details on how that particular transporter works. Details regarding each of these ZIP transporter proteins have been reviewed elsewhere [168].

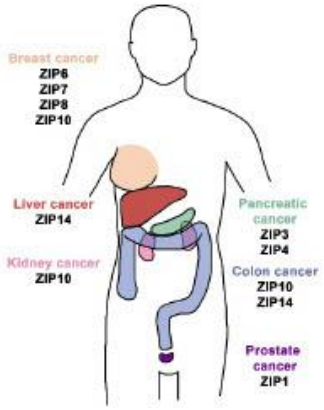

Figure 9. A Schematic showing the association of the members of the LIV-1 Zn-ZIP transporter family and the different cancers that have been implicated these transporters. Redrawn from an imge in Reference [168].

Zinc has been used in several medications including antibacterial ointments. There is also evidence of Zn as an active ingredient in some ancient medicines [169]. The form of Zn(II) in antibacterials is ZnO, possibly in nanoparticle form [170]. Furthermore, Zn and Ni are the metals of choice in the formation of metal-containing complexes that bind to nucleic acid quadruplexes that are currently being investigated for potenital use as anticancer agents [154]. The use of Zn(II)-containing coordination compounds has been reported in animal studies against diabetes [171] which may stem from the fact that it binds with high affinity to regulatory protein tyrosine phosphatases, one of the classes of proteins that uses Zn(II) as a signaling molecule [168,172].

5. Discussion

As described above, all first-row transition elements have applications in medicine whether it is well understood or currently under development. Their involvement ranges from limited applications of non-essential elements such as Sc, for which there is relatively little information available compared to the essential elements such as Fe, Cu, and Zn which have numerous applications.

For some of the elements, the potential for essentiality is debated in the literature, but these issues are complex because trace elements such as V are often administered as an impurity with other supplements such as Fe-supplements. Furthemore, as in the case of Ni, its presence in the human gut serves a protective function by eliminating pathogenic species that otherwise might invade the human gut. However, strictly defined, non-essential elements are elements that do not have a defined role in humans such as Ti, V, Cr, and Ni are known and are surprisingly found to have many applications, particularly when compared to, for example, the essential elements Mn and Co.

It is, however, interesting to note that most essential transition elements are first-row transition elements. Furthermore, the late first-row transition metals, with the exception of Ni, are essential to

humans. This is interesting and presumably a combination of the properties that the elements have as well as the properties of the molecules that make up the biosphere. If proteins were made up from different components, presumably the essential elements would consist of different elements.

6. Conclusions

In this manuscript, we present the entire periodic table of medicines but focus our in detail description on the properties and applications of the first-row transition metal ions in medicine. This compilation of knowledge will inform the reader regarding the applications of the different elements and metal ions in medicine as well as provide a brief but somewhat basic description of each element. In addition, this review highlights the fact that metal ions, as counter ions, bind strongly to proteins or other biological systems and often do so in order to exert their beneficial effects. There are too many potential problems if, for example, a metal ion such as Fe(II) or Fe(III) is not bound efficiently because free ions will engage in Fenton chemistry which will result in the formation of ROS and thus result in toxicity.

The importance of metals in life sciences includes a role as positively charged counterions that coordinate to negatively charged biological residues. Essential metal ions will have a structural or a catalytic function and, thus, bind to proteins, RNA, DNA or other biological structures in order to exert a particular role. This is an overarching role of the first-row transition elements although multiple specific detailed actions for each element exist while exerting this role.

Applications of metal compounds as medicines or diagnostic agents are very different than the corresponding use of organic compounds. This is because the bioprocessing of an organic drug will break down into metabolites, whereas a metal compound will lead to the simple metal ion after bioprocessing. Since the only way to remove a metal ion from a cell is to excrete it, a more likely fate of the metal ion after processing that it will bind to some metabolites that can bind or chelate ions. Such metabolites, in addition to proteins, are naturally occurring ligands in cells such as citrate, phosphates, amino acids, and carbohydrates that will form complexes with any free metal ion when they are located in close proximity to each other. The lifetime of a metal-based drug is therefore extended beyond that of its initial form, and its chemistry should be considered as well as its uptake and excretion of it and compounds formed by chemical and biological processing. The study of metal ions in medicine and any biological system that is charged should include consideration of the speciation. Although speciation chemistry is sometimes ignored, it is of importance for explaining some properties observed with different metal ions. In this review, we included a brief summary of the speciation of the first-row transition metal ions and as such, linked the fundamental aqueous chemistry to the medicinal applications of these metal ions in an attempt to link the chemical properties to that of their respective roles in biological systems and medicine.

Author Contributions: D.C.C. and C.V.C. were both involved in all aspects of the preparation of this manuscript.

Funding: D.C.C. thanks the NSF (Grant CHE-1709564) and the Arthur Cope Foundation administered by the American Chemical Society for funding.

Acknowledgments: D.C.C. and C.V.C. would like to thank Peter Sadler for presenting an early version of a Periodic Table of Medicines at the Gordon Conference Metals in Medicine which stimulated D.C.C. to use various versions of periodic tables of medicines for teaching purposes over the last 15 years. We thank Peter Sadler for his contributions and encouragment of bioinorganic chemists in this area. We also thank Eric Scerri for his role in championing the periodic table over the years and his encourgament to write this manuscript on the Perioid Table of The Medicines.

Conflicts of Interest: The authors declare no conflict of interest.

References

1. Lippard, S.L.; Berg, J.M. *Principles of Bioinorganic Chemistry*; University Science Books: Sausalito, CA, USA, 1994.

2. Song, W.J.; Sontz, P.A.; Ambroggia, X.I.; Tezcan, F.A. Metals in Protein–Protein Interfaces. *Annu. Rev. Biophys.* **2014**, *43*, 409–431. [CrossRef]
3. Weeks, M.E. The discovery of the elements. Chronology. *J. Chem. Educ.* **1933**, *10*, 223–227. [CrossRef]
4. Sigel, H.; Sigel, A. The bio-relevant metals of the periodic table of the elements. *Z. Für Nat.* **2019**, *74*. [CrossRef]
5. Scerri, E.R. *The Periodic Table: Its Story and Its Significance*; Oxford University Press: New York, NY, USA, 2007.
6. Hsia, C.C.W. Respiratory Function of Hemoglobin. *N. Engl. J. Med.* **1998**, *338*, 239–247. [CrossRef]
7. Frey, P.A.; Reed, G.H. The Ubiquity of Iron. *ACS Chem. Biol.* **2012**, *7*, 1477–1481. [CrossRef]
8. Frieden, E. New Perspectives on the Essential Trace Elements. *J. Chem Educ.* **1985**, *62*, 917–923. [CrossRef]
9. Chellan, P.; Sadler, P.J. The elements of life and medicines. *Philos. Trans. A Math. Phys. Eng. Sci.* **2015**, *373*, 56. [CrossRef]
10. Rubino, J.T.; Franz, K.J. Coordination chemistry of copper proteins: How nature handles a toxic cargo for essential function. *J. Inorg. Biochem.* **2012**, *107*, 129–143. [CrossRef]
11. Cotton, F.A.; Wilkinson, G.; Murillo, C.A.; Bochman, M. *Advanced Inorganic Chemistry: A Comprehensive Text*, 6th ed.; John Wiley and Sons: New York, NY, USA, 1999.
12. Housecroft, C.E.; Sharpe, A.G. *Inorganic Chemistry*, 4th ed.; Pearson: Harlow, UK, 2012.
13. Greenwood, N.N. *Chemistry of the Elements*, 2nd ed.; Oxford: Oxford, UK, 1997.
14. Wang, W.; Pranolo, Y.; Cheng, C.Y. Metallurgical processes for scandium recovery from various resources: A review. *Hydrometallurgy* **2011**, *108*, 100–108. [CrossRef]
15. Roberts, W.L.; Rapp, G.R.; Weber, J. *Encyclopedia of Minerals*; Van Nostrand Reinhold Company: New York, NY, USA, 1974.
16. Williams-Jones, A.E.; Vasyukova, O.V. The Economic Geology of Scandium, the Runt of the Rare Earth Element Litter. *Econ. Geol.* **2018**, *113*, 973–988. [CrossRef]
17. Barnebey, O.L.; Bishop, G.M. Differential Iodimetry IV.—The Analysis of Pyrolusite and Other Oxidized Manganese Ores. *J. Am. Chem. Soc.* **1917**, *39*, 1235–1238. [CrossRef]
18. IUPAC. *Compendium of Chemical Terminology (Gold Book)*; IUPAC: Research Triangle Park, NC, USA, 2014; p. 1622.
19. Parkin, G. Valence, oxidation number, and formal charge: Three related but fundamentally different concepts. *J. Chem. Educ.* **2006**, *83*, 791–800. [CrossRef]
20. Levina, A.; Lay, P.A. Mechanistic studies of relevance to the biological activities of chromium. *Coord. Chem. Rev.* **2005**, *249*, 281–298. [CrossRef]
21. Scepaniak, J.J.; Vogel, C.S.; Khusniyarov, M.M.; Heinemann, F.W.; Meyer, K.; Smith, J.M. Synthesis, Structure, and Reactivity of an Iron(V) Nitride. *Science* **2011**, *331*, 1049–1052. [CrossRef]
22. Baes, C.F.; Mesmer, R.E. *The Hydrolysis of Cations*; Wiley: New York, NY, USA, 1976.
23. Horton, D.C.; VanDerveer, D.; Krysztek, J.; Telser, J.; Pittman, T.; Crans, D.C.; Holder, A. Spectroscopic Characterization of L-ascorbic Acid-induced Reduction of Vanadium(V) Dipicolinates: Formation of Vanadium(III) and Vanadium(IV) Complexes from Vanadium(V) Dipicolinate Derivatives. *Inorg. Chim. Acta* **2014**, *420*, 112–119. [CrossRef]
24. Pyrzyńska, K.; Kilian, K.; Pęgier, M. Separation and purification of scandium: From industry to medicine. *Sep. Purif. Rev.* **2018**, *48*, 65–77. [CrossRef]
25. Røyset, J.; Ryum, N. Scandium in aluminum alloys. *Int. Mater. Rev.* **2005**, *50*, 19–44. [CrossRef]
26. Hirano, S.; Suzuki, K.T. Exposure, Metabolism, and Toxicity of Rare Earths and Related Compounds. *Environ. Health Perspect.* **1996**, *104*, 85–95. [CrossRef]
27. Xu, T.; Zhang, M.; Hu, J.; Li, Z.; Wu, T.; Bao, J.; Wu, S.; Lei, L.; He, D. Behavioral deficits and neural damage of *Caenorhabditis elegans* induced by three rare earth elements. *Chemosphere* **2017**, *181*, 55–62. [CrossRef]
28. Tai, P.; Zhao, Q.; Su, D.; Li, P.; Stagnitti, F. Biological toxicity of lanthanide elements on algae. *Chemosphere* **2010**, *80*, 1031–1035. [CrossRef]
29. Majkowska-Pilip, A.; Bilewicz, A. Macrocyclic complexes of scandium radionulides as precursors for diagnostic and therapeutic radiopharmeceuticals. *J. Inorg. Biochem.* **2011**, *105*, 313–320. [CrossRef]
30. Chaple, I.F.; Lapi, S.E. Production and Use of the First-Row Transition Metal PET Radionuclides ^{43,44}Sc, ^{52}Mn, ^{45}Ti. *J. Nucl. Med.* **2018**, *59*, 1655–1659. [CrossRef]

31. Huclier-Markai, S.; Sabatie, A.; Ribet, S.; Kubíček, V.; Paris, M.; Vidaud, C.; Hermann, P.; Cutler, C.S. Chemical and biological evaluation of scandium(III)-polyaminopolycarboxylate complexes as potential PET agents and radiopharmaceuticals. *Radiochim. Acta* **2011**, *99*, 653–662. [CrossRef]
32. Müller, C. Folate-Based Radiotracers for PET Imaging Update and Perspectives. *Molecules* **2013**, *18*, 5005–5031. [CrossRef]
33. Huclier-Markai, S.; Alliot, C.; Kerdjoudj, R.; Mougin-Degraef, M.; Chouin, N.; Haddad, F. Promising Scandium Radionuclides for Nuclear Medicine: A Review on the Production and Chemistry up to In Vivo Proofs of Concept. *Cancer Biother. Radiopharm.* **2018**, *33*, 316–329. [CrossRef]
34. Chakravarty, R.; Goel, S.; Valdovinos, H.F.; Hernandez, R.; Hong, H.; Nickles, R.J.; Cai, W. Matching the Decay Half-Life with the Biological Half-Life: ImmunoPET Imaging with ^{44}Sc-Labeled Cetuximab Fab Fragment. *Bioconjugate Chem.* **2014**, *25*, 2197–2204. [CrossRef]
35. Van Dongen, G.A.; Visser, G.W.; Lub-de Hooge, M.N.; de Vries, E.G.; Perk, L.R. Immuno-PET: A Navigator in Monoclonal Antibody Development and Applications. *Oncologist* **2007**, *12*, 1379–1389. [CrossRef]
36. Verel, I.; Visser, G.W.M.; Boellaard, R.; Stigter-van Walsum, M.; Snow, G.B.; van Dongen, G.A.M.S. ^{89}Zr Immuno-PET: Comprehensive Procedures for the Production of ^{89}Zr-Labeled Monoclonal Antibodies. *J. Nucl. Med.* **2003**, *44*, 1271–1281.
37. Ozcelik, O.; Seydaoglu, G.; Haytac, C.M. Diode lasers for harvesting de-epithelialized palatal graft in the treatment of gingival recession defects: A randomized clinic trial. *J. Clin. Periodontol.* **2016**, *43*, 63–71. [CrossRef]
38. Hakki, S.S.; Korkusuz, P.; Berk, G.; Dundar, N.; Saglam, M.; Bozkurt, B. Comparison of Er,Cr:YSGG Laser and Hand Instrumentation on the Attachment of Periodontal Ligament Fibroblasts to Periodontally Diseased Root Surfaces: An In Vitro Study. *J. Periodontol.* **2010**, *81*, 1216–1225. [CrossRef]
39. Lee, S.; Utsunomiya, A.; Akamatsu, H.; Neishi, K.; Furukawa, M.; Horita, Z.; Langdon, T.G. Influence of scandium and zirconium on grain stability and superplastic ductiles in ultrafine-grained Al–Mg alloys. *Acta Mater.* **2002**, *50*, 553–564. [CrossRef]
40. Buettner, K.M.; Valentine, A.M. Bioinorganic Chemistry of Titanium. *Chem. Rev.* **2012**, *112*, 1863–1881. [CrossRef]
41. Sharma, S.; Sharma, R.K.; Haur, K.; Cátala Torres, J.F.; Loza-Rosas, S.A.; Torres, A.; Saxena, M.; Julin, M.; Tinoco, A.D. Fueling a Hot Debate on the Application of TiO_2 Nanoparticles in Sunscreen. *Materials* **2019**, *12*, 2317. [CrossRef]
42. Davis, J.M.; Long, T.C.; Shatkin, J.A.; Wang, A.; Graham, J.A.; Gwinn, M.; Ranalli, B. *Nanomaterial Case Studies: Nanoscale Titanium Dioxide in Water Treatment and in Topical Sunscreen (Final)*; US Environmental Protection Agency: Washington, DC, USA, 2010; p. 204.
43. Tinoco, A.D.; Eames, E.V.; Valentine, A.M. Reconsideration of Serum Ti(IV) Transport: Albumin and Transferrin Trafficking of Ti(IV) and Its Complexes. *J. Am. Chem. Soc.* **2007**, *130*, 2262–2270. [CrossRef]
44. Oosthuizen, S.J. Titanium: The innovators' metal-Historical case studies tracing titanium process and product innovation. *J. South. Afr. Inst. Min. Metall.* **2011**, *111*, 781–786.
45. Sansone, V.; Pagani, D.; Melato, M. The effects on bone cells of metal ions released from orthopaedic implants. A review. *Clin. Cases Miner. Bone Metab.* **2013**, *10*, 34–40. [CrossRef]
46. Jung, C. About Oxygen, Cytochrome P450 and Titanium: Learning from Ron Estabrook. *Drug Metab. Rev.* **2007**, *39*, 501–513. [CrossRef]
47. Tshuva, E.Y.; Miller, M. Coordination Complexes of Titanium(IV) for Anticancer Therapy. In *Metallo-Drugs: Development and Action of Anticancer Agents*; Sigel, A., Sigel, H., Freisinger, E., Sigel, R.K.O., Eds.; de Gruyter: Berlin, Germany, 2018; Volume 18, pp. 219–250.
48. Kubacka, A.; Suárez Diez, M.; Rojo, D.; Bargiela, R.; Ciordia, S.; Zapico, I.; Albar, J.P.; Barbas, C.; Martins dos Santos, V.A.P.; Fernádez-Garcia, M.; et al. Understanding the microbial mechanism if TiO_2-based nanocomposite films in a pathogenic bacterium. *Sci. Rep.* **2014**, *4*, 4134. [CrossRef]
49. Chen, Q.; Thouas, G.A. Metallic implant biomaterials. *Mater. Sci. Eng. R* **2015**, *87*, 1–57. [CrossRef]
50. Golaski, M.; Herman, M.; Piekoszewski, W. Toxicological aspects of soluble titanium—A review of in vitro and in vivo studies. *Metallomics* **2016**, *8*, 1227–1242. [CrossRef]
51. Lechner, J.; Noumbissi, S.; von Baehr, V. Titanium implants and silent inflammation in jawbone—A critical interplay of dissolved titanium particles and cytokines TNF-α and RANTES/CCL5 on overall health? *EPMA J.* **2018**, *9*, 331–343. [CrossRef]

52. Makihira, S.; Mine, Y.; Nikawa, H.; Shuto, T.; Iwata, S.; Hosokawa, R.; Kamoi, K.; Okazaki, S.; Yamaguchi, Y. Titanium ion induces necrosis and sensitivity to lipopolysaccharide in gingival spithelial-like cells. *Toxicol. In Vitro* **2010**, *24*, 1905–1910. [CrossRef]
53. Soto-Alvaredo, J.; Blanco, E.; Bettmer, J.; Hevia, D.; Sainz, R.M.; López Cháves, C.; Sánchez, C.; Llopis, J.; Sanz-Medel, A.; Montes-Bayón, M. Evaluation of the biological effect of Ti generated debris from metal implants: Ions and nanoparticles. *Metallomics* **2014**, *6*, 1702–1708. [CrossRef]
54. Huang, J.-H.; Huang, F.; Evans, L.; Glasauer, S. Vanadium: Global (bio)geochemistry. *Chem. Geol.* **2015**, *417*, 68–89. [CrossRef]
55. Crans, D.C.; Amin, S.S.; Keramidas, A.D. Chemistry of relevance to vanadium in the environment. In *Vanadium in the Environment Part 1: Chemistry and Biochemistry*; Nriagu, J.O., Ed.; Wiley and Sons: New York, NY, USA, 1998.
56. Fish, R.H.; Komlenic, J.J. Molecular characterization and profile identifications of vanadyl compounds in heavy crude petroleums by liquid chromatography/graphite furnace atomic absorption spectrometry. *Anal. Chem.* **1984**, *56*, 510–517. [CrossRef]
57. Nriagu, J.O.; Pirrone, N. Vanadium in the atmosphere. In *Vanadium in the Environment Part 1: Chemistry and Biochemistry*; Nriagu, J.O., Ed.; Wiley and Sons: New York, NY, USA, 1998.
58. Fraústo da Silva, J.J.R. Vanadium in biology the case of the *Amanita* toadstools. *Chem. Speciat. Bioavailab.* **1989**, *1*, 139–150. [CrossRef]
59. Bayer, E. Amavadin: The vanadium compound in amanitae. In *Metal Ions in Biological Systems*; Sigel, H., Sigel, A., Eds.; Marcel Dekker, Inc.: New York, NY, USA, 1995; Volume 31, pp. 407–422.
60. Nielsen, F.H. The Nutritional Essentiality and Physiological Metabolism of Vanadium in Higher Animals. In *Vanadium Compounds: Chemistry, Biochemistry, and Therapeutic Applications*; Tracey, A.S., Crans, D.C., Eds.; American Chemical Society: Washington, DC, USA, 1998; Volume 711, pp. 297–307.
61. Leblanc, C.; Vilter, H.; Fournier, J.-B.; Delage, L.; Potin, P.; Rebuffet, E.; Michel, G.; Solari, P.L.; Feiters, M.C.; Czjzek, M. Vanadium haloperoxidases: From the discovery 30 years ago to X-ray crystallographic and V K-edge absorption spectroscopic studies. *Coord. Chem. Rev.* **2015**, *301*, 134–146. [CrossRef]
62. Michibata, H.; Ueki, T. Advances in research on the accumulation, redox behavior, and function of vanadium in ascidians. *Biomol. Concepts* **2010**, *1*, 97–107. [CrossRef]
63. Crans, D.C.; Smee, J.J.; Gaidamauskas, E.; Yang, L. The Chemistry and Biochemistry of Vanadium and the Biological Activities Exerted by Vanadium Compounds. *Chem. Rev.* **2004**, *104*, 849–902. [CrossRef]
64. Pessoa, J.C.; Etcheverry, S.; Gambino, D. Vanadium compounds in medicine. *Coord. Chem. Rev.* **2015**, *301*, 24–48. [CrossRef]
65. Rehder, D. The Bioinorganic Chemistry of Vanadium. *Angew. Chem. Int. Ed. Engl.* **1991**, *30*, 148–167. [CrossRef]
66. Harvey, I.; Arber, J.M.; Eady, R.R.; Smith, B.E.; Garner, C.D.; Hasnain, S.S. Iron K-edge X-ray-absorption spectroscopy of the iron vanadium cofactor of the vanadium nitrogenase from *Azobacter chroococcum*. *Biochem. J.* **1990**, *266*, 929–931.
67. Lee, C.C.; Hu, Y.; Ribbe, M.W. Vanadium Nitrogenase Reduces CO. *Science* **2010**, *329*, 642. [CrossRef]
68. Sipper, D.; Einsle, O. The structure of vanadium nitrogenase reveals an unusual bridging ligand. *Nat. Chem. Biol.* **2017**, *13*, 956–961. [CrossRef]
69. Crans, D.C.; Henry, L.; Cardiff, G.M.; Posner, B.I. Developing Vanadium as an Antidiabetic or Anticancer Drug: A Clinical and Historical Perspective. In *Essential Metals in Medicine: Therputic Use and Toxicity of Metal Ions in the Clinic*; Carver, P.L., Ed.; de Gruyter: Berlin, Germany, 2019; pp. 203–230.
70. Crans, D.C. Antidiabetic, Chemical, and Physical Properties of Organic Vanadates as Presumed Transition-State Inhibitors for Phosphatases. *J. Org. Chem.* **2015**, *80*, 11899–11915. [CrossRef]
71. McLauchlan, C.C.; Peters, B.J.; Willsky, G.R.; Crans, D.C. Vanadium-phosphatase complexes: Phosphatase inhibitors favor the trigonal bipyramidal transition state geometries. *Coord. Chem. Rev.* **2015**, *301*, 163–199. [CrossRef]
72. Cantley, L.C.; Josephson, L.; Warner, R.; Yanagisawa, M.; Lechene, C.; Guidotti, G. Vanadate is a potent (Na,K)-ATPase inhibitor found in ATP from muscle. *J. Biol. Chem.* **1977**, *251*, 7421–7423.
73. Borah, B.; Chen, C.-W.; Egan, W.; Miller, M.; Wlodawer, A.; Cohen, J.S. Nuclear magnetic resonance and neutron diffraction studies of the complex of ribonuclease A with uridine vanadate, a transition-state analogue. *Biochemistry* **1985**, *24*, 2058–2067. [CrossRef]

74. Thompson, K.H.; Lichter, J.; LeBel, C.; Scaife, M.C.; McNeill, J.H.; Orvig, C. Vanadium treatment of type 2 diabetes: A view to the future. *J. Inorg. Biochem.* **2009**, *103*, 554–558. [CrossRef]
75. Thompson, K.H.; Orvig, C. Vanadium in diabetes: 100 years from Phase 0 to Phase I. *J. Inorg. Biochem.* **2006**, *100*, 1925–1935. [CrossRef]
76. Bishayee, A.; Waghray, A.; Patel, M.A.; Chatterjee, M. Vanadium in the detection, prevention and treatment of cancer: The in vivo evidence. *Cancer Lett.* **2010**, *294*, 1–12. [CrossRef]
77. Crans, D.C.; Yang, L.; Haase, A.; Yang, X. Health Benefits of Vanadium and its Potential as an Anticancer Agent. In *Metallo-Drugs: Development and Action of Anticancer Agents*; Sigel, A., Sigel, H., Freisinger, E., Sigel, R.K.O., Eds.; de Gruyter: Berlin, Germany, 2018; Volume 18, pp. 251–280.
78. Selman, M.; Ruosso, C.; Bergeron, A.; Son, H.H.; Krishnan, R.; El-Sayes, N.A.; Varette, O.; Chen, A.; Le Boeuf, F.; Tzelepis, F.; et al. Multi-modal Potentiation of Oncolytic Virotherapy by Vanadium Compounds. *Mol. Ther.* **2018**, *26*, 56–69. [CrossRef]
79. Bergeron, A.; Kostenkova, K.; Selman, M.; Murakami, H.A.; Owens, E.; Haribabu, N.; Arulanandam, R.; Diallo, J.-S.; Crans, D.C. Enhancement of oncolytic virotherapy by vanadium(V) dipicolinates. *BioMetals* **2019**, *32*, 545–561. [CrossRef]
80. Di Bona, K.R.; Love, S.; Rhodes, N.R.; McAdory, D.; Sinha, S.H.; Kern, N.; Kent, J.; Strickland, J.; Wilson, A.; Beaird, J.; et al. CHromium is not an essential trace element for mammals: Effects of a "low-chromium" diet. *J. Biol. Inorg. Chem.* **2011**, *16*, 381–390. [CrossRef]
81. Vincent, J.B. Chromium: Is It Essential, Pharmacologically Relevant, or Toxic? In *Interrelations between Essential Metal. Ions and Human Diseases*; Sigel, A., Sigel, H., Sigel, R.K.O., Eds.; Springer: Dordrecht, The Netherlands, 2013; Volume 13, pp. 171–198.
82. Wu, L.E.; Levina, A.; Harris, H.H.; Cai, Z.; Lai, B.; Vogt, S.; James, D.E.; Lay, P.A. Carcinogenic Chromium(VI) Compounds Formed by Intracellular Oxidation of Chromium(III) Dietary Supplements by Adipocytes. *Angew. Chem. Int. Ed.* **2016**, *55*, 1742–1745. [CrossRef]
83. Valko, M.; Rhodes, N.R.; Moncol, J.; Izakovic, M.; Mazur, M. Free radicals, metals and antioxidants in oxidative stress-induced cancer. *Chem. Biol. Interact.* **2006**, *160*, 1–40. [CrossRef]
84. Jomova, K.; Valko, M. Advances in metal-induced oxidative stress and human disease. *Toxicology* **2011**, *283*, 65–87. [CrossRef]
85. Levina, A.; Pham, T.H.N.; Lay, P.A. Binding of Chromium(III) to Transferrin Could Be Involved in Detoxification of Dietary CHromium(III) Rather than Transport of an Essential Trace Element. *Angew. Chem. Int. Ed.* **2016**, *55*, 8104–8107. [CrossRef]
86. Anderson, R.A. Chromium, glucose intolerance and diabetes. *J. Am. Coll. Nutr.* **1998**, *17*, 548–555. [CrossRef]
87. Schwarz, K.; Mertz, W. Chromium(III) and the Glucose Tolerance Factor. *Arch. Biochem.* **1959**, *85*, 292–295. [CrossRef]
88. Suh, M.; Wikoff, D.; Lipworth, L.; Goodman, M.; Fitch, S.; Mittal, L.; Ring, C.; Proctor, D. Hexavalent chromium and stomach cancer: A systematic review and meta-analysis. *Crit. Rev. Toxicol.* **2019**, 1–20. [CrossRef]
89. Proctor, D.M.; Suh, M.; Campleman, S.L.; Thompson, C.M. Assessment of the mode of action for hexavalent chromium-induced lung cancer following inhalation exposures. *Toxicology* **2014**, *325*, 160–179. [CrossRef]
90. International Agency for Research on Cancer. Chromium(VI) Compounds. Available online: https://monographs.iarc.fr/wp-content/uploads/2018/06/mono100C-9.pdf (accessed on 25 July 2019).
91. Levina, A.; Codd, R.; Dillon, C.T.; Lay, P.A. Chromium in Biology: Toxicology and Nutritional Aspects. In *Progress in Inorganic Chemistry*; Meyer, G.J., Karlin, K.D., Eds.; Wiley and Sons: New York, NY, USA, 2003.
92. Institute of Medicine. *Dietary Reference Intakes for Vitamin A, Vitamin K, Arsenic, Boron, Chromium, Copper, Iodine, Iron, Manganese, Molybdenum, Nickel, Silicon, Vanadium, and Zinc*; National Academic Press: Washington, DC, USA, 2001.
93. Hasan, H. *Manganese*; Rosen Publishing Group: New York, NY, USA, 2008.
94. Chambers, A.; Krewski, D.; Birkett, N.; Plunkett, L.; Hertzberg, R.; Danzeisen, R.; Aggett, P.J.; Starr, T.B.; Baker, S.; Dourson, M.; et al. An exposure-response curve for copper excess and deficiency. *J. Toxicol. Environ. Health Part B* **2010**, *13*, 546–578. [CrossRef]
95. Takeda, A. Manganese action in brain function. *Brain Res. Rev.* **2003**, *41*, 79–87. [CrossRef]
96. Suárez, I.; Bodega, G.; Fernández, B. Glutamine synthetase in brain: Effects of ammonia. *Neurochem. Int.* **2002**, *41*, 123–142. [CrossRef]

97. Umena, Y.; Kawakami, K.; Shen, J.-R.; Kamiya, N. Crystal structure of oxygen-evolving photosystem II at a resolution of 1.9 Å. *Nature* **2011**, *473*, 55–60. [CrossRef]
98. Matés, J.M.; Pérez-Gómez, C.; de Castro, I.N. Antioxidant Enzymes and Human Diseases. *Clin. Biochem.* **1999**, *32*, 595–603. [CrossRef]
99. Li, G.J.; Zhang, L.-L.; Lu, L.; Wu, P.; Zheng, W. Occupational Exposure to Welding Fume among Welders: Alterations of Manganese, Iron, Zinc, Copper, and Lead in Body Fluids and the Oxidative Stress. *J. Occup. Environ. Med.* **2004**, *46*, 241–248. [CrossRef]
100. Jungwirth, U.; Kowol, C.R.; Keppler, B.K.; Hartinger, C.G.; Berger, W.; Heffeter, P. Anticancer Activity of Metal Complexes: Involvement of Redox Processes. *Antioxid. Redox Signal.* **2011**, *15*, 1085–1127. [CrossRef]
101. Batinić-Haberle, I.; Rebouças, J.S.; Spasojević, I. Superoxide Dismutase Mimics: Chemistry, Pharmacology, and Therapeutic Potential. *Antioxid. Redox Signal.* **2010**, *13*, 877–918. [CrossRef]
102. Triller, M.U.; Hsieh, W.-Y.; Pecoraro, V.L.; Rompel, A.; Krebs, B. Preparation of Highly Efficient Manganese Catalase Mimics. *Inorg. Chem.* **2002**, *41*, 5544–5554. [CrossRef]
103. Aschner, M.; Erikson, K.M.; Dorman, D.C. Manganese Dosimetry: Species Differences and Implications for Neurotoxicity. *Crit. Rev. Toxicol.* **2005**, *35*, 1–32. [CrossRef]
104. Martinez-Finley, E.J.; Gavin, C.E.; Aschner, M.; Gunter, T.E. Manganese neurotoxicity and the role of reactive oxygen species. *Free Radic. Biol. Med.* **2013**, *62*, 65–75. [CrossRef]
105. Kwakye, G.F.; Paoliello, M.M.B.; Mukhopadhyay, S.; Bowman, A.B.; Aschner, M. Manganese-Induced Parkinsonism and Parkinson's Disease: Shared and Distinguishable Features. *Int. J. Environ. Res. Public Health* **2015**, *12*, 7519–7540. [CrossRef]
106. Caline, D.B.; Chu, N.S.; Huang, C.C.; Lu, C.S.; Olanow, W. Manganism and idiopathic parkinsonism: Similarities and differences. *Neurology* **1994**, *44*, 1583–1586. [CrossRef]
107. Thévenod, F. Iron and Its Role in Cancer Defense: A Double-Edged Sword. In *Metallo-Drugs: Development and Action of Anticancer Agents*; Sigel, A., Sigel, H., Freisinger, E., Sigel, R.K.O., Eds.; de Gruyter: Berlin, Germany, 2018; pp. 437–467.
108. Nelson, D.L.; Cox, M.M. *Lehinger Principles of Biochemistry*, 5th ed.; W.H. Freeman: New York, NY, USA, 2008.
109. Blumenthal, I. Carbon monoxide poisoning. *J. R. Soc. Med.* **2001**, *94*, 270–272. [CrossRef]
110. Crichton, R. *Iron Metabolism: From Molecular Mechanisms to Clinical Consequences*, 4th ed.; Wiley and Sons: Chichester, UK, 2016.
111. Sangkhae, V.; Nemeth, E. Regulation of the Iron Homeostatic Hormone Hepcidin. *Adv. Nutr.* **2017**, *8*, 126–136. [CrossRef]
112. Vessières, A. Iron Compounds as Anticancer Agents. In *Metal-based Anticancer Agents*; Casini, A., Vessières, A., Meier-Menches, S.M., Eds.; The Royal Society of Chemistry: Croyden, UK, 2019; pp. 62–90.
113. Valko, M.; Morris, H.; Cronin, M.T.D. Metals, Toxicity, and Oxidative Stress. *Curr. Med. Chem.* **2005**, *12*, 1161–1208. [CrossRef]
114. Braga, S.S.; Silva, A.M.S. A New Age for Iron: Antitumoral Ferrocenes. *Organometallics* **2013**, *32*, 5626–5639. [CrossRef]
115. Kowalski, K. Recent developments in the chemistry of ferrocenyl secondary natural product conjugates. *Coord. Chem. Rev.* **2018**, *366*, 91–108. [CrossRef]
116. Kondratskyi, A.; Kondratskyi, K.; Abeele, F.V.; Gordienko, D.; Duboid, C.; Toillon, R.-A.; Slomianny, C.; Lemière, S.; Delcourt, P.; Dewailly, E.; et al. Ferroquine, the next generation antimalarial drug, has antitumor activity. *Sci. Rep.* **2017**, *7*, 15896. [CrossRef]
117. Whitnall, M.; Howard, J.; Ponka, P.; Richardson, D.R. A class of iron chelators with a wide spectrum of potent antitumor activity that overcome resistance to chemotherapeutics. *Proc. Natl. Acad. Sci. USA* **2006**, *103*, 14901–14906. [CrossRef]
118. Rosa, L.; Cutone, A.; Lepanto, M.S.; Paesano, R.; Valenti, P. Lactoferrin: A Natural Glycoprotein Involved in Iron and Inflammatory Homeostasis. *Int. J. Mol. Sci.* **2017**, *18*, 1985. [CrossRef]
119. Dorazio, S.J.; Olatunde, A.O.; Tsitovich, P.B.; Morrow, J.R. Comparison of divalent transition metal ion paraCEST MRI contrast agents. *J. Biol. Inorg. Chem.* **2014**, *19*, 191–205. [CrossRef]
120. Kuźnik, N.; Wyskocka, M. Iron(III) Contrast Agent Candidates for MRI: A Survey of the Structure-Effect Relationship in the Last 15 Years of Study. *Eur. J. Inorg. Chem.* **2016**, *2016*, 445–458. [CrossRef]

121. Tsitovich, P.B.; Gendron, F.; Nazarenko, A.Y.; Livesay, B.N.; Lopez, A.P.; Shores, M.P.; Autschbach, J.; Morrow, J. Low-Spin Fe(III) Macrocyclic Complexes of Imidazole-Appended 1,4,7-Triazacyclononane as Paramagnetic Probes. *Inorg. Chem.* **2018**, *57*, 8364–8374. [CrossRef]
122. Viljoen, J.J.; Weir, L.; Fietz, S.; Cloete, R.; Loock, J.; Philibert, R.; Roychoudhury, A.N. Links Between the Phytoplankton Community Composition and Trace Metal Distribution in Summer Surface Waters of the Atlantic Southern Ocean. *Front. Mar. Sci.* **2019**, *6*, 295. [CrossRef]
123. Hodgkin, D.C.; Kamper, J.; MacKay, M.; Pickworth, J.; Trueblood, K.N.; White, J.G. Structure of vitamin B_{12}. *Nature* **1956**, *178*, 64–66. [CrossRef]
124. Hunt, A.; Harrington, D.; Robinson, S. Vitamin B_{12} deficiency. *Br. Med. J.* **2014**, *349*, g5226. [CrossRef]
125. Fortin, J.-L.; Waroux, S.; Giocanti, J.P.; Capellier, G.; Ruttimann, M.; Kowalski, J.-J. Hydroxocobalamin for poisoning caused by ingestion of potassium cyanide: A case study. *J. Emerg. Med.* **2008**, *39*, 320–324. [CrossRef]
126. Jelkmann, W. Erythropoietin after a century of research: Younger than ever. *Eur. J. Haematol.* **2007**, *78*, 183–205. [CrossRef]
127. Munteanu, C.R.; Suntharalingam, K. Advances in cobalt complexes as anticancer agents. *Dalton Trans.* **2015**, *44*, 13796–13808. [CrossRef]
128. Mjos, K.D.; Orvig, C. Metallodrugs in Medicinal Inorganic Chemistry. *Chem. Rev.* **2014**, *114*, 4540–4563. [CrossRef]
129. Martínez-Bulit, P.; Garza-Ortiz, A.; Mijangos, E.; Barrón-Sosa, L.; Sánchez-Bartéz, F.; Garcia-Mora, I.; Flores-Parra, A.; Contreras, R.; Reedijk, J.; Barba-Behrens, N. 2,6-Bis(2,6-diethylphenyliminomethyl)pyridine coordination compounds with cobalt(II), nickel(II), copper(II), and zinc(II): Synthesis, spectroscopic characterization, X-ray study and in vitro cytotoxicity. *J. Inorg. Biochem.* **2015**, *142*, 1–7. [CrossRef]
130. Casini, A.; Vessières, A.; Meier-Menches, S.M. Heterometallic Complexes as Anticancer Agents. In *Metal-Based Anticancer Agents*; Casini, A.; Vessières, A.; Meier-Menches, S.M. The Royal Society of Chemistry: Croyden, UK, 2019; pp. 143–168.
131. Singh, N.; Jang, S.; Jo, J.-H.; Kim, D.H.; Park, D.W.; Kin, I.; Kim, H.; Kang, S.C.; Chi, K.-W. Coordination-Driven Self-Assembly and Anticancer Potency Studies of Ruthenium-Cobalt-Based Heterometallic Rectangles. *Chem. Eur. J.* **2016**, *22*, 16157–16164. [CrossRef]
132. EPA. Radionuclide Basics: Cobalt-60. Available online: https://www.epa.gov/radiation/radionuclide-basics-cobalt-60 (accessed on 18 June 2019).
133. Yoshiya, K.; Sato, T.; Omori, S.; Maruyama, S. The Birthplace of Proto-Life: Role of Secondary Minerals in Forming Metallo-Proteins through Water-Rock Interaction of Hadean Rocks. *Orig. Life Evol. Biosph.* **2018**, *48*, 373–393. [CrossRef]
134. Boer, J.L.; Mulrooney, S.B.; Hausinger, R.P. Nickel-dependent metalloenzymes. *Arch. Biochem. Biophys.* **2013**, *544*, 142–152. [CrossRef]
135. Nim, Y.S.; Wong, K.-B. The Maturation Pathway of Nickel Urease. *Inorganics* **2019**, *7*, 85. [CrossRef]
136. Zambelli, B.; Ciurli, S. Nickel and Human Health. In *Interrelations between Essential Metal Ions and Human Diseases*; Sigel, A., Sigel, H., Sigel, R.K.O., Eds.; Springer: New York, NY, USA, 2013; Volume 13, pp. 321–357.
137. Kusters, J.G.; van Vliet, A.H.M.; Kuipers, E.J. Pathogenesis of *Helicobacter pylori* Infection. *Clin. Microbiol. Rev.* **2006**, *19*, 449–490. [CrossRef]
138. Duerig, T.; Pelton, A.; Stöckel, D. An overview of nitinol medical applications. *Mater. Sci. Eng. A* **1999**, *273*, 149–160. [CrossRef]
139. Martin, S.F.; Esser, P.R.; Weber, F.C.; Jakob, T.; Freudenberg, M.A.; Schmidt, M.; Goebler, M. Mechanisms of chemical-induced innate immunity in allergic contact dermatitis. *Allergy* **2011**, *66*, 1152–1163. [CrossRef]
140. Vilar, R. Nucleic Acid Quadruplexes and Metallo-Drugs. In *Metallo-Drugs: Development and Action of Anticancer Agents*; Sigel, A., Sigel, H., Freisinger, E., Sigel, R.K.O., Eds.; De Gruyter: Berlin, Germany, 2018; pp. 325–350.
141. Sauvage, J.-P. Transition Metal-Containing Rotaxanes and Catenanes in Motion: Toward Molecular Machines and Motors. *Acc. Chem. Res.* **1998**, *31*, 611–619. [CrossRef]
142. Beuning, C.N.; Mestre-Voegtlé, B.; Faller, P.; Hureau, C.; Crans, D.C. Measurement of Interpeptidic Cu(II) Exchange Rate Constants by Static Fluorescence Quenching of Tryptophan. *Inorg. Chem.* **2018**, *57*, 4791–4794. [CrossRef]

143. Alberts, B.; Bray, D.; Hopkin, K.; Johnson, A.; Lewis, J.; Raff, M.; Roberts, K.; Walter, P. *Essential Cell Biology*, 4th ed.; Garland Science: New York, NY, USA, 2014.
144. Iwata, S.; Ostermeier, C.; Ludwig, B.; Michel, H. Structure at 2.8Å resolution of cytochrome c oxidase from *Paracoccus denitrificans*. *Nature* **1995**, *376*, 660–669. [CrossRef]
145. Tsukihara, T.; Aoyama, H.; Yamashita, E.; Tomizaki, T.; Yamaguchi, H.; Shinzawa-Itoh, K.; Nakashima, R.; Yaono, R.; Yoshikawa, S. The Whole Structure of the 13-Subunit Oxidized Cytochrome c Oxidase at 2.8Å. *Science* **1996**, *272*, 1136–1144. [CrossRef]
146. Brewer, G.J. Copper in medicine. *Curr. Opin. Chem. Biol.* **2003**, *7*, 207–212. [CrossRef]
147. Cobbett, C.; Goldsbrough, P. Phytochelatins and Metallothioneins: Roles in Heavy Metal Detoxification and Homeostasis. *Annu. Rev. Plant Biol.* **2002**, *53*, 159–182. [CrossRef]
148. Cruces-Sande, A.; Rodríguez-Pérez, A.; Herbello-Hermelo, P.; Bermejo-Barrera, P.; Méndez-Álvarez, E.; Labandeira-García, J.L.; Soto-Otero, R. Copper Increases Brain Oxidative Stess and Enhances the Ability of 6-Hydroxydopamine to Cause Dopaminergic Degeneration in a Rat Model of Parkinson's Disease. *Mol. Neurobiol.* **2019**, *56*, 2845–2854. [CrossRef]
149. Atrián-Blasco, E.; Gonzalez, P.; Santoro, A.; Alies, B.; Faller, P.; Hureau, C. Cu and Zn coordination to amyloid peptides: From fascinating chemistry to debated pathological relevance. *Coord. Chem. Rev.* **2018**, *371*, 38–55. [CrossRef]
150. Schleper, B.; Stuerenburg, H.J. Copper deficiency-associated myelopathy in a 46-year-old woman. *J. Neurol.* **2001**, *248*, 705–706. [CrossRef]
151. Kumar, N. Copper Deficiency Myelopathy (Human Swayback). *Mayo Clin. Proc.* **2006**, *81*, 1371–1384. [CrossRef]
152. Marzano, C.; Pelleri, M.; Tisato, F.; Santini, C. Copper Complexes as Anticancer Agents. *Anti-Cancer Agents Med. Chem.* **2009**, *9*, 185–211. [CrossRef]
153. Denoyer, D.; Clatworthy, S.A.S.; Cater, M.A. Copper Complexes in Cancer Therapy. In *Metallo-Drugs: Development and Action of Anticancer Agents*; Sigel, A., Sigel, H., Freisinger, E., Sigel, R.K.O., Eds.; De Gruyter: Berlin, Germany, 2018; pp. 469–506.
154. Santini, C.; Pellei, M.; Gandin, V.; Porchia, M.; Tisato, F.; Marzano, C. Advances in Copper Complexes as Anticancer Agents. *Chem. Rev.* **2014**, *114*, 815–862. [CrossRef]
155. Kellett, A.; Molphy, Z.; McKee, V.; Slator, C. Recent Advances in Anticancer Copper Compounds. In *Metal-based Anticancer Agents*; Casini, A., Vessières, A., Meier-Menches, S.M., Eds.; The Royal Society of Chemistry: Croyden, UK, 2019; pp. 91–119.
156. Ala, A.; Walker, A.P.; Ashkan, K.; Dooley, J.S.; Schlisky, M.L. Wilson's disease. *Lancet* **2007**, *369*, 397–408. [CrossRef]
157. Kaneshiro, B.; Aeby, T. Long-term safety, efficacy, and patient acceptability of the intrauterine Copper T-308A contraceptive device. *Int. J. Womens Health* **2010**, *2*, 211–220. [CrossRef]
158. Stanford, J.B.; Mikolajczyk, R.T. Mechanisms of action of intrauterine devices: Update and estimation of postfertilization effects. *Am. J. Obstet. Gynecol.* **2002**, *187*, 1699–1708. [CrossRef]
159. Sifri, C.D.; Burke, G.H.; Enfield, K.B. Reduced health care-associated infections in an acture care community hospital using a combination of self-disinfecting copper-impregnated composite hard surfaces and linens. *Am. J. Infect. Control* **2016**, *44*, 1565–1571. [CrossRef]
160. Perelshtein, I.; Ruderman, Y.; Perkas, N.; Beddow, J.; Singh, G.; Vinatoru, M.; Joyce, E.; Mason, T.J.; Blanes, M.; Mollá, K.; et al. The sonochemical coating of cotton withstands 65 washing cycles at hospital washing standards and retains its antibacterial properties. *Cellulose* **2013**, *20*, 1215–1221. [CrossRef]
161. Ataie, N.J.; Hoang, Q.Q.; Zahniser, M.P.D.; Tu, Y.; Milne, A.; Petsko, G.A.; Ringe, D. Zinc Coordination Geometry and Ligand Binding Affinity: The Structural and Kinetic Analysis of the Second-Shell Serine 228 Residue and the Methionine 180 Residue of the Aminopeptidase from *Vibrio proteolyticus*. *Biochemistry* **2008**, *47*, 7673–7683. [CrossRef]
162. Bauer, B.A. Zinc for Colds: The Final Word? Available online: https://www.mayoclinic.org/diseases-conditions/common-cold/expert-answers/zinc-for-colds/faq-20057769 (accessed on 26 June 2019).
163. Maret, W.; Li, Y. Coordination Dynamics of Zinc in Proteins. *Chem. Rev.* **2009**, *109*, 4682–4707. [CrossRef]
164. Berg, J.M.; Shi, Y. The Galvanization of Biology: A Growing Appreciation for the Roles of Zinc. *Science* **1996**, *271*, 1081–1085. [CrossRef]

165. Humphrey, W.; Dalke, A.; Schulten, K. VMD: Visual Molecular Dynamics. *J. Mol. Graph.* **1996**, *14*, 33–38. [CrossRef]
166. Elrod-Erickson, M.; Benson, T.E.; Pabo, C.O. High-resolution structures of variant Zif268–DNA complexes: Implications for understanding zinc finger–DNA recognition. *Structure* **1998**, *6*, 451–464. [CrossRef]
167. Lichten, L.A.; Cousins, R.J. Mammalian Zinc Transporters: Nutritional and Physiologic Regulation. *Annu. Rev. Nutr.* **2009**, *29*, 153–176. [CrossRef]
168. Ziliotto, S.; Ogle, O.; Taylor, K.M. Targeting Zn(II) Signalling to Prevent Cancer. In *Metallo-Drugs: Development and Action of Anticancer Agents*; Sigel, A., Sigel, H., Freisinger, E., Sigel, R.K.O., Eds.; De Gruyter: Berlin, Germany, 2018; Volume 18, pp. 507–530.
169. Giachi, G.; Pallecchi, P.; Romualdi, A.; Ribechini, E.; Lucejko, J.J.; Colombini, M.P.; Lippi, M.M. Ingredients of a 2,000-y-old medicine revealed by chemical, mineralogical, and botanical investigations. *Proc. Natl. Acad. Sci. USA* **2012**, *110*, 1193–1196. [CrossRef]
170. Xie, Y.; He, Y.; Irwin, P.L.; Jin, T.; Shi, X. Antibacterial Activity and Mechanism of Action of Zinc Oxide Nanoparticles against *Campylobacter jejuni*. *Appl. Environ. Microbiol.* **2011**, *77*, 2325–2331. [CrossRef]
171. Sakurai, H.; Kojima, Y.; Yoshikawa, Y.; Kawabe, K.; Yasui, H. Antidiabetic vanadium(IV) and zinc(II) complexes. *Coord. Chem. Rev.* **2002**, *226*, 187–198. [CrossRef]
172. Bellomo, E.; Singh, K.B.; Massarotti, A.; Hogstrand, C.; Maret, W. The metal face of protein tyrosine phosphatase 1B. *Coord. Chem. Rev.* **2016**, *327–328*, 70–83. [CrossRef]

Appendix X: The Interfacial Interactions of Glycine and Short Glycine Peptides in Model Membrane Systems

This manuscript is published in the *International Journal of Molecular Science*.[1]

Van Cleave partook in this work, but it was previously used in Kaitlin A. Doucette's thesis.

References

1. Doucette, K.A.; Chaiyasit, P.; Calkins, D.L.; Martinez, K.N.; Van Cleave, C.; Knebel, C.A.; Tongraar, A.; Crans, D.C. The Interfacial Interactions of Glycine and Short Glycine Peptides in Model Membrane Systems. *Int. J. Mol. Sci.* **2021**, *22*, 162.

International Journal of
Molecular Sciences

MDPI

Article

The Interfacial Interactions of Glycine and Short Glycine Peptides in Model Membrane Systems

Kaitlin A. Doucette [1,2], Prangthong Chaiyasit [3], Donn L. Calkins [2], Kayli N. Martinez [2], Cameron Van Cleave [2], Callan A. Knebel [2], Anan Tongraar [3] and Debbie C. Crans [1,2,*]

[1] Cell and Molecular Biology Program, Colorado State University, Fort Collins, CO 80523, USA; Kaitlin.Doucette@colostate.edu
[2] Department of Chemistry, Colorado State University, Fort Collins, CO 80523, USA; dlcalkinscsu@gmail.com (D.L.C.); kmarti11@berkeley.edu (K.N.M.); Cameron.Van_Cleave@colostate.edu (C.V.C.); callan.knebel@rams.colostate.edu (C.A.K.)
[3] School of Chemistry, Institute of Science, Suranaree University of Technology, Nakhon Ratchasima 30000, Thailand; aomchaiyasit@gmail.com (P.C.); anan_tongraar@yahoo.com (A.T.)
* Correspondence: debbie.crans@colostate.edu; Tel.: +1-970-491-7635

Abstract: The interactions of amino acids and peptides at model membrane interfaces have considerable implications for biological functions, with the ability to act as chemical messengers, hormones, neurotransmitters, and even as antibiotics and anticancer agents. In this study, glycine and the short glycine peptides diglycine, triglycine, and tetraglycine are studied with regards to their interactions at the model membrane interface of Aerosol-OT (AOT) reverse micelles via ^{1}H NMR spectroscopy, dynamic light scattering (DLS), and Langmuir trough measurements. It was found that with the exception of monomeric glycine, the peptides prefer to associate between the interface and bulk water pool of the reverse micelle. Monomeric glycine, however, resides with the N-terminus in the ordered interstitial water (stern layer) and the C-terminus located in the bulk water pool of the reverse micelle.

Keywords: glycine; reverse micelles; AMPs; pK_a; ^{1}H NMR

Citation: Doucette, K.A.; Chaiyasit, P.; Calkins, D.L.; Martinez, K.N.; Van Cleave, C.; Knebel, C.A.; Tongraar, A.; Crans, D.C. The Interfacial Interactions of Glycine and Short Glycine Peptides in Model Membrane Systems. *Int. J. Mol. Sci.* **2021**, *22*, 162. https://doi.org/10.3390/ijms22010162

Received: 30 November 2020
Accepted: 22 December 2020
Published: 26 December 2020

1. Introduction

Small peptides play an essential role in a variety of biological functions, acting as chemical messengers, intra- and intercellular mediators, hormones, and neurotransmitters [1–3]. Peptides also play an important role as antibiotics, such as bacitracin and colistin, as well as antimicrobial peptides (AMPs, also referred to as host defense peptides) [4–6]. AMPs are peptides produced by multicellular organisms as part of the innate immune response found in all classes of life and function as a defense against pathogenic microbes. They exert this function in a number of ways, such as the suppression of biofilm formation, induction of the dissolution of existing biofilms, and attracting phagocytes via chemotaxis to induce non-opsonic phagocytosis [5,7,8]. In addition to their antimicrobial function, recently, it has been found that AMPs may also have anticancer activity; they are able to trigger cytotoxicity of a number of cancer cells through the interaction of the amphipathic or cationic peptide with the plasma membrane of the cell, which selectively exposes negatively charged phosphatidylserine lipids [9,10]. The combination of the function of AMPs as antimicrobial agents as well as anticancer agents makes them a promising starting point for antimicrobial and anticancer drug design [11–14].

In order to exert their antimicrobial or anticancer properties, AMPs must interact with the plasma membrane of the bacterial or cancer cell [5,15]. This interaction with the membrane is associated with their mechanism of action, which can include disruption of the membrane, disruption of membrane-associated physiological processes such as cell wall synthesis, or even translocation across the membrane for interaction with a cytoplasmic

target [5,16–18]. The interactions of these small peptides are dependent on a variety of variables such as size, amino acid composition, secondary structure, and amphiphilic behavior, and their mechanism of action is generally unknown with the exceptions of a few representative examples [8,9,19,20]. Additionally, AMP interactions with the membrane depend on the composition of the membrane itself, as they tend to be attracted more to negatively charged membranes such as bacterial membranes or plasma membranes of cancer cells, which selectively expose negatively charged phosphatidylserine lipids [10,21]. Because of this, AMPs prefer membranes with a high concentration of anionic lipids, those that maintain a high electrical potential gradient, and membranes that tend to lack cholesterol [5,22,23]. It is thus important to study the interactions of peptides at a membrane interface using a small representative amino acid and a membrane mimetic interface (Figure 1A) to determine the molecular placement of the molecules at the membrane as well as the manner by which they interact.

Of the twenty amino acids that are found in peptides, glycine (G, Figure 1B) is both the smallest and the most versatile [24]. Having only a hydrogen atom as its substituent, it is the only amino acid that is achiral, and as such, it is compatible with hydrophilic environments, and although it is not directly soluble in for example isooctane (Figure S1) it can partition toward hydrophobic regions in inhomogenous environments. In addition, it has many biological functions, one of the most notable of which as a simple inhibitory and excitatory neurotransmitter, and as such, it is a logical representative amino acid for investigation of simple peptide and amino acid interactions with a membrane, and in addition, there have been numerous reports of glycine-rich AMPs [25–28].

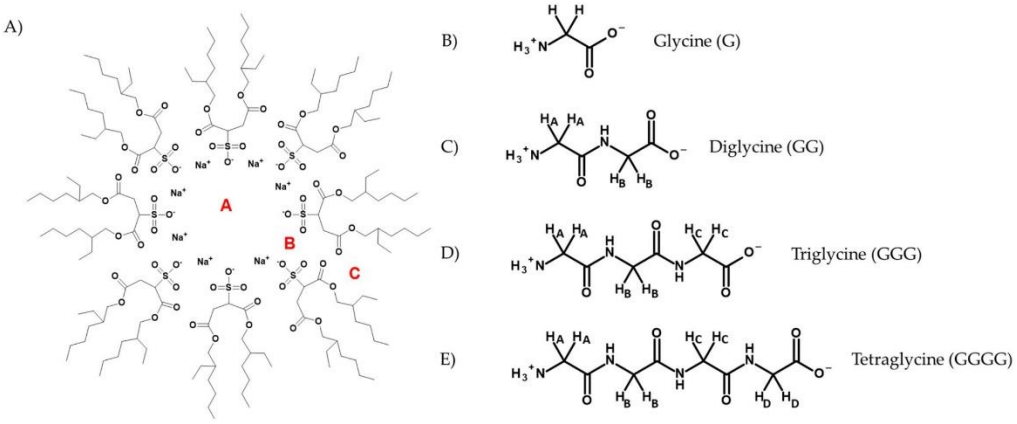

Figure 1. The structure of glycine (G) analogs and schematic of the Aerosol-OT reverse micelle (AOT RM) model system. (**A**) A schematic of a simplified structure of an RM. "A" represents the bulk water pool, "B" is the interfacial region of the RM in the region of the charged AOT head groups, and "C" represents association in the more hydrophobic region of the RM in the region of the acyl groups, hydrophobic tails, and isooctane solvent. (**B**) The amino acid G at physiological pH. (**C**) Structure of diglycine (GG), with protons labeled corresponding to proton peaks analyzed by ^{1}H NMR (**D**) Structure of triglycine (GGG) with protons labeled corresponding to proton peaks analyzed via ^{1}H NMR. (**E**) Structure of tetraglycine (GGGG), with protons labeled corresponding to proton peaks analyzed via ^{1}H NMR.

Because we are interested in obtaining molecular information on how simple peptides interact with membrane interfaces, we will use monomeric, dimeric, trimeric, and tetrameric G-containing peptides, hereafter referred to as G, GG, GGG, and GGGG (Figure 1B–E). To study how these small peptides behave near cellular membranes, we use a reverse micellar (RM) system (Figure 1A) which consists of a self-assembled ternary system containing surfactant, organic solvent, and water [29–32]. The surfactant, in this case, is Aerosol-OT (AOT), also known as sodium 2-diethylhexylsulfosuccinate, which arranges

itself such that the water pool is contained by the negatively charged head groups of the AOT, and surfactant tails extend outward into the organic solvent—in this case, isooctane (2,2,4-trimethylpentane) [33,34]—and commonly, water droplets contained in this system range from a size of 1 to 10 nm [35,36]. The RM system provides both a hydrophilic and hydrophobic environment at a negatively charged interface, making it a good model system to investigate the interactions of molecules with membrane interfaces [37,38].

To investigate the interactions of G and G-containing peptides with model membranes, it is of interest to determine its location within the RM. That is, whether it is located near the charged AOT heads, bulk water pool, or in the ordered, interstitial water between the charged interface and the water pool, referred to as the stern layer [39]. Furthermore, the location of the molecule of interest may be sensitive to the local pH of the RM interior [40,41].

In this study, we use AOT RMs and Langmuir monolayers to gain insight into how G and G-based peptides interact with simple membrane model systems. Specifically, we investigate here the interaction of G, GG, GGG, and GGGG with an AOT RM interface and with dipalmitoyl phosphatidylcholine (DPPC) and dipalmitoyl ethanolamine (DPPE) monolayers to determine the interactions and placement of G compounds at a model membrane interface to mimic non-cancerous and human cells.

2. Results

The chemical shifts of G, GG, GGG, and GGGG were examined by ^{1}H NMR spectroscopy to compare their chemical shifts in aqueous solution with those peaks obtained in the environment of the RM model membrane (Sections 2.1–2.4). Solutions containing each of the G compounds were made at varying pH values to determine the pK_a values of each in both aqueous environment and in the environment of the RM (summarized in the Discussion section, Figure S2), and representative NMR spectra for each compound in RM and D_2O as well as exact chemical shift values are given in the Supplemental Materials. Each of these compounds showed a slight difference in chemical shift values between RMs and the compound alone in D_2O, indicating a difference in environment for the probe molecule. These data give some structural information about the location of the probe within the reverse micelle. The systems were also investigated using dynamic light scattering (DLS) to verify formation of the RMs and to examine the impact of the G compounds on the RM system (Section 2.5).

In Section 2.6, we further support the observations made in this paper in Sections 2.1–2.5 by using Langmuir trough measurements. These studies used a natural lipid as well as a different method, and this was done to investigate whether the conclusion obtained by using the microemulsions system could be confirmed and extended to studies of physiological lipids and human cells.

2.1. ^{1}H NMR Spectroscopy of L-Glycine (G) in RM

A series of samples with RMs of size w_0 10 (where w_0 = [AOT]/[H_2O]) were made containing G at varying pH values by adding 200 mM G solution in D_2O at the pH specified to the appropriate volume of 750 mM AOT solution dissolved in isooctane. The chemical shifts of these were recorded using ^{1}H NMR spectroscopy and chemical shifts are compared with the representative spectra shown (Figure 2A, Figures S2–S6). The pK_a values were calculated (Figure S2) from the spectra both in D_2O and in microemulsions are listed in Table 2 in the Discussion section. Values obtained from G in aqueous and RM environments show that the pK_a of the C-terminus differs very little between aqueous and RM environments, but the N-terminus differs significantly, with a pK_a value of 10.7 in D_2O and 8.51 in the RM model membrane. This difference, or lack thereof, in pK_a values between the two environments gives some information about the environments surrounding the carboxy- and amine-terminal ends of G within the RM [42]. Because there is little change between the carboxyl pK_a in RM and D_2O, this suggests that this portion of the compound is in an environment that is the same. In the context of the RM model system, this observation is consistent with the C-terminus being in the stern layer/aqueous

environment directed toward the bulk water pool (Figure 1A). The significant decrease in pK_a between aqueous and RM environments for the amine-terminal end of G indicates a significant change in environment, such that the amine-terminal end is located near or in the charged region of the RM interface.

It is likely that the experimental N-terminal pK_a of G in RM is lower than what is reported in the literature due to the higher ionic strength near the charged interface. In pure aqueous solution, the amine is free to hydrogen-bond to the carboxyl moiety of the amino acid, forming an energetically favorable five-membered ring and stabilize the amine. However, in high ionic strength solutions, this H-bonding may be disrupted by the presence of counterions, which are known to accumulate near the interface of the AOT (Figure 1A) [43,44], lowering the pK_a of the N-terminus. Additionally, this H-bonding phenomenon could be disrupted by the interaction of the amine with the sulfonate groups on the AOT head groups. This disruption of H-bonding is consistent with the lowering of the pK_a values in the reverse micelle, which contains more Na^+ ions, the presence of charged sulfonate groups, and, therefore, a higher ionic strength.

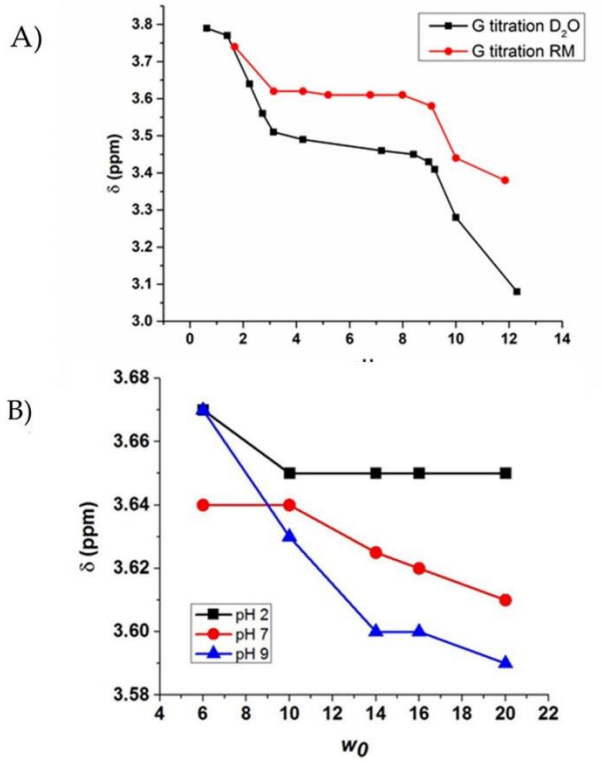

Figure 2. (**A**) Comparison of ^{1}H NMR chemical shifts of G in aqueous and RM environments. (**B**) The ^{1}H NMR chemical shift of G is plotted with increasing w_0 at pH 2, 7, and 9. Error bars have been included in the plot; however, due to minimal error, they are not visible beyond the symbols used in the graph.

To further support this conclusion, experiments were performed in which the size of the RM containing the G solutions was varied so that the chemical shifts could be analyzed as a function of increasing vesicle size to give further information about their placement within the RM system. The pH of the G solutions used to prepare the RMs was varied at representative pH values: alkaline pH (pH 9), neutral/physiological pH (pH 7.4), and acidic pH (pH 2). From this experiment, it was found that as the size of the water pool in the RM increased, the chemical shift of the G peak in the neutral- and alkaline-pH RM environments decreased and approached its shift value in D_2O alone, which is 3.55 at pH 2 and 7.4 (Figure 2B). This suggests that the neutral and negatively charged forms of G, predictably, are not attracted to the interfacial region of the RM due to their charges not interacting with the negatively charged AOT heads [45]. As the vesicle size increases, the interstitial water region becomes less ordered and more analogous to bulk water, and as a result, the compounds that are not highly attracted to the polar interface begin to transition to water that behaves more as bulk water. However, in the case of G at pH 2, the carboxylate moiety is fully protonated, leading to an overall +1 charge of the molecule. As a result, the positive charge of the molecule interacts with the negatively charged polar heads of the AOT consistently, leading to the plateau in chemical shift as the size of the RM increases.

To test the hypothesis that as the vesicle size increases at neutral and alkaline pH, the chemical shift of G approaches that of its shift in pure aqueous environment, experiments were performed in which the pK_a of G was calculated in a w_0 30 RM (12.4-nm diameter) instead of the w_0 10 (6.8-nm diameter) that was previously used [35]. These experiments showed that the carboxy-terminal pK_a in this larger vesicle stayed the same at 2.5, but the amine-terminal pK_a decreased significantly to 9.6 from 8.51, a value much closer to the pK_a when G is in an aqueous environment under ionic strength (Figure 2). This is consistent with our hypothesis that G is likely positioned such that the N-terminus is in the interstitial water region of the RM facing the negatively charged interface, while the C-terminus is located closer to the bulk water pool of the RM [45]. As the size of the RM increases, the interstitial water region becomes less ordered and behaves more as bulk water, and the N-terminus is in a more aqueous-like environment; the pK_a reflects this as it increases with larger vesicle size (Figures S7 and S8).

2.2. ^1H NMR Spectroscopy of Diglycine (GG) in RM

In a similar fashion to G, ^1H NMR spectroscopy of solutions containing GG in the RM model membrane system and aqueous solution was recorded and analyzed to identify any differences in chemical shift that may occur as a result of confinement by w_0 10 RM. Chemical shift values are plotted and compared between environments, with representative spectra for each given in the Supplementary Materials (Figure 3; Figures S9–S12).

The solution pH values and resulting pK_a that was calculated show that GG displays a small increase in chemical shift from aqueous environment to the RM, indicating that the compound is in a slightly more charged environment consistent with the interfacial water layer containing the Na^+ counterions (Figure 1A). However, this change in pK_a values from aqueous to RM is small, with a pK_a of 2.85 in D_2O and 2.99 in RM for the C-terminal CH_2, and 8.60 in D_2O and 8.48 for the N-terminal CH_2.

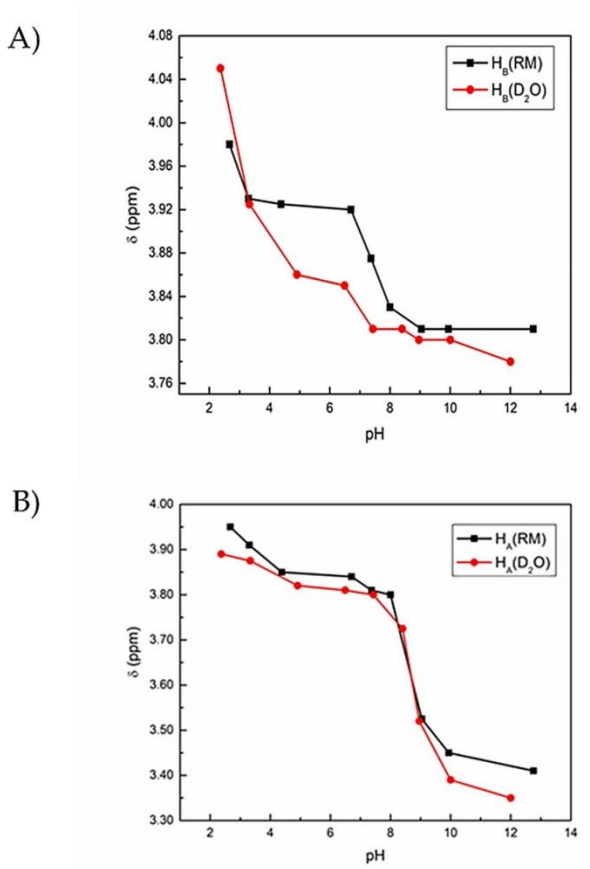

Figure 3. Chemical shifts of GG as a function of pH in D_2O and RM samples based on ^1H NMR spectroscopic studies of GG at varying pH values. RMs of size w_0 10 were formed with 200 mM solutions of GG in D_2O. Error bars on the graph are smaller than the symbols used. (**A**) ^1H NMR chemical shift values of protons B (CH_2 near N-terminus) of GG measured at different pH values in D_2O, with the proton labeling scheme shown in Figure 1C. (**B**) ^1H NMR chemical shift values of protons A (CH_2 near C-terminus) of GG measured at different pH values in RMs, with the proton labeling scheme shown in 1C.

2.3. ^1H NMR Spectroscopy of Triglycine (GGG) in RM

Solutions containing GGG were also studied in comparison in D_2O and RMs of w_0 10 using ^1H NMR to investigate its potential interactions within the confines of the RM. Results obtained from solutions of GGG are similar to those obtained from GG in that there is little change in the chemical shifts of the solutions in aqueous environment and in the AOT RM (Figure 4). There was little change in the pK_a of the N- and C-terminal ends of the peptide, with the C-terminal pK_a in D_2O at 3.18, and in RM, 3.27, and the N-terminal pK_a in D_2O was at 8.29, and in RM, 8.11.

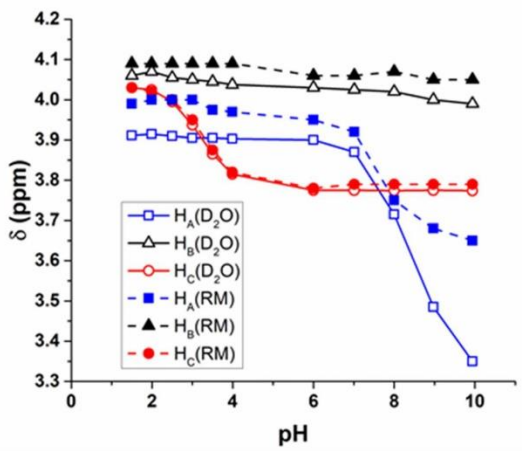

Figure 4. GGG proton shifts compared at varying pH values in aqueous (D_2O) and RM environments, as determined by ^{1}H NMR spectroscopy. RMs of size w_0 10 were formed with 200 mM GGG in D_2O. Error bars on the graph are smaller than the symbols used. GGG protons are labeled according to Figure 1D.

We further explored this observation that the chemical shift of the C-terminal CH_2 remains relatively unchanged between aqueous and RM environments, consistent with the interpretation that the C-terminal end of the peptide resides within the bulk water pool of the RM or the molecule has folded over on itself. The chemical shift of the middle CH_2 at all pH values tested was slightly elevated in the RM as compared to D_2O, consistent with being located in a more charged environment, and the N-terminal CH_2 protons show the most change in chemical shift, with values in the RM being higher than those of D_2O, consistent with being located in a more charged environment or, possibly, if it is in a folded conformation (Figure 4; Figures S13–S16). However, similarly to those calculated for GG, there is little change in the calculated pK_a values with differences of only 0.1 pH unit.

2.4. ^{1}H NMR Spectroscopy of Tetraglycine (GGGG) in RM

Aqueous solutions of GGGG at varying pH values and corresponding AOT RMs were analyzed via ^{1}H NMR spectroscopy, similarly to the other G compounds above. The results obtained from GGGG in terms of pK_a differences are small, as was found for the GGG and GG peptides. The pK_a value found for the C-terminal end of the peptide in D_2O was determined to be 3.05, and that in RM was determined to be 2.82. The pK_a value found for the N-terminal end of GGGG was found to be 7.75 in D_2O and 7.94 within the RM. These small differences may be attributed to the slight changes in the environment of the RM as compared to aqueous solution and suggest that the peptide itself resides between the interface of the RM and the stern layer. The increased pK_a of the N-terminal protons as well as the slightly decreased pK_a of the C-terminal protons indicate that the zwitterionic form of GGGG is equally or more stable in the RM, which is also consistent with the compound being between the bulk water and interface of the RM (Figure 5A; Figures S17–S20).

It is also worth noting, when looking at the chemical shifts of the middle protons (H_B and H_C) of the compound, the difference in shift is $\leq$0.1 ppm, indicating that the environment is essentially the same between the two systems (Figure 5B).

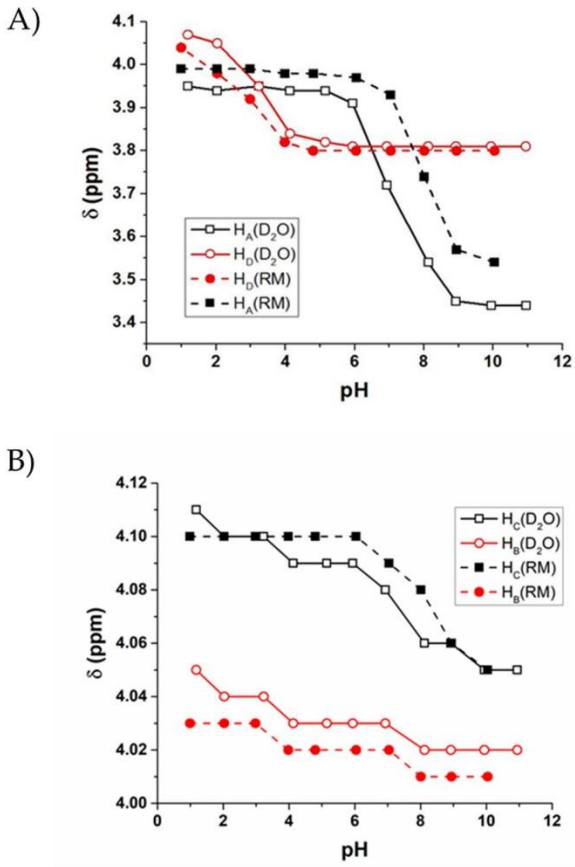

Figure 5. Chemical shift values as determined by ^{1}H NMR of GGGG at varying pH values in RM and D_2O with peaks corresponding to labels in Figure 1D. RMs of size w_0 10 were formed with 200 mM GGGG in D_2O. Error bars on graph are smaller than symbols used. (**A**) N- and C- terminal CH_2 protons of GGGG in D_2O and RM, or protons A and D as labeled in Figure 1E. (**B**) Interior CH_2 protons on N- or C-terminal side of GGGG in D_2O and RM, or protons B and C as labeled in Figure 1E.

2.5. Dynamic Light Scattering of RM Samples

To verify that RMs formed in the microemulsion samples, the solutions were subjected to DLS analysis. RMs of sizes of w_0 20 were made as representatives for these investigations instead of the w_0 10 RMs used to perform the ^{1}H NMR measurements, as it is much easier both to measure the size as well as to visualize changes with the larger (8.9 nm) w_0 20 RM than w_0 10 (6.8 nm) [35]. The results are summarized in Table 1. Measurements were taken for each solution of RM containing 200 mM G compounds in deionized water (diH_2O) and the corresponding RM sample with no probe molecule in the diH_2O. As seen in Table 1, in the larger w_0 20 RM, to better visualize any changes, the size of the RMs did not significantly change by the addition of G, GG, GGG, or GGGG and the values observed are in agreement with the literature value of 8.9 nm for a w_0 20 RM [35].

Table 1. Dynamic light scattering (DLS) size measurements of RM containing each of the G peptides. Each of these measurements was taken at pH 7.

Sample	w_0 20 RM Diameter (nm)	w_0 20 RM Std. Dev. (nm)
Control	9.5	0.44
G	9.5	0.43
GG	9.2	0.47
GGG	9.2	0.36
GGGG	9.3	0.39

2.6. Compression Isotherms of Langmuir Monolayers Containing Glycine

In this study, Langmuir monolayers with the lipids dipalmitoyl phosphatidylcholine (DPPC) and dipalmitoyl phosphatidylethanolamine (DPPE), which are two of the most abundant phospholipids found in biological membranes and carry an overall neutral charge, were also used to investigate the effect that glycine has on a biological membrane [46]. Compression isotherm data are plotted as the percent difference in the area per molecule of monolayers containing both lipid and glycine from those containing no glycine versus the surface pressure, as shown in Figure 6 [47]. At pH 4, 6, 7, and 8, DPPC monolayers containing glycine all exhibit a similar trend in which monolayers with glycine present have an expanded area at low surface pressure, but the amount of expansion decreases as surface pressure increases.

However, at pH 6 and 7, monolayers exposed to glycine always remain at least slightly expanded from the control. At pH 4, monolayers with glycine transition from expanded to contracted around 30–35 mN/m, which is what is commonly regarded as physiological surface pressure [48,49]. The pH 8 monolayer with glycine transitioned from expanded to condensed around 25 mN/m. The pH 9 monolayer with glycine in the subphase remained relatively near to the control monolayer at all pressures, though slightly condensed. Importantly, at physiological-like conditions at pH 7 with glycine in the subphase and DPPC as the lipid, the monolayer was 4–5% expanded relative to the control, implying that some glycine was positioned at the interface, as opposed to the subphase or the acyl chains of the DPPC. Overall, DPPC monolayers with glycine in the subphase have a trend of expanding the monolayer at lower surface pressures and then transition to only a slight expansion, or to condensing the monolayer as surface pressure increases. At pH 7, which is the most physiologically relevant pH used in this study, the monolayer remains expanded relative to the control, which suggests that glycine interacts weakly with the interface (Figure 6A).

DPPE monolayers, then, followed nearly the same trend at pH 4, 6, and 8; all are 15–20% expanded relative to the control at a surface pressure of 5 mN/m and decreased as surface pressure increased. All three monolayers reached an equilibrium of remaining approximately 5% expanded relative to the control at 35 mN/m. Much like with the DPPC monolayers, the pH 9 monolayer remained relatively constant, remining between 1.8% and 2.4% expanded relative to the control throughout compression. While glycine slightly condensed DPPC at pH 9, it slightly expanded DPPE at the same pH. Interestingly, pH 7 differs greatly between DPPC and DPPE. For DPPE, the pH 7 monolayer is 5% expanded relative to the control at 5 mN/m and then becomes condensed between 10 and 15 mN/m. The monolayer remains slightly condensed, and at physiological surface pressure, the monolayer exposed to glycine is approximately 2–3% condensed relative to the control.

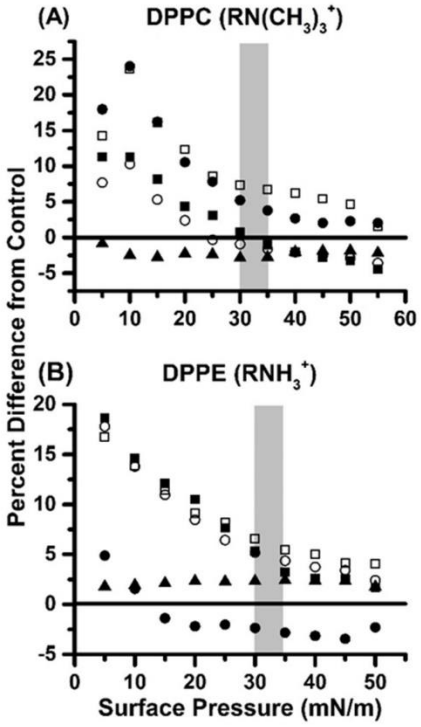

Figure 6. Calculated percent difference between the area per molecule of control Langmuir monolayers and monolayers with glycine in the subphase for (**A**) dipalmitoyl phosphatidylcholine (DPPC) and (**B**) dipalmitoyl ethanolamine (DPPE). R represents the phosphate group, glycerol, and saturated C_{16} tails. Symbols each represent a different pH, where solid squares are pH 4, hollow squares are pH 6, solid circles are pH 7, hollow circles are pH 8, and solid triangles are pH 9. The region shaded in grey represents physiological surface pressure. Exact values and errors for all points are reported in Tables S1 and S2.

Since the measured values are within the calculated error, the glycine-exposed monolayer is not experimentally different from the control. Overall, DPPE monolayers with glycine in the subphase at all pH values but seven follow similar patterns to each other, in which the monolayer is expanded 15–20% at lower surface pressures and decreases to 5% expansion as the surface pressure increases (Figure 6B). Interestingly, at pH 7, the monolayer exposed to glycine becomes slightly condensed and does not follow patterns typical of the other pH values, and the experimental error is such that there is no statistical difference between glycine-exposed and control monolayers. This suggests that glycine may interact with the membrane interface, but it does not do so strongly.

3. Discussion

The studies described above determine pK_a measurements of G-containing peptides and, in doing so, compare the data of small G-peptides in aqueous solution and associated with the AOT interface. The longer G peptides, in the case of GGG and GGGG, have chemical shifts in the same region as the AOT and overlap in chemical shifts, as can be seen in Figures S15 and S19. G and GG are found to appear in a region where AOT and isooctane peaks are not observed; however, GGG and GGGG show signals in the same region as the

AOT, therefore limiting observation of the signals of these short G-containing peptides. As a result, a subtraction method was utilized in which the AOT RM spectra containing no compound were subtracted from AOT RM spectra containing the G compound of interest. Analyzing the spectra using the subtraction method described in the experimental section allowed us to calculate the chemical shifts for all G compounds and was also used to obtain the pK_a results, summarized in Table 2. The pK_a values were calculated for both the R-group protons near the C-terminus and the N-terminus of the G peptides in both aqueous environment and the environment of the RM. The resulting pK_a values calculated in this work are summarized in Table 2 for all the systems investigated in this work and detailed in the descriptions below.

Table 2. Comparison of experimental pK_a values obtained for G compounds in aqueous (D_2O) and w_0 10 RM systems, shown with 95% confidence intervals, with literature aqueous pK_a values.

Compound	System	pK_a(1): This Work, Carboxylic Acid	pK_a(1) lit.	pK_a(2): This Work, Protonated Amine	pK_a(2) lit.
G	D_2O	2.51 ± 0.03	2.46 [50]	10.7 ± 0.05	9.60 [50]
	RM	2.49 ± 0.02		8.51 ± 0.06	
GG	D_2O	2.85 ± 0.08	3.15 [50]	8.60 ± 0.10	8.10 [50]
	RM	2.99 ± 0.04		8.48 ± 0.04	
GGG	D_2O	3.18 ± 0.03	3.18 [50]	8.29 ± 0.04	7.87 [50]
	RM	3.27 ± 0.02		8.11 ± 0.07	
GGGG	D_2O	3.05 ± 0.08	3.25 [50]	7.75 ± 0.12	7.98 [50]
	RM	2.82 ± 0.09		7.94 ± 0.14	

Our hypothesis that G is likely positioned such that the N-terminus is near or in the interstitial water region of the RM either facing the negatively charged interface or actually associated with the interface is in line with previous observations and predictions with other charged molecules [51,52]. This pattern was observed for all the G peptides to different degrees, with the largest change for G. The larger difference for G can be explained because this is a smaller amphiphilic molecule, and penetration of the interface by the N-terminus will impact the amphiphilic molecule more than with peptides. Although penetration will bring the C-terminus closer to the interface, little change is observed in the pK_a of the C-terminal, suggesting that the N-terminal is loosely associated with the interface and not deeply penetrated in the interface (Figure 7). This difference in the pK_a of the protonated amine of G may also be due to the presence of ions at the RM interface; in pure water, G forms an energetically favorable five-membered ring between the protons of the positively charged amine and the negatively charged oxygen on the carboxyl group, which is disrupted by the presence of ions at the RM interface where the N-terminus is likely located. This will result in a lower pK_a, as shown in Table 2. The changes in the pK_a value of the amino terminus in the three G-peptides, by contrast, are much smaller. Differences in pK_a between different sizes of RMs containing G suggest that there may be some subtle differences in the specific location of the amino terminus of these G peptides as anticipated, because the charge distributions are somewhat different depending on the specific conformation of the molecule. Importantly, modest change is observed in the pK_a value of the C-terminus consistent with its environment changing much less compared to the aqueous and microemulsion preparations of the G compounds, consistent with their location closer to or in the bulk water pool of the RM as expected if the environment changed little [45].

The presented data for all the G peptides investigated indicate that they all interact with the interface, albeit in different ways. The smallest G, which is a zwitterion at neutral pH, is likely to interact more strongly with the interface based on the large changes in the pK_a of the free amine part of the peptide. As we demonstrated with aniline, the observed differences are likely to be caused by changes in location and not due to an inherent difference in pK_a values in the new environment [52]. This may also be due to the disruption

of the favorable five-membered ring that is formed by the positively charged protons on the amine and the negatively charged oxygen on the carboxylate group in water by the presence of Na^+ at the RM interface, as mentioned previously. In the case of the GG, GGG, and GGGG peptides, the observed difference is much less and there are also variations in the direction of the change; for G, GG, and GGG, the pK_a value decreased (acidity increased) in the presence of the interface, whereas in the case of GGGG, the pK_a value increased (acidity decreased). In order to obtain more information on this system, we examined the interactions of glycine with lipid interfaces in the Langmuir monolayer system. Since the majority of responses were observed with glycine, we limited these studies with glycine but examined its response in a pH-dependent manner (Section 2.6). These results showed that glycine is likely to associate with the lipid interface at near-neutral pH, hence confirming the observations made with the microemulsion system.

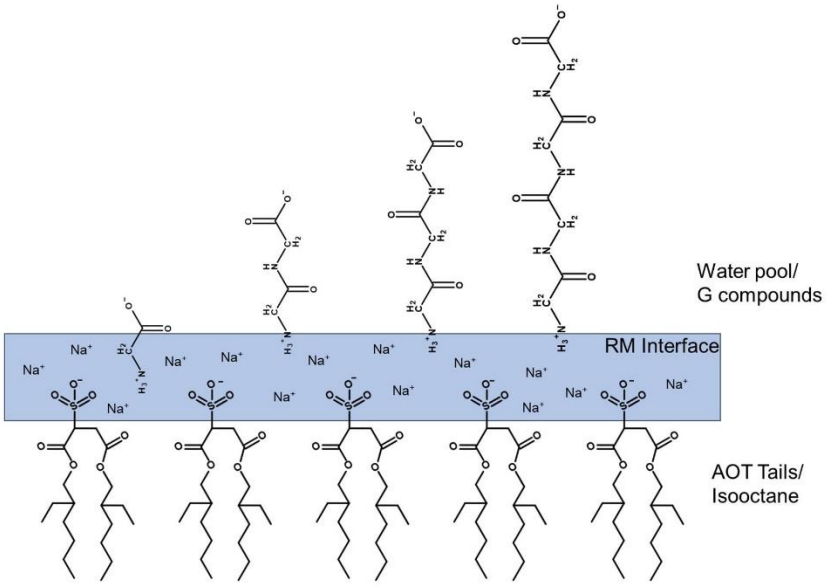

Figure 7. Schematic figure depicting the likely positioning of the G compounds used in this study relative to the RM interface. G compounds depicted here are shown in a linear conformation; however, it is likely that longer G compounds such as GGG and GGGG rotate around C-C bonds in solution such that the conformation of the molecule may be bent as discussed previously, but the C-terminal end is still located at the bulk water pool.

Comparison of the pK_a values in aqueous solution and near RM interfaces is most valuable when considering the inherent differences between the two systems and recognizing that the aqueous solution can change significantly depending on the other ions in solution and overall ionic strength. Previous work done with GGG in aqueous solution found that GGG adopts a U-shaped conformation in the presence of Na^+ and SO_3^- [53], with no similar studies being found for GG or GGGG. In this study, it was found that there is a strong interaction between the sodium ions and the sulfite, which then interacts with the protonated amine of GGG, favoring a bending that adopts a U shape. A similar phenomenon may be occurring in the RM systems in which the Na^+ ions interact with the sulfate groups on the AOT surfactant molecules, which then interact more strongly with the protonated amine. This would be consistent with the increase in chemical shift of the protonated amine for GGGG in RM as compared to its shift in D_2O (Table 2). Additionally, the increased pK_a of the N-terminal protons as well as the slightly decreased pK_a of

C-terminal protons indicates that the zwitterionic form is equally or more stable in the RM, consistent with being at the edge of the bulk water pool of the RM between the bulk water and interface (Figure 5A,B; Figure 7).

These results imply that it is unlikely that peptides containing numerous glycine residues will have a strong effect as membrane-penetrating peptides for use in the development of novel antibacterial or anticancer therapeutics, unless there are other amino acids present which are more likely to interact with a membrane interface, such as lysine. Even in the context of the reverse micelle, which has a strongly negatively charged interface to mimic the exposure of phosphatidylserine residues by cancerous cells, there is little to no interaction of the G peptides with the RM interface, indicating that even when the interface has a negative charge characteristic to bacterial or cancerous cells, there is still no penetration of the interface by a peptide, despite numerous reports of glycine-rich AMPs [26–28]. This result stands in contrast with studies with G alone, which is found to interact with the interface. Together, these results suggest that for AMP peptides to be effective in penetrating membranes, residues other than G are necessary for the action of these peptides. This is consistent with the fact that many AMP peptides contain significantly higher concentrations of lysine residues and/or aromatic residues such as phenylalanine and tyrosine in addition to higher concentrations of glycine than the average presence of these amino acids in other proteins due to the two physical features required for antimicrobial peptide activity: charge and hydrophobicity [54–56].

4. Materials and Methods

4.1. General Materials

The following materials were purchased and used without purification: glycine HCl (G, Mallinckrodt, Madison, WI, USA, 99.0%), diglycine (GG, Sigma-Aldrich, St. Louis, MO, USA, 99.0%), triglycine acid (GGG, Sigma-Aldrich, 99.0%), tetraglycine (GGGG, Aurum Pharmatech, Franklin Park, NJ, USA, >96%), activated charcoal (carbon 6–12 mesh), 2,2,4-trimethylpentane (isooctane) (Sigma-Aldrich, 99.0%), deuterium oxide (Sigma-Aldrich, 99.0% deuterium), and 4,4,-dimethyl-4-silapentane-1-sulfonic acid sodium salt (DSS, Wilmad, Buena, NJ, USA). The chemicals methanol (>99%), citric acid anhydrous (>99.5%), sodium citrate dihydrate (>99%), sodium hydroxide (>99%), and hydrochloric acid were purchased from Fisher Scientific. The lipids 1,2-dipalmitoyl-*sn*-glycero-3-phosphocholine (DPPC, >99%) and 1,2-dipalmitoyl-*sn*-glycero-3-phosphoethanolamine (DPPE, >99%) were purchased from Avanti Polar Lipids (Alabaster, AL, USA). Sodium Aerosol-OT (AOT) (bis(2-ethylhexyl)sulfosuccinate sodium salt, Sigma-Aldrich, $\geq$99.0%) was purified as described previously to remove an acidic impurity [57]. Briefly, 50.0 g of AOT was dissolved into 150 mL of methanol to which 15 g of activated charcoal was added. This suspension was stirred for 2 weeks. After mixing, the suspension was filtered to remove the activated charcoal. The filtrate was then dried under rotary evaporation at 50 °C until the water content was below 0.2 molecules of water per AOT as determined by ^{1}H NMR spectroscopy [58]. The pH of aqueous solutions was measured at 25 °C on an Orion 2STAR pH meter (Thermo Fisher Scientific, Waltham, MA, USA) prior to formation of the AOT RM in isooctane. The pH was adjusted throughout the experiment using varying concentrations of NaOH or HCl dissolved in diH_2O or D_2O, depending on experimental need. NaOH or HCl dissolved in D_2O is referred to as NaOD or DCl, respectively, and the pH was adjusted to consider the presence of deuterium (pD = 0.4 + pH) [58,59]. The pD is customarily referred to as pH and will be referenced as such for the remainder of this manuscript.

4.2. Preparation of Samples for Analysis

4.2.1. Preparation of Stock Solutions of G, GG, GGG and GGGG for ^{1}H NMR and Dynamic Light Scattering

Each of the 200 mM stock solutions used in the ^{1}H NMR experiments were prepared with 2.00×10^{-3} mol each of G, GG, GGG, and GGGG dissolved in 10 mL D_2O in a

volumetric flask and pH-adjusted to the appropriate value as needed for the overall concentration of 200 mM. Each of the 50 mM stock solutions used for dynamic light scattering experiments were prepared with 5.0×10^{-3} mol each of G, GG, GGG, and GGGG and dissolved in 10 mL diH_2O.

All stock solutions were sonicated until clear, if not already, and all stock solutions were pH-adjusted with DCl or HCl and NaOD or NaOH, depending on experimental need. The pH of the stock solutions was measured at 25 °C with an Orion 2STAR pH meter. The pH values were measured directly in D_2O, and the pH was adjusted to the presence of deuterium (pD) and is referred to as pH rather than pD, as stated previously [59–61].

4.2.2. Preparation of AOT-Isooctane Stock Solution and RMs Containing G, GG, GGG, and GGGG for ^{1}H NMR

A 750 mM AOT-isooctane stock solution was prepared by dissolving 7.5×10^{-3} mol AOT in 10 mL isooctane. This mixture was sonicated and vortexed until clear, approximately 15 min. Once dissolved, the solution was equilibrated to ambient room temperature. RMs of w_0 values of 6, 10, 14, 16, and 20, where w_0 = [H_2O]/[AOT], were prepared by combining appropriate volumes of the appropriate prepared stock AOT stock solution, depending on experimental need, and appropriate volumes of 200 mM stock solutions of G, GG, GGG, or GGGG to create the desired size of RM.

4.2.3. Preparation of AOT-Isooctane Stock Solution and RMs Containing G, GG, GGG, and GGGG for Dynamic Light Scattering

The 200 mM AOT-isooctane solution was prepared by dissolving 2.00×10^{-3} mol AOT in 10 mL isooctane. This mixture was sonicated and vortexed until clear, approximately 15 min. Once dissolved, the mixture was equilibrated to ambient room temperature. To prepare the RM solutions, specific volumes of AOT stock solution and aqueous 50 mM G stock solution were combined to a total of 5 mL to form RM sizes of w_0 10 and 20 (w_0 = [H_2O]/[AOT]). This mixture was vortexed until clear, consistent with the formation of RMs.

4.2.4. Preparation of Lipid Stock Solutions and Aqueous Subphase

Sodium phosphate buffer (20 mM) was prepared in distilled deionized water and adjusted to pH 6.00, 7.00, 8.00, and 9.00 (±0.02) with either 1.0 M HCl or 1.0 M NaOH. Sodium phosphate citrate buffer (20 mM) was prepared in distilled deionized water and adjusted to pH 4.00 ± 0.02 in the same manner as the sodium phosphate buffers. Glycine subphase (1 mM) was prepared by dissolving 75.0 ± 0.1 mg glycine into one liter of the previously prepared buffers. The pH was readjusted to the previously mentioned values with 1.0 M HCl or 1.0 M NaOH. Stock solutions of DPPC and DPPE were prepared by dissolving 0.025 mmol of powdered phospholipid into 5.0 ± 0.1 mL of freshly prepared 9:1 chloroform methanol (v:v).

4.3. Methods

4.3.1. ^{1}H NMR Spectroscopy and Analysis of D_2O and RM Samples

The ^{1}H NMR experiments were performed using a 400 MHz Varian (Gloucester, MA, USA) ^{1}H NMR spectrometer using standard parameters (1 s relaxation time, 25 °C temperature control, and 45° pulse angle). The aqueous samples were referenced to an internal DSS sample. RM samples were referenced to the isooctane methyl peak at δ = 0.90 ppm as has been previously reported and were originally referenced to tetramethylsilane [51]. The resulting spectra were referenced, baseline-corrected, normalized, and analyzed using MestReNova version 10.0.1.

The pK_a values were determined by plotting chemical shifts of the samples at their varying pH values in D_2O and w_0 10 RMs and calculating the first derivative of the best fit curve using OriginPro version 9.1 [62]. In order to do this, a plot was made of ppm vs. pH and the curve was fitted in Origin using the reference described in [62] for monofunctional

acids. In order to do this, half of the bifunctional curve of ppm vs. pH was plotted and a best fit line was applied. From here, the first derivative was calculated to give the final pK_a value for both the carboxyl- and amine-terminal protons (Figure S2).

In the case of peaks corresponding to GGG and GGGG in RMs, these shifts were often masked by the AOT peaks, as shown in Figure 8. As a result, a technique was employed in which worked up spectra were analyzed by MestReNova version 10.0.1, and after baseline correction, normalization, and referencing, the arithmetic function in MestReNova was used to subtract control spectra containing no probe molecule from spectra which did contain probe molecules (Figures S15 and S19).

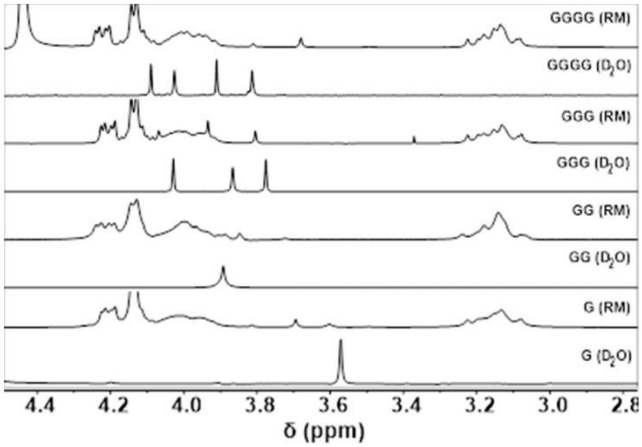

Figure 8. A comparison of each of the studied compounds and their chemical shifts as determined by ^{1}H NMR in w_0 10 reverse micelles (RMs) and D_2O. Spectra beginning from the bottom correspond to G, GG, GGG, and GGGG in D_2O and RM alternately at pH 7. Asterisk in the GGG RM spectrum denotes acetone impurity.

4.3.2. Langmuir Trough Instrument Preparation

Compression isotherms were obtained with a Kibron μTrough XS (stainless steel; Helsinki, Finland) equipped with a hydrophobic Teflon ribbon barrier. The trough was cleaned thoroughly with three isopropanol washes, three ethanol washes, and a water rinse before each experiment. Excess water was evaporated with compressed air. The wire probe used as a Wilhelmy plate was flamed with a Bunsen burner to remove lipids before each experiment.

After cleaning, approximately 50 mL of 20 mM buffer or 1 mM glycine in 20 mM buffer was added to the trough. The subphase surface was then cleaned with vacuum aspiration to remove dust contamination. The surface was considered clean when the surface pressure remained at 0.0 ± 0.5 mN/m throughout a full compression.

4.3.3. Formation, Compression Measurement, and Calculation of Langmuir Monolayers

Either DPPC or DPPE (20 μL, 20 nmol) was added to the surface in a drop-wise manner with a glass Hamilton syringe (50 μL) followed by a 15-min equilibration period. Monolayers were compressed at a speed of 10 mm/min (5 mm/min on each side). The temperature of the subphase was maintained at 25 °C by an external water bath. All experiments were run in triplicate, and the data presented were obtained by averaging the triplicate measurements.

The percent difference between control monolayers and monolayers with glycine present in the subphase was calculated with Equation (1), where A_{gly} is the area of mono-

layers with glycine present and A_{con} is the area of control monolayers. Calculations were performed at every 5 mN/m of surface pressure.

$$\%diff = (\frac{A_{gly} - A_{con}}{A_{con}}) \times 100 \quad (1)$$

4.3.4. Dynamic Light Scattering (DLS)

Dynamic light scattering (DLS) experiments were performed using the Malvern Instrument (Malvern Instruments Limited, UK) MAN0486 [36,51]. DLS and the autocorrelation method of analyzing scattering were used to measure the hydrodynamic radius of AOT RMs, with temperature controlled at 25.0 °C. Each sample was equilibrated for 600 s at 25 °C and then run for 10 scans per acquisition for a minimum of ten measurements for every solution, with and without G compounds, at neutral pH (7.4) for each w_0 value. A 1-mL aliquot of sample was required for measurement. The viscosity (0.4670 cP) and refractive index (1.391) were needed for RM size determination in the isooctane solvent used in this work [57]. The photons scattered by the RMs were collected at a 173° angle. Data processing was carried out using the Zetasizer version 7.11 software.

5. Conclusions

Studies exploring the interaction of G, GG, GGG, and GGGG compounds with model membrane interfaces measured in microemulsions (AOT RMs) using ^{1}H NMR spectroscopy and DLS indicate that G peptides prefer to locate themselves at the edge of the charged reverse micellar interface, between the water pool and interface at the stern layer. This location is different for the single amino acid G, which is penetrated further into the interface. These findings are supported by the calculated pK_a values of the G compounds in both aqueous and RM systems. Minor differences were observed for the pK_a values and the chemical shift between the aqueous and micellar environments, indicating similarity between the environments that the G peptides are inhabiting. Larger changes were observed for the amine group on the G amino acid, suggesting that the N-terminus is further anchored into the interface. This finding is also consistent with studies done with Langmuir monolayers containing DPPE and DPPC exposed to glycine; in the case of DPPC, at physiological pH, the interface remains only slightly expanded relative to the control, indicating weak interaction with the interface. At physiological pH, there was no significant difference between DPPE monolayers exposed to glycine and the control. In the case of the short G peptides GG, GGG, and GGGG, it is likely that they associate with the RM interface by orienting themselves such that the N-termini interact weakly with the RM interface and the C-termini oriented towards the bulk water pool of the RM (Figure 7).

The case of G is very different from that of its longer peptides. In an aqueous environment, the protons on the positively charged amine hydrogen bond with the negatively charged carboxyl end and form an energetically favorable five-membered ring. This may explain the large difference between the pK_a measured in the aqueous environment compared to the reverse micellar environment. In the RM, this hydrogen bonding is disrupted, likely by the presence of the Na^+ counterions. Additionally, the observed gradually decreasing chemical shift of G at pH 7 and 9 indicates that the amino acid is likely placed in the interstitial water layer between the interface and the bulk water pool. As the RM grows larger and the water becomes more similar to bulk water, the chemical shift approaches a shift more analogous to that in D_2O, consistent with the G moving from the interface into the interior water pool. This conclusion is very important because of the role of G as a neurotransmitter; that is, for G to function and propagate a signal to be received after it has been confined within synaptic vesicles and excreted through the synapse. These results suggest that in the large synaptic vesicle (40 nm), it is not likely that G will have any significant interactions with the membrane interface and is readily released for uptake [63].

Considering that AMPs (host defense peptides) generally contain a high level of G as well as other key amino acids (Lys, Phe/Tyr) it was of interest to determine the effects of G and G peptides to obtain a better understanding how specific amino acid residues and their

corresponding peptides interact with membranes. The data suggest that the amino acid G does associate with the membrane whereas the G peptides interact less strongly with a membrane and likely function to increase the hydrophobicity of reported AMPs which are glycine-rich. These studies support the interpretation that the properties of AMP peptides are more related to other amino acids such as Lys and aromatic amino acids with regard to translocation of these peptides across a membrane for anticancer or antimicrobial activities.

Supplementary Materials: Supplementary materials can be found at https://www.mdpi.com/1422-0067/22/1/162/s1. Figure S1. NMR spectra documenting the insolubility of glycine (G) in isooctane; Figures S2–S4. ^{1}H NMR spectra at different pH values of G in D_2O, a plot of ^{1}H NMR chemical shifts as a function of pH of G in D_2O and a representative calculation of the pK_a of the bifunctional amino acids/peptides used in this manuscript.; Figures S5 and S6. ^{1}H NMR spectra at different pH values of G in RM and plot of ^{1}H NMR chemical shifts as a function of pH of G in RM; Figures S7 and S8. ^{1}H NMR spectra at different pH values of G in w_0 30 RM and a plot of ^{1}H NMR chemical shifts as a function of pH of G in w_0 30 RM; Figures S9 and S10. ^{1}H NMR spectra at different pH values of diglycine (GG) in D_2O and a plot of ^{1}H NMR chemical shifts as a function of pH of GG in D_2O; Figures S11 and S12. ^{1}H NMR spectra at different pH values of GG in RM and a plot of ^{1}H NMR chemical shifts as a function of pH of GG in RM; Figures S13 and S14. ^{1}H NMR spectra at different pH values of triglycine (GGG) in D_2O and a plot of ^{1}H NMR chemical shifts as a function of pH of GGG in D_2O; Figures S15 and S16. Subtraction example of ^{1}H NMR spectrum of GGG in RM and plot of ^{1}H NMR chemical shifts as a function of pH of GGG in RM; Figures S17 and S18. ^{1}H NMR spectra at different pH values of tetraglycine (GGGG) in RM and a plot of ^{1}H NMR chemical shifts as a function of pH of GGGG in D_2O; Figures S19 and S20. Subtraction example of ^{1}H NMR spectrum of GGGG in RM and a plot of ^{1}H NMR chemical shifts as a function of pH of GGGG in RM; Table S1 Percent difference values for DPPC-Glycine Langmuir monolayers; Table S2. Percent difference values for DPPE-Glycine Langmuir monolayers.

Author Contributions: Conceptualization, D.C.C.; methodology, D.C.C., K.A.D., P.C., D.L.C. and C.V.C.; software, K.A.D. and D.C.C.; validation, K.A.D., P.C. and C.V.C.; formal analysis, K.A.D., P.C., C.V.C. and D.C.C.; investigation, K.A.D., P.C., D.L.C., K.N.M., C.V.C. and C.A.K.; resources, D.C.C., K.A.D. and C.V.C.; data curation, D.C.C. and C.V.C.; writing—original draft preparation, D.C.C. and K.A.D.; writing—review and editing, K.A.D. and D.C.C.; visualization, K.A.D., C.V.C. and D.C.C.; supervision, D.C.C.; project administration, D.C.C.; funding acquisition, A.T. All authors have read and agreed to the published version of the manuscript.

Funding: D.C.C. thanks the Arthur P. Cope foundation and Colorado State University for the funds partially funding this work. P.C. and A.T. thank the Thailand Research Fund (TRF), under the Royal Golden Jubilee Ph.D. Program, and Suranaree University of Technology for funding P.C.'s visit to Colorado State University. K.N.M. thanks the NSF REU program with grant number NSF CHE-1461040.

Acknowledgments: We acknowledge the effort by Mary Fisher for preliminary experiments and Christopher D. Rithner for technical assistance.

Conflicts of Interest: The authors declare no conflict of interest.

Abbreviations

AMPs	Antimicrobial peptides, also known as host defense peptides
AOT	Aerosol-OT
DLS	Dynamic Light Scattering
DPPC	Dipalmitoyl phosphatidylcholine
DPPE	Dipalmitoyl phosphatidylethanolamine
G	Glycine
GG	Diglycine
GGG	Triglycine
GGGG	Tetraglycine
NMR	Nuclear Magnetic Resonance
RMs	Reverse Micelles

References

1. Malandrino, N.; Smith, R.J. Synthesis, secretion, and transport of peptide hormones. In *Principles of Endocrinology and Hormone Action, Endocrinology*; Belfiore, A., LeRoith, D., Eds.; Springer: Cham, Germany, 2018; pp. 29–42.
2. Snyder, S.H. Brain peptides as neurotransmitters. *Science* **1980**, *209*, 976–983. [CrossRef] [PubMed]
3. Peters, G.H.; Werge, M.; Elf-Lind, M.N.; Madsen, J.J.; Velardez, G.F.; Westh, P. Interaction of neurotransmitters with a phospholipid bilayer: A molecular dynamics study. *Chem. Phys. Lipids* **2014**, *184*, 7–17. [CrossRef] [PubMed]
4. Gallo, R.L.; Murakami, M.; Ohtake, T.; Zaiou, M. Biology and clinical relevance of naturally occurring antimicrobial peptides. *J. Allergy Clin. Immunol.* **2002**, *110*, 823–831. [CrossRef] [PubMed]
5. Fjell, C.D.; Hiss, J.A.; Hancock, R.E.; Schneider, G. Designing antimicrobial peptides: Form follows function. *Nat. Rev. Drug Discov.* **2012**, *11*, 37–51. [CrossRef]
6. Ambroggio, E.E.; Separovic, F.; Bowie, J.H.; Fidelio, G.D.; Bagatolli, L.A. Direct visualization of membrane leakage induced by the antibiotic peptides: Maculatin, citropin, and aurein. *Biophys. J.* **2005**, *89*, 1874–1881. [CrossRef]
7. Zasloff, M. Antimicrobial peptides of multicellular organisms. *Nature* **2002**, *415*, 389–395. [CrossRef]
8. Brogden, K.A. Antimicrobial peptides: Pore formers or metabolic inhibitors in bacteria? *Nat. Rev. Microbiol.* **2005**, *3*, 238–250. [CrossRef]
9. Roudi, R.; Syn, N.L.; Roudbary, M. Antimicrobial peptides as biologic and immunotherapeutic agents against cancer: A comprehensive overview. *Front. Immunol.* **2017**, *8*, 1320. [CrossRef]
10. Tornesello, A.L.; Borrelli, A.; Buonaguro, L.; Buonaguro, F.M.; Tornesello, M.L. Antimicrobial peptides as anticancer agents: Functional properties and biological activities. *Molecules* **2020**, *25*, 2850. [CrossRef]
11. Hancock, R.E.; Sahl, H.-G. Antimicrobial and host-defense peptides as new anti-infective therapeutic strategies. *Nat. Biotechnol.* **2006**, *24*, 1551–1557. [CrossRef]
12. Peschel, A.; Sahl, H.-G. The co-evolution of host cationic antimicrobial peptides and microbial resistance. *Nat. Rev. Microbiol.* **2006**, *4*, 529–536. [CrossRef] [PubMed]
13. Zandsalimi, F.; Talaei, S.; Noormohammad Ahari, M.; Aghamiri, S.; Raee, P.; Roshanzamiri, S.; Yarian, F.; Bandehpour, M.; Zohrab Zadeh, Z. Antimicrobial peptides: A promising strategy for lung cancer drug discovery? *Expert Opin. Drug Discov.* **2020**, *15*, 1343–1354. [CrossRef] [PubMed]
14. Maravilla, E.; Le, D.P.; Tran, J.J.; Chiu, M.H.; Prenner, E.J.; Weers, P.M. Apolipophorin III interaction with phosphatidylglycerol and lipopolysaccharide: A potential mechanism for antimicrobial activity. *Chem. Phys. Lipids* **2020**, *229*, 104909. [CrossRef] [PubMed]
15. Felício, M.R.; Silva, O.N.; Gonçalves, S.; Santos, N.C.; Franco, O.L. Peptides with dual antimicrobial and anticancer activities. *Front. Chem.* **2017**, *5*, 5. [CrossRef]
16. Chen, Y.; Guarnieri, M.T.; Vasil, A.I.; Vasil, M.L.; Mant, C.T.; Hodges, R.S. Role of peptide hydrophobicity in the mechanism of action of α-helical antimicrobial peptides. *Antimicrob. Agents Chemother.* **2007**, *51*, 1398–1406. [CrossRef]
17. Yeaman, M.R.; Yount, N.Y. Mechanisms of antimicrobial peptide action and resistance. *Pharmacol. Rev.* **2003**, *55*, 27–55. [CrossRef]
18. Chiangjong, W.; Chutipongtanate, S.; Hongeng, S. Anticancer peptide: Physicochemical property, functional aspect and trend in clinical application. *Int. J. Oncol.* **2020**, *57*, 678–696. [CrossRef]
19. Shai, Y. Mode of action of membrane active antimicrobial peptides. *Pept. Sci. Orig. Res. Biomol.* **2002**, *66*, 236–248. [CrossRef]
20. Hale, J.D.; Hancock, R.E. Alternative mechanisms of action of cationic antimicrobial peptides on bacteria. *Expert Rev. Anti Infect. Ther.* **2007**, *5*, 951–959. [CrossRef]
21. Melo, M.N.; Ferre, R.; Castanho, M.A. Antimicrobial peptides: Linking partition, activity and high membrane-bound concentrations. *Nat. Rev. Microbiol.* **2009**, *7*, 245–250. [CrossRef]
22. Teixeira, V.; Feio, M.J.; Bastos, M. Role of lipids in the interaction of antimicrobial peptides with membranes. *Prog. Lipid Res.* **2012**, *51*, 149–177. [CrossRef] [PubMed]
23. Dathe, M.; Wieprecht, T. Structural features of helical antimicrobial peptides: Their potential to modulate activity on model membranes and biological cells. *Biochim. Biophys. Acta BBA Biomembr.* **1999**, *1462*, 71–87. [CrossRef]
24. Wang, W.; Wu, Z.; Dai, Z.; Yang, Y.; Wang, J.; Wu, G. Glycine metabolism in animals and humans: Implications for nutrition and health. *Amino Acids* **2013**, *45*, 463–477. [CrossRef] [PubMed]
25. Eulenburg, V.; Armsen, W.; Betz, H.; Gomeza, J. Glycine transporters: Essential regulators of neurotransmission. *Trends Biochem. Sci.* **2005**, *30*, 325–333. [CrossRef] [PubMed]
26. Lu, J.; Chen, Z.-W. Isolation, characterization and anti-cancer activity of SK84, a novel glycine-rich antimicrobial peptide from *Drosophila virilis*. *Peptides* **2010**, *31*, 44–50. [CrossRef]
27. Xie, Y.; Wan, H.; Zeng, X.; Zhang, Z.; Wang, Y. Characterization and antimicrobial evaluation of a new Spgly-AMP, glycine-rich antimicrobial peptide from the mud crab Scylla paramamosain. *Fish. Shellfish Immunol.* **2020**, *106*, 384–392. [CrossRef]
28. Rahman, M.S.; Choi, Y.H.; Choi, Y.S.; Yoo, J.C. Glycin-rich antimicrobial peptide YD1 from B. amyloliquefaciens, induced morphological alteration in and showed affinity for plasmid DNA of *E. coli*. *AMB Express* **2017**, *7*, 8. [CrossRef]
29. Sager, W. Systematic study on the influence of impurities on the phase behavior of sodium bis (2-ethylhexyl) sulfosuccinate microemulsions. *Langmuir* **1998**, *14*, 6385–6395. [CrossRef]
30. Ahmad, S.I.; Shinoda, K.; Friberg, S. Microemulsions and phase equilibria. Mechanism of the formation of so-called microemulsions studied in connection with phase diagram. *J. Colloid Interface Sci.* **1974**, *47*, 32–37. [CrossRef]

31. Shinoda, K.; Friberg, S. Microemulsions: Colloidal aspects. *Adv. Colloid Interface Sci.* **1975**, *4*, 281–300. [CrossRef]
32. Giorgio, G.; Colafemmina, G.; Mavelli, F.; Murgia, S.; Palazzo, G. The impact of alkanes on the structure of Triton X100 micelles. *RSC Adv.* **2016**, *6*, 825–836. [CrossRef]
33. Pileni, M. Reverse micelles as microreactors. *J. Phys. Chem. A* **1993**, *97*, 6961–6973. [CrossRef]
34. Quintana, S.S.; Dario Falcone, R.; Silber, J.J.; Mariano Correa, N. Comparison between two anionic reverse micelle interfaces: The role of water-surfactant interactions in interfacial properties. *ChemPhysChem* **2012**, *13*, 115–123. [CrossRef] [PubMed]
35. Maitra, A. Determination of size parameters of water-Aerosol OT-oil reverse micelles from their nuclear magnetic resonance data. *J. Phys. Chem. A* **1984**, *88*, 5122–5125. [CrossRef]
36. Baruah, B.; Roden, J.M.; Sedgwick, M.; Correa, N.M.; Crans, D.C.; Levinger, N.E. When is water not water? Exploring water confined in large reverse micelles using a highly charged inorganic molecular probe. *J. Am. Chem. Soc.* **2006**, *128*, 12758–12765. [CrossRef] [PubMed]
37. Tartaro, G.; Mateos, H.; Schirone, D.; Angelico, R.; Palazzo, G. Microemulsion microstructure (s): A tutorial review. *Nanomaterials* **2020**, *10*, 1657. [CrossRef] [PubMed]
38. Murgia, S.; Palazzo, G.; Mamusa, M.; Lampis, S.; Monduzzi, M. Aerosol-OT in water forms fully-branched cylindrical direct micelles in the presence of the ionic liquid 1-butyl-3-methylimidazolium bromide. *Phys. Chem. Chem. Phys.* **2011**, *13*, 9238–9245. [CrossRef]
39. Tan, H.-S.; Piletic, I.R.; Fayer, M. Orientational dynamics of water confined on a nanometer length scale in reverse micelles. *J. Chem. Phys.* **2005**, *122*, 174501. [CrossRef]
40. Marques, B.S.; Nucci, N.V.; Dodevski, I.; Wang, K.W.; Athanasoula, E.A.; Jorge, C.; Wand, A.J. Measurement and control of pH in the aqueous interior of reverse micelles. *J. Phys. Chem. B* **2014**, *118*, 2020–2031. [CrossRef]
41. Crans, D.C.; Levinger, N.E. The conundrum of pH in water nanodroplets: Sensing pH in reverse micelle water pools. *Acc. Chem. Res.* **2012**, *45*, 1637–1645. [CrossRef]
42. Crans, D.C.; Rithner, C.D.; Baruah, B.; Gourley, B.L.; Levinger, N.E. Molecular probe location in reverse micelles determined by NMR dipolar interactions. *J. Am. Chem. Soc.* **2006**, *128*, 4437–4445. [CrossRef] [PubMed]
43. Harpham, M.R.; Ladanyi, B.M.; Levinger, N.E.; Herwig, K.W. Water motion in reverse micelles studied by quasielastic neutron scattering and molecular dynamics simulations. *J. Chem. Phys.* **2004**, *121*, 7855–7868. [CrossRef] [PubMed]
44. Harpham, M.R.; Ladanyi, B.M.; Levinger, N.E. The effect of the counterion on water mobility in reverse micelles studied by molecular dynamics simulations. *J. Phys. Chem. B* **2005**, *109*, 16891–16900. [CrossRef] [PubMed]
45. Riter, R.E.; Willard, D.M.; Levinger, N.E. Water immobilization at surfactant interfaces in reverse micelles. *J. Phys. Chem. B* **1998**, *102*, 2705–2714. [CrossRef]
46. Farine, L.; Niemann, M.; Schneider, A.; Bütikofer, P. Phosphatidylethanolamine and phosphatidylcholine biosynthesis by the Kennedy pathway occurs at different sites in Trypanosoma brucei. *Sci. Rep.* **2015**, *5*, 16787. [CrossRef]
47. Mahadeo, M.; Prenner, E.J. Differential impact of synthetic antitumor lipid drugs on the membrane organization of phosphatidic acid and diacylglycerol monolayers. *Chem. Phys. Lipids* **2020**, *229*, 104896. [CrossRef]
48. Nobre, T.M.; Pavinatto, F.J.; Caseli, L.; Barros-Timmons, A.; Dynarowicz-Łątka, P.; Oliveira, O.N., Jr. Interactions of bioactive molecules & nanomaterials with Langmuir monolayers as cell membrane models. *Thin Solid Film.* **2015**, *593*, 158–188.
49. Zasadzinski, J.A.; Ding, J.; Warriner, H.E.; Bringezu, F.; Waring, A.J. The physics and physiology of lung surfactants. *Curr. Opin. Colloid Interface Sci.* **2001**, *6*, 506–513. [CrossRef]
50. Serjeant, E.P.; Dempsey, B. *Ionisation Constants of Organic Acids in Aqueous Solution*; Pergamon: Oxford, UK, 1979; Volume 23.
51. Crans, D.C.; Trujillo, A.M.; Bonetti, S.; Rithner, C.D.; Baruah, B.; Levinger, N.E. Penetration of negatively charged lipid interfaces by the doubly deprotonated dipicolinate. *J. Org. Chem.* **2008**, *73*, 9633–9640. [CrossRef]
52. Sripradite, J.; Miller, S.A.; Johnson, M.D.; Tongraar, A.; Crans, D.C. How interfaces affect the acidity of the anilinium ion. *Chem. Eur. J.* **2016**, *22*, 3873–3880. [CrossRef]
53. Schwartz, C.P.; Uejio, J.S.; Duffin, A.M.; England, A.H.; Kelly, D.N.; Prendergast, D.; Saykally, R.J. Investigation of protein conformation and interactions with salts via X-ray absorption spectroscopy. *Proc. Natl. Acad. Sci. USA* **2010**, *107*, 14008–14013. [CrossRef] [PubMed]
54. Zasloff, M. Magainins, a class of antimicrobial peptides from Xenopus skin: Isolation, characterization of two active forms, and partial cDNA sequence of a precursor. *Proc. Natl. Acad. Sci. USA* **1987**, *84*, 5449–5453. [CrossRef] [PubMed]
55. Nguyen, L.T.; Haney, E.F.; Vogel, H.J. The expanding scope of antimicrobial peptide structures and their modes of action. *Trends Biotechnol.* **2011**, *29*, 464–472. [CrossRef] [PubMed]
56. Wang, Z.; Wang, G. APD: The antimicrobial peptide database. *Nucleic Acids Res.* **2004**, *32*, D590–D592. [CrossRef]
57. Peters, B.J.; Groninger, A.S.; Fontes, F.L.; Crick, D.C.; Crans, D.C. Differences in interactions of benzoic acid and benzoate with interfaces. *Langmuir* **2016**, *32*, 9451–9459. [CrossRef]
58. Stahla, M.L.; Baruah, B.; James, D.M.; Johnson, M.D.; Levinger, N.E.; Crans, D.C. H-1 NMR studies of aerosol-OT reverse micelles with alkali and magnesium counterions: Preparation and analysis of MAOTs. *Langmuir* **2008**, *24*, 6027–6035. [CrossRef]
59. Samart, N.; Beuning, C.N.; Haller, K.J.; Rithner, C.D.; Crans, D.C. Interaction of a biguanide compound with membrane model interface systems: Probing the properties of antimalaria and antidiabetic compounds. *Langmuir* **2014**, *30*, 8697–8706. [CrossRef]
60. Crans, D.C.; Schoeberl, S.; Gaidamauskas, E.; Baruah, B.; Roess, D.A. Antidiabetic vanadium compound and membrane interfaces: Interface-facilitated metal complex hydrolysis. *J. Biol. Inorg. Chem.* **2011**, *16*, 961–972. [CrossRef]

61. Koehn, J.T.; Magallanes, E.S.; Peters, B.J.; Beuning, C.N.; Haase, A.A.; Zhu, M.J.; Rithner, C.D.; Crick, D.C.; Crans, D.C. A synthetic isoprenoid lipoquinone, menaquinone-2, adopts a folded conformation in solution and at a model membrane interface. *J. Org. Chem.* **2017**, *83*, 275–288. [CrossRef]
62. Peters, B.J.; Van Cleave, C.; Haase, A.A.; Hough, J.P.B.; Giffen-Kent, K.A.; Cardiff, G.M.; Sostarecz, A.G.; Crick, D.C.; Crans, D.C.J.L. Structure dependence of pyridine and benzene derivatives on interactions with model membranes. *Langmuir* **2018**, *34*, 8939–8951. [CrossRef]
63. Zhang, B.; Koh, Y.H.; Beckstead, R.B.; Budnik, V.; Ganetzky, B.; Bellen, H.J. Synaptic vesicle size and number are regulated by a clathrin adaptor protein required for endocytosis. *Neuron* **1998**, *21*, 1465–1475. [CrossRef]

Appendix XI: Permissions for Figures

Permissions for figures reproduced in Chapter 1.

ELSEVIER LICENSE
TERMS AND CONDITIONS

May 23, 2021

This Agreement between Ms. Cameron Van Cleave -- Cameron Van Cleave ("You") and Elsevier ("Elsevier") consists of your license details and the terms and conditions provided by Elsevier and Copyright Clearance Center.

License Number	5074900133805
License date	May 23, 2021
Licensed Content Publisher	Elsevier
Licensed Content Publication	Advances in Colloid and Interface Science
Licensed Content Title	Membrane interactions in drug delivery: Model cell membranes and orthogonal techniques
Licensed Content Author	Ada-Ioana Bunea,Stine Harloff-Helleberg,Rafael Taboryski,Hanne Mørck Nielsen
Licensed Content Date	Jul 1, 2020
Licensed Content Volume	281
Licensed Content Issue	n/a
Licensed Content Pages	1
Start Page	102177
End Page	0

Type of Use	reuse in a thesis/dissertation
Portion	figures/tables/illustrations
Number of figures/tables /illustrations	1
Format	both print and electronic
Are you the author of this Elsevier article?	No
Will you be translating?	No
Title	Interactions of biologically active molecules, cofactors, cations, and drugs with model membranes
Institution name	Colorado State University
Expected presentation date	Jun 2021
Portions	Figure 2, representation of cell membrane
Requestor Location	Ms. Cameron Van Cleave Colorado State University Campus Delivery 1872 FORT COLLINS, CO 80523 United States Attn: Ms. Cameron Van Cleave
Publisher Tax ID	98-0397604
Total	0.00 USD
Terms and Conditions	

LIST OF ABBREVIATIONS

AOT – aerosol-OT, dioctyl sulfosuccinate (Chapter 1, Chapter 2, Chapter 4)

$CDCl_3$ – deuterated chloroform (Chapter 2)

CF – 5(6)-carboxyfluorescein (Chapter 4)

CT – terminal carbon (Chapter 3)

DCl – deuterated hydrochloric acid (Chapter 2, Chapter 4)

D_2O – deuterium oxide (Chapter 2, Chapter 4)

DLS – dynamic light scattering (Chapter 2, Chapter 4)

DMSO – dimethylsulfoxide (Chapter 2)

DPPC – 16:0 PC, dipalmitoylphosphatidylcholine (Chapter 1, Chapter 2, Chapter 3, Chapter 4)

DPPE – 16:0 PE, dipalmitoylphosphatidylcholine (Chapter 1, Chapter 2, Chapter 3, Chapter 4)

DTT – dithiothreitol (Chapter 2)

HCl – hydrochloric acid (Chapter 2, Chapter 3, Chapter 4)

MD – molecular dynamics (Chapter 3)

MDL – menadiol (Chapter 2, Chapter 5)

MEN – menadione (Chapter 2, Chapter 5)

MeOD – deuterated methanol (Chapter 2)

MK – menaquinone (Chapter 1, Chapter 2, Chapter 3, Chapter 5)

NaOD – deuterated sodium hydroxide (Chapter 2, Chapter 4)

NaOH – sodium hydroxide (Chapter 2, Chapter 3, Chapter 4)

NOESY – nuclear Overhauser effect spectroscopy (Chapter 2)

NMR – nuclear magnetic resonance (Chapter 1, Chapter 2, Chapter 3, Chapter 4, Chapter 5)

POA – pyrazinoic acid (Chapter 1, Chapter 4, Chapter 5)

POA_C – neutral species of pyrazinoic acid (Chapter 4)

POA_N – charged species of pyrazinoic acid, pyrazinoate (Chapter 4)

POPC – 16:0-18:1 PC, phosphatidylcholine (Chapter 3)

PZA, pyrazinamide (Chapter 1, Chapter 3, Chapter 5)

ROESY – rotating-frame Overhauser effect spectroscopy (Chapter 2)

RM – reverse micelle (Chapter 1, Chapter 2, Chapter 4, Chapter 5)

UQ – ubiquinone (Chapter 3, Chapter 5)

UV-vis – ultraviolet-visible light spectroscopy (Chapter 2)